Stability Evaluation and Analysis of Underground Space Engineering

Lead Guest Editor: Ping Xiang
Guest Editors: Shehata Eldabie Abdel Raheem and Upaka Rathnayake

Stability Evaluation and Analysis of Underground Space Engineering

Stability Evaluation and Analysis of Underground Space Engineering

Lead Guest Editor: Ping Xiang
Guest Editors: Shehata Eldabie Abdel Raheem and
Upaka Rathnayake

Zhaofei Chu, China
Wonseok Chung, Republic of Korea
Donato Ciampa, Italy
Gian Paolo Cimellaro, Italy
Francesco Colangelo, Italy
Romulus Costache, Romania
Liviu-Adrian Cotfas, Romania
Antonio Maria D'Altri, Italy
Bruno Dal Lago, Italy
Amos Darko, Hong Kong
Arka Jyoti Das, India
Dario De Domenico, Italy
Gianmarco De Felice, Italy
Stefano De Miranda, Italy
Maria T. De Risi, Italy
Tayfun Dede, Turkey
Sadik O. Degertekin, Turkey
Camelia Delcea, Romania
Cristoforo Demartino, China
Giuseppe Di Filippo, Italy
Luigi Di Sarno, Italy
Fabio Di Trapani, Italy
Aboelkasim Diab, Egypt
Thi My Dung Do, Vietnam
Giulio Dondi, Italy
Jiangfeng Dong, China
Chao Dou, China
Mario D'Aniello, Italy
Jingtao Du, China
Ahmed Elghazouli, United Kingdom
Francesco Fabbrocino, Italy
Flora Faleschini, Italy
Dingqiang Fan, Hong Kong
Xueping Fan, China
Qian Fang, China
Salar Farahmand-Tabar, Iran
Ilenia Farina, Italy
Roberto Fedele, Italy
Guang-Liang Feng, China
Luigi Fenu, Italy
Tiago Ferreira, Portugal
Marco Filippo Ferrotto, Italy
Antonio Formisano, Italy
Guoyang Fu, Australia
Stefano Galassi, Italy

Junfeng Gao, China
Meng Gao, China
Giovanni Garcea, Italy
Enrique García-Macías, Spain
Emilio García-Taengua, United Kingdom
DongDong Ge, USA
Khaled Ghaedi, Malaysia
Khaled Ghaedi, Malaysia
Gian Felice Giaccu, Italy
Agathoklis Giaralis, United Kingdom
Ravindran Gobinath, India
Rodrigo Gonçalves, Portugal
Peilin Gong, China
Belén González-Fonteboa, Spain
Salvatore Grasso, Italy
Fan Gu, USA
Erhan Güneyisi, Turkey
Esra Mete Güneyisi, Turkey
Pingye Guo, China
Ankit Gupta, India
Federico Gusella, Italy
Kemal Hacıefendioğlu, Turkey
Jianyong Han, China
Song Han, China
Asad Hanif, Macau
Hadi Hasanzadehshooiili, Canada
Mostafa Fahmi Hassanein, Egypt
Amir Ahmad Hedayat, Iran
Khandaker Hossain, Canada
Zahid Hossain, USA
Chao Hou, China
Biao Hu, China
Jiang Hu, China
Xiaodong Hu, China
Lei Huang, China
Cun Hui, China
Bon-Gang Hwang, Singapore
Jijo James, India
Abbas Fadhil Jasim, Iraq
Ahad Javanmardi, China
Krishnan Prabhakan Jaya, India
Dong-Sheng Jeng, Australia
Han-Yong Jeon, Republic of Korea
Pengjiao Jia, China
Shaohua Jiang, China

MOUSTAFA KASSEM iD, Malaysia
Mosbeh Kaloop iD, Egypt
Shankar Karuppannan iD, Ethiopia
John Kechagias iD, Greece
Mohammad Khajehzadeh iD, Iran
Afzal Husain Khan iD, Saudi Arabia
Mehran Khan iD, Hong Kong
Manoj Khandelwal, Australia
Jin Kook Kim iD, Republic of Korea
Woosuk Kim iD, Republic of Korea
Vaclav Koci iD, Czech Republic
Loke Kok Foong, Vietnam
Hailing Kong iD, China
Leonidas Alexandros Kouris iD, Greece
Kyriakos Kourousis iD, Ireland
Moacir Kripka iD, Brazil
Anupam Kumar, The Netherlands
Emma La Malfa Ribolla, Czech Republic
Ali Lakirouhani iD, Iran
Angus C. C. Lam, China
Thanh Quang Khai Lam iD, Vietnam
Luciano Lamberti, Italy
Andreas Lampropoulos iD, United Kingdom
Raffaele Landolfo, Italy
Massimo Latour iD, Italy
Bang Yeon Lee iD, Republic of Korea
Eul-Bum Lee iD, Republic of Korea
Zhen Lei iD, Canada
Leonardo Leonetti iD, Italy
Chun-Qing Li iD, Australia
Dongsheng Li iD, China
Gen Li, China
Jiale Li iD, China
Minghui Li, China
Qingchao Li iD, China
Shuang Yang Li iD, China
Sunwei Li iD, Hong Kong
Yajun Li iD, China
Shun Liang iD, China
Francesco Liguori iD, Italy
Jae-Han Lim iD, Republic of Korea
Jia-Rui Lin iD, China
Kun Lin iD, China
Shibin Lin, China

Tzu-Kang Lin iD, Taiwan
Yu-Cheng Lin iD, Taiwan
Hexu Liu, USA
Jian Lin Liu iD, China
Xiaoli Liu iD, China
Xuemei Liu iD, Australia
Zaobao Liu iD, China
Zhuang-Zhuang Liu, China
Diego Lopez-Garcia iD, Chile
Cristiano Loss iD, Canada
Lyan-Ywan Lu iD, Taiwan
Jin Luo iD, USA
Yanbin Luo iD, China
Jianjun Ma iD, China
Junwei Ma iD, China
Tian-Shou Ma, China
Zhongguo John Ma iD, USA
Maria Macchiaroli, Italy
Domenico Magisano, Italy
Reza Mahinroosta , Australia
Yann Malecot iD, France
Prabhat Kumar Mandal iD, India
John Mander, USA
Iman Mansouri, Iran
André Dias Martins, Portugal
Domagoj Matesan iD, Croatia
Jose Matos, Portugal
Vasant Matsagar iD, India
Claudio Mazzotti iD, Italy
Ahmed Mebarki iD, France
Gang Mei iD, China
Kasim Mermerdas, Turkey
Giovanni Minafò iD, Italy
Masoomeh Mirrashid iD, Iran
Abbas Mohajerani iD, Australia
Fadzli Mohamed Nazri iD, Malaysia
Fabrizio Mollaioli iD, Italy
Rosario Montuori iD, Italy
H. Naderpour iD, Iran
Hassan Nasir iD, Pakistan
Hossein Nassiraei iD, Iran
Satheeskumar Navaratnam iD, Australia
Ignacio J. Navarro iD, Spain
Ashish Kumar Nayak iD, India
Behzad Nematollahi iD, Australia

Chayut Ngamkhanong (iD), Thailand
Trung Ngo, Australia
Tengfei Nian, China
Mehdi Nikoo (iD), Canada
Youjun Ning (iD), China
Olugbenga Timo Oladinrin (iD), United Kingdom
Oladimeji Benedict Olalusi, South Africa
Timothy O. Olawumi (iD), Hong Kong
Alejandro Orfila (iD), Spain
Maurizio Orlando (iD), Italy
Siti Aminah Osman, Malaysia
Walid Oueslati (iD), Tunisia
SUVASH PAUL (iD), Bangladesh
John-Paris Pantouvakis (iD), Greece
Fabrizio Paolacci (iD), Italy
Giuseppina Pappalardo (iD), Italy
Fulvio Parisi (iD), Italy
Dimitrios G. Pavlou (iD), Norway
Daniele Pellegrini (iD), Italy
Gatheeshgar Perampalam (iD), United Kingdom
Daniele Perrone (iD), Italy
Giuseppe Piccardo (iD), Italy
Vagelis Plevris (iD), Qatar
Andrea Pranno (iD), Italy
Adolfo Preciado (iD), Mexico
Chongchong Qi (iD), China
Yu Qian, USA
Ying Qin (iD), China
Giuseppe Quaranta (iD), Italy
Krishanu ROY (iD), New Zealand
Vlastimir Radonjanin, Serbia
Carlo Rainieri (iD), Italy
Rahul V. Ralegaonkar, India
Raizal Saifulnaz Muhammad Rashid, Malaysia
Alessandro Rasulo (iD), Italy
Chonghong Ren (iD), China
Qing-Xin Ren, China
Dimitris Rizos (iD), USA
Geoffrey W. Rodgers (iD), New Zealand
Pier Paolo Rossi, Italy
Nicola Ruggieri (iD), Italy
JUNLONG SHANG, Singapore

Nikhil Saboo, India
Anna Saetta, Italy
Juan Sagaseta (iD), United Kingdom
Timo Saksala, Finland
Mostafa Salari, Canada
Ginevra Salerno (iD), Italy
Evangelos J. Sapountzakis (iD), Greece
Vassilis Sarhosis (iD), United Kingdom
Navaratnarajah Sathiparan (iD), Sri Lanka
Fabrizio Scozzese (iD), Italy
Halil Sezen (iD), USA
Payam Shafigh (iD), Malaysia
M. Shahria Alam, Canada
Yi Shan, China
Hussein Sharaf, Iraq
Mostafa Sharifzadeh, Australia
Sanjay Kumar Shukla, Australia
Amir Si Larbi (iD), France
Okan Sirin (iD), Qatar
Piotr Smarzewski (iD), Poland
Francesca Sollecito (iD), Italy
Rui Song (iD), China
Tian-Yi Song, Australia
Flavio Stochino (iD), Italy
Mayank Sukhija (iD), USA
Piti Sukontasukkul (iD), Thailand
Jianping Sun, Singapore
Xiao Sun (iD), China
T. Tafsirojjaman (iD), Australia
Fujiao Tang (iD), China
Patrick W.C. Tang (iD), Australia
Zhi Cheng Tang (iD), China
Weerachart Tangchirapat (iD), Thailand
Xiaxin Tao, China
Piergiorgio Tataranni (iD), Italy
Elisabete Teixeira (iD), Portugal
Jorge Iván Tobón (iD), Colombia
Jing-Zhong Tong, China
Francesco Trentadue (iD), Italy
Antonello Troncone, Italy
Majbah Uddin (iD), USA
Tariq Umar (iD), United Kingdom
Muahmmad Usman, United Kingdom
Muhammad Usman (iD), Pakistan
Mucteba Uysal (iD), Turkey

Ilaria Venanzi , Italy
Castorina S. Vieira , Portugal
Valeria Vignali , Italy
Claudia Vitone , Italy
Liwei WEN , China
Chunfeng Wan , China
Hua-Ping Wan, China
Roman Wan-Wendner , Austria
Chaohui Wang , China
Hao Wang , USA
Shiming Wang , China
Wayne Yu Wang , United Kingdom
Wen-Da Wang, China
Xing Wang , China
Xiuling Wang , China
Zhenjun Wang , China
Xin-Jiang Wei , China
Tao Wen , China
Weiping Wen , China
Lei Weng , China
Chao Wu , United Kingdom
Jiangyu Wu, China
Wangjie Wu , China
Wenbing Wu , China
Zhixing Xiao, China
Gang Xu, China
Jian Xu , China
Panpan , China
Rongchao Xu , China
HE YONGLIANG, China
Michael Yam, Hong Kong
Hailu Yang , China
Xu-Xu Yang , China
Hui Yao , China
Xinyu Ye , China
Zhoujing Ye , China
Gürol Yildirim , Turkey
Dawei Yin , China
Doo-Yeol Yoo , Republic of Korea
Zhanping You , USA
Afshar A. Yousefi , Iran
Xinbao Yu , USA
Dongdong Yuan , China
Geun Y. Yun , Republic of Korea

Hyun-Do Yun , Republic of Korea
Cemal YİĞİT , Turkey
Paolo Zampieri, Italy
Giulio Zani , Italy
Mariano Angelo Zanini , Italy
Zhixiong Zeng , Hong Kong
Mustafa Zeybek, Turkey
Henglong Zhang , China
Jiupeng Zhang, China
Tingting Zhang , China
Zengping Zhang, China
Zetian Zhang , China
Zhigang Zhang , China
Zhipeng Zhao , Japan
Jun Zhao , China
Annan Zhou , Australia
Jia-wen Zhou , China
Hai-Tao Zhu , China
Peng Zhu , China
QuanJie Zhu , China
Wenjun Zhu , China
Marco Zucca, Italy
Haoran Zuo, Australia
Junqing Zuo , China
Robert Černý , Czech Republic
Süleyman İpek , Turkey

Contents

Research Article

Comprehensive Evaluation and Decision for Goaf Based on Fuzzy Theory in Underground Metal Mine

Rongxing He [iD],[1] **Huan Liu** [iD],[2] **Fengyu Ren** [iD],[1] **Guanghui Li** [iD],[1] **Jing Zhang** [iD],[1] **and Yanjun Zhou**[1]

[1]*School of Resources and Civil Engineering, Northeastern University, Shenyang 110819, China*
[2]*College of Mining Industry, Inner Mongolia University of Technology, Hohhot 010051, China*

Correspondence should be addressed to Huan Liu; gyliuhuan@163.com

In underground metal mines, goaf brings huge safety risks. It is an important part of mine to evaluate goaf stability and determine the best goaf handling measures. However, the evaluation and decision are often separated; they need to be unified. Meanwhile, stability evaluation and decision for goaf are a complex system engineering of rock masses in underground mining, and subjectivity exists in the evaluation and decision process. Under these conditions, it is necessary to minimize subjectivity, and the results of stability evaluation also need to be considered comprehensively in determining handling measures. In this paper, the fuzzy theory was adopted based on the fact that the goaf stability evaluation and handling measure decision were fuzziness. Firstly, the goaf stability model was established by a two-layer fuzzy comprehensive evaluation. It took into account 12-factor indexes of goaf with engineering empirical approaches and divided them into 3 categories according to their engineering categories. The model improved the applicability of the goaf stability evaluation results, and the results were the basis for goaf handling measures as well. Secondly, a decision model of the goaf handling measures was established by multiobjective fuzzy optimization. It consisted of five goaf handling measures and five evaluation indexes. The model provided a comprehensive decision and optimal scheme for goaf handling. Two models were also applied to the Paishanlou gold mine and achieved a good handling result. The practical application showed that the two models were feasible.

1. Introduction

In underground metal mines, a goaf is formed. When the ore is mined and the mined-out area is not filled, especially the room and pillar mining, it forms many goafs of different sizes, shapes, and buried depths. In 2015, according to the survey results of 457 large and medium-sized mines in 25 provinces and cities conducted by the State Administration of Work Safety of China, there are 432 million m³ goaf, 80% of the goaf is below 10000 m³, but the remaining 20% of the goaf is above 10000 m³ and the total volume accounts for more than 50%. In particular, the number of goafs above 30000 m³ is less than 6%, but the volume accounts for 30% of the total [1].

The harm of the underground goaf is significant to the mine. Firstly, during the long-term creep and groundwater action, the strengths of surrounding rock and pillar decrease, the pillars occur continuously unstable or the roof suddenly caving, and at the same time, shock gas and waves are caused. These bring huge safety risks to personnel, equipment, facilities, buildings, etc. On November 6, 2005, a large-scale collapse accident occurred in Xingtai gypsum mines in China, which caused a large number of casualties including 37 deaths and 38 injuries, and a total of 88 living rooms on the surface were destroyed. The direct property loss was up to 7.74 million RMB [2]. Secondly, during the process of mining, the surrounding rock in the goaf is affected by blasting vibration, which

leads to the development of fractures in the rock mass. This may lead to the formation of fracture connection networks and water inrush accidents. Accidents may submerge the tunnel and cause losses. On the afternoon of March 28, 2009, a water burst accident occurred in the old goaf of the Xishimen iron mine, which caused 8 people to die. Therefore, timely and appropriate goaf handling is the most fundamental measure to eliminate the safety threat. And the stability evaluation of the goaf is the basis for determining the goaf handling measures.

The stability of goaf is restricted by many factors, such as rock strength, joint conditions, groundwater, goaf parameters, and engineering factors. These factors are interrelated with each other. Therefore, the stability evaluation of the goaf is an extremely complex system engineering. The evaluation of goaf stability is a comprehensive evaluation for the goaf risk degree. The evaluation results have important guiding significance for determining goaf handling measures and timing. Swift and Reddish [3] considered the probabilistic approach to analyze stability problems. Yavuz [4] proposed a method for estimating the distance to return of the cover pressure and the stress distribution in the goaf. Hu and Li [5] presented a Bayes discriminant analysis method to identify the risk of complicated goafs in mines. Wang et al. [6] analyzed the creep failure of a roof stratum seated on pillars in the mined-out area through a newly developed visco-elastic model. Zhou et al. [7] proposed an approach to forecasting large-scale goaf instability that combined particle swarm optimization and support a vector machine. Sun et al. [8] proposed a three-zone model to analyze and evaluate the stability of the goaf. Hu et al. [9] built the RS-TOPSIS model to predict the hazard degree of goafs based on the results of the expert investigation. Zhang et al. [10] developed a susceptibility assessment system to define the risk from mine collapse for coalfields across the mining area based on the principles of fuzzy mathematics and the analytical hierarchy process. Li et al. [11] proposed a method to calculate releasable space in strata based on the characteristics of pore distribution in the rock strata above the goaf. Xiao et al. [12] established the hazard evaluation model of goaf by using information entropy and unascertained measurement theory. Guo et al. [13] established a risk assessment model with seven main assessment factors for expressway construction site instability based on fuzzy theory. In these studies, the influencing factors are considered in detail. However, goaf stability is affected by many uncertain factors and the influence degree of each factor is also different. These factors and the evaluation results have certain fuzziness and subjectivity. Therefore, it is a good way to combine the fuzzy theory with the classical comprehensive evaluation method. This will make the evaluation results as objective as possible and obtain more appropriate evaluation results.

For the goaf left by underground mining, there are usually four goaf handling measures: closing, caving,

reinforcing, and filling. However, the specific conditions of each mine are different, the positions and shape characteristics of each goaf are also different, and the goaf handling measures are often different. Therefore, it is an important part of the mine to determine the best goaf handling measures in terms of technology, economy, safety, and reliability according to various factors affecting the decision-making of handling measures.

In this paper, based on the goaf stability evaluation and decision-making of goaf handling measures that are fuzzy, the fuzzy theory is adopted to establish a stability evaluation model and a decision model for goaf in underground metal mines. In the establishment process, evaluation and decision are considered comprehensively. These models are applied to the Paishanlou gold mine.

2. Establishment of Goaf Stability Model

The two-layer fuzzy comprehensive evaluation mathematical model (in Figure 1) is adopted for the goaf stability evaluation, and the processes are as follows.

2.1. Determination of Factor. There were many factors affecting goaf stability, which could be summarized as the factors of rock mass quality, goaf parameters, and induced factors. The factors of rock mass quality could refer to rock mass classification standards, such as Q classification [14, 15], RMR classification [16, 17], MRMR classification [18, 19], and engineering rock mass classification standard [20]. These factors included rock uniaxial compressive strength, rock point load strength, rock quality index RQD, joint spacing, intactness index of the rock mass, volumetric joint count of the rock mass, and joint occurrence. The uniaxial compressive strength and the point load strength both represented the rock strength, and the point load test was a more practical, time-saving, and economical method compared to the uniaxial compressive strength [21]. Many studies [22–25] also have shown that the point load strength has a good correlation with the uniaxial compressive strength. Therefore, the point load strength was chosen to represent the strength rock. The RQD, joint spacing, intactness index of the rock mass, and volumetric joint count of the rock mass [26] all represented the characteristics of the joint, and these factors were related or the same parameter was reflected in different aspects. Considering the convenience of field measurement, the intactness index of the rock mass was determined to represent the joint characteristics. Another factor was the joint occurrence. The study [20] has shown that the angle between the joint occurrence and the goaf direction affects the stability of the rock mass. Because the joint occurrence was complex in the actual rock mass, and it was difficult to study the influence of each joint occurrence, the dominant joint occurrence was selected.

The goaf parameters mainly included the goaf span, goaf area, goaf volume, goaf buried depth, goaf height, height
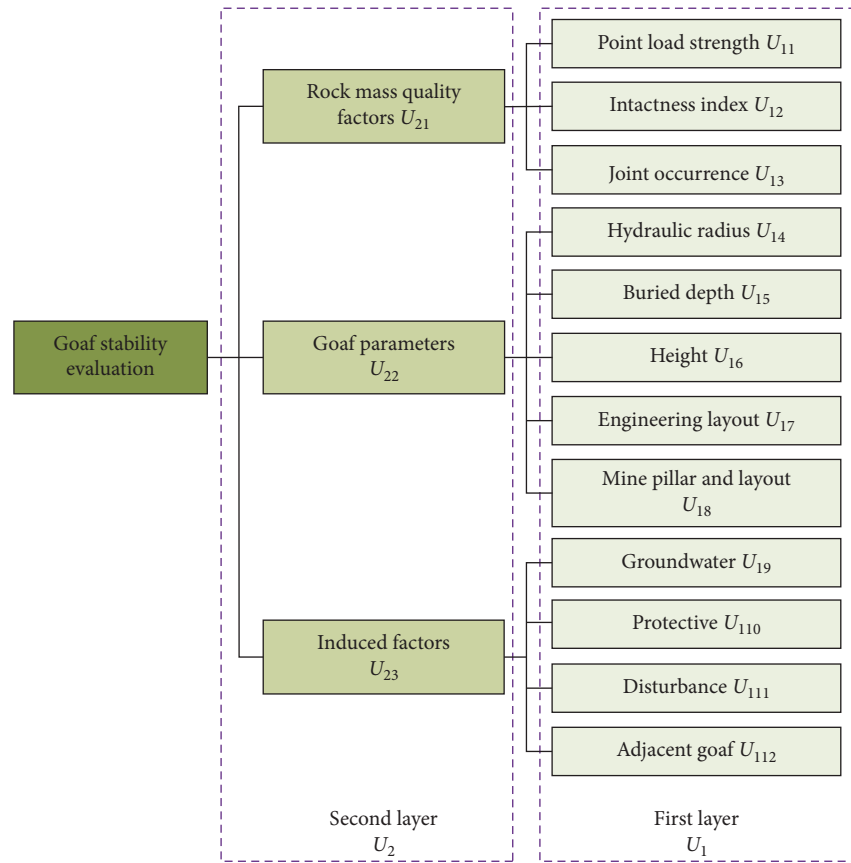
FIGURE 1: Two-layer fuzzy comprehensive evaluation mathematical model.

span ratio, goaf shape, goaf engineering layout, and mine pillar and layout. Among them, the hydraulic radius could be used to express the goaf span, goaf area, goaf volume, goaf height, height span ratio, and goaf shape. The hydraulic radius refers to the ratio of area to the perimeter of the goaf.

The induced factors of the goaf could be summarized as groundwater, protective measures, mining disturbance, and influence of adjacent goaf.

Based on the above analysis, the actual application, and site conditions of the mine, the factor set U_1 was established; $U_1 = \{U_{11}, U_{12}, U_{13}, U_{14}, U_{15}, U_{16}, U_{17}, U_{18}, U_{19}, U_{110}, U_{111}, U_{112}\} = \{$point load strength, intactness index of the rock mass, dominant joint occurrence, hydraulic radius, goaf buried depth, goaf height, engineering layout, mine pillar and layout, groundwater, protective measures, mining disturbance, adjacent goaf$\}$. These factors are shown in Figure 1.

2.2. Factor Layer and Assessment Ranks.
Due to the fact that many factors affected goaf stability, if a single-layer fuzzy comprehensive evaluation was adopted, the factor weight might not be determined, or the weight value was too small, which led to the distortion of the evaluation results. For this

reason, 12 factors in the first layer were divided into 3 categories according to their engineering categories, which were integrated into 3 factors in the second layer; that is, $U_2 = \{U_{21}, U_{22}, U_{23}\} = \{$rock mass quality factors, goaf parameters, induced factors$\}$. The specific factor layering and meaning are shown in Figure 1.

The assessment ranks were a set reflecting goaf stability. Generally, a 4-rank classification was used; that is, $V = \{V_1, V_2, V_3, V_4\} = \{$stable I, basically stable II, understable III, unstable IV$\}$. Among them, the stable I indicated that the goaf did not need to be handled and monitored. The basically stable II indicated that the goaf needed to be handled and monitored to ensure safe production within the affected area. Understable III indicated that the goaf needed to be handled and monitored, and emergency plans needed to be formulated. The unstable IV indicated that handling measures needed to be taken immediately and strengthen monitoring, and personnel and equipment within its affected area must be evacuated immediately.

Based on the factor layer and assessment ranks, each factor index was divided into 4 levels according to the stability classification of the engineering rock mass. In addition, the results are shown in Table 1; there are both

TABLE 1: The classification of goaf stability.

Factor index		Assessment ranks			
		Stable I	Basically II	Understable III	Unstable IV
Rock mass quality factors U_{21}	Point load strength U_{11}	>10 MPa	4~10 MPa	2~4 MPa	0~2 MPa
	Intactness index U_{12}	>0.75	0.75~0.55	0.55~0.35	0.35~0
	Dominant joint occurrence U_{13}	Very favorable	Favorable	General	Unfavorable
Goaf parameters U_{22}	Hydraulic radius U_{14}	<15 m	15~30 m	30~45 m	>45 m
	Buried depth U_{15}	<100 m	100~200 m	200~400 m	>400 m
	Goaf height U_{16}	<8 m	8~20 m	20~30 m	>30 m
	Engineering layout U_{17}	Very reasonable	Reasonable	General	Unreasonable
	Mine pillar and layout U_{18}	Pillars and layout standard	Pillars and layout not standard	No pillars or layout not standard, start breaking	No pillars or layout not standard, serious breaking
Induced factors U_{23}	Groundwater U_{19}	<35 L•min^{-1}	35~55 L•min^{-1}	55~70 L•min^{-1}	>70 L•min^{-1}
	Protective measures U_{110}	Very reasonable	Reasonable	General	Unreasonable
	Mining disturbance U_{111}	No impact	Weak	Influence	Great influence
	Adjacent goaf U_{112}	No	Small	Some	Many
Quantized range V_r		0.75~1.00	0.50~0.75	0.25~0.50	0.00~0.25

qualitative and quantitative factor indexes. The membership degree of each qualitative factor index could be obtained by counting the frequency by several measuring personnel, such as U_{13} dominant joint occurrence, U_{17} engineering layout, U_{18} mine pillar and layout, U_{110} protective measures, U_{111} mining disturbance, and U_{112} adjacent goaf. The membership degree of each quantitative factor index could be determined by measuring the value and membership function, such as the U_{11} point load strength, U_{12} intactness index of the rock mass, U_{14} hydraulic radius, U_{15} goaf buried depth, U_{16} goaf height, and U_{19} groundwater.

2.3. Membership Function.
In order to determine the membership degree of each quantitative factor index and make the model more effective, the original measured value was normalized, and the input data were in the [0, 1] interval. The normalized formula is

$$f\left(U_{ij}\right) = q_{i\,\min} + \frac{q_{i\,\max} - q_{i\,\min}}{p_{i\,\max} - p_{i\,\min}}\left(U_{ij} - p_{i\,\min}\right), \quad (1)$$

$$f\left(U_{ij}\right) = q_{i\max} - \frac{q_{i\,\max} - q_{i\,\min}}{p_{i\,\max} - p_{i\,\min}}\left(U_{ij} - p_{i\,\min}\right), \quad (2)$$

where $f(U_{ij})$ is the normalized value; U_{ij} is the original measured value; $p_{i\max}$ and $p_{i\min}$ are the maximum values and minimum of the original measured value, respectively; $q_{i\max}$ and $q_{i\min}$ are the maximum values and minimum of the quantitative range corresponding to the original measured value, respectively; Formula (1) shows that the larger U_{ij} is, the more stable of the goaf. Formula (2) is that the larger U_{ij} is, the more unstable it is.

After normalizing the original measured value, it was necessary to establish the membership function of each quantitative factor index, and the membership degree could be calculated. According to the conclusion that different membership functions were equivalent by Su et al. [27], this paper used the fuzzy reasoning method to establish membership functions based on the characteristics of fuzzy sets.

In rock engineering, the membership function usually adopted the intermediate type. That was, the membership degree was 0.5 at the endpoint of the interval range and the state was the fuzziest. The membership degree was 1 at the middle point and the neighborhood of the interval range and the state was the clearest. The membership function formula is

$$A_4\big(f(U_{ij})\big) = \begin{cases} 1, & f(U_{ij}) \le 0.125 + \delta, \\[2mm] \dfrac{f(U_{ij})}{2\delta - 0.25} + \dfrac{\delta - 0.375}{2\delta - 0.25}, & 0.125 + \delta < f(U_{ij}) \le 0.375 - \delta, \\[2mm] 0, & f(U_{ij}) > 0.375 - \delta, \end{cases}$$

$$A_3\big(f(U_{ij})\big) = \begin{cases} 0, & f(U_{ij}) \le 0.125 + \delta, \\[2mm] \dfrac{f(U_{ij})}{0.25 - 2\delta} - \dfrac{\delta + 0.125}{0.25 - 2\delta}, & 0.125 + \delta < f(U_{ij}) \le 0.375 - \delta, \\[2mm] 1, & 0.375 - \delta < f(U_{ij}) \le 0.375 + \delta, \\[2mm] \dfrac{f(U_{ij})}{2\delta - 0.25} + \dfrac{\delta - 0.625}{2\delta - 0.25}, & 0.375 + \delta < f(U_{ij}) \le 0.625 - \delta, \\[2mm] 0, & f(U_{ij}) > 0.625 - \delta, \end{cases}$$

$$A_2\big(f(U_{ij})\big) = \begin{cases} 0, & f(U_{ij}) \le 0.375 + \delta, \\[2mm] \dfrac{f(U_{ij})}{0.25 - 2\delta} - \dfrac{\delta + 0.375}{0.25 - 2\delta}, & 0.375 + \delta < f(U_{ij}) \le 0.625 - \delta, \\[2mm] 1, & 0.625 - \delta < f(U_{ij}) \le 0.625 + \delta, \\[2mm] \dfrac{f(U_{ij})}{2\delta - 0.25} + \dfrac{\delta - 0.875}{2\delta - 0.25}, & 0.625 + \delta < f(U_{ij}) \le 0.875 - \delta, \\[2mm] 0, & f(U_{ij}) > 0.875 - \delta, \end{cases}$$

$$A_1\big(f(U_{ij})\big) = \begin{cases} 0, & f(U_{ij}) \le 0.625 + \delta, \\[2mm] \dfrac{f(U_{ij})}{0.25 - 2\delta} - \dfrac{\delta + 0.625}{0.25 - 2\delta}, & 0.625 + \delta < f(U_{ij}) \le 0.875 - \delta, \\[2mm] 1, & 0.875 - \delta < f(U_{ij}), \end{cases}$$

$$(3)$$

where δ is the neighborhood value centered on the middle point, and the membership degrees are 1 in the neighborhood range.

2.4. Fuzzy Judgment of First Layer Factor. According to formulas (1) to (3), the membership degree of each quantitative factor index was calculated. Combining the membership degrees of the qualitative factor index, a fuzzy comprehensive evaluation matrix could be established. Based on the three categories, three fuzzy comprehensive evaluation matrixes could be established:

$$
R_{21} = \begin{array}{cccc} \text{I} & \text{II} & \text{III} & \text{IV} \\ \left[\begin{array}{cccc} A_1(f(U_{11})) & A_2(f(U_{11})) & A_3(f(U_{11})) & A_4(f(U_{11})) \\ A_1(f(U_{12})) & A_2(f(U_{12})) & A_3(f(U_{12})) & A_4(f(U_{12})) \\ A_1(f(U_{13})) & A_2(f(U_{13})) & A_3(f(U_{13})) & A_4(f(U_{13})) \end{array}\right] \begin{array}{c} U_{11} \\ U_{12} \\ U_{13} \end{array} \end{array}
$$

$$
R_{22} = \begin{array}{cccc} \text{I} & \text{II} & \text{III} & \text{IV} \\ \left[\begin{array}{cccc} A_1(f(U_{14})) & A_2(f(U_{14})) & A_3(f(U_{14})) & A_4(f(U_{14})) \\ A_1(f(U_{15})) & A_2(f(U_{15})) & A_3(f(U_{15})) & A_4(f(U_{15})) \\ A_1(f(U_{16})) & A_2(f(U_{16})) & A_3(f(U_{16})) & A_4(f(U_{16})) \\ A_1(f(U_{17})) & A_2(f(U_{17})) & A_3(f(U_{17})) & A_4(f(U_{17})) \\ A_1(f(U_{18})) & A_2(f(U_{18})) & A_3(f(U_{18})) & A_4(f(U_{18})) \end{array}\right] \begin{array}{c} U_{14} \\ U_{15} \\ U_{16} \\ U_{17} \\ U_{18} \end{array} \end{array}
\qquad (4)
$$

$$
R_{23} = \begin{array}{cccc} \text{I} & \text{II} & \text{III} & \text{IV} \\ \left[\begin{array}{cccc} A_1(f(U_{19})) & A_2(f(U_{19})) & A_3(f(U_{19})) & A_4(f(U_{19})) \\ A_1(f(U_{110})) & A_2(f(U_{110})) & A_3(f(U_{110})) & A_4(f(U_{110})) \\ A_1(f(U_{111})) & A_2(f(U_{111})) & A_3(f(U_{111})) & A_4(f(U_{111})) \\ A_1(f(U_{112})) & A_2(f(U_{112})) & A_3(f(U_{112})) & A_4(f(U_{112})) \end{array}\right] \begin{array}{c} U_{19} \\ U_{110} \\ U_{111} \\ U_{112} \end{array} \end{array}
$$

where $A_k(f(U_{ij}))$ is the membership degree; R_{21} is the evaluation matrix of the rock mass quality; R_{22} is the evaluation matrix of the goaf parameter; R_{23} is the evaluation matrix of the induced factor.

After establishing the fuzzy comprehensive evaluation matrixes, it needed to determine the weight of the first layer factor. In the evaluation of goaf stability, each factor index had a different influence on goaf stability, and it was necessary to determine the weight of each factor index. Weight was an important part of the comprehensive evaluation. Among the methods to determine the weight, the analytic hierarchy process (AHP) was an effective method to determine the weight coefficient.

The AHP [28, 29] divided a complex system into several levels and factors. By comparing the importance of the two factors, the weight coefficient was determined. It was an effective multiobjective planning method in system engineering. The essence of AHP was a kind of decision-making thinking mode, which combined qualitative analysis and quantitative analysis in the decision-making process. The steps of AHP were as follows: determination of judgment object and factors, establishment of a judgment matrix, calculation of the order of the relative importance, and consistency check.

The object was the stability of the goaf, and the factors had three sets included $U_{21} = \{U_{11}, U_{12}, U_{13}\}$, $U_{22} = \{U_{14}, U_{15}, U_{16}, U_{17}, U_{18}\}$, and $U_{23} = \{U_{19}, U_{110}, U_{111}, U_{112}\}$. In the judgment matrix, the value reflected the relative importance. Generally, the judgment matrix was obtained by the scale method of 1~9 and its reciprocal. The judgment matrix can be established as follows:

$$
P_{21} = \begin{array}{ccc} U_{11} & U_{12} & U_{13} \\ \left[\begin{array}{ccc} 1 & 1/3 & 3 \\ 3 & 1 & 5 \\ 1/3 & 1/5 & 1 \end{array}\right] \begin{array}{c} U_{11} \\ U_{12} \\ U_{13} \end{array} \end{array}
$$

$$
P_{22} = \begin{array}{ccccc} U_{14} & U_{15} & U_{16} & U_{17} & U_{18} \\ \left[\begin{array}{ccccc} 1 & 5 & 3 & 7 & 6 \\ 1/5 & 1 & 1/3 & 3 & 2 \\ 1/3 & 3 & 1 & 4 & 3 \\ 1/7 & 1/3 & 1/4 & 1 & 1/2 \\ 1/6 & 1/2 & 1/3 & 2 & 1 \end{array}\right] \begin{array}{c} U_{14} \\ U_{15} \\ U_{16} \\ U_{17} \\ U_{18} \end{array} \end{array}
\qquad (5)
$$

$$
P_{23} = \begin{array}{cccc} U_{19} & U_{110} & U_{111} & U_{112} \\ \left[\begin{array}{cccc} 1 & 2 & 2 & 3 \\ 1/2 & 1 & 1 & 2 \\ 1/2 & 1 & 1 & 2 \\ 1/3 & 1/2 & 1/2 & 1 \end{array}\right] \begin{array}{c} U_{19} \\ U_{110} \\ U_{111} \\ U_{112} \end{array} \end{array}
$$

where P_{21} is the judgment matrix of rock mass quality, P_{22} is the judgment matrix of goaf parameters, and P_{23} is the judgment matrix of induced factors.

In the order of the relative importance, the maximum eigenvalue of P_{21} with $\lambda_{21\max} = 3.04$, and the eigenvector X_{21} is as follows:

$$X_{21} = \begin{matrix} U_{11} & U_{12} & U_{13} \\ \begin{bmatrix} 0.37 & 0.92 & 0.15 \end{bmatrix} \end{matrix} \tag{6}$$

The fuzzy relative weight coefficient was obtained by normalizing the eigenvector X_{21}. The weight vector C_{21} is

$$C_{21} = \begin{matrix} U_{11} & U_{12} & U_{13} \\ \begin{bmatrix} 0.26 & 0.64 & 0.10 \end{bmatrix} \end{matrix} \tag{7}$$

The maximum eigenvalue of P_{22} with $\lambda_{22\max} = 5.13$; the eigenvector X_{22} is as follows:

$$X_{22} = \begin{matrix} U_{14} & U_{15} & U_{16} & U_{17} & U_{18} \\ \begin{bmatrix} 0.88 & 0.20 & 0.40 & 0.09 & 0.13 \end{bmatrix} \end{matrix} \tag{8}$$

The weight vector C_{22} is

$$C_{22} = \begin{matrix} U_{14} & U_{15} & U_{16} & U_{17} & U_{18} \\ \begin{bmatrix} 0.52 & 0.11 & 0.24 & 0.05 & 0.08 \end{bmatrix} \end{matrix} \tag{9}$$

The maximum eigenvalue of P_{23} with $\lambda_{23\max} = 4.01$; the eigenvector X_{23} is as follows:

$$X_{23} = \begin{matrix} U_{19} & U_{110} & U_{111} & U_{112} \\ \begin{bmatrix} 0.78 & 0.42 & 0.42 & 0.22 \end{bmatrix} \end{matrix} \tag{10}$$

The weight vector C_{23} is

$$C_{23} = \begin{matrix} U_{19} & U_{110} & U_{111} & U_{112} \\ \begin{bmatrix} 0.42 & 0.23 & 0.23 & 0.12 \end{bmatrix} \end{matrix} \tag{11}$$

In the consistency check, it was necessary to check whether the weight was reasonable. The formula of the consistency index (CI) is as follows:

$$CI = \frac{\lambda_{\max} - n}{n - 1}, \tag{12}$$

where n is the number of factors.

The consistency ratio CR can be obtained as follows:

$$CR = \frac{CI}{RI}, \tag{13}$$

where RI is the average random consistency index. n is 3, 4, and 5, and RI is 0.52, 0.89, and 1.12, respectively.

When the CR was less than 0.10, it showed that the judgment matrix satisfied the consistency test; that is, the distribution of the weight coefficient was reasonable. The results were $CI_{21} = 0.02$, $CR_{21} = 0.04$, $CI_{22} = 0.033$, $CR_{22} = 0.029$, $CI_{23} = 0.003$, and $CR_{23} = 0.004$. These results showed that the distribution of the weight coefficient was reasonable.

After the weight vector C_{2i} and the fuzzy comprehensive evaluation matrix R_{2i} were determined, fuzzy subset B_{2i} could be obtained through a fuzzy linear change.

$$B_{21} = C_{21} \circ R_{21} = \begin{matrix} \text{I} & \text{II} & \text{III} & \text{IV} \\ \begin{bmatrix} b_{11} & b_{12} & b_{13} & b_{14} \end{bmatrix} \end{matrix}$$

$$B_{22} = C_{22} \circ R_{22} = \begin{matrix} \text{I} & \text{II} & \text{III} & \text{IV} \\ \begin{bmatrix} b_{21} & b_{22} & b_{23} & b_{24} \end{bmatrix} \end{matrix} \tag{14}$$

$$B_{23} = C_{23} \circ R_{23} = \begin{matrix} \text{I} & \text{II} & \text{III} & \text{IV} \\ \begin{bmatrix} b_{31} & b_{32} & b_{33} & b_{34} \end{bmatrix} \end{matrix}$$

where "$\circ$" is a synthetic operator for weight vector C_{2i} and fuzzy comprehensive evaluation matrix R_{2i}.

2.5. Fuzzy Judgment of Second Layer Factor.

Based on the fuzzy comprehensive evaluation matrix of the first layer, the fuzzy comprehensive evaluation matrix R of the second layer can be established:

$$R = \begin{bmatrix} B_{21} \\ B_{22} \\ B_{23} \end{bmatrix} = \begin{matrix} \text{I} & \text{II} & \text{III} & \text{IV} \\ \begin{bmatrix} b_{11} & b_{12} & b_{13} & b_{14} \\ b_{21} & b_{22} & b_{23} & b_{24} \\ b_{31} & b_{32} & b_{33} & b_{34} \end{bmatrix} \end{matrix} \begin{matrix} U_{21} \\ U_{22} \\ U_{23} \end{matrix} \tag{15}$$

The next was to determine the weight of the second layer factor. AHP was still used to determine the weight of the second layer factor. The judgment object was goaf stability. The set of judgment factors was $U_2 = \{U_{21}, U_{22}, U_{23}\}$. When determining the relative importance value in judgment matrix P, the main basis was the current research results or scoring value in the common evaluation methods. The judgment matrix P could be obtained.

$$P = \begin{matrix} U_{21} & U_{22} & U_{23} \\ \begin{bmatrix} 1 & 1/3 & 3 \\ 3 & 1 & 6 \\ 1/3 & 1/6 & 1 \end{bmatrix} \end{matrix} \begin{matrix} U_{21} \\ U_{22} \\ U_{23} \end{matrix} \tag{16}$$

In the order of the relative importance, the maximum eigenvalue of P with $\lambda_{\max} = 3.02$; the eigenvector X is as follows:

$$X = \begin{matrix} U_{21} & U_{22} & U_{23} \\ \begin{bmatrix} 0.35 & 0.93 & 0.14 \end{bmatrix} \end{matrix} \tag{17}$$

The fuzzy relative weight coefficient was obtained by normalizing the eigenvector X. The weight vector is

$$C = \begin{matrix} U_{21} & U_{22} & U_{23} \\ \begin{bmatrix} 0.25 & 0.65 & 0.10 \end{bmatrix} \end{matrix} \tag{18}$$

In the consistency check, the consistency index CI was 0.01, and the consistency ratio CR was 0.02 and less than 0.10, which showed that the distribution of the weight coefficient was reasonable.

(a)

(b)
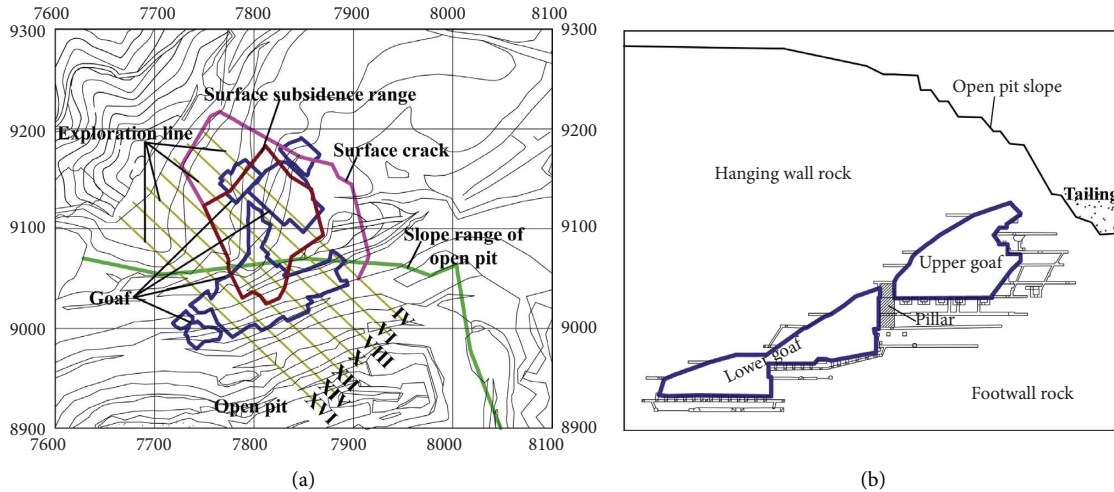
FIGURE 2: The situation of goafs. (a) The location of the open pit and goafs. (b) The section of exploration line X.

After the weight vector C and the fuzzy comprehensive evaluation matrix R were determined, fuzzy subset B could be obtained through a fuzzy linear change. That is,

$$B = C \circ R = \begin{matrix} \text{I} & \text{II} & \text{III} & \text{IV} \\ [b_1 & b_2 & b_3 & b_4] \end{matrix} \tag{19}$$

According to the principle of maximum membership, the maximum value $b_{\max} = \max\{b_i\}$ was obtained, and the value of i was 1 to 4. The rank of $b_{\max} = \max\{b_i\}$ was the rank of comprehensive evaluation.

2.6. Application in Paishanlou Gold Mine. The Paishanlou gold mine belongs to the China National Gold Group, which is the key enterprise in Northeast China. The Paishanlou gold deposit is a large-scale hydrothermal gold deposit. The surrounding rock is mylonite, and the remote rock is primary mylonite and mylonitic rock. The dip angle of the ore body is 35°~55°. The ore body is located between the elevations of 465~−30 m. After open pit mining to +300 m, the mine transferred to underground mining. Due to the slow dip angle of the ore body and the increase the production capacity, the open stope method is adopted in the two middle sections of 300 m and 225 m, forming large-scale discontinuous goafs (in Figure 2).

The horizontal area of the goafs has reached 11250 m^2 above the 275 m level, and the volume is approximately 500000 m^3. The roof of the goaf obliquely intersects with the surface. In the section of exploration line X (in Figure 2(b)), the dip angle of the goaf roof is 25°–35°, the surface boundary is the open-pit mining boundary, and the boundary slope angle is 29°–50°. The thinnest thickness of the goaf roof is only 36 m. The original open pit is used to store dry toxic tailings. The design storage elevation is +420 m. The locations of the open pit and goaf are shown in Figure 2(a).

Therefore, it was urgent to evaluate goaf stability in the Paishanlou gold mine. According to the results of the stability evaluation and the technical conditions of the mine, the optimal goaf handling measures were determined. The ultimate goals

TABLE 2: Stability evaluation of upper goaf and lower goaf.

Index	Goaf	
	Upper	Lower
U_{11}	4.3 MPa	5.2 MPa
U_{12}	0.20	0.28
U_{13}	General	General
U_{14}	32 m	26 m
U_{15}	36 m	175 m
U_{16}	75 m	75 m
U_{17}	General	General
U_{18}	Serious breaking	Pillars standard
U_{19}	45 L•min^{-1}	32 L•min^{-1}
U_{110}	General	General
U_{111}	Weak	Great
U_{112}	Small	Small
B	[0.07 0.21 0.35 0.37]	[0.08 0.47 0.15 0.31]
Ranks	IV, III	II

were to achieve safe mining of ore bodies and safe management of goafs. Then, stability evaluation of the upper goaf and lower goaf was carried out by the goaf stability model. The indexes and results are shown in Table 2.

As shown in Table 2, the stability rank of the upper goaf is unstable IV based on the principle of maximum membership. However, the membership in unstable IV is close to membership in understable III, and the stability ranks of the upper goaf are unstable IV and understable III. The stability rank of the lower goaf is basically II. The results showed that the goafs need to be handled to ensure safe mining, and these results were the basis for goaf handling measures as well.

3. Establishment of the Goaf Decision Model

In the process of the goaf decision model, many uncertain factors were involved, such as the geological conditions of the mine, goaf stability, goaf location, goaf shape, and filling of the goaf. Different goaf handling measures had different handling costs, handling effects, and time required for handling. They also depend on the specific production situations of the mine. The

TABLE 3: The index and the relative membership for goaf handling measures.

Goaf	Measure	Index					
		p_{s1}	p_{s2}	p_{s3}	p_{s4}	p_{s5}	u_j
Upper	d_{s1}	1.14	1.29	3.43	250	80	0.15
	d_{s2}	5.29	1.14	1.57	45	50	0.78
	d_{s3}	7.42	6.71	5.86	288	40	0.93
	d_{s4}	3.57	7.14	7.86	382	300	0.27
	d_{s5}	5.14	9.14	9.14	440	360	0.41
Lower	d_{s1}	1.86	1.14	3.57	160	80	0.20
	d_{s2}	6.29	1.86	3.43	45	50	0.94
	d_{s3}	5.57	3.71	5.57	390	120	0.66
	d_{s4}	5.29	5.46	7.86	424	260	0.50
	d_{s5}	6.14	9.14	9.43	517	300	0.65

feasibility and other indexes were also different for the goaf with different stability ranks. Therefore, the advantages and disadvantages of goaf handling measures were fuzzy. And multiobjective fuzzy optimization theory could make a good comprehensive evaluation of the goaf handling effect and obtain the optimal handling scheme.

3.1. Multiobjective Fuzzy Optimization.

For the goaf handling measures, there were usually four categories: closing, caving, reinforcing, and filling. Each category also included a series of subhandling measures, such as filling could be divided into waste rock dry filling, tailings filling, and cemented filling, and caving could be divided into induced natural caving and blasting caving. Considering the mine situation, the goaf handling measures were preliminarily determined, which were $D_s = \{d_{s1}, d_{s2}, d_{s3}, d_{s4}, d_{s5}\} =$ {blasting and caving, induced natural caving, waste rock dry filling, tailings filling, cemented filling}.

The comprehensive indexes of goaf handling mainly included necessity, feasibility, requirements of laws and regulations, treatment effect, handling cost and work efficiency, and handling time. The necessity of handling was determined according to the goaf stability evaluation results, the results in Table 2, and mining status showed that goaf handling was necessary. The feasibility mainly considered safety (based on the goaf stability evaluation) and construction conditions. Therefore, the evaluation index set P_s was determined, $P_s = \{p_{s1}, p_{s2}, p_{s3}, p_{s4}, p_{s5}\} =$ {feasibility, requirements of laws and regulations, handling effect, handling cost, handling time}. According to the five goaf handling measures and five evaluation indexes, the index characteristic matrix is expressed as

$$X = (x_{ij})_{5 \times 5} = \begin{matrix} & d_{s1} & d_{s2} & d_{s3} & d_{s4} & d_{s5} \\ \begin{bmatrix} x_{11} & x_{12} & x_{13} & x_{14} & x_{15} \\ x_{21} & x_{22} & x_{23} & x_{24} & x_{25} \\ x_{31} & x_{32} & x_{33} & x_{34} & x_{35} \\ x_{41} & x_{42} & x_{43} & x_{44} & x_{45} \\ x_{51} & x_{52} & x_{53} & x_{54} & x_{55} \end{bmatrix} & \begin{matrix} p_{s1} \\ p_{s2} \\ p_{s3} \\ p_{s4} \\ p_{s5} \end{matrix} \end{matrix} \quad (20)$$

where x_{ij} is the characteristic value of index i and measure j.

In the process of fuzzy optimization or decision-making, in order to solve the possible objectivity of membership and the subjective in the process of determination, the relative membership matrix was established by using the index relative membership. For larger and better indexes (handling effect, feasibility, requirements of laws and regulations), the relative membership formula is

$$r_{ij} = \frac{x_{ij} - \bigwedge_j x_{ij}}{\bigvee_j x_{ij} - \bigwedge_j x_{ij}}. \quad (21)$$

For smaller and better indexes (necessity of handling, handling cost, handling time), the relative membership formula is

$$r_{ij} = \frac{\bigvee_j x_{ij} - x_{ij}}{\bigvee_j x_{ij} - \bigwedge_j x_{ij}}, \quad (22)$$

where r_{ij} is the relative membership degree of index i and measure j; $\vee$ and $\wedge$ are the characteristics of taking large and taking small, respectively.

The index characteristic matrix X is transformed into the index relative membership matrix by formulas (21) and (22); that is,

$$R_s = \begin{matrix} & d_{s1} & d_{s2} & d_{s3} & d_{s4} & d_{s5} \\ \begin{bmatrix} r_{11} & r_{12} & r_{13} & r_{14} & r_{15} \\ r_{21} & r_{22} & r_{23} & r_{24} & r_{25} \\ r_{31} & r_{32} & r_{33} & r_{34} & r_{35} \\ r_{41} & r_{42} & r_{43} & r_{44} & r_{45} \\ r_{51} & r_{52} & r_{53} & r_{54} & r_{55} \end{bmatrix} & \begin{matrix} p_{s1} \\ p_{s2} \\ p_{s3} \\ p_{s4} \\ p_{s5} \end{matrix} \end{matrix} \quad (23)$$

The relative membership degree of the superior measure is

$$G = (g_1, g_2, g_3, g_4, g_5)^T = (1, 1, 1, 1, 1)^T. \quad (24)$$

The relative membership degree of the inferior measure is

$$B_s = (b_{s1}, b_{s2}, b_{s3}, b_{s4}, b_{s5})^T = (0, 0, 0, 0, 0)^T. \quad (25)$$

In the goaf handling system, the weight vector W_s is

$$W_s = (w_{s1}, w_{s2}, w_{s3}, w_{s4}, w_{s5})^T. \quad (26)$$

The weight vector W_s was still determined by AHP, and the judgment matrix is

(a)

(b)

(c)
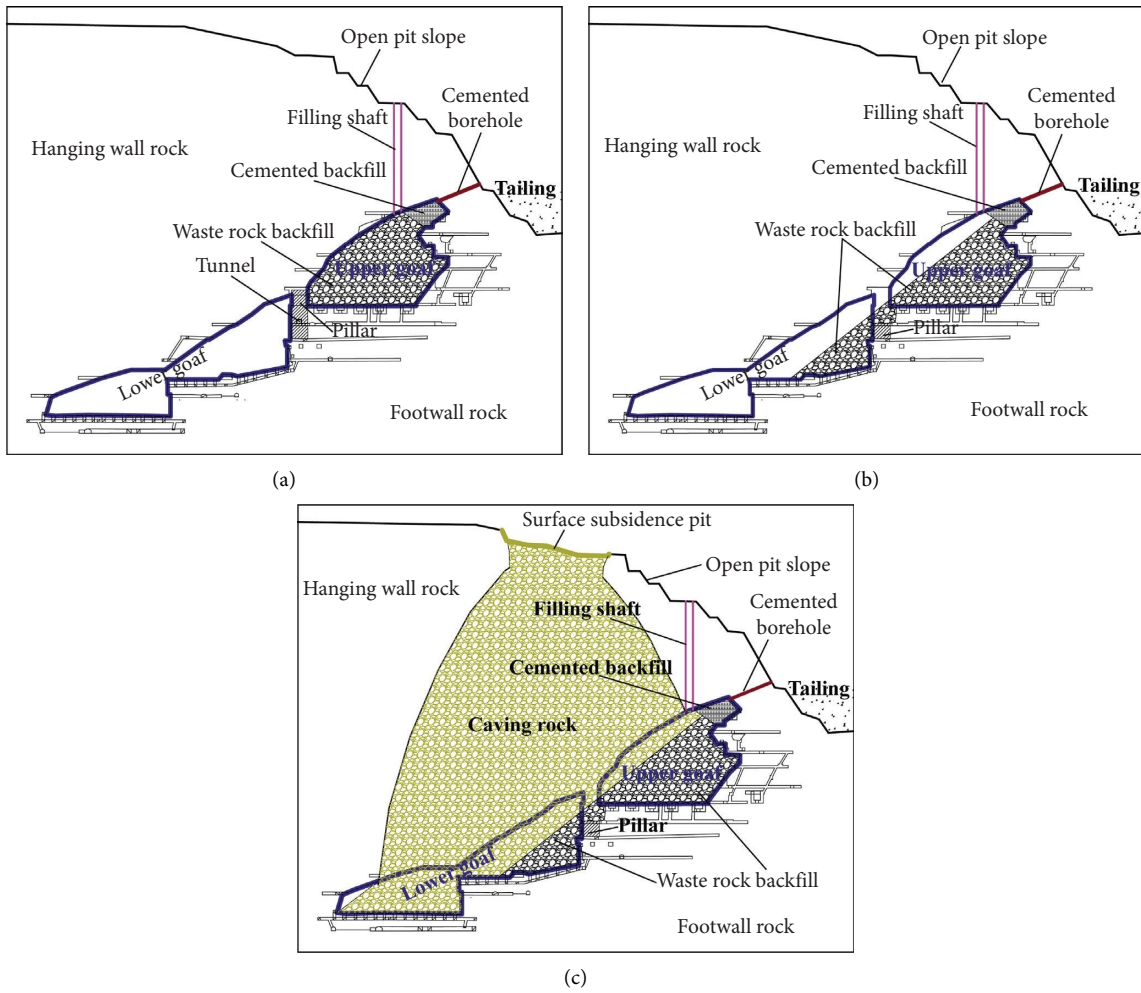
Figure 3: Comprehensive handling measure. (a) Filling the upper goaf. (b) Connecting the upper goaf with the lower goaf. (c) Filling the lower goaf.

(a)

(b)

Figure 4: The filling process by mining truck. (a) Waste rock filling. (b) Loess filling.

(a)

(b)

(c)

(d)

FIGURE 5: Cover of surface subsidence pit. (a) Surface subsidence pit. (b) Filling process. (c) Covering process. (d) Covering process.

$$P_s = \begin{array}{c} \begin{array}{ccccc} p_{s1} & p_{s2} & p_{s3} & p_{s4} & p_{s5} \end{array} \\ \begin{bmatrix} 1 & 3 & 4 & 2 & 2 \\ 1/3 & 1 & 2 & 1/2 & 1/2 \\ 1/4 & 1/2 & 1 & 1/2 & 1/2 \\ 1/2 & 2 & 2 & 1 & 2 \\ 1/2 & 2 & 2 & 1/2 & 1 \end{bmatrix} \begin{array}{c} p_{s1} \\ p_{s2} \\ p_{s3} \\ p_{s4} \\ p_{s5} \end{array} \end{array} \quad (27)$$

Calculating the maximum eigenvalue $\lambda_{\max} = 5.11$ of the judgment matrix P_s, the consistency index CI was 0.028, and the consistency ratio CR was 0.025 and less than 0.10. That is, the weight vector W_s is

$$\begin{aligned} W_s &= (w_{s1}, w_{s2}, w_{s3}, w_{s4}, w_{s5})^T \\ &= (0.38, 0.12, 0.09, 0.23, 0.18)^T. \end{aligned} \quad (28)$$

In fuzzy theory, the weighted optimal distance D_{jg} is

$$D_{\text{jg}} = u_j p \sqrt{\sum_{i=1}^{5} \left[w_{si} \left(g_i - r_{ij} \right) \right]^p}. \quad (29)$$

The weighted inferior distance D_{jb} is

$$D_{\text{jb}} = (1 - u_j) p \sqrt{\sum_{i=1}^{5} \left[w_{si} \left(r_{ij} - b_i \right) \right]^p}, \quad (30)$$

where p is the distance parameter and $p = 1$ is the Hamming distance.

The optimization criterion was that the sum of the weighted optimal distance square and the weighted inferior distance square was the smallest. That is,

$$\min \left\{ F(u_j) = \left(D_{\text{jg}}^2 + D_{\text{jb}}^2 \right) \right\}. \quad (31)$$

Finding the derivative of formula (31), and making it equal to zero, the solution is

$$u_j = \frac{1}{1 + \left\{ \sum_{i=1}^{5} \left[w_{si} (1 - r_{ij}) \right]^p / \sum_{i=1}^{5} \left[w_{si} r_{ij} \right]^p \right\}^{2/p}}. \quad (32)$$

Formula (32) was a fuzzy optimization theory model of the goaf handling measures. In the set of measures that meet the index constraints, the measure with the highest relative membership degree u_j was the satisfactory measure, and the sequence of u_j from the largest to the smallest was the satisfactory sequence.

3.2. Application in Paishanlou Gold Mine. To determine the goaf handling measures, a group of nine experts scored and calculated the feasibility, requirements of laws and regulations, handling effect, handling cost, and handling time for

(a)   (b)   (c)
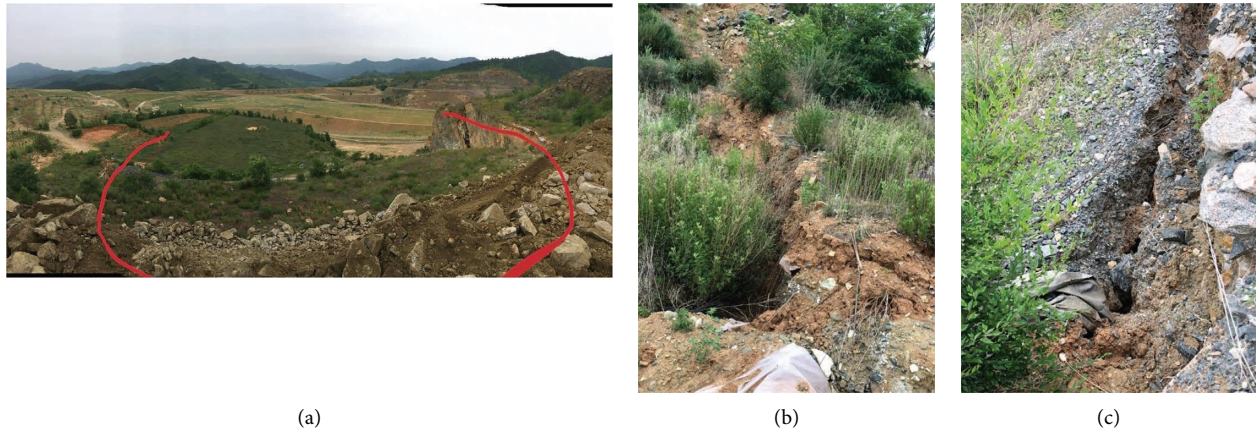
FIGURE 6: The present situation of handling results. (a) Surface subsidence. (b) Surface cracks. (c) Surface cracks.

five goaf handling measures. The experts were composed of mining technicians, mine leaders, material planners, and university researchers. Then, the highest and the lowest scores were removed, respectively, and the mean value of the remaining results was taken. Among them, the feasibility, treatment effect, and requirements of laws and regulations were all scored on the 10-point system. The final score and calculation results are shown in Table 3. Then, the relative membership degree u_j is calculated by the multiobjective fuzzy optimization model (in Table 3).

The results of fuzzy optimization for the goaf decision are shown in Table 3, the handling measure of the upper goaf is waste rock dry filling, and the handling measure of the lower goaf is induced natural caving. However, considering the relevance of goafs (in Figure 2) and the urgency of handling, a comprehensive handling measure is proposed as shown in Figure 3. Firstly, the filling shaft is drilled in the open pit slope to fill the upper goaf with waste rock (in Figure 3(a)). The mining truck is used to fill the upper goaf quickly (in Figure 4(a)), and the total amount of waste rock filling is $372000 \, m^3$. After the upper goaf is filled, the cemented filling is carried out at the top of the upper goaf, to better protect the stability of the slope.

Secondly, the tunnel is excavated in the pillar of the upper and lower goaf, and blasting medium-length holes are drilled so that the upper and lower goaf is connected by blasting and this engineering induces natural caving of the rock mass above the goaf (in Figure 3(b)). Two days after blasting, a surface subsidence pit is formed, and it has a depth of 10 to 43 m and a total area of 10451 m^2 (as shown in Figure 5(a)).

Finally, the surface subsidence pit is filled with waste rock and covered with soil (in Figure 5). When the subsidence pit is stable, the waste rock in the waste rock field is transported by mining trucks, and the subsidence pit is filled from north to south (in Figure 3(c)). By September 2012, the landform was basically restored, and the total amount of waste rock filled is $333566 \, m^3$. After the completion of waste rock filling, the engineering of covering with new soil is carried out in layers (in Figure 5). The first layer is covered with 0.5 m loess (in

Figure 4(b)), after leveling, the protection against osmosis fabric is covered, and then the new soil is covered with a 0.5 m loess layer to protect against osmosis fabric. In the spring of 2013, soybean, corn, and other crops were planted on the new soil, to prevent soil erosion and achieve economic benefits.

4. Conclusions

To comprehensively solve the safety risks from goafs in underground metal mines, minimize subjectivity in the evaluation and decision process, and comprehensively consider different handling measures, an evaluation model of goaf stability and a decision model of handling measures were provided based on fuzzy theory.

The goaf stability model was established by the two-layer fuzzy comprehensive evaluation. It took into account 12-factor indexes of goafs with engineering empirical approaches and divided them into 3 categories according to their engineering categories. The membership degree of indexes was determined based on the normalized formula and membership function, and weights were determined by the analytic hierarchy process. This model improved the applicability of the goaf stability evaluation results, and the results were the basis for goaf handling measures. The model was applied to the Paishanlou gold mine. The results showed that the stability ranks of the upper goaf were unstable IV and understable III, and the stability rank of the lower goaf was basically II. In addition, the goaf needed to be handled.

Based on the results of the goaf stability evaluation, the decision model of the goaf handling measures was established by multiobjective fuzzy optimization. It consisted of five goaf handling measures and five evaluation indexes. The model provided a good comprehensive decision and optimal scheme for goaf handling. This model was also applied to the Paishanlou gold mine. The results showed that the handling measure of the upper goaf was waste rock dry filling, and the handling measure of the lower goaf was induced natural caving. These results were integrated with the actual situation of the mine, and a comprehensive handling measure was proposed. That was, the first step was to fill the upper

goaf with waste rock, and cemented filling was also carried out at the top of the upper goaf. The second step was to connect the upper and lower goaf and induce natural caving of the rock mass above the goaf. The third step was to fill the surface subsidence pit with waste rock and cover it with soil.

By 2020, the change in the covered soil in the surface subsidence pit was tracked and observed, as shown in Figure 6. There was small subsidence and some cracks only at the corners, and the integrity of the covered soil was not destroyed. This showed that the comprehensive handling measure was successful. It also showed that the results of goaf stability evaluation and handling measure decisions were correct, and the stability model and decision model for goafs were feasible.

Data Availability

The data used to support the findings of this study are included within the article.

Conflicts of Interest

The authors declare that they have no conflicts of interest.

Acknowledgments

References

[1] H. Ma, N. Liu, Y. Wang, Q. Li, and S. Cheng, "Review on research status of controlling techniques for goaf disaster in metal mine," *Journal of Safety Science & Technology*, vol. 10, no. 10, pp. 75–80, 2014.

[2] J.-A. Wang, X. C. Shang, and H. T. Ma, "Investigation of catastrophic ground collapse in Xingtai gypsum mines in China," *International Journal of Rock Mechanics and Mining Sciences*, vol. 45, no. 8, pp. 1480–1499, 2008.

[3] G. Swift and D. Reddish, "Stability problems associated with an abandoned ironstone mine," *Bulletin of Engineering Geology and the Environment*, vol. 61, no. 3, pp. 227–239, 2002.

[4] H. Yavuz, "An estimation method for cover pressure re-establishment distance and pressure distribution in the goaf of longwall coal mines," *International Journal of Rock Mechanics and Mining Sciences*, vol. 41, no. 2, pp. 193–205, 2004.

[5] Y.-x. Hu and X.-b. Li, "Bayes discriminant analysis method to identify risky of complicated goaf in mines and its application," *Transactions of Nonferrous Metals Society of China*, vol. 22, no. 2, pp. 425–431, 2012.

[6] J.-A. Wang, D. Z. Li, and X. C. Shang, "Creep failure of roof stratum above mined-out area," *Rock Mechanics and Rock Engineering*, vol. 45, no. 4, pp. 533–546, 2012.

[7] J. Zhou, X. Li, S. Hani, S. Wang, and W. Wei, "Identification of large-scale goaf instability in underground mine using particle swarm optimization and support vector machine," *International Journal of Mining Science and Technology*, vol. 23, no. 5, pp. 701–707, 2013.

[8] Y. Sun, X. Zhang, W. Mao, and L. Xu, "Mechanism and stability evaluation of goaf ground subsidence in the third mining area in Gong Changling District, China," *Arabian Journal of Geosciences*, vol. 8, no. 2, pp. 639–646, 2014.

[9] J.-h. Hu, J.-l. Shang, K.-p. Zhou et al., "Hazard degree identification of goafs based on scale effect of structure by RS-TOPSIS method," *Journal of Central South University*, vol. 22, no. 2, pp. 684–692, 2015.

[10] B. Zhang, L. Zhang, H. Yang, Z. Zhang, and J. Tao, "Subsidence prediction and susceptibility zonation for collapse above goaf with thick alluvial cover: a case study of the Yongcheng coalfield, Henan Province, China," *Bulletin of Engineering Geology and the Environment*, vol. 75, no. 3, pp. 1117–1132, 2015.

[11] L. Li, K. Wu, and D.-W. Zhou, "Evaluation theory and application of foundation stability of new buildings over an old goaf using longwall mining technology," *Environmental Earth Sciences*, vol. 75, no. 9, 2016.

[12] H.-p. Xiao, G.-l. Guo, and W. Liu, "Hazard degree identification and coupling analysis of the influencing factors on goafs," *Arabian Journal of Geosciences*, vol. 10, no. 3, 2017.

[13] Q. Guo, Y. Li, X. Meng, G. Guo, and X. Lv, "Instability risk assessment of expressway construction site above an abandoned goaf: a case study in China," *Environmental Earth Sciences*, vol. 7820 pages, 2019.

[14] N. Barton, R. Lien, and J. Lunde, "Engineering classification of rock masses for the design of tunnel support," *Rock Mechanics*, vol. 6, no. 4, pp. 189–236, 1974.

[15] N. Barton, "Some new Q-value correlations to assist in site characterisation and tunnel design," *International Journal of Rock Mechanics and Mining Sciences*, vol. 39, no. 2, pp. 185–216, 2002.

[16] Z. T. Bieniawski, "Engineering classification of jointed rock masses," *The Civil Engineering in South Africa*, vol. 15, pp. 335–343, 1973.

[17] Z. T. Bieniawski, *Classification of Rock Masses for Engineering: The RMR System and Future Trends*, Pergamon Press, New York, 1993.

[18] D. H. Laubscher, "A geomechanics classification system for the rating of rock mass in mine design," *JS Afr. Inst. Metall*, vol. 90, no. 10, pp. 257–273, 1990.

[19] D. H. Laubscher, "Cave mining-the state of the art," *Journal of the South African Institute of Mining and Metallurgy*, vol. 94, no. 10, pp. 279–293, 1994.

[20] "Ministry of Water Resources of the People's Republic of China," *Standard For Engineering Classification of Rock Mass*, China Planning Press, Beijing, 2014.

[21] F. Ren, H. Liu, R. He, G. Li, and Y. Liu, "Point load test of half-cylinder core using the numerical model and laboratory tests: size suggestion and correlation with cylinder core," *Advances in Civil Engineering*, vol. 2018, pp. 1–11, 2018.

[22] D. W. Hobbs, "A simple method for assessing the uniaxial compressive strength of rock," *International Journal of Rock Mechanics and Mining Sciences & Geomechanics Abstracts*, vol. 1, no. 1, pp. 5–15, 1963.

[23] J. A. Franklin, "Suggested method for determining point load strength," *International Journal of Rock Mechanics and Mining Sciences & Geomechanics Abstracts*, vol. 22, no. 2, pp. 51–60, 1985.

[24] D. A. Mishra and A. Basu, "Use of the block punch test to predict the compressive and tensile strengths of rocks,"

International Journal of Rock Mechanics and Mining Sciences, vol. 51, pp. 119–127, 2012.

[25] T. N. Singh, A. Kainthola, and A. Venkatesh, "Correlation between point load index and uniaxial compressive strength for different rock types," *Rock Mechanics and Rock Engineering*, vol. 45, no. 2, pp. 259–264, 2012.

[26] R. He, H. Liu, F. Ren, G. Li, and J. Zhang, "A fuzzy comprehensive assessment approach and application of rock mass cavability in block caving mining," *Mathematical Problems in Engineering*, vol. 2019, pp. 1–13, 2019.

[27] Y. Su, M. He, and X. Sun, "Equivalent characteristic of membership function type in rock mass fuzzy classification," *Journal of University of Science and Technology Beijing*, vol. 29, no. 7, pp. 670–675, 2007.

[28] T. L. Saaty, "How to make a decision: the analytic hierarchy process," *European Journal of Operational Research*, vol. 48, no. 1, pp. 9–26, 1990.

[29] W. J. Hurley, "The analytic hierarchy process: a note on an approach to sensitivity which preserves rank order," *Computers & Operations Research*, vol. 28, no. 2, pp. 185–188, 2001.

Research Article

Experimental Study on Double Row Micropiles and Anchors Composite Retaining Structure in Deep Fill Site

Wenfeng Liu [ID],[1] Jie Mao [ID],[1] Hongxing Zhao [ID],[1] and Guangbiao Shao [ID][2,3]

[1]*Shandong Institute of Geophysical & Geochemical Exploration, Jinan 250013, China*
[2]*School of Civil Engineering, Shandong Jianzhu University, Jinan 250101, China*
[3]*Key Laboratory of Building Structural Retrofitting and Underground Space Engineering (Shandong Jianzhu University), Ministry of Education, Jinan 250101, China*

Correspondence should be addressed to Guangbiao Shao; shaogb@sdjzu.edu.cn

In recent years, with the continuous advancement of urbanization in China and the gradual increase in the utilization scale of underground space, foundation pits may build in a narrow and compact environment. Meanwhile, miscellaneous fill layers in the city may cause construction difficulties when new foundation pits are excavated and supported. While we focus on the above problems, new retaining structure forms which are safe and economical are urgently needed. In this study, based on the excavation in a deep filling site in Jinan, the double row micropiles and anchors composite retaining structure is monitored under excavation, loading, and unloading conditions by installing sensors and testing. The stress and axial force distribution of the front and back row micropiles and anchors in the composite retaining system under different excavation depths and different loads are analyzed. The performance changes of the front and back row micropiles under different conditions and the contribution of anchors at different depths to the structure resistance during excavation and loading tests are discussed. The results show that double row steel piles and anchors composite retaining structure is feasible when excavating deep fill site in the urban area. In the composite retaining system, the stress of the front pile is greater than the back pile, the back pile has a lag when it starts working, and the axial force of the middle and upper anchor is greater than that of the bottom anchor.

1. Introduction

With the continuous progress of urbanization in China, the scale of underground excavation in urban areas is gradually increasing, and a large number of deep and complex foundation pits for new construction projects are emerging [1]. With the continuous expansion of underground space of excavation scale, the construction difficulty is increasing. The increasingly complex surrounding environment in the urban area leads to the boundary of excavation construction close to the existing buildings. Therefore, reinforced concrete vertical retaining members with larger stiffness and anchor or strut are often used as foundation pit retaining structures. But these traditional structure type in the excavation has several problems, such as high cost, low construction speed, and go against to the environmental protection of the construction industry [2]. It should also be

noted that the new construction site in the city is often distributed with relatively deep under-consolidated miscellaneous fill. Due to the short backfill time and the complicated component, miscellaneous fill shows some properties of low strength and poor self-stability. These undesirable characteristics cause higher support requirements for excavations. In order to solve these adverse factors, a new retaining structure type form with good construction performances such as rapid construction, low cost, and high bearing capacity is urgently needed.

As a new kind of retaining structure used in excavation engineering in recent years, steel pipe pile has been applied in some excavation and slope engineering. This structure form has several advantages, such as good construction efficiency, high mechanical performance, low cost, and environment friendly. However, the research of theoretical calculation on steel pipe pile retaining structure form lags

behind the practical application. This lead to severely restricts the promotion and application of this retaining structure in building excavation construction.

At present, plenty of research works were carried out on the retaining system of steel pipe pile and pile-anchor retaining structures in deep soil-filled excavation engineering. According to the simulation results of some model tests and finite element analysis, Wang [3] pointed out that with the increase of excavation depth, the transition point of pile positive and negative bending moment gradually moved downward, and the pile load on the top of the slope would aggravate the damage of the pile-soil system. Shi [4] found that under the same conditions, the axial force of soil nails in normal nail walls is smaller than that in steel pipe pile composite soil nailing wall, the cooperative work of steel pipe pile and soil nail limits the lateral displacement at the initial stage of excavation, soil nail material has been fully used. Wang, et al. [5] introduced a superthick backfill subgrade instance of Qianjiang-Zhangjiajie-Changde Railway in China and carried out an experimental and numerical study. Xu [6] revealed the deformation law of steel pipe micropile composite soil nailing wall and conducted a parameter sensitivity analysis on steel pipe piles. Han et al. [7] and Ding et al. [8] investigated the damage constitutive model of grouting and concrete, respectively. Sun et al. [9] introduced a new iterative process to find the bending moment and shear capacity of the micropile section, and give a new design method for micropiles for earth slope stabilization. Fu et al. [10] believed that the horizontal displacement and bending moment of cantilever double-row grouting steel pipe pile support gradually decreased with the increase of pile row spacing. However, when the row spacing is too large, pile-soil interaction will decrease. Qi et al. [11] combined with offshore engineering, tested the vertical static load test of steel pipe piles by deploying weak reflection Bragg grating sensors and achieved good results. Shao et al. [12] monitored deep and miscellaneous fill foundation pit with a pile-anchor support system and prestressed anchor cable combined with a channel steel lattice beam, and the monitoring results showed that both structures could effectively control the deformation of excavation construction. Thompson [13] studied the load transfer law of single and double steel pipe piles under lateral load by using the shear box model method. Richards and Rothbauer [14] studied the working performance of micropiles under soil lateral loading. Prat [15] presents a numerical investigation of a micropile retaining wall, and discussed the influence of overestimation soil strength and underestimation loads.

Therefore, it is generally important to obtain a proper understanding of how the micropile structure works in excavation construction. Existing research mainly adopted field tests, numerical simulations, and model tests to study single-row or double-row cantilever steel pipe piles. However, the research of double row micropiles and anchors composite retaining structure in miscellaneous fill soil is almost blank, existing results are not suitable for guiding this structure type construction. To the best of our knowledge, little work has been done on the working mode of micropile and anchor in several construction situations of excavation. In addition,
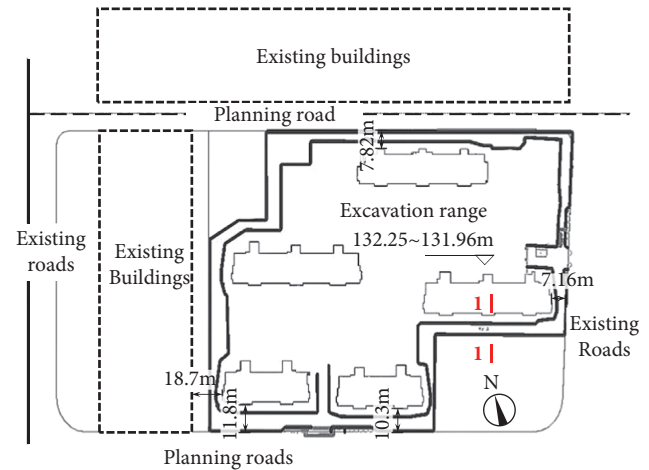
FIGURE 1: Surrounding environment of this excavation engineering.

vibrating wire sensors may be interfered by the field construction in the test process, and the survival ratio and data reliability will be reduced. Therefore, sensors should be properly selected and arranged during the field test.

In this study, we will first introduce the actual building excavation project of a deep soil-filled site in Jinan and explain the structure form of double row steel pipe piles composite supporting system. After this, introduce the plan of field tests of this foundation pit in excavation and loading conditions that were conducted. Based on the measured data of piles and anchors, the results of field tests will then be discussed. Finally, some important conclusions from this work will be presented.

2. Practical Case of Foundation Pit

2.1. Project Overview. The construction site is located in Shizhong District, Jinan, Shandong province. The miscellaneous fill of this site is mainly silty clay, construction trash, and domestic garbage. The thickness of this soil layer filled is 1.10~18.40 m, and the average value is 9.44 m. Investigation of the hydrogeological environment showed that there is no underground water trace in the depth range of the proposed site. The investigation of the engineering environment showed that the silty clay layer is under the miscellaneous fill layer of this site. The foundation type of the proposed main structure is the pile-raft composite foundation. The retaining structure of this excavation project adopts the double row micropiles and anchors composite retaining structure. The construction unit adopts a vertical excavation plan, and the excavation depth is 5.70~7.14 m. There are existing roads to the east and west of the construction boundary, planning roads will be built close to the north and south boundary, and existing residential building areas were located to the west and north boundary. The specific distribution of the construction area and surrounding environment is shown in Figure 1.

2.2. Design of Composite Retaining Structure. The safety level of the excavation project retaining structure of this
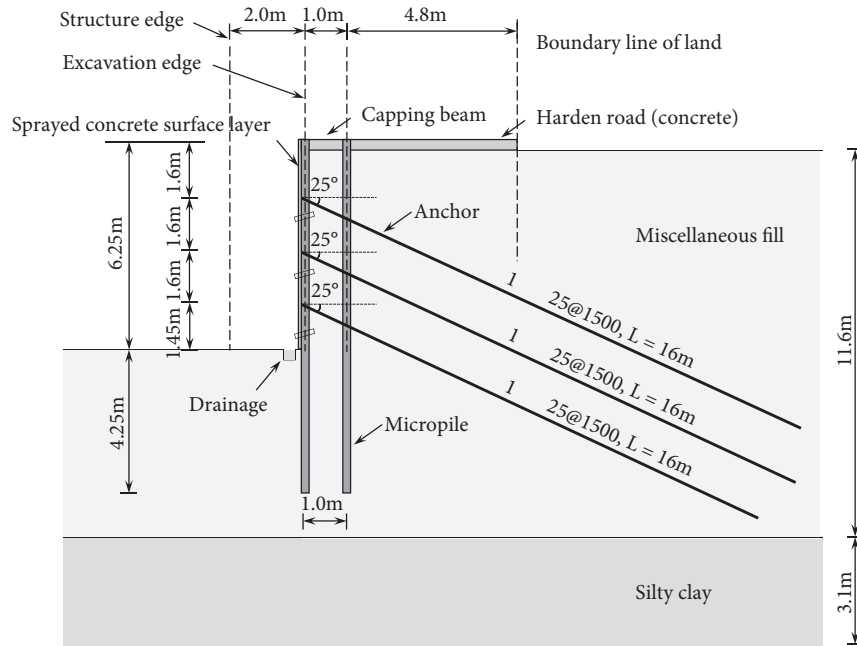
FIGURE 2: Typical section of double row steel pipe micropile composite retaining structure.

construction project is level 2, and its design work life is 18 months. The distance between the foundation line of the external wall and the bottom line of the vertical slope is 2.0 m. The schematic diagram of typical section 1-1 (shown in Figure 1) of the composite retaining structure system of double row steel pipe micropiles is shown in Figure 2. The outer diameter of the steel pipe which the micropile used is 159 mm, and the pipe thickness is 8 mm. Steel pipes should be placed in the pre-bored hole, then start cement grout pouring. Reinforced concrete cast-in-place capping beam that geometry is 1300 × 300 mm is set on the double row micropile top, and the beam is integrated with the surrounding hardened road by the cast-in-place concrete process. This excavation section is designed with three prestressed steel bar anchors, all of them have a dip Angle of 25° and a locking value of 50 kN. The horizontal spacing of each anchor is 1.5 m and the vertical spacing is 1.6 m. One steel bar (type is HRB400, diameter = 25 mm) is adopted for the anchor body, and a transverse channel steel waist beam is arranged at the anchor head. The excavation was divided into three stages. After the completion of each layer of excavation, anchors and 80 mm steel mesh hanging shotcrete surface layer belonging to this layer are constructed.

2.3. Construction Process. In the field construction of double row steel pipe micropile composite retaining structure, the hole sinking and grouting of steel pipe pile are first carried out. After the construction of steel pipe piles is completed, the reinforced anchor and shotcrete surface layer are applied along with the layered excavation of soil until the excavation reaches the basement. Figure 3 shows the key construction process of the double row steel pipe micropile composite retaining structure.

3. Field Test of Foundation Pit Excavation and Loading Condition

3.1. Field Test Scheme. The typical double-row steel pipe micropile composite retaining structure position of 1-1 section which was located on the south side of the excavation area was selected as the test area. The supporting structure layout of the test area is shown in Figure 4. In this field test, different sensors were installed to double-row steel pipe piles and steel anchor rods. Continuous monitoring was carried out for the double row steel pipe pile composite retaining structure in the excavation process and the loading-unloading process at the slope top of the foundation pit. Based on the monitoring data obtained, the working situation and retaining mechanism of the double row steel pipe micropile and steel bar anchor in deep miscellaneous fill excavation are analyzed. To ensure the accuracy of the test results, sensors were arranged for three groups of adjacent double-row steel pipe piles (i.e., every single pile from 1# to 6# in Figure 4) and one group of anchors.

Specifically, the steel pipe pile surface along the length of a certain distance arranged on the surface of the pile, to sense the deformation and internal force changes of the steel pipe pile under different working conditions, the sensor type selected ZX-FBG-S02D steel structure strain sensor with a range of $\pm 1500 \mu \varepsilon$, accuracy 0.5% F.S. The data acquisition device is TV-200 portable fiber grating demodulation instrument. By getting the central wavelength drift caused by deformation and temperature of the grating from this device, the relationship between wavelength drift and strain or temperature is established according to the following formula:

$$\frac{\Delta \lambda_B}{\lambda_B} = (1 - P_e)\varepsilon + (\alpha + \xi)\Delta T, \tag{1}$$
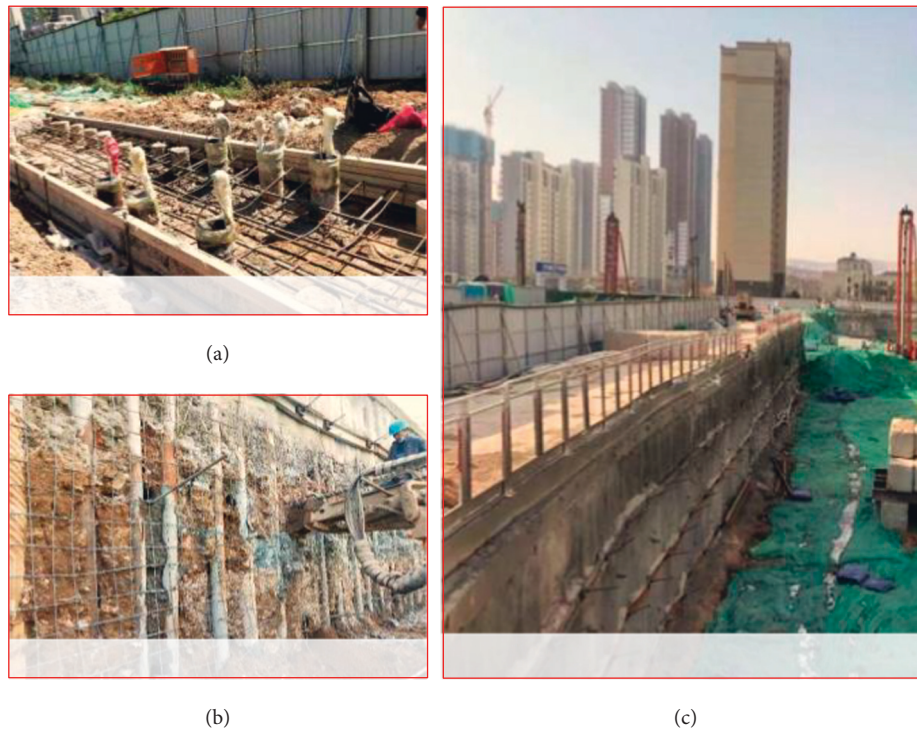
FIGURE 3: Double row steel pipe pile composite support construction process. (a) Micropiles and capping beam. (b) Anchor construction. (c) Excavation completed.
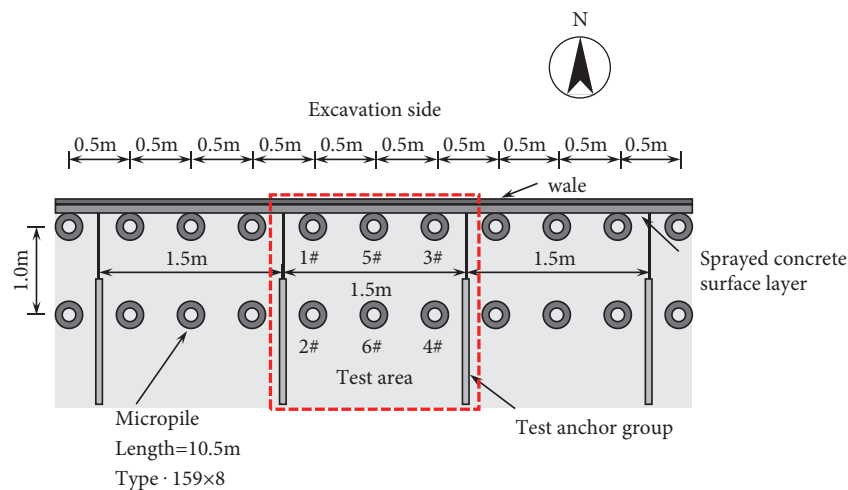
FIGURE 4: Layout plan of double row micropiles and anchors composite retaining structure test area.

where λ_B and $\Delta\lambda_B$ are the central wavelength and its variation value of FBG respectively, P_e is the effective elastic-optical coefficient, ε is the strain variable perceived by the fiber sensor, and α and ζ are the thermal expansion coefficient and thermal-optical coefficient of the fiber sensor respectively.

Through the above formula, the change of the perceived physical quantity can be obtained according to the change of the central wavelength of the fiber Bragg grating. The fiber grating strain sensor layout scheme and testing equipment are shown in Figure 5.

The fiber Bragg grating (FBG) steel bar axial force sensors are arranged on the free part and the anchor part to obtain the axial force variation of the anchor body under different working conditions. ZX-FBG-F100 steel bar axial force sensors are selected for the anchor monitoring, with the range of 0~400 MPa and the accuracy of 0.5% F·S. Axial force sensors are installed by welding, and its basic principle is the same as that of the fiber Bragg grating strain gauge. The difference is that the axial force sensors indirectly calculate the steel bar stress and axial force through the strain perceived by the grating. In this study, TV-200 portable fiber Bragg grating demodulation instrument is used for data collection for both two different sensor types. The layout scheme and testing equipment of the FBG reinforcement

(a)

(b)

(c)
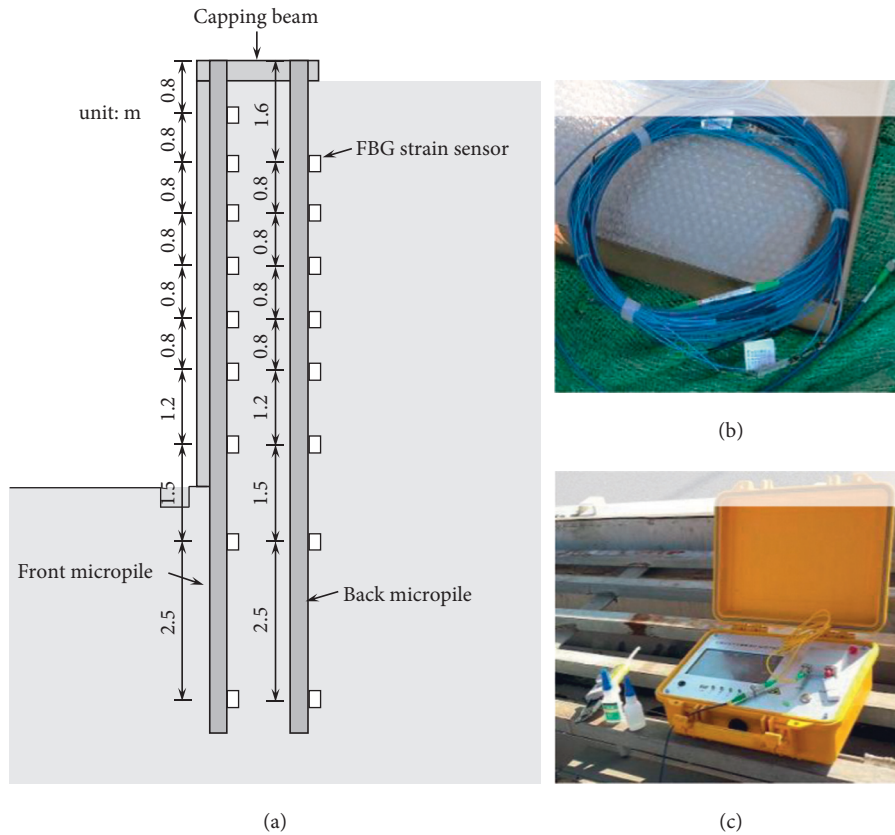
FIGURE 5: Micropile sensors layout plan and testing equipment. (a) Experimental setup of micropile. (b) FBG strain sensor. (c) FBG signal demodulator.
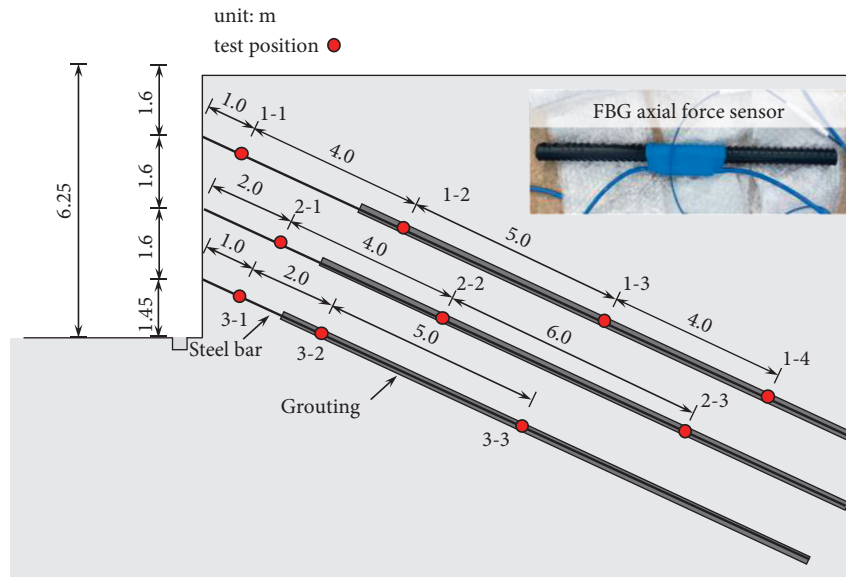
FIGURE 6: Anchor sensor layout.

dynamometer for reinforcement anchors are shown in Figure 6.

3.2. Sensor Installation. Because the using environment of geotechnical sensors is generally bad, it is vulnerable to failure and disturbance. In order to ensure the safety of the test sensors during the installation and use phase, it is necessary to protect and encapsulate them. To reduce the effect on the performance of the sensor installation and protection measures, patch type grating strain sensor using bonding agent paste in polishing surface of the steel pipe

(a)

(b)

FIGURE 7: Steel pipe pile and anchor sensor installation. (a) Installation of FBG strain sensor. (b) Installation of FBG axial force sensor.

pile, using anhydrous alcohol clean the paste surface before paste. After being pasted firmly, put all the single fiber Bragg grating strain sensors in series, and grating position coating glue to seal sensors. The transmission fiber was fixed by adhesive tape and protected by structural adhesive coating along the length of the fiber. The fiber end was left on the top of the slope for data collection.

When fiber Bragg grating reinforcement was arranged on the anchor body. The anchor body for this test was cut off at the predetermined measuring point of the test scheme, and then the anchor was welded with the sensor connector. Finally, a layer of structural adhesive was coated on the surface of the anchor for protection. Sensors installation of pile body and anchor is shown in Figure 7.

3.3. Field Test of Supporting Internal Force under Excavation Condition

3.3.1. Stress Variation of Steel Pipe Micropile under Excavation Condition. After all kinds of sensors were set up, the initial strain value of all sensors was measured as the starting value before the excavation work started, and the body edge of the front and back pile strain was monitored during the excavation. Due to the interference of the construction process, the data of some measuring points could not be obtained or the distortion was serious. Therefore, a group of double-row steel pipe micropiles (1# and 2# piles) with relatively complete data collection were selected for analysis.

Figure 8 shows the stress distribution of the front and back steel pipe micropiles when the soil is excavated to 2.5 m and the bottom of the foundation pit (at this time, the excavation depth is 6.25 m and the embedded depth of steel pipe micropiles is 4.25 m). The stress value is converted by the strain value, to get strain data, the strains were measured
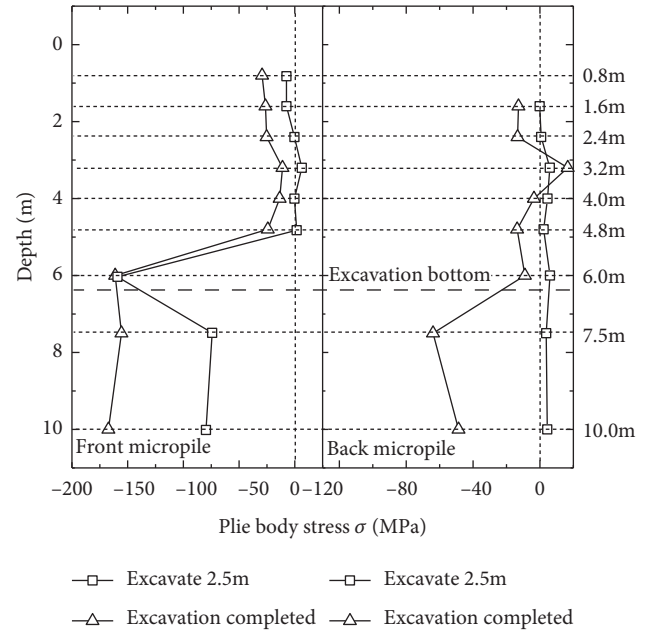
FIGURE 8: Stress distribution of pile at different excavation depths.

by the fiber Bragg grating strain gauge and obtained by conversion according to (2) according to the elastic theory. The E_s is the elastic modulus of steel, value is 2.06×10^5 MPa.

$$\sigma_s = \frac{\Delta\lambda_B}{(1 - P_e)\lambda_B} \cdot E_s. \tag{2}$$

With the construction of the layered excavation of excavation project, the stress distribution of the cross-section of the double row steel pipe micropiles changed significantly, and the internal force distribution situation of the front and back micropile was very different. When the soil was excavated to 2.5 m, the front pile stress in the depth range of 0~4.8 m did not change significantly, but there was a mutation point of pile stress at the 6.0 m measuring point, which was 161.1 MPa.

According to the data of each measuring point below the mutation point, the pile body stress gradually decreases with the increase of depth. When excavated to the bottom of the excavation, the stress distribution in the steel pipe micropile was similar to that in the 2.5 m excavation, and the micropile stress increased further. The stress in the upper part of the micropile increased by about 20 MPa in the range of 0~4.8 m, while the stress increment measured below the depth of 6.0 m is about 81.4~87.5 MPa, the increment range is 90%.

In addition, the stress variation of the back steel pipe micropile is significantly different from that of the front steel pipe micropile under the same working conditions. When the soil was excavated to 2.5 m, the stress of the back pile body changed slightly and was evenly distributed along the pile length, and the maximum stress of the pile body is only 6.1 MPa, which reveals that the back steel pipe micropile has not fully entered the working state at this time, and the front steel pipe pile bears most of the soil load. When excavated to the bottom of the pit, the back row micropile gradually works and its stress distribution changes. At this time, part of

the stress of the steel pipe micropile increased in the depth of 0~6.0 m, and tensile stress occur on the soil side of the steel pipe micropile at the measuring point 3.2 m below the excavation slope top. Different from the steel pipe micropile in the front row, the stress value does not abruptly change at the bottom of the excavation pit, and the position of the abrupt change moves down to about 1.5 m from the bottom of the pit. Below the abrupt change point, the pile stress gradually decreases with the increase of the depth. By comparing the same excavation condition front and back row pile body stress distribution, in the mass, the change of stress value of the front steel pipe micropile is greater than the back steel pipe micropile. It is shown that the front steel pipe micropile plays a more important role in bearing soil pressure, and because the front micropile limits the displacement of soil behind the slope surface, and back row micropile bearing capacity is limited. When the excavation continues, because the soil displacement increases further, the back row steel pipe micropile begins to work and contribute to its capacity, so there is an obvious lag in the work situation of the back row steel pipe micropile.

Therefore, some emphasis should be placed on points of the design composite double row steel pipe micropiles retaining structure. Considering the large force of the front row steel pipe micropiles, the section parameters of the front row steel pipe micropiles may be appropriately increased, and the section parameters of the back steel pipe micropiles may be reduced as appropriate, by this way to improve the mechanical performance and economy of this kind of composite support structure. In addition, it can be seen from the deformation and stress distribution of the back row piles that the micropile body stress above the embedded section changes little, while the stress value of the micropile below the foundation pit bottom is large.

3.3.2. Stress Variation of Anchor under Excavation Condition.

Figure 9 shows the axial force test results of the group of three test anchors from top to bottom. Among them, the data of measuring points 1-4 of the top anchor and measuring points 2-3 of the anchor in the second row are partially missing. According to the test results, when the construction of the upper anchor was completed, the axial force of the anchor is small and evenly distributed due to the shallow excavation depth. With the gradual excavation of the soil, the axial force of the anchor increases by 45%~60%, and the axial force of the anchor along its length is still evenly distributed.

During the middle anchor was prestressed to excavation finished, the axial force of the middle anchor is larger than other anchors in different layers, and its axial peak value is about 135 kN, The axial force increases evenly and gradually with the excavation process.

Axial force values of the bottom anchor at each measuring point are small under different working conditions, indicating that the double row steel pipe micropiles and the upper anchor can effectively suppress the deformation of the supporting soil. In addition, the axial force of the bottom anchor body attenuated significantly when it was transferred
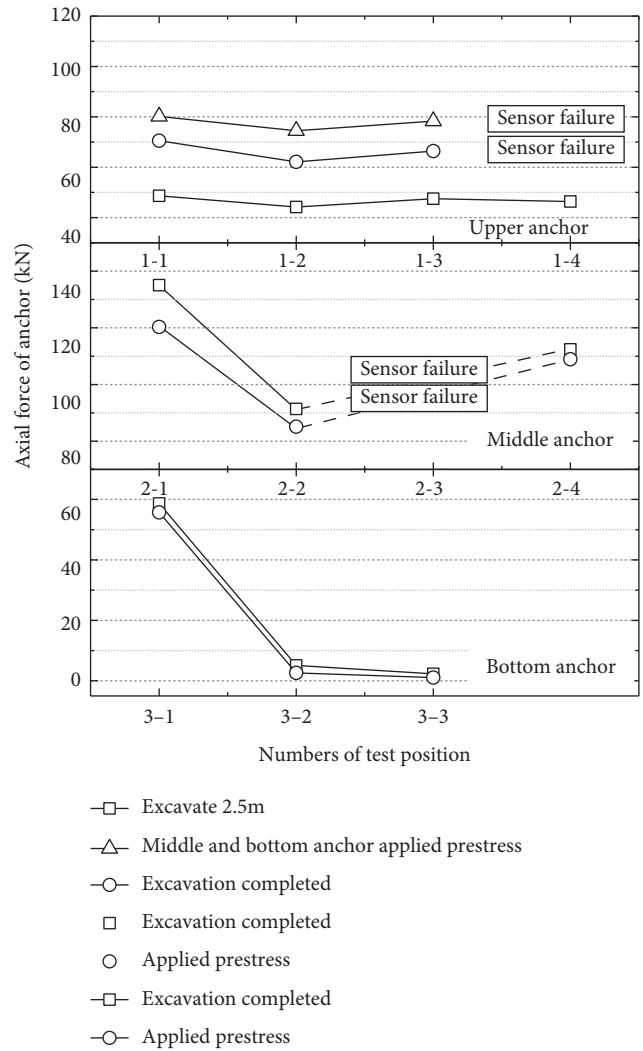
FIGURE 9: Axial force distribution of each row of anchors under different working conditions.

from the free part to the anchor part, while the axial force tended to be stable within the measuring point 3-2~3-3 in the anchor part, and the axial force of the anchor part was small, only about 5 kN.

3.4. Experimental Study on Slope Top Loading and Unloading Test.

After the foundation pit was excavated to the design bottom, in-situ pile foundation testing equipment and counterweight were used to carry out loading and unloading tests on the top of the foundation pit slope, and the variation tendency of pile stress and axial force of anchor in double row steel pipe micropile composite retaining system with or without load is analyzed.

In this section, the distance between the load position of counterweight blocks and the edge line of the foundation pit top was 2.0 m, and the load action was divided into two times with each stage load 25 kPa (i.e., apply design load and 2 times design load). Value changes in micropile stress and anchor axial force were recorded after each load stabilization and unloading. The layout of the test site is shown in Figure 10.

FIGURE 10: Arrangement of loading and unloading test.
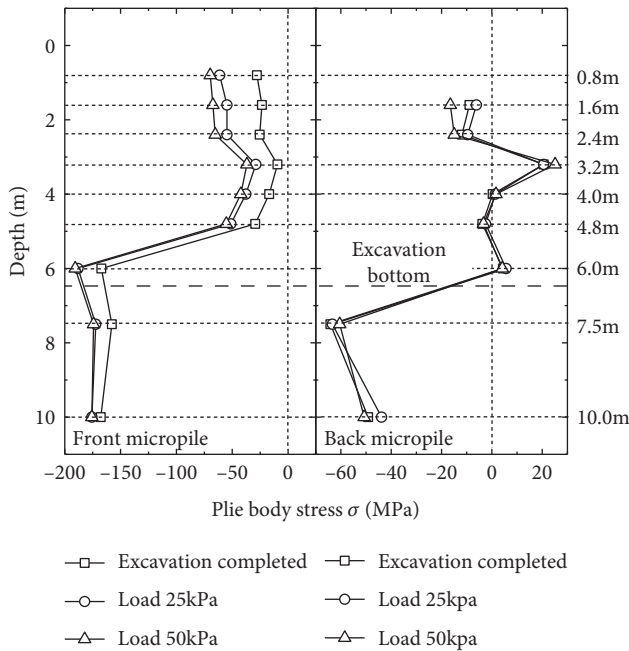
FIGURE 11: Stress distribution of steel pipe pile before and after loading.

FIGURE 12: Comparison of stress distribution of pile in excavation completed, loading, and unloading condition.

3.4.1. Stress Variation of Steel Pipe Micropile under Loading and Unloading Conditions. The change of pile body stress of front and back steel pipe piles during slope top loading are shown in Figure 11. The pile body stress of the front row micropile increases significantly after the initial loading, and the pile body stress above the excavation bottom increases about 115.7%~205.3%. Loading causes a severe impact on the working state of front row piles. Therefore, if the bending stiffness of front row piles is low, the micropile composite structure may lead to excessive deformation, buckling, or even damage during service. These phenomena will cause slope collapse and damage to the foundation pit. The pile body stress of the front row micropiles under the bottom also increases, but the relative increment is smaller than the part above the bottom.

The stress distribution of the pile body has not changed significantly under the two loading conditions of the back pile compared with the unloading condition, and the loading has little influence on the working state of the back pile, which can be almost ignored. This phenomenon reveals that the material of this micropile is partially damaged due to loading and cannot be completely recovered after unloading [8].

Figure 12 shows the comparison of stress distribution of the front and back steel pipe micropiles before loading (i.e., excavation completed), loading stage finished (i.e. apply 50 kPa pressure), and unloading on the foundation slope. After unloading, the pile body stress of the front steel pipe pile has not fully recovered to the state before loading, under the double design load, the unrecoverable plastic deformation occurs in the miscellaneous fill soil, and the pile body stress of the back steel pipe micropile has slightly changed in the whole process. The reason for this phenomenon may be explained that the under-consolidated miscellaneous fill soil behind the excavation surface being deformed due to the loading. The recoverable deformation of the soil after unloading is small. After unloading, the front row steel pipe piles are constrained by the soil and cannot return to the initial state before deformation. The back row steel pipe micropiles are less affected by this factor due to their small stress and deformation. There is no significant change in the stress of the back row micropile before and after unloading.

3.4.2. Variation of Axial Force of Anchor Rod under Loading and Unloading Conditions. In the process of unloading, the distribution of axial force along the anchor body of three test anchors in the group was tested. The axial force test results of

Figure 13: Axial force distribution of each row of anchor rod body before and after loading.

increment percent is about 45~60%. However, the anchor axial force of other layers did not change a lot. This means during the foundation pit excavation, the proportion of earth pressure that is resistant by upper anchors is gradually increased. Thus, attention should be paid to the upper anchor in the design work.

In the Experimental study on slope top loading and unloading test, With the increase of the slope top load, the absolute value of the front pile stress increases obviously, and the absolute value of pile stress increases with the increase of depth. The back pile stress increases not obviously. Under the condition of slope top load, the absolute value of the front pile is larger than that of the back pile. When slope top load = 25 kPa, the maximum stress of the front pile is about 2.45 times that of the back pile. When slope top load = 50 kPa, the maximum stress of the front pile is about 2.9 times of that of the back pile. It shows the importance of the front pile in this composite retaining structure. The performance of these test anchors in the loading and unloading test reveals that during the first loading process, the miscellaneous filling soil behind the excavation is consolidated, resulting in the redistribution of the stress field so that the axial force of anchors does not change significantly in the second loading and unloading process. At the same time, the displacement of miscellaneous fill behind the excavation caused by the loading on the top of the slope is constrained by double-row steel pipe micropiles and upper anchor anchors. The influence range of loading on the support system is limited to the middle and upper layers of the excavation slope, so the axial force of the bottom anchor body is effectively reduced.

the anchor body in each layer are shown in Figure 13. The axial force of the first row of anchor increased significantly after the first loading of 25 kPa. After the loading increased to 50 kPa and the unloaded phase, the axial force of the tested anchor did not increase or decrease significantly. Similar to the upper anchor, the axial force of the middle anchor also increased significantly during the first loading phase, and the overall stress distribution and values of the anchor changed little during the subsequent loading and unloading process. After the first loading phase, the axial force of the free part of the bottom anchor was decreasing, and the axial force of the anchor part is similar to that before loading, but there is no significant floatation in the axial force of the bottom anchor in the subsequent loading and unloading process.

4. Discussion

4.1. Test Result Analysis. During the whole process of excavation, the absolute value of stress of the front pile is larger than that of the back pile, and the maximum value of the front pile is about 2.16~2.42 times that of the back pile. With the excavation of the foundation pit to the bottom, the axial force of upper anchors presents a sharp change, the

4.2. Suitability of Double Row Steel Piles Composite Structure in Deep Fill Site. Due to the low strength and complex composition of deep fill soil, the retaining structure form of the foundation pit excavation is limited. Step-slope excavation and soil nailing wall may cause large deformation when use in deep foundation pit with poor soil strength. Due to the large boulder and construction waste in the deep filling soil, it is difficult to carry out cement soil mixing reinforcement and high-pressure rotary jet grouting reinforcement. The reinforced concrete pile or wall retaining structure may lead to high cost, long construction period, and large consumption of cement materials, using these structure forms is not helpful for environmental protection.

As a new composite retaining structure, double row steel piles and anchors composite retaining structure has several advantages, such as short construction period, low cement consumption, and better retaining performance (compared to soil nail and soil reinforcement method). But it needs to be pointed out that the bending stiffness of this composite structure is weaker than the large reinforced pile or wall retaining structure. Therefore, with the increase of foundation pit design depth, its economy gradually decreases, and its optimal application depth is 6~10 m.

4.3. Other Possible Applications in Civil Engineering. The application instance of double row steel piles and anchors

composite retaining structure in a deep fill site showed that this retaining structure form is suitable for supporting weak soil layers. Meanwhile, its good economic property makes it easier to promote applications. Besides the foundation pit excavation engineering, this retaining structure form also has the suitability for slope sliding resistance structure or reinforced measures, or other engineering projects.

5. Conclusions

In this study, field tests for the double row steel piles and anchors composite retaining structure in a deep fill site with excavation and loading conditions were carried out. Based on these test results, the distribution of double row micropile stress and anchor axial force of piles is revealed. Some main conclusions can be drawn:

(1) It is feasible to apply the double row steel pipe micropile composite retaining system to the excavation in the deep miscellaneous fill area. In addition, material strength advantages of steel pipe pile and steel bar anchor can be brought into full play.

(2) During the excavation, the absolute value of stress of the front pile is larger than that of the back pile, and the maximum value of the front pile is about 2.16~2.42 times that of the back pile. The stress of the back pile in the double row steel piles and anchors composite retaining structure system is less than the front one, the soil load is preferentially borne by the front pile. There is a lag before the back pile starts working. In loading and unloading tests, the loading on the top of the slope has a severe impact on the working state of the front row piles and the influence on the back pile is relatively small. After unloading, the stress of the pile body of the front pile does not completely recover to the initial state, while the stress of the back pile body has slightly changed. Based on the above experimental results, the engineering economy may be improved by reducing the bending stiffness of the back pile or enhancing the bending stiffness of the front pile. Meanwhile, it is important to control the stacking on the top of the slope.

(3) The field test shows that the axial force of the middle and upper anchor is greater than the bottom anchor of the foundation pit. With the excavation of the foundation pit, the axial force of upper anchors presents a sharp change, the increment percent is about 45~60%. While the axial force value of the bottom anchor is small under different working conditions. Resistance redundancy of structure components like middle and upper anchors should be increased in the design phase of the excavation project.

(4) Optimal application depth in deep fill foundation pit of the double row steel piles and anchors composite retaining structure is 6~10 m. Based on the performance and the good economy of this composite structure, besides the foundation pit excavation engineering, this composite structure form may have the suitability for slope sliding resistance structure or reinforced measures, or other engineering projects.

Data Availability

Some or all data that support the findings of this study are available from the corresponding author upon reasonable request.

Conflicts of Interest

There is no conflicts of interest regarding the publication of this paper.

References

[1] J. Liu and X. Hou, *Foundation Pit Engineering Manual*, pp. 139-140, China Construction Industry Press, Beijing, 1997, in Chinese.

[2] Z. L. Chen, J. Y. Chen, and H. Liu, "Present status and development trends of underground space in Chinese cities: evaluation and analysis," *Tunnelling and Underground Space Technology*, vol. 71, pp. 253–270, 2018.

[3] P. Wang, *Analysis of Mechanical Response of Deep Foundation Pit Micropile Supporting*, Chang'an University, Xi'an, China, 2018, in Chinese.

[4] Y. Shi, *Study the Model Test and the Design Method of Miniature Steel Pipe Piles Composite Soil Nailing wall*, Nan'chang University, Jiang'xi, China, 2015, in Chinese.

[5] J. Wang, J. Han, J. Chen et al., "Experimental and numerical study on the dynamic response of a superthick backfill subgrade under high-speed railway loading: a case study of Qianjiang-Zhangjiajie-Changde Railway," *Journal of Construction Engineering and Management*, vol. 148, 2022.

[6] Z. Xu, *Based on Deformation Control of Composite Soil Nailing Wall with Steel Micro-pile Finite Element Analysis Method and Application*, University of Jinan, Jinan, Shandong, P. R. China, 2016, in Chinese.

[7] J. Han, D. Liu, Y. Guan et al., "Study on shear behavior and damage constitutive model of tendon-grout interface," *Construction and Building Materials*, vol. 320, Article ID 126223, 2022.

[8] F. Ding, X. Wu, and P. Xiang, "New damage ratio strength criterion for concrete and lightweight aggregate concrete," *ACI Structural Journal*, vol. 118, no. 6, pp. 165–178, 2021.

[9] S. W. Sun, B. Z. Zhu, and J. C. Wang, "Design method for stabilization of earth slopes with micropiles," *Soils and Foundations*, vol. 53, no. 4, pp. 487–497, 2013.

[10] T. Fu and X. Lu, "Finite element analysis of double row grouting steel pipe pile foundation pit support structure," *Smart city*, no. 3, 202 pages, 2017, in Chinese.

[11] L. Qi, Z. Meng, and C. Sun, "Static load test of steel pipe pile based on weak-reflection fiber gratings," *Building Structure*, vol. 51, no. S2, pp. 1645–1650, 2021, in Chinese.

[12] G. Shao, J. Sun, and W. Huanwei, "Design and construction technology of foundation pit supporting on heavy

miscellaneous fill layer," *Building Technology*, vol. 42, no. 8, pp. 727–730, 2011, in Chinese.

[13] M. J. Thompson, "Experimental load transfer of piles subject to lateral movement," in *Proceedings of the Transportation Scholars Conference*, Iowa, IA, USA, 2004.

[14] T. D. Richards and M. J. Rothbauer, "Lateralloads on pin piles(micropiles)," in *Proceedings of the Geosupport Conference*, pp. 158–174, Orlando, FL, USA, December 2004.

[15] P. C. Prat, "Numerical investigation into the failure of a micropile retaining wall," *Computers and Geotechnics*, vol. 81, pp. 262–273, 2017.

Research Article

Full-Scale Laboratory Test of Cutting Large-Diameter Piles Directly by Shield Cutterhead

Yuqing Wang,[1] Xinyu Wang [ID],[2] Yangyang Xiong,[1] Zhuangzhi Yang,[1] and Jie Zhang[1]

[1]*China Railway Tunnel Group Co Ltd., Guangzhou 511458, China*
[2]*School of Civil Engineering, Henan Polytechnic University, Jiaozuo 454000, China*

Correspondence should be addressed to Xinyu Wang; wangxinyu2010@163.com

Based on the TBM tunnel of Red Line of Tel Aviv in Israel, this paper carried out laboratory tests of shield cutting concrete and reinforced concrete piles and investigated cutting performance of cutter, failure model of rebars, length of damaged rebars, and cutter vibration. The results indicate that under the condition of low tunneling speed and rotating speed, vibration of the cutterhead is small, and vibration of the center cutterhead is more obvious in the radial direction of the cutterhead. Cross sections of broken rebars mainly consist of shear section, tensile-shear section, tensile-compressive section, and bending section. Considering the tunnel status, it is recommended to adopt excavation speed of 3~5 mm/min, and rotating speed of 1.0~1.3 r/min. While cutting RC piles, the principle of "low excavation speed, high rotating speed, and less disturbance" is recommended. Cutting with disc cutters is efficient and the torque of which is stable but the length of the rebars got from cutting varies a lot. It is recommended that majorities of the cutters shall be disc cutters and supplemented with drag bits and tear cutters.

1. Introduction

In order to solve the problem of traffic congestion and make full use of the underground space, subway/metro tunnels have been constructed in cities worldwide. Due to the complex construction environment in cities and limitations of alignment planning of the tunnel, tunnels adjacent to the existing piles of buildings appear frequently [1–4]. In particular cases, tunnels are passing through the existing piles [5–7]. The shield tunneling method is widely used in tunnel engineering, for its advantage of safety, efficiency, high mechanization degree, and small disturbance. Compared to the methods of tunnel rerouting and pile underpinning [6, 8], cutting the piles directly using the shield cutter is more economical and efficient when shield tunnels pass through the existing reinforced concrete (RC) piles, and it has wide application prospects. During the process of shield cutting piles, parameters configuration of cutter and shield working is crucial. Therefore, it is important to execute laboratory or field tests of cutting RC piles by shield cutterhead before practical engineering application.

In recent years, most studies mainly focus on the effects of shield tunneling on existing pile foundation [1, 2, 9–14], and report related to cutting the RC piles by shield is few. Based on the construction of Suzhou metro in China, field test of shield cutting RC piles was carried out, wear and damage of the modified rippers were studied by Li et al. [7]. Wang et al. [15–17] presented a field test on shield cutting of obstacle piles, and the shield working parameters were analyzed. Based on the construction of shield cutting of bridge piles, Yuan et al. [18] studied feasibility of a new style cutter for shield cutting large-diameter RC Piles. Field test of shield cutting was presented by Chen et al. [19] to investigate variation characteristics and cutting parameters. Du et al. [20] and Xu et al. [21] executed laboratory tests of direct cutting RC piles by shield cutterhead, combination scheme of disc and tearing cutters, and reasonable cutting parameters were proposed.

Cutting the piles directly using the shield has been used in some practical engineering. However, as an emerging technology, cutting the RC piles directly by shield is not mature yet. The shield cutter which is specifically used to cut

the obstacle RC piles is still absent. Variation characteristics of cutter and cutting parameters are still in the exploratory stage and phenomena of cutter wear and cutterhead wound by rebar are widespread in practical engineering.

Based on the TBM tunnel of Red Line of Tel Aviv in Israel, laboratory tests of shield cutting concrete and reinforced concrete piles were carried out, cutting performance of cutter, failure model of rebars, length of damaged rebars, and cutter vibration were investigated through the TBM comprehensive experimental platform, thus to provide reasonable cutting parameters for cutting pile foundation in the TBM tunnel segment.

2. Project Overview

Red Line of Tel Aviv LRT project (Western Segment) is located in center of Tel Aviv in Israel. TBM tunnel (Western Segment) located between Herzl Street and Ben Gurion station is the major part of the underground works, as shown in Figure 1. It consists of twin-bore single-track tunnels with segmental lining with an inside diameter of 6.5 m having a total length of approximately 5.5 km. The shield with a diameter of 7.54 m, a maximum thrust force of 55000 kN, a nominal torque of 12000 kN·m, and a maximum rotating speed of 3.8 r/min is adopted to build the tunnel.

TBMs will be launched a Herzl shaft, then bore through Allenby station, and be lifted out at Karlibach station. The tunnels will underpass the Ayalon river and the railway tracks (Figure 2) between the Galei Gil shaft and the Arlozorov station. On both sides of the Ayalon river bed, Ayalon retaining wall structures are located. The eastern retaining wall is located about 20 m from the Galei Gil launching shaft and supports Ayalon North highway. The western retaining wall supports the railway tracks and is located about 30 m from the Galei Gil launching shaft. These retaining walls are partially supported by piles, as described in detail in the next clause. The TBM will encounter these obstacles immediately after launching. On the west bank of the river, an L-shape reinforced concrete retaining wall on pile shafts foundations was constructed, the foundation of this wall consists of two rows of piles with a diameter of 1 m and 12 m in depth. And pile foundations intruded into the tunnel are listed in Table 1.

3. Experiment Design

In order to verify the performance of shield cutter in directly cutting square and circular piles, disc cutters are installed on the cutter head and square and circular piles are symmetrically arranged in the rock disc. The pile foundation is made of C35 grade concrete, and M5 grade cement mortar is filled between the square and the circular piles.

The parameters measured in the experiment mainly include the performance of the cutter in cutting circular and square piles, the vibration characteristics of the cutters, the failure form of the steel bars, and the shield tunneling parameters. On this basis, the feasibility of cutting circular and square piles by cutter is evaluated.

3.1. Arrangement of Cutters. Fourteen 17-inch cutters with a constant cross-section are adopted in both working conditions, including six double-edge cutters (1#-6#) and eight single-edge cutters (7#-14#), as shown in Figure 3.

3.2. Arrangement of Piles in Rock Disc. In the experiment, piles are similar to Ayalon River piles that TBM#6 and TBM# 5 will be encountered. In order to simulate Ayalon piles, the circle-section pile and the square-section pile are paralleled and placed to be cast. The diameter and reinforcement of the circle-section pile and the square-section pile are approximately the same as Ayalon piles.

The diameter of the rock disc of the TBM comprehensive platform [22] is 2500 mm, the cutting diameter of the cutter is 2280 mm and the thickness of the simulated rock layer is 500 mm. The square and circular piles are arranged in parallel in the same rock disc at a ratio of 1 : 1. The circular piles form a structure with a diameter of 1200 mm and the square piles with a size of 450 mm × 400 mm. The two structures are symmetrically arranged in the disc, spaced at 280 mm. The main reinforcement bars of the circular and square piles are made of Φ25 threaded steel, and the stirrups are Φ12 plain round bars.

In order to simulate the condition, where the piles are buried deep and the built-in steel bars extend longer, the main bars and stirrups are welded and fixed during the experiment, and the top of the piles is covered with a 50 mm-thick test tunneling layer. The circular and square piles are arranged in the rock disc as shown in Figure 4.

3.3. TBM Comprehensive Experimental Platform. The TBM comprehensive experimental platform [22] of the State Key Laboratory of Shield Machine and Boring Technology is adopted in the experiment, as shown in Figure 5. The TBM comprehensive experimental platform mainly consists of a mechanical structure, hydraulic pump station, tunneling device, rotating device, spiral conveyer, and its control system. It is used either vertically or horizontally to conduct experiments on various concrete samples with its cutters made of different materials and at different cutter spacings, cutting speeds, and feed rates. Based on these statistics, the cutting efficiency and cutter service life are analyzed, thus providing cutters of appropriate material with appropriate arrangements for different projects. The experimental parameters of the TBM comprehensive experimental platform are listed in Table 2.

4. Experiment Results Analysis

4.1. Parameters of TBM Comprehensive Platform

4.1.1. Initial Value of Force on Cutter. Figure 6 shows the data of the total thrust and penetration speed of the cutters before they contact the rock disc (idle thrust). In this stage, the piles have not been cast by the cutters, and the trends of the tunneing speed can be divided into two periods: (1) From the period of 9 : 44 : 03 to 9 : 45 : 21, the maximum
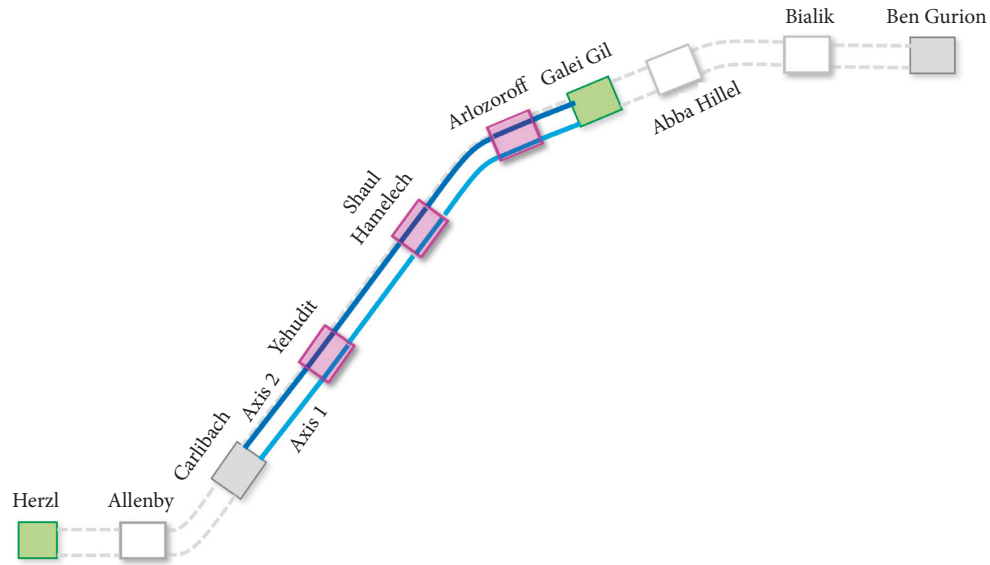
FIGURE 1: Red line.

FIGURE 2: Aylalon river.

penetration speed fed back by the cutter head is 53.7 mm/min, and the maximum thrust reaches 1778.2 kN. When the penetration speed of the cutters is controlled at 50.7–53.7 mm/min, it is generally positively correlated with the total thrust. The total thrust increases with the increase of the penetration speed control value and then remains stable at 1765.6–1778.2 kN. (2) At the period of after time 9 : 45 : 21, when the penetration speed of the cutters sharply decreases from 53.7 mm/min to zero at the time of 9 : 45 : 21, the total thrust would not decrease as rapidly. After time 9 : 45 : 21, the total thrust firstly decreases from 1778.2 kN at the time of 9 : 45 : 21 to 1465.4 kN at the time of 9 : 45 : 47. Then, it remains stable at 1595.8–1637.6 kN with increasing penetration speed of the cutters.

The cutters stop penetrating forward and are in an idling state. By controlling the rotating speed at 0.36–0.48 r/min, the torque fluctuates at 28.4–30.2 kN·m. Figure 7 shows the torque and rotating speed under idling conditions.

4.1.2. Cutting of Concrete Layer by Cutters. Set the penetration speed of the cutters. The average feedback value is 9.47 mm/min and the rotating speed is 0.61 r/min. The total thrust and torque when cutting the concrete layer are shown in Figure 8. It can be seen that the total thrust and torque of the cutters gradually increase at the constant penetration speed and rotating speed mentioned above, and the two parameters are strongly correlated.

Figure 9 shows the variation of the feedback values of cutter penetration and rotating speed when cutting the concrete layer. As can be seen from the figure, due to the step characteristics of the cutter in concrete breaking, the vibration amplitude of penetration varies greatly, ranging from 0 mm/min to 38.78 mm/min. Compared with the set value, the cutter torque varies little, ranging from 0.516 kN·m to 0.662 kN·m.

However, the cutter penetration speed and rotating speed mentioned above cannot meet the requirements for stable and efficient concrete breaking, and it is necessary to increase the rotating speed or change the penetration speed.

Increase the penetration speed, The average feedback value is 17.25 mm/min. The variation of total thrust and torque over time is shown in Figure 10. It can be found that when the penetration speed is increased, the total thrust and torque grow rapidly. The instantaneous maximum total thrust reaches 3862.5 kN, and the instantaneous maximum torque reaches 387.1 kN·m. When driving at the maximum penetration speed for a moment, the cutters get stuck and gradually stop rotating, and the torque gradually decreases to 0.

Set the penetration speed. The average feedback value is 6.47 mm/min. After the rotating speed of the cutters is increased to 1.03 r/min, the variation of the total thrust and torque over time is shown in Figure 11. As demonstrated in this figure, when the rotating speed of the cutters is increased, the total thrust and torque first increase rapidly and then decrease slowly, indicating that compared to a higher

TABLE 1: Pile foundations intruded into the tunnel.

Diameter (m)	Length (m)	Space (m)	Concrete grade	Length of the pile intruded into the tunnel (m)	Number of the pile intruded into the tunnel
1.2	12	2.8	B40	7.84	2
1	12	4.7	B40	7.14	1
1	13.5	1.1	B40	1.7	6

No.	Radius	Space
#14	1119	0
#13	1043	84
#12	959	0
#11	959	84
#10	875	84
#9	791	84
#8	707	84
#7	623	84
#6	539	168
#5	371	70
#4	301	98
#3	203	70
#2	133	98
#1	35	
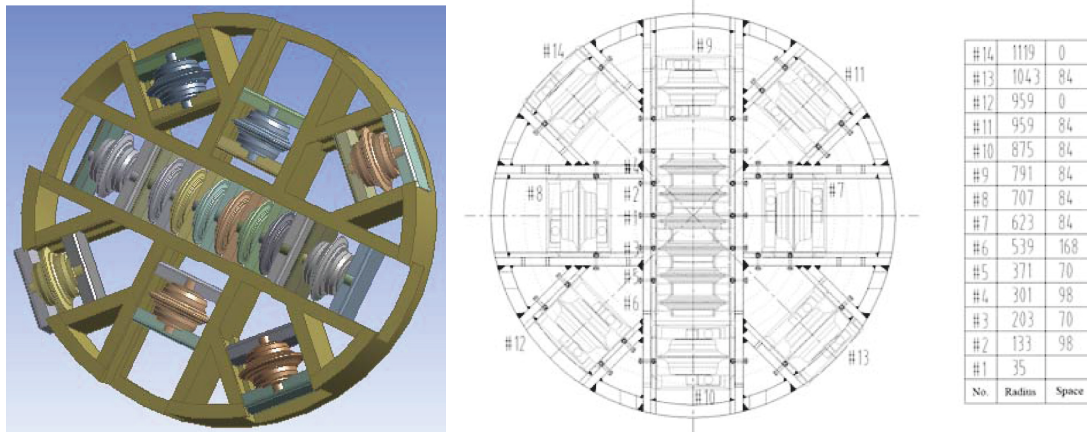
FIGURE 3: Arrangement of cutters.

FIGURE 4: Arrangement of circular and square piles in rock disc.

FIGURE 5: TBM comprehensive experimental platform.

rotating speed, a lower penetration speed results in lower efficiency of concrete breaking and a lower rate of energy utilization.

4.1.3. Cutting of Reinforced Concrete Layer by Cutters. When cutting the reinforced concrete layer, the average feedback value for the penetration speed of the cutters is 10.8 mm/min, and the rotating speed is 0.54 r/min. Figure 12 shows the variation of total thrust and torque over time. As can be seen from the figure, the instantaneous maximum total thrust is 4051.9 kN, and the instantaneous maximum torque is 380.72 kN·m. When the cutters work stably for a

TABLE 2: Main performance parameters of TBM comprehensive experimental platform.

Parameters	Value
Overall dimensions	6880 mm × 4050 mm×5176 mm
Total weight	120T
Max. Cutting diameter	2280 mm
Mould box dimensions	φ2500 mm × 1000 mm
Torque	250 kN·m
Max. Rotating speed	6rpm
Thrust force	400T
Power	250 kW
Cutter size	431.8 mm
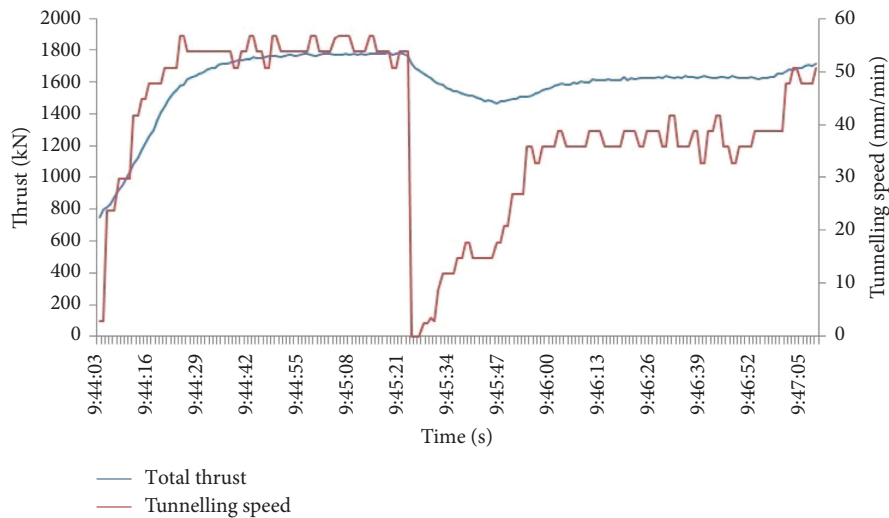
FIGURE 6: Variation of total thrust and penetration speed over time.
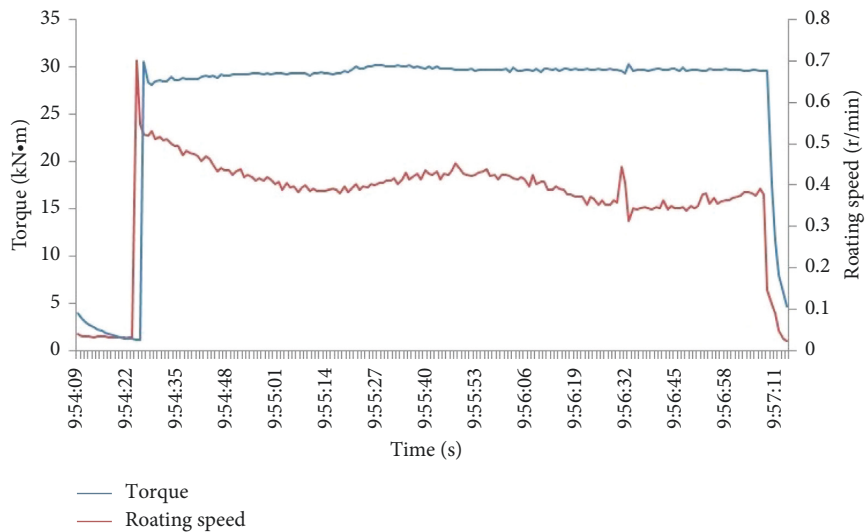
FIGURE 7: Variation of torque and rotating speed over time.

while, the torque reaches its maximum and the cutters get stuck, causing the torque to decrease to 0.

By comparing the thrust and torque during cutting concrete and cutting reinforced concrete (Table 3), it can be found that the thrust and torque needed for cutting concrete are apparently less than those for cutting the rebar layer. Through observation (of noise and vibration) during the test and monitoring of parameters, to ensure efficient excavation
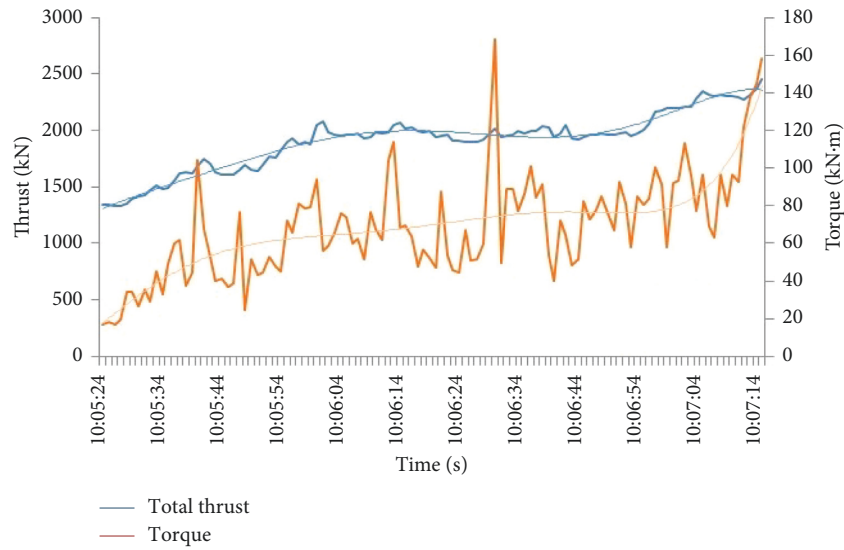
FIGURE 8: Variation of total thrust and torque over time.
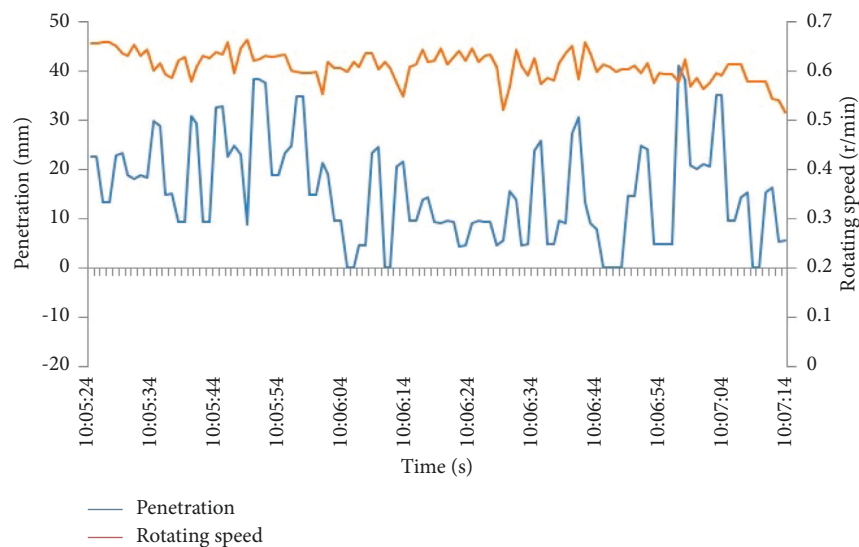
FIGURE 9: Variation of feedback values of penetration and rotating speed over time.

and to avoid stuck of the machine, the most appropriate parameters for cutting C35 concrete with disc cutters are 9.47 mm/min $\leqq$ penetration speed $\leqq$ 17.25 mm/min and rotating speed $\leqq$ 0.61 r/min; for the reinforced concrete, the penetration speed shall be around 8.36 mm/min and no more than 13.30 mm/min. Certainly, increasing the rotating speed could make a higher penetration speed, so it is suggested to set the rotating speed to slightly more than 1.0 r/min.

4.2. Failure Modes of Rebars

4.2.1. Bending Forms of Rebars. Figure 13 shows some of the rebars in the reinforced concrete cut by the cutters. As can be seen from the figure, there are many long rebars in the cut

ones, and some of them are severely bent. This is due to the following three reasons: (1) the rebars are not welded firmly at the ends and the welded points break apart under tensile force when cut by the cutters; (2) the concrete strength is low and is in complicated stress state, which causes the cutter force on the rebars to be transferred to the concrete, resulting in the breaking of the concrete directly under the rebars [23]. Meanwhile, the rebars deform greatly due to compression but their loss of tensile strength is small; and (3) after the ends of the rebars are broken, the rebars are continuously twisted and deformed under the rotation of the cutters.

4.2.2. Cross Section of Broken Rebars. Cross-section types of the rebars broken by the cutters mainly include shear
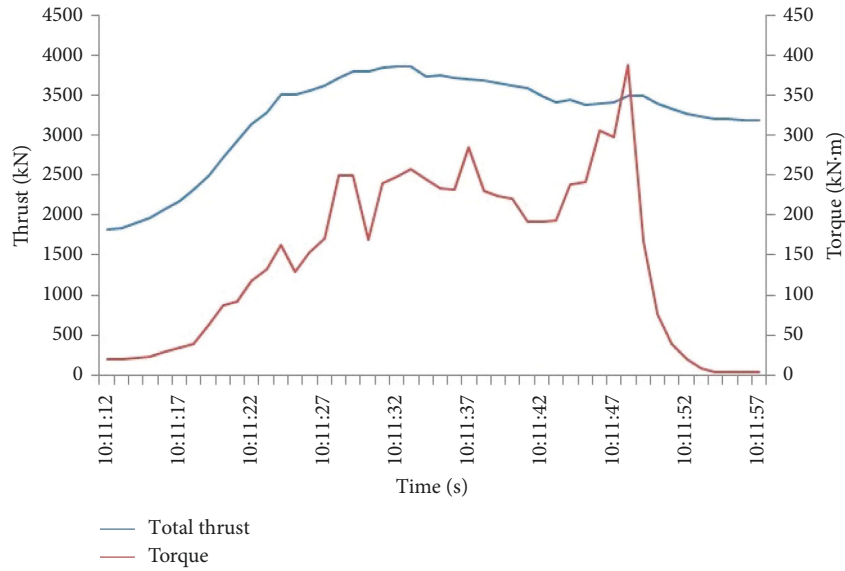
FIGURE 10: Variation of total thrust and torque over time.
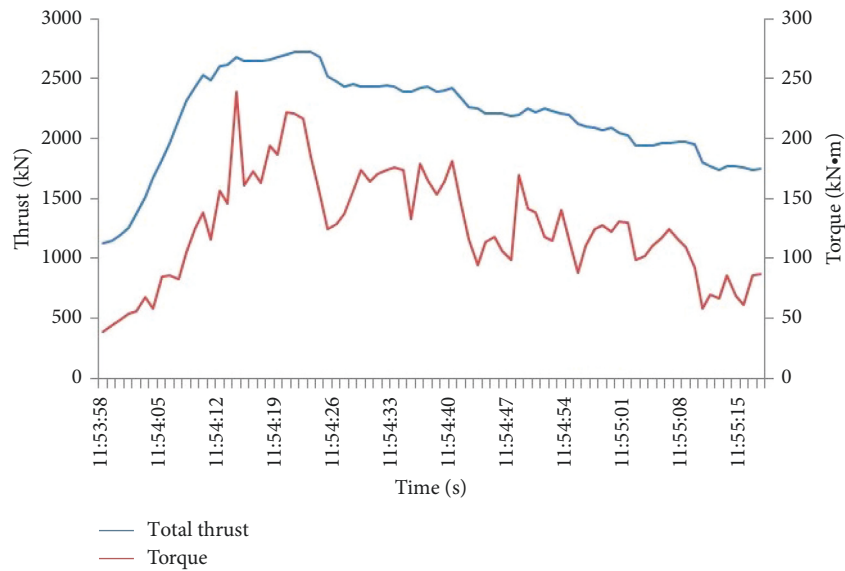
FIGURE 11: Variation of total thrust and torque over time.

section, tensile-shear section, tensile-compressive section, and bending section, as shown in Figure 14. Among them, the shear section is caused by the relative displacement between the rebar directly under the cutter and the one on its side under compression of the cutter. This type of cross section is smooth and reflective, with an obvious sign of one-way movement and accounting for 20% of the total countable sections. The tensile-shear section is caused by the combined action of the tensile stress of the rebar and the shear stress of the cutter. With a sign of one-way movement, it is granular and not smooth, accounting for 30% of the total countable sections. The tensile-compressive section is caused by the combined action of compression and tensile stress on the rebar. Featured by a smaller section area and a granular surface, it accounts for 10% of the total countable sections. The bending section is caused by brittle fracture of the weak surface such as cracks due to bending of the rebar under rotation of the cutter. This type accounts for 40% of the total countable sections.

4.2.3. Length of Damaged Rebars. Statistics of damaged rebars from the testing of cutting C35 reinforced concrete with disc cutters are shown in Figure 15. The damaged rebars include (1) the rebars on both sides damaged by disc cutters, and (2) the rebars damaged by disc cutters on one side and
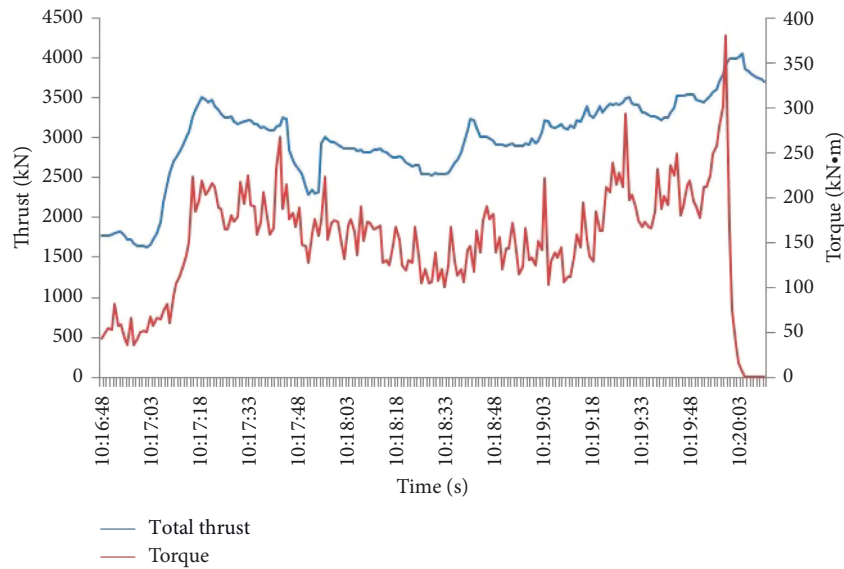
Figure 12: Variation of total thrust and torque over time.

Table 3: Test results for cutting C35 reinforced concrete layer with disc cutters.

Position of cut	Penetration speed (mm/min)	Rotating speed (r/min)	Total thrust (kN)		Torque (kN·m)		Evaluation of test results
			Ave.	Max.	Ave.	Max.	
	9.47	0.61	1942	—	72	—	No stuck, low efficiency
Concrete layer	17.25	0.61	—	3862	—	387	Stuck
	6.47	1.03	—	2500	—	200	No stuck, low efficiency
Reinforced concrete layer	8.36	0.57	2980	3512	206	275	Relatively stable
	13.30	0.51	3200	4052	200	381	Stuck

Figure 13: Rebars in the reinforced concrete cut by the cutters.

damaged between the welded points on the other side. Both sides of the rebars damaged by disc cutters shall be deemed as countable.

It could be concluded from the figure that countable rebars with a length within 0–600 mm constitute 76.92% of the total amount. Countable rebars with a length of more than 1000 mm are of 14.29% of the total amount, which could be argued that after cutting one side of the rebar, stress

is released and thus disc cutters make less damage to the rebars. The rebars are not cut off but twisted, so the shrink of the cross-section is less, making it harder to cut.

4.3. Vibration of Cutters. Table 4 shows the vibration of cutters during the test. It can be seen that when cutting the concrete layer at low excavation speed and low rotating

(a)

(b)

(c)

(d)
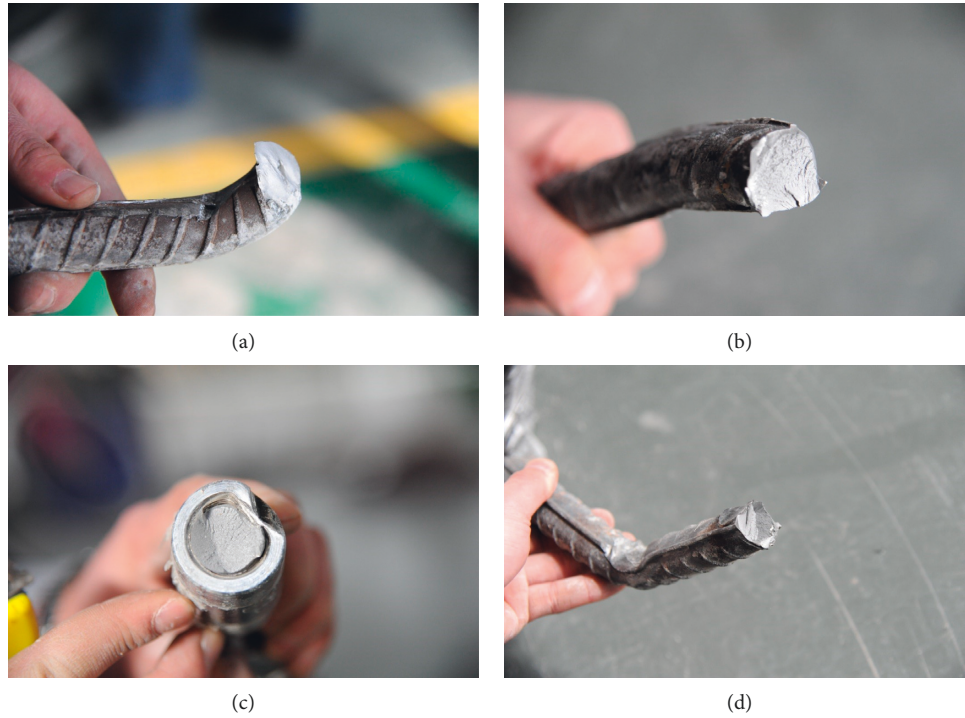
FIGURE 14: Cross section of broken reinforcement. (a) Shear section; (b) Tensile-shear section; (c) Tensile-compressive section; and (d) Bending section.
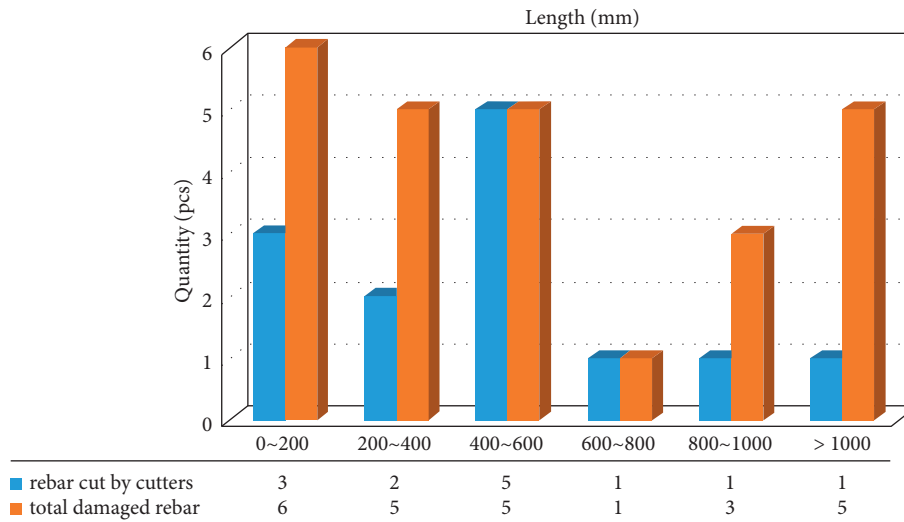
FIGURE 15: Length of damaged rebars.

TABLE 4: Vibration of the cutters.

| Position of cut | Center cutter holder | | 9# cutter holder |
	Axial vibration acceleration of cutter (g)	Radial vibration acceleration of cutter (g)	Circumferential vibration acceleration of cutter (g)
Concrete layer	−0.563–0.495	−0.929–1.077	—
Reinforced concrete layer	−0.952–1.272	−3.714–3.084	−2.188–1.556

Figure 16: Cutters after test.

speed, the vibration acceleration of the center cutter holder is -0.929~1.077 g in the radial direction of the cutter and -0.563~0.495 g in the axial direction of the cutter.

When cutting the reinforced concrete layer, the center cutter holder vibrates violently with an acceleration of -3.714~3.084 g in the radial direction of the cutter, and an acceleration of -0.95 g~1.272 g in the axial direction of the cutter. The vibration acceleration of the 9# cutter holder is -2.188~1.556 g in the circumferential direction of the cutter. Based on the analysis abovementioned, it can be concluded that for the structural design of the TBM comprehensive platform, when cutting the reinforced concrete layer, the vibration of the center cutters is strongest and then weakens as it goes outward.

4.4. Wear of Cutters. As the C35 reinforced concrete layer cut by the cutters is only 500 mm thick, the wear of the cutters cannot be measured. The cutters used in the test are brand new 27-inch cutters provided by China Railway Engineering Equipment Group Co., Ltd. Figure 16 shows the cutters after cutting the C35 reinforced concrete layer.

5. Conclusions

Based on the TBM tunnel of Red Line of Tel Aviv in Israel, laboratory tests of shield cutting concrete and reinforced concrete piles were carried out, cutting performance of cutter, failure model of rebars, length of damaged rebars, and cutter vibration were investigated through the TBM comprehensive experimental platform. Based on the results, the following conclusions could be summarized.

(1) Under the condition of low tunneling speed and rotating speed, vibration of the cutterhead is small, and vibration of the center cutterhead is more obvious in the radial direction of the cutterhead.

(2) Long rebars exist in the cut rebars, and some of them are severely bent. Cross sections of broken rebars mainly consist of shear section, tensile-shear section, tensile-compressive section, and bending section.

(3) Considering the tunnel status, it is recommended to adopt an excavation speed of 3~5 mm/min, rotating speed of 1.0~1.3 r/min. While cutting RC piles, the principle of "low excavation speed, high rotating speed, less disturbance" is recommended to increase the capability of cutting rebars.

(4) Cutting with disc cutters is efficient and torque of which is stable but the length of the rebars got from cutting varies a lot. It is recommended that majorities of the cutters shall be disc cutters and supplemented with drag bits and tear cutters.

Data Availability

All data generated or analyzed during this study are included in this published article.

Conflicts of Interest

The authors declare that they have no conflicts of interest or personal relationships that could have appeared to influence the work reported in this paper.

Acknowledgments

References

[1] C. Liu, Z. X. Zhang, and R. A. Regueiro, "Pile and pile group response to tunnelling using a large diameter slurry shield – case study in Shanghai," *Computers and Geotechnics*, vol. 59, pp. 21–43, 2014.

[2] C. Li, Z. L. Zhong, G. N. He, and X. R. Liu, "Response of the ground and adjacent end-bearing piles due to side-by-side twin tunnelling in compound rock strata," *Tunnelling and Underground Space Technology*, vol. 89, pp. 91–108, 2019.

[3] Y. J. Jeon, S. C. Jeon, S. J. Jeon, and C. J. Lee, "Study on the behaviour of pre-existing single piles to adjacent shield tunnelling by considering the changes in the tunnel face pressures and the locations of the pile tips," *Geomechanics and Engineering*, vol. 21, pp. 187–200, 2020.

[4] K. Huang, Y. W. Sun, D. Q. Zhou, Y. J. Li, M. Jiang, and X. Q. Huang, "Influence of water-rich tunnel by shield tunneling on existing bridge pile foundation in layered soils," *Journal of Central South University*, vol. 28, no. 8, pp. 2574–2588, 2021.

[5] T. Ishimura, M. Metoki, and M. Shimizu, "Development of removed pile method with cutting," *Tunnelling and Underground Space Technology*, vol. 21, no. 3-4, pp. 411-412, 2006.

[6] C. R. Zhang, Y. J. Zhao, Z. Zhang, and B. Zhu, "Case study of underground shield tunnels in interchange piles foundation underpinning construction," *Applied Sciences*, vol. 11, no. 4, p. 1611, 2021.

[7] X. G. Li, D. J. Yuan, X. Q. Jiang, and F. Wang, "Damages and wear of tungsten carbide-tipped rippers of tunneling machines used to cutting large diameter reinforced concrete piles," *Engineering Failure Analysis*, vol. 127, Article ID 105533, 2021.

[8] Q. W. Xu, H. H. Zhu, X. F. Ma et al., "A case history of shield tunnel crossing through group pile foundation of a road

bridge with pile underpinning technologies in Shanghai," *Tunnelling and Underground Space Technology*, vol. 45, pp. 20–33, 2015.

[9] F. Chen, C. He, X. Li, and B. Wang, "Construction schemes for shallow and asymmetrically loaded tunnels crossing below a bridge," *International Journal of Geomechanics*, vol. 20, no. 7, Article ID 04020098, 2020.

[10] Y. Q. Li and W. G. Zhang, "Investigation on passive pile responses subject to adjacent tunnelling in anisotropic clay," *Computers and Geotechnics*, vol. 127, Article ID 103782, 2020.

[11] P. L. Li, Y. Q. Lu, J. X. Lai, H. Q. Liu, and K. Wang, "A comparative study of protective schemes for shield tunneling adjacent to pile groups," *Advances in Civil Engineering*, vol. 2020, pp. 1–16, 2020.

[12] Z. Li, Z. Q. Chen, L. Wang, Z. K. Zeng, and D. G. Gu, "Numerical simulation and analysis of the pile underpinning technology used in shield tunnel crossings on bridge pile foundations," *Underground Space*, vol. 6, no. 4, pp. 396–408, 2021.

[13] Y. X. Zheng, Z. P. Hu, X. Ren, R. Wang, and E. X. Zhang, "The influence of partial pile cutting on the pile-anchor supporting system of deep foundation pit in loess area," *Arabian Journal of Geosciences*, vol. 14, no. 13, p. 1229, 2021.

[14] K. Huang, Y. W. Sun, J. He, X. Q. Huang, M. Jiang, and Y. J. Li, "Comparative study on grouting protection schemes for shield tunneling to adjacent viaduct piles," *Advances in Materials Science and Engineering*, vol. 202119 pages, Article ID 5546970, 2021.

[15] F. Wang, D. J. Yuan, C. W. Dong, B. Han, H. R. Nan, and M. S. Wang, "Study on cutter configuration for directly shield cutting of large-diameter piles," *China Civil Engineering Journal*, vol. 46, no. 12, pp. 127–135, 2013.

[16] F. Wang, D. J. Yuan, C. W. Dong, B. Han, H. R. Nan, and M. S. Wang, "Test study of shield cutting large-diameter reinforced concrete piles directly," *Chinese Journal of Rock Mechanics and Engineering*, vol. 32, no. 12, pp. 2566–2574, 2013.

[17] Y. L. Wang, J. C. Li, and S. M. Liao, "Numerical simulation and measured data analysis of pile group cutting by shield: a case study of running tunnel on line No. 9 of Shenzhen metro," *Tunnel Constrction*, vol. 37, no. 2, pp. 192–199, 2017.

[18] D. J. Yuan, F. Wang, C. W. Dong, B. Han, and M. S. Wang, "Study on new-style cutter for shield cutting large-diameter reinforced concrete pile," *China Journal of Highway and Transport*, vol. 29, no. 3, pp. 89–97, 2016.

[19] H. F. Chen, D. J. Yuan, F. Wang, and M. S. Wang, "Study on shield cutting parameters when cutting big diameter piles," *China Civil Engineering Journal*, vol. 49, no. 10, pp. 103–110, 2016.

[20] C. D. Du, J. Zhang, and Z. X. Tang, "Key technologies of shield direct cutting pile foundation," *Tunnel Constrction*, vol. 39, no. 10, pp. 1–12, 2019.

[21] H. G. Xu, K. Chen, and Z. C. Sun, "Laboratory test of reinforced concrete pile foundation cutting by shield cutterhead," *Tunnel Constrction*, vol. 40, no. 1, pp. 35–42, 2020.

[22] Y. D. Yang, Z. C. Sun, F. Y. Li, B. Zhang, and H. G. Xu, "Research on upgrading of TBM boring modal experiment platform," *Tunnel Constrction*, vol. 40, no. 11, pp. 1570–1577, 2020.

[23] F. Ding, X. Wu, P. Xiang, and Z. Yu, "New damage ratio strength criterion for concrete and lightweight aggregate concrete," *ACI Structural Journal*, vol. 118, no. 6, pp. 165–178, 2021.

Research Article

Grading Evaluation of Goaf Stability Based on Entropy and Normal Cloud Model

Tianxing Ma ⬤,[1] Yun Lin ⬤,[1,2] Xiaobin Zhou ⬤,[1] and Mingzhi Zhang ⬤[1]

[1]*School of Resources and Safety Engineering, Central South University, Changsha 410012, China*
[2]*State Key Laboratory of Strata Intelligent Control and Green Mining Co-Founded by Shandong*
 Province and the Ministry of Science and Technology, Shandong University of Science and Technology, Qingdao 266590, China

Correspondence should be addressed to Yun Lin; yunlin617@163.com

Aiming at the fuzziness and randomness of goaf stability classification, to obtain goaf stability classification more objectively, an entropy weight-normal cloud model for goaf stability classification is proposed. Based on the geological conditions and engineering conditions, 14 indexes that affect the stability of a goaf are selected to establish an evaluation index system, and the weight of each index is determined using the entropy weight method, which makes the weight distribution more objective. Based on the cloud model theory, the cloud numerical characteristics of each evaluation index belonging to goaf stability level are calculated, and a corresponding cloud model is generated. Combined with the entropy weight, the comprehensive certainty degree is calculated, and the evaluation results are obtained. Taking 25 mined-out areas in Xishan mine of Shandong Gold Mining and the Dabaoshan mine as examples, the model is used for stability evaluation, and the evaluation results are basically consistent with the actual situation, which proves the feasibility of the method and provides a new and effective method for stability evaluation of mined-out areas.

1. Introduction

With the rapid development of the economy, the demand for mineral resources is increasing. This demand can only be met by increasing the mining volume of mineral resources. Currently, the main way to obtain mineral resources is through underground mining. This process will inevitably lead to mined-out areas [1], and most shallow resources will be close to depletion after long-term mining. The depth of underground mining is increasing [2], and the stability of goafs is becoming an increasingly prominent problem. Accidents such as goaf collapse, surface collapse, and roof caving often occur [3] and have become one of the main hazard sources of underground mines. Therefore, correctly evaluating the stability of a goaf is very important for safe mine production.

Much research has been performed on the stability of goafs, and results related to accurate detection [4, 5] and

stability evaluation have been achieved. There are mainly two methods used for research on the stability evaluation of goafs: numerical simulations and mathematical statistics. In terms of numerical simulations, Li and Lu [6] initiated the use of ANSYS for goaf stability evaluation, and the evaluation results were mostly consistent with the actual situation. Luo et al. [7] used Surpac to build a three-dimensional model of a mine and Phase2 software to analyse the stability of the goaf, and good results were achieved. Du et al. [3] used GTS-MADIS software to model and analyse the goaf in the Laoyachao Mine. The results were compared with the evaluation results of matter-element analysis and were similar. Kou et al. [8] accurately obtained the spatial shape information of a goaf using CMS and successfully simulated the stability of a goaf using Dimine-FLAC3D. Zhang et al. [9] used Midas-GTS to establish a four-dimensional model, simulated the stability of complex goaf groups based on the improved FLAC3D software, and achieved good results.

Some results have been achieved using the above methods, but a numerical simulation is often limited by assumptions, and the influencing factors of goaf stability are uncertain and complex. Therefore, many researchers have begun to use mathematical statistics to evaluate goaf stability. Based on the unascertained measurement theory, Gong [10] et al. established a goaf risk grade evaluation model, and the evaluation results were consistent with engineering practice. Wang et al. [11] evaluated the stability of a goaf based on the principle of fuzzy mathematics, and the results were consistent with engineering practice. Wang et al. [12] established a support vector machine mining area stability evaluation model, and the grading results were highly consistent with the results of the unconfirmed measurement method. Wang et al. [13] applied the theory of physical element analysis to establish an improved physical element topologizable model for the evaluation of the stability of a mining area and obtained more accurate evaluation results. Tang et al. [14] constructed a neural network model applicable to the evaluation of the stability of a mining area, and the evaluation results obtained were consistent with the actual situation. Jiang et al. [15] established an improved grey target model for the evaluation of the stability of a mining area, considering the influence of the evaluation indicators, which made the evaluation results more accurate. Ding et al. [16] made great contributions to the strength criterion, which has guiding significance for the stability evaluation of goafs.

The above methods have evaluated and graded the stability of goafs using different approaches, and some results were achieved. However, these methods cannot overcome the problem that the influencing factors are very complex and uncertain. However, a cloud model can be used to comprehensively solve the two uncertainty problems of randomness and fuzziness in an evaluation. Therefore, it is very important to introduce a cloud model to evaluate the stability of a goaf. In this paper, combined with the entropy weight method to determine the weight of each evaluation index, the cloud model is used to evaluate goaf stability, and the entropy weight-normal cloud model of goaf stability is established, which provides a new idea for goaf stability evaluation.

2. Entropy Weight-Normal Cloud Goaf Stability Evaluation Model

2.1. Cloud Model Theory. A cloud model, which is a mathematical model proposed by Professor Li [17], is used to realize the qualitative and quantitative transformation of uncertainty concepts. It has been successfully used in data mining, simulation prediction, decision analysis, intelligent control, and other fields.

2.1.1. Definition of a Cloud. Let M be a set represented by exact numerical values, $M = \{x\}$, which is referred to as the universe. C is a qualitative concept in universe M. If the quantitative value $x \in M$ is a random realization of qualitative concept C, the uncertainty of any element x in qualitative concept C $\mu(x) \in [0, 1]$ is a random number with

stable tendency; then, the distribution of x in universe M is called a cloud, and each x is called a cloud drop:

$$\mu : \mathrm{M} \longrightarrow [0, 1] \, \forall x \in \mathrm{M} \, x \longrightarrow \mu(x). \tag{1}$$

If $x \sim N(E_x, E_n'^2)$, is satisfied, where $E_n' \sim N(E_n, H_e^2)$, the uncertainty of C meets the following requirements:

$$\mu(x) = e^{-(x - E_x)^2 / 2E_n'^2}, \tag{2}$$

where $\mu(x)$ is the degree of certainty; x is the variable value; E_x is the expectation; and E_n' is the entropy. Then, the distribution of x in universe M is called a normal cloud distribution. A normal cloud model is the most commonly used and universal cloud model. Many relevant studies have shown that the expectation curves of cloud models with qualitative knowledge in a large part of natural science approximately obey a normal or seminormal distribution [18]. Therefore, this paper uses a normal cloud to evaluate the stability of a goaf.

2.1.2. Digital Characteristics of a Cloud. The digital characteristics of a normal cloud are determined by the expectation E_x. Entropy E_n and hyperentropy H_e as a whole reflect the quantitative characteristics and qualitative concepts of the research object, and expectation E_x is the central value of the qualitative concept in the domain of discourse, that is, the most typical sample of the quantitative concept. Entropy E_n is the measure of the fuzziness of the qualitative concept, which reflects the value range acceptable to the qualitative concept in the domain. Hyperentropy H_e is the measure of uncertainty of entropy, which reflects the dispersion degree of cloud droplets. According to the above cloud model concept, the cloud digital characteristics of the goaf stability evaluation index S for a certain level standard can be calculated according to the following formula [19]:

$$\left. \begin{array}{c} E_x = \dfrac{C_{\max} + C_{\min}}{2} \\[2mm] H_e = K \\[2mm] E_n = \dfrac{C_{\max} - C_{\min}}{6} \end{array} \right\}, \tag{3}$$

where $C_{\min}$ and $C_{\max}$ are the minimum and maximum boundary values of the corresponding grade standards, respectively, and k is a constant that can be adjusted according to the fuzzy threshold of different variables, which is taken as 0.01 in this paper. For variables with unilateral boundaries, such as $(-\infty, C_{\max}]$ or $[C_{\min}, +\infty)$, the default boundary parameters can be determined according to the lower or upper limit of the variable, and then the parameters of the cloud model can be calculated according to equation (3).

2.1.3. Cloud Generator. A cloud generator mainly includes a forward cloud generator and reverse cloud generator. A forward cloud generator can realize the transformation from a qualitative concept to a quantitative value. In other words, a

certain number of cloud droplets are generated according to the three digital characteristics of the cloud model. In contrast, a reverse cloud generator is used to realize the transformation from a quantitative value to a qualitative concept. Since the stability evaluation of a goaf is from qualitative to quantitative, a positive cloud generator is adopted in this paper. The specific algorithm steps are as follows:

(1) Calculation of entropy E_n and hyperentropy H_e based on specific grading metrics

(2) According to the calculated entropy E_n and hyperentropy H_e, a random number e of normal distribution $E_n' \sim N(E_n, H_e^2)$ are generated

(3) Based on specific input value x and expected value E_x, the uncertainty is calculated according to equation (1)

2.2. Goaf Stability Evaluation Index System.

There are many factors affecting goaf stability, and the correlation is complex. Based on the perspective of influence significance, relative independence, ease of obtaining, and ease of quantifying, 14 factors affecting goaf stability are selected as evaluation index factors in this paper [20]. These factors are the influence of the rock mass structure, geological structure, rock quality index, influence of underground visible water and underground water on the surrounding rock, influence of surrounding mining, situation of adjacent goaf, engineering layout, span, area, height, size and layout of the ore pillar, burial depth, and goaf specification, which are expressed as S_1, S_2, S_3, S_4, S_5, S_6, S_7, S_8, S_9, S_{10}, S_{11}, S_{12}, S_{13}, and S_{14}, respectively. The rock quality index, span, area, height, and buried depth are divided into grades I, II, III, and IV, which represent extremely stable, stable, unstable, and extremely unstable classifications, respectively, according to the actual measured data. The classification standards are shown in Table 1. The rock mass structure, geological structure, underground visible water, influence of an underground water body on the surrounding rock, influence of surrounding mining, situation of an adjacent goaf, engineering layout, size and layout of the ore pillar, and specifications of the goaf are determined using a semiquantitative method. The values 1, 2, 3, and 4 correspond to grades I, II, III, and IV, respectively. The classification standards are shown in Table 2. Classification criteria refer to relevant research results [21].

2.3. Determination of the Weight of the Evaluation Index Based on the Entropy Weight Method.

The weight reflects the role of an evaluation index affecting the stability of the goaf in the overall evaluation. In this paper, the entropy weight method is used to determine the weight. Generally, the smaller the information entropy of an index is, the greater the degree of variation, the greater the amount of information it provides, and the more significant its role in the comprehensive evaluation. The weight of the corresponding index is also larger [22], so the weight of each index can be calculated through the variation degree of the index. The specific calculation steps are as follows:

TABLE 1: Classification and assignment of quantitative indexes for goaf stability evaluation.

Indicator	Stability level			
	Level I	Level II	Level III	Level IV
Rock quality (S_3), %	>60	50~60	40~50	<40
Span (S_9), m	<40	80~40	80~120	>120
Area (S_{10}), m^2	<800	800~1200	800~1200	>2700
Height (S_{11}), m	<8	8~20	20~30	>30
Depth (S_{13}), m	<100	100~200	200~400	>400

(1) Build a judgement matrix. If there are m evaluation objects and n evaluation indexes, the value of the j-th index corresponding to the i-th object is x_{ij}, and the original information evaluation matrix X can be constructed:

$$X = \begin{bmatrix} x^{11} & x^{12} & \cdots & x^{1j} \\ x^{21} & x^{22} & \cdots & x^{2j} \\ \vdots & \vdots & \vdots & \vdots \\ x^{i1} & x^{i2} & \cdots & x^{ij} \end{bmatrix}. \quad (4)$$

(2) Normalize the matrix X when the indicator is as large as possible:

$$y_{ij} = \frac{x_{ij} - \min_j(x_{ij})}{\max_j(x_{ij}) - \min_j(x_{ij})}. \quad (5)$$

When the index is as small as possible,

$$y_{ij} = \frac{\max_j(x_{ij}) - x_{ij}}{\max_j(x_{ij}) - \min_j(x_{ij})}. \quad (6)$$

(3) Calculate the contribution of the j-th index and the i-th object:

$$P_{ij} = \frac{y_{ij}}{\sum_{i=1}^{m} y_{ij}}. \quad (7)$$

If $P_{ij} = 0$, define $\ln P_{ij} = 0$.

(4) Calculate the information entropy of each index. The information entropy of the j-th index is calculated as follows:

$$E_j = -\ln(m)^{-1} \sum_{i=1}^{m} P_{ij} \ln P_{ij}. \quad (8)$$

(5) Calculate the weight of each indicator. The weight of the j-th indicator is calculated as follows:

$$\omega_{ij} = \frac{1 - E_j}{n - \sum E_j}. \quad (9)$$

2.4. Comprehensive Uncertainty.

The cloud droplets of each evaluation index are generated using a forward cloud generator, and specific data x are input to obtain the membership degree $\mu(x)$ of each evaluation index. Then, combined with the weight of each evaluation index calculated using the entropy weight method, the comprehensive

TABLE 2: Classification and assignment of qualitative indexes for goaf stability evaluation.

| Stability level | Assignment | Rock mass structure (S_1) | Geological structure (S_2) | Underground visible water (S_4) | Influence of groundwater on surrounding rock (S_5) | Influence factor | | | | Pillar size layout (S_{12}) | Specification and shape of goaf (S_{14}) |
						Impact of surrounding mining (S_6)	Adjacent empty space (S_7)	Project layout (S_8)		
Level I	1	Complete block structure	No fault and fold	No drenching trace	No water impact	The mining area is not affected by blasting operation	There is no adjacent empty area within the affected area	Reasonable	Code for pillar layout	$\theta < 1$
Level II	2	Layered structure	Small fold influence	Visible water trace of rainfall	Less impact on water body	The impact of blasting operation in the mining area is small	There is no adjacent empty area within the affected area	More reasonable	There are pillars but they are not standard	$1 \leq \theta < 2$
Level III	3	Structural fragmentation	Partial cutting or folding of fault has great influence	Heavy rainfall and drenching	General impact on water body	Large impact of blasting operation in mining area	The area and quantity of empty areas within the scope of influence are large, but they are scattered	Partially reasonable	There is no pillar or the layout is not standard and starts to be damaged	$2 \leq \theta < 3$
Level IV	4	Loose structure	Fault penetrates rock mass	Rain in rainy season	Great impact on water body	The mining area has a great impact on blasting operation	The area of empty areas within the influence range is large, the number is large, and the adjacent areas are close	Less reasonable	There is no pillar or the layout is very irregular and seriously damaged	$2 \leq \theta < 3$

uncertainty is calculated according to equations (1) and (6).
fd6

$$U = \sum_{j=1}^{m} \mu(x)\omega_j, \tag{10}$$

where $\mu(x)$ is the uncertainty of each index and ω_j is the weight of the evaluation index.

2.5. Specific Implementation Process. The basic idea of establishing a goaf stability evaluation model based on an entropy weight cloud model is to select evaluation indexes and corresponding classification standards according to the actual goaf situation and relevant data, determine the corresponding weight of each index with the entropy weight method for specific goaf data, and determine the cloud digital characteristics according to the classification standards of each index. A cloud model of each index and each grade is generated based on a forward cloud generator, and the membership degree of each index corresponding to each grade is calculated according to the measured data. Finally, the stability evaluation results of the goaf are obtained according to the maximum membership degree principle. The specific process is shown in Figure 1.

3. Engineering Application Examples

The Xishan mine of Shandong Gold Mining and the Dabaoshan mine are taken as examples. Based on the actual situation, a total of 25 goafs, 12 goafs [12] in the Xishan mine, and 13 goafs [10] in the Dabaoshan mine are selected. The value of each evaluation index is taken. The specific situation of each goaf is shown in Table 3.

3.1. Determination of the Weight of Each Index. According to the above steps, the entropy weight method is used to determine the weight of each index. When normalizing the data, the larger the rock quality (S_3) index is, the better, which is calculated using equation (5), and the smaller the other 13 indexes are, the better, which is calculated using equation (6). The weight calculation results of each index are shown in Table 4.

3.2. Cloud Model Generation. Based on the theory of a normal cloud model, the numerical feature expectation E_x, entropy E_n and superentropy H_e of the cloud model are determined according to the grading criteria of the stability evaluation index of the mining area and equation (3), and a sufficient number of cloud drops are generated using MATLAB 2016a with a forward cloud generator to generate the cloud model corresponding to each index. The cloud models for five of the rock mass indicators, span, area, height, and depth of burial are shown in Figure 2.
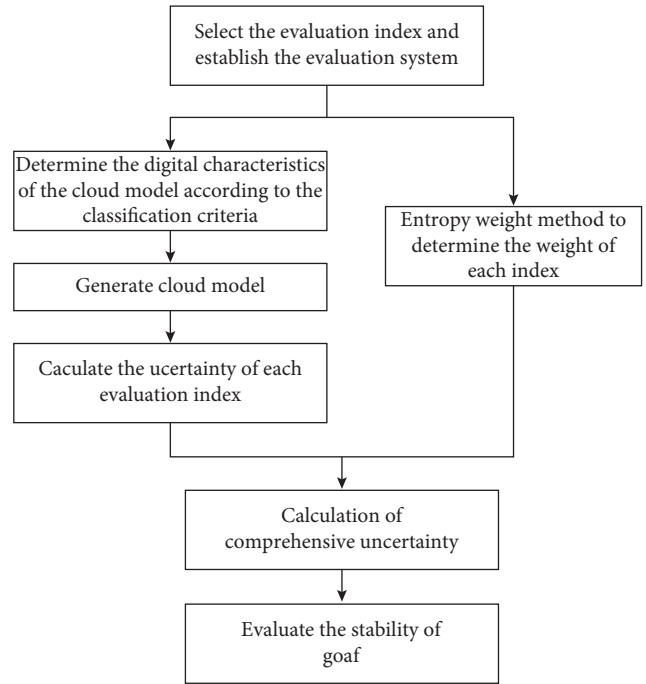
FIGURE 1: Stability evaluation process of goaf.

3.3. Goaf Stability Evaluation Results. The goaf stability evaluation results are determined by the membership degree of each evaluation index and the weight of each index in the cloud model. Goaf No. 17 is taken as an example to demonstrate the calculation process. First, according to the cloud model and the 14 corresponding index data of the goaf, the uncertainty of each index value belonging to goaf stability level 4 is generated. The comprehensive uncertainty is calculated using the weight sum equation (10) of each index determined in Table 4. The results are $U_I = 0.5808$, $U_{II} = 0.2693$, $U_{III} = 0.0378$, $U_{IV} = 0.0005$, and $U_I > U_{II} > U_{III} > U_{IV}$; see Table 5 for the specific data. According to the maximum comprehensive certainty value, it can be concluded that the evaluation result of the goaf is grade I, which represents an extremely stable goaf, and is consistent with the actual situation.

According to the above process, the stability evaluation results of the 25 goafs are calculated and compared with their actual situations, as shown in Table 6. The results show that the evaluation results are essentially consistent with the actual situation, which shows that the application of the entropy weight cloud model to evaluate goaf stability is effective and feasible. At the same time, there are many complex factors affecting goaf stability. Using the entropy weight method to determine the weight can reduce the influence of subjective factors and make the evaluation results more objective. Moreover, goaf stability is a qualitative concept. The use of a cloud model can realize the qualitative and quantitative transformation of the uncertainty concept and can convert the fuzziness and randomness of a goaf into a quantitative

TABLE 3: Measured data of influencing factors and indicators of goaf stability.

| Sample serial number | Goaf stability evaluation index | | | | | | | | | | | | | |
	S_1	S_2	S_3	S_4	S_5	S_6	S_7	S_8	S_9	S_{10}	S_{11}	S_{12}	S_{13}	S_{14}
1	1	1	59	2	3	3	2	3	125	896	170	1	71	2
2	4	4	39	3	3	4	4	2	75	703	30	1	160	2
3	2	2	38	3	3	1	4	3	185	852	145	4	298	2
4	4	4	39	2	3	1	2	4	115	734	100	4	396	4
5	4	4	58	2	3	4	4	1	445	1705	140	1	82	1
6	3	3	51	3	4	1	3	1	65	221	35	2	439	1
7	4	4	46	3	3	2	4	2	30	34	30	3	66	1
8	1	1	54	1	3	3	2	2	45	67	15	4	63	2
9	1	1	57	3	1	2	3	4	60	87	40	4	225	3
10	4	4	36	2	4	3	2	3	80	110	25	1	129	3
11	3	3	38	2	2	3	3	2	65	82	30	2	152	4
12	3	3	47	1	3	2	4	2	25	40	45	1	125	3
13	3	1	38	2	2	4	4	2	85	5190	15	4	260	2
14	2	2	56	2	2	4	4	1	60	1230	8	3	260	2
15	3	3	35	2	2	4	4	2	62	2560	14.5	4	290	3
16	3	3	47	2	2	4	4	3	160	6890	26.3	4	305	4
17	2	1	55	1	1	1	1	1	26	2870	15.8	2	305	1
18	2	1	57	2	2	4	4	1	96	2260	21	3	335	2
19	1	1	67	2	2	1	1	1	60	1200	10	1	335	1
20	1	2	53	3	3	4	4	2	85	3970	60	4	240	2
21	1	2	59	1	1	1	1	1	40	2260	15	1	305	2
22	1	1	62	2	2	1	1	1	35	1450	13	1	290	1
23	1	1	52	2	2	3	3	1	35	2590	6	1	201	1
24	1	1	55	1	1	3	3	1	65	2430	12	1	208	1
25	1	1	54	1	1	3	3	1	68	1800	10	1	208	2

Row group labels: Samples 1–12 belong to "Xishan mine of Shandong gold mining"; samples 13–25 belong to "Dabaoshan mine".

TABLE 4: Entropy of evaluation indices.

Evaluating indicator	S_1	S_2	S_3	S_4	S_5	S_6	S_7
Entropy weight	0.1151	0.0953	0.0055	0.0302	0.0596	0.1249	0.2028
Evaluating indicator	S_8	S_9	S_{10}	S_{11}	S_{12}	S_{13}	S_{14}
Entropy weight	0.0609	0.0090	0.0241	0.0268	0.1363	0.0328	0.0834

(a)   (b)

FIGURE 2: Continued.

(c)

(d)

(e)
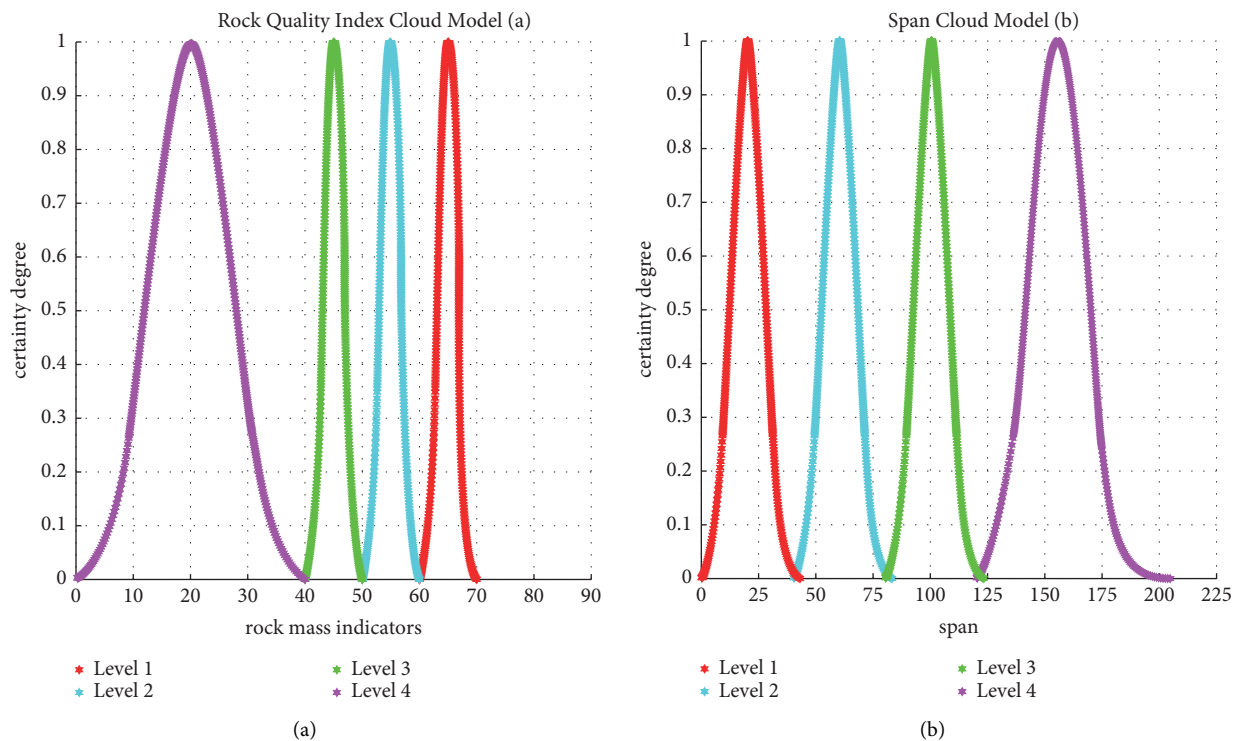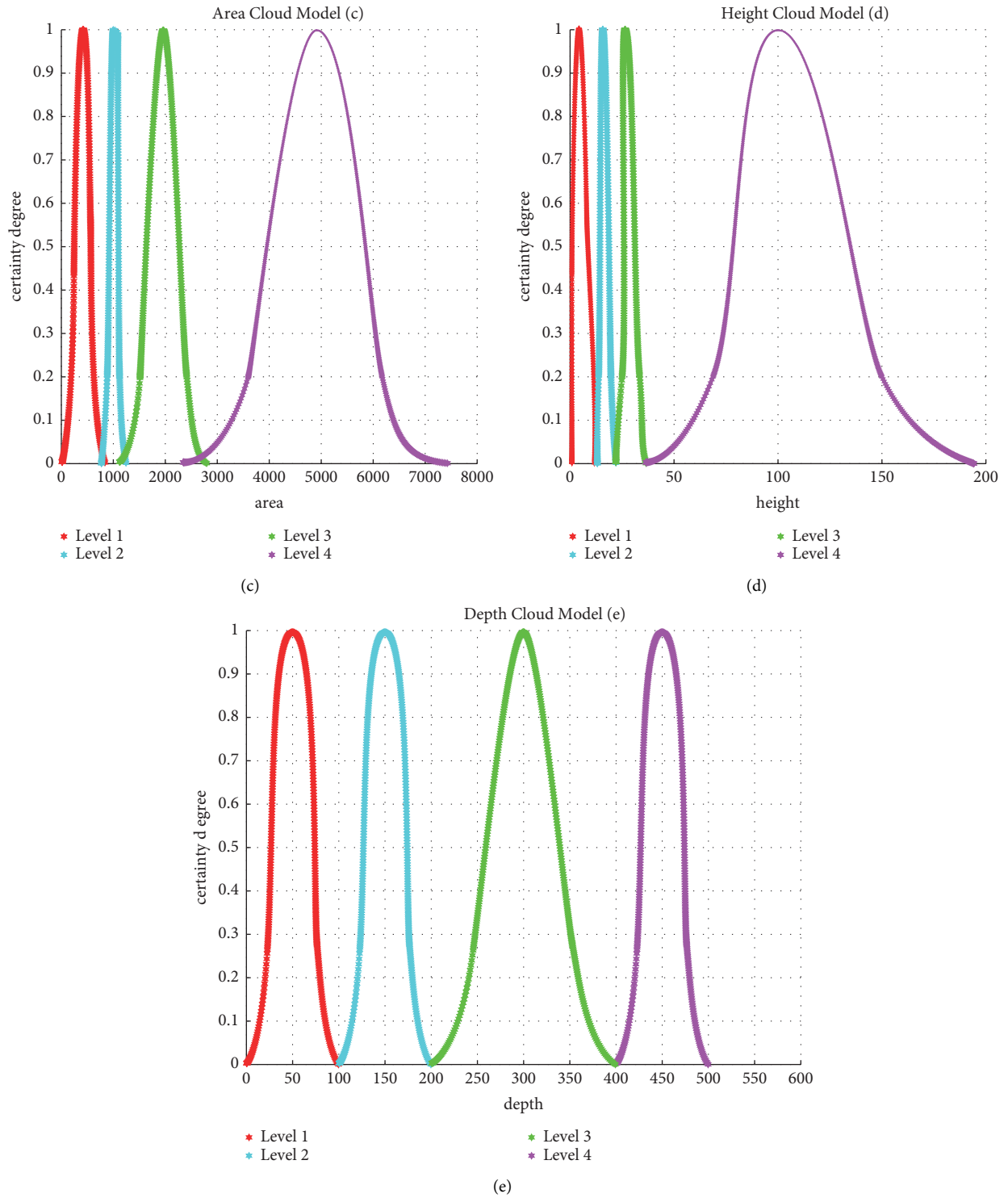
FIGURE 2: Each evaluation index belongs to the cloud model of the goaf stability level.

TABLE 5: Calculation data of stability evaluation of sample 19 goaf.

Evaluating indicator	Weighting	Degree of certainty			
		I	II	III	IV
S_1	0.1151	0	1	0	0
S_2	0.0953	1	0	0	0
S_3	0.0055	0	0	1	0
S_4	0.0302	1	0	0	0
S_5	0.0596	1	0	0	0
S_6	0.1249	1	0	0	0
S_7	0.2028	1	0	0	0
S_8	0.0609	1	0	0	0
S_9	0.0090	0.6672	0	0	0
S_{10}	0.0241	0	0	0.005261	0.03494
S_{11}	0.0268	0	0.6682	0	0
S_{12}	0.1363	0	1	0	0
S_{13}	0.0328	0	0	0.9894	0
S_{14}	0.0834	1	0	0	0

TABLE 6: Evaluation results of goaf stability and comparison with the actual situation.

Sample	Comprehensive uncertainty				Discrimination results	Actual level
	U (I)	U (II)	U (III)	U (IV)		
1	0.2663	0.3237	0.2460	0.1224	II	II
2	0.1374	0.1725	0.1887	0.4429	III ~ IV	III
3	0.1251	0.1998	0.1868	0.4702	III ~ IV	III
4	0.1254	0.2361	0.1553	0.5175	IV	IV
5	0.2858	0.0333	0.0610	0.5826	IV	IV
6	0.2831	0.1431	0.3516	0.1820	III	III
7	0.1207	0.1905	0.2298	0.4133	III ~ IV	III
8	0.2816	0.3716	0.1894	0.1363	II	II
9	0.1888	0.1949	0.3252	0.2925	III	III
10	0.2457	0.2501	0.2963	0.1750	III	III
11	0.0139	0.3924	0.4433	0.0835	III	III
12	0.1901	0.1992	0.2585	0.2996	III ~ IV	III
13	0.0954	0.2613	0.1318	0.4779	IV	IV
14	0.0611	0.3965	0.1570	0.3278	II	II
15	0.0004	0.1884	0.3260	0.4642	IV	IV
16	0	0.0958	0.3240	0.5614	IV	IV
17	0.5808	0.2693	0.0379	0.0005	I	I
18	0.1562	0.3276	0.1732	0.3278	II ~ III	II
19	0.8189	0.1058	0.0190	0.0027	I	I
20	0.1152	0.1777	0.1029	0.4759	IV	IV
21	0.7335	0.2023	0.0390	0.0000	I	I
22	0.8197	0.1168	0.0328	0.0011	I	I
23	0.5008	0.0934	0.3299	0.0000	I	I
24	0.5843	0.0229	0.3362	0.0000	I	I
25	0.5008	0.0915	0.1426	0.0000	I	I

value of certainty. Therefore, the use of a cloud model has advantages in representing the uncertainty of goaf stability and makes the evaluation results more accurate.

4. Conclusion

In this paper, a cloud model is used to evaluate goaf stability. Taking 25 goafs as samples, 14 factors affecting their stability are selected. According to the actual data, the hierarchical model of each influencing factor is established and solved. Combined with the actual data from the Xishan and

Dabaoshan mining area of the Shandong gold mining industry, the cloud model is used to evaluate 25 mined-out areas, and the classification results are compared with the actual situation.

The accuracy of model forecast is 96% with high accuracy. In addition, the predicted results of No. 2, 3, 7, 12, and 18 samples are of high risk level, which indicates that the predicted results are conservative and are beneficial to prevent goaf collapse. This method provides a new idea for mine safety production and goaf treatment and has important theoretical and practical significance.

Data Availability

The data of this paper are available, and the data come from other papers.

Disclosure

This paper was completed under the guidance of Professor Yun Lin.

Conflicts of Interest

The authors declare that they have no conflicts of interest.

Acknowledgments

References

[1] C. Feng, J. Li, W. Yu, Y. Xue, and B. Li, "Mechanism study of abandoned stope disposal in Dongtongyu Gold Mine," *Goad*, vol. 23, no. 11, pp. 11–15, 2002.

[2] H. Zhou, H. Xie, and J. Zuo, "Developments in Researches on mechanical Behaviors of rocks under the condition of high ground pressure in the depths," *Advances in Mechanics*, vol. 25, no. 1, pp. 91–99, 2005.

[3] K. Du, X. Li, K. Liu, and X.-X. Zhao, "Comprehensive evaluation of underground goaf risk and engineering application," *Journal of Central South University*, vol. 42, no. 9, pp. 2802–2811, 2011.

[4] F. Ma, "Accurate detection method of concealed goof in an iron mine," *Metal Mine*, vol. 479, pp. 196–199, 2016.

[5] X. W. Han, X. D. Zhang, Y. Wang et al., "Short- and long-term outcomes of kidney transplants with kidneys lavaged by retrograde perfusion technique," *Chronic diseases and translational medicine*, vol. 1, no. 3, pp. 163–168, 2015.

[6] J. Li and Z. Lu, "Application of ANSYS in safety assessment of abandoned stope stability," *China Molybdenum Industry*, vol. 30, no. 5, pp. 13–17, 2006.

[7] Z. Luo, X. Liu, Y. Wu, W. Liu, and B. Zhang, "Study on cavity stability numerical simulation based on coupling of Surpac and Phase2," *Journal of Liaoning Technical University (Natural Science)*, vol. 27, no. 4, pp. 485–488, 2008.

[8] X. Kou, W. Li, L. Wang, and X. Wu, "Evaluation and analysis of stability of mined- out area based on the CMS and DIMINE- FLAC3D coupling technique," *Mineral Engineering Research*, vol. 25, no. 1, pp. 31–35, 2010.

[9] F. Zhang and W. Li, "Number simulation analysis on the stability of complex group goaf and study on its control measures," *Mining Research and Development*, vol. 39, no. 9, pp. 41–45, 2019.

[10] F. Gong, X. Li, L. Dong, and X. Liu, "Underground goaf risk evaluation based on uncertainty measurement theory," *Chinese Journal of Rock Mechanics and Engineering*, vol. 171, no. 4356, pp. 323–330, 2008.

[11] X. Wang, S. Xie, Q. Zhang, and B. Zhao, "Stability analysis of mined-out area based on fuzzy mathematical comprehensive evaluation," *Journal of Kunming University of Science and Technology*, vol. 35, no. 1, pp. 9–13, 2010.

[12] H. Wang, X. Li, L. Dong, K. Liu, and H. Tong, "Classification of goaf stability based on support vector machine," *Journal of Safety Science and Technology*, vol. 10, no. 10, pp. 154–159, 2014.

[13] W. Wang, Z. Luo, L. Xiong, and N. JIa, "Research of goaf stability evaluation based on improved matter-element extension model," *Journal of Safety and Environment*, vol. 15, no. 1, pp. 21–25, 2015.

[14] S. Tang, H. Tang, and H. Guo, "Design of e-procurement system of coal enterprises based on cloud computing," *Journal of Xi'an University of Science and Technology*, vol. 32, no. 2, pp. 234–238+278, 2012.

[15] H. Jiang, Y. Ye, N. Hu, Q. Wang, and M. Wu, "Improved grey target model for risk evaluation of goaf," *Nonferrous Metals Engineering*, vol. 11, no. 7, pp. 96–106, 2021.

[16] F. Ding, X. Wu, P. Xiang, and Z. Yu, "New damage ratio strength criterion for concrete and lightweight Aggregate concrete," *ACI Structural Journal*, vol. 118, no. 65, pp. 165–178, 2021.

[17] D. Li, H. Mei, and X. Shi, "Membership clouds and membership cloud generators," *Computer und Recht D*, vol. 32, no. 6, pp. 15–20, 1995.

[18] Y. Gong, "Comprehensive assessment on ecological risk of Hexi Corridor urbanization based on normal cloud model and entropy weight," *Journal of Arid Land Resources & Environment*, vol. 26, no. 5, pp. 169–174, 2012.

[19] Y. Wang, H. Jing, Q. Zhang, L. Wei, and Z. Xu, "A normal cloud model-based study of grading prediction of rock burst intensity in deep underground engineering," *Rock and Soil Mechanics*, vol. 36, no. 4, pp. 1189–1194, 2015.

[20] Y. Guo, *Study on Stability Classification and Intelligent Prediction of Complex Goaf in Metal Mine*, Central South University, Changsha, China, 2012.

[21] X. Wang, Y. Ke, D. Yan, and S. Wang, "Underground goaf risk evaluation based on entropy weight and matter element analysis," *China Safety Science Journal*, vol. 22, no. 6, pp. 71–78, 2012.

[22] H. Wang, X. Li, L. Dong, K. Liu, and H. Tong, "Classification of goaf stability based on support vector machine," *China safety production science and Technology*, vol. 10, no. 10, pp. 154–159, 2014.

Research Article

Nonlinear Vibrations of an Axially Moving Beam with Fractional Viscoelastic Damping

Zhe Zhang,[1] Hongxiang Yang [ID],[2] Zhongjin Guo,[3] Lili Zhu,[2] and Weiyan Liu[3]

[1]*College of Civil Engineering, Hunan University of Technology, Zhuzhou, Hunan 412007, China*
[2]*School of Information Science and Technology, Taishan University, Taian, Shandong, China*
[3]*School of Mathematics and Statics, Taishan University, Taian, Shandong, China*

Correspondence should be addressed to Hongxiang Yang; tsuyhx@tsu.edu.cn

The nonlinear vibrations of an axially moving viscoelastic beam under the transverse harmonic excitation are examined. The governing equation of motion of the viscoelastic beam is discretized into a Duffing system with nonlinear fractional derivative using Galerkin's method. The viscoelasticity of the moving beam is described by the fractional Kelvin–Voigt model based on the Caputo definition. The primary resonance is analytically investigated by the averaging method. With the aid of response curves, a parametric study is conducted to display the influences of the fractional order and the viscosity coefficient on steady-state responses. The validations of this study are given through comparisons between the analytical solutions and numerical ones, where the stability of the solutions is determined by the Routh–Hurwitz criterion. It is found that suppression of undesirable responses can be achieved via changing the viscosity of the system.

1. Introduction

The model of axially moving systems that play essential roles is always observed in a wide range of engineering devices, such as power transmission belts, magnetic tapes, paper sheets, chains, pipes conveying fluids, aerial tramways, and fiber textiles. Therefore, research on the dynamic behaviors of such systems has been conducted in the past decades and is still of interest today [1–3]. Especially, the problems of axially moving beams and micro/nano scaled beams axially loaded have widely been tackled in the analysis of some aspects, such as free vibration [4], stability analysis [5, 6], discretization approaches [7], modeling techniques [8], different solution methods [9, 10], and nonlinear dynamics [5–20]. In the architectural design and construction industry, the materials that exhibit excellent damping characteristics have been widely utilized to fabricate structures to enhance their performance from the viewpoint of vibration control. A growing body of research activities has therefore been appearing to explore the nonlinear vibrations of axially moving viscoelastic beams [4–18]. To better understand the

damping mechanism, some classical constitutive models such as Kelvin–Voigt [5–19] and three-parameter Zener model [20] are adopted to effectively describe the dynamical responses of the viscoelastic materials. Although the classical models contain combinations of elastic and viscous elements, they do not have sufficient parameters to handle the different shapes of the hysteresis loops reflecting the nature of viscoelastic materials and structures. Consequently, the fractional calculus [21] has been introduced in constitutive relations to obtain a satisfactory solution for the real viscoelastic responses of the materials over a large range of frequency [22, 23]. Although there remain some mathematical issues unsolved, the fractional calculus-based modern viscoelasticity problems are becoming the focus of attention [24–32].

This research is devoted to investigating the dynamic behavior of an axially moving viscoelastic beam under a transverse harmonic excitation. It is assumed that the material of the beam obeys the Kelvin–Voigt model based on the fractional Caputo definition. Remarkably speaking, by one-term Garlerkin's technique, the governing equation of

the beam is discretized into a nonlinear Duffing type equation that has the nonlinear fractional operator [26–29]. The first order averaging method is utilized to derive the modulation equations governing the steady state amplitudes and phases of the system. Then, the stability of the solution is studied by the Routh–Hurwitz criterion [33]. Finally, the results of representative calculations are described and briefly discussed from the vibration control point of view.

2. Equation of Motion

The present study considers a uniform axially moving viscoelastic beam, shown in Figure 1, with density ρ, cross-sectional area A, and moment of inertial I. The initial tension is represented by P_0. The beam travels at a constant axial speed v between two motionless ends separated by distance L and is subjected to an external transverse force $F(x, T)$. Here, it is assumed that the excitation is spatially uniform and temporally harmonic: $F(X, T) = F \cos(WT)$, where T and X represent the time and the axial coordinate, respectively. Only the bending vibration described by the transverse displacement $U(X, T)$ is considered here, and Newton's second law of motion yields

$$\rho A\left(\frac{\partial^2 U}{\partial T^2} + 2v\frac{\partial^2 U}{\partial X \partial T} + v^2\frac{\partial^2 U}{\partial X^2}\right) = \frac{\partial}{\partial X}\left[(P_0 + A\sigma(X,T))\frac{\partial U}{\partial X}\right]$$
$$- \frac{\partial^2 M(X,T)}{\partial X^2} + F\cos(WT),$$

(1)

where $\sigma(X, T)$ and $M(X, T)$ are the disturbed axial stress and bending moment, respectively.

The viscoelasticity of the beam material obeys the fractional Kelvin–Voigt model [27, 28, 30] and its constitutive relationship is given as follows:

$$\sigma(X,T) = E_0\varepsilon_L(X,T) + E_1 D_C^\alpha[\varepsilon_L(X,T)].$$

(2)

In which E_0 represents the Young's modulus and E_1 denotes the viscoelastic coefficient. To reveal the geometric nonlinearity owing to the small but finite stretching of the beam, we adopt the Lagrangian strain $\varepsilon_L(X, T)$, which is defined by

$$\varepsilon_L(X,T) = \frac{1}{2}\left[\frac{\partial U(X,T)}{\partial X}\right]^2.$$

(3)

In equation (2), D_C^α denotes the α-order fractional differentiation operator with respect to time T in the Caputo sense given by [21].

$$D_C^\alpha(f) = \begin{cases} \frac{1}{\Gamma(m-\alpha)}\int_0^T \frac{f^m(\tau)}{(T-\tau)^{\alpha+1-m}}d\tau, & m-1 < \alpha < m, \\ \\ \frac{d^m}{dT^m}f, & \alpha = m\,(\text{a positive integer}), \end{cases}$$

(4)

where Γ is the well-known gamma function. Moreover, for a slender beam, the linear moment-curvature relation is adopted.

$$M(X,T) = (E_0 + E_1 D_C^\alpha)I\frac{\partial^2 U(X,T)}{\partial X^2}.$$

(5)

Substitution of equations (2), (3) and (5) into equation (1), yields the governing equation of transverse motion of the axially viscoelastic beam

$$\rho A\left(\frac{\partial^2 U}{\partial T^2} + 2v\frac{\partial^2 U}{\partial X \partial T} + v^2\frac{\partial^2 U}{\partial X^2}\right) - P_0\frac{\partial^2 U}{\partial X^2} + E_0 I\frac{\partial^4 U}{\partial X^4}$$
$$+ E_1 I D_C^\alpha\left(\frac{\partial^4 U}{\partial X^4}\right) = \frac{3}{2}AE_0\left(\frac{\partial U}{\partial X}\right)^2\frac{\partial^2 U}{\partial X^2}$$
$$+ \frac{1}{2}AE_1\frac{\partial^2 U}{\partial X^2}D_C^\alpha\left[\left(\frac{\partial U}{\partial X}\right)^2\right]$$
$$+ AE_1\frac{\partial U}{\partial X}D_C^\alpha\left(\frac{\partial U}{\partial X}\cdot\frac{\partial^2 U}{\partial X^2}\right) + F\cos(WT).$$

(6)

In the present investigation, the boundary conditions are taken to be simply supported, i.e.,

$$U(0,T) = U(L,T) = 0,$$
$$\frac{\partial^2 U(0,T)}{\partial X^2} = \frac{\partial^2 U(L,T)}{\partial X^2} = 0.$$

(7)

Using the following dimensionless scheme,

$$x = \frac{X}{L},$$
$$t = \frac{T}{L}\sqrt{\frac{P_0}{\rho A}},$$
$$\omega = WL\sqrt{\frac{\rho A}{P_0}},$$
$$u = \frac{U}{L},$$
$$\gamma = v\sqrt{\frac{\rho A}{P_0}},$$
$$k_f = \sqrt{\frac{E_0 I}{P_0 L^2}},$$
$$\eta = \frac{E_1 I}{P_0 L^2}\sqrt{\left(\frac{P_0}{\rho AL^2}\right)^\alpha},$$
$$k_1 = \sqrt{\frac{AE_0}{P_0}},$$
$$k_2 = \frac{AE_0}{2P_0}\sqrt{\left(\frac{P_0}{\rho AL^2}\right)^\alpha},$$
$$p = \frac{\pi FL}{4P_0}.$$

(8)
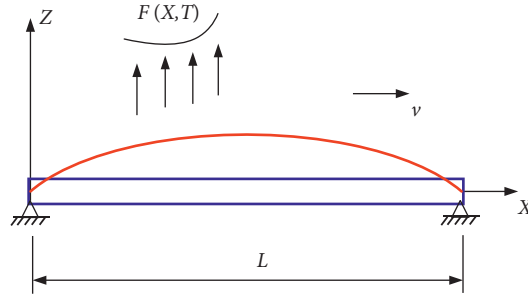
FIGURE 1: Schematic of an axially moving beam.

Equation (6) becomes

$$\frac{\partial^2 u}{\partial t^2} + 2\gamma \frac{\partial^2 u}{\partial x \partial t} + \left(\gamma^2 - 1\right)\frac{\partial^2 u}{\partial x^2} + k_f^2 \frac{\partial^4 u}{\partial x^4} + \eta D_C^\alpha \left(\frac{\partial^4 u}{\partial x^4}\right) = \frac{3}{2}k_1^2\left(\frac{\partial u}{\partial x}\right)^2 \frac{\partial^2 u}{\partial x^2} + k_2\left\{\frac{\partial^2 u}{\partial x^2}D_C^\alpha\left[\left(\frac{\partial u}{\partial x}\right)^2\right] + 2\frac{\partial u}{\partial x}D_C^\alpha\left(\frac{\partial u}{\partial x} \cdot \frac{\partial^2 u}{\partial x^2}\right)\right\}$$

$$\tag{9}$$

$$+ \frac{4}{\pi}p\cos(\omega t).$$

With boundary conditions

$$u(0,t) = u(1,t) = 0,$$

$$\frac{\partial^2 u(0,t)}{\partial x^2} = \frac{\partial^2 u(1,t)}{\partial x^2} = 0. \tag{10}$$

3. Steady State Responses and Stability Analysis

In this study, one term Galerkin's method is applied to discretize equation (9), and its solution is assumed to be as follows:

$$u(x,t) = q(t)\sin(\pi x), \tag{11}$$

where $q(t)$ is the modal coordinate of the beam. Then, a nonlinear fractional ordinary differential equation is derived as follows:

$$q + \pi^4 \eta D_C^\alpha q + \frac{3}{4}k_2 \pi^4 q D_C^\alpha\left(q^2\right)$$

$$+ \pi^2\left(\pi^2 k_f^2 + 1 - \gamma^2\right)q + \frac{3}{8}k_1^2 \pi^4 q^3 = p\cos(\omega t). \tag{12}$$

For simplicity in the following analysis, equation (12) is rewritten as follows:

$$\ddot{q} + \mu_1 D_C^\alpha q + \mu_2 q D_C^\alpha\left(q^2\right) + \omega_0^2 q + k_n q^3 = p\cos(\omega t). \tag{13}$$

With

$$\mu_1 = \pi^4 \eta,$$

$$\mu_2 = \frac{3}{4}k_2 \pi^4,$$

$$\omega_0 = \pi\sqrt{\pi^2 k_f^2 + 1 - \gamma^2}, \tag{14}$$

$$k_n = \frac{3}{8}k_1^2 \pi^4.$$

Remarkably, equations (12) or (13) is a nonlinear Duffing type equation having a nonlinear fractional operator $D_C^\alpha(q^2)$ [26–28].

In what follows, the primary resonance of the fractional system described by (13) will be investigated by the linear averaging method. We mainly focus on examining the effects of the damping parameters and the fractional order on the steady state response of the beam. The stability of the stationary solutions is examined by the Routh–Hurwitz criterion [33].

To obtain the primary resonance of the fractional oscillator (equation (13)), we introduce a small parameter ε. We detune the primary resonance by setting $\omega_0^2 = \omega^2 + \varepsilon\sigma$. Then, equation (13) is rewritten as follows:

$$\ddot{q} + \omega^2 q = -\varepsilon\left[\mu_1 D_C^\alpha q + \mu_2 q D_C^\alpha\left(q^2\right) + \sigma q + k_n q^3 - p\cos(\omega t)\right], \tag{15}$$

where the parameter ε merely serves to indicate the assumed smallness of the terms without any physical meaning. The solution at $\varepsilon = 0$ can be written in the form as follows:

$$q = A\cos\theta, \theta = \omega t + \varphi, \tag{16}$$

where A and φ are integration constants determined by the initial conditions. When $\varepsilon \neq 0$ the approximate solution near the primary resonant frequency region can be viewed as a perturbation of the solution given by (16). In this case, A and φ are slowly varying functions of time t such that their derivatives are of $o(\varepsilon)$. According to the averaging method, we assume that the solution of the system takes the following form:

$$q = A\cos\theta \text{ and } \dot{q} = -A\omega\sin\theta, \tag{17}$$

which implies

$$\dot{A}\cos\theta - A\dot{\varphi}\sin\theta = 0. \tag{18}$$

Differentiating the second equation in equation (17) with respect to t gives the following equation:

$$\ddot{q} = -\omega\left(\dot{A}\sin\theta + A\dot{\varphi}\cos\theta\right) - \omega^2 q. \tag{19}$$

Substituting equations (17) and (19) into equation (14) leads to the following equation:

$$\begin{cases} \dot{A} = \dfrac{\varepsilon}{\omega}\sin\theta\, G(x,t), \\[3mm] \dot{\varphi} = \dfrac{\varepsilon}{A\omega}\cos\theta\, G(x,t), \end{cases} \tag{20}$$

where $G = \mu_1 D_C^\alpha q + \mu_2 q D_C^\alpha(q^2) + \sigma q + k_n q^3 - p\cos\omega t$.

Based on the averaging method, the right-hand side of equation (20) can be replaced by its averages over one period when G is a periodic function with respect to t. However, owing to the presence of the fractional derivative in equation (20), an infinite interval should be considered, and we have the following equation:

$$\begin{aligned} &\mathrm{Aver}\left[\left(D_C^\alpha q^m\right)\begin{pmatrix}\cos\theta \\[1mm] \sin\theta\end{pmatrix}\right] \\[3mm] &= \lim_{T\to\infty}\frac{1}{T}\int_0^T \left(D_C^\alpha q^m\right)\begin{pmatrix}\cos\theta \\[1mm] \sin\theta\end{pmatrix}\mathrm{d}\theta,\quad m = 1,2. \end{aligned} \tag{21}$$

Since we consider the steady state only, the fractional order derivative of q can be easily derived approximately based on the fractional definition given in equation (4) [21, 27, 32], as follows:

$$D_C^\alpha q \approx \omega^\alpha A\cos\left(\theta + \frac{\alpha\pi}{2}\right),$$

$$q D_C^\alpha\left(q^2\right) \approx \frac{1}{4}(2\omega)^\alpha A^3\cos\left(\theta + \frac{\alpha\pi}{2}\right). \tag{22}$$

Subsequently, the average in equation (21) can also be integrated over one period, when the fractional derivative of q is replaced by the respective approximation in equation (22). Then, we have the averaged equation (20) as follows:

$$\begin{cases} \dot{A} \approx \dfrac{\varepsilon}{2\omega\pi}\displaystyle\int_0^{2\pi}\sin\theta\,\widetilde{G}(A,\theta)\mathrm{d}\theta, \\[4mm] \dot{\varphi} = \dfrac{\varepsilon}{2\omega\pi A}\displaystyle\int_0^{2\pi}\cos\theta\,\widetilde{G}(A,\theta)\mathrm{d}\theta, \end{cases} \tag{23}$$

where

$$\begin{aligned} \widetilde{G} &= \sigma A\cos\theta + A\omega^\alpha\left(\mu_1 + 2^{\alpha-2}\mu_2 A^2\right)\cos\left(\theta + \frac{\alpha\pi}{2}\right) \\[2mm] &\quad + 2^{\alpha-2}\mu_2\omega^\alpha A^3\cos\left(3\theta + \frac{\alpha\pi}{2}\right) \\[2mm] &\quad + \frac{k_n}{4}A^3\cos^3\theta - p\cos(\omega t). \end{aligned} \tag{24}$$

A direct calculation yields

$$\begin{cases} \dot{A} = -\dfrac{\varepsilon}{2\omega}\left(f_{11}A + f_{12}A^3 + p\sin\varphi\right), \\[4mm] \dot{\varphi} = \dfrac{\varepsilon}{2\omega A}\left(f_{21}A + f_{22}A^3 - p\cos\varphi\right), \end{cases} \tag{25}$$

where

$$f_{11} = \mu_1\omega^\alpha\sin\left(\frac{\alpha\pi}{2}\right),$$

$$f_{12} = 2^{\alpha-2}\mu_2\omega^\alpha\sin\left(\frac{\alpha\pi}{2}\right),$$

$$f_{21} = \sigma + \mu_1\omega^\alpha\cos\left(\frac{\alpha\pi}{2}\right),$$

$$f_{22} = 2^{\alpha-2}\mu_2\omega^\alpha\cos\left(\frac{\alpha\pi}{2}\right) + \frac{3}{4}k_n. \tag{26}$$

The small parameter ε is reduced in equation (25) by introducing a slow time scale $\widetilde{t} = \varepsilon t$, and we have the following equation:

$$\begin{cases} A' = -\dfrac{1}{2\omega}\left(f_{11}A + f_{12}A^3 + p\sin\varphi\right), \\[4mm] \varphi' = \dfrac{1}{2\omega A}\left(f_{21}A + f_{22}A^3 - p\cos\varphi\right). \end{cases} \tag{27}$$

where $A' = dA/d\widetilde{t}$. The steady state conditions $A' = \varphi' = 0$ give the following equation:

$$\begin{cases} A^2\left[\left(f_{11} + f_{12}A^2\right)^2 + \left(f_{21} + f_{22}A^2\right)^2\right] = p^2, \\[3mm] \tan\varphi = -\left(f_{11} + f_{12}A^2\right)\left(f_{21} + f_{22}A^2\right)^{-1}. \end{cases} \tag{28}$$

Then, the variation of the amplitude A and phase φ of the steady state primary response as a function of the fractional order. External excitation as well as other control parameters can be determined by these two equations.

In what follows, the stability of the solutions of the system in the neighborhood of the equilibrium state is approximately analyzed by exploring the eigenvalues of the Jacobian matrix of equation (27) evaluated at the fixed points of interest. In order to do that, the small disturbances of the response amplitude and phase $\Delta A = A - \overline{A}$ and $\Delta\varphi = \varphi - \overline{\varphi}$, are introduced and substituted into equation (27). Then, the linearized equation is obtained as follows:

$$\begin{pmatrix}\dfrac{\mathrm{d}\Delta A}{\mathrm{d}t} \\[4mm] \dfrac{\mathrm{d}\Delta\varphi}{\mathrm{d}t}\end{pmatrix} = J\big|_{(\overline{A},\overline{\varphi})}\begin{pmatrix}\Delta A \\[2mm] \Delta\varphi\end{pmatrix}, \tag{29}$$

where

$$J|_{(\overline{A},\overline{\varphi})} = \begin{pmatrix} \dfrac{\partial F_1}{\partial A} & \dfrac{\partial F_1}{\partial \varphi} \\[2mm] \dfrac{\partial F_2}{\partial A} & \dfrac{\partial F_2}{\partial \varphi} \end{pmatrix}\Bigg|_{(\overline{A},\overline{\varphi})}, \tag{30}$$

with

$$\frac{\partial F_1}{\partial A}\bigg|_{(\overline{A},\overline{\varphi})} = -\frac{1}{2\omega}\left(f_{11} + 3f_{12}\overline{A}^2\right),$$

$$\frac{\partial F_1}{\partial \varphi}\bigg|_{(\overline{A},\overline{\varphi})} = -\frac{\overline{A}}{2\omega}\left(f_{21} + f_{22}\overline{A}^2\right),$$

$$\frac{\partial F_2}{\partial A}\bigg|_{(\overline{A},\overline{\varphi})} = \frac{1}{2\omega\overline{A}}\left(f_{21} + 3f_{22}\overline{A}^2\right),$$

$$\frac{\partial F_2}{\partial \varphi}\bigg|_{(\overline{A},\overline{\varphi})} = -\frac{1}{2\omega}\left(f_{11} + f_{12}\overline{A}^2\right). \tag{31}$$

The eigenfunction of the linearized equation (29) is as follows:

$$\lambda^2 + a\lambda + b = 0, \tag{32}$$

with

$$\begin{cases} a = -\dfrac{1}{\omega}\left(f_{11} + 2f_{12}\overline{A}^2\right), \\[4mm] b = \dfrac{1}{4\omega^2}\left[\left(f_{11} + 3f_{12}\overline{A}^2\right)\left(f_{11} + f_{12}\overline{A}^2\right) + \left(f_{21} + f_{22}\overline{A}^2\right)\left(f_{21} + 3f_{22}\overline{A}^2\right)\right]. \end{cases} \tag{33}$$

From the Routh–Hurwitz criterion [33], the steady-state response is asymptotically stable if and only if the real parts of the eigenvalues are negative. It can be obtained by the following equation:

$$a < 0 \text{ and } b > 0. \tag{34}$$

4. Verifications and Numerical Simulations

In the following, a parametric investigation in primary resonance conditions has been conducted to reveal the influences of the control variables on the steady state responses of the beam from the vibration control point of view. The approximate results have been achieved and illustrated by frequency- and forcing amplitude-response curves, in which the solid lines stand for the stable results and the dotted ones correspond to the unstable results. The distinction between the stable solutions and unstable ones is determined by the inequalities (equation (34)) using the Routh–Hurwitz criterion [33]. In calculations, the system parameters in equation (12) have been taken as follows [14]: $k_1 = 33.526$, $k_2 = 0.05$, $k_f = 0.173$, and $\gamma = 0.6$.

4.1. Effects of Fractional Order on System Response.
In Figures 2 and 3, the forcing frequency ω near the natural frequency ($\omega_0 \approx 3.038$) has been chosen as a bifurcation parameter. The forcing amplitude-response curves are depicted in Figure 4.

The influence of the fractional order α on the dynamic behavior of the viscoelastic system is firstly investigated. The response curves for several cases: $\alpha = 0.6, 0.8$, and 1.0 are plotted with a frequency range near the natural frequency of the system in Figure 2. It is seen apparently that when $\alpha = 0.6$, as the forcing frequency grows gradually from 4 the stable responses increase until a saddle node bifurcation occurs at $P (\omega \approx 9.592)$ and another saddle node happens at $Q (\omega \approx 7.547)$, by which a bistable interval or the hysteresis area can be calculated. For this bistable interval, there are two stable attractors and one unstable attractor in between. This is a typical characteristic of Duffing oscillator due to its cubic nonlinearity in primary resonance [33]. As the forcing frequency increases gradually from point P, the response jumps down from the resonance branch to the non-resonance branch and the system experiences a saddle node bifurcation at point P. Correspondingly, starting at a high forcing frequency on the nonresonance branch, the response undergoes a conversion to the resonance branch again through a jump up at another saddle node bifurcation point Q. In the response curve for $\alpha = 0.8$, although the jump phenomena exist, the positions of the jumps $P' (\omega \approx 7.192)$ and $Q' (\omega \approx 7.096)$ are shifted to the left, and the width of the jump region (i.e., the hysteresis area) is shrunk obviously. Additionally, the response amplitudes of the system are attenuated at the same time. With the further increase of the fractional order, the hysteresis domain decreases. Eventually, as α increases beyond a certain critical value, the jumps can be eliminated, which is manifested in Figure 2 when $\alpha = 1$. It means that the fractional order can stabilize the system.

In addition, the amplitude-response curves are also depicted in Figure 4 to verify the above conclusions, where the response amplitudes are plotted as the function of forcing amplitude. Similar conclusions can easily be drawn.
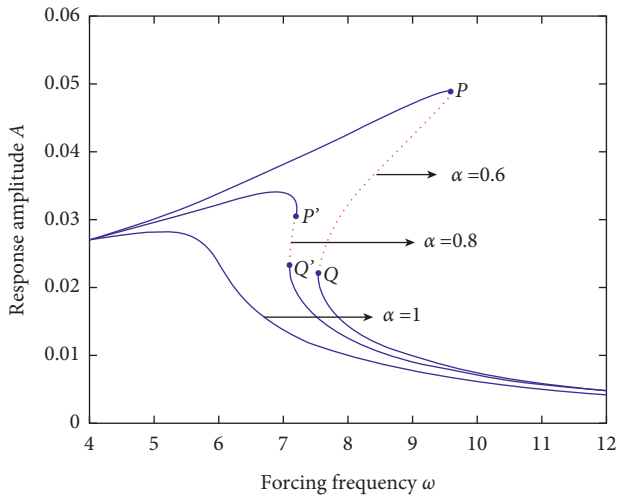
FIGURE 2: Forcing frequency-response curves for $\eta = 0.04$ and $p = 0.6$.
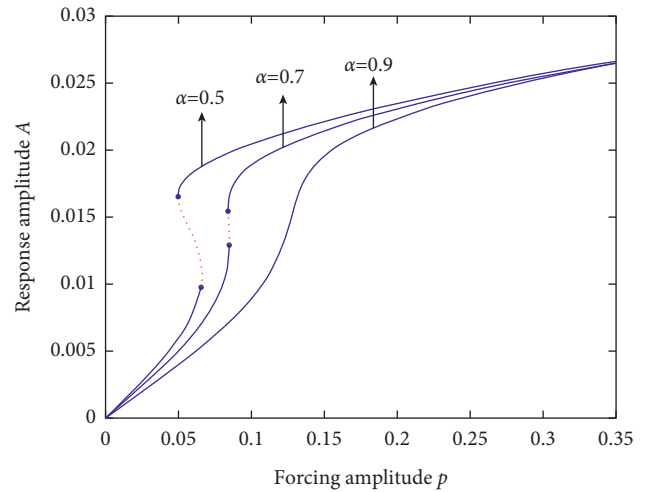
FIGURE 4: Forcing amplitude-response curves for $\eta = 0.02$ and $\omega = 4.6$.
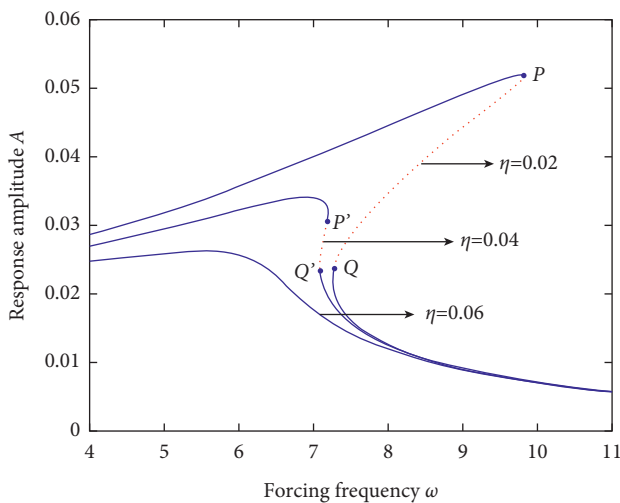
FIGURE 3: Frequency-response curves for $p = 0.6$ and $\alpha = 0.8$.

FIGURE 5: Comparisons of the analytical and numerical solutions when $p = 0.6$. The solid and dotted lines stand for the stable analytical and the unstable analytical solutions, respectively, and the asterisk marks the numerical result.

4.2. Effects of Viscoelastic Coefficient on the Dynamic Behaviors. The influence of the viscoelastic coefficient η on the dynamic behavior of the viscoelastic system is then investigated and graphically presented by the frequency-response curves for different coefficients, that is $\alpha = 0.5, 0.7,$ and 0.9 in Figure 3. It is found that the influences of the parameter η are much similar to those of the fractional order α. When $\eta = 0.02$ for example, with the excitation frequency is gradually growing, the amplitude of the stable response continuously rises until the first limit point $P(\omega \approx 9.821)$, at which the solution becomes unstable through a saddle node bifurcation. Contrarily, as the forcing frequency decreases, the amplitude exhibits a saddle node bifurcation at the jump-up point $Q(\omega \approx 7.288)$. Moreover, the hysteresis area is shrunk and eventually eliminated as the viscoelastic coefficient η increases. At the same time, the response amplitudes are attenuated for the cases having a relatively large viscoelastic coefficientη.

4.3. Verifications. To verify the previous discussions, the analytical results have been compared with the numerical solutions achieved from the direct numerical integration technique. The primary resonance of the system is shown in Figure 5, in which the control parameter-set adopted is chosen as $\eta = 0.04$, $k_1 = 33.526$, $k_2 = 0.05$, $k_f = 0.173$, $\gamma = 0.6$, $\alpha = 0.6$, and $p = 0.6$. Depicted in Figure 5, the stability of the dynamic solutions, such as the "stability limit," is shown by the conditions that are given in (34). Also, one can observe that the analytical results achieve good agreement with the solutions by the numerical technique.

5. Conclusions

By the averaging technique, in the present investigations, the primary resonant response of the axially moving viscoelastic

beam system has been analytically investigated from the viewpoint of vibration control. The influences of different system parameters, such as fractional order and the viscoelastic coefficient, on the dynamic responses of the viscoelastic beam are graphically illustrated. From the investigation, the following conclusions have been made:

(1) It has shown that the hysteresis or jump phenomenon occurs owing to the existence of multiple solutions on response curves, while the hysteresis area contracts with the increase of the fractional order or viscoelastic coefficient.

(2) A critical value of these two parameters exists, beyond which the hysteresis region can be eliminated. The increase in them reduces the vibration amplitudes.

(3) Both the fractional order and viscoelastic coefficient are powerful factors in stabilizing the system.

Data Availability

The data used to support the findings of this study are available from the corresponding author upon request.

Disclosure

A preprint of this paper [34] has previously been presented on Engineering Archive (doi: 10.31224/osf.io/2wsv6).

Conflicts of Interest

The authors declare that they have no conflicts of interest.

Acknowledgments

References

[1] C. D. Mote, "On the nonlinear oscillation of an axially moving string," *Journal of Applied Mechanics*, vol. 33, no. 2, pp. 463-464, 1966.

[2] L. Ying-hui, G. Qing, J. Kai-lin, and Y. Xue-gang, "Dynamic responses of viscoelastic axially moving belt," *Applied Mathematics and Mechanics*, vol. 24, no. 11, pp. 1348–1354, 2003.

[3] K. Marynowski and T. Kapitaniak, "Dynamics of axially moving continua," *International Journal of Mechanical Sciences*, vol. 81, pp. 26–41, 2014.

[4] O. Civalek and O. Kiracioglu, "Free vibration analysis of Timoshenko beams by DSC method," *International Journal for Numerical Methods in Biomedical Engineering*, vol. 26, no. 12, pp. 1890–1898, 2010.

[5] L. Q. Chen and X. D. Yang, "Stability in parametric resonance of axially moving viscoelastic beams with time-dependent speed," *Journal of Sound and Vibration*, vol. 284, no. 3-5, pp. 879–891, 2005.

[6] B. Akgöz and Ö. Civalek, "A size-dependent beam model for stability of axially loaded carbon nanotubes surrounded by Pasternak elastic foundation," *Composite Structures*, vol. 176, pp. 1028–1038, 2017.

[7] G. C. Zhang, H. Ding, L. Q. Chen, and S. P. Yang, "Galerkin method for steady-state response of nonlinear forced vibration of axially moving beams at supercritical speeds," *Journal of Sound and Vibration*, vol. 331, no. 7, pp. 1612–1623, 2012.

[8] L. Q. Chen and X. D. Yang, "Steady-state response of axially moving viscoelastic beams with pulsating speed: comparison of two nonlinear models," *International Journal of Solids and Structures*, vol. 42, no. 1, pp. 37–50, 2005.

[9] S. H. Chen, J. L. Huang, and K. Y. Sze, "Multidimensional Lindstedt–Poincaré method for nonlinear vibration of axially moving beams," *Journal of Sound and Vibration*, vol. 306, no. 1-2, pp. 1–11, 2007.

[10] L. Q. Chen and H. Ding, "Steady-state responses of axially accelerating viscoelastic beams: approximate analysis and numerical confirmation," *Science in China - Series G: Physics Mechanics and Astronomy*, vol. 51, no. 11, pp. 1707–1721, 2008.

[11] X. D. Yang and W. Zhang, "Nonlinear dynamics of axially moving beam with coupled longitudinal transversal vibrations," *Nonlinear Dynamics*, vol. 78, no. 4, pp. 2547–2556, 2014.

[12] X. D. Yang and L. Q. Chen, "Non-linear forced vibration of axially moving viscoelastic beams," *Acta Mechanica Solida Sinica*, vol. 19, no. 4, pp. 365–373, 2006.

[13] H. Ding and L. Q. Chen, "Approximate and numerical analysis of nonlinear forced vibration of axially moving viscoelastic beams," *Acta Mechanica Sinica*, vol. 27, no. 3, pp. 426–437, 2011.

[14] M. H. Ghayesh, "Nonlinear forced dynamics of an axially moving viscoelastic beam with an internal resonance," *International Journal of Mechanical Sciences*, vol. 53, no. 11, pp. 1022–1037, 2011.

[15] X. Y. Mao, H. Ding, and L. Q. Chen, "Forced vibration of axially moving beam with internal resonance in the super-critical regime," *International Journal of Mechanical Sciences*, vol. 131-132, pp. 81–94, 2017.

[16] H. Ding, G. C. Zhang, L. Q. Chen, and S. P. Yang, "Forced vibrations of supercritically transporting viscoelastic beams," *Journal of Vibration and Acoustics*, vol. 134, no. 5, pp. 4825–4829, 2012.

[17] H. Ding, X. Y. Mao, and L. Q. Chen, "Periodic response of an axially high-speed moving beam under 3:1 internal resonance," *Journal of Physics: Conference Series*, vol. 744, Article ID 012117, 2016.

[18] Y. H. Li, Y. H. Dong, Y. Qin, and H. W. Lv, "Nonlinear forced vibration and stability of an axially moving viscoelastic sandwich beam," *International Journal of Mechanical Sciences*, vol. 138-139, pp. 131–145, 2018.

[19] X. Y. Mao, H. Ding, C. Lim, and L. Q. Chen, "Super-harmonic resonance and multi-frequency responses of a super-critical translating beam," *Journal of Sound and Vibration*, vol. 385, pp. 267–283, 2016.

[20] K. Marynowski and T. Kapitaniak, "Zener internal damping in modelling of axially moving viscoelastic beam with time-dependent tension," *International Journal of Non-linear Mechanics*, vol. 42, no. 1, pp. 118–131, 2007.

[21] I. Podlubny, *Fractional Differential Equations: An Introduction to Fractional Derivatives, Fractional Differential*

Equations, to Methods of Their Solution and Some of Their Applications, Academic Press, San Diego, CL, USA, 1999.

[22] M. Francesco, Fractional Calculus and Waves in Linear Viscoelasticity: An Introduction to Mathematical Models, Imperial College Press, London, 2010.

[23] Y. A. Rossikhin and M. V. Shitikova, "Application of fractional calculus for dynamic problems of solid mechanics: novel trends and recent results," Applied Mechanics Reviews, vol. 63, no. 1, Article ID 010801, 2010.

[24] A. C. Galucio, J. F. Deü, and R. Ohayon, "Finite element formulation of viscoelastic sandwich beams using fractional derivative operators," Computational Mechanics, vol. 33, no. 4, pp. 282–291, 2004.

[25] R. Lewandowski and M. Baum, "Dynamic characteristics of multilayered beams with viscoelastic layers described by the fractional Zener model," Archive of Applied Mechanics, vol. 85, no. 12, pp. 1793–1814, 2015.

[26] M. Sjöberg and L. Kari, "Nonlinear isolator dynamics at finite deformations: an effective hyperelastic, fractional derivative, generalized friction model," Nonlinear Dynamics, vol. 33, no. 3, pp. 323–336, 2003.

[27] A. Y. T. Leung, H. X. Yang, P. Zhu, and Z. J. Guo, "Steady state response of fractionally damped nonlinear viscoelastic arches by residue harmonic homotopy," Computers & Structures, vol. 121, pp. 10–21, 2013.

[28] L. Q. Chen, W. J. Zhao, and J. W.Zu, "Transient responses of an axially accelerating viscoelastic string constituted by a fractional differentiation law," Journal of Sound and Vibration, vol. 278, no. 4-5, pp. 861–871, 2004.

[29] A. Y. T. Leung, H. X. Yang, and P. Zhu, "Bifurcation of a duffing oscillator having nonlinear fractional derivative feedback," International Journal of Bifurcation and Chaos, vol. 24, no. 3, Article ID 1450028, 2014.

[30] T. Z. Yang and B. Fang, "Stability in parametric resonance of an axially moving beam constituted by fractional order material," Archive of Applied Mechanics, vol. 82, no. 12, pp. 1763–1770, 2012.

[31] Y. Li and Y. Tang, "Analytical analysis on nonlinear parametric vibration of an axially moving string with fractional viscoelastic damping," Hindawi Mathematical Problems in Engineering, vol. 2017, Article ID 1393954, 9 pages, 2017.

[32] R. Lewandowski and P. Wielentejczyk, "Nonlinear vibration of viscoelastic beams described using fractional order derivatives," Journal of Sound and Vibration, vol. 399, no. 7, pp. 228–243, 2017.

[33] A. H. Nayfeh and D. T. Mook, Nonlinear Oscillations, Wiley-Interscience, New York, NY, USA, 1979.

[34] H. X. Yang, P. Zhu, L. L. Zhu, and W. Y. Liu, "Nonlinear dynamics of an axially moving beam with fractional viscoelastic damping," Engineering Archive, 2019.

Research Article

Time-Frequency Characteristics of Ground Motion and Seismic Response Analysis of Typical Structures in the Yangbi Earthquake in Yunnan Province

Qin Xu,[1] Shaofeng Chai ⓘ,[2,3] Shihu Zhou,[1] Liqun Bao,[1] and Quan Li[1]

[1]*Lanzhou Institute of Technology, Lanzhou 730050, China*
[2]*Key Laboratory of Earthquake Engineering and Engineering Vibration of China Earthquake Agency,*
Institute of Engineering Mechanics, China Earthquake Agency, Harbin 150080, Heilongjiang, China
[3]*Key Laboratory of Loess Earthquake Engineering of China Earthquake Administration & Gansu Province, Lanzhou 730000,*
Gansu, China

Correspondence should be addressed to Shaofeng Chai; chaishaofeng520@163.com

The ground motion records obtained by the CDSMON during the Ms6.4 earthquake in Yangbi, Yunnan Province, on May 21, 2021, were subjected to routine processing such as baseline correction and filtering. The nonstationary time-frequency characteristics of ground motion signals were analysed by the wavelet transform, and the acceleration response spectrum characteristics of typical stations under different epicentral distances, magnitudes, and site conditions were analysed. Finite element software was used to establish a model to analyse the seismic response of a typical three-span continuous beam bridge. The maximum peak ground acceleration (PGA) of this earthquake (720.29 gal) was obtained from 53YBX in the NS direction at the epicentral distance of 8.6 km. The energy at station 53YBX was mainly concentrated in 0–15 Hz range, and the low-frequency component energy caused great damage to buildings with natural frequencies in this frequency band. The Sa value near the origin of the earthquake is relatively large, as the distance from the epicentre increases, the predominant period of Sa also gradually increases, and the high-frequency component diminishes. With the increase in earthquake magnitude, the Sa peak increased, and the long-period component became more obvious. The soil station had more obvious long-period components than the bedrock station, which is consistent with the amplification result of the response spectrum of overburden thickness to surface acceleration. The earthquake had little influence on the pier displacement of the three-span continuous beam bridge with a fundamental period of 0.77 s but had a great influence on the bending moment at the bottom of the piers.

1. Introduction

According to the measurement of the China Earthquake Networks Center, at 21 : 48 on May 21, 2021, an Ms6.4 earthquake occurred in Yangbi County, Dali Prefecture, Yunnan Province. The epicentre was located at 25.67°N and 99.87°E, and the focal depth was 8 km. The earthquake belongs to a typical foreshock-mainshock-aftershock event. More than 350 seismicities occurred before the mainshock, including five earthquakes with a magnitude of Ms4.0 or above. The largest foreshock was the Ms5.6 earthquake at 21 : 21 on May 21, 2021, with the epicentre at 25.67°N and 99.87°E, a focal depth of 10 km, and a distance from the

Ms6.4 mainshock of 6 km. After the mainshock, the Yunnan regional seismic network recorded rich sequences of aftershocks. As of May 26, 2021, 2426 aftershocks above magnitude 0 have been recorded. The largest aftershock was the Ms5.2 earthquake at 22 : 31 on May 21, 2021, with the epicentre at 25.59 N and 99.97°E) and a focal depth of 8 km [1]. The seismogenic fault of this earthquake was a NW-trending secondary fault on the west side of the Weixi-Qiaohou fault, which is dominated by dextral strike-slip motion [2, 3]. On May 25, the Yunnan Provincial Seismological Bureau issued the intensity map of the Ms6.4 Yangbi earthquake in Yunnan Province, which shows that the maximum intensity of this earthquake was VIII and that

the area of intensity VI and above was approximately 6600 km^2, involving 6 counties and cities of Dali Prefecture.

The China Digital Strong Motion Observation Network (CDSMON) captured abundant records of strong ground motions after the earthquake. Chen and Li [4] conducted conventional processing such as filtering on the ground motion records, analysed the attenuation patterns and duration characteristics of the ground motion amplitude, and compared the recorded acceleration response spectra of stations with different epicentral distances. Tian et al. [5] compared and analysed the acceleration response spectra of 6 stations with the nearest epicentral distances and largest amplitudes. The aforementioned studies analysed the frequency domain characteristics of ground motion mainly based on acceleration response spectra.

Ground motion records belong to nonstationary time-varying signals, and their energy and frequency will change greatly with time [6]. Conventional signal processing methods cannot well reflect the time dependence of frequency components, while the wavelet transform and wavelet packet transform are time-frequency analysis methods suitable for nonstationary signals [7, 8]. Therefore, based on the conventional processing of ground motion records such as baseline correction and filtering, the wavelet and wavelet packet transforms are introduced to analyse their time-frequency characteristics. In the analysis of acceleration response spectra, in addition to the comparative analysis of the response spectrum characteristics of different epicentral distances, the response spectrum characteristics of different earthquake magnitudes at the same stations and the response spectrum characteristics of stations with similar epicentral distances but different site conditions, such as soil and bedrock, are comparatively analysed. In addition, a typical finite element model of a continuous beam bridge is established to analyse the stress of the model under the Ms6.4 earthquake in Yangbi, Yunnan Province. This study further explores the influence pattern of the nonstationary ground motion signal on the time-frequency characteristics of the structure, which has more in-depth research value and significance.

2. Collection and Processing of Strong Motion Records

Baseline correction, filtering, and other conventional data processing [9] were conducted on the uncorrected acceleration records. (1) The average value of acceleration recorded 20 s before the time of recording the original acceleration was calculated and subtracted from the recorded original acceleration, and then, the recorded zero drift was adjusted. (2) The acceleration records after zero-line adjustment were subjected to bidirectional high-pass filtering through a digital filter (4th-order Butterworth) in the cutoff frequency range of 0.01–100 Hz selected according to the Nyquist sampling rate. (3) The corrected acceleration records were filtered according to the Interim Code for computing the instrumental seismic intensity in the cutoff frequency range of 0.1–10 Hz, and the instrumental seismic intensities were computed. The basic information and related parameters of typical strong earthquake records

corresponding to the strong motion stations of the Ms6.4 earthquake are shown in Table 1. The maximum peak ground acceleration (PGA) of this earthquake (720.29 gal) was obtained from 53YBX (Yangbi Station that is 8.6 km far from the epicentral distance) in the NS direction. The records obtained in this earthquake were mostly far-field records and rarely near-field records.

3. Wavelet and Wavelet Packet Analysis

The wavelet transform and wavelet packet transform are tools of signal analysis and time-frequency analysis methods suitable for nonstationary signals [10]. The wavelet transform inherits and develops the idea of localization in the short-time Fourier transform (STFT) [11], which makes up for the shortcomings that the window width cannot be applied to any frequency and provides a time-frequency window that changes with frequency [12]. As a generalization and extension of the wavelet transform, the wavelet packet transform can provide a more refined signal analysis method [13]. Compared with the conventional Fourier transform and wavelet transform, the advantage of the wavelet packet transform is that it divides the time-frequency plane more finely and improves the resolution of the high-frequency component of the signal [14].

3.1. Wavelet Transform Analysis.
Considering that the waveform of a Daubechies wavelet is very similar to that of a ground motion velocity pulse in terms of high compactness, smoothness, and approximate symmetry [15], Daubechies 8 was used as the wavelet basis in this study. The time-frequency analysis of the ground motion signal of the Ms6.4 earthquake is carried out using a one-dimensional continuous wavelet transform [16]. The strong motion records in three directions (EW, NS, and UD) obtained at station 53YBX were selected for wavelet analysis. The analysis results are shown in Figure 1. In the frequency domain, the overall low-frequency signal energy is strong, the high-frequency signal energy is weak, and the energy in three directions is mainly concentrated in the 0–15 Hz range. In the time domain, there are two energy peaks in the EW and NS directions at 32–34 s and 36–38 s and one energy peak in the UD direction at 36–38 s. In general, the energy peak in the UD direction has a larger width and lower wavelet coefficients than those in the EW and NS directions.

3.2. Wavelet Packet Transform Analysis.
In this study, Daubechies 8 was still used as the wavelet base for wavelet packet decomposition. The sampling rate of the strong seismograph was 200 Hz. Considering the requirements of resolution and refinement, five-layer wavelet packet decomposition was selected, so the minimum frequency bandwidth was 1.5625 Hz. In addition, the sequence number sorting disorder occurs in wavelet packet decomposition. The MATLAB program was written using the method proposed in a past study [17] to realize the function of frequency sorting with a node sequence number. The frequency band energy ratio was intercepted within 0.1, and Figures 2–4 show the

TABLE 1: Typical strong motion records and some related parameters of the Ms 6.4 earthquake at epicentral distances of less than 200 km.

Station code	Station type	Epicentral distance (km)	PGA/cm/s/s			PGV/cm/s			Instrumental intensity
			EW	NS	UD	EW	NS	UD	
53YBX	Soil	8.6	−379.88	−720.29	−448.36	30.26	−29.4	−7.32	8.9
53DLY	Soil	31.3	−116.41	−108.25	−91.02	−8.45	11.48	2.24	6.95
53YPX	Soil	40.0	−44.94	−65.16	—	3.43	−7.39	—	—
53BTH	Rock	67.7	7.36	6.97	−6.05	0.53	−0.74	0.64	3.29
53BCJ	Soil	72.6	−22.5	−24.3	−18	−2.7	2.47	1.37	5.12
53LKT	Rock	103.5	−10.15	9.66	−12.84	−0.53	−0.48	−0.32	3.51
53SDX	Soil	124.0	19.06	−27.34	9.61	3.25	−4.49	0.78	5.39
53YRH	Soil	145.1	−6.2	−4.41	3.12	−0.64	0.57	0.24	3.09
53LLP	Soil	160.0	−2.41	−3.17	−1.56	−0.34	0.23	−0.11	2.23
51PZF	Soil	184.6	−2.39	2.74	−1.11	0.33	−0.34	0.18	2.17
53MST	Soil	190.2	−5.1	4.8	2.49	0.48	1.02	−0.26	3.2
51PZT	Soil	198.9	−4.95	4	−1.2	−0.26	0.26	0.08	2.41

(a)

(b)

(c)
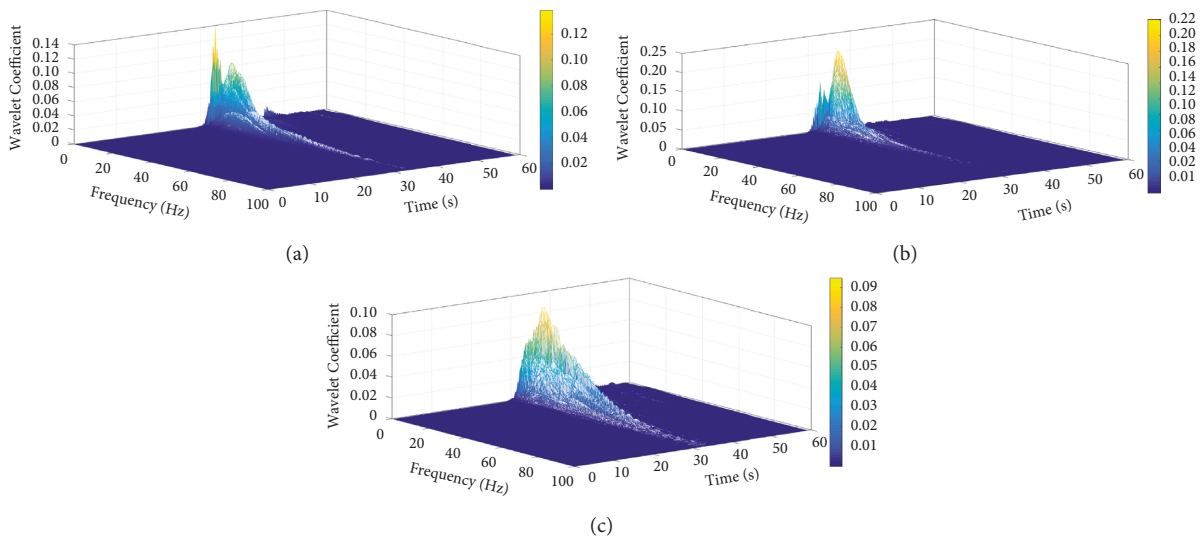
FIGURE 1: Wavelet time-frequency analysis of earthquake records at 53YBX: (a) east-west; (b) north-south; and (c) vertical.

distribution of the seismic energy spectrum of the Ms6.4 earthquake at stations with different epicentral distances.

The energy in the EW and NS directions at 53YBX (8.6 km from the epicentre), which was closest to the epicentre, is mainly distributed in the first 8 modes (0–12.5 Hz), the energy in the UD direction is more widely distributed in the first 13 modes (0–20.3 Hz), the energy in the EW direction peaks in the 0–1.6 Hz range, and the energy in the NS direction peaks in the 4.7–6.2 Hz range. There is no sudden increase in energy in the frequency band in the UD direction, and the width of the dominant energy band accounts for a large proportion. For 53DLY (31.3 km from the epicentre), the energy in the EW and NS directions is mainly distributed in the first 10 modes (0–15.6 Hz), the energy in the UD direction is distributed in the first 11 modes (0–17.2 Hz), the energy in the EW and NS direction peaks in the 0–1.6 Hz range, and the energy in the UD direction peaks in the 9.4–10.9 Hz range. For 53BCJ (72.6 km from the epicentre), the energy in the EW and NS directions is mainly distributed in the first 3 modes (0–4.7 Hz), the energy in the UD direction is distributed in the first 5 modes

(0–7.8 Hz), and the energy peaks in the 0–1.6 Hz range is distributed in all three directions. It is found that the width of dominant energy band at stations with different distances from the epicentre of the same earthquake is greater in the UD direction than in the EW and NS directions. With the increase in epicentral distance, the width of the characteristic energy frequency band becomes narrower, the dominant energy is more concentrated in low-frequency bands, and the high-frequency energy decreases.

4. Characteristics of the Acceleration Response Spectra

The acceleration response spectrum is an important basis and method for engineering seismic design. Calculating and analysing the acceleration response spectra are helpful to understand the frequency-domain characteristics of strong earthquake acceleration near the epicentre and directly show the maximum response of structures with different natural periods to earthquakes [18].

(a)

(b)

(c)
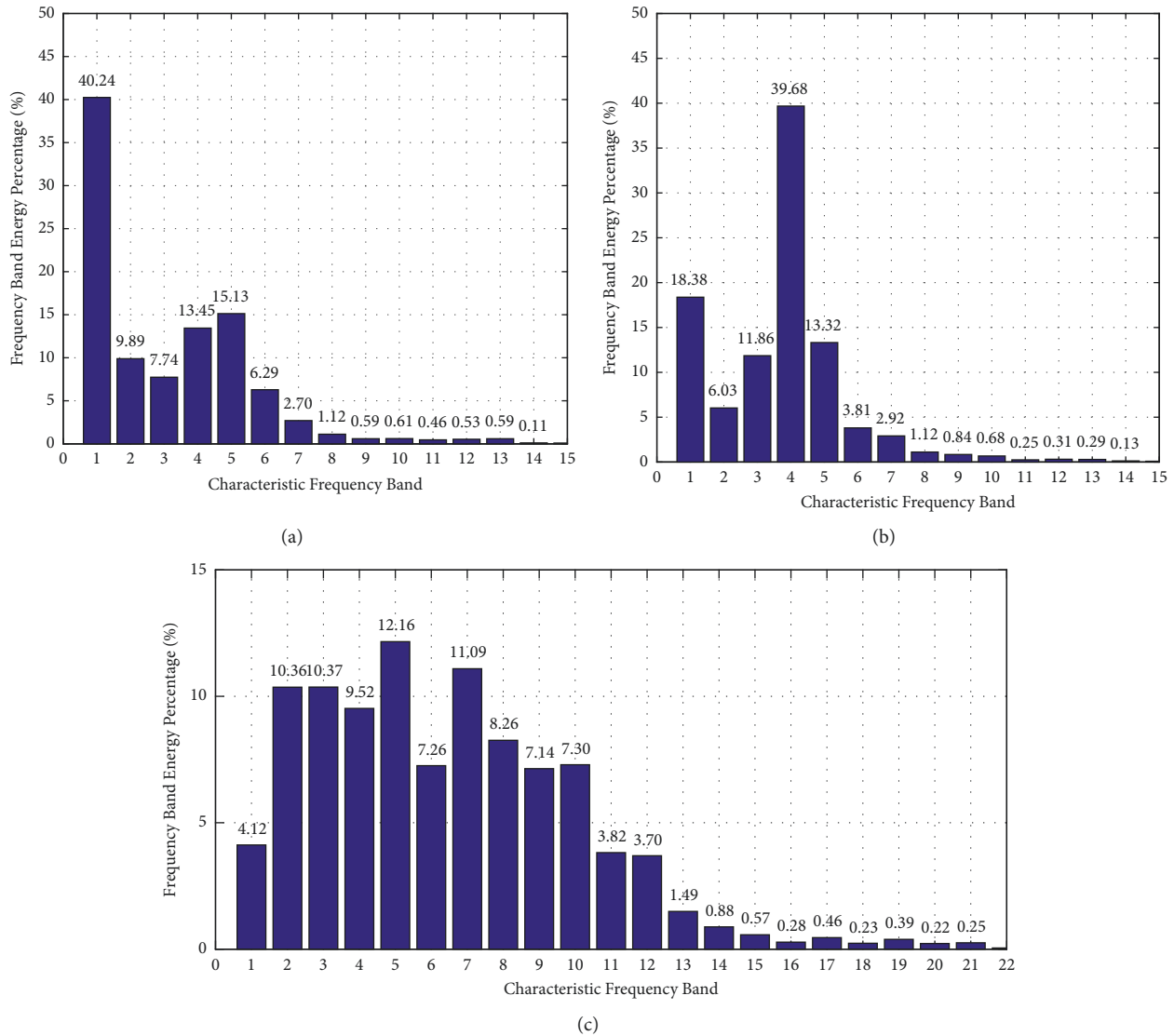
FIGURE 2: Energy probability distribution of earthquake records at 53YBX (8.6 km from the epicentre): (a) east-west; (b) north-south; (c) and vertical.

4.1. Acceleration Response Spectra of Stations at Different Epicentral Distances.

Acceleration response spectra (Sa) of three soil stations (53YBX, 53DLY, and 53BCJ) with different distances from the epicentre of the Ms6.4 earthquake were selected and compared with the seismic design response spectra of the areas where the stations are located (Code for Seismic Design of Buildings (GB 50011–2010)). Station 53YBX is located in Yangbi Yi Autonomous County. For station 53YBX, the seismic fortification intensity is VIII, the design basic seismic acceleration is 0.20 (m/s^2), and the design ground motion group is the third group. The seismic fortification intensity for stations 53DLY and 5BCJ is VIII. As can be seen from Figure 5, there is similarity between the Sa spectra in the three directions of 53YBX (EW, NS, and UD), the predominant period of which is around 0.04–0.09 s. The Sa value in the directions of EW and NS is higher compared with the design spectrum of intensity VIII rare earthquake within 0.1 s. When the period is smaller than

1.2 s, the Sa is higher than the design spectrum of intensity VIII fortification earthquake; in the UD direction, the Sa is higher than the design spectrum of intensity VIII rare earthquake within 0.2 s, and after 3 s, the Sa attenuates to near 0 g. The 53DLY three direction predominant periods of Sa are approximately 0.05–1.1 s, and the Sa is lower than the design spectrum of intensity VIII rare earthquake. When the period is smaller than 1.2 s, the Sa in the EW and NS directions is higher than the design spectrum of intensity VIII frequent earthquake, and in the UD direction, the Sa is higher than the code design spectrum of intensity VIII frequent earthquake within 0.1 s. The Sa in the three directions at station 53BCJ is lower than the design spectrum of intensity VIII frequent earthquake, and the predominant period of Sa is approximately 0.15–1.5 s. The comparison shows that the Sa value near the origin of the earthquake is relatively large. As the distance from the epicentre increases, the predominant period of Sa is also gradually increasing,

(a)

(b)

(c)
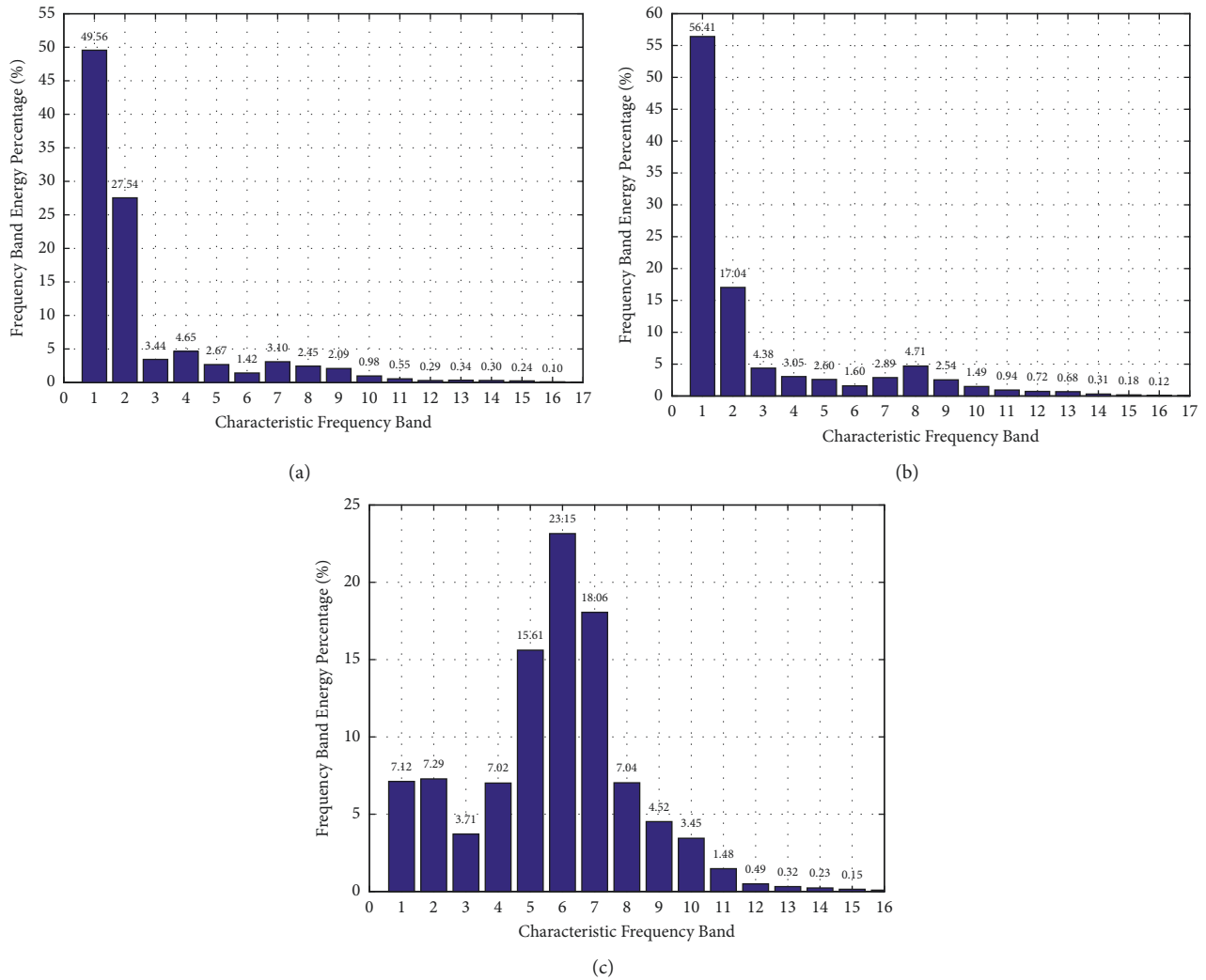
FIGURE 3: Energy probability distribution of earthquake records at 53DLY (31.3 km from the epicentre): (a) east-west; (b) north-south; and (c) vertical.

the high-frequency component diminishes, and the Sa spectrum shifts to the long period on the whole, which is attributed to the attenuation of the ground motion through the propagation medium. Consequently, the maximum response of the structure is reduced as well.

4.2. Acceleration Response Spectra of Different Earthquake Magnitudes at the Same Station. Three earthquakes (Ms6.4, Ms5.6, and Ms5.2) at the 53YBX station were selected, and their Sa was comparatively analysed (Figure 6). The Sa values of Ms6.4 in three directions within 0.09 s are higher relative to the design spectrum of intensity VIII rare earthquake, while those of Ms5.6 in the directions of EW and NS within 0.1 s are higher compared with the design spectrum of VII rare earthquake, the Sa values in the direction of UD is lower than the design spectrum of intensity VIII rare earthquakes and higher than the design spectrum of intensity VII rare earthquakes with this period and those of Ms5.2 within 0.09 s are higher in comparison with the design spectrum of intensity VIII rare earthquake in the direction of NS. As

revealed by the comparison, the Sa spectra of the three earthquakes are consistent in the same direction, and the Sa values in the direction of NS at the same station with different magnitudes of earthquake are greater than in the directions of EW and UD. With an increase in magnitude of the earthquake, the Sa peak value rises and the long-period component becomes more significant.

4.3. Acceleration Response Spectra of Soil and Bedrock Stations with Similar Epicentral Distances. A soil station 53BCJ (epicentral distance is 72.6 km) and a bedrock station 53BTH (epicentral distance is 67.7 km) with similar distances from the epicentre of the same Ms6.4 earthquake were selected. According to the intensity values of the two stations (Table 1), the instrument intensity of the two stations reaches 3.29 and 5.12, respectively. Therefore, the intensity VI frequent and fortification seismic design spectrum is adopted for comparison. As shown in Figure 7, the Sa tridirectional value curve of 53BCJ is lower compared with the intensity VI fortification seismic design spectrum, with the
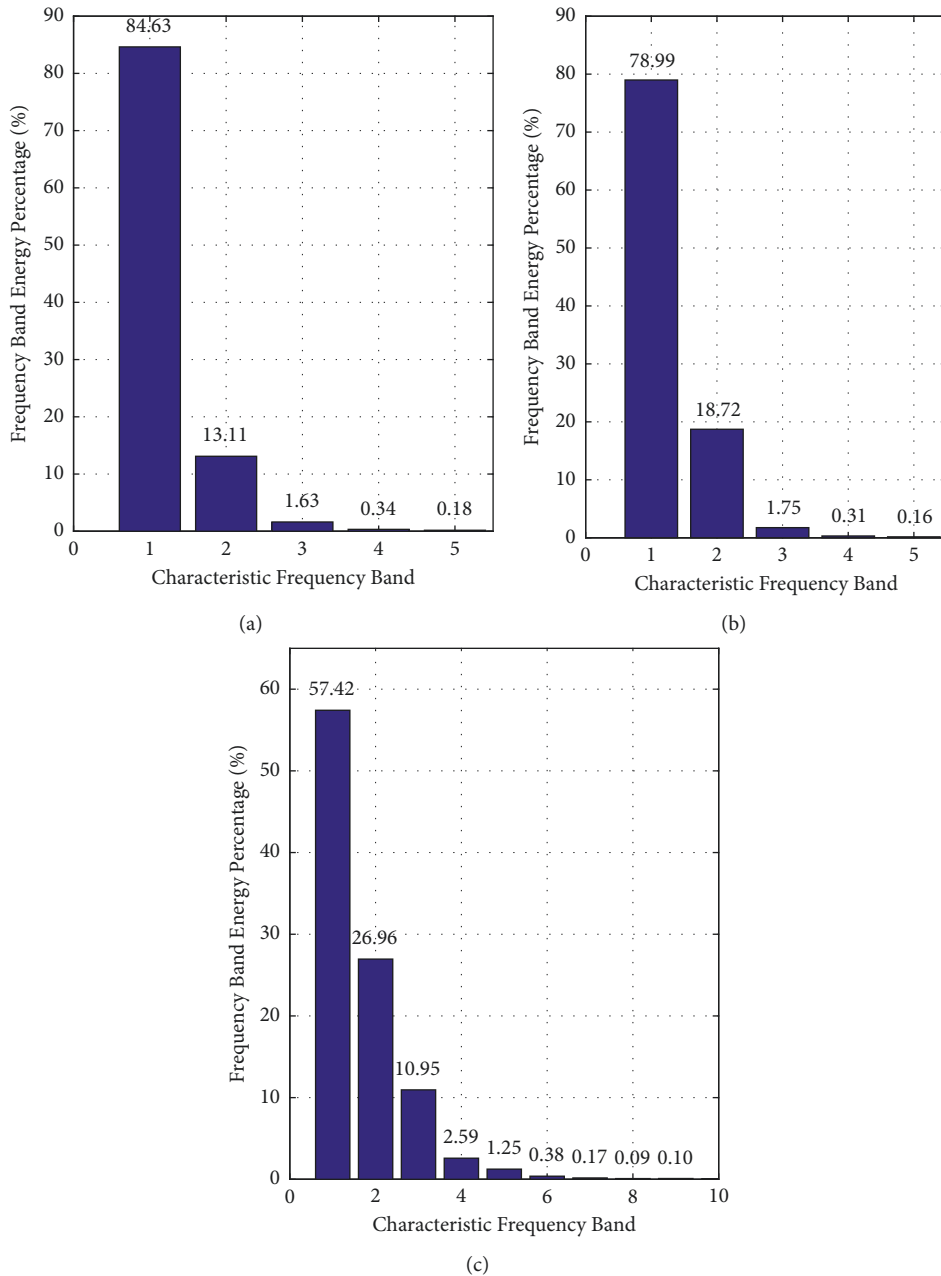
FIGURE 4: Energy probability distribution of earthquake records at 53BCJ (72.6 km from the epicentre): (a) east-west; (b) north-south; and (c) vertical.

values after 0.2 s in the directions of NS and EW reaching a level that is higher than the intensity VI frequent seismic design spectrum, and the Sa tri-directional values curve of 53BTH is lower compared with the intensity VI seismic design spectrum. According to the comparison, the soil station (53BCJ) has a high peak Sa value and long-cycle component relative to the bedrock station (53BTH), the process of Sa attenuation is slowed, and the overall response spectrum curve shifts to the right. The analysis reveals that site conditions tend to have a significant impact on ground motion and that soil field causes a more evident amplification effect on the acceleration response of ground surface than bedrock. Such amplification is not confined to being manifested in the long-cycle part. Instead, the Sa amplitude

of the short-cycle part also increases, which exerts a widespread influence on buildings. The specific amplification factor is related to the thickness of soil overburden [19–21], which is worthy of further study.

5. Seismic Response Analysis of Typical Structures

As the lifeline project of urban construction, the seismic safety of road and bridge structures is of great significance to ensure the normal operation of social, political, and economic life, as well as post-earthquake rescue and reconstruction [22]. In this section, the finite element model of a typical three-span reinforced concrete continuous beam

(a)

(b)

(c)
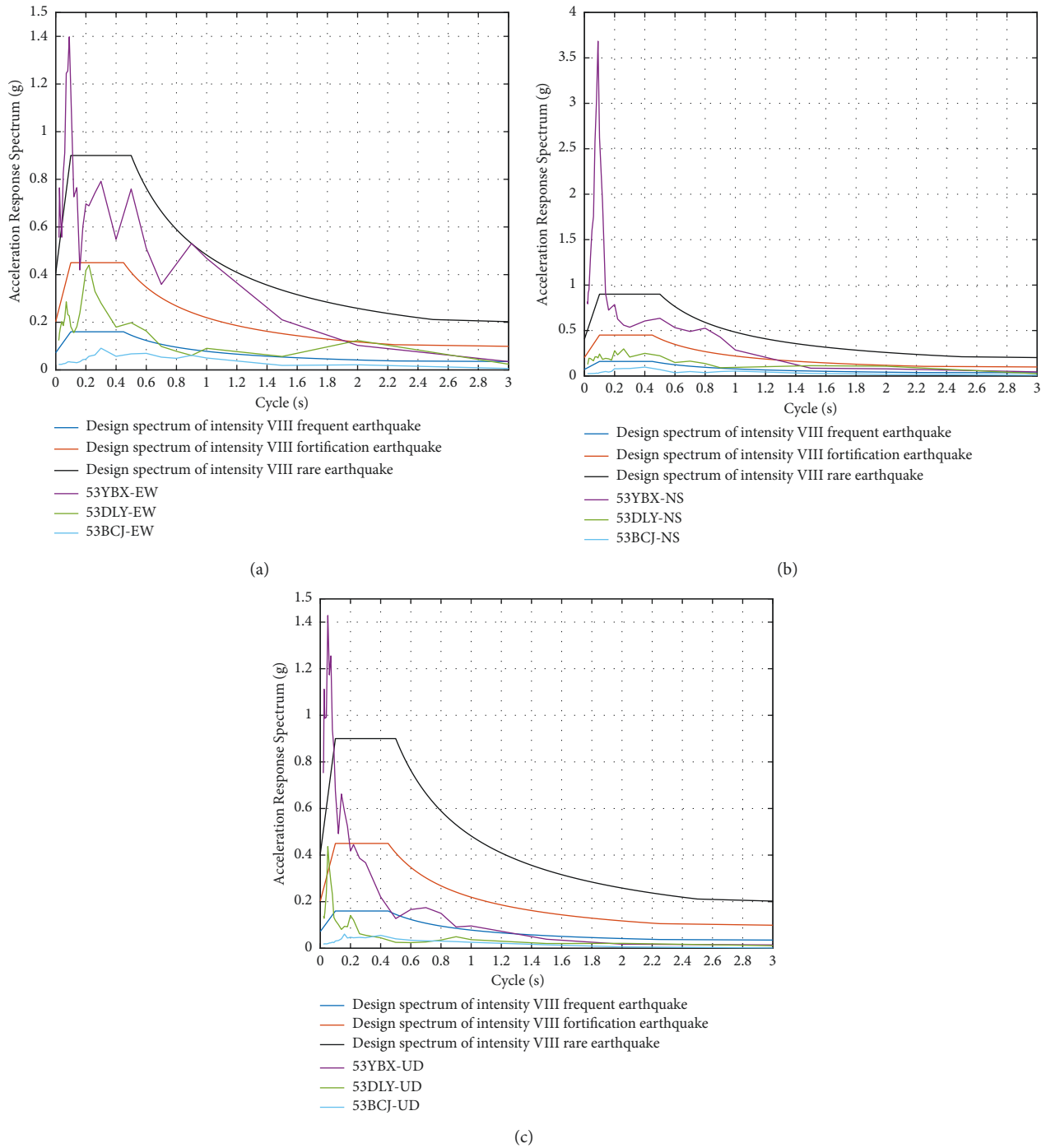
FIGURE 5: Comparison of acceleration response spectra (Sa) and code design spectra among stations with different epicentral distances: (a) east-west; (b) north-south; and (c) vertical. Note: all acceleration response spectra involved in this section are acceleration response spectra (Sa) with a damping ratio of 5%.

bridge is established to simulate the stress on the bridge under an earthquake, analyse the influence of the parameters of the bridge in the seismic response, and lay a foundation for future seismic research [23].

5.1. Project Overview. A continuous girder bridge is characterized by large structural stiffness, small deformation, few expansion joints, and a smooth and comfortable surface for driving, so it is widely used in the development of modern bridges. In this study, a three-span $(40 + 70 + 40)$ m continuous beam bridge was selected as the model [24]. The bridge elevation is shown in Figure 8. The bridge superstructure is a reinforced concrete continuous box girder, and the substructure consists of rectangular gravity piers [25]. The size of each pier is $8 \, \text{m} \times 3.5 \, \text{m} \times 5.0 \, \text{m}$. The diameter of
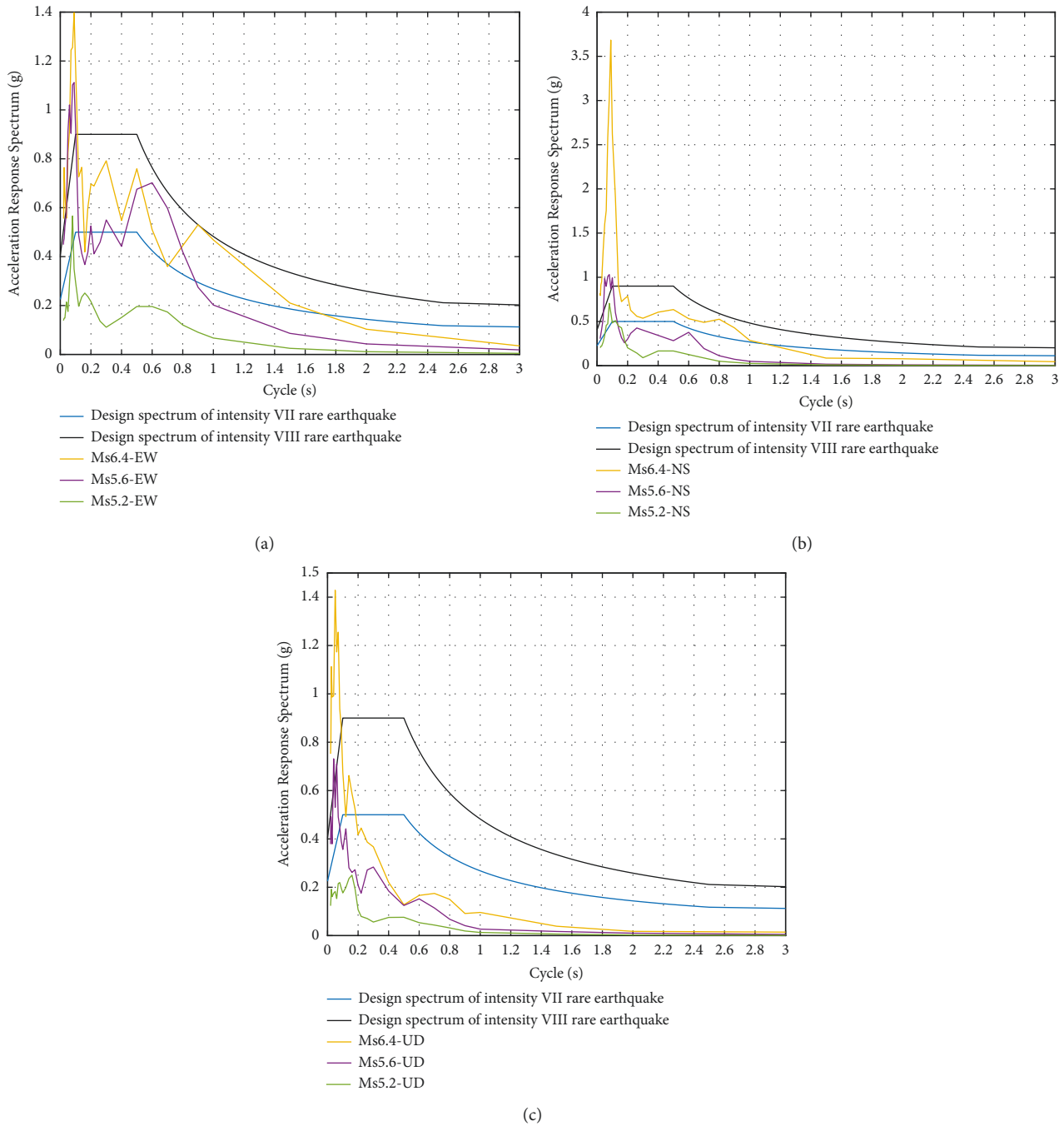
FIGURE 6: Comparison of acceleration response spectra (Sa) and code design spectra among the MS6.4, MS5.6, and MS5.2 earthquakes: (a) east-west; (b) north-south; and (c) vertical.

the main reinforcement of a pier is 28 mm, the diameter of the other reinforcement is 16 mm, the foundation is pile cap foundation, and the foundation conditions were added according to the geological survey data. The pier helps to ensure ductility and higher bearing capacity. Considering the E1 and E2 stages, the response of the pier of the bridge structure under the earthquake is studied and analysed [26].

5.2. Define the Constitutive Relationship of Reinforced Concrete. During the seismic analysis of the bridge, the

$M - \varphi$ curve shall be defined according to the requirements of the specification. For the reinforced concrete pier, the concrete in the core area shall be calculated as constrained concrete [27], and the concrete within the thickness of the protective layer shall be calculated as unconstrained concrete. The corresponding ultimate compressive strain of concrete is calculated according to the Mander constitutive relationship, and the reinforcement and section data are imported. The hysteretic model of reinforcement constitutive relationship is based on the

(a)

(b)

(c)
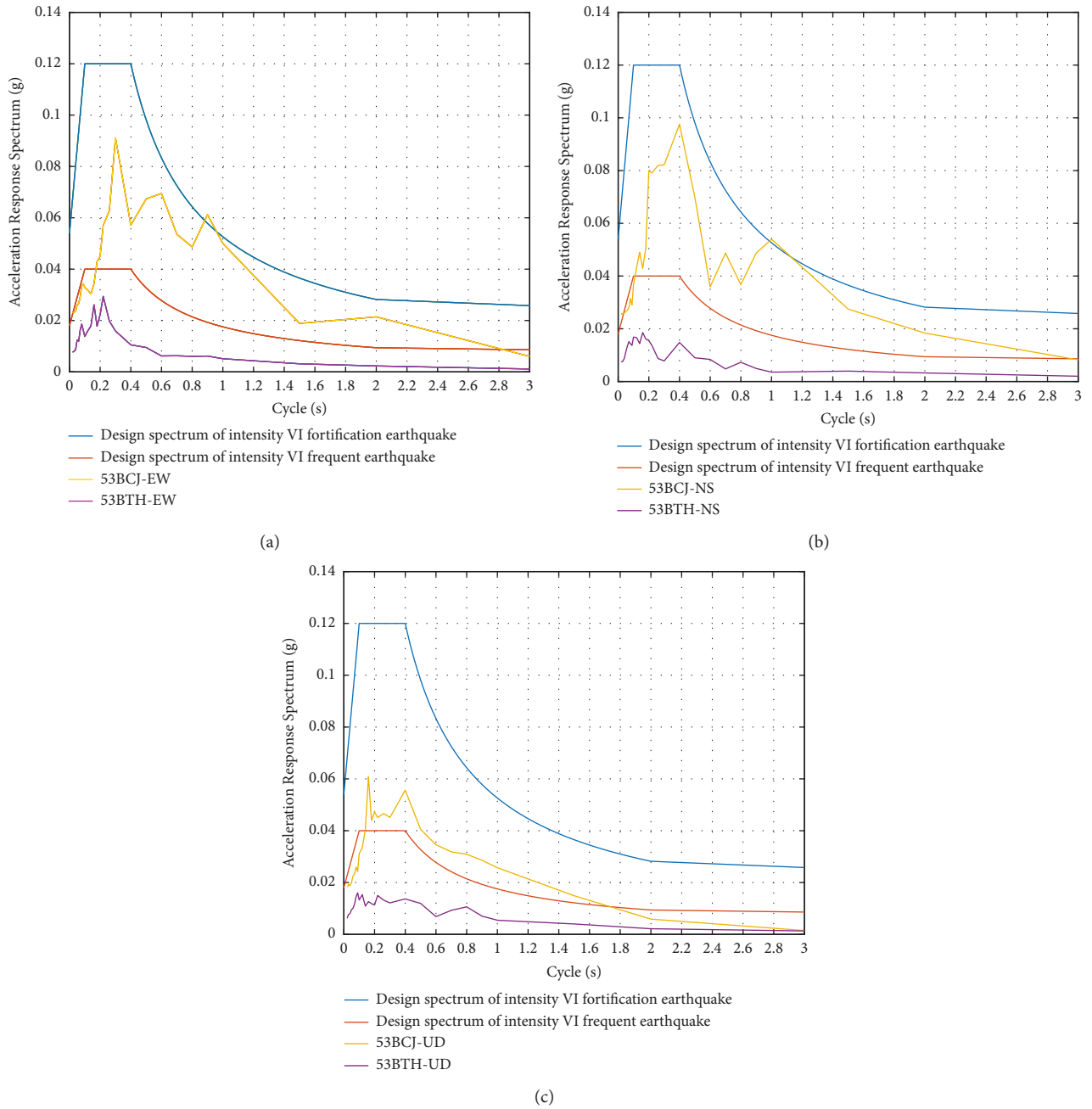
FIGURE 7: Comparison of acceleration response spectra (Sa) and code design spectra between a soil station (53BCJ) and a rock station (53BTH): (a) east-west; (b) north-south; and (c) vertical.
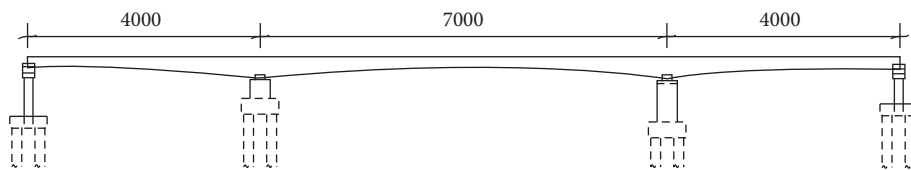
FIGURE 8: Bridge elevation.
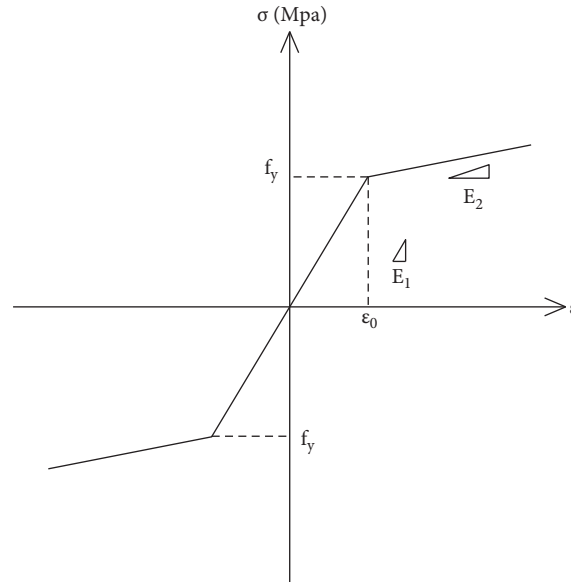
FIGURE 9: Constitutive relation of reinforcement.
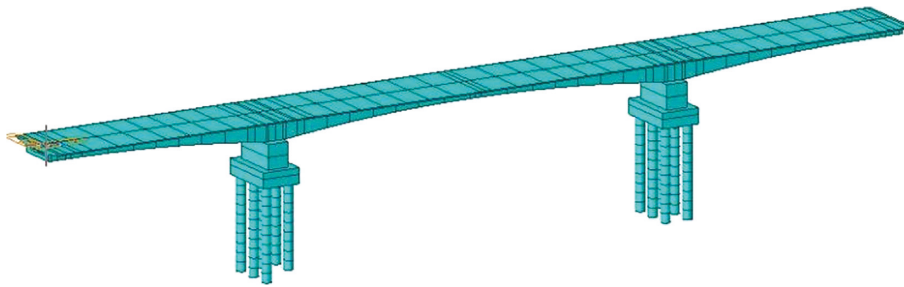
FIGURE 10: Finite element division of bridge elements.

double broken line model, in which Fy is 345 MPa, E1 is 210 Gpa, and E2 is 1% of E1 (Figure 9).

5.3. *Finite Element Model and Modal Analysis.* The dynamic calculation model of the bridge was established by Midas Civil software [28]. A total of 113 nodes were established for the whole bridge and divided into 96 units. The beam end and beam bottom were simplified as general support constraints [29], the superstructure and substructure were elastically connected, and the parts of the substructure were also elastically connected (Figure 10). The method was used to calculate the stiffness of the pile foundation in all directions. The structural load was converted into mass. The eigenvectors were computed using the Lanczos method, and the number of vibration modes was 110 [30]. The first 10 natural frequencies of the bridge structure and the cumulative participation mass of the first 110 modes were considered (Tables 2 and 3). The fundamental period of the bridge was 0.77 s, which is relatively small. The period basically changed in the first 5 modes. The cumulative participation mass of the first 67 modes exceeded 90% in the X and Y directions but did not exceed 90% in the Z direction until the 105th mode. The distribution of the

TABLE 2: First 10 natural frequencies and natural periods of the bridge structures.

Mode	Natural angular frequency (rad/sec)	Natural frequency (cycle/sec)	Natural period (sec)
1	8.213	1.307	0.765
2	8.737	1.391	0.719
3	11.445	1.822	0.549
4	14.957	2.380	0.420
5	15.356	2.444	0.409
6	17.089	2.720	0.368
7	20.840	3.317	0.301
8	25.400	4.043	0.247
9	34.298	5.459	0.183
10	40.157	6.391	0.156

three-dimensional cumulative participation rate of the first 110 modes is shown in Figure 11.

5.4. *Time History Conversion Response Spectrum.* Consider that the time history analysis results are lower than the response spectrum results, to better reflect the impact of the earthquake on the bridge structures [31]. This study uses Midas Civil software to convert the three-dimensional

TABLE 3: Cumulative participation mass of the first 110 vibration modes of the bridge structures.

Mode	Vibration mode participation mass/ X (%)	Vibration mode participation mass/ Y (%)	Vibration mode participation mass/Z (%)
1	0	70.47	0
2	0	70.47	25.89
3	75.74	70.47	25.89
4	76.62	70.47	25.89
5	76.62	70.47	73.97
6	76.62	70.47	73.97
7	77.83	70.47	73.97
8	77.83	70.47	73.97
9	77.83	70.47	74.05
10	77.83	70.47	74.05
. . .	. . .	. . .	. . .
67	90.17	92.87	77.69
. . .	. . .	. . .	. . .
105	90.17	92.87	94.35
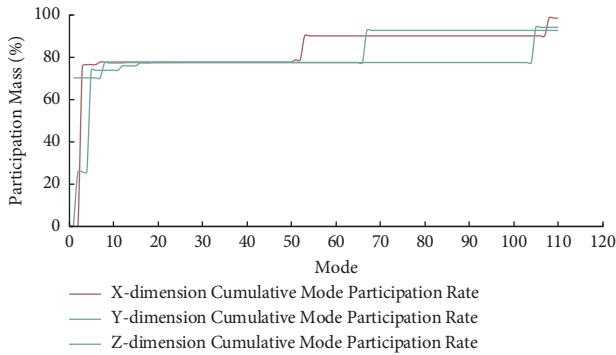
FIGURE 11: Three-dimensional cumulative mode participation rate.

(a)

(b)

FIGURE 12: Three-dimensional cumulative mode participation rate: (a) E1 and (b) E2.

TABLE 4: Bending moment of pier (unit: kN m).

Pier	E1	E2	Conversion response spectrum
Pier top	53290.7	104141.3	56216.8
Pier bottom	30877.6	43904.3	48833.0

TABLE 5: Pier displacement (unit: mm).

Pier	E1	E2	Conversion response spectrum
Pier top	22.01	39.2	12.1
Pier bottom	17.8	33.7	10.4

seismic wave of the Ms6.4 earthquake at 53YBX into the response spectrum, hereinafter referred to as the converted response spectrum, and then compares the converted response spectrum with the displacement and internal force of the response spectrum under E1 and E2 in the Specifications for Seismic Design of Highway Bridges [32].

The seismic fortification intensity of the area where the earthquake was located (Yangbi Yi Autonomous County, Yunnan Province) is VIII, the Ci values are 0.5 and 1.7, respectively, under the seismic importance factors E1 and E2, the zoning characteristic period is 0.45 s, the PGA is 0.2 g, the bridge type is class B, the damping ratio is 0.05, and other relevant parameters were selected according to the Specifications for Seismic Design of Highway Bridges (2020). The response spectra are fitted (Figure 12).

Using the Midas Civil software, the maximum bending moment and displacement of the pier top and bottom of the bridge under E1 and E2 stages were solved according to the Specifications for Seismic Design of Highway Bridges, and the results were compared with the calculation results based on the time history seismic wave conversion response spectrum (Tables 4 and 5). The results show that the earthquake has little effect on the displacement of the bridge piers, which is much smaller than those at E1 and E2 stages.

The maximum bending moment generated at the top of the bridge piers exceeds the E1 design bending moment by 5.5%, which is 53.1% lower than the E2 design bending moment. The maximum bending moment generated at the bottom of the piers exceeds the E1 design bending moment by 58.2% and exceeds the E2 design bending moment by 11.2%, indicating that the earthquake had a greater impact on the bottom of the bridge piers and that the pier bottom might have entered the plastic stage. The specific checking calculation needs further investigation of the boundary constraints and pier reinforcement design.

6. Conclusion

The ground motion records obtained in Yangbi, Yunnan Province, on May 21, 2021, were processed by filtering and other conventional processing. The time-frequency analysis of ground motion signals was carried out using wavelet,

wavelet packet, and acceleration response spectra. A model was established to analyse the seismic response of a typical three-span continuous beam bridge, which provides important reference materials for the investigation of ground motion characteristics and engineering seismic damage in Southwest China. The following conclusions can be drawn:

(1) The maximum PGA of the Ms6.4 earthquake occurred at station 53YBX. The low-frequency signal energy is strong, and the energy is mainly concentrated in the 0–15 Hz range.

(2) With the increase in epicentral distance, the characteristic frequency bandwidth of an energy spectrum becomes narrower, the dominant energy is more concentrated in the low-frequency band, and the high-frequency energy decreases.

(3) The Sa value near the origin of the earthquake is relatively large. With an increase in magnitude of the earthquake, the Sa peak value rises and the long-period component becomes more significant; the site conditions tend to have a significant impact on ground motion and that soil field causes a more evident amplification effect on the acceleration response of ground surface than bedrock.

(4) This earthquake has little effect on pier displacement, which is far less than the design response spectrum of E1 and E2 stages. The maximum bending moment generated at the top of the pier is less than the E2 design bending moment, and the maximum bending moment generated at the bottom of the pier is greater than the E2 design bending moment, indicating that the earthquake has a greater impact on the bottom of the bridge pier, and the bottom of the pier may have entered the plastic stage.

Data Availability

Data for this study are provided by the Institute of Engineering Mechanics, China Earthquake Administration.

Conflicts of Interest

The authors declare that they have no conflicts of interest.

Acknowledgments

References

[1] F. Long, Y. P. Qi, and G. X. Yi, "Relocation of the Ms6.4 Yangbi earthquake sequence on May21,2021 in yunnan Province and its seismogenic structure analysis," *Chinese Journal of Geophysics*, vol. 64, no. 8, pp. 2631–2646, 2021.

[2] C. Y. Li, J. Y. Zhang, and W. Wang, "The seismogenic fault of the 2021 Yunnan Yangbi Ms6.4 earthquake," *Seismology and Geology*, vol. 43, no. 3, pp. 706–721, 2021.

[3] W. Wang, J. He, X. Wang et al., "Rupture process models of the Yangbi and Maduo earthquakes that struck the eastern Tibetan Plateau in May 2021," *Science Bulletin*, vol. 67, no. 5, pp. 466–469, 2022.

[4] B. Chen and H. J. Li, "Characteristics of strong ground motions during the May 21, 2021 M6.4 Yangbi, Yunnan earthquake," *Journal of Nanjing University of Technology (Natural Science Edition)*, vol. 37, no. 4, pp. 81–90, 2021.

[5] W. T. Tian, J. H. Dong, and B. Yang, "Basic characteristics of the three elements of strong ground motion of the Yangbi Ms6.4 earthquake inYun nan Province," *China Earthquake Engineering Journa*, vol. 63, no. 4, pp. 760–766, 2021.

[6] P. R. Beaudet, J. K. He, X. Wang, and Y. Zhou, "Synthesis of nonstationary seismic signals," *Bulletin of the Seismological Society of America*, vol. 60, no. 5, pp. 1615–1624, 1970.

[7] S. Mukherjee and V. K. Gupta, "Wavelet-based characterization of design ground motions," *Earthquake Engineering & Structural Dynamics*, vol. 31, no. 5, pp. 1173–1190, 2003.

[8] H. Y. Yu, D. Wang, and Y. Q. Yang, "The preliminary analysis of strong ground motion characteristics from the Ms8.0 wenchuan earthquake," *Earthquake Engineering and Engineering Dynamics*, vol. 29, no. 1, pp. 1–13, 2009.

[9] L. Hong and C. H. Li, "Wavelet transform and application in signal processing," *Machine Building and Automation*, vol. 41, no. 3, pp. 131–133, 2012.

[10] K. Gurley and A. Kareem, "Applications of wavelet transforms in earthquake, wind and ocean engineering," *Engineering Structures*, vol. 21, no. 2, pp. 149–167, 1999.

[11] J. Allen, "Short term spectral analysis, synthesis, and modification by discrete Fourier transform," *IEEE Transactions on Acoustics, Speech, & Signal Processing*, vol. 25, no. 3, pp. 235–238, 1977.

[12] J. Morlet, G. Arens, E. Fourgeau, and D. Glard, "Wave propagation and sampling theory-Part I: complex signal and scattering in multilayered media," *Geophysics*, vol. 47, no. 2, pp. 203–221, 1982.

[13] M. Stephane, *A Wavelet Tour of Signal Processing*, Elsevier, Pittsburgh, 1999.

[14] D. F. Zhao, G. Y. Chen, and S. Chen, "Analysis of time-frequency characteristics of shaking table test data of subway underground station structure with different stiffness," *Journal of Nanjing University of Technology (Natural Science Edition)*, vol. 37, no. 4, pp. 77–84, 2015.

[15] M. P. Fargues, H. F. Overdyk, R. Wang, and Y. Zhou, "Wavelet-based detection of frequency hopping signals," in *Proceedings of the Conference Record of the Thirty-First Asilomar Conference on Signals, Systems and Computers (Cat. No.97CB36136)*, no. 1, pp. 515–519, Pacific Grove, CA, USA, November 1997.

[16] S. P. Wang, W. G. Zhang, and G. Y. Zhang, "Identification of structural parameters from free vibration data using Gabor wavelet transform," *Mechanical Systems and Signal Processing*, vol. 147, no. 2, pp. 107–114, 2020.

[17] X. Jin, L. C. Kang, and Y. P. Ou, "Acceleration spectrum attenuation relation for small and moderate earthquakes in Fujian region," *J Earthquake Engineering and Engineering Dynamics*, vol. 29, no. 5, pp. 52–58, 2009.

[18] N. C. Nigam and P. C. Jennings, "Calculation of response spectra from strong-motion earthquake records," *Bulletin of the Seismological Society of America*, vol. 59, no. 2, pp. 909–922, 1969.

[19] B. Mohraz, "A study of earthquake response spectra for different geological conditions," *Bulletin of the Seismological Society of America*, vol. 66, no. 3, pp. 915–935, 1976.

[20] P. K. Malhotra, "Smooth spectra of horizontal and vertical ground motions," *Bulletin of the Seismological Society of America*, vol. 96, no. 2, pp. 506–518, 2006.

[21] E. Kuribayashi, T. Iwasaki, Y. Iida, and K. Tuji, "Effects of seismic and subsoil conditions on earthquake response spectra," *International conference on microzonation for safer construction research and application*, vol. 2, pp. 668–671, 1972.

[22] Q. Han, X. Du, J. Liu, Z. Li, L. Li, and J. Zhao, "Seismic damage of highway bridges during the 2008 Wenchuan earthquake," *Earthquake Engineering and Engineering Vibration*, vol. 8, no. 2, pp. 263–273, 2009.

[23] F. X. Ding, W. Xia, x. Ping, and W. Y. Zhi, "New damage ratio strength criterion for concrete and lightweight aggregate concrete," *ACI Structural Journal*, vol. 118, no. 6, pp. 165–178, 2021.

[24] H. A. Mohamed, M. M. Husain, and A. M. Aboraya, "Progressive collapse of RC box girder bridges due to seismic actions," *Advances in Civil Engineering*, vol. 2020, no. 2, Article ID 1919683, 17 pages, 2020.

[25] S. Talatahari, V. P. Singh, A. H. Alavi, and F. Kang, "Soft computing methods in civil engineering," *The Scientific World Journal*, vol. 2015, no. 1, Article ID 605871, 2 pages, 2015.

[26] J. Deng, T. Liu, W. Xie, and W. Lu, "Study on repaired earthquake-damaged bridge piers under seismic load," *Advances in Materials Science and Engineering*, vol. 2015, Article ID 295392, 10 pages, 2015.

[27] W. G. Corley, "Applicability of seismic design in mitigating progressive collapse," in *Proceedings of the National Workshop on Prevention of Progressive Collapse*, p. 13, Rosemont, IL, USA, July 2002.

[28] H. Wibowo, S. S. Reshotkina, and D. T. Lau, N. L. St John's, Modeling progressive collapse of RC bridges during earthquakes," in *Proceedings of the CSCE Annual General Conference 2009: On the Leading Edge*, p. 11, Canada, May 2009.

[29] C. Akogul and O. Celik, "Effect of elastomeric bearing modeling parameters on the seismic design of RC highway bridges with precast concrete girders," in *Proceedings of the 14th World Conference on Earthquake Engineering (14WCEE)*, Beijing, China, October 2008.

[30] A. Chopra, *Dynamics of Structures: Aeory and Applications to Earthquake Engineering*, Prentice-Hall, Englewood Cliffs, NJ, USA, 1995.

[31] Z. Sun, D. Wang, X. Du, and B. Si, "Rapid repair of severely earthquake-damaged bridge piers with flexural-shear failure mode," *Earthquake Engineering and Engineering Vibration*, vol. 10, no. 4, pp. 553–567, 2011.

[32] N. Shome, C. A. Cornell, P. Bazzurro, and J. E. Carballo, "Earthquakes, records, and nonlinear responses," *Earthquake Spectra*, vol. 14, no. 3, pp. 469–500, 1998.

Research Article

Mechanical Properties of the Shear Failure of Rock Masses with Prefabricated Sinusoidal Fractures

Limei Tian,[1,2] Hongzhou Zhang,[2] Wei Hong,[1] Yunxia Zhang,[2] Jinghua Zhang,[3] and Wenhui Tan [ORCID][1]

[1]*School of Civil and Resource Engineering, University of Science and Technology Beijing, Beijing 100083, China*
[2]*Institute of Architectural Civil Engineering, Langfang Normal University, Langfang 065000, China*
[3]*China Petroleum Pipeline Engineering Corporation, Langfang 065000, China*

Correspondence should be addressed to Wenhui Tan; wenhui.t@ustb.edu.cn

A large number of sinusoidal fractures exist in the open-pit slopes of mines, and the mechanical properties of shear failure are of great significance to the stability of the open-pit slope. Sandstone specimens containing sinusoidal fractures with different undulated heights were prefabricated by the CNC sand-wire-electrode cutting technology to explore the effect of sinusoidal fractures on the mechanical properties of shear failure of rock masses. The TFD-20H/50J rock shear testing machine was used for shear tests on sinusoidal-fracture sandstone with different undulated heights. In the shear loading process, the prefabricated-fracture sandstone specimens with different undulated heights have the fracture-compacting stage, linear-elastic changing stage, bottom-up stage, and residual strength stage. Before peak strength, the sinusoidal prefabricated-fracture rock masses with different undulated heights have the precursory characteristics of decreased stress, which can provide an early warning for the instability and failure of rock masses. The undulated height of sinusoidal fractures significantly affects the fracture initiation and propagation of specimens. Fractures occur and develop from the prefabricated fractures at low undulated height (≤10 mm) to multiple ways under the high undulated height (>10 mm); that is, fractures occur at the prefabricated fractures and the end of specimens simultaneously. With the increased undulated height, the fractures expand from parallel to the slope of the prefabricated fractures to perpendicular to the prefabricated fractures. The fracture propagation direction of sinusoidal-fracture rock masses with different undulated heights is mainly from the middle of the slope surface of prefabricated fractures to the end. It is the main direction of the shear failure of sinusoidal prefabricated fractures, and the monitoring of weak planes should be strengthened in the actual slope engineering.

1. Introduction

The sloped rock masses of an open-pit mine usually have a large number of irregular structural planes, among which fractures are particularly critical to the physical and mechanical properties of rock masses. The shear-failure mechanical property of rock masses is a vital index, widely used in studying the stability of rock engineering. In slope engineering, the landslides of rock masses are usually closely related to the shear strength of slopes, with various fractures, joints, interlayers, sliding surfaces, and faults in rock masses. In the process of landslides of rock masses, the physical and mechanical properties of fractures play a crucial role in fracture initiation, expansion, and damage, and the stability of the slope is also a prerequisite for the safe production of open-pit mines. Therefore, it is vital to study the influence mechanism of fracture geometries on shear failure in fractured rock masses to explore the engineering stability of rock masses [1–3].

The material and structure of rock masses play a decisive role in the mechanical properties and law of rock-mass failure [4–8]. The common shear failure modes of rock masses along the structural plane are as follows in practical engineering: slipping damage to dam foundations [5],

Figure 1: Specimens of fractures with different undulated heights.
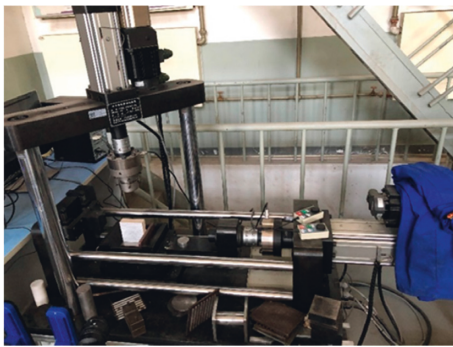
Figure 2: Shear testing machine of rocks.

unstable slipping of the sloped rock masses under low stress [6], disasters caused by static force, fault-slip earthquakes [7], and structural-plane slipped rock burst under high stress [8].

Therefore, the shear-failure mechanical properties and failure laws of structural planes of rock masses have attached great importance to rock mechanics. Scholars have studied them using indoor shear tests and numerical simulation methods [9–15]. Li et al. used cement mortar to make zigzag fractures with different undulated heights [16, 17]. Direct shear tests are performed to analyze the shear-failure mechanical properties and failure laws of zigzag fractures with different undulated heights. Zhang et al. [18] also used cement mortar to produce regular zigzag-fracture specimens with different undulated heights. The shear test studied the effects of different normal stress on the failure mechanical properties of specimens.

Foreign scholars have also studied zigzag fractures. Patton proposed a formula for calculating the shear strength of zigzag-fracture specimens [19], which has considerable limitations. Only extreme states under high/low normal stress can be investigated, and the failure of specimens cannot be well expressed under moderate normal stress. Zhang et al. used PFC^{2D} (discrete-element, particle-flow software) for numerical simulations on the specimens with different structural-plane values to analyze the strength characteristics of isotropic and heterogenic structural planes [20]. V. Sarfarazi et al. used PFC^{2D} to study the failure modes of square specimens with two horizontal fractures under the shearing action [21]. The failure modes are mainly affected by the overlap of joints, while shear strength is closely related to the failure mode.

At present, studies on irregular fractures in indoor shear tests and numerical simulations mostly consider regular zigzag fractures. A large number of sinusoidal fractures exist on the surface of the fractured rock masses of the open-pit mine slope in practical engineering, e.g., Hebei Heishan iron mine, Xigou limestone mine stope slope, and Yuebao open-pit mine. Therefore, the work prefabricated the rock masses with sinusoidal fractures and different undulated heights for shear tests. The test results have a certain reference for the safety of open-pit mines and other projects.

2. Materials and Methods

2.1. Specimen Preparation.
In this test, sandstone was used as the sample material, and the geometric size of the rock masses with prefabricated fractures was $100 \times 100 \times 30$ mm. The SK7740 CNC sand-wire-cutting machine was used to prepare sinusoidal fractures, and the undulated heights of fractures were 5, 10, 15, 20, and 30 mm (see Figure 1).

2.2. Test Equipment and Loading Conditions.
The TFD-20H/50J rock shear testing machine was used in the test (see Figure 2), and the normal load was first applied to specimens. The load was applied to 0.5 kN by the displacement control of 3 mm/min and then applied to 3 kN by the load control of 0.1 kN/s. Normal stress was kept stable at 3 kN, and tangential stress was loaded at a loading rate of 0.5 mm/min.

DIC equipment was used to monitor the surface deformation of specimens after pretreatment to analyze the deformation properties of specimens in the shearing process. The surface of the test piece was marked before the DIC test. First, spray a uniform layer of white primer on the side of the sample, and then spray uniform and irregularly distributed black paint speckles. A CCD camera was used to monitor the displacement changes of speckle images on the side of specimens in the shearing process. The image acquisition rate was 23 frames per second, which was used to obtain the instantaneous process of the shearing failure of specimens.
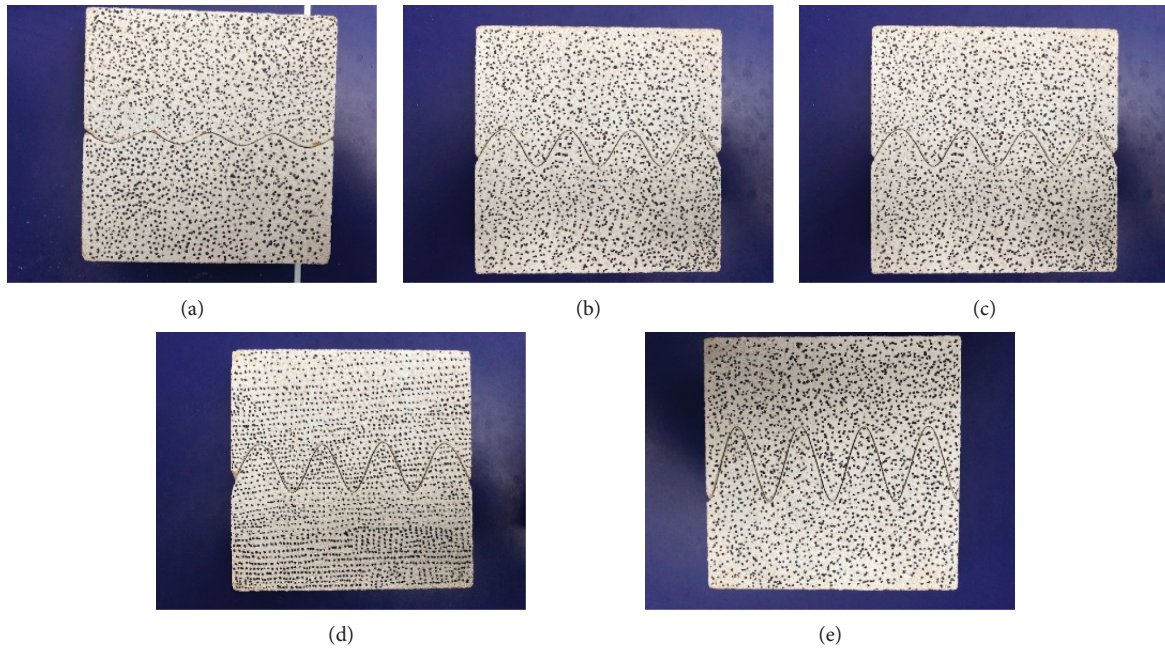
FIGURE 3: Specimens after marking. (a) Undulation of 5 mm. (b) Undulation of 10 mm. (c) Undulation of 15 mm. (d) Undulation of 20 mm. (e) Undulation of 30 mm.
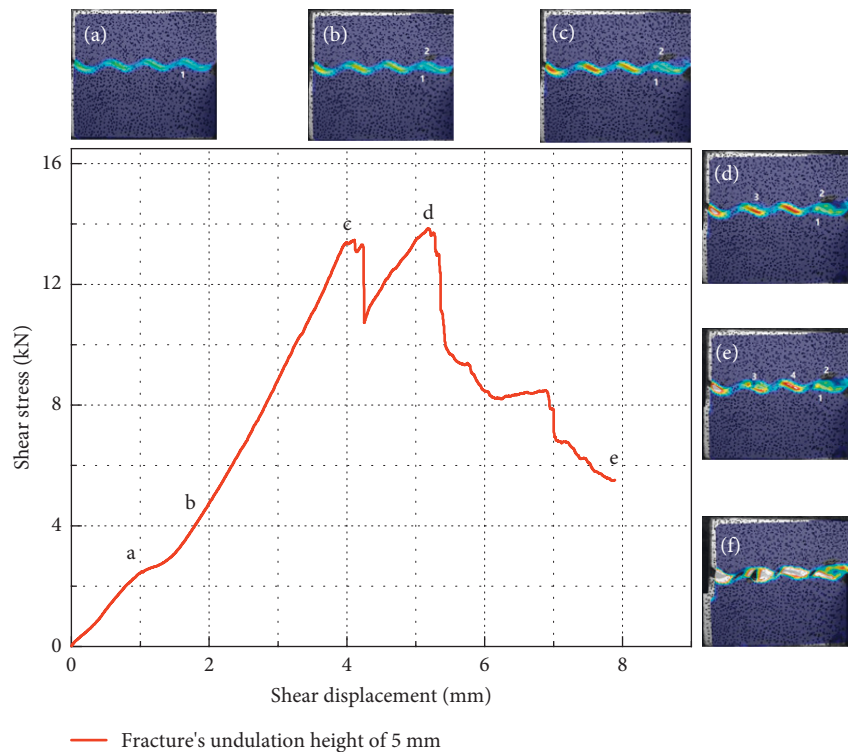
FIGURE 4: Shear stress-shear displacement curve of the specimen with an undulated height of 5 mm.

After the test, the monitoring images in acquisition cards were input into the computer for data processing. The monitoring range of strain could reach 0.005–2000%, which could meet the monitoring needs of shear tests. Surface-marked specimens are presented in Figure 3 for monitoring with DIC.

3. Results and Discussion

3.1. Analysis of Shear Stress-Shear Displacement Properties of Specimens under Direct Shearing. The work only analyzed the specimens with the prefabricated-fracture undulated heights of 5 and 30 mm due to the manuscript's length limit
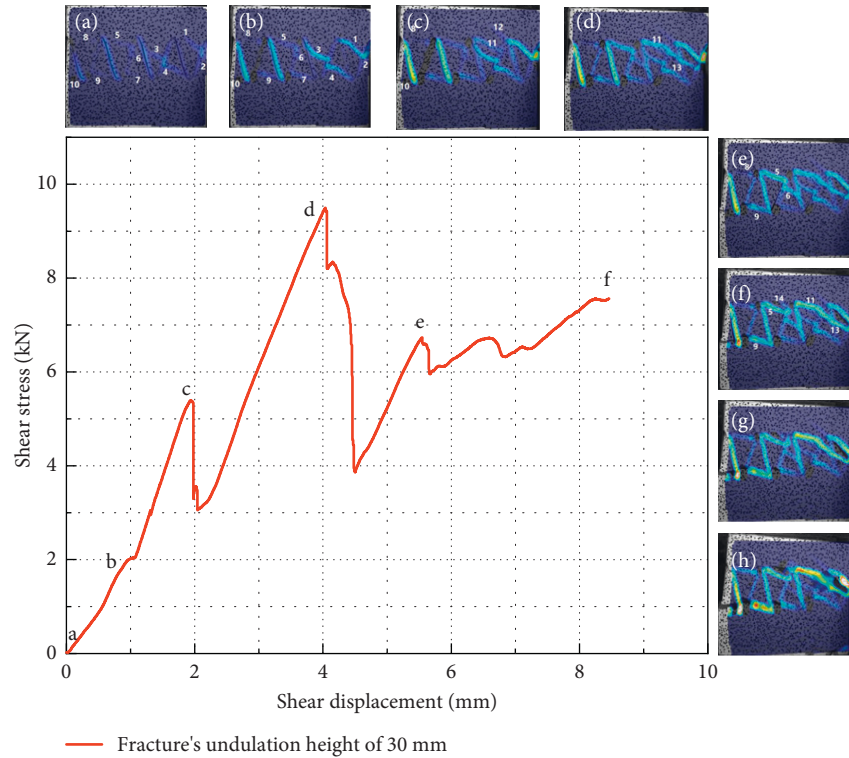
FIGURE 5: Shear stress-shear displacement curve of the specimen with an undulated height of 30 mm.

to analyze the shear stress-shear displacement properties of specimens under direct shearing. The details are as follows.

Figure 4 shows the shear stress-shear displacement curves of specimens with a prefabricated-fracture undulated height of 5 mm under the direct shear test as well as the development process of fractures. The characteristics of the shear stress-shear displacement curves are divided into four stages: the fracture-compacting stage, linear-elastic changing stage, bottom-up stage, and residual strength stage. The properties of each stage are as follows.

Fracture-compacting stage (ab): the shear stress-shear displacement curve is concave upward. The increment of the shear displacement decreases with increased shear stress, indicating that the prefabricated fractures of specimens and the internal fine original fractures close and compact under shear stress.

Linear-elastic changing stage (bc): the shear stress-shear strain curve presents a straight-line shape and obeys Hooke's law. With increased shear stress, fractures 1 and 2 occurred and gradually extended under stress (see Figures 4 (a) and (b)). Since the tiny fractures produced are not enough to reduce the overall shear strength of specimens, shear stress continues to increase.

Bottom-up stage (cd): this stage is characterized by the tendency of specimens' shear stress to decrease first and then increase. The stress value at point d is greater than that at point c, indicating that point d is the peak shear stress of specimens. That increased shear stress makes the fractures expand continuously, resulting in local damage to specimens; therefore, shear stress decreases immediately.
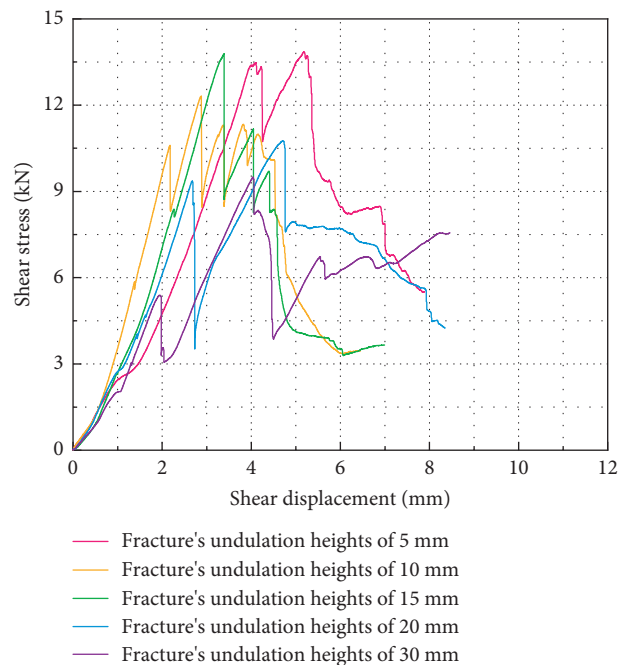
FIGURE 6: Shear stress-shear displacement curves of specimens with fractures having different undulated heights.

However, local damage is not enough to reduce the overall bearing capacity, and specimens still have a high bearing capacity. Thus, the shear stress of specimens continues to increase. Figure 4(e) shows new fractures that appear in specimens and develop in this process.
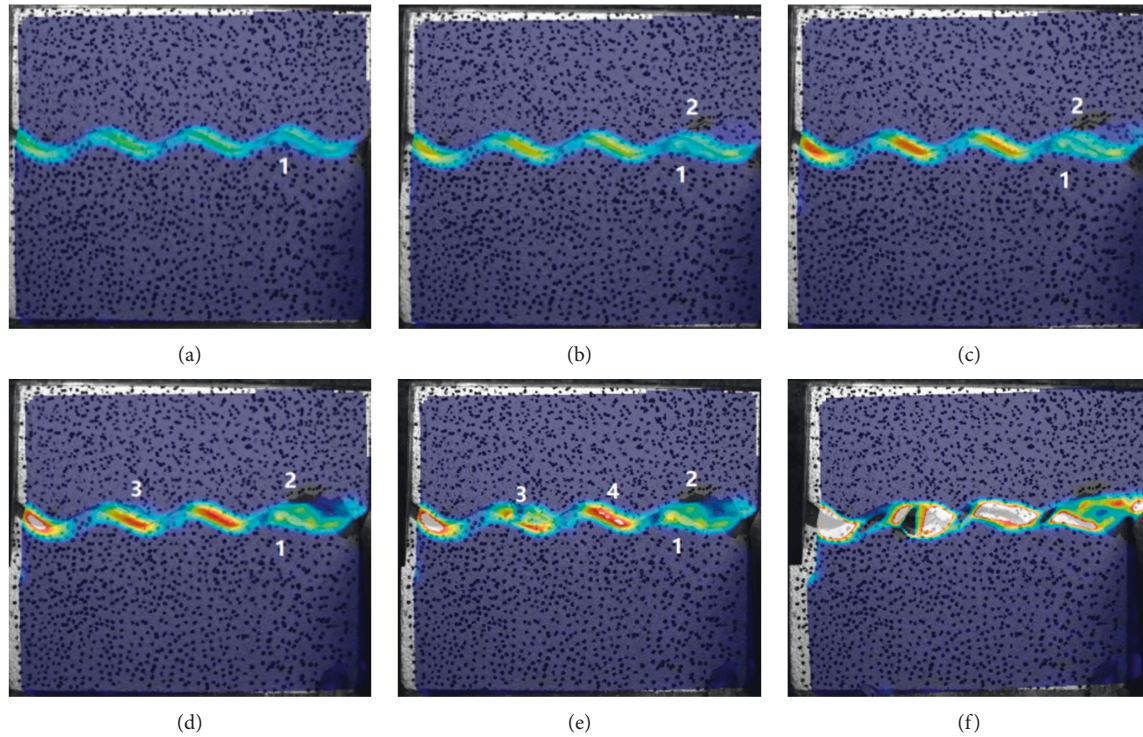
FIGURE 7: Failure process of the specimen with an undulated height of 5 mm under DIC monitoring.

Residual strength stage (de): fractures are further expanded under shear stress during this period. Damage occurs at the prefabricated sinusoidal fractures, causing large-scale fractures to penetrate each other and the specimens to lose most of their bearing capacity. At this time, the strength of the specimens is provided by internal friction force, and Figure 4(f) shows the final failure of the specimens.

Figure 5 shows the shear stress-shear displacement curve of the specimen with the prefabricated-fracture undulated height of 30 mm in the direct shear test as well as the development process of fractures. According to the properties of the shear stress-shear displacement curve, it is divided into five stages: the fracture-compacting stage, linear-elastic changing stage, first and second bottom-up stages, and residual strength stage.

Fracture-compacting stage (ab): the shear stress-shear displacement curve is concave upward. The increment of the shear displacement decreases with increased shear stress, indicating that the prefabricated fractures of specimens and the internal fine original fractures close and compact under shear stress.

The linear-elastic changing stage (bc): the shear stress-shear displacement curve presents a straight-line shape and obeys Hooke's law. Fractures occur and expand. In Figure 5(a), fractures 1, 2, 3, 4, and 5 occur and expand with the large undulated height due to compression of shear stress.

The 1st bottom-up stage (cd): this stage is similar to the bottom-up stage with an undulated height of 5 mm. However, the specimens with an undulated height of 30 mm rise more after the curve descends. Figure 5(c) shows that local

fractures occur at the top and middle of sinusoidal fractures, which decreases the bearing capacity and descends the curve. However, the fractures are small, and no major penetration occurs. There is still a strong bearing capacity, so the curve continues to rise.

The 2nd bottom-up stage (de): this stage is different from the 1st bottom-up stage, and its bottom and up sections are located after the shear stress peak. With the further expansion and penetration of fractures, the strengthening of the squeezing action near the top of the sinusoidal fracture causes the entire part of the specimen to be damaged. As a result, the specimen is unstable, and shear failure occurs, which decreases shear stress instantaneously. However, the deformation diagram shows that the damaged specimen still has bearing capacity under the squeezing action and friction, which increases shear stress again.

The residual strength stage (ef): fractures extend and penetrate under shear stress, and the overall strength of the specimen is seriously affected and eventually destroyed. In Figures 5(f) and 5(g), fractures 9 and 10 penetrate, and so do fractures 11 and 13, which significantly affect the overall strength of the specimen, and the specimen is gradually damaged.

The shear stress-shear displacement curves of the specimens with different undulated heights (see Figure 6) are used to explore the effect of prefabricated fractures with different undulated heights on the shearing effect of the specimens. Under the shearing action, the initiation and propagation of fractures are reflected in the shear stress-shear displacement diagram, and the shear stress-shear displacement curves show that the sandstone specimens
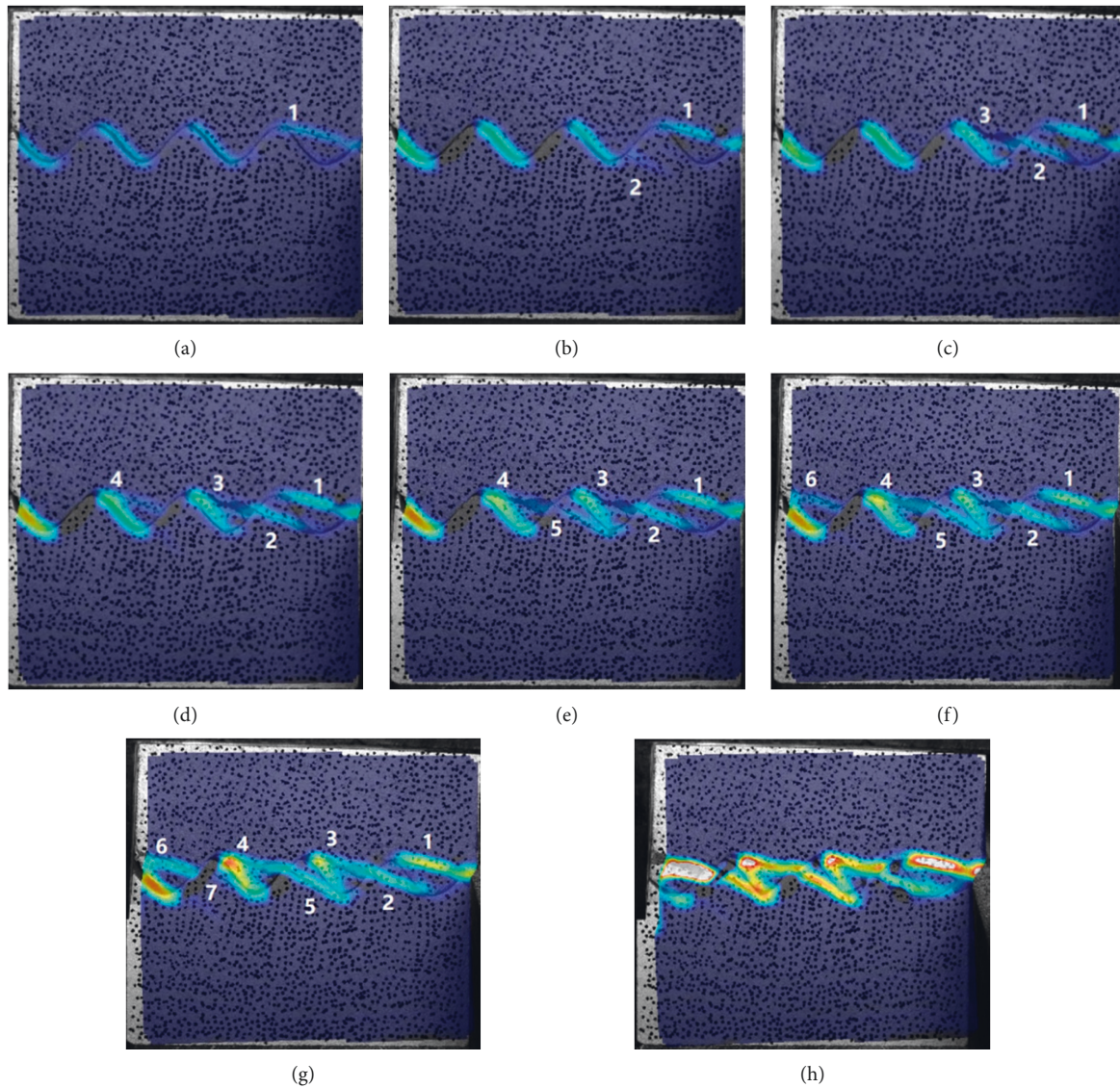
FIGURE 8: Failure process of the specimen with an undulated height of 10 mm under DIC monitoring.

with prefabricated fractures and different undulated heights have experienced the fracture-compacting stage, linear-elastic changing stage, bottom-up stage, and residual strength stage. At the first bottom-up stage, it rises from a relatively small stress value to peak strength. Before reaching peak strength, the rock masses with prefabricated fractures experience a brief local failure, which has few effects on the overall strength of specimens. The rock masses still have a strong bearing capacity.

The first decrease of shear stress can provide an early warning for the failure and instability characteristics of the subsequent rock masses. According to the analysis of the shear stress-shear displacement curves, shear stress does not rapidly decrease to a minimum value after the specimens reach peak strength. Instead, it goes through multiple bottom-up stages and enters a stable stage, indicating that the specimen still has certain strength after peak strength and can maintain a certain bearing capacity.

3.2. Fracture-Extension Process of Specimens in the Direct Shear Test. Figure 7 shows the fracture-expansion process of the specimen when the undulated height of the prefabricated fracture is 5 mm. Under shear stress, the fracture-development position is the stress concentration area inside the prefabricated fracture. Figure 7(a) shows that fracture 1 occurs at the bottom of the sinusoidal fracture and expands along the slope to the middle of the next sloped fracture. At the initial stage of the shear loading, the main force direction of the specimen is approximately parallel to the slope surface and prone to failure. Meanwhile, fracture 2 expands with further increased shear stress, parallel to shear stress. It eventually penetrates with the tip of the prefabricated fracture and suffers failure (see Figures 7(b) and 7(c)). The prefabricated fracture has a major influence on the fracture propagation direction of specimens.

Then fracture 3 occurs, and its position is farther from fractures 1 and 2. As stress concentration appears, fracture
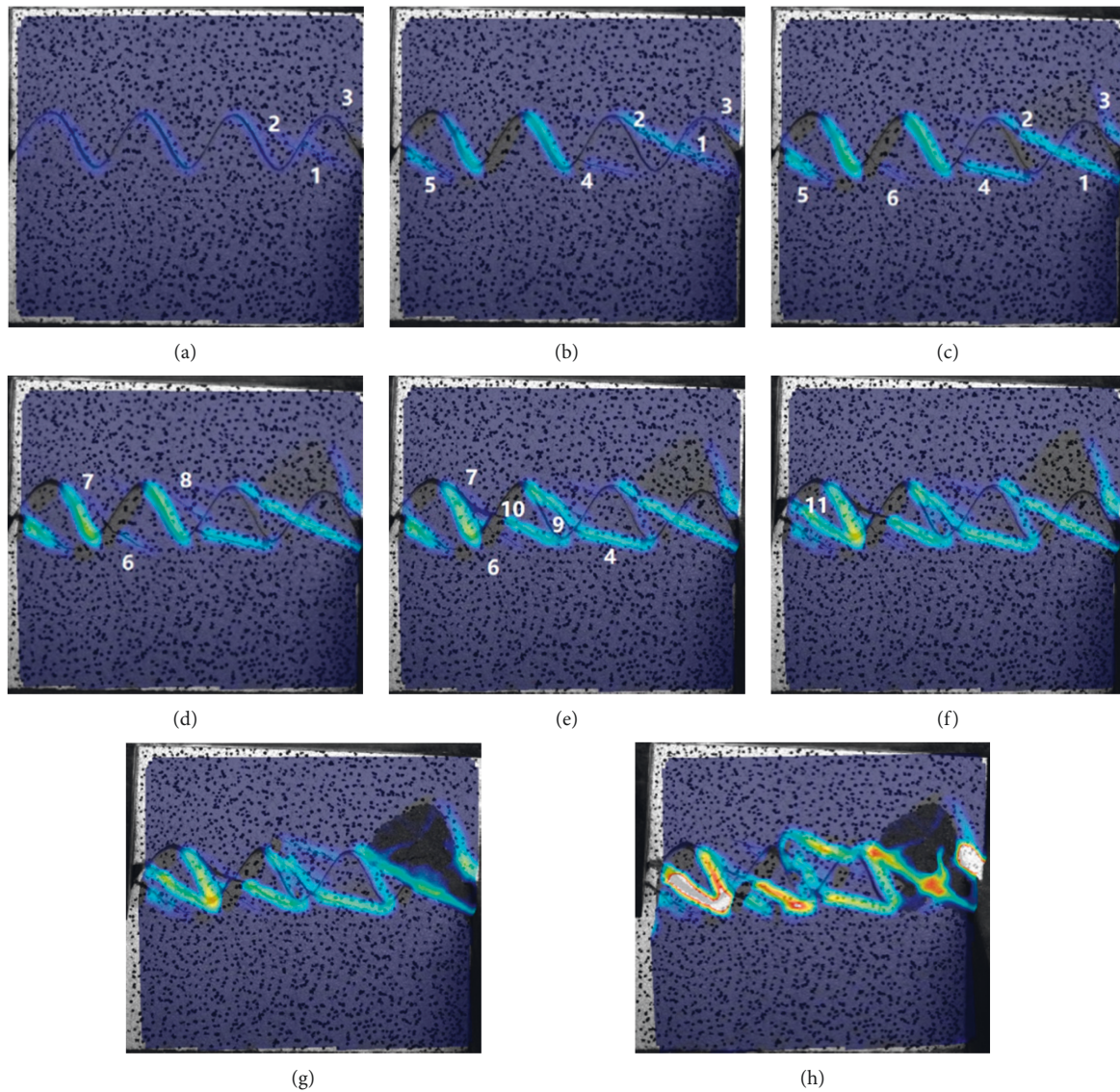
FIGURE 9: Failure process of the specimen with an undulated height of 15 mm under DIC monitoring.

initiation begins. Fracture 3 and prefabricated fractures penetrate with increased shear stress. Meanwhile, prefabricated fracture 4 in the connecting parts of fractures 1, 2, and 3 also occurs and expands rapidly (see Figures 7(d) and 7(e)) because fractures penetrate each other. Finally, the four fractures are fully expanded and penetrated, and the specimen suffers a shear failure. Figure 7(f) shows the final failure.

Figure 8 shows the fracture-expansion process of the specimen when the undulated height of the prefabricated fracture is 10 mm. The fracture-development location is still the stress concentration area inside the prefabricated fracture. However, compared with the specimen with an undulated height of 5 mm, there are obvious differences in stress concentration parts. The squeezing effect on the top of the prefabricated fracture is more intense and stress concentration is more obvious due to the "climbing" effect in the shearing process. Therefore, fracture 1 expands from

the top of the prefabricated fracture to the end of the specimen under stress, and fracture 2 also expands (see Figures 8(a) and 8(b)). As shear stress gradually increases, fractures 3 and 4 also develop. However, Figures 8(c) and 8(d) show that fractures 3 and 4 both occur from the top of the sinusoidal fracture and expand to the middle, parallel to the wave direction of the sinusoidal fracture. Meanwhile, fracture 3 and the prefabricated fracture penetrate each other under the influence of fracture 2, so the specimen loses part of the bearing capacity. Sinusoidal fractures under the shearing action play a leading role in the development, expansion, and penetration of the fractures in the specimen.

With the action of shear stress, fracture 5 occurs from the bottom of the sinusoidal fracture and expands to the middle, which has the same expansion characteristics as fractures 3 and 4. At this point, the specimen has lost most of its bearing capacity (see Figures 8(e) and 8(f)). Finally, fractures 6 and 7

(a)

(b)

(c)

(d)

(e)

(f)

(g)

(h)
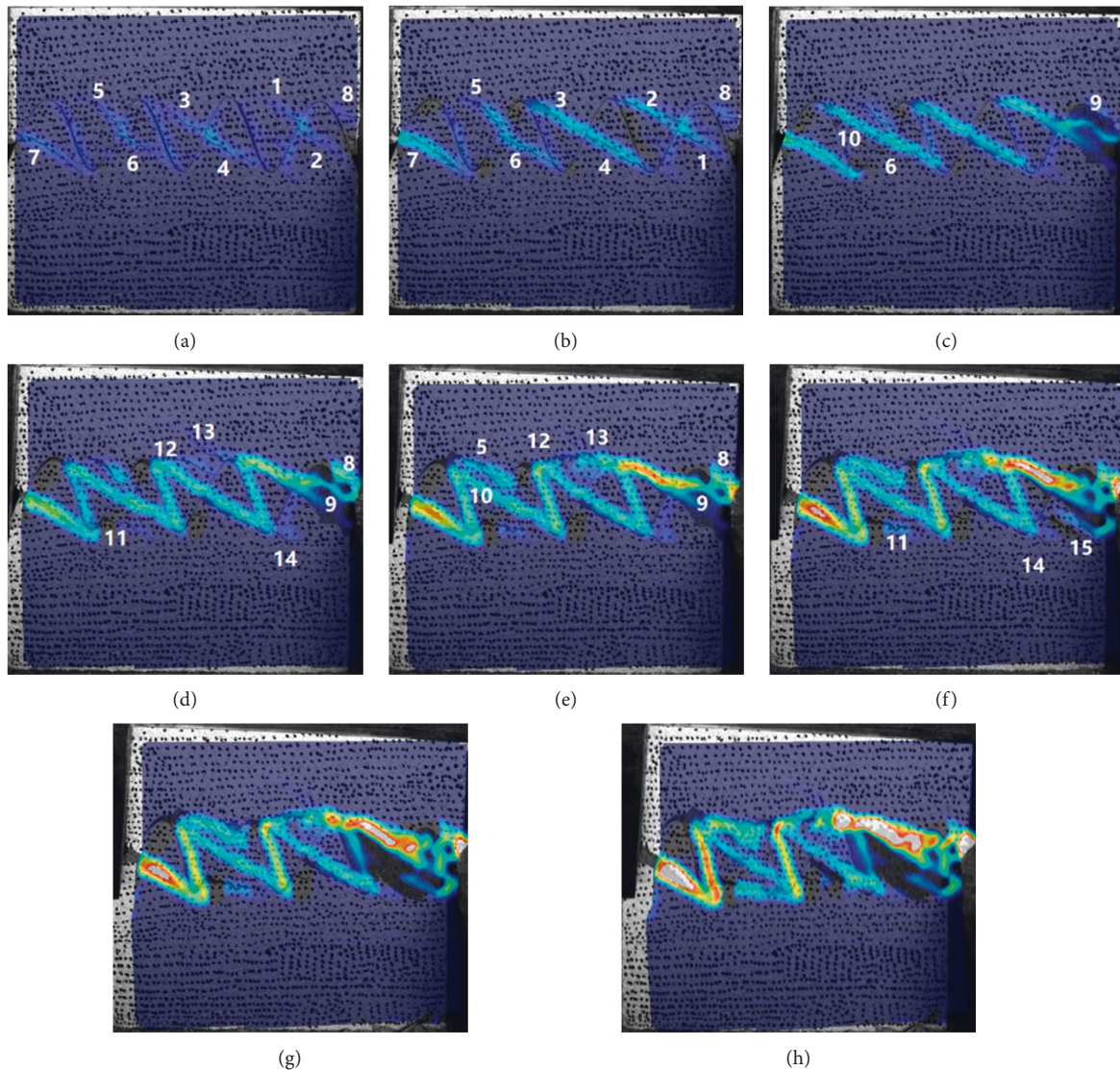
FIGURE 10: Failure process of the specimen with an undulated height of 20 mm under DIC monitoring.

gradually develop to the failure of the specimen in the same way (see Figures 8(g) and 8(h)).

The above fracture propagation process shows that when the undulated height of the prefabricated fracture is 10 mm, the development direction of fractures is mainly parallel to the "climbing" section of the sinusoidal fracture. It is the dominant direction of the failure of the specimen, and the monitoring of this direction should be strengthened in the actual slope engineering.

Figure 9 shows the fracture-extending process of the specimen with an undulated height of 15 mm. Fractures 1 and 2 still occur from the stress concentration zone in the middle of the sinusoidal fracture, and fracture 3 is also generated at the end of the specimen (see Figure 9(a)). With gradually increased shear stress, fractures 4, 5, and 6 expand (see Figures 9(b) and 9(c)). The above three fractures appear from the middle and lower parts of the sinusoidal fracture and develop perpendicular to the fracture, which is approximately parallel to the shearing direction. The increased

undulated height of the prefabricated sinusoidal fracture changes the direction of the weak planes of rock masses. At this time, fractures 1 and 2 penetrate each other under stress, forming a penetrated fracture, which affects the bearing capacity of the specimen. After occurring from the top of the sinusoidal fracture, the fracture develops in the middle and gradually penetrates the existing fracture. Some secondary cracks also occur in the specimen. The final specimen is damaged under shear stress (see Figures 9(f)–9(h)).

Figure 10 shows the fracture-expansion process of the specimen with an undulated height of the prefabricated fracture of 20 mm. The fracture development is in the stress concentration area. Fractures occur and expand from the middle of the prefabricated fracture to the end, and some are also generated at the end of the specimen. With increased shear stress, fractures 1, 2, 3, 4, 5, 6, and 7 occur and expand from the stress concentration area inside the fracture; fracture 8 appears from the end of the specimen (see Figure 10(a)). Under shear stress, fractures 1 and 2, fractures
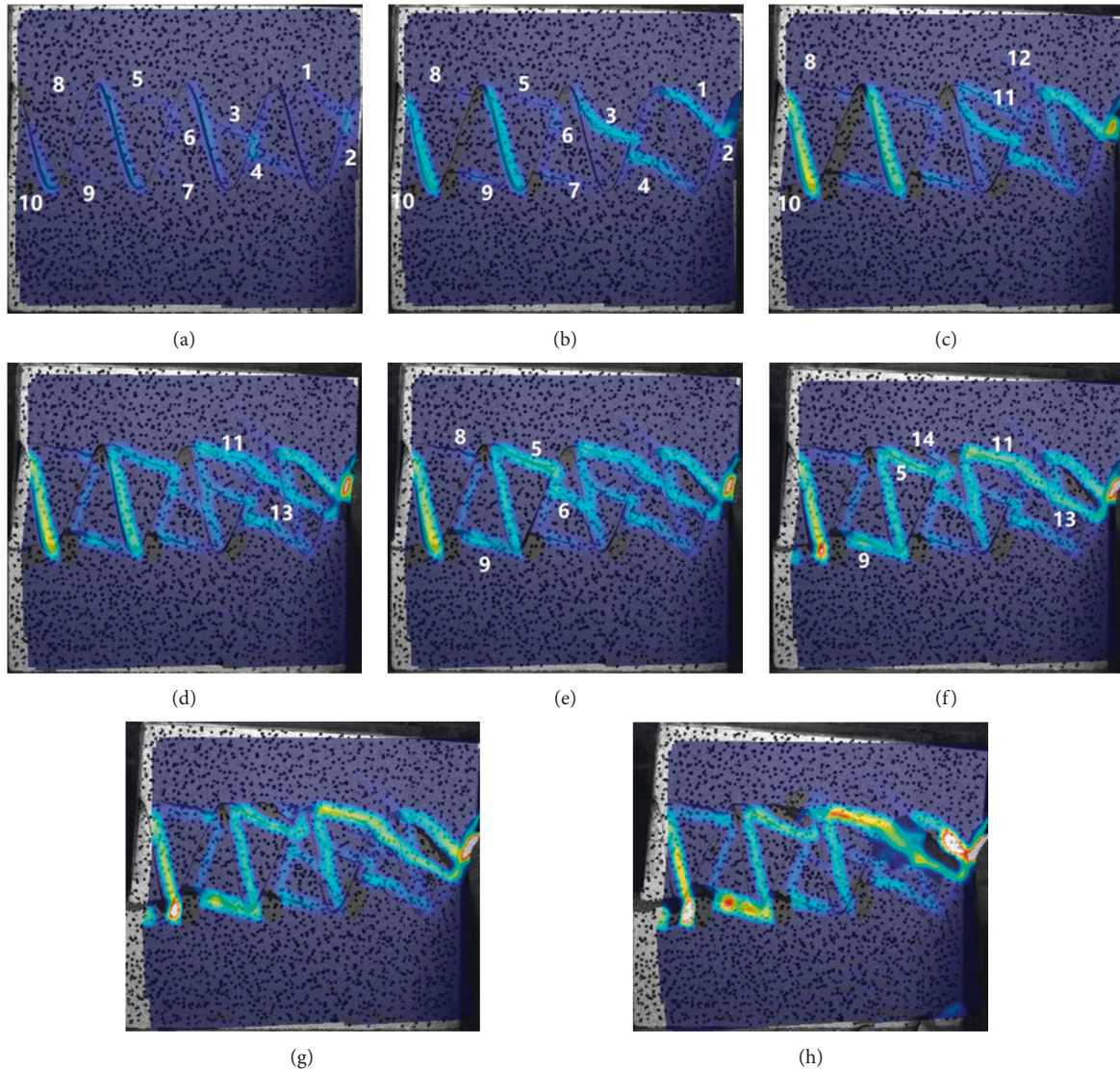
FIGURE 11: Failure process of the specimen with an undulated height of 30 mm under DIC monitoring.

3 and 4, and fractures 5 and 6 further expand and penetrate each other.

Fracture 7 also penetrates with the prefabricated fracture, and the strength of the specimen is affected (see Figure 10(b)). Then, the tip of the prefabricated fracture is partially destroyed, and fracture 9 occurs at the end of the specimen and penetrates with the prefabricated fracture. After arising, fracture 10 penetrates with fracture 6 under shear stress (see Figure 10(c)). Multiple fractures gradually penetrate each other under stress. Fractures 12, 13, and 14 occur and expand, and fractures 12 and 13 penetrate each other after rapid extension; fractures 5 and 10 also penetrate. At this time, the shear resistance of the specimen is greatly reduced (see Figures 10(d) and 10(e)). Finally, fracture 11 penetrates with the prefabricated fracture. The specimen generates a large number of tiny fractures, which eventually causes the failure of the specimen (see Figures 11(f)–11(h)).

Figure 11 shows the fracture-extension process of the specimen with an undulated height of the prefabricated fracture of 30 mm. The undulated height is the maximum explored in the work. Figures 11(a) and 11(b) show that the fractures occur near the end of the sinusoidal prefabricated fracture and extend to the other end. When the undulated height increases, stress concentration near the tooth tip is more obvious in the shearing process, and the bearing capacity is weak. Therefore, it causes the first fracture there. Fractures 1, 3, 4, 5, 6, 7, 8, and 9 arise from the internal stress concentration areas of the prefabricated fractures. Fractures 2 and 10 are generated at the left and right ends of the specimen, respectively, and fracture 2 quickly penetrates with the prefabricated fracture and causes partial failure of the specimen. The expanded direction of fractures is perpendicular to the prefabricated fracture (see Figures 11(a) and 11(b)).

With increased shear stress, fractures 8 and 10 gradually form the penetrated path between the end and prefabricated fracture, and fractures 11 and 12 occur and expand (see Figure 11(c)). Fracture 11 generates secondary fracture 13

and penetrates with the prefabricated fracture (see Figure 11(d)). Fractures 5 and 6, fractures 5 and 9, and fractures 11 and 13 penetrate under stress. According to the stress cloud diagram, fractures 5, 9, 11, and 13 are located in the stress concentration area. At this time, the strength of the specimen is seriously affected, and a new fracture 14 occurs (see Figures 11(e) and 11(f)). Finally, the specimen is damaged under shear stress (see Figures 11(g) and 11(h) for results).

To sum up, with the increased undulated height of prefabricated fractures, fractures expand from the stress concentration area inside the prefabricated fracture to the stress concentration area and the end of specimens. For specimens with undulated heights of 5 and 10 mm, fractures only develop from the stress concentration area inside the prefabricated fracture. For the specimens with the undulated heights of 15, 20, and 30 mm, the fracture occurs and expands from the end of the specimen except for the stress concentration area. With the increased undulated height, the fracture expands from parallel to the slope of the prefabricated fracture to perpendicular to the prefabricated fracture. For the specimen with an undulated height of 5 mm, the fracture propagation direction is parallel to the slope of the prefabricated fracture.

For those with undulation heights of 10, 15, 20, and 30 mm, the fracture-expansion direction is approximately perpendicular to the prefabricated fracture. Fractures increase with the increased undulated height. Based on DIC monitoring, specimens with the undulated heights of 5, 10, and 15 mm have 4, 7, and 11 fractures, respectively; when the undulated heights are 20 and 30 mm, there are 15 and 14 fractures, respectively. Although the undulated height of prefabricated fractures changes, fractures expand from the middle to the end of the slope surface of the prefabricated fracture. This direction is the main fracture direction in the shear failure of the sinusoidal prefabricated fracture, and the monitoring of the weak plane should be strengthened in the actual slope engineering.

4. Conclusions

Taking sandstone as the research object, the work performed the direct shear test of sinusoidal fractures with different undulated heights to study the influences of the undulated heights on the shear stress-shear displacement characteristics of the sinusoidal-fracture specimens and the fracture-evolving process. The following conclusions were obtained by the comparative analysis of the results:

(1) During the shear test, the prefabricated-fracture sandstone specimens with different undulated heights had the fracture-compacting stage, linear-elastic changing stage, bottom-up stage, and residual strength stage.

(2) Under the shearing action, the rock masses with the sinusoidal prefabricated fractures of different undulated heights had the precursory characteristics of decreased stress before peak strength. However, it had little effect on the overall strength of the

specimen, so the feature could be used for early warning of instability and failure of rock masses. After the peak, the stress of the specimen appeared several times at the bottom-up stage and finally entered a stable stage, indicating that the specimen still had a certain bearing capacity after failure.

(3) The undulated height of the sinusoidal fracture significantly affected the fracture initiation and propagation of the specimen. The fracture occurred and developed from the prefabricated fracture at a low undulated height (≤10 mm) to multiple ways at a high undulated height (>10 mm); that is, the fracture occurred at the prefabricated fracture and the end of the specimen simultaneously. With the increased undulated height, the fracture expands from parallel to the slope of the prefabricated fracture to perpendicular to the prefabricated fracture.

(4) On the whole, the fracture development of rock masses of sinusoidal fractures with different undulated heights had commonalities. That is, the fracture expanded from the middle slope of the prefabricated fracture to the end, which was the main fracture direction in the shear failure of the sinusoidal prefabricated fractures. In the actual slope engineering, the monitoring of the weak plane should be strengthened.

Data Availability

The experimental data used to support the findings of this study are included within the article.

Conflicts of Interest

The authors declare that there are no conflicts of interest regarding the publication of this paper.

Acknowledgments

References

[1] C. C. Xia and Z. Q. Sun, *Joint Mechanics of Engineering Rock Mass*, Tong ji University Press, Shanghai, China, 2002.

[2] H. Zhou, F. Z. Meng, and C. Q. Zhang, "Shear failure characteristics of structural plane and its application in studying slip-type rockburst," *Chinese Journal of Rock Mechanics and Engineering*, vol. 34, no. 9, pp. 1729–1738, 2015.

[3] D. Stead and A. Wolter, "A critical review of rock slope failure mechanisms: the importance of structural geology," *Journal of Structural Geology*, vol. 74, no. 5, pp. 1–23, 2015.

[4] F. Ding, X. Wu, P. Xiang, and Z. Yu, "New damage ratio strength criterion for concrete and lightweight Aggregate concrete," *ACI Structural Journal*, vol. 118, no. 6, 2021.

[5] M. R. Li, Y. Chen, and L. Zhang, "Influence and treatment of the stability of gravity dam foundation with multiple structures under complex geological conditions," *Rock and Soil Mechanics*, vol. S1, pp. 328–333, 2014.

[6] Q. Xu, D. X. Zhang, and G. Zheng, "Failure mode and stability analysis of the left bank abutment slope of jinping I hydropower station in the construction period," *Chinese Journal of Rock Mechanics and Engineering*, vol. 6, pp. 1183–1192, 2009.

[7] Y. S. Pan, L. G. Wang, and M. T. Zhang, "Theoretical and experimental research on the occurrence of fault rock burst," *Chinese Journal of Rock Mechanics and Engineering*, vol. 06, p. 642, 1998.

[8] C. Zhang, X.-T. Feng, H. Zhou, S. Qiu, and W. Wu, "Case histories of four extremely intense rockbursts in deep tunnels," *Rock Mechanics and Rock Engineering*, vol. 45, no. 3, pp. 275–288, 2012.

[9] J. L Pan, M. F Cai, P. Li, and Q.-F. Guo, "A damage constitutive model of rock-like materials containing a single crack under the action of chemical corrosion and uniaxial compression," *Journal of Central South University*, vol. 29, no. 2, pp. 486–498, 2022.

[10] Y. J. Jiang, S. H. Zhang, and H. J. Luan, "Numerical simulation of dynamic contact characteristics of rock-mass structural plane under shear loads," *Journal of China Coal Society*, vol. 47, no. 1, pp. 233–245, 2022.

[11] S. G. Du, Y. J. Lv, and Z. Y. Luo, "Combined test system and primary application of the shear strength and size effect of the rock-mass structural plane," *Chinese Journal of Rock Mechanics and Engineering*, vol. 40, no. 7, pp. 1337–1349, 2021.

[12] M. Ma, Q. Guo, J. Pan, C. Ma, and M. Cai, "Optimal support solution for a soft rock roadway based on the drucker-prager yield criteria," *Minerals*, vol. 12, no. 1, p. 1, 2021.

[13] J. Pan, F. Ren, and M. Cai, "Effect of joint density on rockburst proneness of the elastic-brittle-plastic rock mass," *Shock and Vibration*, vol. 2021, Article ID 5574325, 9 pages, 2021.

[14] L. He, Z. M. Zhao, and G. Wu, "Experimental study on the characteristics of shear weakening behaviors of rock-mass structural surface morphology," *Rock and Soil Mechanics*, vol. S2, pp. 1–11, 2020.

[15] J. Pan, X. Wu, Q. Guo, X. Xi, and M. Cai, "Uniaxial experimental study of the deformation behavior and energy evolution of conjugate jointed rock based on AE and DIC methods," *Advances in Civil Engineering*, vol. 2020, Article ID 8850250, 16 pages, 2020.

[16] H. B. Li, B. Liu, and H. P. Feng, "Study on shear deformation characteristics and failure mechanism of simulated rock joint specimens," *Rock and Soil Mechanics*, vol. 7, pp. 1741–1746, 2008.

[17] H. B. Li, H. P. Feng, and B. Liu, "Research on the strength characteristics of rock joints under different shear rates," *Chinese Journal of Rock Mechanics and Engineering*, vol. 12, pp. 2435–2440, 2006.

[18] Q. Z. Zhang, M. R. Shen, and W. Q. Ding, "Mechanical properties of the structural plane under shear," *Hydrogeology & Engineering Geology*, vol. 39, no. 2, pp. 42–47, 2012.

[19] F. D. Patton, "Multiple modes of shear failure in rock," in *Proceedings of the1st Congress of International Society of Rock Mechanics*, Lisbon, Portugal, October 1966.

[20] Y. H. Zhang, D. J. Wang, and H. M. Tang, "Research on shear strength characteristics of heterostructured planes based on the PFC2D numerical test," *Rock and Soil Mechanics*, vol. 37, no. 4, pp. 1031–1041, 2016.

[21] V. Sarfarazi, A. Ghazvinian, W. Schubert, M. Blumel, and H. R. Nejati, "Numerical simulation of the process of fracture of echelon rock joints," *Rock Mechanics and Rock Engineering*, vol. 47, no. 4, pp. 1355–1371, 2014.

Research Article

Numerical Simulation and Application of Zero-Thickness Contact Surface Element with Variable Shear Stiffness on Pile Foundation

You Wang [ID],[1] **Fan Xiong,**[1] **and Jialin Ren**[2]

[1]*School of Civil Engineering, Central South University, Changsha, Hunan 410075, China*
[2]*Shanghai Jianke Project Management Co., Ltd., Shanghai, 200030, China*

Correspondence should be addressed to You Wang; ywang1920@csu.edu.cn

In this study, a contact surface constitutive model with zero-thickness unit and variable shear stiffness was improved based on the statistical damage constitutive model. The model parameters were derived by means of the shear stress-shear displacement curve of the pile-soil contact surface, and the model parameters under different normal stresses were obtained by the linear interpolation method. At the same time, the influence of the interpolation interval range on the model parameters was explored. The shear stiffness adjustment factor was introduced, and the improved pile-soil contact surface constitutive model was applied to the numerical simulation of pile-soil contact surface shear calculations using the fish language embedded in FLAC 3D, and the variation of monopile bearing characteristics and ultimate bearing capacity were investigated and analyzed. The results show that the improved contact surface constitutive model is able to reflect the nonlinear variation of shear stiffness, and that different normal stresses correspond to different fitting parameters, demonstrating the depth effect of the model. The accuracy of the model parameters reduces as the interpolation interval increases, and the interpolation results are more accurate when the interval range is smaller. The numerical model accurately simulates the pile-soil contact surface shear calculation and the monopile bearing calculation, and the simulation results of the ultimate pile bearing capacity are closer to the results computed by the equations in the Chinese code. At the same time, the variation law of pile axial force and pile lateral frictional resistance along the depth direction and the variation of pile ultimate bearing capacity under different working conditions are reasonable, which shows the validity of the contact surface principal structure model and the reasonableness of numerical calculation in this study.

1. Introduction

Pile foundations have a long history and a wide range of applications in the field of civil engineering. Whether a bridge erection is being built, a foundation pit is being supported, or a housing is being constructed, a pile foundation will be used. Scholars currently employ a variety of research methods, including field tests [1, 2], model tests [3, 4], numerical simulations [5–7], and others, to investigate numerous macroscopic problems of pile foundations, including settlement [8–10], deformation [11, 12], and bearing characteristics [13–15], and various explanations are put forward for pile-soil interactions [16–18]. Due to the considerable differences in soil properties, the mechanical properties of the contact surface are also complicated and variable. At the same time, since the pile-soil contact surface

has a significant effect on pile foundation bearing capacity and bearing characteristics, it is required to conduct an in-depth analysis of the pile-soil contact surface.

A contact surface implies the presence of two different materials in touch and interacting, so that their mechanical properties are determined by the combined influence of the two materials [19]. Coulomb proposed an Earth pressure theory as early as the 18th century, based on the friction between soil and walls in practical engineering, which essentially represents the strength attributes of the contact surface within the soil. Since piles are made of concrete, early pile-soil contact surface studies were mainly carried out through soil-concrete contact surface shear tests. Potyondy [20] conducted hundreds of tests to determine the magnitude of contact surface friction and discovered that soil type, moisture content, roughness, and normal stress significantly

affect the contact surface. Shi et al. [21] utilized large cyclic load direct shear tests to evaluate the shear characteristics of the contact surfaces of red clay and concrete under a different number of cycles. Xiong et al. [22] conducted a shear test at the concrete-frozen soil interface and found that the initial moisture content and temperature had a substantial effect on the shear behavior of the frozen pile-soil interface. In addition, experimental studies on pile-soil contact surface shear have been undertaken to determine the soil particle size [23, 24], roughness [25], shear rate [26], and shear path [27].

According to the stress-strain relationship during shear, several conventional contact surface instantiation models have been developed, including the hyperbolic model [28], the elasto-plastic model [29], the rigid-plastic model [30], and the damage model [31]. In response to the results of contact surface experimental studies, the contact surface element theory was proposed to better explain the mechanical behavior of contact surface shear. The contact surface element theory is mainly divided into two types: contact surface element without thickness [32] and element with thickness [33]. Numerous scholars have proposed the contact surface constitutive models under a variety of conditions based on the early investigations [34–37], and numerous studies on contact surface units have been done [38–40]. With the help of continuous strength theory, Yang [41] developed the statistical damage constitutive model of the soil-structure interface from the randomness of the internal damage distribution. This study will expand on the research using this model.

With the advancement of measurement technology and test equipment, related scholars have conducted in-depth studies of the pile-soil contact surface [42–45]. Aldaeef and Rayhani [46] introduced a roughness factor to study the characteristics of the pile-soil interface in permafrost and found that the residual strength of the interface was primarily due to residual interfacial friction and that the roughness factor decreased with decreasing temperature. Zhang et al. [47] employed direct shear tests to determine the mechanical properties of the pile-soil interface in clay soils. They found that roughness, water content, and shear rate were the main influencing factors. For the precast concrete pile-hydraulic soil interface friction problem, Zhao et al. [48] found that the interface friction capacity is highly dependent on the hydraulic soil strength. Additionally, numerical simulations have become a critical tool for investigating pile-soil contact surfaces [49–52]. For example, Wang et al. [53] developed a finite element model based on shear test data to explore the effect of thermal loads and the pile-soil interface on the thermo-mechanical behavior of piles. González et al. [54] developed a BEM-FEM equivalent linear model to analyze the horizontal load response of piles in the case of pile-soil interface degradation.

The majority of the literature on the above-mentioned research focuses on the factors influencing the mechanical properties of the pile-soil interface [46–48, 53, 54], whereas the thickness of the contact surface itself receives less attention. In addition, it is difficult to determine the thickness of the contact surface, which complicates practical

application. At the same time, to facilitate modeling and computation, the model and contact surfaces are typically simplified by using the software's built-in model and setting the shear stiffness of the pile-soil interface to a constant value [50–52]. However, the contact surface shear stiffness is not constant in practice, which significantly impacts the accuracy of the pile-soil numerical simulation. Therefore, it is necessary to develop new contact surface intrinsic structure models.

In order to accurately simulate the pile-soil contact surface unit and its interaction, the effect of contact surface thickness is eliminated, which accounts for the nonlinear variation of shear stiffness at the pile-soil interface. This study develops a new contact surface constitutive relationship independent of the contact surface thickness using the statistical damage constitutive model proposed by Yang and Liu [41]. The first section of the study reviews the literature and analyzes pile-soil contact surface tests, as well as the constitutive model and the pile-soil interface. In the second section, mathematical treatment is used to get the improved contact surface constitutive equations. The following section describes the calculation of the model parameters. The fourth section programs the improved contact surface constitutive model using the FISH language in FLAC3D and applies it to pile-soil contact surface shear numerical simulations. Ultimately, the case study in Section 5 simulates the monopile bearing and analyzes the pile bearing characteristics as well as the final pile bearing capacity under a variety of working conditions.

2. Improved Constitutive Model of Pile-Soil Interface

2.1. Contact Surface Shear Band and Thickness. Under the extrusion of the adjacent soil, normal stress will exist between the pile surface and the soil particles, and the two will be in close contact. After the load is applied to the top of the pile, it tends to move downward, generating static friction at the pile-soil contact surface. When the pile top load gradually increases and exceeds the maximum static friction, the pile will generate downward displacement with respect to the soil; at that point, the static friction is transformed into sliding friction and shear occurs between the two. During the shearing process, shear stress is applied to the soil along the contact surface, casing, and the soil particles to be compressed, dislocated, and slipped amongst one another, before being reorganized and finally reaching a stable condition. Therefore, the soil region adjacent to the contact surface is referred to as the shear band, as illustrated schematically in Figure 1.

The contact surface thickness is difficult to measure since the shear mechanical behavior of the contact surface is affected by numerous factors, including normal stress roughness soil properties. On the relatively smooth surface, shear stress is minimal, and the range of soil influence is small, resulting in a thin contact surface. However, for rough surfaces, the contact surface thickness is typically greater. The schematic diagram is shown in Figure 2.
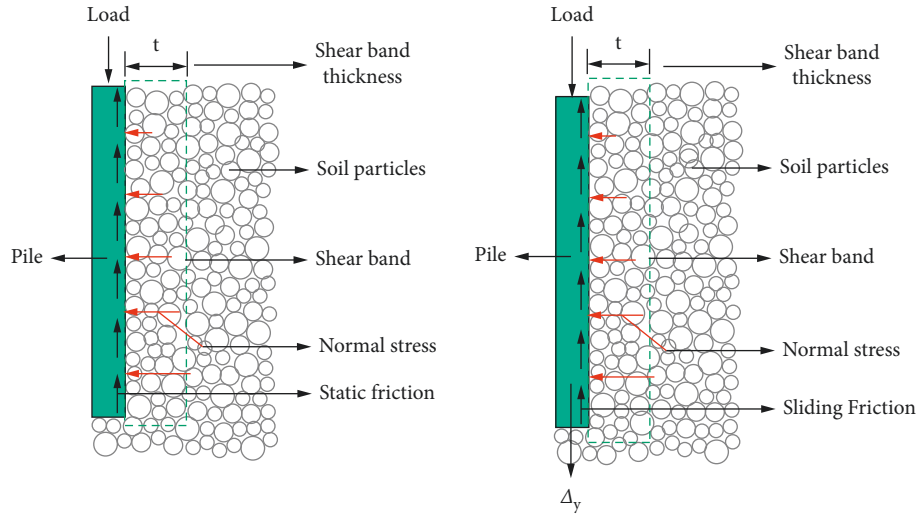
FIGURE 1: Schematic diagram of contact surface shear band.

(a) (b)
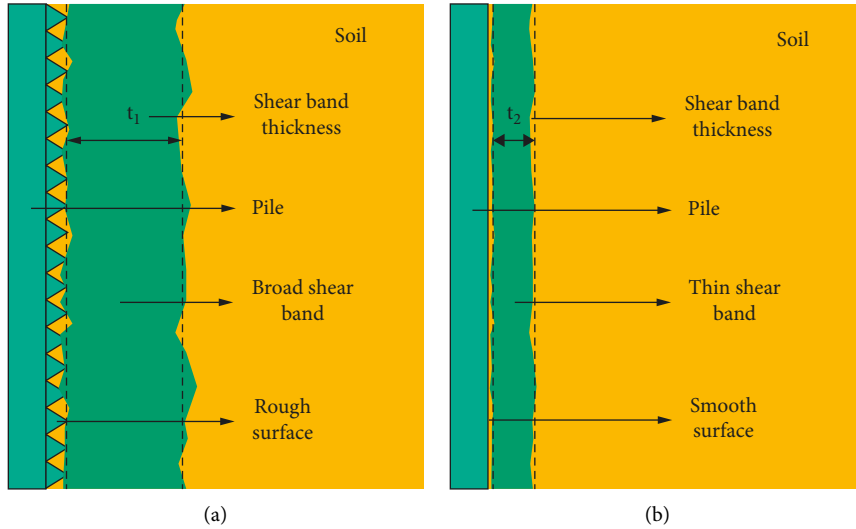
FIGURE 2: Schematic diagram of contact surface thickness. (a) Broad shear band. (b) Thin shear band.

2.2. Improved Contact Surface Constitutive Model. Yang and Liu [41] developed a statistical damage constitutive model for the soil contact surface based on the continuous strength and statistical damage theory, whose expression is as follows:

$$\tau = G\gamma \exp\left[-\left(\frac{\gamma}{F}\right)^m\right], \tag{1}$$

where τ is the shear stress at the pile-soil contact, G is the shear modulus, γ is the shear strain, and m and F are the fitted parameters. Further improvement of this constitutive model is achieved by considering the relatively small thickness of the pile-soil contact surface and assuming that the shear stress and shear strain are uniformly distributed along the contact surface and the shear strain is linearly related to the shear displacement, that is, $\gamma = \lambda\Delta$, where $\lambda = 1/t$ and t is the thickness of the contact surface, allowing equation (1) to be expressed as follows:

$$\tau = G\lambda\Delta\exp\left[-\left(\frac{\lambda}{F}\right)^m \Delta^m\right]. \tag{2}$$

Taking the logarithm of both sides of the above equation, we obtain

$$
\begin{aligned}
Y &= C + DX, \\
Y &= In\left[-\left(\frac{\tau}{G\lambda\Delta}\right)\right], \\
X &= In\Delta, \\
C &= m\left[In\left(\frac{\lambda}{F}\right)\right], \\
D &= m.
\end{aligned}
\tag{3}
$$

Then, considering the displacement Δ of the derivative of equation (2), we can get the shear stiffness k_s and shear displacement of the relationship as follows:

$$k_{si} = G\lambda \, \exp\left[-\left(\frac{\lambda}{F}\right)^m \Delta^m\right] - G\lambda m\Delta^m\left(\left(\frac{\lambda}{F}\right)^m\right)$$
$$\cdot \exp\left[-\left(\left(\frac{\lambda}{F}\right)^m \Delta^m\right)\right]. \tag{4}$$

Let the displacement $\Delta = 0$ and the initial shear stiffness be

$$k_{si} = G\lambda. \tag{5}$$

Then, Y in equation (3) can be expressed as follows:

$$Y = \text{In}\left[-\text{In}\left(\frac{\tau}{k_{si}\Delta}\right)\right]. \tag{6}$$

Therefore, all that is required is to find the initial stiffness k_{si} and to combine it with the points on the contact surface shear test-curve to determine C and D in equation (3). The parameters m and F can be expressed in terms of C and D, respectively:

$$m = D, C = m\left[\text{In}\left(\frac{\lambda}{F}\right)\right]. \tag{7}$$

Substituting equations (5) and (7) into equations (2) and (4) yields

$$\tau = k_{si}\Delta \, \exp\left[-\Delta^D \exp C\right], \tag{8}$$

$$k_s = k_{si} \exp\left[-\Delta^D \exp C\right] - k_{si}D\Delta^D \exp C \, \exp\left[-\Delta^D \exp C\right]. \tag{9}$$

From equations (8) and (9), it can be seen that k_{si} will have a large effect on the fitting effect of the shear process, so in order to ensure the validity of the fitting results, an appropriate solution must be chosen to calculate the initial shear stiffness k_{si}. Considering the presence of slip between the pile and soil and the fact that the shear stiffness at the pile-soil interface does not vary uniformly, a solution approach proposed by Alonso [55] was borrowed. As shown in Figure 3, in the $\tau-\Delta$ curve, the slope of the initial tangent line is the initial shear stiffness: $k_{si} = \tau_{ult}/\Delta_{au}$, and in order to calculate Δ_{au}, the parameter $\chi = \Delta_u/\Delta_{au}$ is introduced to establish the link between Δ_u and Δ_{au} so that the relationship between the initial shear stiffness k_{si} and the ultimate shear stress at the pile-soil interface can be established $k_{si} = \chi\tau_{ult}/\Delta_u$. In the above equation, the ultimate shear stress τ_{ult} and the ultimate shear displacement Δ_u can be derived from the experimental shear curve.

The proposed procedure successfully obtains the initial pile-soil shear stiffness k_{si}, which in turn results in an improved constitutive model of the pile-soil contact surface and the shear stiffness k_s during shear. This method produces k_{si} directly by deriving the displacement Δ in equation (2) and calculating its value without regard for the contact surface thickness. This means that the contact surface constitutive
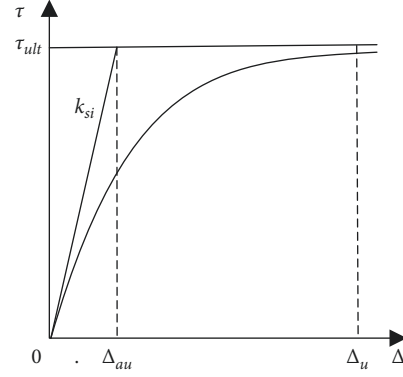
FIGURE 3: Shear stress-shear displacement curve at the pile-soil interface.

model established in this section is not directly related to the contact surface thickness, and because the contact surface thickness has no direct effect on the shear stress and shear stiffness, this study referred to it as the "zero-thickness element."

According to equation (9), shear stiffness varies continuously with shear displacement, which can be utilized to characterize the nonlinear fluctuation of contact surface shear stiffness, and is thus will more accurate. In addition, the shear stiffness-shear displacement relationship in equation (9) is programmatically calculable, which forms the basis for the numerical computation of the monopile bearing characteristics that will be performed in this study.

3. Methodology for Calculating Model Parameters

3.1. Pile-Soil Contact Surface Shear Test. To evaluate the accuracy of the improved pile-soil contact surface intrinsic model presented in the previous subsection, this section uses the data from Yang et al.'s contact surface shear test [56], which includes the following pertinent information:

The test apparatus was modified based on a powered single shear apparatus. The lower box of the shear apparatus was a precast concrete slab to simulate the concrete pile, and the shear stress was directly applied through the right weight. The contact circle diameter between the soil sample and the concrete slab was raised from 61.8 to 88 mm, and the shear area was doubled, reducing stress concentration at the edge of the soil sample and the effect of oblique shear. Figure 4 illustrates the schematic diagram of shear test.

Soil samples were taken from yellow clay excavated from the foundation pit of a new university building. Prior to the test, the soil samples were air dried and then sieved to a fineness of 0.5 mm. The redesigned soil samples were then taken according to the geotechnical test procedure, and the dry density was maintained at $1.63 \, \text{g/cm}^3$ for 1–2 days by stratified compaction. The loading control standard is as follows: (1) the shear displacement is stable under the action of this stage load; (2) the displacement is not stable, but the load of this stage has been applied for 2 minutes and the next load is applied at this time; (3) if the shear displacement
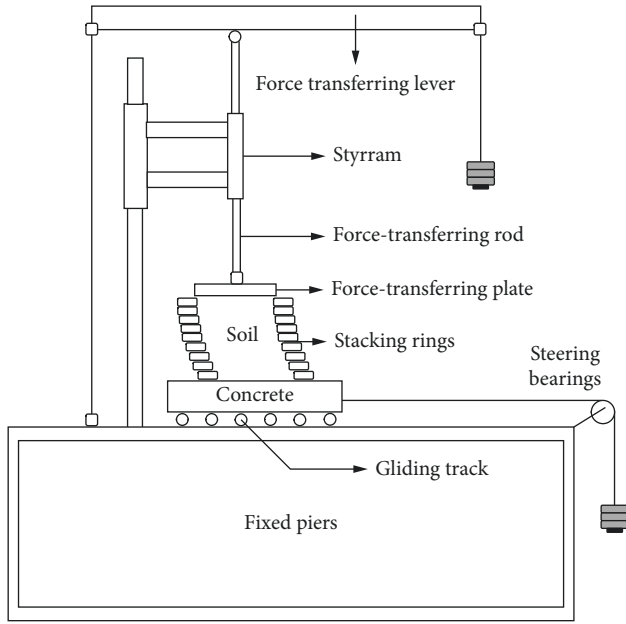
FIGURE 4: Contact surface shear test schematic diagram.

FIGURE 5: Contact surface shear test τ-Δ curve.

TABLE 1: Initial shear stiffness values under different normal stresses.

Normal stress (kPa)	22	55	88	107
Initial shear stiffness (Mpa/m)	135.9	141.03	167.4	234.28

continues to develop under the current load, the soil sample is regarded as destroyed. The contact surface shear stress-shear displacement curves for various normal stresses are shown in Figure 5.

3.2. Calculation of Model Parameters under Different Normal Stresses.

First, the initial shear stiffness k_{si} is determined from $k_{si} = \chi \tau_{ult} / \Delta_u$, where Δ_u is not greatly affected by the normal stress and Δ_u is uniformly taken to be 2.5 mm. To ensure the accuracy of the simulation results, the error analysis coefficient R^2 is introduced to determine the parameter χ, and the expression is as follows:

$$R^2 = 1 - \frac{\sum (y_i - f_i)^2}{\sum (y_i - \overline{y})^2}, \tag{10}$$

where y_i is the experimental stress value, f_i is the simulated stress value, $\overline{y}$ is the average value of the experimental stress. By fitting the experimental data from the literature [56], selecting suitable parameters χ to make the fitting results closer to the experimental data, and then deriving the initial shear stiffness k_{si} at different normal stresses, the results are obtained, as listed in Table 1.

Then, the data k_{si}, τ, and Δ are substituted into equation (3) to obtain the model parameters under different normal stress and the results are listed in Table 2.

Tables 1 and 2 demonstrate that as the normal stress increases, the initial shear stiffness k_{si} of the contact surface increases; additionally, different pile depths correspond to different normal stresses, and changes in normal stresses lead to changes in the values taken for the parameters, indicating that the constitutive model has a depth effect that accurately describes the nonlinear variation in contact surface shear stiffness.

After obtaining the values of the parameters at the four nodes, the next step is to request the values of the parameters at remaining normal stresses. The normal stress range of 22–107 kPa is divided into three intervals: 22–55 kPa, 55–88 kPa, and 88–107 kPa, with the respective intervals of 33 kPa, 33 kPa, and 19 kPa. Because the range of each interval has a minor difference, we may obtain the relevant model parameter values under various normal stress conditions by performing linear interpolation computation on the node parameters.

To prove the effectiveness of the linear interpolation method, this section examines the normal stress of 42 kPa that is included in the range 22–55 kPa, and the corresponding model parameter values are listed in Table 3. Also, the simulation curve for 42 kPa normal stress may be obtained, and the comparison with the shear test curve obtained in reference [56] is displayed in Figure 6.

Figure 6 reveals that the shear stress-shear displacement curves derived from the calculation of the model parameters using the linear interpolation approach fit very well and meet the accuracy requirements, indicating that this method is feasible for calculating the model parameter values.

3.3. Influence of the Range of Normal Stress Interpolation Intervals on the Parameters.

The interpolation interval range of the linear interpolation method may affect the accuracy of interpolation results. Interpolation calculations are performed on the model parameters corresponding to the normal stress 42 kPa, in the interval ranges 22–55 kPa, 22–88 kPa, and 22–107 kPa, and values are 85 kPa, 66 kPa, and 33 kPa, respectively. The model parameters obtained

TABLE 2: Model parameter values under different normal stresses obtained by fitting.

Normal stress (kPa)	χ	Δ_u (mm)	D	C	Correlation coefficient R^2
22	12.5	2.5	0.3648	3.1236	0.9991
55	7.7	2.5	0.4979	3.6888	0.9983
88	6.5	2.5	0.4610	3.4120	0.9992
107	7.8	2.5	0.4350	3.3272	0.9993

TABLE 3: Model parameter values obtained by interpolation under normal stress of 42 kPa.

Normal stress (kPa)	χ	Δ_u (mm)	D	C
42	9.591	2.5	0.44547	3.46615

TABLE 4: Model parameter values obtained by interpolation using different interval regions.

Interval range (kPa)	χ	Δ_u (mm)	D	C
33	9.591	2.5	0.44547	3.46615
66	10.682	2.5	0.39395	3.21100
85	11.394	2.5	0.38132	3.17151
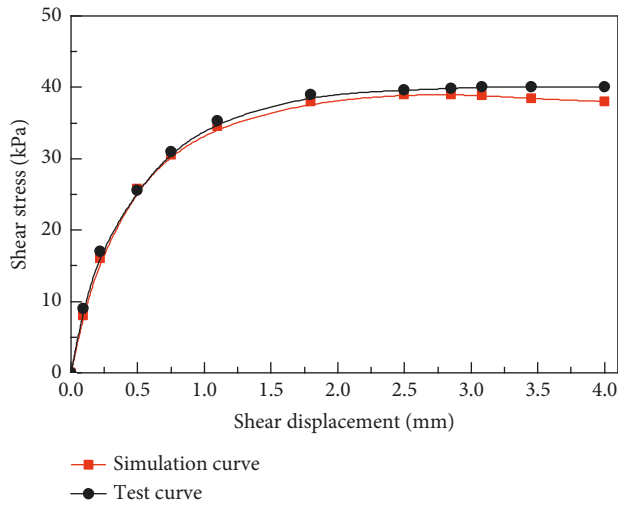
FIGURE 6: Simulation when the normal stress is 42 kPa.
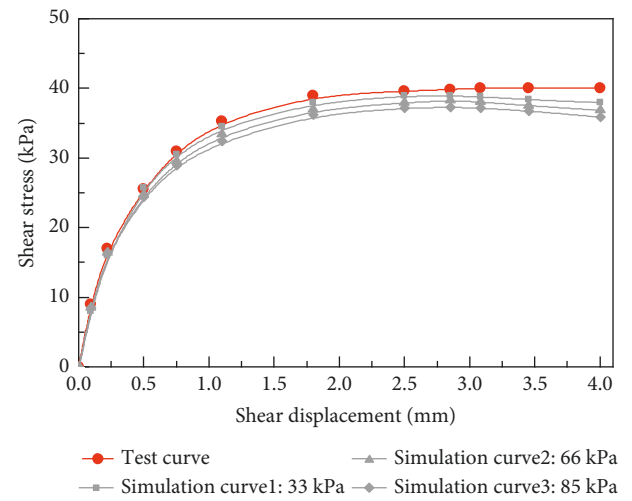
FIGURE 7: Simulation curves obtained using different interpolation regions.

using different interpolation regions for the normal stress 42 kPa are summarized in Table 4.

From the data in Table 4, the corresponding simulation curve can be obtained. The comparison of the simulation and the test curves at 42 kPa normal stress calculated in various interpolation areas is illustrated in Figure 7.

As can be seen from Figure 7, the accuracy of the simulation curve varies with the interpolation interval ranges; from high to low, the accuracy of the simulation curve is 33 kPa, 66 kPa, and 85 kPa, and its accuracy falls as the interpolation area increases. To ensure the accuracy of the model parameters, it is recommended that the interpolation interval should be kept below 40 kPa in order to obtain a reasonable simulation curve depicting the mechanical behavior of the contact surface.

4. Numerical Realization of Improved Constitutive Model

4.1. Numerical Calculation Process Design. Due to the ideal elastoplastic model embedded in FLAC3D having a fixed pile-soil contact surface stiffness, it cannot accurately reflect the nonlinear characteristics. Considering the characteristics of variable shear stiffness and the depth effect of contact

surface as expressed in equation (9), and in order to adapt to the FLAC3D solution method and apply it more accurately to FLAC3D, the shear stiffness adjustment factor is added to equation (9) to obtain the following equation:

$$k_{s,j} = \varphi \left[k_{si,j} \exp\left[-\Delta_j^{D_j} \exp C_j \right] - k_{si} D_j \Delta_j^{D_j} \right.$$
$$\left. \cdot \exp C_j \exp\left[-\Delta_j^{D_j} \exp C_j \right] \right]. \tag{11}$$

where $k_{s,j}$ is the contact surface shear stiffness of the jth node of the contact surface, Δ_j is the shear displacement of the jth node of the contact surface, $k_{si,j}$ is the initial shear stiffness of the jth node of the contact surface, C_j and D_j are model parameter value of the jth node of the contact surface, and φ is the adjustment coefficient for shear stiffness.

The contact surface fish function embedded in FLAC3D may be used to acquire the normal stress value corresponding to the contact surface nodes, and the model parameters under the normal stress can be derived using the approach mentioned above for calculating model parameters. The initial contact surface shear stiffness can be determined by substituting the model parameter values into
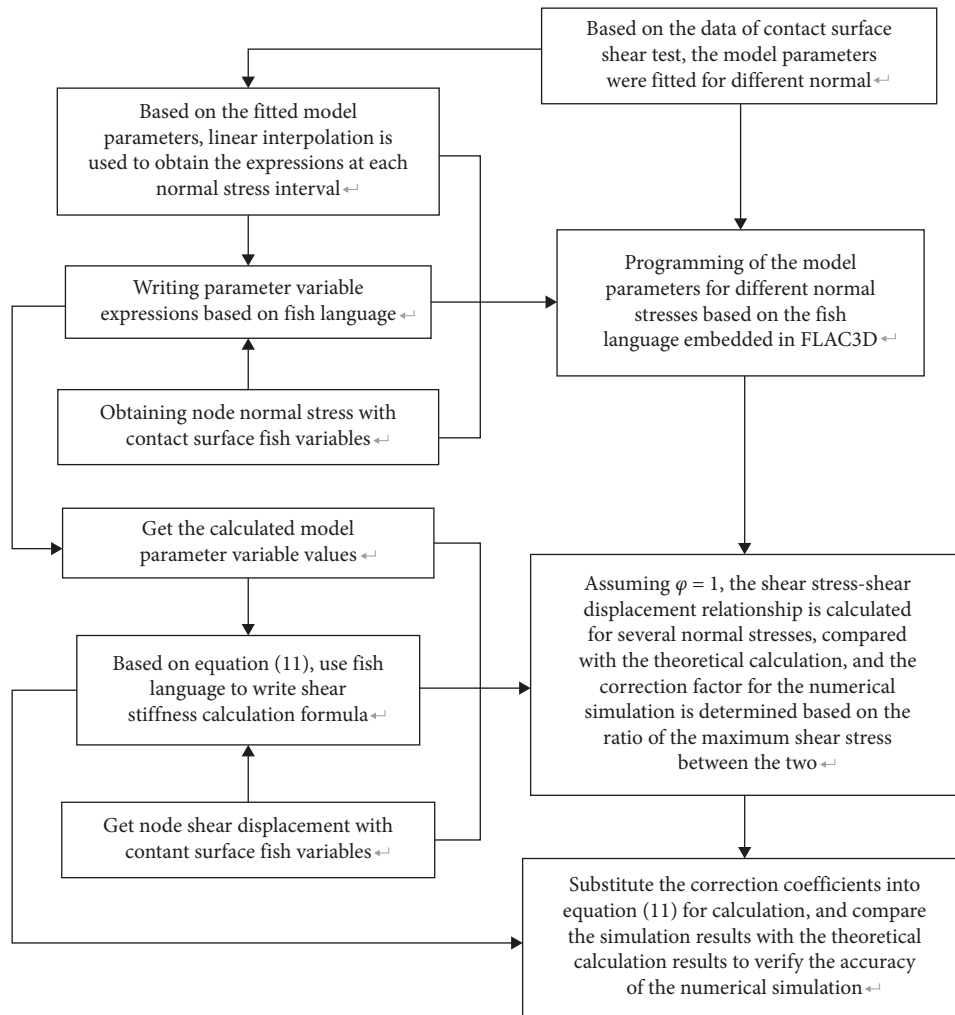
FIGURE 8: Flowchart of FLAC3D model implementation.

equation (9), which is then corrected and the contact surface shear stiffness parameters assigned. The specific implementation and solution process of the shear stiffness adjustment factor are depicted in Figure 8.

4.2. Model Building and Parameter Setting. On the basis of the foregoing, the numerical calculation process was successfully applied using an improved pile-soil contact surface principal structure model. Due to the symmetry of the pile structure and applied loads, a half-pile-soil FLAC3D model is developed here. The diameter of the pile is 0.6 m, and the length is 5.1 m in this model (exposed ground 0.1 m). The soil specifications are as follows: 5 m in thickness, 16 m in length, and 8 m in width; grid division: 2196 units and 3000 nodes (not excluding empty units and nodes). The model is shown in Figure 9.

The numerical calculation model boundary cases are as follows: the top surface is free, the bottom surface is constrained in the Z direction only (except for solid pile), the X direction is constrained in the displacements at the two boundary surfaces at $X = -8$ m and $X = 8$ m, and the Y direction is constrained in the displacements at the two
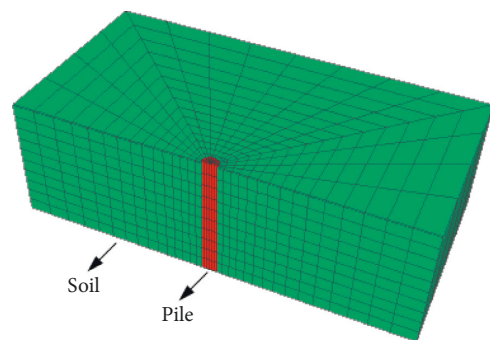
FIGURE 9: Pile-soil FLAC3D shear model.

boundary surfaces at $Y = 0$ m and $Y = 8$ m. The pile was modeled as an elastic model with a bulk modulus of 13.9 GPa and a shear modulus of 10.4 GPa, while the surrounding soil was modeled as a Mohr–Coulomb model. The values of the parameters are listed in Table 5.

According to the shear test results [56], the internal friction angle of the pile-soil contact surface was set at 29.4° and the cohesive force was set to 14.8 kPa. It is sufficient that the normal stiffness is not negligible, and twice the maximum

TABLE 5: Material parameters of soil in the numerical model.

Bulk modulus (MPa)	Shear modulus (MPa)	Cohesion (kPa)	Internal friction angle (°)
16.67	7.69	10	20

normal stiffness of the surrounding unit body was considered to be 292.9 MPa/m based on the numerical calculation experience. Since there is a constant variation in shear stiffness, the contact surface shear stiffness in the interval 22–107 kPa can be computed using the fitted data from Section 3 and the interpolation method. The following solution is proposed for shear stiffnesses in the 0–22 kPa normal stress interval; it is assumed that when the normal stress value is small, the shear stiffness in the 0–22 kPa normal stress interval varies similarly to the 22–55 kPa normal stress range, such that the initial shear stiffness in the 0–22 kPa normal stress interval can be obtained via linear extrapolation.

4.3. Implementation of Numerical Simulation and Comparison with Theoretical Calculation Results. Vertical displacement of the pile can be achieved through the command flow in the software by applying vertical displacement to the pile unit to simulate pile-soil shear, and the greater the vertical displacement, the greater the shear displacement between the pile and the soil. The track of the shear displacement and shear stress is kept during the shear process in order to plot the shear curve. In this study, the ratio of the maximum imbalance force to the typical internal force is less than 10^{-6} as the convergence criterion of the calculation, and the calculation is considered complete when the criterion is met.

However, the range of values for the normal stress is rather scattered, resulting in insufficient data to be used to determine constant normal stress. Therefore, to simulate the shear stress-shear displacement curves of the nodes at the contact surface of the pile-soil interface under constant normal stress, the normal stress increments are applied to each node using fish language programming to ensure that the nodal normal stress is a certain value, ensuring that the majority of the nodal normal stresses are concentrated around the simulated normal stress value, thereby satisfying the requirement for data acquisition. Four different normal stresses of 16 kPa, 22 kPa, 25 kPa, and 27 kPa are selected below, and the associated shear stress-shear displacement curves are obtained through simulation using the shear stiffness adjustment factors for the four cases, as listed in Table 6. The shear stress-shear displacement curves obtained numerically were then compared to those derived using the improved contact surface constitutive structure model, which is displayed in Figure 10.

In this section, the improved pile-soil contact surface was put to the numerical calculation software FLAC3D, and the contact surface shear calculation was successfully completed, yielding a numerical simulation graph of shear stress-shear displacement. As can be seen from the comparison graph of the results, the numerical and theoretical results are quite similar, and the fitting degree is quite high. Additionally, when the normal stress is in the range of 0–22 kPa, the linear extrapolate approach can be used to solve the shear stiffness

TABLE 6: Adjustment coefficient of shear stiffness under different normal stress.

Normal stress (kPa)	Shear stiffness adjustment factor
16	0.99
22	0.99
25	1.02
27	1.02
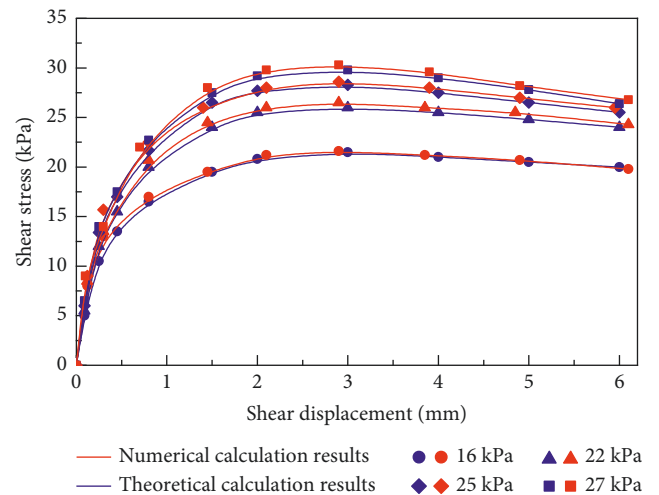
FIGURE 10: Comparison of the theoretical and numerical calculation results under different normal stresses.

more accurately. Using equation (10) to calculate the correlation coefficient of the two, when the normal stress is 16 kPa, 22 kPa, 25 kPa, and 27 kPa, the correlation coefficients are 0.9832, 0.9826, 0.9844, and 0.9851, respectively, all of which are close to 1. Therefore, the numerical calculation can be regarded as precise.

5. Case Study

5.1. Numerical Calculation of Ultimate Bearing Capacity of Single Pile. In this section, the simulation and analysis of monopile load bearing will be introduced with the pile-soil shear model. Considering that the shear stress-shear displacement curves for the selected pile-soil indoor shear tests exhibit lateral resistance hardening characteristics, this section will further optimize the implementation path of the model reflecting lateral resistance hardening in FLAC3D. As shown in equation (9), when $\Delta = (D\exp C)^{-1/D}$, the shear stiffness $k_s = 0$ and the shear stress is at its maximum value, it can be assumed that when the shear stiffness is less than or equal to 0, the shear stress is maintained constant to reflect the lateral resistance hardening characteristics of the pile-soil contact surface during the shear process, and the above idea can be implemented in FLAC3D through fish language

programming. According to the data in Table 6, the shear stiffness adjustment factor can be assumed as 1 during the numerical calculation process. In the line of the above ideas, the calculation program of the previous section for the pile-soil shear process can be modified to perform the numerical calculation for single pile bearing.

Due to the symmetry of the pile foundation structure and the added load, only half of the model needs to be built. The model specifies the following pile parameters: diameter 0.6 m and length 5.1 m (exposed ground 0.1 m). The soil specifications are as follows: 8 m in soil thickness, 16 m in length, 8 m in width, and 3492 cells and 4205 nodes of the grid. The model is depicted in Figure 11. The numerically calculated boundary cases of the model are as follows: the top surface is the free surface; in the X direction, the displacements of the two boundary surfaces at $X = -8$ m and $X = 8$ m are constrained; in the Y direction, the displacements of the two boundary surfaces at $Y = 0$ m and $Y = 8$ m are constrained (except for the solid pile); in the Z direction, the surface at $Z = -8$ m is constrained. The pile and soil model parameters are the same as in the numerical pile-soil shear simulation approach described previously.

The pile-soil interface constitutive model is based on the lateral resistance hardening model given previously, with the remaining parameters identical to those in Figure 9. To execute the numerical simulation of the bearing capacity of a single pile, the pile top is loaded incrementally at a rate of 40 kPa. The ultimate bearing capacity of a single pile is determined by observing the dramatic shift of pile foundation settlement, and the load-settlement curve is seen in Figure 12.

As displayed in Figure 12, when the load applied to the top of the pile is minimal, the load-settlement curve changes essentially linearly. However, when the applied load reaches a critical value, the settlement displacement of the top of the pile reduces steeply as the load increases. The settlement curve presented in Figure 8 follows a pattern similar to that observed during the static load test of the monopile, which has a bearing capacity of approximately 760 kPa under such conditions.

5.2. Applied Research on Pile Foundation Bearing Characteristics

5.2.1. Numerical Analysis of Axial Stresses in Piles.
Figure 13 describes the variation of axial stresses within the pile body as the function of pile top load. As can be seen from the figure, the pile is subjected to vertical loads of 120 kPa, 240 kPa, 360 kPa, 480 kPa, 600 kPa, and 720 kPa, respectively. As the load increases, the axial stress in the pile body increases accordingly, resulting in a compressed stress state throughout the pile foundation. Within the ultimate bearing capacity of the pile foundation, the axial stress at the same position on the pile body grows essentially linearly with the vertical load.

Axial pile stresses exhibit the same variation rule under different vertical loads, which can be summarized as follows: as the depth of the pile foundation increases, the axial pile
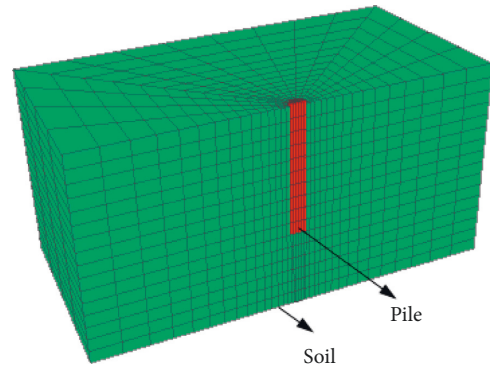
Figure 11: Pile bearing calculation model.
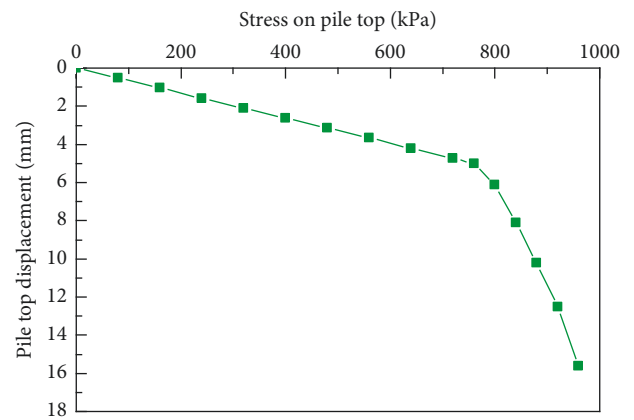
Figure 12: Load-settlement curve obtained by numerical calculation.
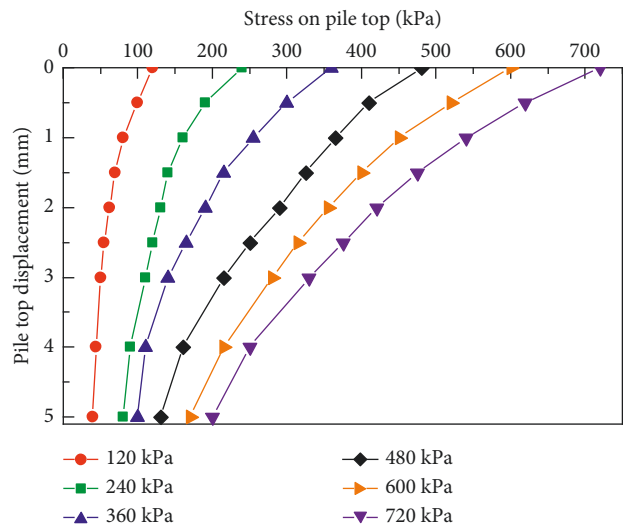
Figure 13: Axial stress curve of pile body under different pile top loads.

stresses gradually decrease and the pile end resistance values drop, indicating that the pile side frictional resistance carries the majority of the pile top load. The axial stress of pile diminishes nonlinearly with depth at all levels of load. The slope of the curve is greater in the upper soil part, revealing a

faster rate of change, whereas the slope of the curve declines in the lower soil part, revealing a slower rate of change. This suggests that the axial force of the upper part of the pile drops rapidly, while the lower part slows down and tends to remain stable.

5.2.2. Numerical Analysis of Pile Side Friction Resistance.
Figure 14 depicts the variation curves for pile lateral friction resistance under various pile top loads. As the pile top load increases, the pile side frictional resistance increases proportionately, and the pile side frictional resistance caused by the soil at the upper part of the pile perimeter is greater. During the loading process, the upper part of the pile is compressed, resulting in downward displacement relative to the soil, while the pile side is also subjected to the upward frictional resistance of the soil; thus, the pile top load is transferred to the soil around the pile through the frictional resistance, resulting in decreasing pile axial stress with depth.

When the load value on the pile top is increased, the load is transferred from top to bottom, increasing the compression and displacement of the pile body. The relative displacement between the pile and the lower soil occurs, and the friction of the lower soil layer of the pile body is gradually exerted. This demonstrates that the lateral friction of the upper and lower soil layers of the pile is not synchronized, but that the friction of the upper soil layer of the pile plays a role first. If the load continues to increase, the resistance at the pile end will begin to play out until it reaches the bearing limit of the bearing layer, and the pile top displacement will increase significantly, resulting in damage.

From the above analysis, it is clear that the simulation results for the variation curves of axial stress and lateral frictional resistance of the pile under vertical load are consistent with the conventional pile foundation load transfer law, which more accurately simulates the top-down pile top load transfer.

5.3. Theoretical Calculation of Monopile Bearing Capacity.
There are numerous requirements and methods in various codes for calculating the vertical bearing capacity of a single pile; but in general, the bearing capacity of the pile is divided into two parts: pile side friction and pile end resistance. The pile side friction is determined by the different rock layers traversed by the pile, and different coefficients are chosen, but the method of calculation is based on friction theory, whereas the pile end resistance is primarily determined by the lithology of the bearing layer and the load transfer mechanism.

According to the Chinese code—"Code for Design on Subsoil and Foundation of Railway Bridge and Culvert" [57], the axial compressive bearing capacity of a single pile can be computed using the following equation:

$$[P] = \frac{1}{2} U \sum f_i l_i + m_0 A [\sigma], \tag{12}$$

where U is the perimeter of the pile section, f_i is the ultimate frictional resistance of the soil layer on the side of the pile, l_i
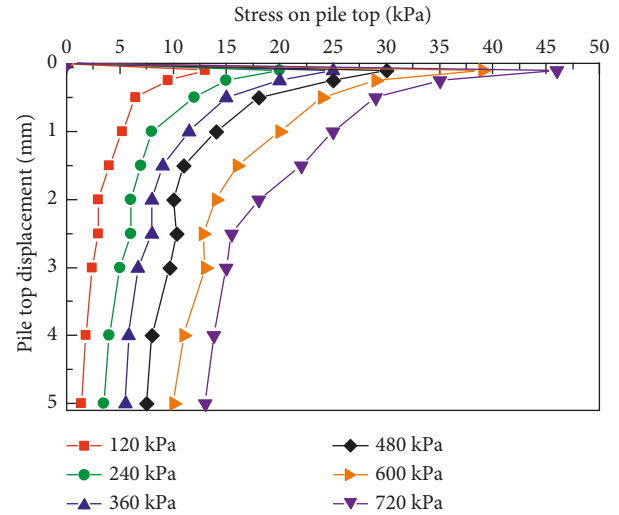
FIGURE 14: Curves of pile side friction resistance under different pile top loads.

TABLE 7: Pile bearing capacity parameter values.

U (m)	f_i (kPa)	l_i (m)	m_0	A (m^2)	$[\sigma]$ (kPa)
0.6π	38	5	0.8	0.09π	240

is the thickness of the soil layer on the side of the pile, m_0 is the discount factor for the support force at the base of the pile, A is the area of the base of the pile, and $[\sigma]$ is the allowable bearing capacity of the foundation soil at the base of the pile. Based on the basic parameters of the pile foundation model in this section and the provisions of the code on the relevant coefficients, the above parameters are obtained, as listed in Table 7.

By substituting the coefficients from Table 7 into equation (12), the theoretical value of the ultimate bearing capacity of the single pile can be obtained. After calculation, the final bearing capacity is about 233.36 kN, which is then divided by the pile area to get around 825 kPa. In comparison to the numerical calculation result of 760 kPa, the theoretical calculation value is 825 kPa, and the discrepancy between the two values is stable at 10%. This reveals that the theoretical calculation results provide a more robust verification of the numerical simulation's correctness.

5.4. Analysis of Influencing Factors of Ultimate Bearing Capacity of Single Pile.
To facilitate comprehension of the application of the improved contact surface constitutive model and to further verify the validity of the model, this subsection will simulate the ultimate bearing capacity of a single pile with varying pile lengths and soil moduli.

5.4.1. Effect of Different Pile Lengths.
In Section 5.1, the length of the pile in the model is 5 m in length and 0.6 m in diameter. Keeping the pile diameter constant and changing the length of the pile, models with pile lengths of 7.5 m, 10 m, and 12.5 m, were established to investigate the effect of varying pile lengths on the ultimate bearing capacity of the
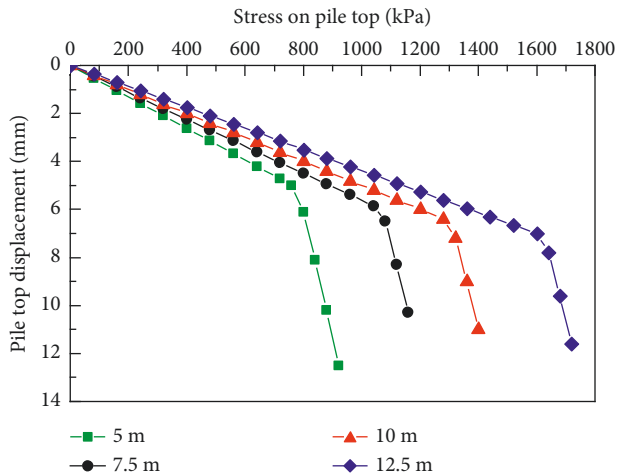
FIGURE 15: Load-settlement curves of piles with different pile lengths.

FIGURE 16: Pile load-settlement curves for different soil moduli.

monopile. To minimize the influence of boundary effects, the model height is adjusted to double the length of the pile, and the remaining material characteristics and boundary conditions remain unchanged. The model loading scheme is still loaded incrementally with 40 kPa, and the settlement of pile tops is recorded for each load step. Figure 15 illustrates the load-settlement curves for various pile lengths. The inflection point of the curve represents the ultimate bearing capacity of the single pile.

As shown in Figure 15, the pile top settlement increases linearly with increasing load at the commencement of loading. After the inflection point of the curve, the settlement accumulated rapidly and the pile foundation is damaged. The longer the pile length is, the less settlement there will be under the same load. At the same time, the ultimate bearing capacity of a pile foundation grows with the pile length increases. This is because as the pile length increases, the pile side frictional resistance increases bearing capacity, and the pile axial force is transferred more to the pile perimeter soil, which reduces pile body compression and pile bottom soil compression. Therefore, increasing the pile length can reduce settlement and improve the pile bearing capacity.

5.4.2. Effect of Different Soil Moduli. The pile length of 5 m and the pile diameter of 0.6 m are maintained, but the soil modulus around the pile is altered. To test the effect of different soil deformation moduli on the ultimate bearing capacity of the monopile, the soil deformation modulus was set to 10 MPa, 16.67 MPa, and 20 MPa. The remaining material characteristics and boundary conditions remain unchanged, as does the loading method. The load-settlement curves for the pile with varying soil moduli around the pile are plotted in Figure 16.

As depicted in Figure 16, the variation pattern of pile Q-S curves with varying soil moduli is similar to that of Q-S curves with varying pile lengths, where settlement initially increases linearly and then rapidly increases once the inflection point appears. Increases in the soil modulus
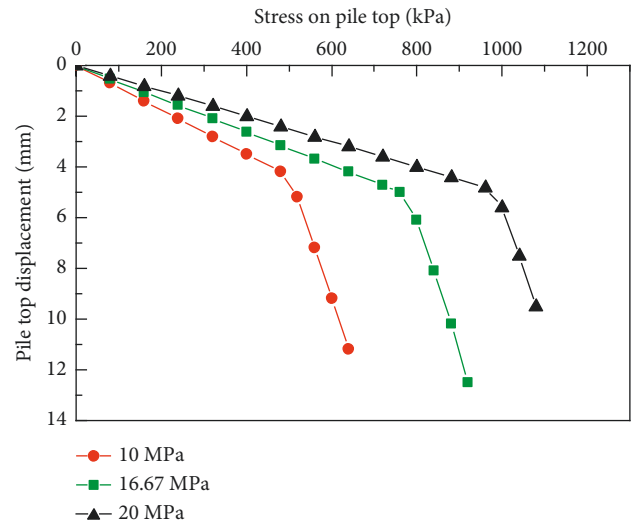
surrounding the pile result in a decrease in the settlement at the top of the pile and an increase in ultimate bearing capacity. This corresponds to the impact of lengthening the pile. When the soil modulus around the pile increases, the pile lateral frictional resistance increases as well. Because the soil at the bottom of the pile gets stronger, its bearing capacity increases and the compression deformation decreases, and increasing the soil modulus can reduce settlement and enhance the pile bearing capacity.

As can be observed from the above analysis, the simulation results for the ultimate bearing capacity of a single pile under various pile lengths and soil moduli are consistent with the actual pile bearing capacity variation law, which more accurately simulates the pile bearing capacity variation law.

This section applies an improved constitutive model of the pile-soil interface to the simulation of single pile bearing capacity, verifies the ultimate bearing capacity of a single pile, analyzes the variation law of pile axial force and pile side friction, and investigates the influence of pile length and soil modulus around the pile on the ultimate bearing capacity of a single pile. The case study proves the effectiveness of the improved constitutive model, which has a certain engineering application value.

6. Conclusion

The constitutive model of the pile-soil interface with variable shear stiffness and zero thickness element is improved using the original contact surface model. At the same time, the numerical simulation of the new constitutive model is realized, as well as a case study of a single pile is carried out. The following conclusions are drawn:

(1) The improved constitutive model is capable of describing the nonlinearity of the contact surface shear stiffness, and it is beneficial to program computation and numerical simulation research, laying the foundation for further contact surface and single pile bearing numerical calculations.

(2) Combined with the data from the shear test, the parameter calculation method is proposed. The parameter values for various normal stresses can be determined by linear interpolation, which reflects the depth effect of the model. Because the accuracy of the model parameters reduces as the interpolation area increases, it is recommended that the interpolation interval be kept small.

(3) Implementing an improved constitutive model of the pile-soil interface in FLAC 3D is proposed, as is the usage of a linear extrapolation method for the shear stiffness in the normal stress range of 0–22 kPa. The model and calculation procedure successfully simulate pile-soil shear, and the numerical results are in good agreement with the theoretical results, which accurately depict the nonlinear stiffness of the contact surface.

(4) The improved constitutive model is used in the bearing simulation of a single pile. The case study demonstrates that during pile top load transfer, the upper soil part of the pile provides more pile lateral friction resistance than the lower soil part because the pile and upper soil body are the first to be displaced relative to one another. By increasing the pile length and the soil modulus around the pile, settlement can be reduced and the pile bearing capacity increased. The feasibility of the model is verified by comparing the calculated results to the equations in the Chinese code, which serves as a guide for engineering practice.

Data Availability

The data used to support the findings of this study are included in the article.

Conflicts of Interest

The authors declare that they have no conflicts of interest.

Acknowledgments

References

[1] L. Gao, C. Han, Z. Xu, Y. Jin, and J. Yan, "Experimental study on deformation monitoring of bored pile based on BOTDR," *Applied Sciences*, vol. 9, no. 12, p. 2435, 2019.

[2] X. Wang, "Field test investigation of the pile jacking performance for prefabricated square rigid-drainage piles in saturated silt sandy soils," *Advances in Civil Engineering*, vol. 2019, pp. 1–11, Article ID 4587929, 2019.

[3] Z. Feng, H. Hu, R. Zhao et al., "Experiments on reducing negative skin friction of piles," *Advances in Civil Engineering*, vol. 2019, Article ID 4201842, 2019.

[4] C. Yao, J. Takemura, and J. Zhang, "Centrifuge modeling of single pile-shallow foundation interaction in reverse fault," *Soil Dynamics and Earthquake Engineering*, vol. 141, Article ID 106538, 2021.

[5] Q. Xu, Z. Bao, T. Lu, H. Gao, and J. Song, "Numerical simulation and optimization Design of end-suspended pile support for soil-rock composite foundation pit," *Advances in Civil Engineering*, vol. 2021, pp. 1–15, Article ID 5593639, 2021.

[6] F. Liu, J. Yi, P. Cheng, and H. Yao, "Numerical simulation of set-up around shaft of XCC pile in clay," *Geomechanics and Engineering*, vol. 21, no. 5, pp. 489–501, 2020.

[7] J. Li, D. R. Fuhrman, X. Kong, M. Xie, and Y. Yang, "Three-dimensional numerical simulation of wave-induced scour around a pile on a sloping beach," *Ocean Engineering*, vol. 233, Article ID 109174, 2021.

[8] X. Jin, T.-H. Wang, W.-C. Cheng, Y. Luo, and A. Zhou, "A simple method for settlement evaluation of loess-pile foundation," *Canadian Geotechnical Journal*, vol. 56, no. 11, pp. 1690–1699, 2019.

[9] M. Shakeel and C. W. W. Ng, "Settlement and load transfer mechanism of a pile group adjacent to a deep excavation in soft clay," *Computers and Geotechnics*, vol. 96, pp. 55–72, 2018.

[10] M. R. Kaloop, J. W. Hu, and E. Elbeltagi, "Pile-raft settlements prediction under coupled static-dynamic loads using four heuristic regression approaches," *Shock and Vibration*, vol. 2018, pp. 1–10, Article ID 3425461, 2018.

[11] H. Wang, Z. Lv, H. Qin, and J. Zhang, "Deformation control method of the antislide pile under trapezoidal load in the Zhangjiawan landslide," *Advances in Civil Engineering*, vol. 2020, pp. 1–14, Article ID 1405610, 2020.

[12] P. Yu and X. Fu, "Study on vertical bearing deformation behavior of single pile considering Poisson's effect," *Journal of Railway Science and Engineering*, vol. 18, no. 4, pp. 901–907, 2021.

[13] Z. Feng, J. Huo, H. Hu et al., "Research on corrosion damage and bearing characteristics of bridge pile foundation concrete under a Dry-Wet-Freeze-Thaw Cycle," *Advances in Civil Engineering*, vol. 2021, pp. 1–13, Article ID 8884396, 2021.

[14] Y. Dong, Z. Feng, H. Hu, J. He, Q. Zhang, and F. Wang, "The horizontal bearing capacity of composite concrete-filled steel tube piles," *Advances in Civil Engineering*, vol. 2020, pp. 1–15, Article ID 3241602, 2020.

[15] Q. Wang, Z. Hu, Y. Ji, J. Ma, and W. Chen, "Centrifugal model test based bearing characteristics and analytical model of uplift pile in combined composite ground," *Rock Mechanics and Rock Engineering*, vol. 55, 2022.

[16] L. Qu, X. Ding, G. Kouroussis, and C. Zheng, "Dynamic interaction of soil and end-bearing piles in sloping ground: numerical simulation and analytical solution," *Computers and Geotechnics*, vol. 134, Article ID 103917, 2021.

[17] S. Zhang, J. Zhang, Y. Ma, and R. Y. S. Pak, "Vertical dynamic interactions of poroelastic soils and embedded piles considering the effects of pile-soil radial deformations," *Soils and Foundations*, vol. 61, no. 1, pp. 16–34, 2021.

[18] D. Kong, M. Deng, and Z. Zhao, "Seismic interaction characteristics of an inclined straight alternating pile group-soil in liquefied ground," *Advances in Civil Engineering*, vol. 2019, pp. 1–12, Article ID 3758286, 2019.

[19] D. K. Feng, *Three-dimensional Constitutive Laws, Mechanism and Model of Gravel-Structure Interfaces*, Tsinghua University, Beijing, 2012.

[20] J. G. Potyondy, "Skin friction between various soils and construction materials," *Géotechnique*, vol. 11, no. 4, pp. 339–353, 1961.

[21] X. Shi, J. Zhang, G. Deng, F. Meng, J. Xu, and B. Liu, "Experimental research on shearing property of red clay-concrete interface under cyclic loading," *Journal of Railway Science and Engineering*, vol. 11, no. 3, pp. 88–93, 2014.

[22] M. Xiong, P. He, Y. Mu, and X. Na, "Modeling of concrete-frozen soil interface from direct shear test results," *Advances in Civil Engineering*, vol. 2021, pp. 1–11, Article ID 7260598, 2021.

[23] H. Cheng, X. Wang, J. Zhang, and Z. Wu, "Effects of particle size on shear behavior of interface between coarse-grained soil and concrete," *Journal of Basic Science and Engineering*, vol. 26, no. 1, pp. 145–153, 2018.

[24] L.-J. Su, W.-H. Zhou, W.-B. Chen, and X. Jie, "Effects of relative roughness and mean particle size on the shear strength of sand-steel interface," *Measurement*, vol. 122, pp. 339–346, 2018.

[25] G. Han, Y. Zhou, R. Liu, Q. Tang, X. Wang, and L. Song, "Influence of surface roughness on shear behaviors of rock joints under constant normal load and stiffness boundary conditions," *Natural Hazards*, vol. 112, no. 1, pp. 367–385, 2022.

[26] A. Martinez and H. H. Stutz, "Rate effects on the interface shear behaviour of normally and overconsolidated clay," *Géotechnique*, vol. 69, no. 9, pp. 801–815, 2019.

[27] D. K. Feng and J. M. Zhang, "Influence of shear paths on 3D cyclic behaviors of the gravel-structure interface," *China Civil Engineering Journal*, vol. 51, no. 9, pp. 84–91+101, 2018.

[28] R. E. Goodman, R. L. Taylor, and T. L. Brekke, "A model for the mechanics of jointed rock," *Journal of the Soil Mechanics and Foundations Division*, vol. 94, no. 3, pp. 637–659, 1968.

[29] C. S. Desai, M. M. Zaman, J. G. Lightner, and H. J. Siriwardane, "Thin-layer element for interfaces and joints," *International Journal for Numerical and Analytical Methods in Geomechanics*, vol. 8, no. 1, pp. 19–43, 1984.

[30] G. W. Clough and J. M. Duncan, "Finite element analyses of retaining wall behavior," *Journal of the Soil Mechanics and Foundations Division*, vol. 97, no. 12, pp. 1657–1673, 1971.

[31] M. Boulon and R. Nova, "Modelling of soil-structure interface behaviour a comparison between elastoplastic and rate type laws," *Computers and Geotechnics*, vol. 9, no. 1-2, pp. 21–46, 1990.

[32] Z. Z. Yin, H. Zhu, and G. Xu, "Deformation and mathematical simulation of interface between soil and structural materials," *Chinese Journal of Geotechnical Engineering*, vol. 3, pp. 14–22, 1994.

[33] C. S. Desai and Y. Ma, "Modelling of joints and interfaces using the disturbed-state concept," *International Journal for Numerical and Analytical Methods in Geomechanics*, vol. 16, no. 9, pp. 623–653, 1992.

[34] M. Saberi, C.-D. Annan, and J.-M. Konrad, "Three-dimensional constitutive model for cyclic behavior of soil-structure interfaces," *Soil Dynamics and Earthquake Engineering*, vol. 134, Article ID 106162, 2020.

[35] Q. Gao, Z. Wen, Z. Zhou, A. Brouchkov, D. Wang, and R. Shi, "A creep model of pile-frozen soil interface considering damage effect and ice effect," *International Journal of Damage Mechanics*, vol. 31, no. 1, pp. 3–21, 2022.

[36] W. Zhong, D. Ouyang, X. Yang, J. Wang, Q. Guo, and K. J. Hu, "Effect of the in situ leaching solution of ion-absorbed rare earth on the mechanical behavior of basement

[37] X. Cao and J. Li, "A shear damage model of the interface between soil and sulfate-corroded concrete," *Construction and Building Materials*, vol. 293, Article ID 123450, 2021.

[38] X.-x. Qian, H.-n. Yuan, Q.-m. Li, and B.-y. Zhang, "Comparative study on interface elements, thin-layer elements, and contact analysis methods in the analysis of high concrete-faced rockfill dams," *Journal of Applied Mathematics*, vol. 2013, pp. 1–11, Article ID 320890, 2013.

[39] I. P. Damians, Y. Yan, A. Lloret, R. J. Bathurst, and A. Josa, "Equivalent Interface Properties to Model Soil-Facing Interactions with Zero-Thickness and Continuum Element Methodologies," *Fundamentals to Applications in Geotechnics*, IOS Press, Amsterdam, pp. 1065–1072, 2015.

[40] L. Rouleau, A. Legay, and J.-F. Deü, "Interface finite elements for the modelling of constrained viscoelastic layers," *Composite Structures*, vol. 204, pp. 847–854, 2018.

[41] L. D. Yang and Q. J. Liu, "Research on statistical damage model for soil-structure interface," *Chinese Journal of Underground Space and Engineering*, vol. 2, no. 1, pp. 79–83, 2006.

[42] P. Staubach, J. Wichtmann, and T. Wichtmanna, "Mortar contact discretisation methods incorporating interface models based on Hypoplasticity and Sanisand: application to vibratory pile driving," *Computers and Geotechnics*, vol. 146, Article ID 104677, 2022.

[43] Y. Zhao, X. Mao, Q. Wu, W. Huang, and Y. Wang, "Study on shear characteristics of interface between frozen soil and pile during thawing process in permafrost area," *Advances in Civil Engineering*, vol. 2022, pp. 1–12, Article ID 1755538, 2022.

[44] S. Yazdani, S. Helwany, and G. Olgun, "Influence of temperature on soil-pile interface shear strength," *Geomechanics for Energy and the Environment*, vol. 18, pp. 69–78, 2019.

[45] W. Zhou, Z. Guo, L. Wang, J. Li, and S. Rui, "Effect of cyclic jacking on sand-pile interface shear behaviour," *Soil Dynamics and Earthquake Engineering*, vol. 141, Article ID 106479, 2021.

[46] A. A. Aldaeef and M. T. Rayhani, "Pile-soil interface characteristics in ice-poor frozen ground under varying exposure temperature," *Cold Regions Science and Technology*, vol. 191, Article ID 103377, 2021.

[47] M. Zhang, S. Sang, Y. Wang, and X. Bai, "Factors influencing the mechanical characteristics of a pile-soil interface in clay soil," *Frontiers of Earth Science*, vol. 7, 2020.

[48] J. Zhou, J. Yu, X. Gong, M. H. El Naggar, and R. Zhang, "The effect of cemented soil strength on the frictional capacity of precast concrete pile-cemented soil interface," *Acta geotechnica*, vol. 15, no. 11, pp. 3271–3282, 2020.

[49] N. Terfaya, A. Berga, M. Raous, and N. Abou-Bekr, "A contact model coupling friction and adhesion: application to pile/soil interface," *International Review of Civil Engineering (IRECE)*, vol. 9, no. 1, p. 20, 2018.

[50] W. D. Wang, Y. H. Li, and J. B. Wu, "Pile-soil interface shear model of super long bored pile and its FEM simulation," *Rock and Soil Mechanics*, vol. 33, no. 12, pp. 3818–3832, 2012.

[51] Y. Yin, B. Y. Zhang, H. N. Yuan, and X. Sun, "Experimental and numerical study on interface direct shear tests," *Journal of Hydroelectric Engineering*, vol. 37, no. 6, pp. 84–92, 2018.

[52] R. C. Qiu and J. S. Ai, "FLAC3D-based study on sensitivity of pile-soil interface parameters by static load test of single pile," *Subgrade Engineering*, vol. 2, pp. 164–169, 2019.

[53] D. Wang, L. Lu, and P. Cui, "Simulation of thermo-mechanical performance of pile geothermal heat exchanger

(PGHE) considering temperature-depend interface behavior," *Applied Thermal Engineering*, vol. 139, pp. 356–366, 2018.

[54] F. González, L. A. Padrón, J. J. Aznárez, and O. Maeso, "Equivalent linear model for the lateral dynamic analysis of pile foundations considering pile-soil interface degradation," *Engineering Analysis with Boundary Elements*, vol. 119, pp. 59–73, 2020.

[55] E. E. Alonso, A. Josa, and A. Ledesma, "Negative skin friction on piles: a simplified analysis and prediction procedure," *Géotechnique*, vol. 34, no. 3, pp. 341–357, 1984.

[56] L. J. Yang, W. Wang, and T. H. Lu, "A study on laboratory simple shearing test of pile-soil interface," *Highways*, vol. 8, no. 8, pp. 209–212, 2008.

[57] TB 10093-2017, "National Railway Administration of the People's Republic of China," *Code for Design on Subsoil and Foundation of Railway Bridge and Culvert, TB 10093-2017*, China Railway Publishing House, China, 2017.

Review Article

Review on the Development of Mining Method Selection to Identify New Techniques Using a Cascade-Forward Backpropagation Neural Network

Mohamed E. I. Abdelrasoul [1,2] **Guangjin Wang** [1] **Jong-Gwan Kim** [3] **Gaofeng Ren** [4] **Mohamed Abd-El-Hakeem Mohamed** [5] **Mahrous A. M. Ali** [6] **and Wael R. Abdellah** [2]

[1]*Faculty of Land Resources Engineering, Kunming University of Science and Technology, Kunming 650093, China*
[2]*Department of Mining and Metallurgical Engineering, Faculty of Engineering, University of Assiut, Assiut, P.O. Box 71515, Egypt*
[3]*Department of Energy and Resources Engineering, Chonnam National University, Gwangju, Republic of Korea*
[4]*Wuhan University of Technology, School of Resources and Environmental Engineering, Luoshi Road 122, Wuhan, Hubei 430070, China*
[5]*Electric Department, Faculty of Engineering-Qena, 83513, Al-Azhar University, Cairo, Egypt*
[6]*Mining and Petroleum Engineering Department, Faculty of Engineering-Qena, 83513, Al-Azhar University, Cairo, Egypt*

Correspondence should be addressed to Guangjin Wang; wangguangjin2005@163.com

The most crucial event in a mining project is the selection of an appropriate mining method (MMS). Consequently, determining the optimal choice is critical because it impacts most of the other key decisions. This study provides a concise overview of the development of multiple selection methods using a cascade-forward backpropagation neural network (CFBPNN). Numerous methods of multicriteria decision-making (MCDM) are discussed and compared herein. The comparison includes several factors, such as applicability, subjectivity, qualitative and quantitative data, sensitivity, and validity. The application of artificial intelligence is presented and discussed using CFBPNN. The Chengchao iron mine was selected for this investigation to pick the optimum mining method. The results revealed that cut and fill stoping is the most appropriate mining method, followed by sublevel and shrinkage stoping methods. The least appropriate method is open-pit mining, followed by room and pillar and longwall mining methods.

1. Introduction

Mining methods are techniques for extracting mineral resources from the Earth's surface. Owing to the difficulties associated with the lithological and mechanical properties of mineral deposits, a unique exploitation technique cannot be employed to extract all of them. When extracting ore deposit, it is critical to employ either technique that has the greatest conceptual coherence with the geomechanical and lithological conditions of that mineral deposit. For the employed extraction method, it eventually has to be cost effective compared with alternative methods [1]. The

selection of the mining method (MMS) refers to the procedure for picking an ideal extraction technique for mineral deposit. It is hard to switch the picked method, manipulate, and/or swap it with another after the MMS process has been finalized, and the mining of ore deposit has begun using the proposed approach [2]. Because this alternative is typically expensive, the entire project may become uneconomical. Therefore, the selection of the mining method, MMS, seems to be an irrevocable step in mine planning [3]. However, choosing an extraction method for ore deposit is entirely reliant on the resource's ambiguous lithological and geomechanical properties. Due to such ambiguity, no positive

value can be ascribed to any of these attributes. For example, mineral resources might not be allocated a positive slope or volume if precise numbers are used [4]. The basic goal in selecting how to mine ore deposits is to develop an ore extraction technique that is fully appropriate within the given conditions. Before deciding on an exploitation technique, it is crucial to know the important characteristics that each mining method requires. MMS is primarily influenced by several factors, including ore deposit geometry (e.g., size, shape, and dip), subsurface properties (e.g., mineral composition, lithology, homogeneity, deformation, and erosional), geomechanical characteristics of rocks and ore (e.g., elastic deformation, in situ stresses, consolidation, competency, and various physical properties), economical aspects (e.g., stockpile weight, rate of production, and mine life) [5].

MMS requires the study, assessment, and evaluation of selection factors, a duty which is frequently completed by engineers according to their mining knowledge, expertise, and intuition. Because of the complexity of the assignment, it can be accomplished significantly more effectively by someone who has a thorough understanding of the subject. It is critical to imitate a human expert's judgment and comprehension. The MMS problem is a comprehensive system from the standpoint of system theory. The characteristics of this system are as follows [6]:

(1) There are multiple attributes to consider while choosing a mining method.

(2) The popularity of the orebody, product demand, enterprise index, and other factors influences the choice of the mining approach.

(3) Relationships between components are intricate. These components are linked to excessive ambiguity, both in structures and in content.

(4) There are multiple dimensions in choosing a mining strategy. The MMS system comprises subsystems, each of which has its own set of subsystems. Mining machines, ore-dressing machines, and processing machines, for example, are all parts of the running machine. Consequently, the MMS system is a massive system with multiple dimensions.

(5) An open machine is the mining strategy of choice. This type of system communicates with external systems regularly by exchanging materials, energy, and statistics.

(6) Information is often ambiguous. Statistics in the technology, economy, geology, and other fields are usually unclear in the exploitation system.

(7) Environmental factors must be considered during the manufacturing process. The main factor is the complex geology of the orebody; as a result, the exploitation system is difficult to explain using a mathematical model.

(8) The machine is in a state of flux. The specifications of the machine, in terms of area and time, often change.

When deciding on an appropriate mining method for ore deposits, various criteria must be considered. Numerous techniques, such as the Nicholas, modified Nicholas, and UBC methods, were designed to assess the appropriate method for ore extraction. Unfortunately, none of such methods consider the weight values for every factor that influences the MMS. Thus, this study aims to provide a review of the development of MMS tools explaining the advantages and disadvantages of each one and provides a new technique based on the application of a cascade-forward backpropagation neural network (CFBPNN), which is adopted as a case study in the Chengchao iron mine.

The rest of the paper is structured as follows. Section 2 focuses on the development of MMS tools. Multicriteria decision-making (MCDM) methods are discussed in Section 3. In Section 4, the MMS employing soft computing and artificial intelligence is discussed. Section 5 discusses the MMS using the application of CFBPNN (Chengchao iron mine case study). Finally, in Section 6, conclusions, recommendations, and suggestions for future work are presented, respectively.

2. Development of MMS Tools

Researchers have investigated the challenges of MMS. Numerous techniques have been generated to evaluate the appropriate extraction strategies for mineral deposits with respect entirely to their natural and geomechanical characteristics. The first qualitative classification scheme for underground method selection was developed by Boshkov and Wright [4]. Consequently, their system assumes that surface mining is no longer an option. Morrison proposed a system based on the width of ore, guide type, and strain energy accumulation [7]. Nicholas and Mark [1, 8] proposed a quantitative device. The device is based on a series of steps, categorized as follows:

The geometry and mineral composition of the ore

The characteristics of the ore zone and host rocks (e.g., hanging wall (HW) and footwall (FW))

A numerical rating based entirely on the addition of scores

Applying a weighting factor to the categories

Hartman and Mutmansky [6], Laubscher [9], Marano and Everitt [10], Bandopadhyay and Venkatasubramanian [11], Agoshkov et al. [12], Mutagwaba and Terezopoulos [13], Miller-Tait et al. [14], Hamrin [15], Tatiya [16], Basu [17], Kahriman and Karadogan et al. [18, 19], Kesimal and Bascetin [20], Clayton et al. [21], Guray et al. [22], Wei et al. [23], Shahriar et al. [24], Mihaylov [25], Miranda and Almeida [26], and Bascetin [27] have written several papers on MMS. MMS techniques are classified into three categories: qualitative techniques, numerical rating techniques (scoring), and decision-making models. Table 1 provides a brief history of proposed approaches to MMS and their main issues.

Despite the perceived advantages of these approaches, a scientific method for MMS that links subjective and objective decision-making is still lacking. Hence, a few MMS choices are primarily based entirely on experience, wherein

TABLE 1: Summary of the existing mining method selection (MMS) techniques and main issues associated with them.

Author(s)	Year	Characteristics	Drawbacks
Peele, Church	1941	Uses broad descriptions of thickness, dip, and strength of ore and strength of rock	Only used when there are similar situations in popular methods
Morrison	1976	The criteria for selecting a mining method are overall descriptors of ore size, type of rock support, and buildup of strain energy	The preference for one method over another is determined by various combinations of ground conditions
Nicholas	1981	Numerically rates the characteristics of ore deposit based on lithological and geomechanical properties of ore and host rocks	The chosen mining method is the result of combining evaluation and high ranking
Laubscher	1981	Based on a rock mass classification system that takes into account expected mining effects on rock mass strength	The preferred method is solely determined by the rock mass classification system
Hartman	1987	The decision is made based on the lithological and geomechanical characteristics of ore deposits	A flow chart must be created to define the mining method
Loubscher	1990	If the area available for undercutting is large enough, this method can be modified to include the hydraulic radius, making it feasible for more competent rock	The classification must be altered in order to link rock mass rating to hydraulic radius
Nicholas	1993	Altering the selection procedure by incorporating a weighting factor [28]	
Miller, Pakalnis, and Poulin	1995	The Nicholas approach has been modified to demonstrate more emphasis on stoping methods, better portraying typical Canadian mining design practices	Insufficient and inadequate for conducting accurate and robust MMS process

the outcome of the technique used is the only much like the deposit without absolutely catering to the distinctiveness of the deposit in question. Consequently, the mining industry cannot gain sufficient confidence in the previously implemented approaches. Most of the choices cannot be quantified; consequently, there is a need for a scientific method to select the mining technique. Table 1 lists the existing MMS methods and their main drawbacks.

3. Methods of Multicriteria Decision-Making (MCDM)

A modern method for MMS uses MCDM tools for resources within the process [29]. MCDM is efficient at enabling selection; nevertheless, its use really has not gained widespread acceptance in the mining industry, primarily in MMS [30]. MCDM methods are widely used in a wide range of industries, including manufacturing, management of water resources, quality assurance, mass transit, and product innovation, and they provide a platform for further MMS research [31].

The following decision-making strategies have been used within the MMS process: AHP, PROMETHEE, TOPSIS, TODIM, VIKOR, ELECTRE, and GRA. However, they are no longer widely used within the mining industry, and recent work extends on available research of MCDM methods because they allow for similar exploration in MMS [32]. Furthermore, OCRA, ARAS, COPRAS, CP, and SAW are supplemental decision-making techniques, since no recent evidence could encounter their application within the mining industry [32, 33]. MCDM methods have been used to entail final choice. To acknowledge importance of MCDM methods, their contributions to various decision-making processes must be emphasized. The availability of a technique allows for the use of a variety of MCDM approaches. These tools, regrettably, can be unaffordable and are not

always tailored to certain situations. Furthermore, acquiring a tool is only cost effective if it will be used multiple times. Furthermore, no unique strategy is appropriate for all situations, and each approach has benefits and drawbacks that vary depending on the context. Table 2 lists the various MCDM approaches.

4. MMS Using Soft Computing (SC) and Artificial Intelligence

Several studies on MMS have been conducted using MCDM methods. However, some of these studies failed to account for parameter uncertainty. Fuzzy logic could be employed to counteract this uncertainty [31, 96, 97]. Yun and Huang have integrated a fuzzy scheme into the MMS [98, 99]. This technique is broken down into three steps. During the first phase, fuzzy relation equations are derived to calculate Hamming intervals between both the lithological design for the proposed mining method and the geotechnical qualities of the mine that had been built. The technical and economic values of each suggested mining methods are approximated in the second phase employing statistical data from mines with similar circumstances. In the last phase, several goal decisions will be determined based entirely on the outcomes of the first and second stages [100].

Bitarafan and Ataei proposed a method for assigning weights to distinguishing criteria [101]. In the proposed method [102], Yager's technique is used wholly in a fuzzy various ruling method [103] and a fuzzy primacy technique introduced by Hipel has been used. One unique aspect is that the technique adopted accelerating primitives to reflect the relevance of the criteria provided, that can substantially raise the quality of the metrics having equivalent requirements to the ore deposit. Alternatively, it may be decreased drastically [104]. Such technique has been effectively implemented in MMS in one of the anomalies in Iran's GoleGohar iron mine,

TABLE 2: Summary of the various MCDM methods.

MCDM method	Description	Advantages	Disadvantages
AHP	Saaty created it to enable the decision-makers make more organized decisions [34, 35]. A multilevel hierarchical structure of objectives, criteria and alternatives is used [36]. Evaluate the significance of key measurements before correlating possible options with regard to each factor. Eventually, calculate the utmost preference of each decision option and also the overall score of the decision options [37]	Simple to be adopted, and its scale can be adapted to meet the needs of various decision-making situations [38]. Its popularity arises from the belief that it requires less data than other MCDM methods and can manage evaluation criteria [39]. When data are measured on different scales, it can be normalized and aggregated later [40]. It is accurate in taking decisions because of its potential to prove the consistency of the independent expert assessment [41]	As the list of considerations to be matched grows, calculations can become challenging. The ultimate determination (overall score of options) may be impacted by increasing the scale of relative importance [38]. As stated earlier in the section, AHP is only valid with positive reciprocal matrices [40]
PROMETHEE	In 1982, it was firstly created by Brans and Vincke [42]. The PROMETHEE, for each alternative, calculates both positive and negative flows ($\Phi+$, $\Phi-$), respectively, based on the weight assigned to each criterion [43]. PROMETHEE I through VI was created to serve as outranking methods. In each criterion, alternatives are compared in pairs [44]	Can compare a finite set of alternatives to competing criteria [45]. Pair-wise comparison is no longer necessary once options are removed or provided during the assessment. It is employed to select the optimal underground ore transportation and mining method [46]. Calculations are very complicated; therefore, the method is only suitable for experts	Because of the scarcity of selection guidelines, decision-makers find it hard to set up preference limits and thresholds [47]. The uncertainty of the set up limits is also not wholly responsible for, despite the fact that a parametric analysis is then conducted [48]. The subjective input of preferences adds to the uncertainty [49]
TOPSIS	In 1981, Hwang and Yoon addressed TOPSIS, which stands for order preferences by similarity to ideal solution [50]. Ranks the alternatives according to the distance between the ideal positive and negative solutions [51, 52]. The TOPSIS method's best alternative is the one that comes closest to the positive ideal solution [53, 54]	TOPSIS allows to reach the right solution faster than most MCDM methods. Its logic is sound and easy to grasp. Furthermore, the significance of weight vectors could be incorporated into the comparative process [55]. A polyhedron could be used to depict the effectiveness of options and metrics, and the estimation process is then straightforward [56]. The method is suitable when the indicators of alternatives do not vary very strongly	TOPSIS lacks a component that checks for inconsistency between judgment and expressed preferences [57]. Because TOPSIS cannot elicit weights, it must focus solely on alternative measuring strategies such as AHP [58]. TOPSIS application might be invalid if the weights are not accurate [59]. Simple computational steps, solid mathematical foundations, and a method that is simple to understand [60]
TODIM	Tomada de Decisao interactive multicriteria have been developed in the early 1990s by Gomes and Lima to assist throughout the list of options in which the selection should successfully maintain a choice in the event of a crisis [61]. Main idea has to use the overall value to determine each alternative's dominance over the others and then evaluate and rank the alternatives [62]	In terms of behavioral decision-making, it is effective since it considers the decision-psychological maker's virtues and therefore can catch damage and lack of certainty [63]. The attenuation parameter, that would be adjusted, will portray the decision-maker's risk tolerance [64]. Even professionals with no prior knowledge of MCDM describe the method as an easy-to-implement tool [65, 66]	Inability to acknowledge the uncertainty associated and imprecision in decision-making [67]. In the TODIM method, any two alternatives must be compared, which results in high computational complexity [68]. Interactive attributes can be used with positive or negative criteria interactions and crisp values [69]
VIKOR	Opricovic [70] proposed this method to solve situations with contradictory and quasi requirements [71]. Presuming that agreement is reasonable for dealing with conflict, the selection seeks the fairly close answer to the perfect, and all defined requirements are used to take active steps [72, 73]	It is very simple because it has the fewest steps for calculating the ranking order [74]. Could go with the expansion functionality of the "most of" and the least specific remorse of the "competitor" [75, 76]. A helpful aid, especially once the choice has not yet addressed his or her priorities at the outset of the method [77]. Enables to calculate the distance between the second-best option and the first	Looking for a compromise ranking order, i.e., a compromise between pessimistic and expected solutions. Another flaw is the use of complex-linear normalization in the calculation formula [78]. The use of complex normalization is required for all of the matrix's elements, which typically have different metrics, to be obtained as dimensionless units [79]

TABLE 2: Continued.

MCDM method	Description	Advantages	Disadvantages
ELECTRE	Roy invented it in 1968. Various ELECTRE methods have since been developed [80] used to classify a number of options by analyzing data in a decision matrix [81]. In the pair-wise correlation of alternatives, consistency and disharmony are used [82]	Capable of dealing with both qualitative and quantitative criteria [83]. ELECTRE was employed in civil and environmental engineering [84]. Examples of these applications include power efficiency, sustainable use of natural resources, environment protection, nutrition, security, healthcare, design, and mechatronics. To select the best surface mining technology [85]	ELECTRE occasionally fails to sort the alternatives into different ranks [86]. The weakness of ELECTRE's normal ranking arises from the need of supplemental limit, and the ranking of the alternative is dependent on the size of this limit, so there is no "correct value" [87]
GRA	Deng proposed it in 1982 to find solutions involving uncertainty and missing information [88]. Grey prediction model, grey relational analysis (GRA), grey decision, grey programming, and grey control are the five components of the grey prediction model [89]. This method treats each alternative as a data sequence. It then looks at how similar each alternative is to the reference sequence [90]	The analyzed results are reliant on the raw data, and the calculation procedure is simple and straightforward [91, 92]. There are no restrictions on sample size or normally distributed data, and the computational method is simple [93]. Ability to provide methods for ranking alternatives that do not necessitate a large sample size or any sample distribution. Very popular and useful tools for analyzing various relationships among discrete information and making decisions in various situations	There is a lack of mathematical principles to discuss its history, rules, and restrictions [94]. The most relative relational degree from the probabilistic linguistic positive ideal solution is used to select an alternative [95]
OCRA, ARAS, COPRAS, SAW, CP		Rapid development of methods for dealing with real-world problems [32]	The method has seen limited application in mining engineering [32]

and the block-caving technique has been selected as the optimal mining technique. Ataei et al. adopted the analytic hierarchy process (AHP) to resolve MMS issue in Golbini No. 8 deposit in Jajarm, Iran [39]. They developed an AHP structure of 13 metrics and six alternatives, and 17 professionals from different tasks were selected to create pairs contrast matrices. According to the findings, the reduce-and-fill mining approach has been opted as the most appropriate approach out of six alternatives [105].

One disadvantage of the AHP is that the decision-making instinct may be expressed as a genuine value. Yet another flaw of the AHP is the incorrect treatment of inherent ambiguity within the pair-wise contrast procedure, as well as judgment size prejudices [106]. To eliminate such disadvantages, Naghadehi et al. [106] employed the fuzzy analytical hierarchy process (FAHP) to MMS [107, 108]. Weights of primary criteria in the FAHP system were determined using a fuzzy set of rules, and six suggested mining techniques have been listed using the AHP [33]. The suggested technique has been adopted in Jajarm Bauxite mine in Iran, and the traditional reduce-and-fill method was chosen as the most suitable extraction technique [109, 110]. Azadeh et al. [28] developed Nicholas' [111] quantitative rating approach, and the ambiguity of the decision-makers' judgments was expressed using trapezoidal fuzzy numbers. The method comprised AHP models labeled as "technical" and "economic" operation. A case study has been adopted at

the northern anomaly of the Choghart iron mine in Iran to confirm the advanced method and compare it with the Nicholas method [112].

Namin et al. [113] proposed a fuzzy mining approach with interrelation criteria (FMMSIC), which is a hybrid decision-support system that combines the fuzzy analytic network process (FANP) [114] and fuzzy entropy (FE) [115]. The FANP and FE were used for preliminary weighting [50], and a revised fuzzy method for ordering priorities matching to the optimal situation (TOPSIS) [116] has been employed for the MMS ranking procedure. A case study of the Gole Gohar deposit in southern Iran was conducted to confirm the validity of the FMMSIC [117]. 11 underground mining strategies and 16 MMS-related conditions have been taken into account as proposed strategies and requirements for the choice process [118]. Finally, the block-caving method has been selected as the best suitable mining technique for this mine, which has been supported by numerous expert opinions. Table 3 summarizes relevant studies on MMS using SC technologies and MCDM methods and includes some guiding references for using SC in MMS.

Despite significant efforts by researchers, no MMS system can address the entire scope of the MMS issues. Latest MMS research has typically concentrated on allocating weight elements to standards and attempting to model the precise notion techniques of decision-makers [106]. To cut a size of the MMS, proposed mining strategies

TABLE 3: Summary of first representative MMS studies using SC technologies and MCDM methods.

Author	Soft computing technologies					MCDM methods	
	EXS	FUA	ANN	YAM	FUE	AHP	TOPSIS
Yun and Huang [98]		✓					
Bandopadhyay and Venkatasubramanian [11]	✓						
Gershon et al. [119]	✓						
Xiaohua [120]	✓		✓				
Guray et al. [22]	✓						
Bitarafan and Ataei [101]		✓					
Ataei et al. [39]		✓		✓			
Yavuz [121]						✓	
Naghadehi et al. [106]				✓		✓	
Azadeh et al. [28]		✓					
Namin et al. [113]		✓			✓	✓	✓
Gupta and Kumar [122]						✓	
Yavuz [121]					✓	✓	

EXS, expert system; FUA, fuzzy algorithm; ANN, artificial neural network; YAM, Yagar's method; FUE, fuzzy entropy; MCDM, multiple-criteria decision-making; AHP, analytic hierarchy process; TOPSIS, technique for order performance by similarity to ideal solution.

might be suggested prior to executing the MMS system. However, this results in the software of a completely subjective technique. In addition, because many mines are transitioning from surface to underground mining after completing surface exploitation, neither of the evolved MMS structures can manage more than one sequential transition from open pit to underground mining.

Artificial intelligence (AI) or computing intelligence (CI), which has been used in the discovery of minerals recently, has improved over the years. Moreover, the use of statistics is also becoming popular. The importance of relevant information retrieval through massive data collection was emphasized [123]. As the demand for extensive data grows, so does the recognition of statistical processing fields such as statistics mining, massive statistics, machine learning, and synthetic intelligence [124].

Artificial neural networks (ANNs) are a class of massively parallel architectures that can be used to study and generalize from experience in order to provide significant solutions to problems, even if the input data contain mistakes and are imperfect. As a result, the use of ANNs is an effective approach for solving a variety of technically challenging issues. Primarily, the processing elements of a neural network are similar to the neurons within the brain, which include many simple computational elements organized in layers. A neural network has to be trained on the experimental results associated with material in order to predict its behavior. Therefore, if these findings have adequate information relevant to that material behavior, then the trained neural network will not only replicate these results but also approximate the results of different material.

An ANN is a technique that mimics the human mind's analyzing and problem-solving abilities. It is adaptable, highly parallel, reliable, and tolerant to fix faults [125]. In the implementation of synthetic neural networks, expertise is addressed as numeric weights that can be employed to extract correlations within data that are hard to express analytically. This iterative manner adapts the network parameters to reduce the sum of squared approximation errors. Neural networks could be applied to simulate sophisticated relationships rather than using simplified assumptions, which are likely to be employed in linear approaches.

The specific benefits of ANNs are their capabilities to address every linear and nonlinear relationship, their applicability to directly observe these relationships from the data used, the fact that they no longer need to maintain an in-depth record of structures and interactions within the systems, and that they are regarded as final black-box models. For prediction employing the trained network, ANN systems can be used to repeat experiments several times, which can be useful considering that experiments are difficult and in some cases impossible [126, 127]. Since the 1980s, there was a remarkable rise in the use of neural networks to solve a variety of problems [128, 129]. The multilayer perceptron (MLP), radial basis functions (RBFs), recurrent neural networks (RNNs), and echo state networks (ESNs) [130] are among the neural networks that can be used [131, 132]. Lv and Zhang [133] established the TCSMMPM-ANN to decide the suitable thick coal seam mining method to overcome the problems of traditional MMS and address economic and technical index predictions. Chen and Shixiang [134] designed a genetic algorithm ANN to optimize the connection weights and thresholds in the optimal BP network and established a nonlinear relation between the mining method and geological conditions in a thin coal seam working face. However, due to the small sample size and highly advanced background, the BP network built in this study should be improved on a regular basis. Özyurt and Karadogan [135] developed a model using ANN and game theory, which provides solutions if ANNs are continuously trained, benefiting from technological developments and new findings without requiring expert opinion or detailed research in the relevant publication.

ANN models can recognize patterns that link input variables to their corresponding outputs in complex biological systems for prediction. Methods for improving the network performance include determining the optimal

network architecture and suitable number of training cycles using different input combinations. One of them is cascade-forward backpropagation.

5. MMS Using CFBPNN (Case Study)

As illustrated in Figure 1 [136], the CFBP model is similar to feedforward (FF) networks; nevertheless, two-layer FF networks could be used to monitor any input-output relationship, whilst FF networks with more layers could be used to visualize intricate interactions more quickly. In terms of using the BP algorithm for the weight update, the CFBPNN model is analogous to the FFBPNN model. However, a key feature of this network is that each layer of neurons is linked to the ones before it [137]. A CFBPNN, like other FF networks, contains a single or multiple interrelated hidden layers and activation functions. Neurons have private biases, and their connections have different weights. A set of modified weights should be determined in ANN modelling in such a way that the estimator error is kept to bare essentials [138].

When using the BP algorithm to update weights, a CFBPNN is similar to an FFBPNN. Most crucial component, however, is each layer of neurons is linked to the layers before it. To maximize the response of the CFBPNN, the characteristics of tan-sigmoid transfer, log-sigmoid transfer, and pure linear limit have all been determined. The mean squared error (MSE) in equation (1), the root mean squared error (RMSE) in equation (2), and R^2 in equation (3) were calculated to demonstrate the effectiveness of the algorithms.

$$\text{MSE} = \left[\sum_{1}^{n} ((\text{Qexp} - \text{Qcal}) \mid n)^2 \right], \quad (1)$$

$$\text{RMSE} = \sqrt{\frac{1}{2} \sum_{1}^{n} \left[((\text{Qexp} - \text{Qcal}) \mid n)^2 \right]}, \quad (2)$$

$$R^2 = \sum_{1}^{n} \left[((\text{Qexp} - \text{Qcal}) \mid n)^2 \right], \quad (3)$$

where Qexp represents the measured value, Qcal represents the computed values, and n counts the set of observations.

CFBPNN models are like FFBPNN models in which they incorporate a weighted link from an input to every layer as well as from each layer to the subsequent layers. In some circumstances, the CFBP approach outperforms the FFBP method according to Mitra et al. [130].

$$\text{f}\left(\text{net}_j\right) = \frac{1}{\left(1 + e^{-\text{netj}}\right) \sum_{1}^{n} \left[((\text{Qexp} - \text{Qcal}) \mid n)^2 \right]}, \quad (4)$$

$$\text{f}\left(\text{net}_j\right) = \text{net}.$$

The yield of the chosen mining tactics was predicted using a schematic of a trainable CFBP. As previously discussed, the training level is critical. Backpropagation and quick-propagation training strategies are widely common
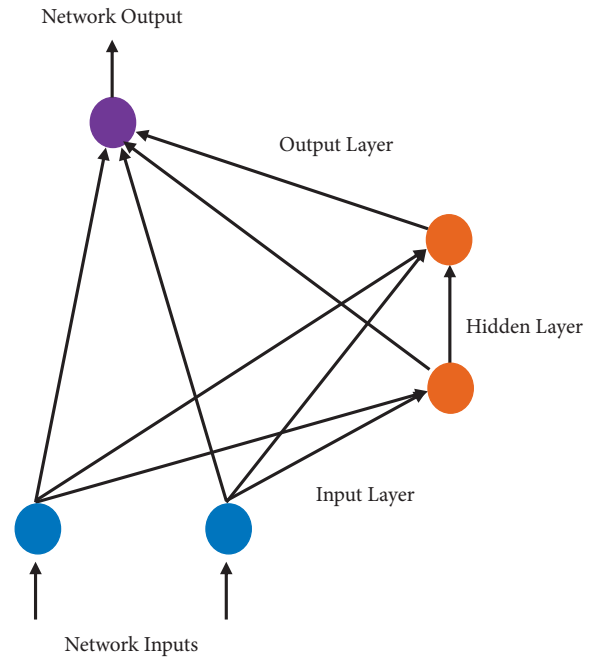
Figure 1: Cascade correlation neural network.

employed strategies. Consequently, the backpropagation approach was adapted to be implemented at the training level according to the method of Lashkarbolooki et al. [139] and its benefits in the current study. Specifically, the Levenberg–Marquardt backpropagation technique has been utilized due to its speed and accuracy. As a result, the proposed ANN model is transformed into one trained with the Levenberg–Marquardt algorithm [140]. The number of concealed layers is reduced and improved at the next level. As Cybenko [140] stated, a network with only a single concealed layer may mimic nearly every nonlinear relation; thus, for the proposed ANN model, just one concealed layer is used. The second essential criterion is the optimal number of neurons in the hidden layer. The number of neurons in the hidden layer is difficult to determine due to a limited number of neurons results in a network with low precision, whereas a larger number results in overfitting and poor interpolation quality because the risk of overtraining increases as the number of neurons increases [141]. There are four steps in the proposed technique for MMS using CFBPNN:

Step 1. The ANN's weight (W) and bias (b) values, as illustrated in Figure 2, were calculated using the MATLAB toolbox's trainable cascade-forward backpropagation and then entered in an Excel sheet.

Step 2. Equation (5) is used to calculate the output of the first layer (K) in the Excel spreadsheet function, and the results are shown in Section 5.2.

$$K1 = \frac{2}{(1 + \text{EMP}(-2 \times (\text{SUM}(O1))))} - 1. \quad (5)$$

Step 3. Equation (6) is used to determine the output of the second layer (rank of the selection technique) in the Excel sheet.

Figure 2: Subsidence features at China's Chengchao iron ore mine. Image courtesy of Google Earth, taken in 2018.

$$R = \text{SUM}(\text{Column02}) + K \times \text{W21W1} + b2. \qquad (6)$$

Step 4. The approach is chosen, and its name is shown in the Excel sheet by changing approximation rank values to integer values using the *V* function.

5.1. Gathering Data and Site Investigation.
Chengchao iron mine is a major iron ore and pellet ore production base for the Wuhan Iron and Steel Group Company and thus a huge identified underground iron mine in China. Between the Huaiyang Shield and Jiangnan Ancient Land, the Chengchao mining area is situated west of the lower Yangtze depression. It is a part of the western wing of the frontal arc of the Huaiyang epsilon structure. As indicated in Figure 2, the mining area is located near the East-West structural belt, which includes Mufushan as the major orebody in the south, the Liangzi Lake depression with a Neocathaysian structure in the west, and the South Huaiyang fault in the north.

The mining industry has a complex structure. Sedimentary, magmatic, and metamorphic rocks have been found in the Chengchao mining area. Anhydrite deposits were found in the contact zone between marble and granite, iron ores are found near the contact zone between diorite and granite, and skarns, which are in the shape of a pulse or a lens, are found near the contact zone between hornfels and granites. The eastern and western mining zones of the mine are separated by the geological exploration line 15. There are numerous ore deposits in the mining areas. Numbers I, II, III, IV, V, VI, VII, and others are the most typical iron ore bodies. Numbers II, III, VI, and VII are large-scale iron ores. The orebodies are mainly irregular lenticular in shape and slanted southward. Branching, compounding, expansion, and contraction are common occurrences in orebodies and ore sections. Table 4 summarizes the main geomechanical properties of the rock and ore in a mine case study.

5.2. Results.
To maximize the CFBPNN response, the tan-sigmoid transfer, log-sigmoid transfer, and pure linear limit characteristics are first determined. This is illustrated

Table 4: Characteristic of underground mining rock.

Characteristics of ore		
Geometry/form	T, tabular	
Width of ore, m	*N*, thin 17.5	Characterization Amplitude
Dip angle of ore, degrees	70°	
Allocation of grade levels	G, gradational G, gradational	Characterization Amplitude
Depth below surface, m	SH, shallow 210, m	Characterization Amplitude
Ore	M, medium 60	Characterization Amplitude
Hanging wall	VW, very weak 45	Characterization Amplitude
Footwall	VW, very weak 45	Characterization Amplitude
Ore	VW, very weak 40	
Hanging wall	W, weak 35	
Footwall	W, weak 40	

in Figure 3. The UBC criteria were converted to weights, and the load was determined using mining techniques (benefits are given the most weight, while risks are given the least, as in the mining methods). Table 5 summarizes the findings.

Table 6 summarizes the output of the first CFBPNN stage, which involves utilizing the MATLAB toolbox to compute the ANN weight (W) and bias (b) values using trainable CFBP. Table 7 presents the MMS results and findings based on the CFBPNN application. Ten mining methods were used to select the best method based on the assigned weights (*w*) and bias (b), as listed in Table 7. These parameters were calculated using a number of input parameters, including ore shape, thickness, dip angle, depth below surface, rock mass classification systems (such as RQD), and rock structure rating (RSR). CFBPNN was used to estimate the rank of each parameter in relation to the mining method. According to the findings, the cut and fill stopping method is the most effective.

5.3. Discussion.
The following layer properties have been employed based on the findings, which represent the integration of the method specifications and the real layer set: a dip of 70°, underground depth of 210 m, and RQD of 60 (moderate) and 45 (very weak) in the hanging wall. The cut and fill stoping method was superior to the other methods due to its suitability for all previous layer specifications. Figure 4 depicts the main design of the cut and fill stoping mining technique, which is the ideal mining method.

The Chengchao iron mine has been extracted using a sublevel caving method that eliminated the need for sill pillars. This is a type of bulk mining technique in which the
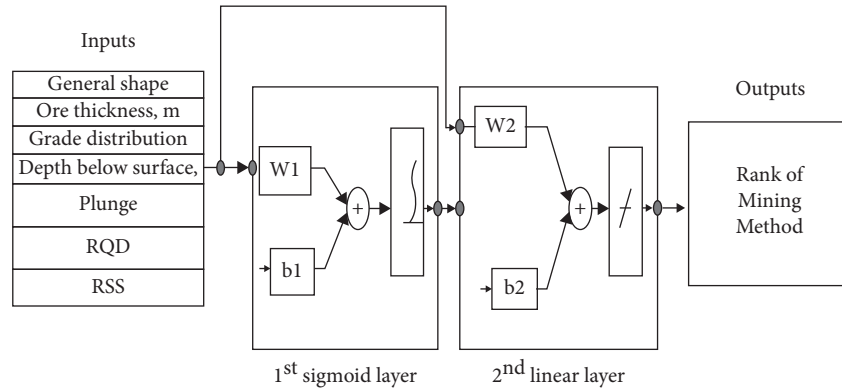
FIGURE 3: Trainable cascade-forward backpropagation ANN adopted to decide the suitable mining method.

TABLE 5: Weights of the various parameter assignments based on the mining methods.

	Parameter/mining methods	Open pit	Block caving	Sublevel stoping	Sublevel caving	Longwall	Room and pillar	Shrinkage stoping	Cut and fill stoping	Top slicing	Square set stoping
1	General shape	0.8	0.8	0.6	0.6	0	0	0	0.2	0.2	0
2	Ore thickness, m	0.8	0.8	0.6	0.8	0	0	0	0	0.2	0
3	Grade distribution	0.6	0.6	0.8	0.6	0.8	0.8	0.6	0.4	0.4	0
4	Depth, m	0.8	0.4	0.6	0.6	0.4	0.6	0.6	0.4	0.4	0.2
5	Plunge	0.2	0.8	0.8	0.8	0	0	0.8	0.8	0	0.4
6	Ore zone	0.6	0	0.8	0	0.4	0.9	0.6	0.6	0	0
7	RQD Hanging wall	0.8	0.4	0.8	0.4	0.6	0.9	0.8	0.6	0.6	0
8	Foot wall	0.8	0.4	0.6	0.6	0	0	0.6	0.4	0.4	0
9	Ore zone	0.6	0	0.8	0.4	0.2	0.9	0.8	0.6	0	0
10	RSS Hanging wall	0.8	0	0.6	0.25	0.4	0.9	0.8	0.4	0.4	0
11	Foot wall	0.8	0.2	0.6	0.4	0	0	0.6	0.4	0.25	0

TABLE 6: Values for weight (W) and bias (b) derived from the MATLAB toolbox.

Property/input	w1	w21 w2	b1	b2
General shape	5.4438	3.4113	8.803278	6.128579
Thickness of ore	12.4184	0.0339		
Distribution of grade levels	−12.5975	−5.4184		
Subsurface depth	−0.1821	−1.4329		
Dip angle	11.1132	0.301		
Rock quality designation (RQD) index	6.8993	2.6115		
Rockmass Structure Rate (RSR)	−22.7358	0.7069		
		−2.78847		

movement of blasted ore and caved waste rock is controlled by gravity. To relieve ground pressure, backed down rock masses from overlying country rock have been used to replace mined-out regions caused by ore extraction [142]. The caved zone, which is composed of caved rock masses, can come as a result above the mined-out area, inferring vertical caving. In addition, above the fallen rock mass, a joint may be developed. Consequently, this type of mass underground mining can cause severe ground surface disruption. As the excavation of the subterranean orebody continues, the caving of the overlying country rock caves ultimately propagates to the

ground surface, causing it to collapse [143]. According to Zhang et al. [144], the movement of strata at the Chengchao iron mine can be classified into six categories: vertical subsidence, toppling slip, toppling, deformation, deformation accumulation, and undisturbed areas. As a result, when a large-scale orebody is mined, large-scale collapse at the ground surface is common. According to the CFBPNN rank presented in Table 8, sublevel caving is ranked No. 4. According to the overall score assigned to all ore attributes, the findings reveal metrics for selection to use when deciding between different mining processes.

Table 7: Results of using CFBPNN for MMS with the given parameters.

Mining method	No.		Rank	O2	O1	b2	b1	w21 w2	w1	Properties/ input
		Rank	2.72904	4.35504	6.128579	8.803278	3.4113	5.4438	0.8	
Open-pit mining	1		7.933731	0.01356	4.96736			0.0339	12.4184	0.4
Block caving	2	**Method 8**		−3.25104	−7.5585			−5.4184	−12.5975	0.6
Sublevel stoping	3	**Cut and fill stoping**		−0.85974	−0.10926			−1.4329	−0.1821	0.6
Sublevel caving	4			0.0301	1.11132			0.301	11.1132	0.1
Longwall mining	5			0.26115	0.68993			2.6115	6.8993	0.1
Room and pillar	6			0.42414	−13.6415			0.7069	−22.7358	0.6
Shrinkage stoping	7			7.933731	−1.38231			−2.78847		
Cut and fill stoping	8				−0.88147					
Top slicing	9									
Square set stoping	10									

The bold value means the optimal selected mining method.
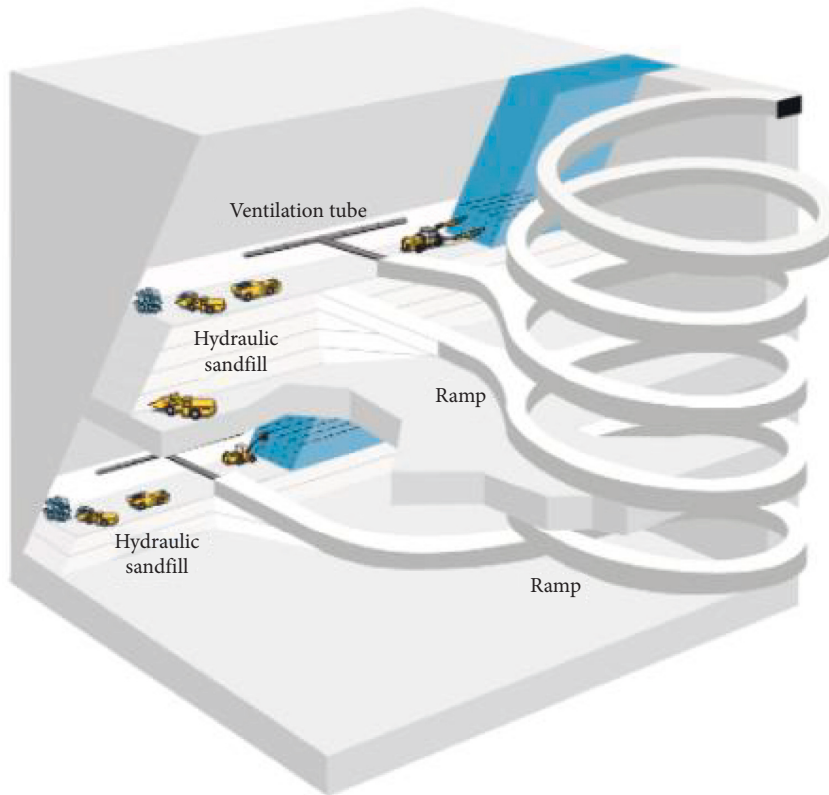
Figure 4: Cut and fill stoping.

TABLE 8: Ranking of all mining methods using CFBPNN.

Mining method	Final Rank
Open pit	10
Block caving	5
Sublevel stoping	2
Sublevel caving	4
Longwall mining	8
Room and pillar	9
Shrinkage stoping	3
Cut and fill stoping	**1**
Top slicing	6
Square set stoping	7

The bold means the best mining method based on the results.

6. Conclusions

Various criteria must be considered when deciding on an appropriate mining method for ore deposits. Several techniques, including the Nicholas, modified Nicholas, and UBC methods, were created to investigate the appropriate mining methods for mineral deposits. Unfortunately, none of these methods consider the weight values for every factor that influences the MMS. As a result, this study takes into account the weight values for each parameter that influences the mining method selection. In comparison to other studies, this is the first to try a new technique called CFBPNN, which was implemented in the Chengchao iron ore mine to select the most appropriate (safe) mining method. The findings of this study can be summarized as follows:

(1) The primary goal of this review is to study in detail the development of different tools that are earlier used in decision-making for MMS and their application, functionality, advantages, and disadvantages.

(2) A newly proposed technique for MMS based on the application of CFBPNN was presented and illustrated, which is easier to apply and more accurate than traditional tools.

(3) The CFBPNN method is used in this paper to determine appropriate mining methods for the Chengchao iron mine under various conditions. The most effective mining method is cut and fill stoping.

(4) Based on the total score assigned to all ore properties, the results offer metrics that could be used to select among various mining methods.

Users should understand the MMS tools described and recognize that the suggested method is a simplified approach and will only be helpful if the theoretical background behind ANN is understood. If the factors and methods in the results section are not sufficient, an appropriate criteria and alternatives could be included to the database for the investigated problem. For effective and reliable results, changes in the final rank have to be monitored and recorded using at least two MMS tools in the suggested way.

The suggested model was introduced without correlation to other MMS methods, which is a limitation. As a result, future research could look into other MMS tools and their impact on final rankings. The second limitation is that some of the publications have been translated into English. As a result, in the future, more publications will need to be reviewed to learn more about MMS tools. CFBPNN algorithms for selecting a proper MMS can be developed in future research once the problem has been described and organized, so determining the optimal method will be convenient.

Abbreviations

AHP:	Analytic hierarchy process
AI:	Artificial intelligence
ANN:	Artificial neural network
ARAS:	Additive ratio assessment approach
CFBPNN:	Cascade forward backpropagation neural network
CI:	Computing intelligence
COPRAS:	Complex proportional assessment approach
CP:	Constraint programming
ELECTRE:	ELimination Et Choix Traduisant la REalité (elimination and choice translating reality)
GRA:	Grey relational analysis
MCDM:	Multicriteria decision-making
MMS:	Mining method selection
OCRA:	Operational competitiveness rating analysis
PROMETHEE:	Preference ranking organization method for enrichment evaluation
SAW:	Simple additive weighting
TODIM:	Portuguese acronym for interactive multicriteria decision-making
TOPSIS:	Technique for order of preference by the similarity to ideal solution
VIKOR:	Vlsekriterijumska Optimizacija I Kompromisno Resenje (multicriteria optimization and compromise solution).

Conflicts of Interest

The authors declare that they have no conflicts of interest.

References

[1] D. E. Nicholas, "Selection procedure," in *Mining Engineering Handbook*, H. Hartman, Ed., pp. 2090–2105, SME, New York, NY, USA, 1993.

[2] Z. Li, Y. Zhao, and H. Zhao, "Assessment indicators and methods for developing the sustainability of mining communities," *The International Journal of Sustainable Development and World Ecology*, vol. 15, no. 1, p. 35, 2008.

[3] M. Straka and D. Malindzak, "Algorithms of capacity balancing of printing machineries for Alfa Foils, as planning system," *Acta Montanistica Slovaca*, vol. 14, no. 1, pp. 98–102, 2009.

[4] S. Boshkov and F. Wright, "Basic and parametric criteria in the selection, design and development of underground mining systems," *SME Mining Engineering Handbook*, SME-AIME, vol. 1, p. 12, New York, NY, USA, 1973.

[5] F. Samimi Namin, K. Shahriar, and S. Karimi Nasab, "Fuzzy decision making for mining method selection in third

anomaly gol-E-gohar deposit," in *Proceedings of the 18th International Mining Congress and Exhibition of Turkey (I MCET)*, Ankara, Turkey, June 2003.

[6] H. L. Hartman and J. M. Mutmansky, *Introductory Mining Engineering*, John Wiley & Sons, Hoboken, NJ, USA, 2002.

[7] R. G. K. Morrison, *A Philosophy of Ground Control: A Bridge Between Theory and Practice*, Department of Mining and Metallurgical Engineering, McGill University, Montreal, Canada, 1976.

[8] D. Nicholas and J. Mark, "Feasibility study–selection of a mining method integrating rock mechanics and mine planning," in *Proceedings of the 5th Rapid Excavation and Tunneling Conference*, San Francisco, CA, USA, May 1981.

[9] D. H. Laubscher, "Selection of mass underground mining methods," *Design and Operation of Caving and Sublevel Stoping Mines*, pp. 23–38, 1981.

[10] G. Marano and A. Everitt, "Selection of mining method and equipment for Block 58, Shabanie Mine, Zimbabwe," in *Proceedings of the African Mining Conference*, Harare, Zimbabwe, August 1987.

[11] S. Bandopadhyay and P. Venkatasubramanian, "Rule-based expert system for mining method selection," *CIM (Canadian Institute Mining and Metallurgy) Bulletin;(Canada)*, vol. 81, no. 919, 1988.

[12] M. Agoshkov, S. Borisov, and V. Boyarsky, "Classification of ore deposit mining systems," *Mining of Ores and Non-Metalic Minerals*, pp. 59–62, 1988.

[13] W. Mutagwaba and N. Terezopoulos, "Knowledge-based system for mine method selection," *Transactions of the Institution of Mining and Metallurgy. Section A. Mining Industry*, vol. 103, 1994.

[14] L. Miller-Tait, R. Panalkis, and R. Poulin, "UBC mining method selection," in *Proceedings of the Mine Planning and Equipment Selection Symposium*, Calgary, Canada, November 1995.

[15] H. Hamrin, "Choosing underground mining method techniques in underground mining," *Mining Engineering Handbook*, pp. 45–85, SME, Canonsburg, PA, USA, 1988.

[16] R. Tatiya, "Computer assisted economic analysis to select a stoping method," *CIM Bulletin*, vol. 91, no. 1023, pp. 82–86, 1998.

[17] A. Basu, "A mining method selection expert system with prototype with an Australian case study," in *Proceedings of the Mine Planning and Equipment Selection*, pp. 73–78, Dnipropetrovsk, Ukraine, June 1999.

[18] A. Kahriman, *Selection of Optimum Underground Mining Method for Kayseri Pynarbapy-Pulpynar Chrome Ore*, Middle East Technical University, Ankara, Turkey, 2000.

[19] A. Karadogan, A. Bascetin, and A. Kahriman, "A new approach in selection of underground mining method," in *Proceedings of the International Conference Modern Management of Mine Producing*, Varna, Bulgaria, June 2001.

[20] A. Kesimal and A. Bascetin, "Application of fuzzy multiple attribute decision making in mining operations," *Mineral Resources Engineering*, vol. 11, no. 1, pp. 59–72, 2002.

[21] C. Clayton, R. Pakalnis, and J. Meech, "A knowledge-based system for selecting a mining method," in *Proceedings of the IPPM Conference*, Calgary, Canada, July 2002.

[22] C. Guray, N. Celebi, V. Atalay, and A. Pasamehmetoglu, "Ore-age: a hybrid system for assisting and teaching mining method selection," *Expert Systems with Applications*, vol. 24, no. 3, pp. 261–271, 2003.

[23] Y. Wei, Y. Fan, and W. Xu, "An integrated methodology for decision making of mining method selection," *International Journal of Manufacturing Technology and Management*, vol. 5, no. 1/2, p. 10, 2003.

[24] K. Shahriar, V. Shariati, and F. S. Namin, "Geomechanical characteristics study of deposit in underground mining method selection process," in *Proceedings of the 11th ISRM Congress*, OnePetro, Lisbon, Portugal, July 2007.

[25] G. Mihaylov, *A Model and Procedure for Selecting Underground Mining Methods*, World Mining Congress, Tehran. Iran, 2005.

[26] C. Miranda and C. Almeida, "Mining methods selection based on multi criteria models," *Application of computes and operation research in the mineral industry*, CRC Press, London, UK, 2005.

[27] A. Bascetin, "A decision support system using analytical hierarchy process (AHP) for the optimal environmental reclamation of an open-pit mine," *Environmental Geology*, vol. 52, no. 4, pp. 663–672, 2007.

[28] A. Azadeh, M. Osanloo, and M. Ataei, "A new approach to mining method selection based on modifying the Nicholas technique," *Applied Soft Computing*, vol. 10, no. 4, pp. 1040–1061, 2010.

[29] R. Chaudhari, J. Vora, D. M. Parikh, V. Wankhede, and S. Khanna, "Multi-response optimization of WEDM parameters using an integrated approach of RSM–GRA analysis for pure titanium," *Journal of the Institution of Engineers: Series D*, vol. 101, no. 1, pp. 117–126, 2020.

[30] K. Yoon, *Systems Selection by Multiple Attribute Decision Making*, Kansas State University, Manhattan, Kansas, 1980.

[31] F. S. Namin, K. Shahriar, A. Bascetin, and S. H. Ghodsypour, "Practical applications from decision-making techniques for selection of suitable mining method in Iran," *Gospodarka Surowcami Mineralnymi*, vol. 25, pp. 57–77, 2009.

[32] V. D. Baloyi and L. Meyer, "The development of a mining method selection model through a detailed assessment of multi-criteria decision methods," *Results in Engineering*, vol. 8, Article ID 100172, 2020.

[33] W. Banda, "A fuzzy techno-financial methodology for selecting an optimal mining method," *Natural Resources Research*, vol. 29, no. 5, pp. 3047–3067, 2020.

[34] T. Saaty, *The Analytic Hierarchy Process*, Vol. 70, Mcgraw Hill, New York, NY, USA, 1980.

[35] P. Kluge and D. F. Malan, "The application of the analytical hierarchical process in complex mining engineering design problems," 2011.

[36] Q. Guo, H. Yu, Z. Dan, and S. Li, "Mining method optimization of gently inclined and soft broken complex ore body based on AHP and TOPSIS: taking miao-ling gold mine of China as an example," *Sustainability*, vol. 13, no. 22, Article ID 12503, 2021.

[37] K. D. Balt, "A methodology for implementing the analytical hierarchy process to decision-making in mining," 2016.

[38] M. Velasquez and P. T. Hester, "An analysis of multi-criteria decision making methods," *International Journal of Operational Research*, vol. 10, no. 2, pp. 56–66, 2013.

[39] M. Ataei, M. Jamshidi, F. Sereshki, and S. M. E. Jalali, "Mining method selection by AHP approach," *Journal of the South African Institute of Mining and Metallurgy*, vol. 108, no. 12, pp. 741–749, 2008.

[40] C. Musingwini and R. Minnitt, "Ranking the efficiency of selected platinum mining methods using the analytic hierarchy process (AHP)," in *Proceedings of the 3rd International Platinum Conference 'Platinum in Transformation'*, The Southern African Institute of Mining and Metallurgy, Sun City, South Africa, October 2008.

[41] E. Cheng and H. Li, "Utility of consistency measure in the analytic hierarchy process," *Construction Innovation*, vol. 3, no. 4, pp. 231–247, 2003.

[42] J.-P. Brans and P. Vincke, "Note—a preference ranking organisation method: (the PROMETHEE method for multiple criteria decision-making)," *Management Science*, vol. 31, no. 6, pp. 647–656, 1985.

[43] J.-P. Brans and Y. De Smet, "PROMETHEE Methods," in *Multiple Criteria Decision Analysis*, pp. 187–219, Springer, Berlin, Germany, 2016.

[44] G. Anand and R. Kodali, "Selection of lean manufacturing systems using the PROMETHEE," *Journal of modelling in management*, vol. 3, 2008.

[45] V. Tomić, Z. Marinković, and D. Janošević, "PROMETHEE method implementation with multi-criteria decisions," *Facta Universitatis – Series: Mechanical Engineering*, vol. 9, no. 2, pp. 193–202, 2011.

[46] M. Iphar and S. Alpay, "A mobile application based on multi-criteria decision-making methods for underground mining method selection," *International Journal of Mining, Reclamation and Environment*, vol. 33, no. 7, pp. 480–504, 2019.

[47] A. Sultana and A. Kumar, "Ranking of biomass pellets by integration of economic, environmental and technical factors," *Biomass and Bioenergy*, vol. 39, pp. 344–355, 2012.

[48] V. M. Athawale and S. Chakraborty, "Facility layout selection using PROMETHEE II method," *Iup Journal of Operations Management*, vol. 9, 2010.

[49] K. Hyde, H. R. Maier, and C. Colby, "Incorporating uncertainty in the PROMETHEE MCDA method," *Journal of Multi-Criteria Decision Analysis*, vol. 12, no. 4-5, pp. 245–259, 2003.

[50] C.-L. Hwang and K. Yoon, "Methods for multiple attribute decision making," in *Multiple Attribute Decision Making*, pp. 58–191, Springer, Berlin, Germany, 1981.

[51] D. L. Olson, "Comparison of weights in TOPSIS models," *Mathematical and Computer Modelling*, vol. 40, no. 7-8, pp. 721–727, 2004.

[52] H.-S. Shih, H.-J. Shyur, and E. S. Lee, "An extension of TOPSIS for group decision making," *Mathematical and Computer Modelling*, vol. 45, no. 7-8, pp. 801–813, 2007.

[53] J. Wu, J. Sun, Y. Zha, and L. Liang, "Ranking approach of cross-efficiency based on improved TOPSIS technique," *Journal of Systems Engineering and Electronics*, vol. 22, no. 4, pp. 604–608, 2011.

[54] Y.-J. Lai, T.-Y. Liu, and C.-L. Hwang, "Topsis for MODM," *European Journal of Operational Research*, vol. 76, no. 3, pp. 486–500, 1994.

[55] M. S. García-Cascales and M. T. Lamata, "On rank reversal and TOPSIS method," *Mathematical and Computer Modelling*, vol. 56, no. 5-6, pp. 123–132, 2012.

[56] E. Tajvidi Asr, M. Hayaty, R. Rafiee, M. Ataie, and S. E. Jalali, "Selection of optimum tunnel support system using aggregated ranking of SAW, TOPSIS and LA methods," *International Journal of Operational Research*, vol. 5, no. 4, pp. 49–63, 2015.

[57] S. Cheng, C. W. Chan, and G. H. Huang, "Using multiple criteria decision analysis for supporting decisions of solid waste management," *Journal of Environmental Science and Health, Part A*, vol. 37, no. 6, pp. 975–990, 2002.

[58] A. Aghajani and M. Osanloo, "Application of AHP-TOPSIS method for loading-haulage equipment selection in open pit mines," in *Proceedings of the 27th International Mining Convention*, Veracruz, Mexico, October 2007.

[59] E. K. Zavadskas, A. Mardani, Z. Turskis, A. Jusoh, and K. M. Nor, "Development of TOPSIS method to solve complicated decision-making problems—an overview on developments from 2000 to 2015," *International Journal of Information Technology and Decision Making*, vol. 15, no. 3, pp. 645–682, 2016.

[60] S. Chakraborty, P. Chatterjee, and P. P. Das, "A DoE–TOPSIS method-based meta-model for parametric optimization of non-traditional machining processes," *Journal of Modelling in Management*, vol. 14, 2019.

[61] D. Zindani, S. R. Maity, S. Bhowmik, and S. Chakraborty, "A material selection approach using the TODIM (TOmada de Decisao Interativa Multicriterio) method and its analysis," *International Journal of Materials Research*, vol. 108, no. 5, pp. 345–354, 2017.

[62] L. A. D. Rangel, L. F. A. M. Gomes, and F. P. Cardoso, "An application of the TODIM method to the evaluation of broadband internet plans," *Pesquisa Operacional*, vol. 31, no. 2, pp. 235–249, 2011.

[63] J. Huang, Z. S. Li, and H.-C. Liu, "New approach for failure mode and effect analysis using linguistic distribution assessments and TODIM method," *Reliability Engineering & System Safety*, vol. 167, pp. 302–309, 2017.

[64] S. m. Yu, J. Wang, and J. q. Wang, "An extended TODIM approach with intuitionistic linguistic numbers," *International Transactions in Operational Research*, vol. 25, no. 3, pp. 781–805, 2018.

[65] L. A. D. Rangel, L. F. A. M. Gomes, and R. A. Moreira, "Decision theory with multiple criteria: an aplication of ELECTRE IV and TODIM to SEBRAE/RJ," *Pesquisa Operacional*, vol. 29, no. 3, pp. 577–590, 2009.

[66] H. Dehghani, A. Siami, and P. Haghi, "A new model for mining method selection based on grey and TODIM methods," *Journal of Mining and Environment*, vol. 8, no. 1, pp. 49–60, 2017.

[67] Y. Kazancoglu and S. Burmaoglu, "ERP software selection with MCDM: application of TODIM method," *International Journal of Business Information Systems*, vol. 13, no. 4, p. 435, 2013.

[68] E. A. Adali, A. T. Işik, and N. Kundakci, "Todim method for the selection of the elective courses," *European Scientific Journal*, vol. 12, pp. 314–324, 2016.

[69] D. Zhang, X. Bao, and C. Wu, "An extended TODIM method based on novel score function and accuracy function under intuitionistic fuzzy environment," *International Journal of Uncertainty, Fuzziness and Knowledge-Based Systems*, vol. 27, no. 6, pp. 905–930, 2019.

[70] S. Opricovic, "Programski paket VIKOR za visekriterijumsko kompromisno rangiranje," in *Proceedings of the 17th International Symposium on Operational Research SYM-OP-IS*, Belgrade, Serbia, 1990.

[71] N. Caterino, "A comparative analysis of decision making methods for the seismic retrofit of RC buildings," in *Proceedings of the the 14 th World Conference on Earthquake Engineering*, Bejing, China, October 2008.

[72] V. Thiagarasu and V. Rengaraj, "A MADM model with VIKOR method for decision making support systems," *International Journal of Computer Science and Software Engneering*, vol. 2, no. 1, pp. 63–81, 2015.

[73] A. R. Fallahpour and A. R. Moghassem, "Evaluating applicability of VIKOR method of multi-criteria decision making for parameters selection problem in rotor spinning," *Fibers and Polymers*, vol. 13, no. 6, pp. 802–808, 2012.

[74] M. A. M. Ali, J. G. Kim, Z. H. Awadallah, A. M. Abdo, and A. M. Hassan, "Multiple-criteria decision analysis using TOPSIS: sustainable approach to technical and economic evaluation of rocks for lining canals," *Applied Sciences*, vol. 11, no. 20, p. 9692, 2021.

[75] J. H. Kim and B. S. Ahn, "The hierarchical VIKOR method with incomplete information: supplier selection problem," *Sustainability*, vol. 12, no. 22, p. 9602, 2020.

[76] A. Mardani, E. Zavadskas, K. Govindan, A. Amat Senin, and A. Jusoh, "VIKOR technique: a systematic review of the state of the art literature on methodologies and applications," *Sustainability*, vol. 8, no. 1, p. 37, 2016.

[77] S. Opricovic and G.-H. Tzeng, "Compromise solution by MCDM methods: a comparative analysis of VIKOR and TOPSIS," *European Journal of Operational Research*, vol. 156, no. 2, pp. 445–455, 2004.

[78] A. Puška, "RANGIRANJE INVESTICIONIH PROJEKATA korišcenjem VIKOR METODE," *Singidunum scientific review/singidunum revija*, vol. 8, no. 2, 2011.

[79] M. Mančev, "Service quality management in the libraries at the University of Niš Faculties using the VIKOR method," *Journal INFO Theca*, vol. 14, no. 1, pp. 15–25, 2013.

[80] A. Kangas, J. Kangas, and J. Pykäläinen, "Outranking methods as tools in strategic natural resources planning," *Silva Fennica*, vol. 35, no. 2, 2001.

[81] O. Yavuz, "Supplier selection process using ELECTRE I decision model and an application in the retail sector," *İşletme Araştırmaları Dergisi*, vol. 5, no. 4, pp. 210–226, 2013.

[82] A. H. Azadnia, G. Pezhman, Z. M. S. Muhamad, Y. W. Kuan, and S. Safian, "Supplier selection: a hybrid approach using ELECTRE and fuzzy clustering," in *Proceedings of the International Conference on Informatics Engineering and Information Science*, Springer, Kuala Lumpur, Malaysia, November 2011.

[83] A. Afshari, M. Mojahed, R. Yusuff, T. Hong, and M. Ismail, "Personnel selection using ELECTRE," *Journal of Applied Sciences*, vol. 10, no. 23, pp. 3068–3075, 2010.

[84] J.-j. Peng, J. q. Wang, H. y. Zhang, and X. h. Chen, "An outranking approach for multi-criteria decision-making problems with simplified neutrosophic sets," *Applied Soft Computing*, vol. 25, pp. 336–346, 2014.

[85] B. F. Hobbs and P. Meier, "Energy decisions and the environment: A Guide to the Use of Multicriteria Methods," vol. 28, Springer science & business media, Berlin, Germany, 2012.

[86] C. Stojanovic, D. Bogdanovic, and S. Urosevic, "Selection of the optimal technology for surface mining by multi-criteria analysis," *Kuwait Journal of Science*, vol. 42, no. 3, 2015.

[87] P. Bodziony, Z. Kasztelewicz, and P. Sawicki, "The problem of multiple criteria selection of the surface mining haul trucks," *Archives of Mining Sciences*, vol. 61, no. 2, pp. 223–243, 2016.

[88] K. Hanbin, "Grey numbers in multiple criteria decision analysis and conflict resolution," University of Waterloo, Waterloo, Canada, 2014.

[89] E. G. Satolo, C. Leite, R. D. Calado, G. A. Goes, and D. D. Salgado, "Ranking lean tools for world class reach through grey relational analysis," *Grey Systems: Theory and Application*, vol. 8, no. 4, pp. 399–423, 2018.

[90] W. Wu, "Grey relational analysis method for group decision making in credit risk analysis. EURASIA Journal of Mathematics," *Science and Technology Education*, vol. 13, no. 12, pp. 7913–7920, 2017.

[91] H. Hasani, S. A. Tabatabaei, and G. Amiri, "Grey relational analysis to determine the optimum process parameters for open-end spinning," *Journal of Engineered Fibers and Fabrics*, vol. 7, no. 2, pp. 81–86, 2012.

[92] S.-T. Lin, S. J. Horng, B. H. Lee et al., "Application of grey-relational analysis to find the most suitable watermarking scheme. International Journal of Innovative Computing," *Information and Control*, vol. 7, no. 9, pp. 5389–5401, 2011.

[93] Y. Kuo, T. Yang, and G.-W. Huang, "The use of a grey-based Taguchi method for optimizing multi-response simulation problems," *Engineering Optimization*, vol. 40, no. 6, pp. 517–528, 2008.

[94] S. Wang and Jl Zhang, "Study on coal mines accidents based on the grey relational analysis," *Journal of Coal Science and Engineering*, vol. 14, no. 1, pp. 81–84, 2008.

[95] J. Bao, J. Johansson, and J. Zhang, "Evaluation on safety benefits of mining industry occupational health and safety management system based on DEA model and grey relational analysis," *International Journal of Engineering and Technology*, vol. 10, no. 1, pp. 82–88, 2018.

[96] F. Saki, H. Dehghani, B. Jodeiri Shokri, and D. Bogdanovic, "Determination of the most appropriate tools of multi-criteria decision analysis for underground mining method selection—a case study," *Arabian Journal of Geosciences*, vol. 13, no. 23, p. 1271, 2020.

[97] G.-H. Tzeng and J.-J. Huang, *Multiple attribute decision making: Methods and Applications*, CRC press, Boca Raton, FL, USA, 2011.

[98] Q. Yun and G. Huang, "A fuzzy set approach to the selection of mining method," *Mining Science and Technology*, vol. 6, no. 1, pp. 9–16, 1987.

[99] F. A. Ooriad, M. Yari, R. Bagherpour, and M. K. Esfahani, "The development of a novel model for mining method selection in a fuzzy environment; case study: tazareh Coal Mine, Semnan Province, Iran," *Rudarsko-geološko-naftni zbornik*, vol. 33, no. 1, pp. 45–53, 2018.

[100] L. A. Zadeh, "Fuzzy sets," in *Fuzzy Sets, Fuzzy Logic, and Fuzzy Systems: Selected Papers by Lotfi A Zadeh*, pp. 394–432, World Scientific, Singapore, 1996.

[101] M. Bitarafan and M. Ataei, "Mining method selection by multiple criteria decision making tools," *Journal of the South African Institute of Mining and Metallurgy*, vol. 104, no. 9, pp. 493–498, 2004.

[102] R. R. Yager, "Fuzzy decision making including unequal objectives," *Fuzzy Sets and Systems*, vol. 1, no. 2, pp. 87–95, 1978.

[103] K. W. Hipel, "Fuzzy set methodologies in multicriteria modeling," *Fuzzy Information and Decision Processes*, pp. 279–287, 1982.

[104] G. Tian, Z. Guo, and S. Li, "Optimization of tawa landslide treatment scheme based on the AHP-fuzzy comprehensive evaluation method," in *Proceedings of the IOP conference series: Earth and environmental science*, IOP Publishing, Changsha, China, September 2020.

[105] T.-C. Wang and Y.-H. Chen, "Applying fuzzy linguistic preference relations to the improvement of consistency of fuzzy AHP," *Information Sciences*, vol. 178, no. 19, pp. 3755–3765, 2008.

[106] M. Z. Naghadehi, R. Mikaeil, and M. Ataei, "The application of fuzzy analytic hierarchy process (FAHP) approach to selection of optimum underground mining method for Jajarm Bauxite Mine, Iran," *Expert Systems with Applications*, vol. 36, no. 4, pp. 8218–8226, 2009.

[107] D.-Y. Chang, "Applications of the extent analysis method on fuzzy AHP," *European Journal of Operational Research*, vol. 95, no. 3, pp. 649–655, 1996.

[108] H. Yu, N. Wang, and J. Pan, "Application of fuzzy extension analytic hierarchy process in location selection of logistics center," in *Journal of Physics: Conference Series*, vol. 1995, no. 1, IOP Publishing, Article ID 012035, 2021.

[109] O. Dogan, "Process mining technology selection with spherical fuzzy AHP and sensitivity analysis," *Expert Systems with Applications*, vol. 178, Article ID 114999, 2021.

[110] M. Ataei, H. Shahsavany, and R. Mikaeil, "Monte Carlo Analytic Hierarchy Process (MAHP) approach to selection of optimum mining method," *International Journal of Mining Science and Technology*, vol. 23, no. 4, pp. 573–578, 2013.

[111] H. L. Hartman and SME, *SME mining engineering handbook*, Vol. 2, Society for mining, metallurgy, and exploration denver, Englewood, CO, USA, 1992.

[112] Z. Fu, X. Wu, H. Liao, and F. Herrera, "Underground mining method selection with the hesitant fuzzy linguistic gained and lost dominance score method," *IEEE Access*, vol. 6, pp. 66442–66458, 2018.

[113] F. S. Namin, K. Shahriar, A. BAscetin, and S. H. Ghodsypour, "FMMSIC: a hybrid fuzzy based decision support system for MMS (in order to estimate interrelationships between criteria)," *Journal of the Operational Research Society*, vol. 63, no. 2, pp. 218–231, 2012.

[114] T. L. Saaty and L. G. Vargas, "Diagnosis with dependent symptoms: bayes theorem and the analytic hierarchy process," *Operations Research*, vol. 46, no. 4, pp. 491–502, 1998.

[115] A. De Luca and S. Termini, "A definition of a non-probabilistic entropy in the setting of fuzzy sets theory," *Information and Control*, vol. 20, no. 4, pp. 301–312, 1972.

[116] M. Javanshirgiv and M. Safari, "The selection of an underground mining method using the fuzzy topsis method: a case study in the Kamar Mahdi II fluorine mine," *Mining Science*, vol. 24, 2017.

[117] H. Karimnia, H. Bagloo, "Optimum mining method selection using fuzzy analytical hierarchy process–Qapiliq salt mine, Iran," *International Journal of Mining Science and Technology*, vol. 25, no. 2, pp. 225–230, 2015.

[118] W.-z. Liang, G. Zhao, H. Wu, and Y. Chen, "Optimization of mining method in subsea deep gold mines: a case study," *Transactions of Nonferrous Metals Society of China*, vol. 29, no. 10, pp. 2160–2169, 2019.

[119] M. Gershon, S. Bandopadhyay, and V. Panchanadam, "Mining method selection: a decision support system integrating multi-attribute utility theory and expert systems," in *Proceedings of the 24th international symposium on the application of computers in mine planning (APCOM)*, Montreal, Canada, October 1993.

[120] W. Y. T. G. C. Xiaohua, "A study on the neural network based expert system for mining method selection," *Computer Applications and Software*, vol. 5, 1995.

[121] M. Yavuz, "The application of the analytic hierarchy process (AHP) and Yager's method in underground mining method selection problem," *International Journal of Mining, Reclamation and Environment*, vol. 29, no. 6, pp. 453–475, 2015.

[122] S. Gupta and U. Kumar, "An analytical hierarchy process (AHP)-guided decision model for underground mining method selection," *International Journal of Mining, Reclamation and Environment*, vol. 26, no. 4, pp. 324–336, 2012.

[123] C. Qi, A. Fourie, Q. Chen, and Q. Zhang, "A strength prediction model using artificial intelligence for recycling waste tailings as cemented paste backfill," *Journal of Cleaner Production*, vol. 183, pp. 566–578, 2018.

[124] M. E. Yetkin and M. K. Özfırat, "selection of thick coal seam mining method using analytic hierarchy process," *ITEGAM-JETIA*, vol. 5, no. 20, pp. 6–11, 2019.

[125] Y. H. Hu and J.-N. Hwang, "Handbook of neural network signal processing," CRC press, Boca Raton, FL, USA, 2002.

[126] L. Wang, B. Yang, R. Wang, and X. Du, "Extraction of pepsin-soluble collagen from grass carp (Ctenopharyngodon idella) skin using an artificial neural network," *Food Chemistry*, vol. 111, no. 3, pp. 683–686, 2008.

[127] A. R. Khanchi, M. K. Mahani, M. Hajihosseini, M. G. Maragheh, M. Chaloosi, and F. Bani, "Simultaneous spectrophotometric determination of caffeine and theobromine in Iranian tea by artificial neural networks and its comparison with PLS," *Food Chemistry*, vol. 103, no. 3, pp. 1062–1068, 2007.

[128] M. Fullana, F. Trabelsi, and F. Recasens, "Use of neural net computing for statistical and kinetic modelling and simulation of supercritical fluid extractors," *Chemical Engineering Science*, vol. 55, no. 1, pp. 79–95, 2000.

[129] J.-Z. Yin and Q. Q. A. Q. Xu, "Experiments and numerical simulations of supercritical fluid extraction for hippophae rhamnoides l seed oil based on artificial neural networks," *Industrial & Engineering Chemistry Research*, vol. 44, no. 19, pp. 7420–7427, 2005.

[130] P. Mitra, P. C. Barman, and K. S. Chang, "Coumarin extraction from cuscuta reflexa using supercritical fluid carbon dioxide and development of an artificial neural network model to predict the coumarin yield," *Food and Bioprocess Technology*, vol. 4, no. 5, pp. 737–744, 2011.

[131] M. Izadifar and F. Abdolahi, "Comparison between neural network and mathematical modeling of supercritical CO2 extraction of black pepper essential oil," *The Journal of Supercritical Fluids*, vol. 38, no. 1, pp. 37–43, 2006.

[132] M. Khajeh, M. G. Moghaddam, and M. Shakeri, "Application of artificial neural network in predicting the extraction yield of essential oils of Diplotaenia cachrydifolia by supercritical fluid extraction," *The Journal of Supercritical Fluids*, vol. 69, pp. 91–96, 2012.

[133] W. Y. Lv and Z. H. Zhang, "Application of thick coal seam mining method prediction model based on artificial neural network," *Advanced Materials Research*, vol. 962–965, pp. 242–246, 2014.

[134] W. Chen and T. Shixiang, "Evolving neural network using genetic algorithm for mining method evaluation in thin coal seam working face," *International Journal of Mining and Mineral Engineering*, vol. 9, no. 3, p. 228, 2018.

[135] M. C. Özyurt and A. Karadogan, "A new model based on artificial neural networks and game theory for the selection of underground mining method," *Journal of Mining Science*, vol. 56, no. 1, pp. 66–78, 2020.

[136] O. De Jesus and M. T. Hagan, "Backpropagation algorithms for a broad class of dynamic networks," *IEEE Transactions on Neural Networks*, vol. 18, no. 1, pp. 14–27, 2007.

[137] M. H. Beale, M. T. Hagan, and H. B. Demuth, *Neural Network Toolbox User's Guide*, pp. 77–81, The MathWorks, Portola Valley, CA, USA, 2010.

[138] F. Nami and F. Deyhimi, "Prediction of activity coefficients at infinite dilution for organic solutes in ionic liquids by artificial neural network," *The Journal of Chemical Thermodynamics*, vol. 43, no. 1, pp. 22–27, 2011.

[139] M. Lashkarbolooki, A. Z. Hezave, and A. Babapoor, "Correlation of density for binary mixtures of methanol+ ionic

liquids using back propagation artificial neural network," *Korean Journal of Chemical Engineering*, vol. 30, no. 1, pp. 213–220, 2013.

[140] G. Cybenko, "Approximation by superpositions of a sigmoidal function," *Mathematics of Control, Signals, and Systems*, vol. 5, no. 4, p. 455, 1992.

[141] K. Levenberg, "A method for the solution of certain nonlinear problems in least squares," *Quarterly of Applied Mathematics*, vol. 2, no. 2, pp. 164–168, 1944.

[142] K. Xia, C. Chen, Y. Deng et al., "In situ monitoring and analysis of the mining-induced deep ground movement in a metal mine," *International Journal of Rock Mechanics and Mining Sciences*, vol. 109, pp. 32–51, 2018.

[143] Y. Abolfazlzadeh and M. Hudyma, "Identifying and describing a seismogenic zone in a sublevel caving mine," *Rock Mechanics and Rock Engineering*, vol. 49, no. 9, pp. 3735–3751, 2016.

[144] C. Zhang, M. Kang, J. Fu, and W. Song, "Study on the law and mechanism of strata movement induced by caving mining of slowly inclined large and thick orebody," 2021.

Research Article

Influence of Different Excavation Sequence of Double-Side Heading Method on Supporting Structure

Chengkun Ling,[1] Yanmei Ruan,[2] Pengbo Wu,[1] Jin Li,[1] Jin Zhao [ID],[3] and Bingxiang Yuan [ID][3]

[1]*China Railway Tenth Bureau Group Urban Rail Transit Engineering Co.,Ltd., Guangzhou 510000, Guangdong, China*
[2]*Guangzhou Metro Design and Research Institute Co., Ltd., Guangzhou 510030, Guangdong, China*
[3]*Guangdong University of Technology School of Civil and Transportation Engineering, Guangzhou 510006, Guangdong, China*

Correspondence should be addressed to Bingxiang Yuan; yuanbx@gdut.edu.cn

The double-side heading method is often used in the construction of large-span and large-section tunnels. The excavation of the pilot tunnel is complex, so the construction efficiency is low. Based on the underground excavation tunnel project of a subway in Guangzhou, the section excavation sequence of the traditional double-side heading method is optimized according to the actual situation. Midas/GTS software is used for finite element analysis, the displacement and internal force of ground settlement and support structure under two different section excavation sequences are calculated, and the calculation results are compared with the field monitoring data. The calculation results show that the influence of the two excavation sequences on the displacement of the supporting structure is not much different, but the influence on the internal force of the supporting structure is obviously different. The stress value of the supporting structure caused by the optimized excavation sequence is larger, especially the temporary inverted arch, but it is within the controllable range. The optimized excavation sequence increases the construction work surface, greatly improves the construction efficiency, and reduces the project cost, which can provide a reference for the construction of urban subway tunnels under similar engineering conditions in the future.

1. Introduction

With the rapid development of urban transportation facilities, more and more tunnel projects have emerged. Due to the relatively dense population and buildings on the ground in the city, many underground pipe piles foundations, and subway lines, tunnel engineering has high requirements for construction safety, and any carelessness may result in an accident [1, 2]. The construction of an underground tunnel will disturb the surrounding buildings (structures), which will lead to the deformation of buildings, and even threaten the life safety of relevant personnel in serious cases [3–5]. Therefore, the deformation and stability control of the underground tunnel is the key technical links in urban tunnel engineering [6–9].

Compared with other tunnel excavation methods, the double-side heading method has advantages in controlling surface subsidence and surface horizontal displacement [10–12]. For the double-side heading method, many scholars at home and abroad had in-depth studies on the safety and stability of the structure [13–17], soil particle properties [18–22], and the deformation law of the surrounding rock [23–25] in the construction process using the methods of field monitoring [26–28], model experiment [29–31], and numerical simulation analysis [32–34], but there are few studies on the optimization of the construction method. Due to the number of excavation sections, complex construction process, high construction cost, and slow construction speed of the double-side heading method, it needs to be optimized [35]. Zeng [36] optimized the excavation section of the double-side heading method, increased the area of the upper excavation section, and improved the construction efficiency; Yang et al. [37] optimized the supporting structure of the tunnel crossing the pebble soil layer, which well

controlled the surface settlement and reduced the construction risk; Li et al. [38] optimized the construction step of double-side heading method, adopted the excavation form of upper and lower sections, reserved core rock pillars in the middle soil layer, accelerated the construction progress, and improved the overall stability of the tunnel.

The influence of the construction step on supporting structure has not been discussed in-depth in the above studies. Based on this, an underground excavation tunnel of a subway station in Guangzhou is taken as the engineering background of this article. The tunnel has a large cross-section, and there is a large height difference between the lower pilot tunnel of the transverse passage and the upper pilot tunnel of the main line tunnel when the construction is completed. It is difficult to transport workers, machines, and materials. Therefore, the excavation sequence has been optimized. Midas/GTS software was used for finite element analysis. Combined with the field monitoring data, the displacement and internal force of the supporting structure under different excavation sequences were compared to analyze the safety and stability of the structure. Finally, a reasonable excavation sequence was selected after careful consideration of construction cost, construction period, and construction safety. The optimized construction scheme not only ensured the safety and stability of tunnel structure but also greatly improved the construction efficiency, which provides some reference for tunnels under similar engineering conditions.

2. Engineering Overview

The underground excavation tunnel interval is located at about 300 m east of the intersection of West side of Whampoa Avenue and Xiancun Road, which is connected to the east end of Xiancun Station. Two open-cut shafts were set up, and the rest were underground excavation channel. The left line is 163.845 m long and goes through the Whampoa Avenue Tunnel in parallel, and the vault is about 16.9 m from the bottom of the Whampoa Avenue Tunnel. The right line is 51.72 m long and is laid below the south side of Whampoa Avenue, and the vault is about 25 m from the ground. The crossover between the left and right lines is 37.35 m long. The general layout of the underground excavation tunnel interval is shown in Figure 1.

The construction method for the tunnel adopted the double-side heading method. The construction sequence was to excavate the upper section, construct the supporting structure, and then excavate the lower section after the construction of the upper section was completed. The daily footage of construction was 1 m. The finite element model was modeled and analyzed based on this working condition.

3. Construction Optimization Scheme

The main principle of the double-side heading method is to divide the large section of the tunnel into small sections using the middle wall, and each small section can be divided into upper and lower pilot tunnels to avoid stress concentration. The specific section is shown in Figure 2. The

common excavation sequence of sections is that the left and right sections are constructed first and the support system is formed in time, and then the middle section is constructed, namely, ①-④-②-⑤-③-⑥. The optimized excavation sequence of the section is to excavate the upper left and right pilot tunnels first, then the upper middle pilot tunnel, then the lower left and right pilot tunnels, and finally the lower middle pilot tunnel, namely, ①-②-③-④-⑤-⑥.

4. Numerical Simulation

4.1. Calculation Model and Boundary Conditions. The model strata from top to bottom were plain fill, medium coarse sand, plastic residual soil, strongly weathered pelitic siltstone, moderately weathered pelitic siltstone, and slightly weathered pelitic siltstone. The model included shaft, transverse passage, main line tunnel, and foundation pit above the tunnel. According to Saint-Venant's principle, when the size of the model is 3 to 5 times the tunnel span, the influence of the boundary effect on the model can be ignored [39]. Therefore, the boundary of the overall model was 120 m in the X direction, 140 m in the Y direction, and 50 m in the Z direction. The total number of model elements was 130161, and the total number of mesh nodes was 76573, as shown in Figure 3.

4.2. Material Constitutive and Parameters. The Mohr–Coulomb constitutive model was adopted for plain fill, medium coarse sand, plastic residual soil, and strongly weathered pelitic siltstone [40]. The moderately weathered and slightly weathered pelitic siltstone adopted the modified Mohr–Coulomb constitutive model because of their relatively complete rock structure and hard rock quality. Supporting structures such as shotcrete, bolt, grid steel frame, and section steel adopted the elastic constitutive model. The physical and mechanical parameters of each material are shown in Table 1.

The initial support of transverse passage and tunnel adopted the form of grid steel frame and shotcrete, and the elastic modulus of initial support was calculated by the method of stiffness equivalence [41]. The equivalent elastic modulus of initial support was calculated to be 25.382 Gpa, and the equivalent elastic modulus of the temporary support was 29.064 Gpa.

4.3. Simulated Construction Steps. The original construction scheme and the optimized construction scheme were compared using numerical simulation. The original construction scheme was scheme I and the optimized construction scheme was scheme II. The specific construction steps of scheme I were as follows (S stands for construction steps).

(1) Initial stress field analysis (IS): activate the original strata, gravity, and boundary condition in the numerical model and cleared the displacement to simulate the state when the tunnel was not excavated.

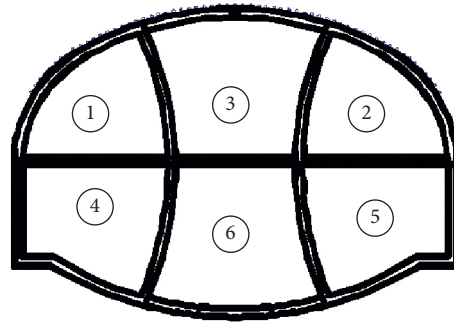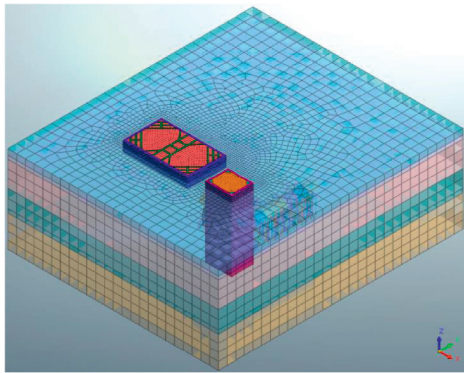FIGURE 1: General layout of underground excavation tunnel interval.

FIGURE 2: Construction process of double-side heading method.
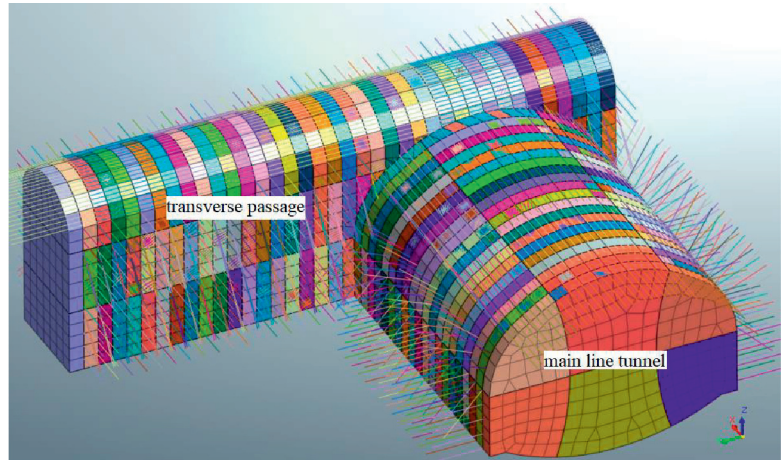
(a) (b)

FIGURE 3: Double-side heading method model. (a) Overall model. (b) Main tunnel model.

(2) Excavate shaft and foundation pit and construct the supporting structure (S2)

(3) Excavate the upper (S3–S40), middle (S41–S78), and lower (S79–S116) pilot tunnels of transverse passage and construct the supporting structure

(4) Excavate the 1 and 2 (S117), 4 and 5 (S118), 3 (S119), and 6 pilot tunnels (S120) of the mainline tunnel in sequence, and the supporting structures of each pilot tunnel were constructed after one construction step

Repeat the above steps until the construction was completed; scheme I included 159 construction steps in total.

The specific construction steps of scheme II were as follows:

(1) Initial stress field analysis (IS): activate the original strata, gravity, and boundary condition in the numerical model and clear the displacement to simulate the state when the tunnel was not excavated.

(2) Excavate the shaft and foundation pit and construct the supporting structure (S2).

(3) Excavate the upper (S3–S40) and middle (S41–S78) pilot tunnels of transverse passage and construct the supporting structure.

TABLE 1: Physicomechanical parameters of material.

Material name	Elastic modulus/ (MPa)	Bulk density/(kN/ m^3)	Cohesion/ (kN/m^2)	Internal friction angle/ (°)	Strata thickness /(m)
Plain fill	12.6	19.0	10.0	9.0	3.2
Medium-coarse sand	16.0	20.0	0	30.0	2.0
Plastic residual soil	22.0	22.0	18.6	18.0	14.6
Strongly weathered pelitic siltstone	50.0	21.0	45.0	30.0	10.0
Moderately weathered pelitic siltstone	200.0	25.6	180.0	32.0	2.2
Slightly weathered pelitic siltstone	400.0	26.0	450.0	35.0	18.0
C25 shotcrete	23000.0	25.0			
Initial support	25383.0	25.0			
Temporary support	29064.0	25.0			
Bolt	206000.0	78.5			

(4) Excavate the 1 and 2 (S79) and 3 pilot tunnels (S80) of the main line tunnel in sequence, and the supporting structures of each pilot tunnel were constructed after one construction step.

(5) Repeat the above steps until the construction of the upper section of main line tunnel is completed (S79–S99).

(6) Excavate the lower (S100–S137) pilot tunnel of transverse passage and construct the supporting structure.

(7) Excavat the 4 and 5 tunnels (S138) and 3 pilot tunnels (S80) of main line tunnel in sequence, and the supporting structure of each pilot tunnel were constructed after one construction step;

Repeat the above steps until the construction was completed, and scheme II included 159 construction steps in total.

5. Results

5.1. Analysis of Surface Settlement of Transverse Passage. After simulation calculation, the surface settlement curve of the transverse passage with the construction steps as the abscissa was drawn, as shown in Figure 4, where the monitoring section is $Y = 70$ m.

Figure 4 shows that the final surface settlement of the transverse passage is 11.77 mm. The biggest impact on the surface settlement of the transverse passage was the excavation of the upper pilot tunnel of the transverse passage, and the settlement value was about 8.22 mm, accounting for 69.8% of the total settlement value. The second was the excavation of the upper pilot tunnel of the main line tunnel, and the settlement value increased from 9.19 mm to 10.99 mm, accounting for 15.3% of the total settlement value. The excavation of the middle and lower pilot tunnels of the transverse passage and the lower pilot tunnel of the main line tunnel had little impact on the surface settlement of the transverse passage. The reason was that the initial support was timely constructed after the excavation of the upper section, which played a role in supporting and limiting the vertical displacement of the soil. Therefore, the excavation of the upper pilot tunnel of the transverse passage

was a key construction process, and monitoring should be strengthened during on-site construction.

The surface settlement data of the transverse passage at section $Y = 70$ m in the numerical model was selected for comparison and analysis with the field monitoring data. The on-site construction progress was that the construction of the upper pilot tunnel of the transverse passage had been completed, and the middle pilot tunnel had been excavated for 6 m. The comparison results are shown in Figure 5.

Figure 5 shows that the trend of the surface settlement results of the transverse passage in the field monitoring data and numerical simulation was basically the same, but the settlement value of field monitoring was larger than the numerical simulation. The final settlement value of field monitoring was 13.69 mm, which was 66.6% larger than the result of the numerical simulation. The reason why the numerical simulation results were small was that the model ignored the influence of groundwater [42, 43]. Only self-weight stress was considered in rock and soil mass, and the influence of tectonic stress was ignored. The deformation of rock and soil mass was considered to be isotropic. These simplifications and assumptions made the numerical simulation results smaller than the actual settlement value.

5.2. Displacement Analysis of Initial Support of Tunnel. The displacement value of initial support was extracted according to the monitoring points shown in Figure 6, where the monitoring surface was located at $X = 50$ m and the corresponding tunnel excavation distance was 10 m. Figure 7 shows the displacement diagram of initial support under different schemes. As can be seen from the figure, the settlement value from large to small of the tunnel was vault, spandrel, hance, and arch foot. The settlement value of the right initial support was slightly larger than that of the left because there was a foundation pit above the left initial support, which reduced the soil press upside, so the settlement of the left initial support was smaller. For scheme I, when the excavation surface did not reach the monitoring surface, some areas of the monitoring point had slight displacement. After the excavation reached the monitoring surface, the displacement of the initial support increased with the advancement of the excavation surface and finally tended to be stable.
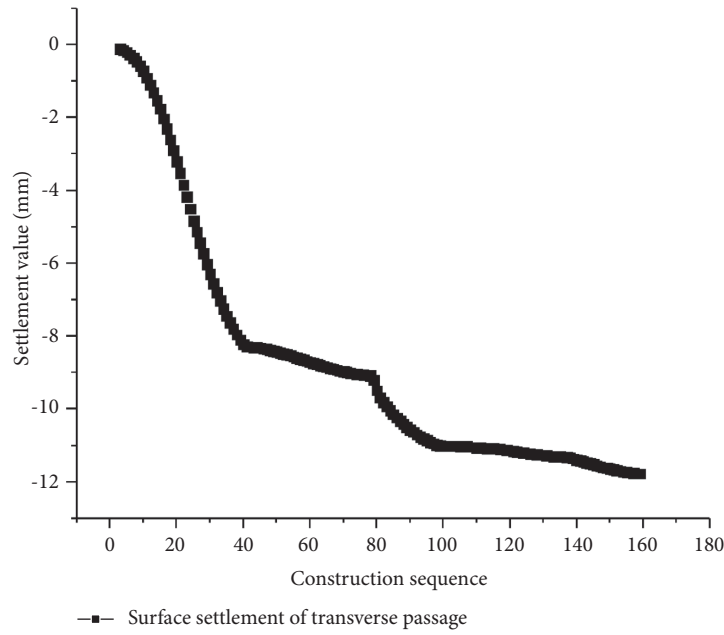
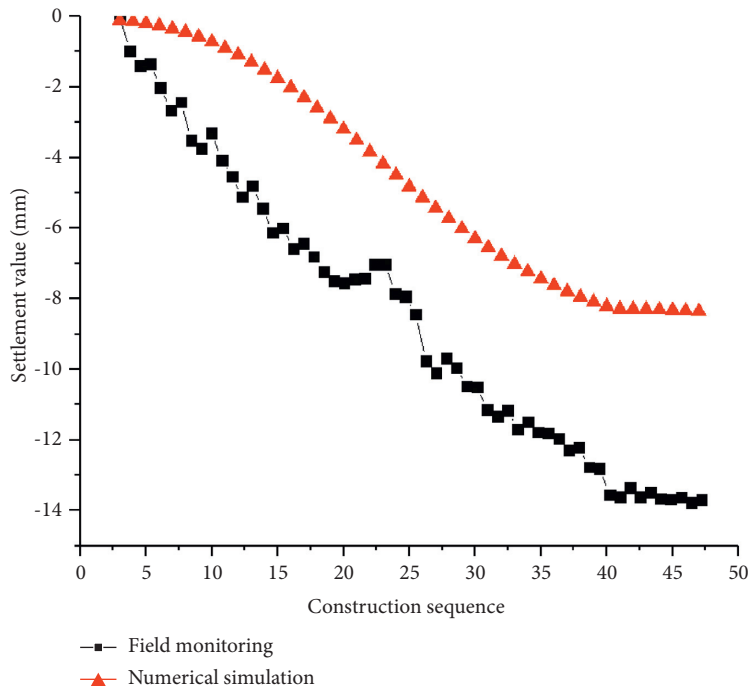FIGURE 4: Time-history curve of surface settlement of transverse passage.

FIGURE 5: Comparison of the time-history curve of surface settlement of transverse passage.

For scheme II, the influence of tunnel excavation on the initial support was divided into two parts. The first part was the excavation of the upper section of the tunnel. At this time, the vault and spandrel had a large settlement, and the settlement of the hance was small. The second part was the excavation of the lower section of the tunnel, which had a small impact on the overall initial support. The excavation of the lower pilot tunnel of the transverse passage had little effect on the displacement of the tunnel initial support. The

final displacement values of each monitoring point of tunnel initial support under different construction schemes are shown in Table 2.

Table 2 shows that the settlement values of the vault and left and right arch feet in scheme II were 4.6%, 77.8%, and 44.1%, lower than those in scheme I, while the settlement values of the left and right spandrels and hance were 16.4%, 17.7%, and 56.1%, 58.9% higher than those in scheme I, respectively, and the uplift value of the arch bottom was
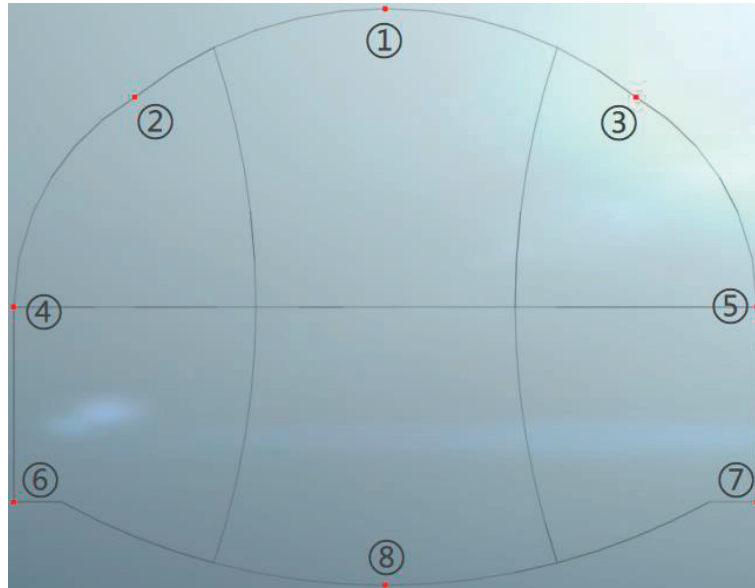
FIGURE 6: Layout diagram of initial support monitoring points.

(a)

(b)
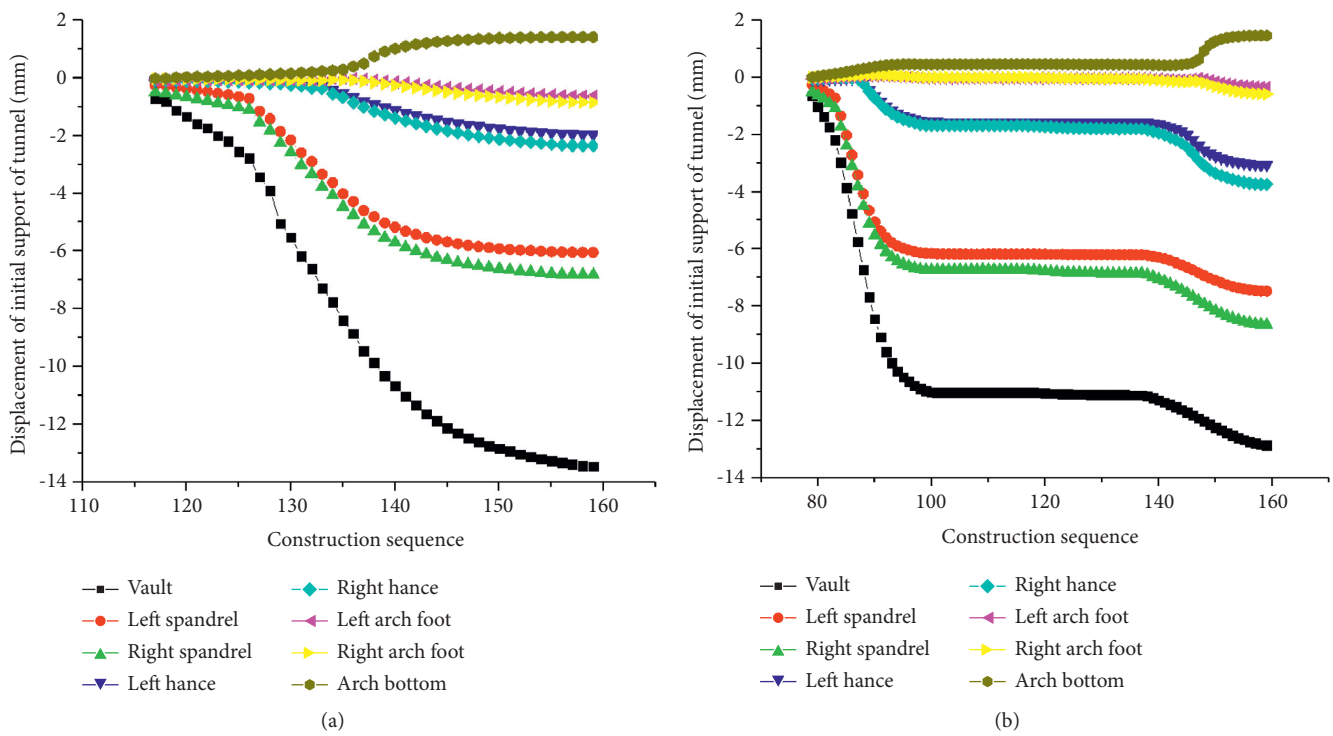
FIGURE 7: Time-history curves of tunnel initial support displacement under different schemes. (a) Time-history curve of tunnel initial support displacement in scheme I. (b) Time-history curve of tunnel initial support displacement in scheme II.

3.5% higher than that in scheme I. The displacement values of the hance and arch foot of the two construction schemes were quite different. The reason was that scheme I was to excavate the sections on both sides first and then excavate the middle section after the initial support on both sides forms a closed loop; scheme II was to excavate the upper section first and then excavate the lower section after the upper section was completed. The support construction sequences of the two construction schemes were different, so the stress conditions of the hance and arch foot were quite different, and the final settlement value was also quite different.

To sum up, the displacement law of initial support caused by different excavation sequences was roughly the same. Scheme II had a slightly greater impact on the displacement of initial support, but within the controllable

TABLE 2: Final displacement value of monitoring points in initial support of tunnel unit: mm.

Scheme	①	②	③	④	⑤	⑥	⑦	⑧
I	−13.4	−6.1	−6.8	−2.0	−2.4	−0.6	−0.9	1.4
II	−12.8	−7.0	−8.0	−3.1	−3.8	−0.4	−0.6	1.5

range. The excavation of 3-pilot tunnel was a key construction process, so it needed to do well in advance support and timely constructed initial support to control the vertical displacement. The excavation of the lower pilot tunnel of the transverse passage had little effect on the completed tunnel support.

5.3. Stress Analysis of Tunnel Supporting Structure.
Figure 8 shows the cloud diagram of the major principle stress of supporting structure when the tunnel excavation of different schemes was completed. As seen from the figure, the major principal stress distribution and value of the tunnel supporting structure of the two schemes were basically the same. In terms of initial support, most of the spandrel and hance were compressed, and a small part was tensioned at the front of the tunnel. Most of the vault and arch bottom were compressed, and a small part was tensioned at the end of the tunnel. In terms of temporary support, most of the temporary inverted arch and the middle wall were tensioned; the part of the temporary inverted arch near both ends of the tunnel and the middle wall near the temporary inverted arch would be compressed. The stress value of the middle wall of the tunnel was greater than that of the temporary inverted arch, and the stress value of the upper middle wall was greater than that of the lower middle wall.

5.3.1. Initial Support of 1-Pilot Tunnel.
The stress value of initial support was extracted according to the monitoring points shown in Figure 9, where the monitoring surface was located at $X = 45$ m, and the corresponding tunnel excavation distance was 5 m. As seen in Figure 8, the stress value of the initial support was symmetrical, so only the left initial support was selected for analysis.
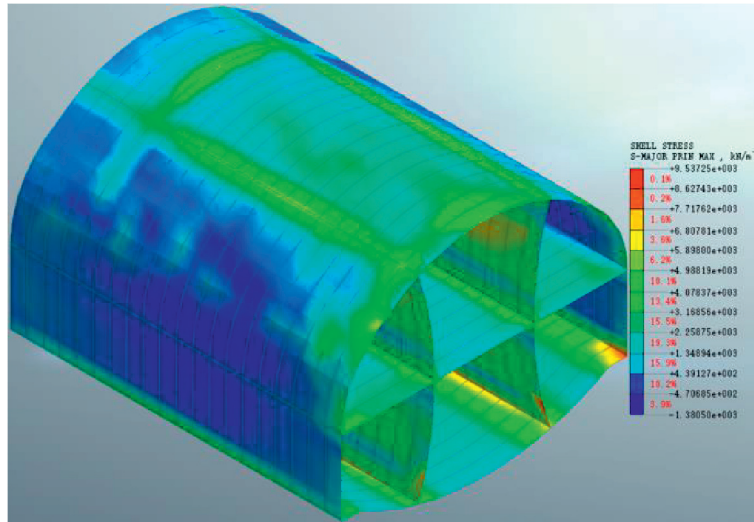
Figure 10(a) shows the time-history curve of initial support stress of the 1-pilot tunnel in scheme II. As seen from the figure, the stress value of the initial support of the 1-pilot tunnel decreased with the excavation of the upper section, and the stress value changed from positive to negative when the excavation reached the end of the upper section. Then, the lower pilot tunnel, different from the transverse passage, was excavated, and the excavation on the side close to the tunnel would slightly increase the compressive stress of the initial support. After the excavation surface passed through the tunnel surface, the stress value of the initial support remained stable. Finally, the lower section of the tunnel was excavated. When the excavation surface had not reached the monitoring surface, the compressive stress value of the initial support increased with the section excavation. After the excavation surface passed through the monitoring surface, the stress value of the initial support basically remained stable.

The time-history curves of the initial support stress of the 1-pilot tunnel of two schemes were compared. Since the excavation of the lower pilot tunnel of the transverse passage had little effect on the stress value of the initial support, this part of the data was discarded during the comparison, and the construction steps were reordered. The comparison of the time-history curve of the initial support stress of the 1-pilot tunnel in the two schemes is shown in Figure 10(b). It could be seen that the variation law of stress value of the initial support of the two construction schemes was basically the same. The stress values of each monitoring point of tunnel initial support under different construction schemes are shown in Table 3. As can be seen from the table, the maximum tensile stress of scheme II was 7.7% higher than that of scheme I, and the maximum compressive stress was 240% higher than that of scheme I. Therefore, the first construction of the supporting structure on both sides could timely distribute the surrounding rock pressure to the lower support, reduced the stress value on the initial support, and was more conducive to the safety of the structure.

5.3.2. Temporary Inverted Arch of 1-Pilot Tunnel.
The stress value of the temporary inverted arch was extracted according to the monitoring points shown in Figure 9. As can be seen from Figure 11, the stress value of the temporary inverted arch of the 1-pilot tunnel in scheme I increased rapidly during early excavation and then decreased slowly with tunnel excavation. The stress value of the temporary inverted arch of the 1-pilot tunnel in scheme II increased continuously when excavating the upper section of the tunnel and reached the peak when excavating the end of the upper section. Then, the excavation of the lower section of the tunnel would rapidly reduce the stress value of the temporary inverted arch and continue to decrease with the excavation. As shown in Table 3, the maximum stress value and the stress value at the completion of tunnel excavation of the temporary inverted arch in scheme II were 173% and 101% higher than those in scheme I, respectively. The stress value of the temporary inverted arch in scheme I would be much less than that in scheme II because the supporting structure on both sides was excavated first. The stress value of the temporary inverted arch in scheme I would be much less than that in scheme II because the supporting structure on both sides was excavated first, and the stress system of the closed space could be formed more quickly.

5.3.3. Middle Wall of 1-Pilot Tunnel.
As can be seen from Figure 12, the overall trend of the stress value of the middle wall in 1-pilot tunnel of the two schemes increased first and then decreased slowly. The difference was that scheme II would cause disturbance to the middle wall when excavating the upper and lower sections, respectively, and the stress value had two fluctuation points.

(a)
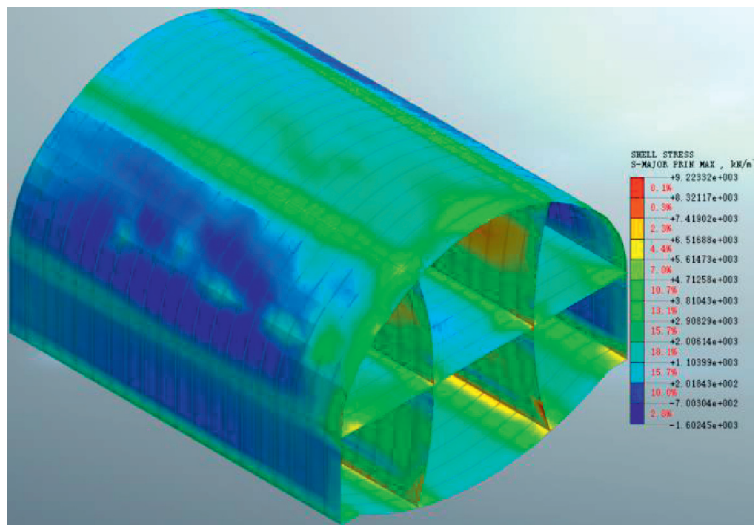
(b)

FIGURE 8: Different schemes of tunnel supporting structure major principle stress cloud diagram. (a) Tunnel supporting structure major principle stress cloud diagram of scheme I. (b) Tunnel supporting structure major principle stress cloud diagram of scheme II.
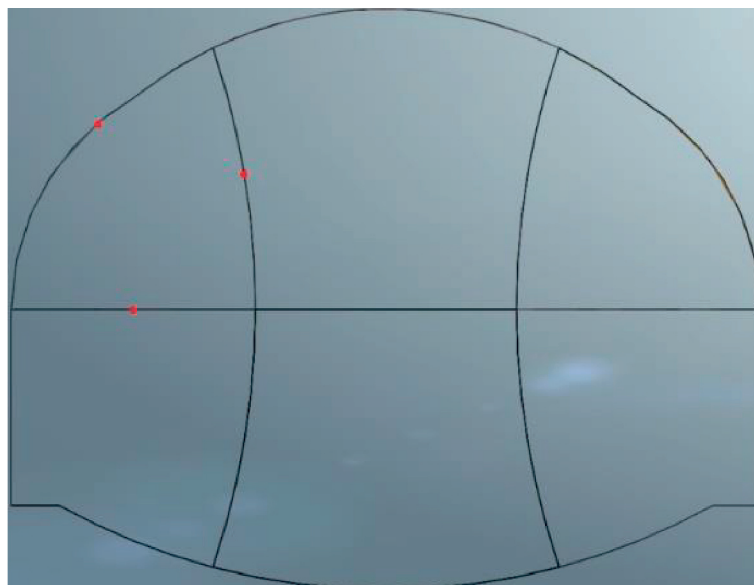
FIGURE 9: The stress value monitoring point layout of supporting structure.
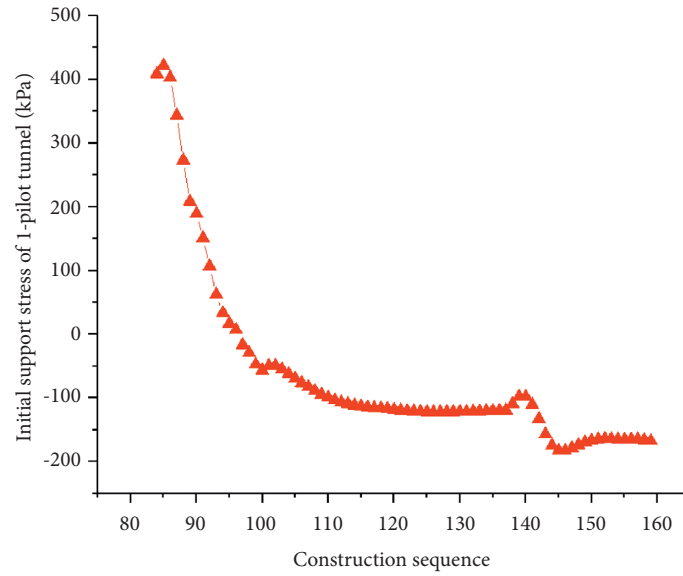
(a)
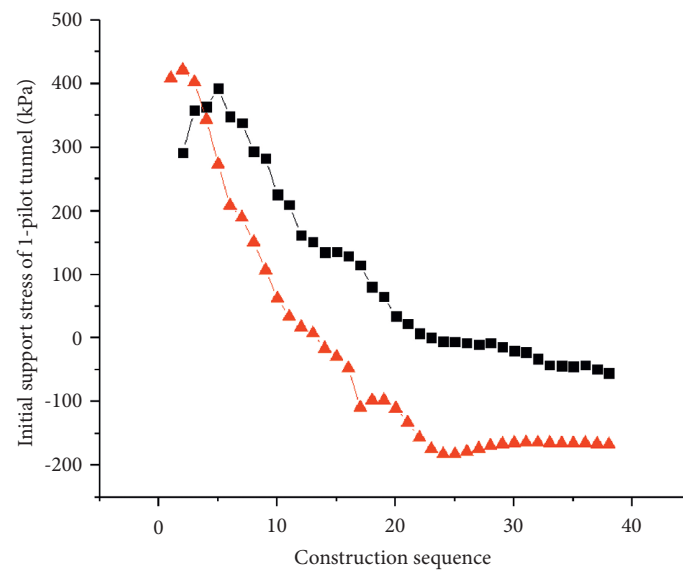
(b)

Figure 10: Time-history curve of initial support stress of 1-pilot tunnel. (a) Time-history curve of the initial support stress of 1-pilot tunnel in scheme II. (b) The comparison of time-history curve of the initial support stress of 1-pilot tunnel in the two schemes.

Table 3: Stress value of each monitoring point of tunnel supporting structure unit: MPa.

Scheme	Maximum stress value of initial support	Stress value at the completion of initial support excavation	Maximum stress value of temporary inverted arch	Stress value at the completion of temporary inverted arch excavation	Maximum stress value of middle wall	Stress value at the completion of middle wall excavation
I	0.39	−0.05	1.95	0.72	7.77	6.17
II	0.42	−0.17	5.33	1.45	8.73	6.51
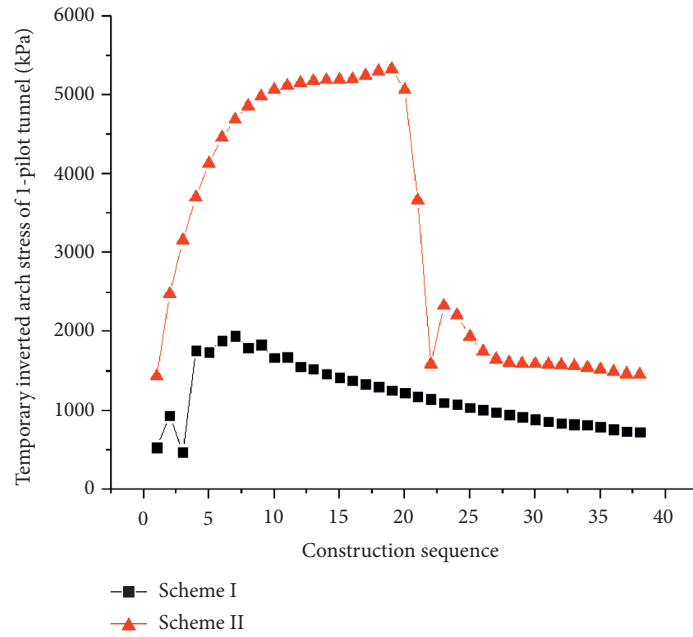
FIGURE 11: Time-history curve of temporary inverted arch stress of 1-pilot tunnel.
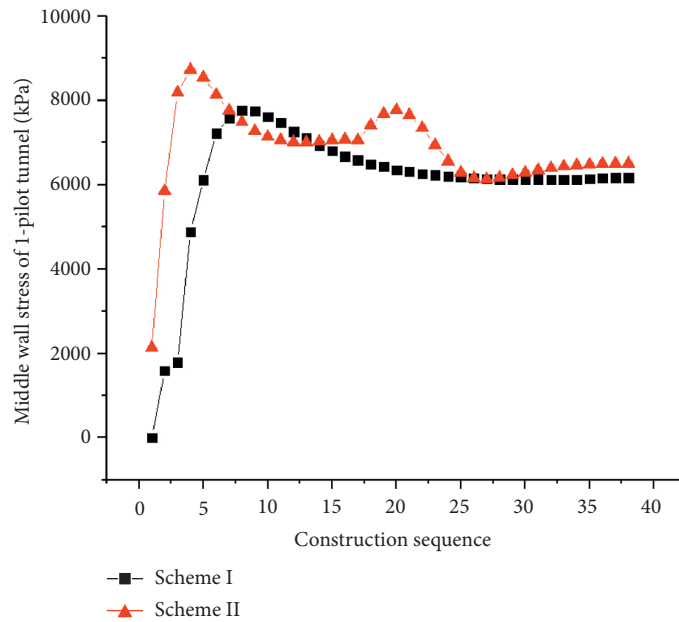
FIGURE 12: Time-history curve of middle wall stress of 1-pilot tunnel.

As shown in Table 3, the maximum stress value and the stress value at the completion of tunnel excavation of the middle wall in scheme II were 12.4% and 5.5% higher than those in scheme I, respectively.

To sum up, the stress values of initial support and temporary support in scheme II were higher than those in scheme I, but both were within the controllable range. Therefore, when scheme II was adopted for construction, it was necessary to strengthen the monitoring of the supporting structure, especially the temporary inverted arch, to ensure the construction safety.

5.3.4. Overall Comparison. Figure 13 shows the overall stress diagram of the tunnel support structure when the tunnel was excavated at 10 m according to different schemes. The stress of the tunnel support structure in scheme I was small in the spandrel, hance, and temporary inverted arch, and the stress was mainly concentrated in the vault, middle wall, arch foot, and arch bottom. The maximum tensile stress was 7.71 MPa located in the middle wall on the right side. The maximum compressive stress was −0.65 MPa located in the initial support on the right side. Because of the construction off the upper part of the supporting structure only,
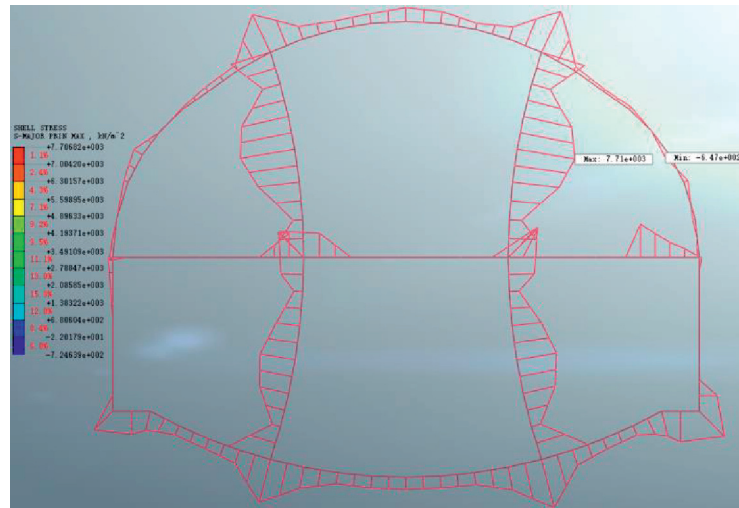
(a)
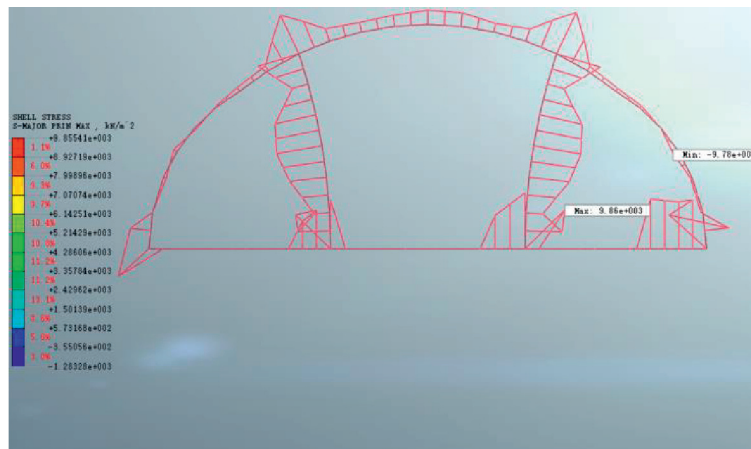
(b)

FIGURE 13: Overall stress diagram of the tunnel support structure. (a) Overall stress diagram of the tunnel support structure in scheme I. (b) Overall stress diagram of the tunnel support structure in scheme II.

the stress of hance and temporary inverted arch in scheme II were larger than that in scheme I. The maximum tensile stress was 9.86 MPa located in the temporary inverted arch on the right side. The maximum compressive stress was −0.98 MPa located in the initial support on the right side. Therefore, the lower part of the structure could share the load of the upper part of the structure and improve the safety and stability of the overall structure.

6. Conclusion

According to the numerical simulation data, after analyzing the surface displacement, displacement, and stress characteristics of the supporting structure of the double-side heading method under different excavation sequences, the conclusions were as follows:

(1) By comparing the numerical simulation date and monitoring data of transverse passage surface settlement, it could be seen that the variation law of surface settlement between the two methods was the same, which showed that the simulation of the deformation law of the stratum by this model was basically consistent. Based on this model, the excavation sequence of the double-side heading method could be qualitatively researched.

(2) Compared with the original construction scheme, the optimized construction scheme had a higher impact on the supporting structure, especially the temporary inverted arch, but it was within the controllable range. The optimized construction scheme first excavated the upper section of the tunnel and then the lower section, which solved the problems of the large height difference in the tunnel and difficulty in transporting workers, machines, and materials, increased the construction work surface, greatly improved the construction efficiency, and shortened the construction period. The optimized construction scheme can provide a reference for the construction of urban subway tunnels under similar engineering conditions in the future.

Data Availability

Conflicts of Interest

The authors declare that they have no conflicts of interest.

Acknowledgments

References

[1] B. B. Yang and Y. Liu, "Application of fractals to evaluate fractures of rock due to mining," *Fractal and Fractional*, vol. 6, no. 2, pp. 1–15, 2022.

[2] B. Yang, S. Du, X. Zhao, D. Tang, and C. Yang, "Decision making of curriculum attainment degree for engineering geology based on fuzzy set theory," *Advances in Civil Engineering*, vol. 2021, Article ID 1743778, 6 pages, 2021.

[3] B. Yuan, Z. Li, Z. Zhao, H. Ni, Z. Su, and Z. Li, "Experimental study of displacement field of layered soils surrounding laterally loaded pile based on Transparent Soil," *Journal of Soils and Sediments*, vol. 21, no. 9, pp. 3072–3083, 2021.

[4] X. Que, Z. Zhu, Z. Niu, and W. Lu, "Estimating the strength and deformation of columnar jointed rock mass based on physical model test," *Bulletin of Engineering Geology and the Environment*, vol. 80, no. 2, pp. 1557–1570, 2021.

[5] Y.-C. Guo, Y.-Y. Ye, G. Guan-Lin, J.-F. Lv, Y.-L. Bai, and J.-J. Zeng, "Effective usage of high strength steel tubes: Axial compressive behavior of hybrid FRP-concrete-steel solid columns," *Thin-Walled Structures*, vol. 154, Article ID 106796, 2020.

[6] B. Yuan, Z. Li, Z. Su, Q. Luo, M. Chen, and Z. Zhao, "Sensitivity of multistage fill slope based on finite element model," *Advances in Civil Engineering*, vol. 2021, Article ID 6622936, 13 pages, 2021.

[7] B. Yang, J. Liu, X. Zhao, and S. Zheng, "Evaporation and cracked soda soil improved by fly ash from recycled materials," *Land Degradation & Development*, vol. 32, no. 9, pp. 2823–2832, 2021.

[8] J. Xiao, X. Long, W. Qu, L. Li, H. Jiang, and Z. Zhong, "Influence of sulfuric acid corrosion on concrete stress-strain relationship under uniaxial compression," *Measurement*, vol. 187, Article ID 110318, 2022.

[9] J. Xiao, Z. M. Xu, Y. K. Murong et al., "Effect of chemical composition of fine aggregate on the frictional behavior of concrete–soil interface under sulfuric acid environment," *Fractal Fract*, vol. 6, no. 1, pp. 1–23, 2022.

[10] C. Liu, "Analysis of influence of different excavation methods on stability of highway tunnel," *Highway Engineer*, vol. 44, no. 1, pp. 130–134, 2019.

[11] Y. C. Zhang, G. W. Hu, and Z. X. Xin, "Comparative analysis and selection of construction methods for large section loess tunnel," *Journal of Railway Engineering Society*, vol. 27, no. 3, pp. 87–92, 2010.

[12] J. Y. Liu, G. Lv, M. Q. Zhang, L. Yue, and D. H. Luo, "Study on extra-large span tunnel excavation methods for Badaling

Great Wall station of Beijing-Zhangjiakou high-speed railway," *Modern Tunnelling Technology*, vol. 56, no. S2, pp. 578–584, 2019.

[13] F. Liu, W. Zheng, L. Li, W. Feng, and G. Ning, "Mechanical and fatigue performance of rubber concrete," *Construction and Building Materials*, vol. 47, pp. 711–719, 2013.

[14] F. Liu, G. Chen, L. Li, and Y. Guo, "Study of impact performance of rubber reinforced concrete," *Construction and Building Materials*, vol. 36, no. 11, pp. 604–616, 2012.

[15] W. Feng, F. Liu, F. Yang, L. Li, and L. Jing, "Experimental study on dynamic split tensile properties of rubber concrete," *Construction and Building Materials*, vol. 165, pp. 675–687, 2018.

[16] Y. Guo, J. Xie, J. Zhao, and K. Zuo, "Utilization of unprocessed steel slag as fine aggregate in normal- and high-strength concrete," *Construction and Building Materials*, vol. 204, pp. 41–49, 2019.

[17] Y. C. Guo, S. H. Xiao, J. J. Zeng, J. Y. Su, T. Z. Li, and Z. H. Xie, "Behavior of concrete-filled FRP tube columns internally reinforced with FRP-steel composite bars under axial compression," *Construction and Building Materials*, vol. 315, pp. 1–18, Article ID 125714, 2022.

[18] Y. Wu, J. Cui, J. Huang, W. Zhang, N. Yoshimoto, and L. Wen, "Correlation of critical state strength properties with particle shape and surface fractal dimension of clinker ash," *International Journal of Geomechanics*, vol. 21, no. 6, Article ID 04021071, 2021.

[19] B. Bai, Q. Nie, Y. Zhang, X. Wang, and W. Hu, "Cotransport of heavy metals and SiO2 particles at different temperatures by seepage," *Journal of Hydrology*, vol. 597, Article ID 125771, 2021.

[20] L. Wang, G. Li, X. Li et al., "Influence of reactivity and dosage of MgO expansive agent on shrinkage and crack resistance of face slab concrete," *Cement and Concrete Composites*, vol. 126, Article ID 104333, 2022.

[21] L. Wang, X. F. Song, H. M. Yang et al., "Pore structural and fractal analysis of the effects of MgO reactivity and dosage on permeability and F–T resistance of concrete," *Fractal and Fractional*, vol. 6, no. 2, pp. 1–17, 2022.

[22] L. Wang, R. Y. Luo, W. Zhang, M. M. Jin, and S. W. Tang, "Effects of fineness and content of phosphorus slag on cement hydration, permeability, pore structure and fractal dimension of concrete," *Fractals*, vol. 29, no. 2, Article ID 2140004, 2021.

[23] B. X. Yuan, M. Sun, L. Xiong, Q. Z. Luo, S. P. Pradhan, and H. Z. Li, "Investigation of 3D deformation of transparent soil around a laterally loaded pile based on a hydraulic gradient model test," *Journal of Building Engineering*, vol. 28, no. 3, Article ID 1010124, 2020.

[24] B. Yuan, M. Sun, Y. Wang, L. Zhai, Q. Luo, and X. Zhang, "Full 3D displacement measuring system for 3D displacement field of soil around a laterally loaded pile in transparent soil," *International Journal of Geomechanics*, vol. 19, no. 5, Article ID 04019028, 2019.

[25] B. Yuan, L. Xiong, L. Zhai et al., "Transparent synthetic soil and its application in modeling of soil-structure interaction using optical system," *Frontiers of Earth Science*, vol. 7, p. 276, 2019.

[26] S. T. Li, Z. S. Tan, and W. T. Du, "Analysis on the mechanical behavior of the small spacing highway tunnel with super large cross section," *China Civil Engineering Journal*, vol. 50, no. S2, pp. 292–296, 2017.

[27] W. Zhou, "Scheme optimization and monitoring analysis of large section shallow buried tunnel on existing highway,"

Journal of Xi'an University of Architecture and Technology, vol. 52, no. 4, pp. 520–527, 2020.

[28] D. P. Ren, "Construction technology of variable Cross-section for Three-line bifurcation and Large-span section of railway tunnel," *Railway Engineering*, vol. 61, no. 12, pp. 105–108, 2021.

[29] S. Q. Liu, J. H. Guo, Y. Yue, and H. W. Shen, "Influence simulation of different underground excavation methods on surface settlement for underground station built in hard rock area," *Urban Mass Transit*, vol. 24, no. 3, pp. 142–146, 2021.

[30] N. Liu, K. Chen, X. Y. Liu, and S. H. Fu, "Study on excavation technology of rock column in double tunnel of subway station," *Journal of Railway Science and Engineering*, vol. 17, no. 9, pp. 2320–2327, 2020.

[31] L. C. Yang, S. H. Zhou, and Y. M. Yao, "Ground surface settlement during excavation of variety span tunnel," *Journal of Tongji University*, vol. 04, pp. 408–412, 2003.

[32] W. Deng, X. F. Shi, G. L. Yang, and H. Q. Zhang, "Analysis of numerical modeling and mechanical characteristics of large section tunnel," *Highway*, vol. 63, no. 3, pp. 253–259, 2018.

[33] Y. L. Zhang, G. Y. Wang, Z. Q. Li, and X. P. Wu, "The study on the influence of excavation parameters of deep buried and large-section tunnel," *Construction Technology*, vol. 43, no. S2, pp. 116–119, 2014.

[34] B. Zhu and X. J. Shi, "Study on construction of long span and soft rock tunnel with numerical simulation," *Applied Mechanics and Materials*, vol. 2733, pp. 438-439, 2013.

[35] Y. L. Shang and Z. Tan, "Optimization of mined construction method for the super-large section Liuhualu station of Guangzhou metro," *Modern Tunnelling Technology*, vol. 56, no. 3, pp. 177–185, 2019.

[36] S. Zeng, "Construction procedure optimization of double-sidewall guide pit method for large-section subsurface excavation subway station," *Municipal Engineer*, vol. 41, no. 1, pp. 152–155, 2019.

[37] Y. Yang, J. L. Huang, B. H. Wan, R. J. Liang, X. J. Wei, and X. Cai, "Research on construction optimization of shallow buried large section railway tunnel crossing pebble soil," *Journal of Railway Science and Engineering*, vol. 18, no. 5, pp. 1240–1247, 2021.

[38] X. D. Li and W. Wang, "Case study on construction of shallow metro tunnel by double side heading method with core rock kept," *Tunnel Construction*, vol. 35, no. 10, pp. 1060–1065, 2015.

[39] H. Rohola, "Advance numerical simulation of tunneling by using a double shield TBM," *Computers and Geotechnics*, vol. 57, 2014.

[40] B. X. Yuan, Z. H. Li, Y. M. Chen et al., "Mechanical and microstructural properties of recycling granite residual soil reinforced with glass fiber and liquid-modified polyvinyl alcohol polymer," *Chemosphere*, vol. 268, no. P1, Article ID 131652, 2021.

[41] Z. Song, Z. Cao, J. Wang, S. Wei, S. Hu, and Z. Niu, "Optimal analysis of tunnel construction methods through cross passage from subway shaft," *Advances in Civil Engineering*, vol. 2018, no. 3, Article ID 5181954, 14 pages, 2018.

[42] B. X. Yuan, Z. J. Li, W. J. Chen et al., "Influence of groundwater depth on pile–soil mechanical properties and fractal characteristics under cyclic loading," *Fractal Fractional*, vol. 6, no. 4, pp. 1–20, 2022.

[43] B. Bai, R. Zhou, G. Cai, W. Hu, and G. Yang, "Coupled thermo-hydro-mechanical mechanism in view of the soil particle rearrangement of granular thermodynamics," *Computers and Geotechnics*, vol. 137, no. 8, Article ID 104272, 2021.

Research Article

Energy Audit of a Residential Building to Reduce Energy Cost and Carbon Footprint for Sustainable Development with Renewable Energy Sources

Anagha Darshan,[1] Naman Girdhar,[1] Rohan Bhojwani,[1] Kanish Rastogi,[1] S. Angalaeswari (ID),[1] L. Natrayan (ID),[2] and Prabhu Paramasivam (ID)[3]

[1]*School of Electrical Engineering, Vellore Institute of Technology, Chennai 600127, Tamil Nadu, India*
[2]*Department of Mechanical Engineering, Saveetha School of Engineering, SIMATS, Chennai 602105, Tamil Nadu, India*
[3]*Department of Mechanical Engineering, College of Engineering and Technology, Mettu University, Metu Zuria 318, Ethiopia*

Correspondence should be addressed to S. Angalaeswari; angalaeswari.s@vit.ac.in, L. Natrayan; natrayanphd@gmail.com, and Prabhu Paramasivam; prabhuparamasivam21@gmail.com

Electricity is a crucial part of our everyday lives. A limited number of resources can be utilized to generate power; hence, one must save these resources or electricity for future utilization. This is only possible by using energy most efficiently. For sustainable development and energy conservation, energy auditing plays an indispensable role. The energy audit is an extensive study that helps to identify energy use among different services and provides opportunities for energy conservation. The literature showed various energy audits conducted at various locations with its analysis. Few were shown that the appliances are responsible for high energy consumption, and few talked about the cost analysis with energy-saving methodologies. This work is proposed to combine the integration of renewable energy sources in a building and the cost-saving due to energy-efficient appliances. This paper tries to observe, infer, and analyze the patterns of energy usage of a residential complex and various measures to reduce energy consumption and cost-saving. A case study is included to analyze the reduction in consumption of energy per unit to make the building energy efficient. A feasibility study is executed to observe the increments in costs. Calculations for auditing will reduce the building's carbon footprint and benefit residents in the form of cost savings in the long run.

1. Introduction

In the residential segment across India, the present electricity consumption is about 25% of the total electricity consumption according to data published (2018-19). The electricity demand in residential buildings is at a simple annual growth rate of 10–14%. This is because of the increasing population economic and technological developments. To ensure that energy usage does not become unmanageable, which now poses a present-day challenge, the issue also provides an opportunity to address and resolve energy management problems in different areas. Energy auditing is efficiently done for energy conservation. The various steps involved are performed by inspecting, surveying, and analyzing energy flow in a building, framework, or system. The result has increased based on analyzing the energy consumption of Two-story buildings in France. In an academic institution located in Nigeria, a study was conducted to project energy consumption on various time scales such as daily, weekly, and annual. It was concluded that HVAC (heating, ventilation, and air conditioning appliances) and gadgets driven by electrical motors consumed 36% and 61.9% of the total energy supplied [1].

The electrical energy consumption at Airport, in Egypt, was analyzed by considering various indoor parameters such as temperature, illuminance, and relative humidity. It was shown that there was a 24.5% reduction in total energy consumption by increasing the air cooler temperature by 2°C

[2]. The energy audit process-based case study in Australia identified the main factors of energy consumption as design, physical conditions, and social-economic buildings' status [3]. In the energy audit carried out in Italy, energy efficiency measures have been selected for identifying the retrofit interventions in the renovation stage of a building. This study and analysis were carried out in a detailed manner with simulation studies and cost analysis. It was observed that the output was not meeting the nZEB (net-zero energy building) criteria; hence, the inclusion of renewable sources has been done with additional cost [4].

Energy auditing can help an individual or a group to identify areas where the amount of energy input into the system can be reduced without adversely affecting the output. The crucial step in energy auditing is identifying opportunities to reduce carbon footprints and energy costs in commercial and industrial real estate applications. An energy audit examines how much energy a household consumes and then develops a method to optimize energy consumption by increasing efficiency. The various coefficients such as annual demand and the cost of the primary source of energy are identified for getting information on the energy-saving methods and its analysis [5]. A large amount of money can be saved in the long run by maximizing the energy efficiency of a residential unit. The usage of energy-efficient devices could help us reduce the cost of energy consumption having the same power output. In [6], the comparative study of efficient and inefficient appliances has been done in Nigeria's residential building. Around 48 percentage savings were obtained in replacing the old with new devices. Moreover, the greenhouse gas emissions and carbon-di-oxide emissions should also be analyzed with the existing components in the building. It is necessary to take steps further to reduce these [7]. It has been observed that the structure of the building and the selection of device are more significant in the power consumption.

The energy consumption purely depends on the architecture with the design and the maintenance due to the usage of the devices. Lighting and thermal play a vital role in energy consumption patterns [8]. An energy audit conducted at Leverett Elementary School revealed that the suggested alternative methods for HVAC systems have given more efficient solution in various aspects such as social, environmental, and economical way [9]. An innovative model based on a multilevel approach was introduced in [10] using a regression model with a combined bottom-up and top-down model approach for residential energy demand in France. Though this paper has given an overview of various factors, there are more challenges such as data collection, reforming the policies, the measures of incentives, enhancement of technical capacity, and the reforms to be considered at the institutional level. The energy usage outline has been evaluated at the buildings located at Central Queensland University, Australia [11]. The survey analyzed the indoor temperature and humidity based on indoor heating and cooling loads. The auditing resulted in a hike in almost 7-8% of the cost to increase 2-3% in energy consumption. The change in energy was mainly due to the

temperature and humidity increase in the outside environment.

Energy audit conducted at Maharaja Surajmal Institute of Technology, Janakpuri, New Delhi for the hostel and mess buildings had given effective energy conservation measures to reduce the cost of energy [12]. It was observed that the replacement of conventional lamps with advanced devices reduced energy usage by one-fourth; the payback period for the replacement was also very economical. Various case studies were carried out in a detailed manner in [13] by taking building construction materials, survey, baseline model, evaluating the energy conservation opportunities, and finally submitting the recommendations for the cost savings. Identifying the utilities having less efficiency was also a major point of consideration. It was given more weightage in the article [14] by carrying out an audit at a residential building in Old Mahabalipuram Road (OMR), Chennai. It was recommended to change the separate cooling systems by centralized cooling units.

Making awareness among the public living in the residential building about energy conservation is the art and heart of energy saving. The study's objective in [15] was to create awareness for the residential building sector and minimize carbon footprint. The simulation was carried out in integrated environmental solution (IES) for the building audit following the guidelines of ASHRAE (American Society of Heating, Refrigerating, and Air-Conditioning Engineers). From the suggestion, there was an energy saving of 6.12% and a cost saving of 24.78% for the simulated building. Most educational institutions could save energy during semester holidays by conducting an energy audit. The six-month data collected from University Tun Hussein Onn Malaysia (UTHM), Johor, Malaysia, namely Kolej Kediaman Tun Dr. Ismail (KKTDI) on four blocks, showed around 88% increase in energy consumption in the semester compared to the holiday period. This study was carried out by considering the building energy index and energy intensity as the main factors for analysis [16].

For small power load estimation, the Morris method is adopted in [17] to deal with the uncertainty of TM22 and TM54 models from a building service of Chartered Institute of Building Service Engineers. It helps the auditors select an optimal assessment strategy for small load estimations. Using the data obtained from the weather stations of various departments, the energy analysis of the photovoltaic plant at the University of Calabria was carried out in TRNSYS simulation software [18]. The results were compared with the Siegel method showing a payback period of five years with cost benefits. An overview of the innovative technological solutions for enhancing the energy performance of a building for energy consumption reduction has been presented in [19]. The authors have given various methods to realize zero energy buildings that could be incorporated into the design stage of a building itself and improve the efficacy of the building energy. The review article [20] elaborated on the data exchange for commercial buildings for the development of BuildingSync during energy audits to support various case studies.

Overview of various standards, roadmaps, and measures for the government's energy savings was reviewed in [21], and the evaluation of various methods, strategies, and applicability to the existing buildings was also presented. The usage of renewable energy sources has become an energy substitution method nowadays. The energy policy related to renewable energy sources with its modelling was given in [22] as a review article by considering the five major countries such as the United States, Germany, Denmark, China, and the United Kingdom. The best two methods for satisfying the energy demand are producing energy by classical and renewable energy methods and enhancing the efficiency of available energy systems [23].

The highlights of the paper are as follows:

(i) Energy audit implementation of a real-time project on a newly constructed building

(ii) Load calculation and distribution analysis for this building with economical cost analysis for various types of flats such as single, double, and triple

(iii) Proposed alternative energy-efficient appliances for the conventional loads for the cost reduction and improved sustainable environment

(iv) Analysis of renewable energy sources such as solar with cost analysis and energy-saving and payback period

This paper aims to conduct the energy audit of an under-construction residential project to optimize the electrical energy consumption and, therefore, make the project more energy-efficient. The energy audit provides a standard or reference point for accessing and overseeing energy consumption throughout the building and provides the methods for guaranteeing optimized energy use across the building. This helps develop ways to decrease energy consumption per unit of product output or lower operating costs and, hence, execute energy auditing [24].

This paper is started with an introduction in the first chapter, which deals with the previously available literature. The second chapter discusses the methodology and the building explanation for the case study. In this chapter, a comparison of conventional energy consumption and energy-efficient equipment consumption is being made. The next chapter includes the integration of renewable energy sources with the payback period calculation. Chapter four discusses the results and inferences, and the importance of GRIHA (Green Rating for Integrated Habitat Assessment) is presented in chapter five. The conclusion is given in chapter six.

2. Methodology

A review program will help focus on variations in the energy costs, availability, and reliability of energy supply, help decide on the appropriate energy mix, identify energy conservation technologies, and retrofit for energy conservation gear. The information and paperwork required during the detailed audit and analysis include energy consumption by type of appliance and usage, energy cost, and tariff data, energy management procedures. In the first stage of auditing, it means to reduce energy use in areas where energy is wasted and reductions will not cause disruptions to the various functions are introduced. This includes replacing less efficient (1 star rated) appliances and lighting systems with more efficient ones (5 stars rated). Each appliance gets rated between one to five stars, with 5 stars meaning it is extremely efficient and provides the best cost savings in the long run. These star labels are issued by the Bureau of Energy Efficiency (BEE) under the Standards and Labelling (S&L) program. The objective is to help the consumer to have an informed choice about the energy savings and thereby the cost-saving potential of household and other equipment that will save the electricity bill. The energy consumption in each case using conventional loads is computed and compared to the energy consumption using energy-efficient loads instead. This comparison has been made in terms of electrical consumption and monetary expenditure. A load distribution can also be inferred from this to see the degree of influence of the particular load on the total electrical consumption. The second stage is to add a solar power system to the building to offset costs further and decrease the building's overall energy and carbon footprint in the long run.

This comparison can be concluded by reducing energy consumption by assessing the difference in total project electrical consumption with efficient appliances. This reduction will give a cost-saving which will be used to see the payback period for the said investments.

2.1. Data Collection. The project is named "Cosmo Empire," developed by Cosmo Group in Gwalior, Madhya Pradesh at around 48 Crore as shown in Figure 1. The site's address is Cosmo Empire, Sirol Main Road, Gwalior, Madhya Pradesh-474001.

The details of the project with its floor plan are given in Figure 2, and its description is as follows:

(i) 8 floors with 16 flats per floor (1BHK-1 flat, 2BHK-9 flats, 3BHK-6 flats)

(ii) Total of 128 flats (1BHK-8 flats, 2BHK-72 flats, 3BHK-48 flats)

(iii) Common area with shops

The floor plan is used to find the number of each type of appliance in a flat and then on a floor and finally the whole building.

2.2. Energy Audit Strategy. Identification of energy consumption and other parameters has been made using detailed calculations, analysis, assumptions, and approximations. First, the load of the building per day with conventional (1-star rating or less efficient) appliances is evaluated and then calculated by replacing them with improved (5 stars rated or more efficient) appliances. Then, the estimation of the cost and payback period for a 40 kW solar power system is done. Finally, the results will be laid out by combining the above measures.

FIGURE 1: Rendering of the finished project.

FIGURE 2: Floor plan.

2.3. Data Analysis

2.3.1. 1BHK (Bedroom-Hall-Kitchen). The layout for the single bedroom is given in Figure 3, and the load calculation with the conventional appliance is presented in Table 1. Load distribution is presented as a chart in Figure 4.

Tables 1 and 2 compare the electricity consumption per day of 1BHK flat type and the estimated appliance cost. The pie chart in Figure 4 shows the percentage distribution of electricity usage per appliance in 1BHK flats. Air conditioning uses 47.8%, followed by the refrigerator, which uses 36.4% of the daily energy. The rest of the appliances are a very small percentage compared to these two. Hence, most energy can be saved if these two appliances are more efficient.

FIGURE 3: 1BHK flat layout.

2BHK flats have 2 AC units. Hence, most energy can be saved if these two appliances are more efficient. The rest of the appliances are a very small percentage compared to these two.

2.3.2. 2BHK. Figure 5 shows the layout for a double bedroom flat. Tables 3 and 4 compare the electricity consumption per day of the 2BHK flat type and the estimated appliance cost.

The pie chart in Figure 6 shows the percentage distribution of electricity usage per appliance in 2BHK flats. Air conditioning uses 63.7%, followed by the refrigerator, which uses 24.3% of the total energy used per day. Compared to 1BHK flats, the air conditioning percentage has increased as
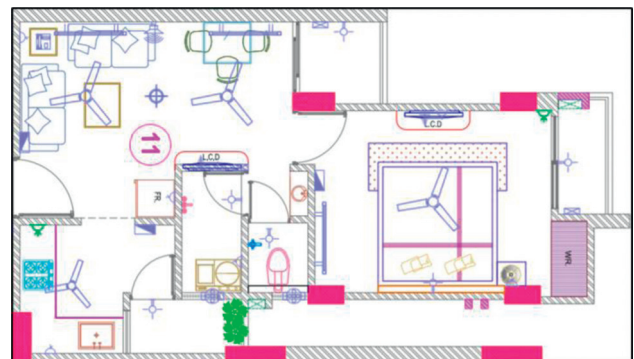
2.3.3. 3BHK. Figure 7 presents the layout and floor plan for the three-bedroom buildings. Tables 5 and 6 compare the electricity consumption of 3BHK flat type per day and the estimated appliance cost.

Table 1: Load calculation—conventional—1BHK.

S. No.	Load type	Load of one appliance (W)	Hours	Nos. per flat	Nos.	Total load of the building (Wh)	Cost per appliance (₹)	Total cost appliance (₹)
1	Tube light	36	7	3	24	6048	54	1296
2	Ceiling fans	78	4.5	4	32	11232	1425	45600
3	LED TV	80	4	1	8	2560	28990	231920
4	Exhaust fans	45	0.5	2	16	360	1150	18400
5	Ceiling light	28	7	1	8	1568	120	960
6	Washing machine	500	2	1	8	8000	17000	136000
7	Refrigerator	359	24	1	8	68928	19600	156800
8	AC	1615	7	1	8	90440	41890	335120
	Total					189136	—	9,26,096
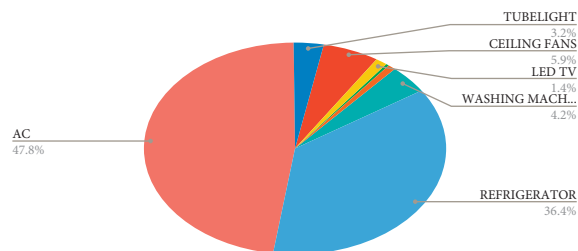
Figure 4: Load distribution—conventional loads—1BHK.

Table 2: Load calculation—improved appliances—1BHK.

S. no.	Load type	Load of one appliance (W)	Hours	Nos. per flat	Nos.	Total load of the building (Wh)	Cost per appliance (₹)	Total cost appliance (₹)
1	Tube light	20	7	3	24	3360	235	5640
2	Ceiling fans	28	4.5	4	32	4032	3800	121600
3	LED TV	80	4	1	8	2560	28990	231920
4	Exhaust fans	35	0.5	2	16	280	1184	18944
5	Ceiling light	16	7	1	8	896	282	2256
6	Washing machine	360	2	1	8	5760	14441	115528
7	Refrigerator	298	24	1	8	57216	34500	276000
8	AC	1440	7	1	8	80640	55990	447920
	Total					154744	—	12,19,808

Figure 5: 2BHK flat layout.

TABLE 3: Load calculation—conventional—2BHK.

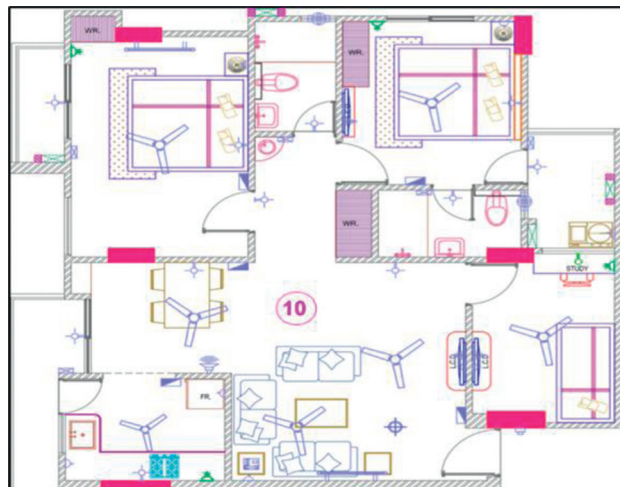| S. no.	Load type	Load of one appliance (W)	Hours	Nos. per flat	Total nos.	Total load of the building (Wh)	Cost per appliance (₹)	Total cost appliance (₹)
1	Tube light	36	7	4	288	72576	54	15552
2	Ceiling fans	78	4.5	4	288	101088	1425	410400
3	LED TV	80	4	2	144	46080	28990	4174560
4	Exhaust fans	45	0.5	2	144	3240	1150	165600
5	Ceiling light	28	7	1	72	14112	120	8640
6	Washing machine	500	2	1	72	72000	17000	1224000
7	Refrigerator	359	24	1	72	620352	19600	1411200
8	AC	1615	7	2	144	1627920	41890	6032160
	Total					2557368	—	1,34,42,112

TABLE 4: Load calculation—improved appliances—2BHK.

S. no.	Load type	Load of one appliance (W)	Hours	Nos. per flat	Nos.	Total load of the building (Wh)	Cost per appliance (₹)	Total cost appliance (₹)
1	Tube light	20	7	4	288	40320	235	67680
2	Ceiling fans	28	4.5	4	288	36288	3800	1094400
3	LED TV	80	4	2	144	46080	28990	4174560
4	Exhaust fans	35	0.5	2	144	2520	1184	170496
5	Ceiling light	16	7	1	72	8064	282	20304
6	Washing machine	360	2	1	72	51840	14441	1039752
7	Refrigerator	298	24	1	72	514944	34500	2484000
8	AC	1440	7	2	144	1451520	55990	8062560
	Total					2151576	—	1,71,13,752
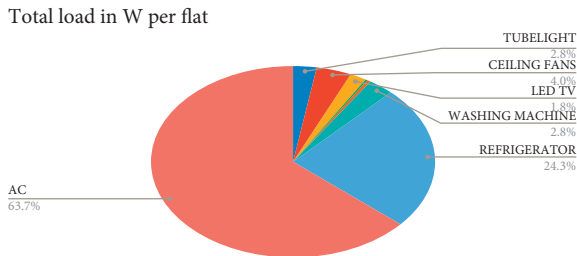
FIGURE 6: Load distribution—conventional loads—2BHK.

FIGURE: 7: 3BHK floor plan.

The pie chart in Figure 8 shows the percentage distribution of electricity usage per appliance in 3BHK flats. Air conditioning uses 61.8%, followed by the refrigerator, which uses 23.6% of the total energy used per day. The rest of the appliances are a very small percentage compared to these two. Compared to 2BHK flats, the AC energy usage has decreased by around 1% as 3BHK flats have more lights and fans.

2.3.4. Common Area. Tables 7 and 8 compare the common area's electricity consumption per day and the estimated appliance cost.

2.3.5. Load Comparison per Flat Type. The various loads with conventional power consumption and replaced new appliances power consumption for all single, dou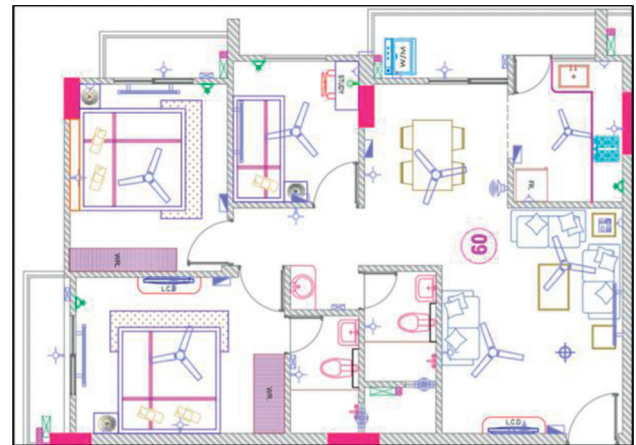ble, and triple bedroom flats are shown in Table 9. The cost-wise comparison for all the flat types with old and new appliances is shown in Figure 9. Energy consumption with the replaced appliances and its cost and payback period are presented in Tables 10 and 11, respectively.

2.3.6. Energy Consumption Details.

2.3.7. Cost and Payback Calculations. The unit rate of electricity is ₹9/unit.

TABLE 5: Load calculation—conventional—3BHK.

S. no.	Load type	Load of one appliance (W)	Hours	Nos. per flat	Nos.	Total load of the building (Wh)	Cost per appliance (₹)	Total cost appliance (₹)
1	Tube light	36	7	4	192	48384	54	10368
2	Ceiling fans	78	4.5	7	336	117936	1425	478800
3	LED TV	80	4	2	96	30720	28990	2783040
4	Exhaust fans	45	0.5	2	96	2160	1150	110400
5	Ceiling light	28	7	1	48	9408	120	5760
6	Washing machine	500	2	1	48	48000	17000	816000
7	Refrigerator	359	24	1	48	413568	19600	940800
8	AC	1615	7	2	96	1085280	41890	4021440
	Total					1755456	—	91,66,608

TABLE 6: Load calculation—improved appliance—3BHK.

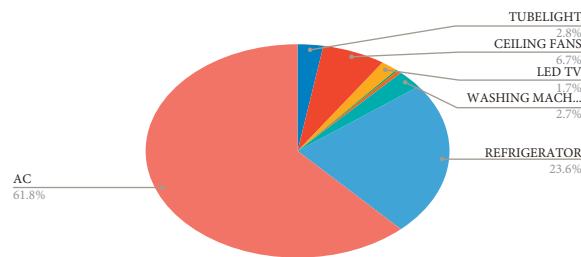| S. no.	Load type	Load of one appliance (W)	Hours	Nos. per flat	Nos.	Total load of the building (Wh)	Cost per appliance (₹)	Total cost appliance (₹)
1	Tube light	20	7	4	192	26880	235	45120
2	Ceiling fans	28	4.5	7	336	42336	3800	1276800
3	LED TV	80	4	2	96	30720	28990	2783040
4	Exhaust fans	35	0.5	2	96	1680	1184	113664
5	Ceiling light	16	7	1	48	5376	282	13536
6	Washing machine	360	2	1	48	34560	14441	693168
7	Refrigerator	298	24	1	48	343296	34500	1656000
8	AC	1440	7	2	96	967680	55990	5375040
	Total					1452528	—	1,19,56,368

FIGURE 8: Load distribution—conventional loads—3BHK.

TABLE 7: Load calculation—conventional—common area.

Load type	Location	Load of one appliance (W)	Nos.	Hours/day	Total load (Wh)	Cost per appliance (₹)	Total cost (₹)
Lift	—	4600	3	24	331200	—	—
Lift	—	6000	1	24	144000	—	—
Tube light	Parking	36	120	8	34560	54	6480
Tube light	Streetlight	36	30	10	10800	54	1620
Tube light	Floor lobby	36	48	10	17280	54	2592
	Total				537840	—	10,692

TABLE 8: Load calculation—improved appliances—common area.

Load type	Location	Load of one appliance (W)	Nos.	Hours/day	Total load (Wh)	Cost per appliance (₹)	Total cost (₹)
Lift	—	4600	3	24	331200	—	—
Lift	—	6000	1	24	144000	—	—
Tube light	Parking	20	120	8	19200	235	28200
Tube light	Streetlight	20	30	10	6000	235	7050
Tube light	Floor lobby	20	48	10	9600	235	11280
	Total				510000	—	46,530

TABLE 9: Load comparison—conventional vs improvised appliances.

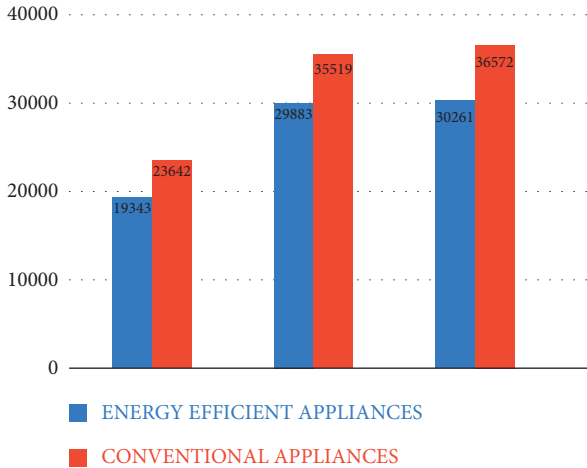|	Conventional appliances total (Wh)	New appliances total (Wh)
1BHK	23642	19343
2BHK	35519	29883
3BHK	36572	30261

FIGURE 9: Difference between energy consumption when conventional loads are used and when improvised appliances are used for 1BHK, 2BHK, and 3BHK.

TABLE 10: Energy usage calculations.

Total project electrical consumption conventionally	5039.800 kWh
Total project electrical consumption with efficient appliances	4268.848 kWh
Reduction in electrical consumption per day	770.952 kWh
Percentage reduction in electrical consumption	15.3%

TABLE 11: Cost saving and payback calculation.

Cost saved	₹6,938.568
Investment	₹67,90,950
Payback period	2.68 years

3. Production of Renewable Energy by the Photovoltaic System (Solar Power)

A proposal is made to put a PV system to produce 40 kW to generate electrical energy. With a 40 kW per day PV system, renewable energy production is above 9% of the total energy usage.

3.1. Working. This system is connected to the electrical grid and allows residents/buildings to use solar energy and power from the grid. In this system, solar PV panels produce direct current (DC) and are fed into a solar inverter that converts it to useable 230V-50 Hz AC. When the panels generate adequate energy, the solar inverter uses no

power from the grid. If the power generated by panels is insufficient, the inverter compensates by drawing power from the grid at night. It will completely switch to the main grid. If the power is in excess, it can be fed to the grid under net metering. The battery is not used for this system as the grid is used as a backup. Solar PV cost quotation and cost savings with payback calculation are shown in Tables 12 and 13.

4. Results

The final cost-saving and its payback period are calculated by taking the electricity unit rate as Rs. 9/unit and given in Table 14. The previously shown results prove that the substitution of energy-efficient appliances in place of conventional equipment has given more cost-saving and energy consumption. In this chapter, the cost reduction is further achieved by integrating renewable energy sources. As shown in Table 14, it is shown that the reduction in energy consumption has been achieved by replacing the appliances and incorporating the solar system. It saves around 2.5 lakhs rupees, which will be getting back in three years as a payback period.

It can be concluded from this project that there is a huge amount of energy and cost-saving potential in the residential sector. By simply swapping less efficient appliances with more efficient ones and installing a PV system, there was a reduction of around 16% in energy consumption, including over 9% of renewable energy production. This was achieved with a surplus cost of around 1.76% of the project's total estimated cost.

Over the next 10 years, the measures are calculated to provide an estimated saving of over 26 crore rupees. In 20 years, the cumulative savings will surpass the total investment made for the construction of the building. As is evident by the data, air conditioning is the single biggest power consumer in the residential power sector. Hence, installing/upgrading to more efficient 5-star rated ACs is a great investment in the long run. It was also observed that huge improvements in energy usage are due to more efficient technologies like BLDC (brushless DC) fans which consume only 28 W of energy compared to normal fans which consume around 80 W.

5. Green Rating for Integrated Habitat Assessment (GRIHA)

The crux of the initiative is "what gets measured." GRIHA attempts to quantify aspects such as energy consumption, waste generation, and renewable energy adoption, to manage, control, and reduce the same to the best possible extent. GRIHA is an independent body now even referred to as a society that looks forward to many architectural aspects of construction projects.

GRIHA is a rating tool that rates a building on certain parameters according to international and national standards and then gives a star rating. Many government bodies regulate India's construction process, whether residential or commercial spaces. This star rating is now getting accepted.

TABLE 12: PV system cost quotation.

Item	Capacity (kWp)	Rate per kWp (₹)	Total price (₹)
Design, manufacture, and supply of 40 kW grid-connected solar PV system complete with a solar module, and other accessories and connecting cables	40	42000	16,80,000
Total			16,80,000

TABLE 13: PV system cost savings and payback calculation.

Per unit cost of grid electricity	9	Rupees
Total energy generated by the PV system per year	52,800	kW
Total saving per year	475200	Rupees
Project cost	16,80,000	Rupees
Payback period	**3.53**	**Years**

TABLE 14: Final cost savings and payback calculation.

Daily energy usage (no energy-saving measures in place)	5039.8 kWh
Reduced energy usage per day (using efficient appliances)	4268.848 kWh
Energy generated by the PV system per day (peak)	40 kWh
Effective total energy usage per day	4228.848 kWh
Reduction in daily total energy usage	810.952 kWh
Reduction in yearly total energy usage	295997 kWh
Percentage reduction in energy usage	16.09%
Total investment cost	8470950 ₹
Total daily savings	7298.568 ₹
Yearly savings	2663977.32 ₹
Payback period	3.179 years

According to the star rating, government bodies provide many incentives so that the construction company and users get a boost while considering the concern of environmental causes. Moreover, many recent real-estate projects have now started taking certification from GRIHA. It is observed that customers prefer many GRIHA rated compared to non-GRIHA affiliated projects.

5.1. Benefits

(i) Energy consumption is reduced without sacrificing the comfort levels of the consumer

(ii) The destruction of natural areas, habitats, and biodiversity is reduced, and soil loss from erosion is also reduced

(iii) Air pollution and water pollution are reduced

(iv) Water consumption is reduced

(v) Waste generation linked to recycling and reuse is limited

(vi) Pollution loads are reduced

(vii) User productivity is increased

(viii) Image and marketability are enhanced to increase the engagement of customers

Therefore, it is recommended that the construction company looks forward to all these incentives and considers all the norms while developing a greener and energy-efficient residential building.

6. Conclusion

The BEE star rating program has successfully spread awareness among the consumers as this rating was very helpful during this project. Data collection about the appliances that did not have the rating proved difficult and ambiguous as most manufacturers do not easily make the energy usage information accessible. This real-time project has been chosen to make the public aware of the importance of energy saving. The various loads in single, double, and three bedrooms, hall, and kitchen rooms have been studied. The cost comparison of all the loads for conventional and energy-efficient devices has been attempted and proved the best method. Solar output has met the load demand, and the building has a better payback period. Hence, it is suggested to have a prior study of the building construction with the cost analysis which will be helpful to reduce the electricity billing and cost reduction. This project proves that investment in energy-saving equipment provides cost benefits in the long run and is better for the planet.

Data Availability

The data used to support the findings of this study are included in the article. Should further data or information be required, these will be made available from the corresponding author upon request.

Conflicts of Interest

The authors declare that there are no conflicts of interest regarding the publication of this paper.

Acknowledgments

References

[1] O. E. Atiba, U. K. Efemwenkiekie, R. O. Olatunji, O. S. Ohunakin, D. S. Adelekan, and O. A. Oyeleke, "Walk-through energy audit of an institutional building," *Journal of Physics: Conference Series*, vol. 1378, no. 3, Article ID 032051, 2019.

[2] A. S. H. Abdallah, M. Ahmed, and M. A.-A. Nayel, "Energy audit and evaluation of indoor environment condition inside assiut international airport terminal building, Egypt," *Ain Shams Engineering Journal*, vol. 12, pp. 2090–4479, 2021.

[3] J. Woo and T. Moore, "An end-user-focused building energy audit: a high-density multi-residential development in melbourne, Australia," in *Energy Performance in the Australian Built Environment. Green Energy and Technology*, P. Rajagopalan, M. Andamon, and T. Moore, Eds., Springer, Singapore, 2019.

[4] A. Lorenzati, I. Ballarini, G. Luca, and V. Corrado, "Social Housing in Italy: Energy Audit and Dynamic Simulation towards a nZEB policy." in *Proceedings of the 16th International Building Performance Simulation Association Conference*, Rome, Italy, January 2020.

[5] M. Sikora and K. Siwek, "Energy audit of the residential building," *Journal of Mechanical and Energy Engineering*, vol. 2, no. 42, pp. 317–328, 2018.

[6] A. Alabi, O. Ogunleye, S. Misra, O. Abayomi-Alli, R. Ahuja, and M. Odusami, "Comparative study of the electrical energy consumption and cost for a residential building with conventional appliances vis-a-vis one with energy-efficient appliances," in *Data, Engineering and Applications*, R. K. Shukla, J. Agrawal, S. Sharma, and G. Singh Tomer, Eds., Springer, Singapore, 2019.

[7] A. G. Gaglia, E. N. Dialynas, A. A. Argiriou et al., "Energy performance of European residential buildings: energy use, technical and environmental characteristics of the Greek residential sector-energy conservation and CO_2 reduction," *Energy and Buildings*, vol. 183, pp. 86–104, 2019.

[8] C. Smalling, "HVAC System Energy Audit for Leverett Elementary School." Biological and Agricultural Engineering Undergraduate Honors Theses," 2019, https://scholarworks.uark.edu/baeguht/66.

[9] E. Hirst, "Improving energy efficiency of existing homes: the Residential Conservation Service, State Energy Policy," *In State Energy Policy*, vol. 12, pp. 85–106, 2019.

[10] F. Belaïd, D. Roubaud, and E. Galariotis, "Features of residential energy consumption: evidence from France using an innovative multilevel modelling approach," *Energy Policy*, vol. 125, pp. 277–285, 2019.

[11] Y. Y. Ghadi and A. M. Baniyounes, "Energy audit and analysis of an institutional building under subtropical climate," *International Journal of Electrical and Computer Engineering*, vol. 8, no. 2, p. 845, 2018.

[12] S. Gupta, R. Kamra, M. Swaroopa, and A. Sharma, "Energy Audit and Energy Conservation for a Hostel of an Engineering Institute," in *Proceedings of the 2018 2nd IEEE Features of Residential Energy Consumption: Evidence from France Using an Innovative Multilevel Modelling Approach International Conference on Power Electronics, Intelligent Control and Energy Systems (ICPEICES)*, pp. 8–12, Delhi, India, October 2018.

[13] M. Krarti, *Energy Audit of Building Systems: An Engineering Approach*, CRC Press, Boca Raton, Florida, 2020.

[14] K. N. Balan and U. Yashvanth, "Energy audit in residential building-replacement of portable air conditioner by an energy efficient centralised air conditioner," *International Journal of Ambient Energy*, vol. 41, no. 2, pp. 179–182, 2020.

[15] A. Joshi, N. Khandelwal, Y. Suryawanshi, and M. Kurulekar, "Energy conservation-residential building, 2020 International Conference and Utility Exhibition on Energy, Environment and Climate Change (ICUE)," in *Proceedings of the 2020 International Conference and Utility Exhibition on Energy, Environment and Climate Change (ICUE)*, pp. 1–5, Delhi, India, October 2020.

[16] A. Mohammed Usman, A. N. Mohammed, M. F. Mohideen, M. F. Mohd Ali, K. Abdullah, and J. Taweekun, "Energy profiling for residential college buildings," *Journal of Advanced Research in Fluid Mechanics and Thermal Sciences*, vol. 81, no. 2, pp. 139–145, 2021, https://doi.org/10.37934/arfmts.81.2.139145.

[17] A. Rodriguez, S. T. Smith, S. T. Smith, and B. Potter, "Sensitivity analysis for building energy audit calculation methods: handling the uncertainties in small power load estimation," *Energy*, vol. 238, Article ID 121511, 2022, https://doi.org/10.1016/j.energy.2021.121511.

[18] D. Mazzeo, N. Matera, P. Bevilacqua, and N. Arcuri, "Energy and Economic Analysis," vol. 8, 2022.

[19] D. Mazzeo and G. Oliveti, "Advanced innovative solutions for final design in terms of energy sustainability of nearly/net zero energy buildings (nZEB)," *Sustainability*, vol. 12, no. 24, Article ID 10394, 2020.

[20] N. Long, K. Fleming, C. CaraDonna, and C. Mosiman, "BuildingSync: a schema for commercial building energy audit data exchange. country unknown/code not available: N. p., 2021," *BuildingSync: a schema for commercial building energy audit data exchange, Developments in the Built Environment*, vol. 7, Article ID 100054.

[21] M. S. Al-Homoud and M. Krarti, "Energy efficiency of residential buildings in the kingdom of Saudi Arabia: review of status and future roadmap," *Journal of Building Engineering*, vol. 36, Article ID 102143, 2021, https://doi.org/10.1016/j.jobe.2020.102143.

[22] Y. Lu, S. Manuel, Z. A. Khan, M. S. Alvarez-Alvarado, and M. Imran, A critical review of sustainable energy policies for the promotion of renewable energy sources, *Sustainability*, vol. 12, no. 12, Article ID 5078, 2020.

[23] S. Soni and Inderpreetkaur, "Analyze energy consumption in a building by energy audit," in *Advances in Power Systems and Energy Management*, N. Priyadarshi, S. Padmanaban, R. K. Ghadai, A. R. Panda, and R. Patel, Eds., Springer, Singapore, Springer, 2021 Lecture Notes in Electrical Engineering.

[24] A. Merabtine, C. Maalouf, A. A. W. Hawila, N. Martaj, and G. Polidori, "Building energy audit, thermal comfort, and IAQ assessment of a school building: a case study," *Building and Environment*, vol. 145, pp. 62–76, 2018.

Research Article

Numerical Modeling of Rock Panels Subjected to Blast Loadings

Haijun Wang [iD],[1,2] **Daiyu Xiong,**[3] **Yun Duan,**[1] **Weiqin Cao,**[4] **Wenru Zhang,**[4] **Peng Jiao,**[4] **Bonan Wang,**[1,2] **Xulin Zhao,**[2] **Yonggang Miao,**[2] **and Le Zhou**[5]

[1]*School of Resource and Civil Engineering, Northeastern University, Shenyang 110819, China*
[2]*BGRIMM Technology Group, Beijing 100160, China*
[3]*China Coal Technology & Engineering Group, Beijing 100160, China*
[4]*Nanjing Yinmao Lead-zinc Mining Co.Ltd., Nanjing 210046, China*
[5]*Changchun Gold Research Institute Co.Ltd., Changchun 130012, China*

Correspondence should be addressed to Haijun Wang; 2957577750@qq.com

In rock engineering problems, the rock is usually subjected to dynamic loads induced by drill, blast and rockburst. Therefore, understanding the dynamic response of rock benefit the safety and productivity of excavation activities. In this study, the response of rock panels under blast loadings is numerically investigated. The uniaxial and triaxial compression tests are firstly conducted in the laboratory to obtain the material property of four types of rocks, including Chuanshan limestone, Gaolishan sandstone, Mineralized limestone and Xixia limestone. Then, a total of 16 numerical simulations are carried out in which each type of rock panel is subjected to TNT blast loadings with four scaled distances, i.e., $0.15 \, \mathrm{m/kg^{1/3}}$, $0.30 \, \mathrm{m/kg^{1/3}}$, $0.60 \, \mathrm{m/kg^{1/3}}$, $1.20 \, \mathrm{m/kg^{1/3}}$. The damage distribution, which is characterized by the effective plastic strain, within the rock panels is quantitatively and qualitatively analyzed. The modelling results demonstrate that the effect of blast loading on the rock is material dependent. For a given scaled distance, the Gaolishan sandstone damages most severely, followed by Xixia limestone, Chuanshan limestone, and mineralized limestone. A critical scaled distance is observed on the limestone panels. When the scaled distance is smaller than the critical value, the damage of limestone panels increases with increasing the scaled distance. Once exceeding the critical value, the damage of limestone panels decreases with the increase of scaled distance. However, such a transitional scaled distance is not observed in the sandstone panels, of which damage decreases gradually with the increases of scaled distance.

1. Introduction

A great many of engineering applications are performed in rock masses, including tunnel excavations, mining activities, and personnel protective structures [1–3]. Consequently, the rock is frequently subjected to dynamic loadings resulted from drill and blast, rockburst, and projectile penetration. Unlike quasi-static loading, the dynamic loading applied on the rock is intensive together with high pressure and high temperature. Therefore, it is of great significance to understand the response of rocks subjected to dynamic loadings, which benefits the safe design and the safety of personnel and device in rock engineering projects.

To date, numerous experiments have been performed in laboratory and filed scale to assess the dynamic response of various rocks. For example, Zhang and Zhao [4] employed the Split and Hopkinson Pressure Bar (SHPB) in conjunction with digital image correlation technique and high-speed camera to explore the mechanical behaviour (e.g., strain localization and evolution, onset of fracture, and material property) of Fangshan marble under dynamic uniaxial compression, Brazilian disc, and notched semi-circular bending tests. They observed that the fracture initiation toughness, tensile strength and uniaxial compression strength of Fangshan marble increases significantly with the increase of strain rate, and the strain rate effect results from the transition of fracture mode. Marurer and Rinehart [5] carried out spherical steel projectile penetration tests on sandstone and granite with various velocities and impact angles. They concluded that the crater formed in the

sandstone and granite is induced by the crushing in front of projectile and the fracturing extension to the free surface, and the crushed and fracturing volumes are relating to the first and second power of impact velocity, respectively. In addition, they noticed that the penetration varies linearly with the impact velocity and is inversely proportional to the specific acoustic resistance of rock. Chi et al. [6] performed blast experiments on six granite cubes with two charge weights, and the fracturing process is monitored with the use of digital correlation technique and high-speed camera. They found that the charge wight influences the number and opening velocity of dominant vertical cracks, the initiation time of macroscopic cracks, and the velocity of fragment.

Numerical approach is an alternative of experiment to investigate the dynamic response of rock materials [7–9]. Compared with experiment, the numerical approach is more cost-effective and easier to repeat. In addition, the numerical approach can be used to investigate the micromechanical parameters that influence the dynamic response of rock, which is difficult to be incorporated in experiments [10]. The commonly used numerical methods include finite element method, finite-discrete element method, discrete element method, peridynamic method, and Smoothed-particle hydrodynamics method [11–13]. Through these methods, the response of rock under various dynamic loadings are explored. For example, Xie et al. [14] investigated the effect of free-surface boundary conditions, in-situ stress and the coefficient of lateral pressure on the granite response subjected to cut blasting with the use of finite element method. An et al. [15] used the discrete element method to evaluate the confinement effect on the on the blasting performance in narrow vein mining, and they found that the blasting confinement results in underbreak or overbreak. Saksala and Ibrahimbegovic [16] developed a combined continuum viscodamage-embedded discontinuity model to figure out the thermal shock weakening effect on the dynamic response of granite, and they reported that the rock gravel and rubble crushing can be enhanced by the heat shock pretreatment. Zhao et al. [17] examined the bedding effect on the dynamic Brazilian tensile strength of coal in the SHPB test with distinct lattice spring method. It is found that the dynamic indirect tensile strength of coal positively correlates to the impact velocity, bedding direction, bedding roughness, and bedding discontinuity. Moreover, much effort has been paid to develop new isotropic and anisotropic constitutive models for more accurately and reasonably describing the rock and rock-like materials' response under dynamic loadings [18–25].

To sum up, the studies mentioned above have provided insights on the dynamic response of rock materials under various dynamic loading scenarios, such as SHPB tests, projectile penetrations and blast loadings. Most of these studies focused on the effect of external factors, e.g., in-situ stress and impact velocity, but the influence of intrinsic factors, including rock types and rock's material property is lesser explored. Therefore, this study aims to numerically investigate the rock response under blast loadings with a special focus on the effect of rock types and explosive configuration. Specially, four types of rock, including Chuanshan limestone, Gaolishan sandstone, Mineralized limestone and Xixia limestone, are selected, and their material properties are first determined with uniaxial and triaxial compression tests in the laboratory. Then, 3D rock panels are established in the finite element tool LS-DYNA [26], and each type of rock panel is subjected to four blast loadings with different scaled distances, i.e., $0.15 \, \text{m/kg}^{1/3}$, $0.30 \, \text{m/kg}^{1/3}$, $0.60 \, \text{m/kg}^{1/3}$, $1.20 \, \text{m/kg}^{1/3}$. Finally, the effects of rock type and scaled distance of TNT on the damage distribution inside rock panels are quantitively and qualitatively discussed.

2. Experimental and Numerical Approaches

2.1. Material Model for Rocks. The Mohr–Coulomb strength criterion is used to describe the mechanical behaviour rock materials herein, which is the one of the most frequently used strength criteria in various rock engineering applications [27]. This criterion relates the shear strength of rock to the constant cohesion and a friction varying with normal stress, and its yield surface is written as

$$\tau_{\text{max}} = C + \sigma_n \tan \varphi, \tag{1}$$

where τ_{max} is the maximum shear stress on any plane; C is the cohesion strength of rock; σ_n is the normal stress on that plane and positive in compression; and φ is the friction angle of rock. The plastic potential function is expressed as

$$g = \beta \sigma_k - \sigma_i + \text{constant}, \tag{2}$$

where σ_k is the maximum principal stress; σ_i is the minimum principal stress; and β is given as

$$\beta = \frac{1 + \sin \varphi}{1 - \sin \varphi}. \tag{3}$$

The damage is described by the plastic strain here, which is formulated as

$$\varepsilon_p = \sqrt{\frac{2}{3} \varepsilon_{ij}^p \cdot \varepsilon_{ij}^p}, \tag{4}$$

where ε_p is the equivalent plastic strain; and ε_{ij}^p is the plastic strain tensor. It is defined here that the damage is formed and then accumulated once the equivalent plastic strain higher than 0.1% [25].

2.2. Parameters Determination. The required parameters of Mohr-Coulomb model can be determined based on the uniaxial and triaxial compression tests on rock materials. Here, four types of rocks, i.e., mineralized limestone, Gaolishan sandstone, Chuanshan limestone, and Xixia limestone, are drilled from the $-475 \, \text{m}$ underground sublevel of a lead-zinc-silver deposit located in Nanjing, China. Then, these rock cores are cut into cylinders with a dimension of $54 \, \text{mm} \times 110 \, \text{mm}$ (diameter × height). Later, these cylinders are ground flat at their two ends. After that, these cylinders are subjected to uniaxial and triaxial compression tests according to the ASTM D7012-14e1 standard method. During the test, a thin layer of Vaseline is put on

(a)   (b)

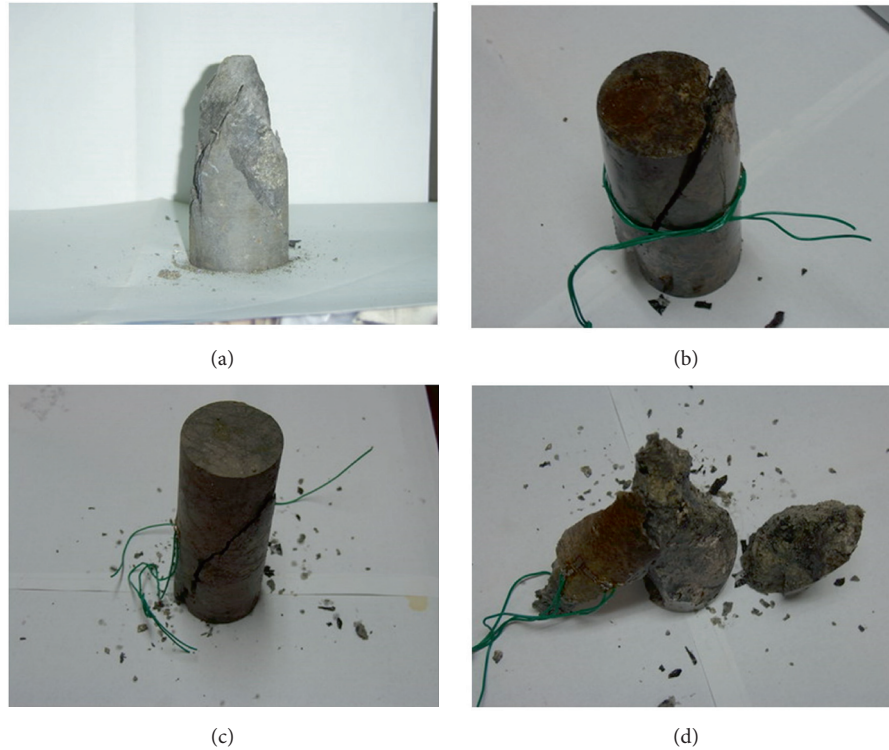(c)   (d)

FIGURE 1: Fracture patterns of mineralized limestone under confining pressure of (a) 0 MPa, (b) 10 MPa, (c) 15 MPa, and (d) 20 MPa.

two ends of the sample to reduce the friction between the sample and the loading platens. The confining pressures include 0 MPa (uniaxial compression), 10 MPa, 15 MPa, and 20 MPa.

The fracture patterns of mineralized limestone under various confining pressures are given as an example and illustrated in Figure 1. It is evident from Figure 1 that when the confining pressure is smaller than 15 MPa, the shear failure is the dominated fracture type of mineralized limestone, and under a high confining pressure (20 MPa in this study) the mineralized limestone fails in a crushing mode. Based on the uniaxial and triaxial compression data of these four rocks, their material properties can be determined as listed in Table 1. In the table, E, v, UCS, and BTS denote Young's modulus, Poisson ratio, uniaxial compressive strength and Brazilian tensile strength, respectively.

2.3. Blast Loading Modelling. The keyword "Load_-Blast_Enhanced" is used to create the air blast pressure history induced by conventional explosives in LS-DYNA [28], which is an empirical function proposed based on a large amount of experimental data. Numerous studies have demonstrated the accuracy and efficiency of this function in modelling the blast loading on panels made of rock-like materials [29, 30], and only the equivalent mass of TNT, type of blast, and the detonation centre of the explosive needs to be predefined in this function. Thus, this keyword is also used to generate the TNT blast loading on the rock panels herein, and its pressure history in a free-air explosion can be described as

$$P(t) = P_{\max}\left(1 - \frac{t}{t_+}\right)\exp\left(-\frac{at}{t_+}\right), \qquad (5)$$

where P is the blast pressure varying with duration time t; $P_{\max}$ is the incident overpressure; t_+ is the positive duration time; and a is waveform number.

The theory and experiments denote that the blast pressure shows a large degree of self-similarity in terms of the scaled distance which is written as

$$Z = \frac{R}{M_e^{1/3}}, \qquad (6)$$

where Z is the scaled distance; R is the distance from explosive centre to the target surface; and M is explosive mass. In this study, four scaled distances are used to investigate the mechanical behaviour of various rock panels subjected to varying degrees of blast loading, i.e., 0.15 m/kg$^{1/3}$ ($R = 0.119$ m, $M = 0.50$ kg), 0.30 m/kg$^{1/3}$ ($R = 0.30$ m, $M = 1.0$ kg), 0.6 m/kg$^{1/3}$ ($R = 0.756$ m, $M = 2.0$ kg), and 1.20 m/kg$^{1/3}$ ($R = 1.905$ m, $M = 4.0$ kg). The generated blast pressure history curves by these four scaled distances are illustrated in Figure 2. As can be seen, with the increase of scaled distance, the maximum incident overpressure on the rock panel's surface decreases from 182.345 MPa to 2.9 MPa, and the arrival time increases from 0.029 ms to 1.2 ms. The negative pressure is also accommodated in the "Load_-Blast_Enhanced" approach using the Friedlander equation [28], and its minimum values are −90.4091 Pa, −90.28 Pa, −60.015 Pa, −102.2 Pa for the scaled distances of 0.15 m/kg$^{1/3}$, 0.30 m/kg$^{1/3}$, 0.6 m/kg$^{1/3}$, and 1.2 m/kg$^{1/3}$, respectively. It is

TABLE 1: Material properties of tocks.

Rock	Density (kg/m^3)	E(MPa)	ν	C (MPa)	ϕ	UCS (MPa)
Mineralized limestone	2725	43722	0.268	5.094	45	78.70
Gaolishan sandstone	2610	28168	0.358	1.146	32	35.14
Chuanshan limestone	2659	26911	0.151	3.438	39	72.92
Xixia limestone	2649	30691	0.141	2.496	34	76.83

(a)

(b)

(c)

(d)
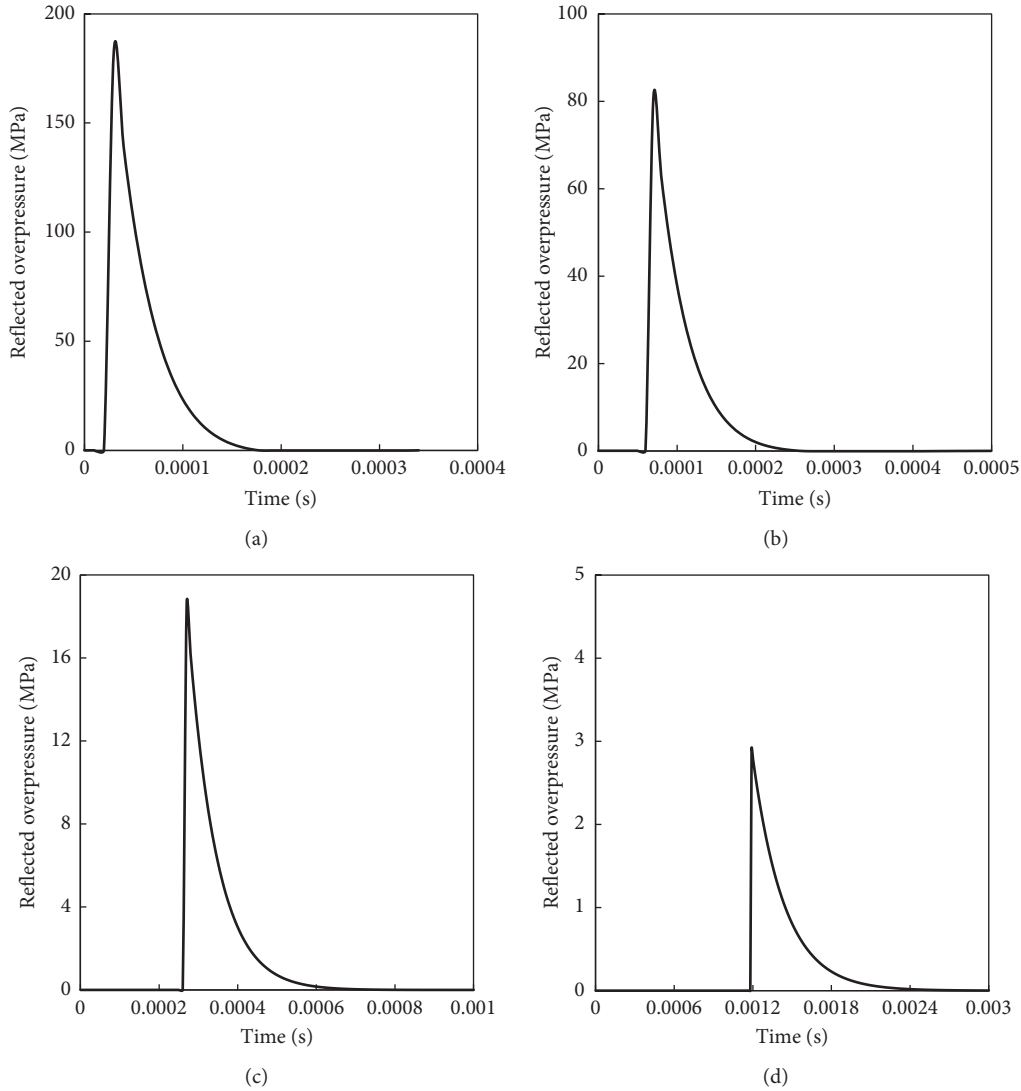
FIGURE 2: Blast pressure history curves for the scaled distance equal to (a) 0.15 m/kg$^{1/3}$, (b) 0.30 m/kg$^{1/3}$, (c) 0.60 m/kg$^{1/3}$ and (d) 1.20 m/kg$^{1/3}$, respectively.

worth mentioning that the blast pressure history is not influenced by the rock type. The density and Chapman-Jouguet detonation velocity of standard TNT in LS-DYNA are 1.57 g/cm3 and 0.693 cm/μs, respectively.

2.4. Numerical Model Setup. A numerical model with a dimension of 700 mm × 700 mm × 75 mm is established with eight-node constant solid stress elements as shown in Figure 3, and the Lagrangian formulation is employed in the modelling. The mesh size is 5 mm, and a total of 294, 000 elements is used in the numerical model after mesh convergence study to avoid mesh dependency as much as possible and make a trade-off between numerical accuracy and computational efficiency. The vertical displacements of two edges along the Y direction in the bottom face are fixed to avoid bouncing back up. Also, the hourglass control is adopted in the explicitly dynamic simulation. Recall that in this study, four kinds of rocks are selected, and each type of rock is subjected to blast load with four scaled distances.
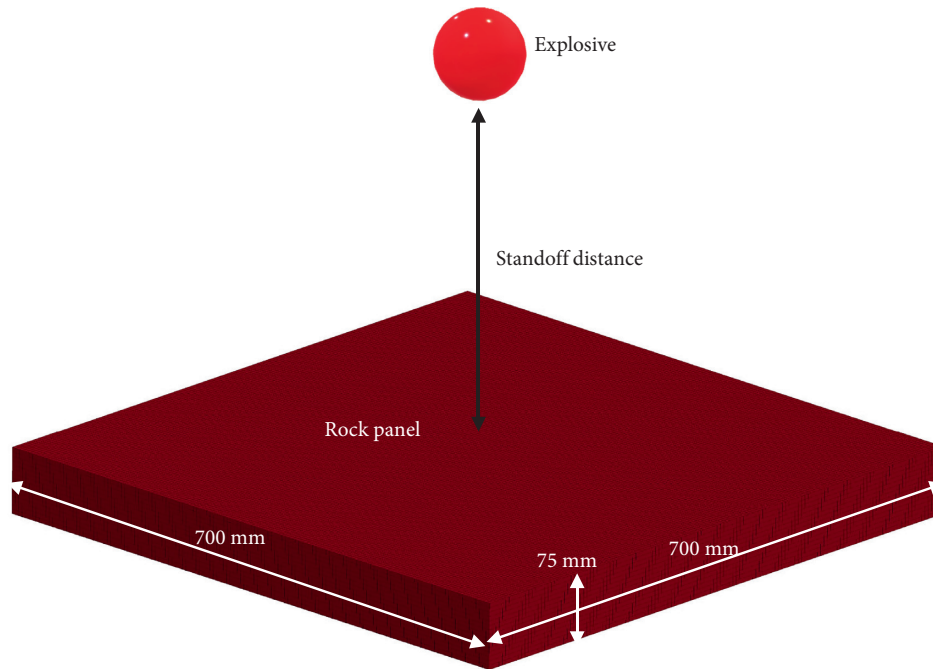
Figure 3: Numerical model setup of rock panel subjected to blast loading.

Therefore, a total of 16 simulations are conducted in this study, and the termination time for each simulation is 0.02 s to ensure the complete blast related response of rock panels. Note that the strength property (e.g., uniaxial compressive and tensile strengths) of rock materials is rate sensitive, and an obvious strength gain can be obtained under high strain rates. The rate sensitivity of rock is material dependent, that is, different types of rock materials show different strength enhancement under the same strain rate. In the numerical modelling, the strain rate effect can be described by using the dynamic increase factor formula. Per the author's knowledge, there is no specified dynamic increase factor formulas for the four kinds of rock materials investigated in this study. In consequence, the strain rate effect on the is not considered here.

3. Results and Discussion

After explosive action, the effective plastic strain distributed within the rock panels are illustrated in Figures 4 and 5. It is worth mentioning that in this study, the finite element with an effective plastic strain (eps) larger than 0 denotes that it has been damaged. Figure 4 plots that the damage decreases with the increasing scaled distance. When the scaled distance is small, i.e., 0.15 m/kg$^{1/3}$, the circular damage area with high eps values localises in the top middle of the rock panels. As the scaled distance increases, the damage pattern changes to a rectangular band across the panel with lower eps values.

The sides views of rock panels in Figure 4 demonstrate that all the panels are overall damaged in flexural mode with eps mainly distributed in the middle span and gradually smeared to the edges. In fact, it is reasonable as such damage pattern absorbs most of the energy generated by the charge explosion. For a given rock type, e.g., the Chuanshan

limestone shown in Figure 4(a), the damage decreases with the increases of scaled distance overall. The diameter of the front face at the side view decreases, but the damage diameter of the distal face at the side view increases first and then decreases as the scaled distance increases. It is interesting to note that the Chuanshan limestone with a scaled distance of 0.15 m/kg$^{1/3}$ is damaged much more severe than the scaled distance of 0.30 m/kg$^{1/3}$ at its distal face where the noticeable bulge is noticed, but its damage diameter of the distal face at side view is smaller. The reason can be explained by the fact that when the scaled distance is small, the local damage occurs in the rock panel centre due to the punching induced by the high-intensity shear force generated by the blast wave [31]. When the scaled distance is big, i.e., 0.30 m/kg$^{1/3}$ or larger, the rock panel is mainly damaged due to the bending force. Note that a similar trend can be concluded for another three types of rock panels as shown in Figures 5(b)–5(d), which is not repeated herein. In addition, it can be observed from Figures 4 and 5 that the Gaolishan sandstone is the most damaged for a given scaled distance, followed by the Xixia limestone, Chuanshan limestone, and mineralized limestone. It is because Gaolishan sandstone has the lowest cohesion strength and friction angle.

To quantify the damage induced by the explosive action with different scaled distances, the probability density of eps in these four types of rocks is illustrated in Figure 6. As seen, for the Chuanshan limestone shown in Figure 6(a), its probability density value of eps = 0 decreases first and then increases, and the lowest probability density value of eps = 0 is noticed in the case of scaled distance equal to 0.30 m/kg$^{1/3}$. Note that a smaller probability density of eps = 0 means that more finite elements are damaged, and thus the Chuanshan limestone panel with a scaled distance of 0.30 m/kg$^{1/3}$ has the largest number of damaged elements. In addition, as the
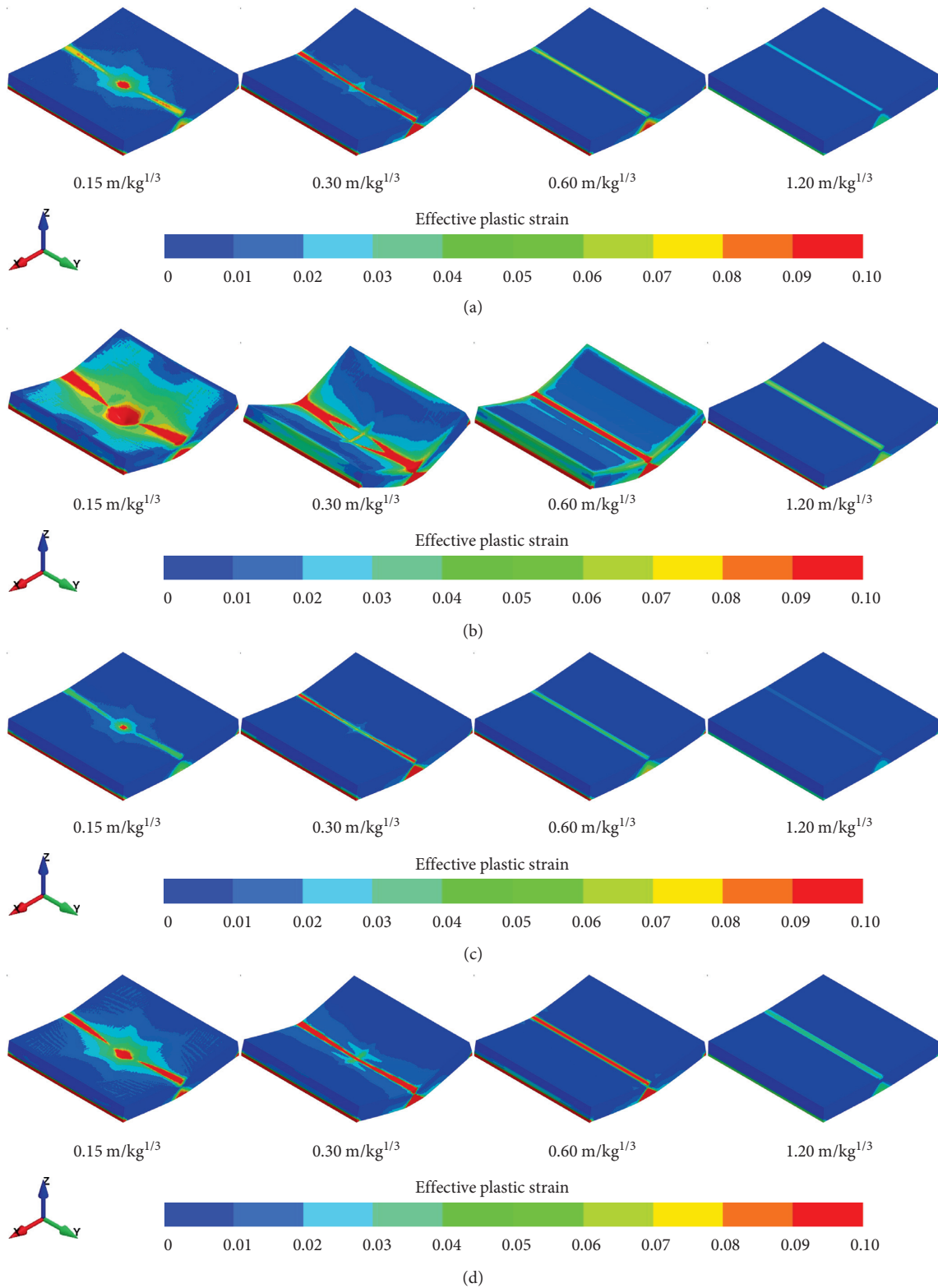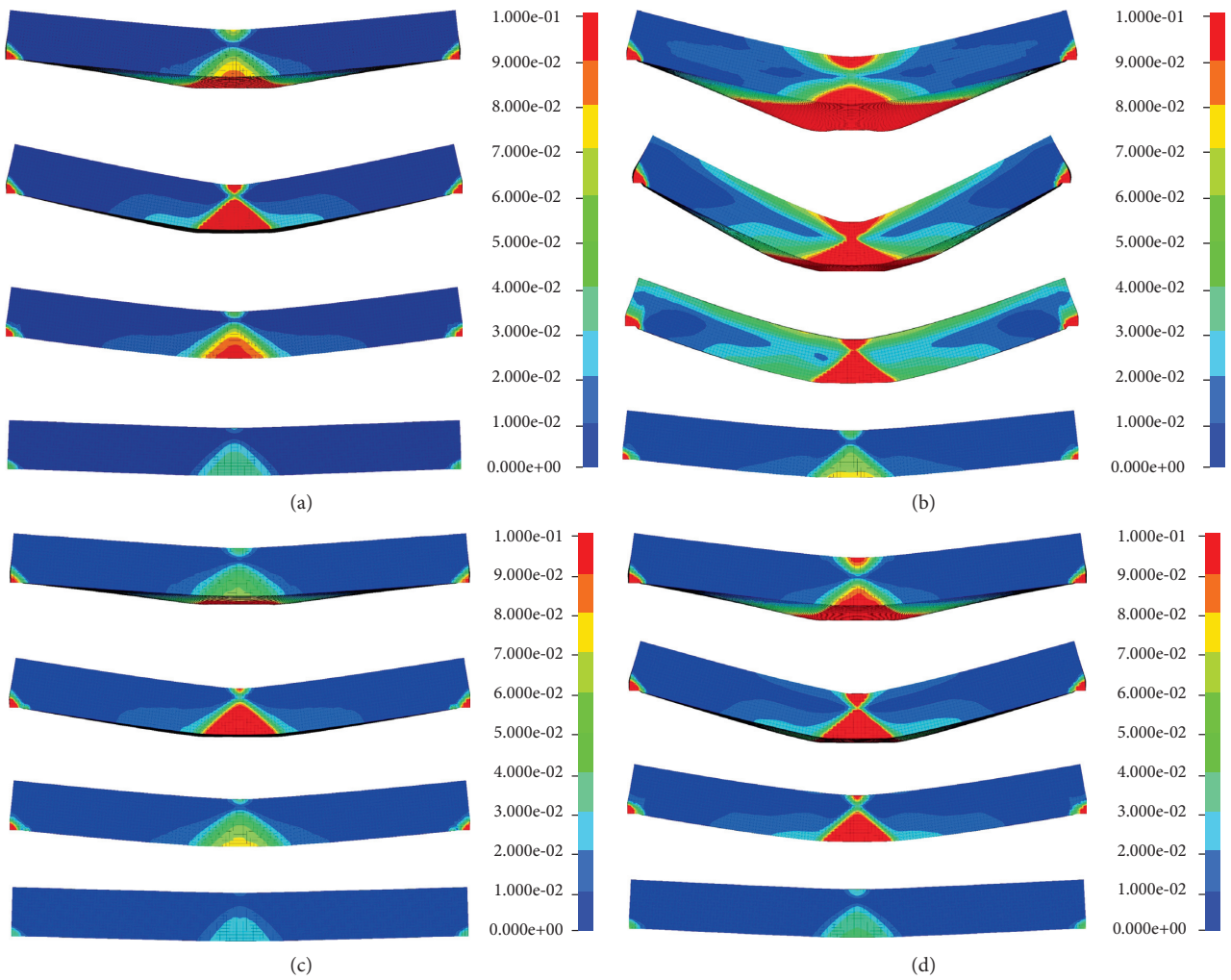
FIGURE 4: Plastic strain distribution in (a) chuanshan limestone, (b) gaolishan sandstone, (c) mineralized limestone, and (d) xixia limestone panels under blast loadings with various scaled distances.

scaled distance increases, the eps corresponding to the peak value of probability density increases first and then decreases. It denotes that their damage degree for these

damaged elements is severest in the Chuanshan limestone panel with a scaled distance of 0.30 m/kg$^{1/3}$. For the Gaolishan sandstone shown in Figure 6(b), it is found that with

FIGURE 5: Plastic strain distribution in (a) chuanshan limestone, (b) gaolishan sandstone, (c) mineralized limestone, and (d) xixia limestone panels after blast loading. In each subplot, the standoff distance from the top to bottom is 0.15 m/kg$^{1/3}$, 0.30 m/kg$^{1/3}$, 0.60 m/kg$^{1/3}$, 1.20 m/kg$^{1/3}$.

FIGURE 6: Continued.

(c)
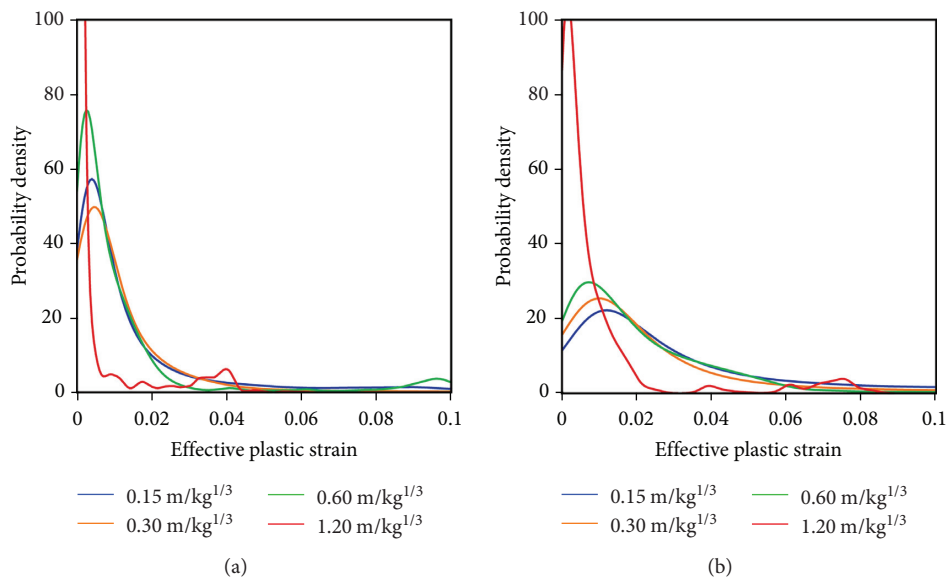
(d)
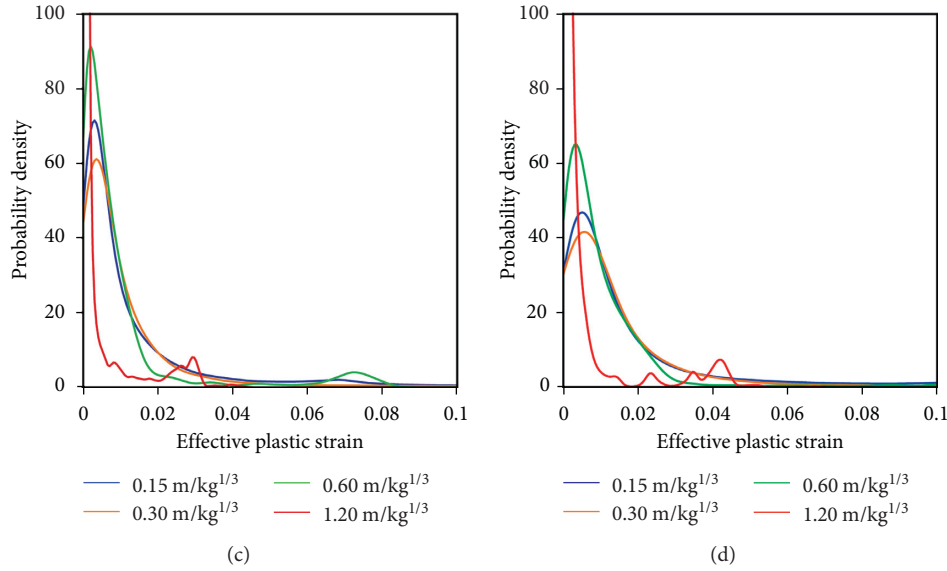
FIGURE 6: Probability density curves of effective plastic strain distribution in (a) chuanshan limestone, (b) gaolishan sandstone, (c) mineralized limestone, and (d) xixia limestone panels under blast loading with different scaled distances.

TABLE 2: Damage percentage of rock panels under blast loadings with various scaled distances.

Rock panel	Scaled distance (m/kg$^{1/3}$)	Damage percentage (%)
Chuanshan limestone	0.15	95.1
	0.30	97.1
	0.60	86.5
	1.20	33.9
Gaolishan sandstone	0.15	99.6
	0.30	99.9
	0.60	95.4
	1.20	75.5
Mineralized limestone	0.15	92.1
	0.30	92.4
	0.60	82.6
	1.20	25.7
Xixia limestone	0.15	97.5
	0.30	97.7
	0.60	90.1
	1.20	47.1

the increase of scaled distance, the probability density of eps = 0 increases significantly. As a result, the number of damaged elements, and the damaged degree decreases with the increase of scaled distance. As for the mineralized limestone and Xixia limestone panels, they behave like the Chuanshan limestone, as shown in Figures 6(c) and 6(d). In fact, the above conclusions can be supported by the average eps of each rock panel. For example, under the scaled distance of 0.15 m/kg$^{1/3}$, 0.30 m/kg$^{1/3}$, 0.60 m/kg$^{1/3}$, 1.20 m/kg$^{1/3}$: (a) the average eps values of the Chuanshan limestone panels are 0.0192, 0.0224, 0.0132, and 0.0037, respectively; (b) the average eps values of the Gaolishan sandstone panels are 0.0472, 0.0471, 0.0320, and 0.0094, respectively; (c) the average eps of the mineralized limestone panels are 0.0152, 0.0181, 0.0104, and 0.0028, respectively; and (d) the average eps of the Xixia limestone panels are 0.0232, 0.0268, 0.0154,

and 0.00429, respectively. In addition, the percentage of damage elements in the rock panels subjected to the blast loadings with different scaled distances are compared in Table 2. It can be seen from Table 2 that the damage percentage shows the same trend as the probability density value illustrated in Figure 6.

4. Conclusions

In this study, the dynamic performance of four types of rock panels (e.g., Chuanshan limestone, Gaolishan sandstone, Mineralized limestone and Xixia limestone) subjected the explosive action with four scaled distances (0.15 m/kg$^{1/3}$, 0.30 m/kg$^{1/3}$, 0.60 m/kg$^{1/3}$, 1.20 m/kg$^{1/3}$) is investigated with the finite element tool. Mohr-Coulomb criterion is used to describe the mechanical behaviour of rock panels, and its

input parameters are determined by the triaxial compression tests with confining pressures between 0 MPa and 20 MPa. The damage, which is represented by the effective plastic strain, induced by the explosive action is qualitatively and quantitively analyzed. The simulation results demonstrate that the effect of scaled distance on the damage distribution of rock panels is material dependent. The Gaolishan sandstone is damaged most severely, followed by the Xixia limestone, Chuanshan limestone, and mineralized limestone for a given scaled distance. Whether the increase of scaled distance leading to a smaller damage degree depends on the rock type. In general, there is a critical scaled distance for most of rocks, e.g., $0.30 \, \text{m/kg}^{1/3}$ in this study. Below this critical value, the scaled distance has a negative impact on the damage degree of rock, but the larger scaled distance leads to a lower damage degree after exceeding this critical value. However, such a critical scaled distance is not observed in the Gaolishan sandstone panels, as the damage induced by explosive action decrease apparently with increasing the scaled distance. The modelling highlights that the blast design and support schemes need to be adjusted when conducting excavation activities in different rock mass, even though these rock masses locate in the same sublevel. In the future study, the heterogeneity rate-dependency of rock's material property need to be taken into account in the blast modelling.

Data Availability

The [DATA TYPE] data used to support the findings of this study are included within the article.

Conflicts of Interest

The authors declare that they have no conflicts of interest.

Acknowledgments

References

[1] S. P. Alavinezhad and H. Shahir, "Determination of Apparent Earth Pressure Diagram for Anchored walls in C–φ Soil with Surcharge," *World Journal of Engineering*, vol. 17, 2020.

[2] Z. Guo, J. Qiu, H. Jiang, J. Xing, X. Sun, and Z. Ma, "Flowability of ultrafine-tailings cemented paste backfill incorporating superplasticizer: insight from water film thickness theory," *Powder Technology*, vol. 381, pp. 509–517, 2021.

[3] P. C. Mishra and M. K. Mohanty, "A Review of Factors Affecting Mining Operation," *World Journal of Engineering*, vol. 17, 2020.

[4] Q. B. Zhang and J. Zhao, "Determination of mechanical properties and full-field strain measurements of rock material under dynamic loads," *International Journal of Rock Mechanics and Mining Sciences*, vol. 60, pp. 423–439, 2013.

[5] W. C. Maurer and J. S. Rinehart, "Impact crater formation in rock," *Journal of Applied Physics*, vol. 31, no. 7, pp. 1247–1252, 1960.

[6] L. Y. Chi, Z. X. Zhang, A. Aalberg, J. Yang, and C. C. Li, "Fracture processes in granite blocks under blast loading," *Rock Mechanics and Rock Engineering*, vol. 52, no. 3, pp. 853–868, 2019.

[7] B. O. Falodun and A. J. Omowaye, "Double-diffusive MHD Convective Flow of Heat and Mass Transfer over a Stretching Sheet Embedded in a Thermally-Stratified Porous Medium," *World Journal of Engineering*, vol. 16, 2019.

[8] A. Khennouf and M. Baheddi, "Bearing Capacity of a Square Shallow Foundation on Swelling Soil Using a Numerical Approach," *World Journal of Engineering*, 2021.

[9] H. Venkatesan and S. Sivamani, "Numerical and Experimental Study of the Combustion Phenomenon when the Compression Ignition Is Fuelled with mineral Diesel," *World Journal of Engineering*, vol. 16, 2019.

[10] M. Dhahri and H. Aouinet, "CFD Investigation of Temperature Distribution, Air Flow Pattern and thermal comfort in Natural Ventilation of Building Using Solar Chimney," *World Journal of Engineering*, vol. 17, 2020.

[11] F. Boussem, A. Belounar, and L. Belounar, "Assumed Strain Finite Element for Natural Frequencies of Bending Plates," *World Journal of Engineering*, 2021.

[12] S. Khalid, F. Khan, Z. Ahmad, and B. Ullah, "Design and Finite Element Analysis of Modular C-Core Stator Tubular Linear Oscillating Actuator for Miniature Compressor," *World Journal of Engineering*, 2021.

[13] A. H. Madadi-Najafabadi and A. Masoumi, "A Study of Rock Ladder Structure Used in Buffer Storage of Iron Ore Pellets: DEM Simulation and Analytical Model," *World Journal of Engineering*, vol. 17, 2020.

[14] L. X. Xie, W. B. Lu, Q. B. Zhang, Q. H. Jiang, G. H. Wang, and J. Zhao, "Damage evolution mechanisms of rock in deep tunnels induced by cut blasting," *Tunnelling and Underground Space Technology*, vol. 58, pp. 257–270, 2016.

[15] L. An, F. T. Suorineni, S. Xu, Y.-H. Li, and Z.-C. Wang, "A feasibility study on confinement effect on blasting performance in narrow vein mining through numerical modelling," *International Journal of Rock Mechanics and Mining Sciences*, vol. 112, pp. 84–94, 2018.

[16] T. Saksala and A. Ibrahimbegovic, "Thermal shock weakening of granite rock under dynamic loading: 3D numerical modeling based on embedded discontinuity finite elements," *International Journal for Numerical and Analytical Methods in Geomechanics*, vol. 44, no. 13, pp. 1788–1811, 2020.

[17] Y. Zhao, G.-F. Zhao, Y. Jiang, D. Elsworth, and Y. Huang, "Effects of bedding on the dynamic indirect tensile strength of coal: laboratory experiments and numerical simulation," *International Journal of Coal Geology*, vol. 132, pp. 81–93, 2014.

[18] R. K. A. A. Rub, "Thermodynamic framework for coupling of elasto-viscoplasticity and nonlocal anisotropic damage for microelectronics solder alloys," *International Journal of Materials and Structural Integrity*, vol. 2, no. 1/2, pp. 106–137, 2008.

[19] R. K. Abu Al-Rub, D.-W. Lee, K. A. Khan, and A. N. Palazotto, "Effective anisotropic elastic and plastic yield properties of periodic foams derived from triply periodic schoen's I-wp minimal surface," *Journal of Engineering Mechanics*, vol. 146, no. 5, Article ID 04020030, 2020.

[20] A. Glema, T. Łodygowski, W. Sumelka, and P. Perzyna, "The numerical analysis of the intrinsic anisotropic microdamage evolution in elasto-viscoplastic solids," *International Journal of Damage Mechanics*, vol. 18, no. 3, pp. 205–231, 2009.

[21] J.-W. W. Ju, J.-L. Chaboche, and G. Z. Voyiadjis, *Damage Mechanics in Engineering Materials*, Elsevier, Amsterdam, Netherlands, 1998.

[22] M. Mukherjee, G. D. Nguyen, A. Mir et al., "Capturing pressure- and rate-dependent behaviour of rocks using a new damage-plasticity model," *International Journal of Impact Engineering*, vol. 110, pp. 208–218, 2017.

[23] T. Saksala, M. Hokka, and V.-T. Kuokkala, "Numerical 3D modeling of the effects of strain rate and confining pressure on the compressive behavior of Kuru granite," *Computers and Geotechnics*, vol. 88, pp. 1–8, 2017.

[24] W. Sumelka, M. Nowak, A. A. Nassr et al., "Dynamic failure of the aluminium plate under air-blast loading in the framework of the fractional viscoplasticity model - theory and validation," *International Journal of Impact Engineering*, vol. 158, Article ID 104024, 2021.

[25] L. Yang, G. Wang, G.-F. Zhao, and L. Shen, "A rate- and pressure-dependent damage-plasticity constitutive model for rock," *International Journal of Rock Mechanics and Mining Sciences*, vol. 133, Article ID 104394, 2020.

[26] S. R. Krishna and N. S. K. Ch, "Analytical Modelling of Ultra-thin white Topping Cement concrete Overlay on Bituminous concrete Pavement Using ANSYS," *World Journal of Engineering*, 2022.

[27] J. Zhao, "Applicability of Mohr-Coulomb and Hoek-Brown strength criteria to the dynamic strength of brittle rock," *International Journal of Rock Mechanics and Mining Sciences*, vol. 37, no. 7, pp. 1115–1121, 2000.

[28] Dyna-LS, *Manual, I. Volume, Version 971*, Livermore Software Technology Corporation, Livermore, California, 2007.

[29] R. Castedo, P. Segarra, A. Alañon, L. M. Lopez, A. P. Santos, and J. A. Sanchidrian, "Air blast resistance of full-scale slabs with different compositions: numerical modeling and field validation," *International Journal of Impact Engineering*, vol. 86, pp. 145–156, 2015.

[30] X. Lin, Y. Zhang, and P. J. Hazell, "Modelling the response of reinforced concrete panels under blast loading," *Materials & Design*, vol. 56, pp. 620–628, 2014.

[31] D.-K. Thai and S.-E. Kim, "Numerical investigation of the damage of RC members subjected to blast loading," *Engineering Failure Analysis*, vol. 92, pp. 350–367, 2018.

Research Article

Analysis of Structural Characteristics of Underground Cavern Group by Simulating All Cavern Excavation

Shaopei Hu [ID],[1] **Chao Su** [ID],[1] **Heng Zhang** [ID],[1] **Enhua Cao**,[1] **Rongyao Yuan** [ID],[1] **and Yunquan Xu**[2]

[1]*College of Water Conservancy and Hydropower Engineering, Hohai University, Nanjing 210098, China*
[2]*PowerChina Kunming Engineering Corporation Limited, Kunming 650000, China*

Correspondence should be addressed to Chao Su; csu_hhu@126.com

The traditional Three-dimensional (3D) model for stability analysis of a large underground cavern group only includes the main powerhouse, the main transformer chamber, the tailrace surge tank, the main electrical wire hall, and part of the diversion tunnel and tailwater tunnel. Other caverns excavation are not taken into consideration, which is inconsistent with the actual project. In this study, a 3D Finite Element Method (FEM) model, including all the cavities, and a 3D simplified model containing only part of the cavities were established based on the actual underground cavern group project. We study the structural characteristics of the cavern group during excavation via 3D nonlinear FEM. At the same time, three numerical calculation schemes are designed for comparison. The results show that the simulated distributions of the stress field, deformation field, and plastic zone of the two numerical models are similar, but the magnitudes of the 3D FEM model, which considers all caverns are generally higher than the simplified model. The difference between the two simulated horizontal displacements of the main powerhouse reaches 53.72%. Therefore, from the perspective of engineering safety and actual construction, it is advisable to adopt the 3D FEM model, including all the cavities, when conducting a simulation analysis of the underground cavern group.

1. Introduction

Hydroelectric power which is an environmentally friendly, cheap, and safe way to obtain electricity can meet the growing electricity demand [1]. Water energy resources are mostly distributed in high mountains and valleys, not suitable for constructing ground buildings. In order to avoid adverse topographic, geological, and climatic factors on the surface, engineers often choose to construct underground powerhouse for the hydropower station. The underground powerhouse is generally composed of large or super-large caverns [2, 3]. A huge underground cavern group's construction process is more complicated than that of a single cavern group due to the mutual influence of several caverns in the cavern group. However, the construction of an extensive underground cavern process is time consuming. Excavation will result in the redistribution of stress in the cavern. The stress field change around the cavern may lead to

the deformation and instability of surrounding rock and rock collapse, which presents a significant threat to the structure, construction equipment and may cause the loss of life and property [4–6]. Therefore, during the excavation of underground caverns of hydropower stations, the stability of the surrounding rocks has always been the focus of the engineering and academic circles.

Many researchers have looked at the stability of the rock that surrounds underground caverns. One of the main reasons for the deformation of the surrounding rock is the ground stress. Before the excavation of the cavern, the rock and soil are generally in a state of natural stress balance, which is called the primary stress state or initial stress state (including self-weight stress and tectonic stress). After the cavern is excavated, the surrounding rock loses its original support and expands into the cavern space [7–9]. Zhang and Wang determined the damage characteristics of deeply buried caverns and the stress distribution characteristics of

the cavern perimeter under different ground stress conditions by numerical model tests [10]. Ma and Zhang discussed the effects of high ground stress, deep unloading and construction processes under complex geological conditions. The comprehensive method combining experiment and simulation reveals law of deformation and failure of surrounding rock of large underground caverns [11]. Dai and Li et al. used a high-resolution micro-seismic monitoring system to assess the stability of underground powerhouses, and developed a comprehensive analysis method that can determine the damaged area and predict the macroscopic deformation of the surrounding rock of the underground powerhouse [12].

Under the action of high initial in-situ stress and excavation unloading of caverns, deep rock masses exhibit unique mechanical behaviors, such as ductility-brittle transition of rock mass, zonal cracking of surrounding rocks, accumulation and sudden release of deformation energy, brittle failure of unloading and so on [13–15]. Li and Wang et al. used the displacement of key points on the sidewall, the volume of the plastic zone and the volume of the crack to characterize the stability of the underground cavern. The optimal layout of underground caverns under different in-situ stress conditions and a modified formula for predicting sidewall displacement are proposed [16]. Zhang and Wang et al. proposed using index of damage degree to describe the Excavation damaged zone (EDZ) via the test results of 38 sets of drilling holes on the high side wall of the main powerhouse [17].

The evaluation of surrounding rock stability is an important research content, reflecting the stability degree of surrounding rock in the process of underground excavation and support and the comprehensive indexes of geological composition, environmental conditions, and engineering factors [18, 19]. Ren and Xu proposed a surrounding rock stability evaluation method that can analyze the deformation stability of surrounding rock and predict the collapse of a rock block quickly by combining DSPEM and RPPMCHE CWIS [20].

For the underground powerhouse of a hydropower station, the layout of the cavern group plays an important role in improving the stability of the surrounding rock of the cavern. Nowadays, great attention has been paid to the selection of the longitudinal axis of the cavern and the distance between the caverns in the design. Researches on the reasonable excavation process, support timing, support strength of the giant underground cavern group and related design theories have become major problems [21, 22]. Using the advantages of PSO and SVM algorithms, Jiang and Su et al. devised an intelligent optimization system for cavern excavation. This approach efficiently reduces the overall volume of the plastic zone and brittle failure of the surrounding rock, according to numerical simulation study [23].

Most of the underground caverns are located in deep canyons. Their geological conditions and geological structures are very complex, including various faults, joints, and weak interlayers [24, 25]. Duan and Feng et al. took the impact of weak interlayers into consideration and proposed

an in-situ observation scheme based on geological monitoring data, revealing the development and failure mechanism of the rock mass failure process [26]. Hao and Azzam used numerical methods (UDEC) to establish induced plastic zones and evaluated the influence of faults on the failure and deformation behavior of rock masses around large underground caverns [27].

In the past, people believed that earthquakes did not damage underground facilities as severely as ground structures. Until the Kobe earthquake in the 1990s, little attention was paid to seismic research on underground facilities [28]. The Daikai subway station was the first urban underground building to be destroyed by seismic forces rather than ground instability [29]. Wang and Chen et al. investigated the seismic response of a huge underground powerhouse's lining structure and suggested an explicit dynamic contact analysis method that took into account the surrounding rock's bonding and damage characteristics as well as the lining interface [30]. Yang and Lu et al. used time-energy density analysis, amplitude spectrum analysis, and finite impulse response (FIR) digital filter methods, and pointed out that the low-frequency components in microseismic records were mainly caused by the instantaneous release of in-situ stress. The high frequency components are mainly caused by explosions [31].

Facts have proved that as the depth increases, the original stress will show a linear or nonlinear increase [32, 33]. The original ground stress caused by the overburden, site conditions, and excavation operations may lead to stress concentration, which can lead to cracks and damage [34, 35]. Rockburst hazards can cause significant damage to the foundation of structures and equipment, and may threaten the safety of workers [36, 37]. Fraadonbeh et al. used two self-organizing maps (SOM) and fuzzy c-means (FCM) robust clustering techniques to explore the relationship between rockburst related parameters [38].

Most of these studies on the stability of underground caverns use three-dimensional simplified models that include the main powerhouse, main transformation chamber, busbar tunnel, some diversion tunnels and tailrace tunnels, or only three main caverns, without considering the impact of the excavation of other caverns on stability.

This paper takes an underground cavern of a hydropower station as the research object, establishes a three-dimensional finite element model including all caverns. And studies the distribution of deformation, stress and plastic zone of the surrounding rock during the excavation of the cavern group. By comparing the calculation results with commonly used three-dimensional simplified models, the influence of different calculation models on the calculation results is analyzed.

2. Project Profile

The underground powerhouse system of an individual project adopts a tail layout, which contains the main and auxiliary powerhouse, the main transformer chamber, the main electrical wire hall, the main transformer transport tunnel, etc (see Figure 1). With an axial direction of N80°W,
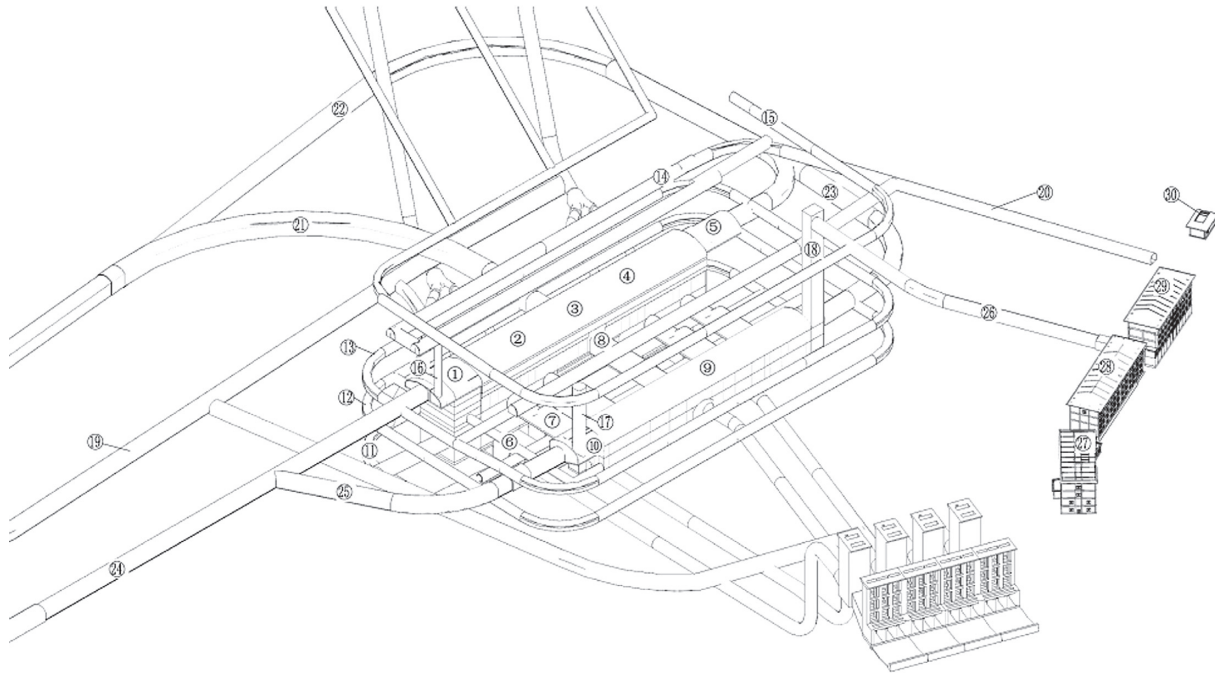
Figure 1: General layout drawing of underground powerhouse cavern group. Remarks: 1. The auxiliary powerhouse; 2, 4. The main powerhouse; 3. The installation room; 9. The main transformer chamber.

the main powerhouse is 169.00 m long, 25.40 m wide, and 54.425 m high. The auxiliary plant is on the right side of the main plant, and the installation space is between Unit 2 and Unit 3. The main transformer chamber is 139.40 m long, 20.20 m wide, and 21.20 m high. It runs parallel to the main powerhouse and is situated on the downstream side of it. The cutway drawing of Unit 4 is shown in Figure 2.

3. Calculation Model and Excavation Scheme

3.1. Numerical Model. A schematic diagram of the full cavern model's (R1) numerical calculation area is shown in Figure 3(a). The orientations of the three coordinate axes are as follows: the X-axis is the direction of the main plant, the direction pointing to the auxiliary plant is positive; the direction perpendicular to the axis of the main plant is the Y-axis, the direction pointing to the main transformation room is positive; the vertical direction is the Z-axis, and upward is positive. The origin is taken at the main center of Unit 1, with an elevation of 451.9 m. The numerical calculation area is 1320 m on the X-axis, 715 m on the Y-axis, and 718 m on the Z-axis. The calculation area includes the main plant, main transformer room, bus tunnel, main transformer transportation tunnel, connection corridor, blower room, exhaust fan room, access tunnel, main power plant delivery, exhaust tunnel, main transformer room delivery, and exhaust tunnel, Diversion tunnel, tailrace tunnel, high-voltage cable flat tunnel, high-voltage cable shaft, maintenance drainage gallery, exhaust shaft, construction branch tunnels 3, 4, 5, and 6, roof anchoring tunnels, and surrounding main powerhouses and main transformer rooms The outer three layers of drainage and anchoring holes while considering the geological structure of the plant area. A total of 649,612 gird

nodes and 3,802,630 eight-node isoparametric elements are used in the 3D computational model (see Figure 3(b)).

The boundary conditions of the model during calculation: the normal displacement is constrained on the $\pm X$ surface of the mountain model, the normal displacement is constrained on the $\pm Y$ surface, $+Z$ (surface) is the free boundary, and the $-Z$ surface is constrained in X, Y, and Z displacements.

A schematic diagram of the Simplified model's (R2) numerical calculation area is shown in Figure 4(a). The orientations of the three coordinate axes are as follows: the X-axis is the direction of the main plant, the direction pointing to the auxiliary plant is positive; the direction perpendicular to the axis of the main plant is the Y-axis, the direction pointing to the main transformation room is positive; the vertical direction is the Z-axis, and upward is positive. The origin is taken at the main center of Unit 1, with an elevation of 451.9 m. The numerical calculation area is 669 m on the X-axis, 550 m on the Y-axis, and 567 m on the Z-axis. The calculation area includes the main powerhouse, main transformer room, four bus tunnels, one main transformer transportation tunnel, one connection corridor, four water diversion tunnels, four tailrace tunnels, collection wells, and the machine room and shaft connected to the powerhouse And part of the access tunnels, wind tunnels, ventilation, and safety tunnels, and also consider the geological structure of the plant area. A total of 102,542 gird nodes and 594,312 eight-node isoparametric elements are used in the 3D computational model (see Figure 4(b)).

The boundary conditions of the model during calculation: the normal displacement is constrained on the $\pm X$ surface of the mountain model, the normal displacement is constrained on the $\pm Y$ surface, $+Z$ (surface) is the free
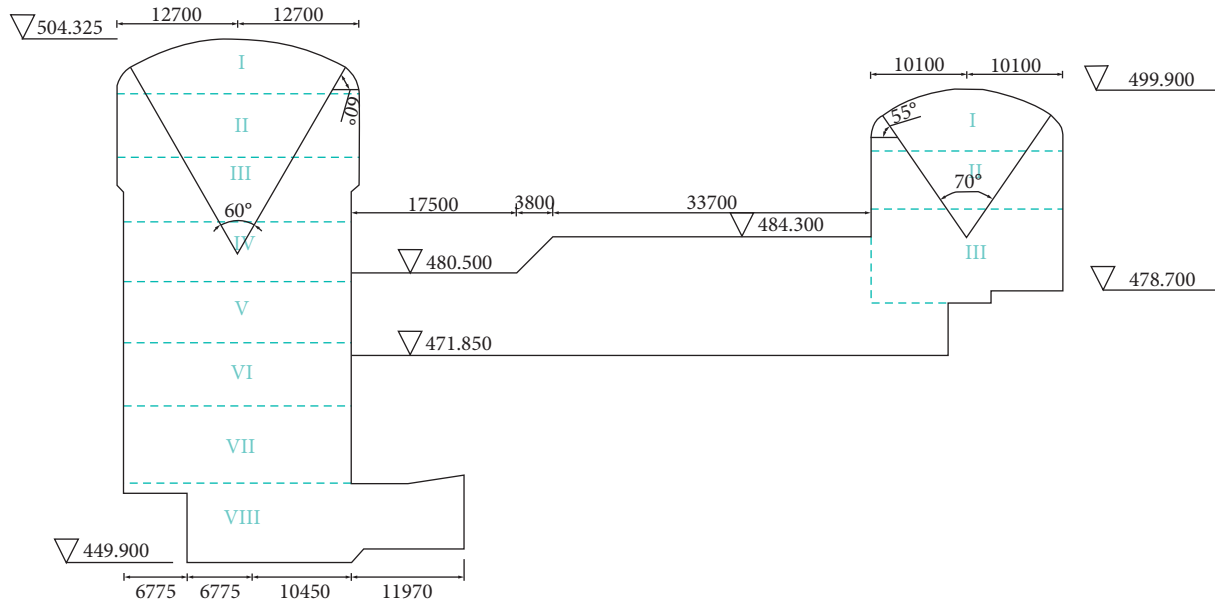
FIGURE 2: The cutway drawing of the Unit 4.

boundary, and the −Z surface is constrained in X, Y, and Z displacements.

3.2. The Modeling Details

3.2.1. Parameter Selection. The initial ground stress was obtained by using the Moore-Coulomb principal structure method. And according to the report of geological exploration, the rock mass is a medium bed~thick layered structure with good integrity. Class III surrounding rocks and class IV surrounding rocks, mainly argillaceous siltstone, account for about 75% and 25%. Table 1 shows the suggested values of the physical and mechanical parameters of surrounding rocks.

3.2.2. Simulation Scheme of Construction Method. According to the construction experience of large underground cavern group at home and abroad, combined with the structural characteristics of underground cavern mentioned in this paper, three excavation calculation schemes are designed for two FEM models.

Excavation calculation Scheme 1 (T1): Model R1, Considering all caverns excavation, each excavation step is shown in Figure 5 below:

Excavation calculation Scheme 2 (T2): Model R2, The main and auxiliary powerhouse, main transformer tunnel, bus tunnel, main transformer transportation tunnel and some diversion tunnel and tailrace tunnel are taken into account for excavation. The excavation chamber of each excavation step is shown in Figure 6 below:

Excavation calculation Scheme 3 (T3): Model R2, Considering the excavation of the main and auxiliary powerhouse and the main transformer chamber, the excavation chamber of each excavation step is shown in Figure 7 below:

4. Results

4.1. Characteristics of the Redistributed Stress after Excavation. Figures 8–10 shows the contour maps of the variation of maximum and minimum principal stress in surrounding rock of the characteristic section obtained after the completion of the three excavation schemes. After the cavern excavation, due to the existence of the initial stress field, the surrounding rock stress field is redistributed, which causes the radial stress of the cavern to be released and the tangential stress changes resulting in a tensile stress distribution around the cave.

The stress distribution of the three excavation schemes is similar. In the initial stage of excavation, the main tensile stress is distributed on the bottom plate because the high side wall is not formed. The top arch has good mechanical performance, and the bottom plate is equivalent to a flat beam, which is easy to be bent, so the maximum main tensile stress mostly occurs at the bottom plate. The high side wall is formed gradually with the excavation, the stress release degree near the side wall is increasing, and the maximum first principal stress is gradually transferred to the side wall. After the excavation of the underground powerhouse is completed, the range of the first principal stress of the cavern group are −5.24 to 0.77 MPa (T1), −5.08 to 0.56 MPa (T2) and −5.23 to 0.57 MPa (T3) respectively ("−" means compressive stress, "+" means tensile stress), and the compressive stress concentration areas are distributed in the downstream arch foot of the main plant, the intersection of the bottom plate and the upstream and downstream sidewalls, and the downstream arch foot of the main transformation chamber Place.

The compressive stress of the main powerhouse is concentrated at the intersection of the arch foot on the downstream side of the top arch and the upstream wall and the floor. The maximum values are −18.93 MPa, −15.13 MPa,
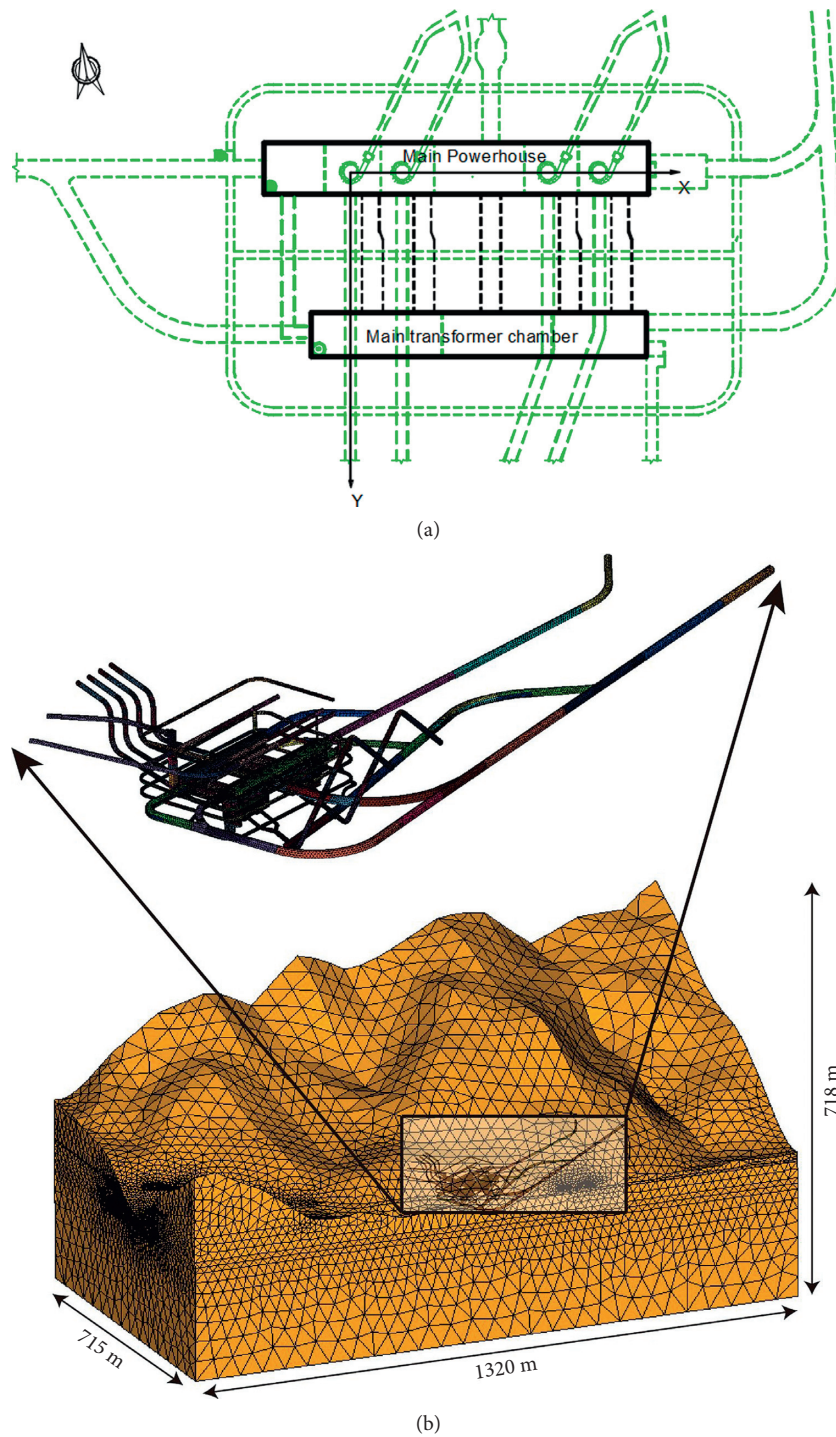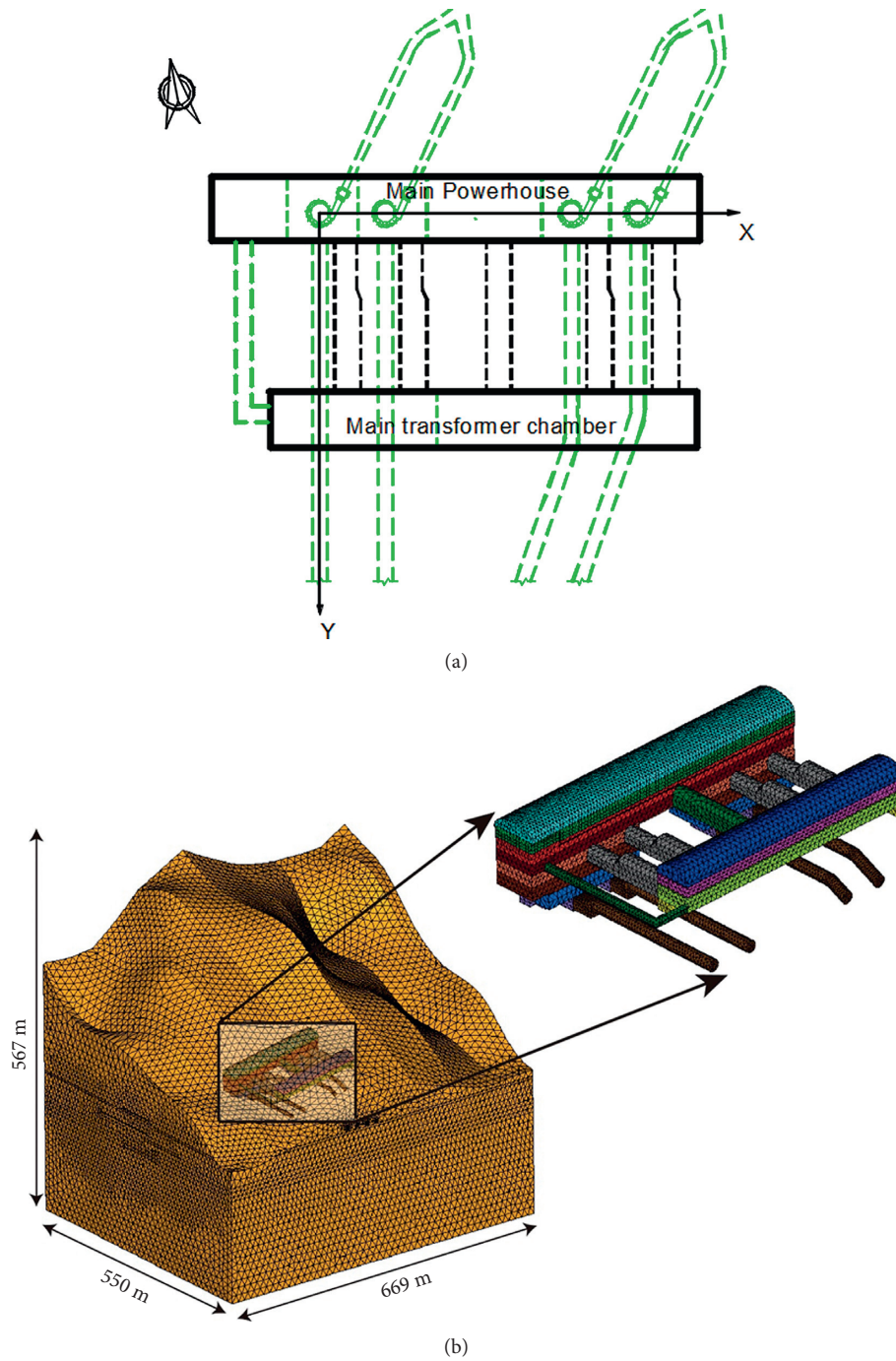
(a)

(b)

FIGURE 3: The computational model R1: (a) Calculation area and model coordinate system origin; and (b) the 3D computational grid model of the Underground powerhouse for excavation.

and −15.80 MPa respectively. Similarly, the compressive stress of the main transformer room is concentrated at the arch foot on the downstream side of the top arch, and attention should be paid to protection. During the entire excavation process, the principal compressive stress did not exceed the surrounding rock's compressive strength.

4.2. Characteristics of the Displacement Distribution after Excavation. Due to the release of in-situ stress, the surrounding rock produces spring back deformation, pointing to the cavern's interior. It shows that under the action of the initial ground stress field, each side surface caused by cavern excavation has a "centripetal" movement trend, and the

(a)

(b)

FIGURE 4: The computational model R2: (a) Calculation area and model coordinate system origin; and (b) the 3D computational grid model of the Underground powerhouse for excavation.

TABLE 1: Parameters of different models.

Type of surrounding rock	Lithology	ρ (kg/m3)	E (GPa)	ν	c (MPa)	φ ($\circ$)
Class III	Fine grain, medium-coarse sandstone	2550	7.5	0.23	0.95	46.4
Class IV	Conglomerate, siltstone	2500	5	0.26	0.5	35
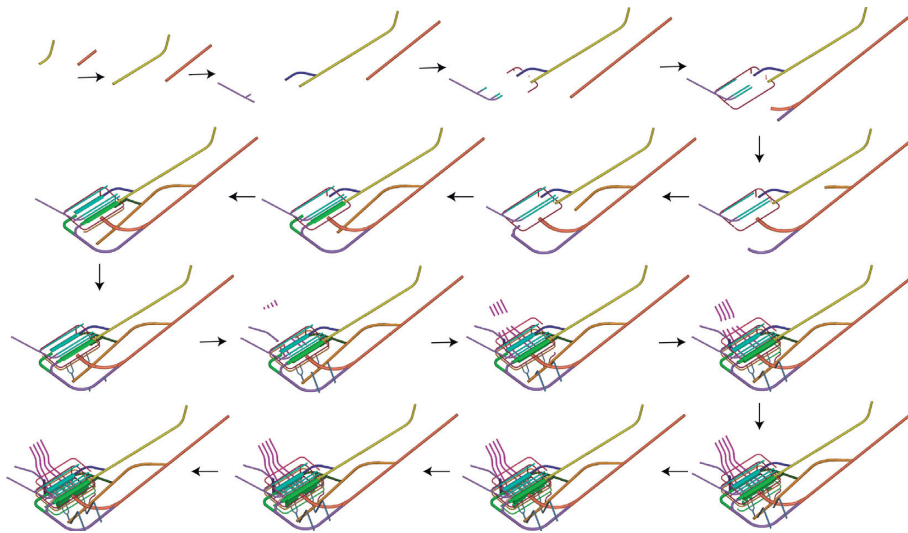
Figure 5: Schematic diagram of the excavation of each excavation step in Scheme T1.
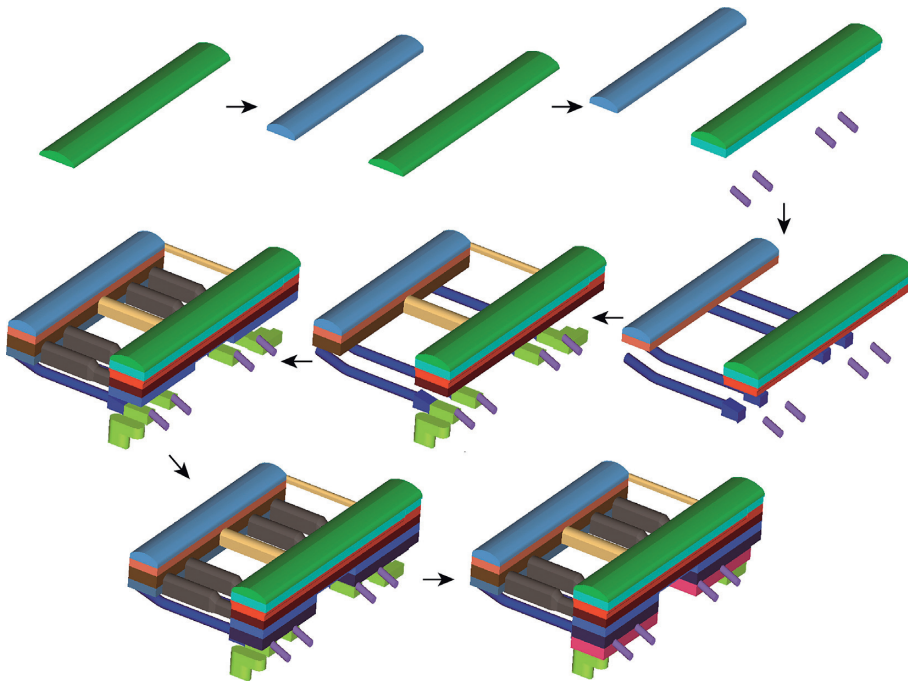
Figure 6: Schematic diagram of the excavation of each excavation step in Scheme T2.

release displacement of surrounding rock excavation attenuates as the distance from the excavation surface increases.

After the cavern excavation, the displacement of the main powerhouse in the roof arch is within the range of −14 to −32 mm. The maximum downward displacement of the top arch lead is 32 mm, and the upward rebound of the bottom plate lead is 39 mm. Simultaneously, the displacements of the upstream and downstream sidewalls of the main powerhouse are within the range of −12∼50 mm and −36∼10 mm (see Figure 11). After the end of the excavation, the maximum horizontal displacement (U2) of the upstream wall perpendicular to the factory building's axis is about

50 mm, which occurs in the upstream wall of the main factory building. The maximum horizontal displacement (U2) of the downstream wall perpendicular to the main factory building axis is about 36 mm, which occurs at the intersection of the bus hole and the main factory building. Moreover, the upstream side wall's deformation is significantly greater than that of the downstream sidewall.

Figure 12 shows the cumulative value of vertical displacement (U3) of the roof and horizontal displacement (U2) of the sidewall in the middle section of unit 4 of the main workshop during each excavation step. It serves to show that the cumulative value of the vertical displacement (settlement of the arch) (see "P1, P2") of the arch roof
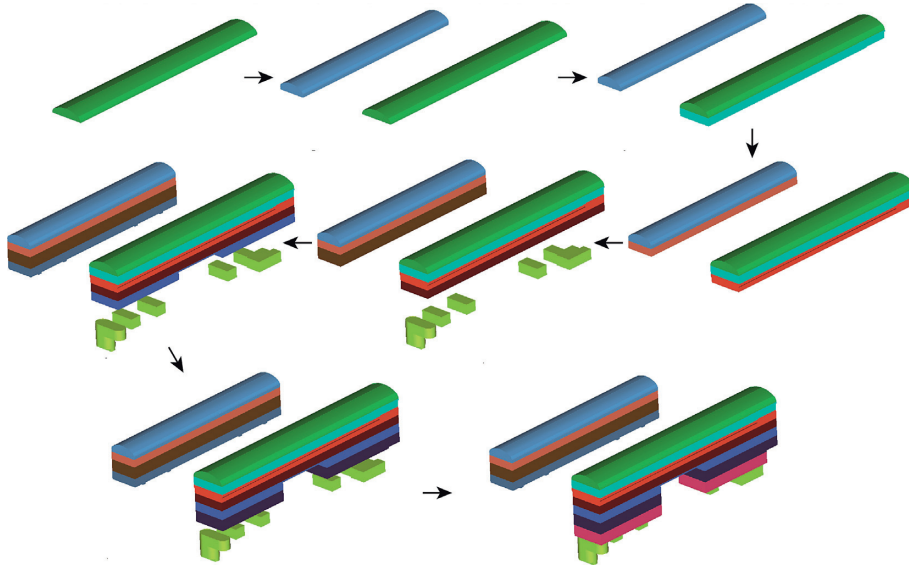
FIGURE 7: Schematic diagram of the excavation of each excavation step in Scheme T3.
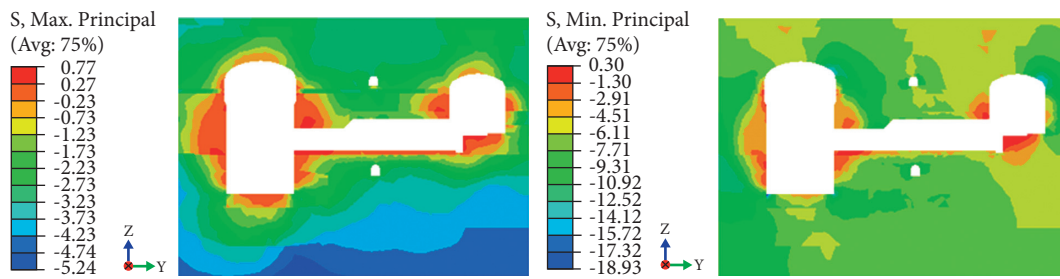

FIGURE 8: Surrounding rock principle stress cloud map (T1: No.4 Unit section) (unit: MPa).
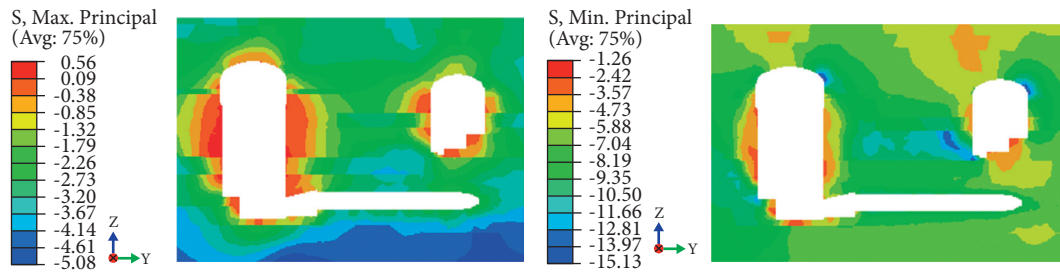

FIGURE 9: Surrounding rock principle stress cloud map (T2: No.4 Unit section) (unit: MPa).
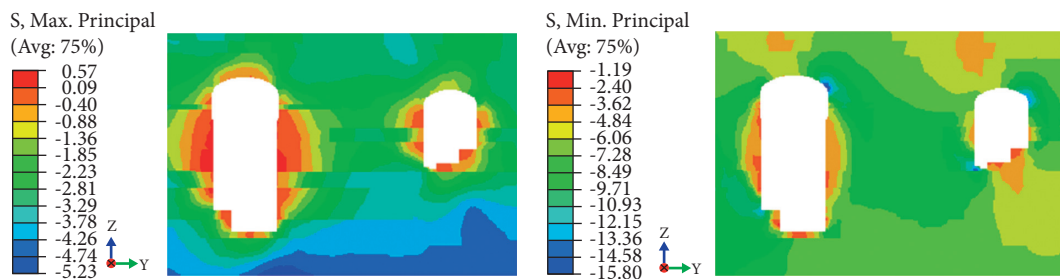

FIGURE 10: Surrounding rock principle stress cloud map (T3: No.4 Unit section) (unit: MPa).
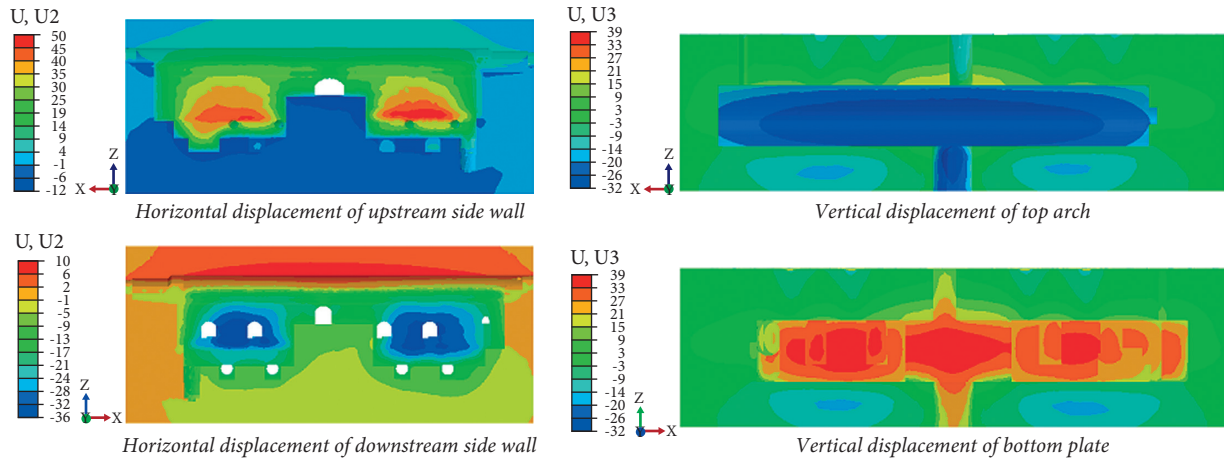
FIGURE 11: Deformation of the surrounding rock of the main powerhouse after excavation (T1: U2 represents *Y*-axial displacement; U3 represents *Z*-axial displacement) (unit: mm).
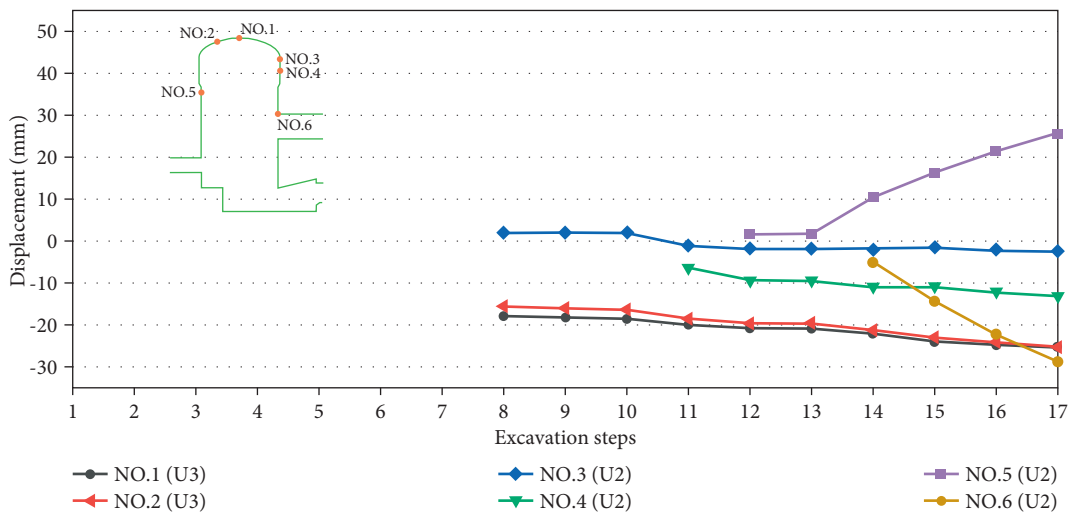
FIGURE 12: Deformation evolution of surrounding rock excavation of the Main Powerhouse. (T1).

continues to increase as the excavation progresses. From the simulation results of the entire 7-story excavation, it can be seen that the excavation of the first and second floors has the most significant impact on the vertical displacement of the vault center of the cavern. When the first layer is excavated, the vertical displacement of the vault will increase by about 17 mm. When the second layer is excavated, the top arch's vertical displacement is increased by about 3 mm. The subsequent excavation steps have little influence on the vertical displacement of the vault center. Each step from the third layer of excavation onwards has no more than 1 mm effect on the vault's vertical displacement. The impact of the vertical displacement of the top arch is gradually decreasing. As the height of the sidewall continues to increase, the horizontal displacement (U2) ("P3~P6") of the sidewall also increases. The numerical simulation results also show that the fourth and fifth floors' excavation will cause obvious deformation of the main building ("P5, P6" in Figure 12).

Like the main powerhouse excavation, each free face of the main transformer room has a "centripetal" movement. The top arch and bottom plate of the main transformer room are mainly plumb displacements. With the gradual increase of the displacement during the excavation, the top arch's vertical displacement after the excavation reaches 23 mm (see Figure 13). The main transformer room's lateral wall is mainly horizontal displacement (U2) perpendicular to the axis of the cave. As the excavation progresses, the lateral wall's height increases continuously, and the horizontal displacement of the lateral wall also increases continuously. After the main transformer chamber excavation, the horizontal displacement of upper and lower walls of the main transformer chamber is within the range of −23~32 mm. The deformation characteristics of the surrounding rock of the main transformer chamber, in which the deformation of the upstream side is greater than that of the downstream side, are near related to the "group tunnel effect" caused by the
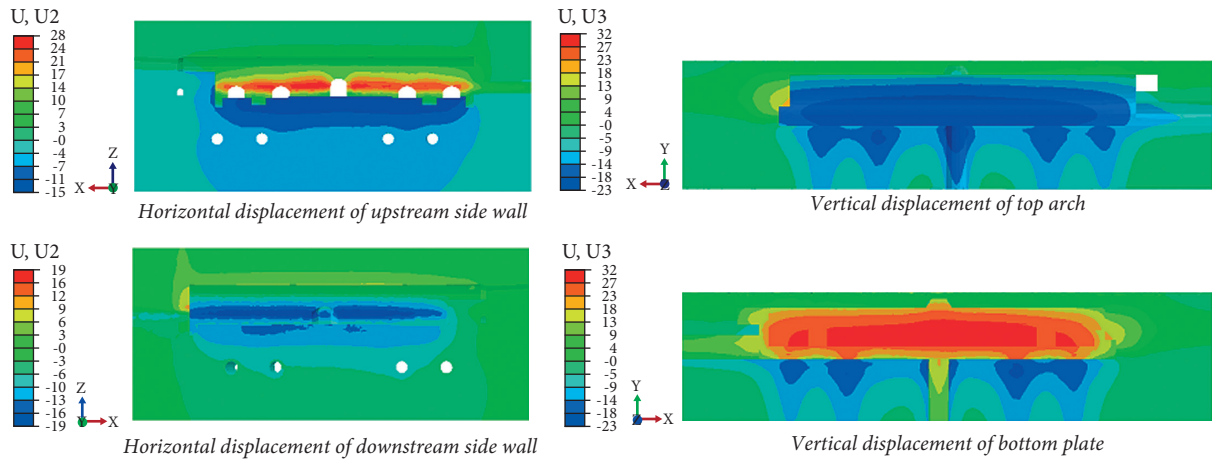
Figure 13: Deformation of the surrounding rock of the main transformer chamber after excavation (T1: U2 represents *Y*-axial displacement; U3 represents *Z*-axial displacement) (unit: mm).
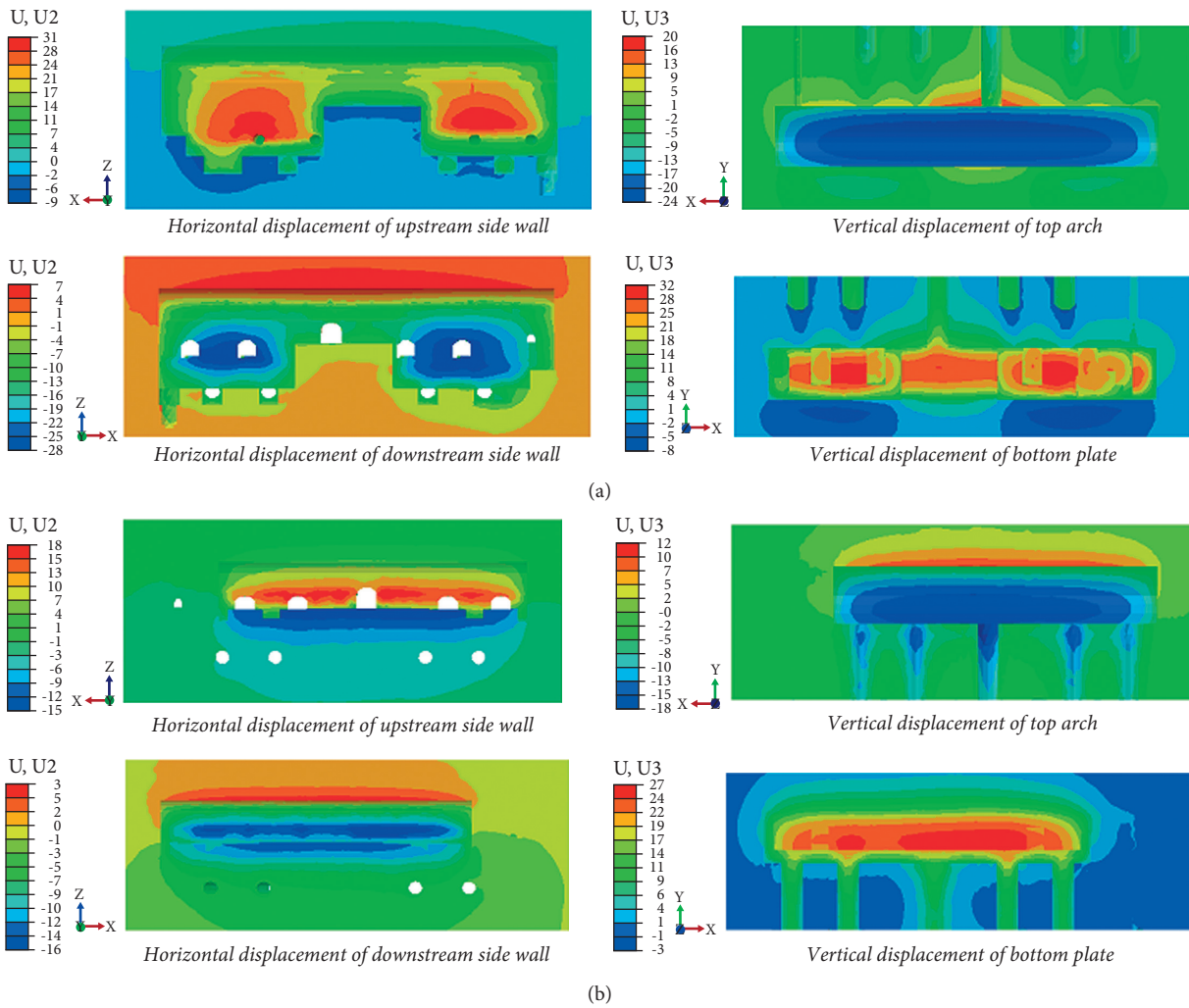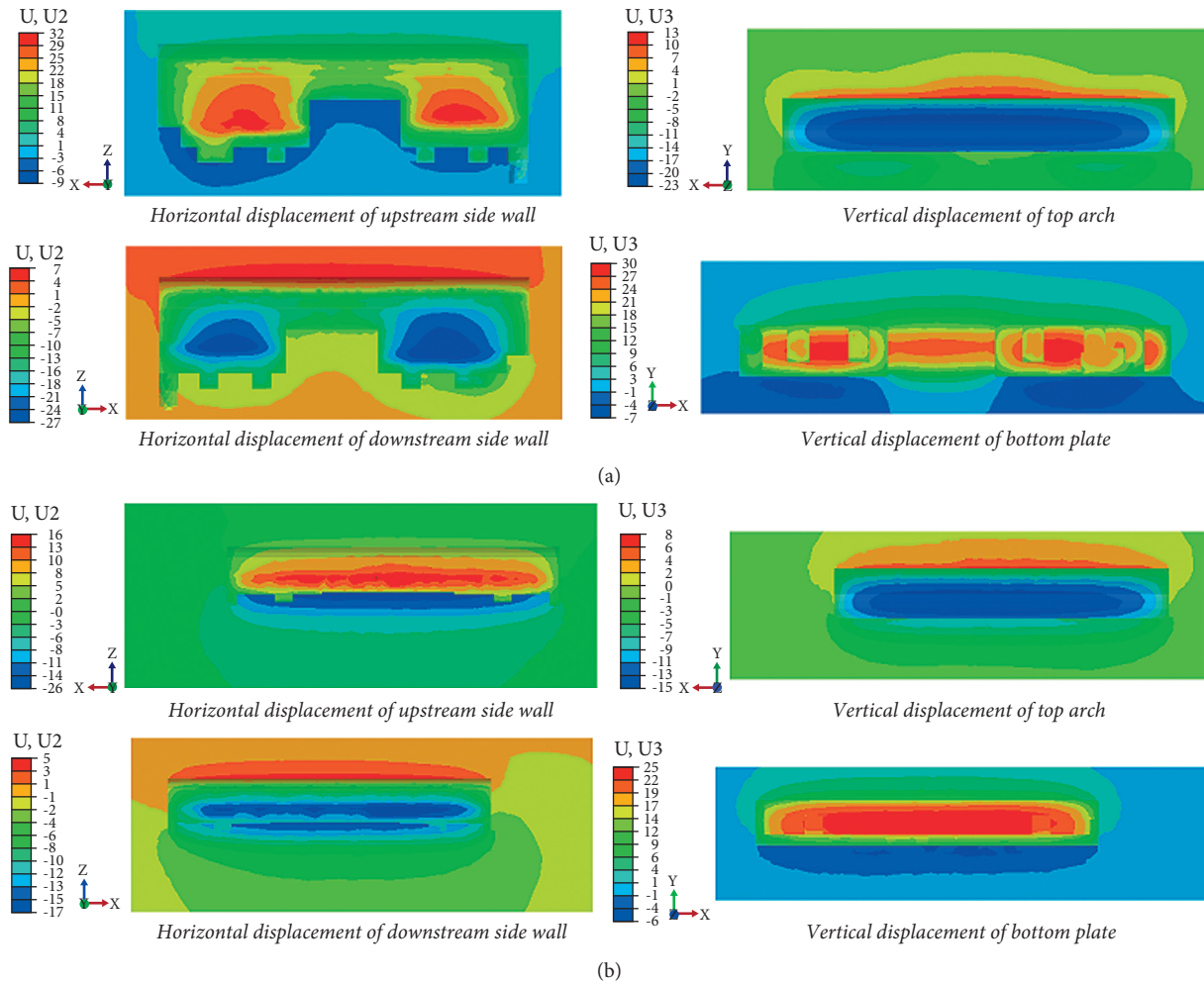

Figure 14: Deformation of the surrounding rock of (a) the main powerhouse and (b) the main transformer chamber after excavation (T2:U2 represents *Y*-axial displacement; U3 represents *Z*-axial displacement) (unit: mm).

FIGURE 15: Deformation of the surrounding rock of (a) the main powerhouse and (b) the main transformer chamber after excavation (T3:U2 represents Y-axial displacement; U3 represents Z-axial displacement) (unit: mm).

TABLE 2: Displacement Distribution around the underground caverns. (unit: mm).

Location		T1	T2	T3
The main powerhouse	Top of the arch	−26.23	−23.36	−20.67
	Upstream side wall	26.33	22.68	21.76
	Downstream side wall	−11.58	−10.35	−9.27
The main transformer chamber	Top of the arch	−16.52	−16.78	−14.56
	Upstream side wall	14.95	15.43	13.28
	Downstream side wall	−11.13	−14.32	−12.36

excavation of the adjacent cavern (main powerhouse and the main electrical wire hall).

Figures 14 and 15 are schematic diagrams of the surrounding displacement of the main powerhouse and the main transformer chamber of the underground cavern after the excavation of T1 and T2 is completed, respectively. Comparing Figures 11 and 13, it can be seen that the displacement change laws are roughly similar. Table 2 shows the displacement values around the hole after the excavation of the three excavation schemes.

4.3. Characteristics of the Plastic Zone Distribution after Excavation.
In the process of excavation, the plastic zone appears obvious, and the distribution of the plastic zone is local. The arch abutment of the main powerhouse appears
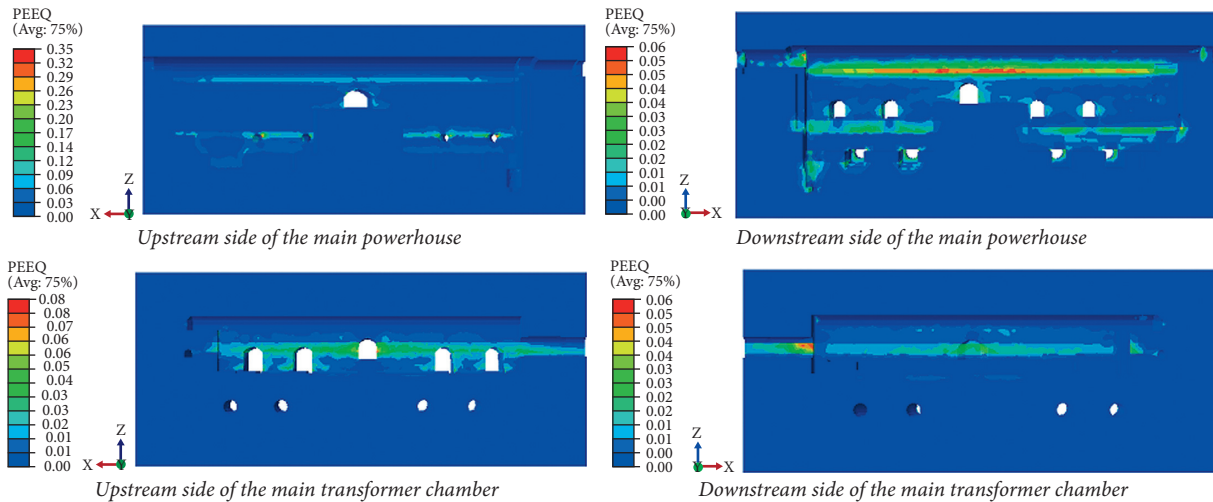
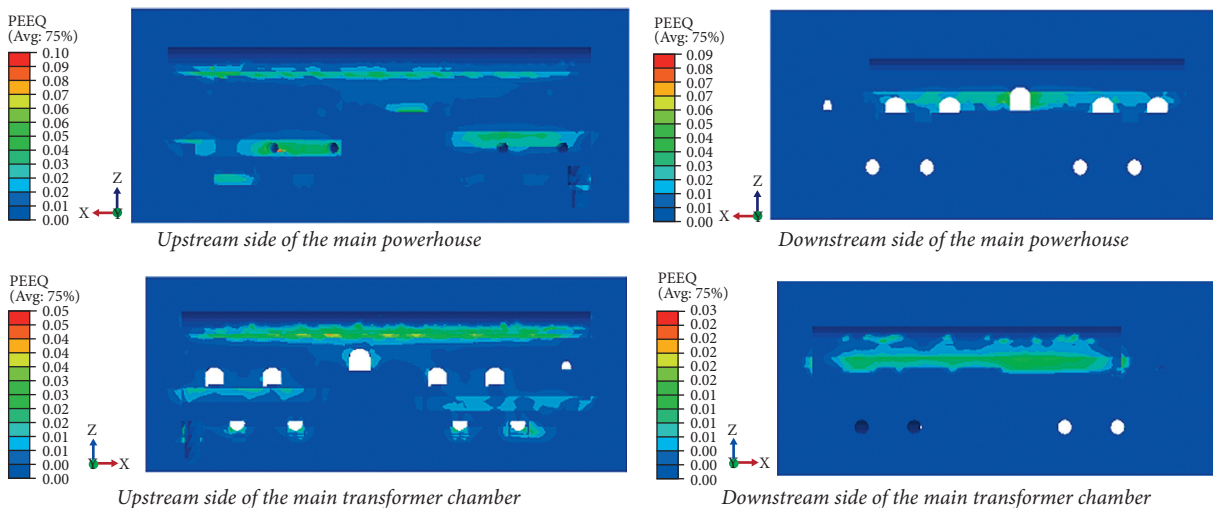FIGURE 16: Plastic zone of the surrounding rock of the caverns after excavation. (T1).

FIGURE 17: Plastic zone of the surrounding rock of the caverns after excavation. (T2).

plastic deformation first and spreads to the depth of surrounding rock with the main powerhouse's excavation. Figures 16–18 are schematic diagrams of the distribution of plastic zones in the upstream and downstream walls of the main powerhouse and the main transformer room after the excavation of the three excavation methods. Table 3 shows the failure depth of plastic zone after excavation.

With the main powerhouse excavation, plastic zones of different degrees appear at the intersection of the upper and lower sidewalls and each cave. It is mainly distributed in the upper and lower sidewalls of the sixth and seventh floors of the main powerhouse, main electrical wire hall, main transformer transportation tunnel, traffic cavity, the horizontal hole underwater diversion, and the intersection with the main powerhouse, and other positions with abrupt shape changes. The main transformer chamber's plastic zone is mainly distributed in the middle area of the sidewall, the roof arch of the main electrical wire hall, and the sidewall of the main transformer transportation tunnel. The plastic zone

distribution on the upstream side of the main transformer room is larger than that on the downstream side due to the excavation of the main electrical wire hall and the main transformer transportation tunnel on the upstream side. There is no plastic zone connecting the main powerhouse, the main transformer chamber, and the workshop's anchorage corridor.

4.4. Comparison of Three Excavation Calculation Schemes. Figure 19 shows the surrounding rock displacement cloud map of the workshop area completed by the cavern group's excavation. It can be seen that the excavation of the auxiliary caves and chambers will affect the deformation of the rock around the main chamber and form a large chamber group effect on the main chamber. The results show that T1, compared with T2 and T3, increases the X-direction displacement of surrounding rocks by 7.59% and 13.91%. The displacement along Y-direction increased by 53.72% and
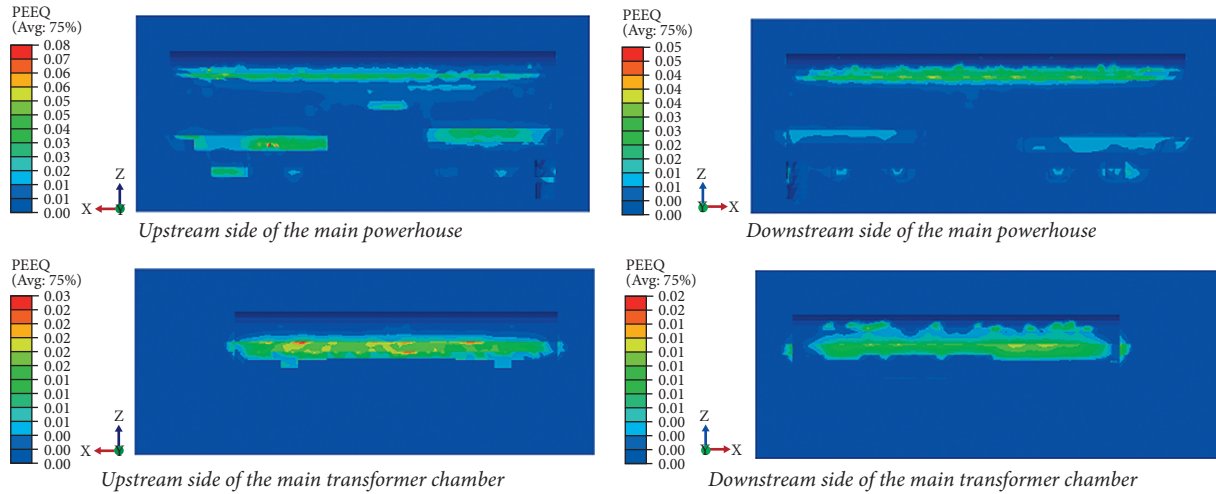
FIGURE 18: Plastic zone of the surrounding rock of the caverns after excavation. (T3).

TABLE 3: Depth of failure zone of surrounding rock. (unit: mm).

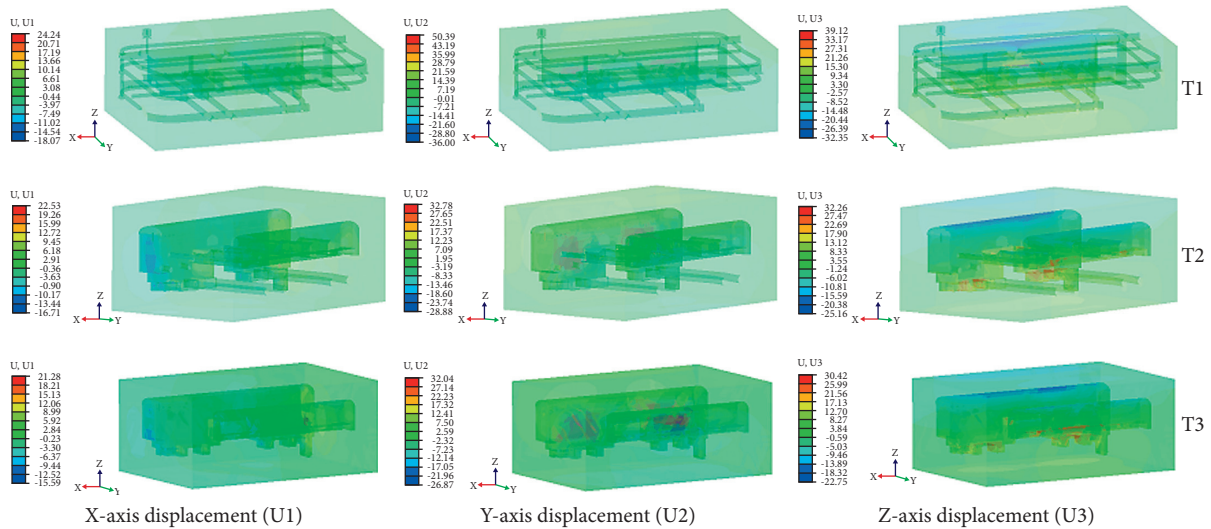| Location		T1	T2	T3
The main powerhouse	Upstream side wall	17.53	14.98	13.58
	Downstream side wall	6.08	5.03	3.86
The main transformer chamber	Upstream side wall	8.65	5.43	2.08
	Downstream side wall	0.52	0.48	0.36

FIGURE 19: Deformation of the surrounding rock of the underground caverns after excavation (unit: mm).

57.27%, respectively. The Z-direction displacement increased by 21.26% and 28.60%, respectively. It can be seen that the excavation of the surrounding cavity has the most significant influence on the Y-direction displacement, followed by the X-direction displacement and the Z-direction displacement. The excavation of all caverns will have a relatively obvious "group tunnel effect."

The contour graphs of the maximum and minimum principal stress changes in the surrounding rock after excavation for the three excavation construction options are shown in Figure 20. In the ABAQUS software, it is ruled that tension stress is complimentary, while pressure stress is negative; therefore, in the figure, S-Max represents the maximum principle stress, while S-Min represents the minimum principal stress.

All the three excavation methods can redistribute the stress of surrounding rock, and the stress is concentrated in the vault and bottom of the three caves. The maximum pressure stress induced by T2 and T3 is −22.20 MPa and −22.28 MPa, respectively, while the maximum pressure
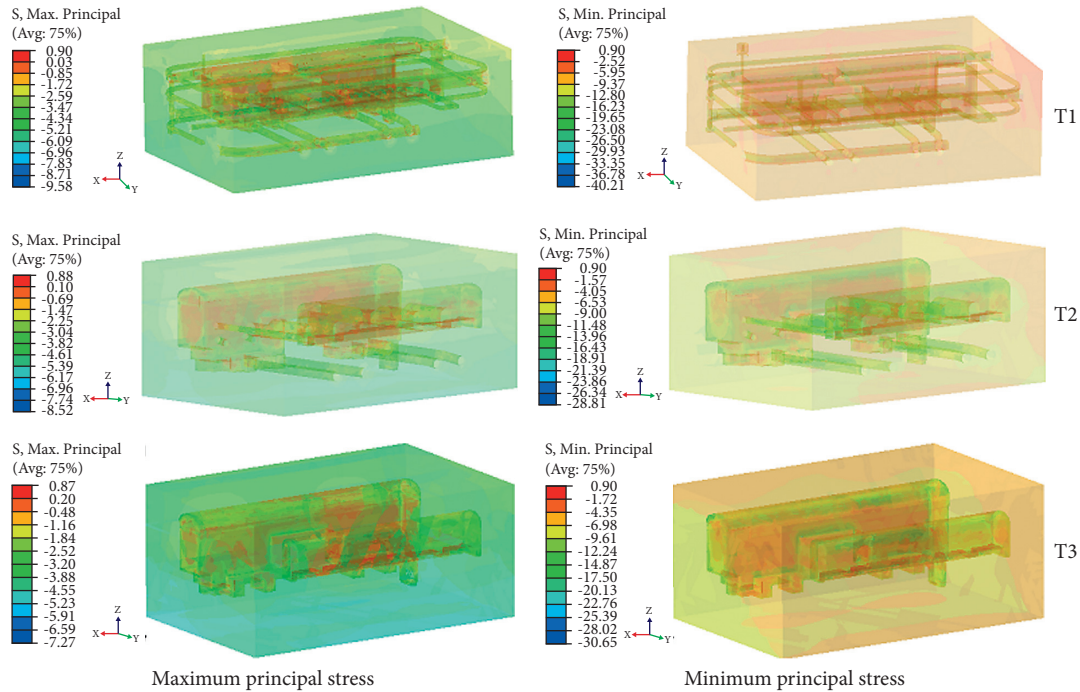
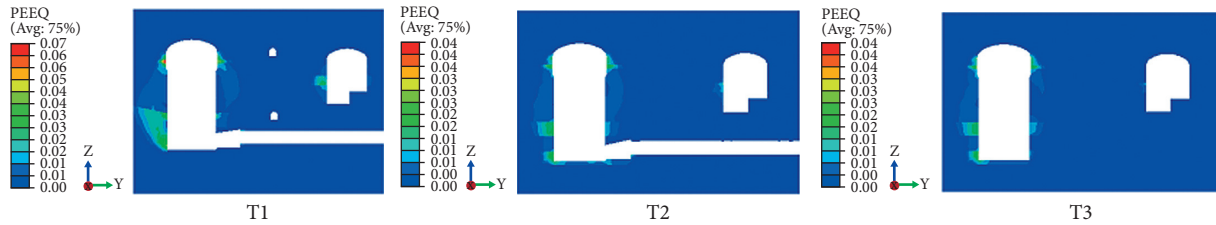FIGURE 20: Surrounding rock principle stress cloud map (unit: MPa).

FIGURE 21: Plastic zone of the surrounding rock at typical section of the caverns after excavation (No.4 Unit section).

stress induced by T1 is −40.21 MPa. They cause tensile stress zones in the surrounding rock, which are concentrated in the upper and lower sidewalls and end walls of the main workshop and main transformer room. T1 tensile stress was the highest at 0.90 MPa. Then T2, 0.88 MPa; The minimum stress provided by T3 is 0.87 MPa. The results show that the excavation of all caverns will affect the stress distribution and stress extreme value of the surrounding rock of the underground powerhouse.

Figure 21 for cavities completed the excavation after the workshop section typical cloud cave surrounding rock plastic zone distribution. Figure 14 shows the T1, T2, and T3 model of plastic zone distribution, plastic zone, mainly in the main factory building abutment, 6 and 7 of the main workshop layer of upstream and downstream of the upstream and downstream sidewall and main transformer chamber second upstream and downstream sidewall, plastic zone than the downstream and upstream wall plastic zone distribution range is significant, the main plant and there is no breakthrough of the plastic zone area between main transformer room.

There is little difference between T2 and T3 in the plastic zone, in which the maximum depth of the plastic zone in the upstream wall of the T2 model is 14 m, and the depth of the plastic zone in the upstream wall of the T3 model is 13 m. The T1 plastic zone was significantly higher than T2 and T3, and the maximum plastic zone depth was 20 m. It indicates that R1 model considers more caves, and its excavation disturbance area is more extensive, which has adverse effects on the surrounding rocks of the main powerhouse and the main transformer chamber. We should pay attention to and strengthen the support strength at the intersection of the arch, the side wall and the opening. During the construction stage, timely support measures should be taken to strengthen random support to prevent large damage and deformation.

5. Conclusions

In this paper, a 3D finite element model including all caverns and a 3D simplified model containing only part of the caverns such as the main powerhouse and the main transformer

chamber are established respectively, and the numerical analysis of the underground cavern group is carried out by using the nonlinear finite element method. In addition, a three-dimensional simplified model is established and three excavation calculation schemes are designed for comparison, and the following conclusions are obtained.

(1) The numerical results using the model of all caverns show that the distribution law of the rock displacement field, stress field and plastic zone around the cave is similar to the results of the numerical model used in the stability analysis of the traditional underground cavern group.

(2) The stress, displacement, and plastic zone of the model containing all the caverns are larger than the model that only contains the main plant, main transformer room, bus tunnel, etc. The maximum horizontal displacement difference of the plant area is 53.72%, and the maximum deviation of the third stress is 39.57%. The maximum difference in the depth of the plastic zone in the workshop area is 30.77%. And the position of the extreme value of stress and displacement also changed.

(3) After the excavation of the auxiliary cavern is completed, there will be places where stress is concentrated. The stress concentration parts should be strengthened to prevent cracking damage. Thereby reducing the probability of rockburst and collapse events and ensuring construction safety.

(4) The excavation of the small caverns around the powerhouse will weaken the integrity of the surrounding rock and have a certain impact on the deformation of the surrounding rock. Three-dimensional finite element models of all caverns.

Based on the above conclusions, it is reasonable to use the numerical simulation analysis of the 3D finite element model including all the caverns. Future work should consider supporting situations on this basis.

Data Availability

The codes used in this paper are available from the author upon request.

Conflicts of Interest

The authors declare that there is no conflict of interest regarding the publication of this paper.

Acknowledgments

References

[1] A. Li, N. Xu, F. Dai, G. Gu, Z. Hu, and Y. Liu, "Stability analysis and failure mechanism of the steeply inclined bedded rock masses surrounding a large underground opening," *Tunnelling and Underground Space Technology*, vol. 77, pp. 45–58, 2018.

[2] N. W. Xu, T. B. Li, F. Dai, B. Li, Y. G. Zhu, and D. S. Yang, "Microseismic monitoring and stability evaluation for the large scale underground caverns at the Houziyan hydropower station in Southwest China," *Engineering Geology*, vol. 188, pp. 48–67, 2015.

[3] N. Xu, F. Dai, B. Li, Y. Zhu, T. Zhao, and D. Yang, "Comprehensive evaluation of excavation-damaged zones in the deep underground caverns of the Houziyan hydropower station, Southwest China," *Bulletin of Engineering Geology and the Environment*, vol. 76, no. 1, pp. 275–293, 2017.

[4] L. Ribeiro e Sousa, "Learning with accidents and damage associated to underground works," in *Geotechnical Risks in Rock Tunnels*, S. Matos and P. Kleberger, Eds., Francis & Taylor, London, UK, 2006.

[5] Y. Li, W. Zhu, J. Fu, Y. Guo, and Y. Qi, "A damage rheology model applied to analysis of splitting failure in underground caverns of Jinping I hydropower station," *International Journal of Rock Mechanics and Mining Sciences*, vol. 71, pp. 224–234, 2014.

[6] Q. Qian and P. Lin, "Safety risk management of underground engineering in China: progress, challenges and strategies," *Journal of Rock Mechanics and Geotechnical Engineering*, vol. 8, no. 4, pp. 423–442, 2016.

[7] W. S. Zhu, B. Sui, X. J. Li, S. C. Li, and W. T. Wang, "A methodology for studying the high wall displacement of large scale underground cavern complexes and it's applications," *Tunnelling and Underground Space Technology*, vol. 23, no. 6, pp. 651–664, 2008.

[8] Y. Zeng and Z. Zhao, "Model testing studies of underground openings," *Chinese Journal of Rock Mechanics and Engineering*, vol. 20, pp. 1745–1749, 2001.

[9] S. Hibino and M. Motojima, "Anisotropic behavior of jointed rock mass around large-scale caverns," in *Proceedings of the 9th ISRM Congress, 1999*, International Society for Rock Mechanics and Rock Engineering, Paris, France, August 1999.

[10] C. Zhang, Z. Wang, and Q. Wang, "Deformation and failure characteristics of the rock masses around deep underground caverns," *Mathematical Problems in Engineering*, vol. 2015, Article ID 230126, 2015.

[11] K. Ma, J. Zhang, Z. Zhou, and N. Xu, "Comprehensive analysis of the surrounding rock mass stability in the underground caverns of Jinping I hydropower station in Southwest China," *Tunnelling and Underground Space Technology*, vol. 104, Article ID 103525, 2020.

[12] F. Dai, B. Li, N. Xu, Y. Fan, and C. Zhang, "Deformation forecasting and stability analysis of large-scale underground powerhouse caverns from microseismic monitoring," *International Journal of Rock Mechanics and Mining Sciences*, vol. 86, pp. 269–281, 2016.

[13] A. Wu, J. Wang, Z. Zhou et al., "Engineering rock mechanics practices in the underground powerhouse at Jinping I hydropower station," *Journal of Rock Mechanics and Geotechnical Engineering*, vol. 8, no. 5, pp. 640–650, 2016.

[14] S. Song, X. Feng, C. Liao, D. Cai, Z. Liu, and Y. Yang, "Measures for controlling large deformations of underground caverns under high in-situ stress condition - a case study of

Jinping I hydropower station," *Journal of Rock Mechanics and Geotechnical Engineering*, vol. 8, no. 5, pp. 605–618, 2016.

[15] M. S. Diederichs, P. K. Kaiser, and E. Eberhardt, "Damage initiation and propagation in hard rock during tunnelling and the influence of near-face stress rotation," *International Journal of Rock Mechanics and Mining Sciences*, vol. 41, no. 5, pp. 785–812, 2004.

[16] X.-J. Li, L.-G. Wang, and W.-M. Yang, "A numerical study of underground cavern stability by geostress characteristics," *Shock and Vibration*, vol. 2016, Article ID 3768453, 2016.

[17] L. Zhang, D. Wang, and J. Dong, "Assessment of the excavation damaged zones in the surrounding rock of an underground powerhouse under high in situ stress using an acoustic velocity detecting method," *Advances in Civil Engineering*, vol. 2020, Article ID 7297260, 2020.

[18] P. Garg and A. Jaiswal, "Estimation of modulus of the caved rock for underground coal mines by back analysis using numerical modelling," *Journal of the Institution of Engineers: Series D*, vol. 97, no. 2, pp. 269–273, 2016.

[19] M. A. Perras, H. Wannenmacher, and M. S. Diederichs, "Underground excavation behaviour of the queenston formation: tunnel back analysis for application to shaft damage dimension prediction," *Rock Mechanics and Rock Engineering*, vol. 48, no. 4, pp. 1647–1671, 2015.

[20] Q. Ren, L. Xu, A. Zhu, M. Shan, J. Gu, and L. Shen, "Comprehensive safety evaluation method of surrounding rock during underground cavern construction," *Underground Space*, vol. 6, no. 1, 2019.

[21] D. Oliveira and M. S. Diederichs, "Tunnel support for stress induced failures in Hawkesbury Sandstone," *Tunnelling and Underground Space Technology*, vol. 64, pp. 10–23, 2017.

[22] P. K. Kaiser and M. Cai, "Design of rock support system under rockburst condition," *Journal of Rock Mechanics and Geotechnical Engineering*, vol. 4, no. 3, pp. 215–227, 2012.

[23] Q. Jiang, G. Su, X.-t. Feng, G. Chen, M.-z. Zhang, and C. Liu, "Excavation optimization and stability analysis for large underground caverns under high geostress: a case study of the Chinese Laxiwa project," *Rock Mechanics and Rock Engineering*, vol. 52, no. 3, pp. 895–915, 2019.

[24] D. Xu, X. Feng, Y. Cui, Q. Jiang, and H. Zhou, "On failure mode and shear behavior of rock mass with interlayer staggered zone," *Rock and Soil Mechanics*, vol. 33, no. 1, pp. 129–136, 2012.

[25] B. Indraratna, D. A. F. Oliveira, and E. T. Brown, "A shear-displacement criterion for soil-infilled rock discontinuities," *Géotechnique*, vol. 60, no. 8, pp. 623–633, 2010.

[26] S.-Q. Duan, X.-T. Feng, Q. Jiang, G.-F. Liu, S.-F. Pei, and Y.-L. Fan, "In situ observation of failure mechanisms controlled by rock masses with weak interlayer zones in large underground cavern excavations under high geostress," *Rock Mechanics and Rock Engineering*, vol. 50, no. 9, pp. 2465–2493, 2017.

[27] Y. H. Hao and R. Azzam, "The plastic zones and displacements around underground openings in rock masses containing a fault," *Tunnelling and Underground Space Technology*, vol. 20, no. 1, pp. 49–61, 2005.

[28] S. Sakurai, S. Akutagawa, K. Takeuchi, M. Shinji, and N. Shimizu, "Back analysis for tunnel engineering as a modern observational method," *Tunnelling and Underground Space Technology*, vol. 18, no. 2-3, pp. 185–196, 2003.

[29] Y. M. A. Hashash, J. J. Hook, B. Schmidt, J. I. Chiang Yao, and C. Yao, "Seismic design and analysis of underground structures," *Tunnelling and Underground Space Technology*, vol. 16, no. 4, pp. 247–293, 2001.

[30] X. Wang, J. Chen, M. Xiao, and D. Wu, "Seismic response analysis of concrete lining structure in large underground powerhouse," *Mathematical Problems in Engineering*, vol. 2017, Article ID 4106970, 2017.

[31] J. Yang, W. Lu, M. Chen, P. Yan, and C. Zhou, "Microseism induced by transient release of in situ stress during deep rock mass excavation by blasting," *Rock Mechanics and Rock Engineering*, vol. 46, no. 4, pp. 859–875, 2013.

[32] J. Sun and S. Wang, "Rock mechanics and rock engineering in China: developments and current state-of-the-art," *International Journal of Rock Mechanics and Mining Sciences*, vol. 37, no. 3, pp. 447–465, 2000.

[33] J. Zhou, X. Li, and X. Shi, "Long-term prediction model of rockburst in underground openings using heuristic algorithms and support vector machines," *Safety Science*, vol. 50, no. 4, pp. 629–644, 2012.

[34] S. Akdag, M. Karakus, A. Taheri, G. Nguyen, and H. Manchao, "Effects of thermal damage on strain burst mechanism for brittle rocks under true-triaxial loading conditions," *Rock Mechanics and Rock Engineering*, vol. 51, no. 6, pp. 1657–1682, 2018.

[35] L. Weng, L. Huang, A. Taheri, and X. Li, "Rockburst characteristics and numerical simulation based on a strain energy density index: a case study of a roadway in Linglong gold mine, China," *Tunnelling and Underground Space Technology*, vol. 69, pp. 223–232, 2017.

[36] W. Blake and D. G. Hedley, *Rockbursts: Case Studies from North American Hard-Rock Mines*, SME, Southfield, MI, USA, 2003.

[37] J. He, L. Dou, S. Gong, J. Li, and Z. Ma, "Rock burst assessment and prediction by dynamic and static stress analysis based on micro-seismic monitoring," *International Journal of Rock Mechanics and Mining Sciences*, vol. 93, no. 93, pp. 46–53, 2017.

[38] R. Shirani Faradonbeh, S. Shaffiee Haghshenas, A. Taheri, and R. Mikaeil, "Application of self-organizing map and fuzzy c-mean techniques for rockburst clustering in deep underground projects," *Neural Computing & Applications*, vol. 32, no. 12, pp. 8545–8559, 2020.

Research Article

Analytical Study on Surface Settlement Troughs Induced by the Sequential Excavation of Adjacent and Parallel Tunnels in Layered Soils

Cong Dong [iD],[1] **Jian Lin** [iD],[1,2] **Guangyong Cao,**[1,2] **Hua Cheng,**[1,3] **Linlin Shi,**[4] **and Xiaohui Zhang**[4]

[1]*Anhui Key Laboratory of Building Structures and Underground Engineering, Anhui Jianzhu University, Hefei, Anhui 230601, China*
[2]*Anhui Jianzhu University College of Civil Engineering, Hefei, Anhui 230601, China*
[3]*Institute of Resources and Environmental Engineering, Anhui University, Hefei, Anhui 230022, China*
[4]*The Fourth Engineering Co., Ltd. of Ctce Group, Hefei, Anhui 230041, China*

Correspondence should be addressed to Jian Lin; linjian@ahjzu.edu.cn

In this paper, the settlement troughs induced by the excavation of adjacent and parallel tunnels in layered soils were studied. Firstly, a trough width parameter calculation method in layered soils was established based on the propagation model of the plastic zone and unloading disturbance zone. Secondly, the mechanism of the superposition disturbance between parallel tunnels is analyzed, and a method for calculating additional settlement trough is proposed. Finally, the applicability of the proposed model was demonstrated with two case studies of the parallel tunnels. The following conclusions were obtained: the difference of soil properties in layered soils had a significant influence on the width parameter of surface settlement trough; a Gaussian curve can describe the additional settlement caused by superimposed disturbance; and finally, the relationship between the ground loss induced by superposition disturbance and the ground loss induced by the preceding tunnel was approximately linear. The model presented in this paper is highly effective and convenient for use in practice and extends the calculation method of surface settlement trough based on the Gaussian curve.

1. Introduction

The settlement of overlying soil above the tunnel is induced by the disturbance of tunnel construction on surrounding soil [1]. The settlement not only affects the stability of surface buildings [2–4], but also jeopardizes the normal use of underground pipelines [5, 6]. The complex structure environment puts forward higher settlement control requirements for tunnel engineering, especially in adjacent and parallel tunnels event. Therefore, the tunneling-induced surface settlement calculation has received extensive attention [7, 8].

Peck [9] proposed that the single tunneling-induced surface settlement trough could be distributed by a Gaussian curve as follows:

$$S(x) = S_{\max} \exp\left[-\frac{x^2}{2i^2}\right], \tag{1}$$

where $S(x)$ is ground settlement; $S_{\max}$ is the maximum surface settlement above the tunnel centerline; x is the horizontal distance from the tunnel centerline; and i is the distance from the tunnel centerline to the curve's inflection point, which is called trough width parameter, as shown in

Figure 1. The empirical methods based on the Gaussian curve have become a generally accepted research model on the surface settlement trough and the interaction of two adjacent and parallel tunnels.

Many measured data in engineering practice show that the surface settlement trough induced by the adjacent and parallel tunnels is asymmetrical [10–12]. It is because the following tunnel was excavated in a brown-field site (previously developed site) [13, 14].

Some scholars have proposed that the surface settlement trough above the following tunnel, which is affected by the preceding excavation, enlarges and shifts. The settlement trough above the following tunnel could be obtained by modifying and moving according to the settlement date of the preceding tunnel. This method is called the modification factor method [15]. Chapman and Hunt [16] proposed the modified function as follows:

$$S_2(x) = \left\{ 1 + \left[k\left(1 - \frac{|B+x|}{2.5 i_1 h} \right) \right] \right\} S_1(x),\qquad(2)$$

where $S_1(x)$ is the surface settlement trough above the preceding tunnel (same as the single tunnel); $S_2(x)$ is the modified surface settlement trough; k is the value of maximum modification; i_1 is the trough width parameter of the preceding tunnel. Dong [15] proposed the deal of maximum modification k could be determined as follows:

$$k = -\frac{1.85B}{2h+D} + 1.002,\qquad(3)$$

where B is the center-to-center spacing of tunnels. Wei and Wei [17] proposed a method of moving settlement trough.

Other scholars proposed that calibration of i and S_{max} is vital during the settlement trough calculation above the following tunnel. Ma et al. [18] converted the Gaussian curve into a linear form, and two numerical methods were used to estimate the settlement parameters induced by parallel tunnels. Zheng et al. [19] investigated the interaction between parallel tunnels by the physical model test, and the differences between the surface settlement troughs above two tunnels were described in terms of parameters.

Many scholars have studied the surface settlement trough induced by adjacent and parallel tunnels with various methods, but the reasons for the changes of surface settlement trough were rarely mentioned from the perspective of interactions. The consistent relationship between model parameters and excavation parameters remains unclear. This paper presents a method for calculating the trough width parameter of surface settlement trough in layered soils. Then, a new calculation method of surface settlement trough above the following tunnel is demonstrated by analyzing the mechanisms of superposition disturbance. Finally, two cases' study is presented to assess the rationale of the proposed model.

2. Calculation of Disturbance Zone and Surface Settlement Trough Induced by Tunnel Excavation in Layered Soils

In order to minimize the detrimental effect of tunneling on surrounding structures, it is necessary to calculate the disturbance zone induced by tunnel excavation accurately. In practical engineering, tunnels are primarily constructed in layered soils. The differences in geotechnical properties significantly affect the plastic zone, unloading disturbance zone, and surface settlement trough.

2.1. Basic Assumptions

(1) The tunnel is excavated in a stratum with a large thickness and covered with multiple soil layers. The surrounding soil is only defined as a standard elastomer.

(2) Instantaneous surface settlement occurs during tunnel excavation, and the ground will not continue to move after the excavation.

(3) The tunnel is excavated in a greenfield, and a Gaussian curve could distribute the settlement trough.

2.2. Plastic Zone and Unloading Disturbance Zone in Layered Soils.
Assuming that there are n layers of soil overlying the tunnel and the tunnel was excavated in the nth layer of soil, h is the distance from the tunnel centerline to the ground surface. In layered soils, h_1 is the thickness of the first soil layer, and so on; h_n is the distance from the tunnel centerline to the interface of the $n-1$th layered soil (Figure 2). The plastic zone and the unloading disturbance zone are calculated by the layered accumulation method.

The tunnel excavation process can be seen as the unloading process of the column hole, and the plastic zone appears in the soil around the tunnel. For the sake of simplicity, the force around the tunnel is assumed to distribute symmetrically. The initial Earth stress and the support force of the tunnel can be calculated as follows:

$$\sigma_0 = \sum_{i=1}^{n} h_i \gamma_i,$$

$$\sigma_a = \sigma_0 \tan^2\left(45° - \frac{\varphi_n}{2}\right) + 2c_n \tan\left(45° - \frac{\varphi_n}{2}\right).\qquad(4)$$

According to the Fenner formula [20], the radius of the plastic zone caused by tunnel construction can be estimated by

$$a = \frac{D}{2}\left[(1 - \sin\varphi_n)\left(\frac{\sigma_0 + c_n \cot\varphi_n}{\sigma_a + c_n \cot\varphi_n}\right) \right]^{(1-\sin\varphi_n/2\sin\varphi_n)},\quad(5)$$

where h_i is the thickness of the i soil layer; γ_i is the unit weight of soil of the ith layer; φ_n is the internal friction angle
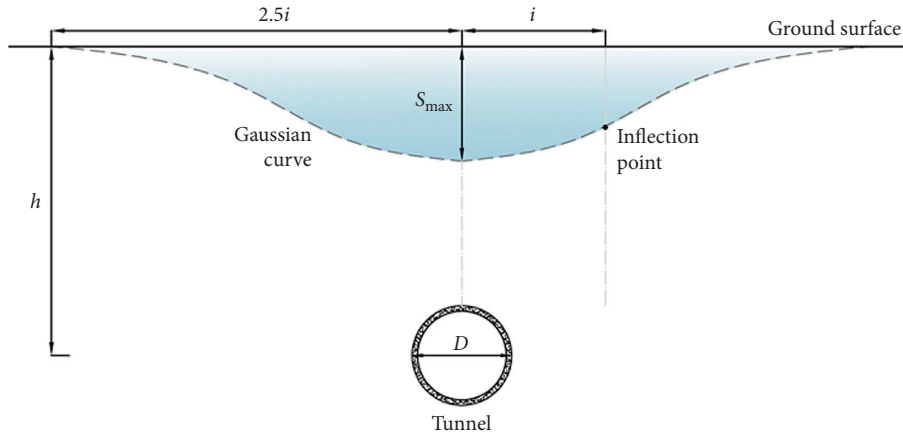
FIGURE 1: Ground settlement trough induced by a single tunnel.

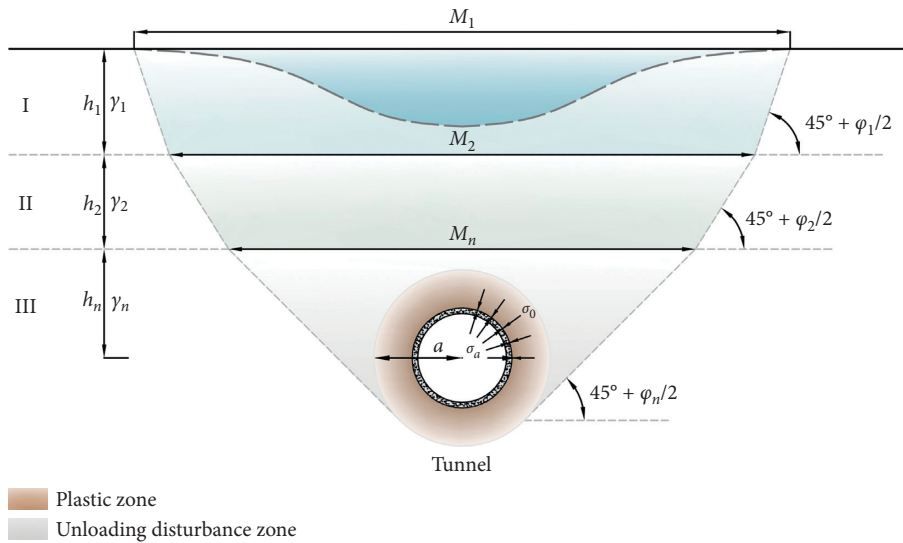Plastic zone
Unloading disturbance zone

FIGURE 2: Plastic zone and unloading disturbance zone in layered soils.

of the soil layer where the tunnel is located; c_n is the cohesion of the soil layer where the tunnel is located.

The unloading disturbance zone is produced due to the stress release of the soil above the plastic deformation zone. The shear failure has taken place at the boundary of the unloading disturbance zone. The failure plane of the unloading disturbance zone is tangent to the shearing disturbance zone, which inclines by an angle $45° + (\varphi/2)$ from the horizontal based on Rankine's Earth pressure theory [21, 22]. Because of the different properties of each soil in layered soils, the failure plane is deflected at the interface between the two soil layers [23, 24]. According to the geometric relationship as shown in Figure 2, the width of the unloading disturbance zone at the interface of the nth soil layer can be calculated as follows:

$$M_n = 2\left(\frac{h_n}{\tan\left(45° + \varphi_n/2\right)} + \frac{a}{\sin\left(45° + \varphi_n/2\right)}\right). \quad (6)$$

Hence, the width of the unloading disturbance zone on the ground is obtained as follows:

$$M_1 = M_n + 2\sum_{i=1}^{n-1} h_i \tan\left(45° + \frac{\varphi_i}{2}\right). \quad (7)$$

2.3. Surface Settlement Trough and Ground Loss of Single Tunnel. According to the above analysis, it can be seen that the unloading disturbance zone and the settlement trough are equal in width. The trough width parameter in the Gaussian curve determines the width of the settlement trough, so there will be a corresponding relationship between the trough width parameter and the width of the settlement trough. Based on a review of a large number of measured data, Stallebrass and Taylor [25] found that the trough width parameter has a linear correlation with the width of settlement trough, as follows:

$$i_1 = \frac{M_1}{5}. \qquad (8)$$

Another key parameter in the Gaussian curve is the maximum ground settlement just above the tunnel centerline, which determines the depth of the settlement trough and has an inevitable relationship with the ground loss induced by the tunnel excavation. Ground loss is defined as the volume of surface settlement trough per unit length of the tunnel. Although there are some calculation methods for ground loss, it is difficult to select parameters and consider factors that influence the ground loss. Attewell and Farme [21] proposed that the calculation formula of ground loss can be obtained by integrating the Gaussian curve as follows:

$$V_{\text{loss}} = \int_{-\infty}^{+\infty} S_{\text{max}} \exp\left(-\frac{x^2}{2i^2}\right) dx = \sqrt{2\pi} i S_{\text{max}}, \qquad (9)$$

where V_{loss} is the ground loss induced by tunnel excavation.

2.4. Surface Settlement Trough above Parallel Tunnels.

Through the statistical analysis of the surface settlement in published case history, it is found that the settlement trough above the parallel tunnels is difficult to describe by a single Gaussian curve. Therefore, Suwansawat and Einstein [12] proposed a superposition calculation method to describe the surface settlement trough above a parallel tunnel. According to the method, the surface settlement trough caused by the excavation of adjacent and parallel tunnels would consist of two components: the surface settlement troughs of the preceding tunnel and the following tunnel. Both troughs caused can be described by Gaussian curve. The first component equals the surface settlement trough induced by the single tunnel. However, the calculation of the second component (i.e., surface settlement trough above the following tunnel) would be the critical point of this method.

3. Calculation of Surface Settlement Trough above the following Tunnel Based on Superposition Technique

The existing calculation models have complex calculation processes and narrow application scope. Therefore, a calculation model of surface settlement trough above the following tunnel with broad applicability is established by analyzing the interaction mechanism between adjacent and parallel tunnels.

3.1. Overlapping Disturbance of Adjacent and Parallel Tunnel.

The soil stability changes in the unloading disturbance area above the preceding tunnel due to the excavation disturbance. The soil in the overlapping zone has been disturbed so that the surface settlement trough above the following tunnel will be larger than the preceding tunnel. In the overlapping zone, the increase of settlement is called additional settlement.

Considering the influence of the overlapping disturbance, it is reasonable that the surface settlement trough

above the following tunnel could divide into two components for calculation. The first component is the surface settlement trough caused by tunnel excavation without considering the interaction and would be equal to the surface settlement trough of a single tunnel. The second component is the asymmetric settlement resulting from the overlapping disturbance in the overlapping zone, as shown in Figure 3. The calculation of asymmetric settlement is the critical point of this method.

3.2. Additional Surface Settlement Trough Induced by Overlapping Disturbance.

The mechanism of soil disturbance in the process of overlapping disturbance is complex, and the additional settlement is the result of various disturbances in the excavation process. It is hard to calculate the surface settlement accurately. As shown in Figure 4, through the analysis of multiple groups of measured data, it could be found that the additional settlement trough caused by the overlapping disturbance also appears as a Gaussian curve, and the settlement characteristics can be described by a Gaussian curve as follows:

$$S'(x) = S'_{\text{max}} \exp\left(\frac{-x'^2}{2i'^2}\right), \qquad (10)$$

where x' is the horizontal distance to the surface; $S'(x)$ is additional surface settlement; i' is the width parameter of additional settlement trough, S'_{max} is the maximum additional settlement. The surface additional settlement trough and soil loss caused by overlapping disturbance are two key points of research.

In order to describe the surface additional settlement trough caused by superposition disturbance, it is necessary to determine the width parameter i' and the maximum additional settlement S'_{max}. As shown in Figure 3, according to the definition and model of overlapping disturbance, the width of surface overlap disturbance is obtained as follows:

$$L = M_1 - B. \qquad (11)$$

And the width parameter of additional settlement trough is obtained based on (8), as follows:

$$i' = \frac{L}{5}. \qquad (12)$$

The maximum additional settlement is closely related to the ground loss in the overlapped disturbance zone.

3.3. Ground Loss Induced by Overlapping Disturbance.

The analysis of additional settlement found that it is difficult to establish a simple corresponding relationship between two adjacent and parallel tunnels in terms of the maximum surface settlement. Considering that the stratum conditions and the construction parameters of the primary and overlapping disturbance zone are similar, a simple correlation between the two adjacent and parallel tunnels can be established through the ground loss. However, the mechanism of soil loss caused by overlapping disturbance is
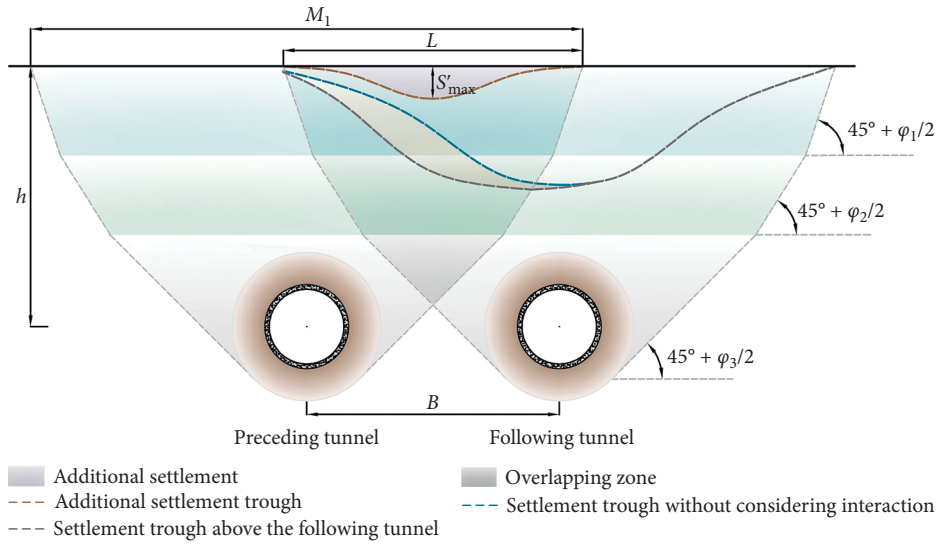
Figure 3: Calculation diagram of calculation method based on superposition theory.
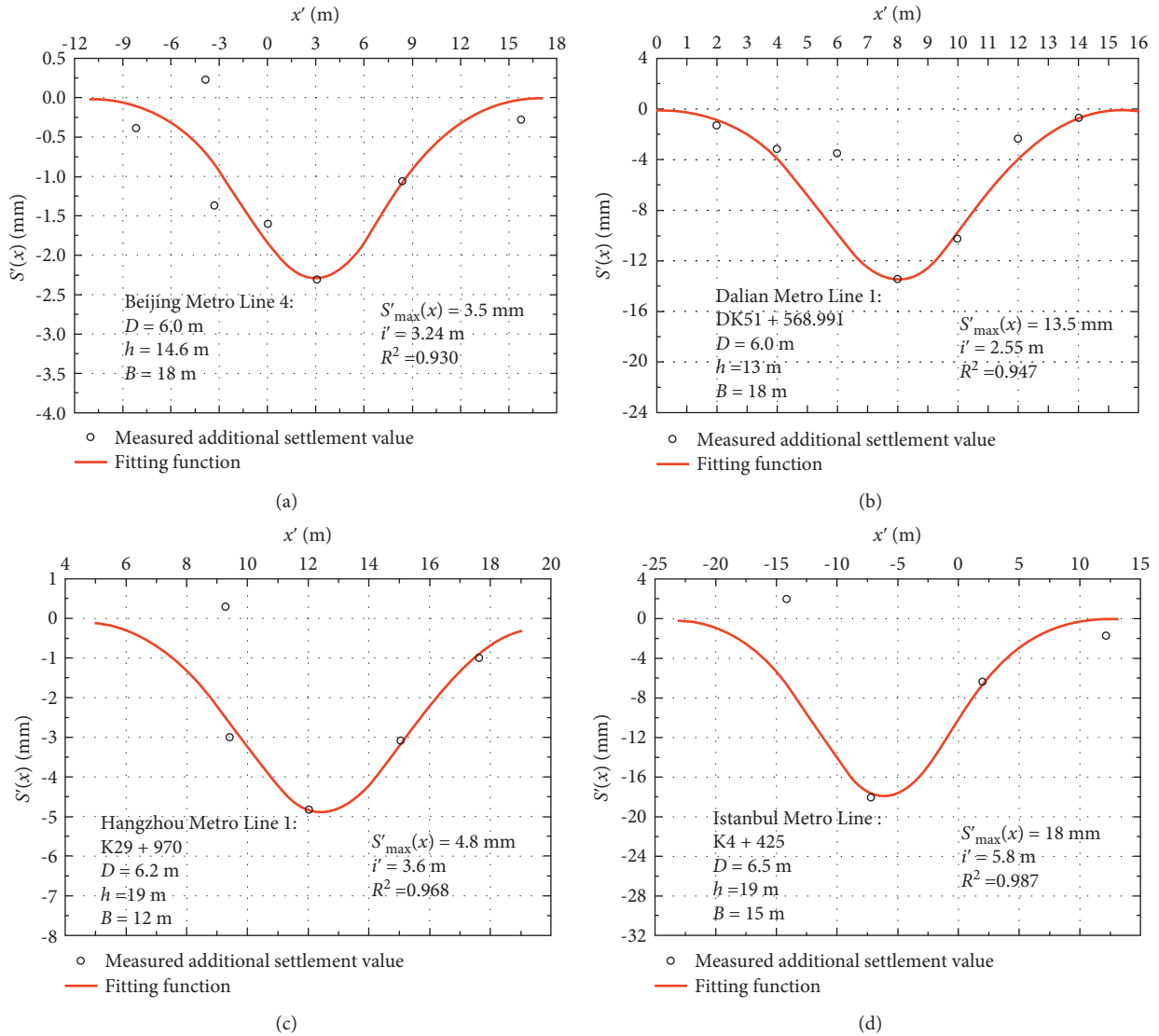

(a)

(b)

(c)

(d)

Figure 4: Comparison between the measured data of additional settlement and the fitting curves. (a) [26]. (b) [27]. (c) [28]. (d) [29].

complex, and it is difficult to monitor accurately. Therefore, the ground loss induced by overlapping disturbance can only be explored based on the existing measured settlement data. The additional settlement data can be obtained according to the following procedure:

(1) Translate the settlement trough of the post-constructed tunnel to the proconstructed tunnel so that the positions of the two tunnels are overlapped.

(2) Subtract the preceding tunnel's settlement from the following tunnel's settlement to obtain an additional surface settlement caused by superposition disturbance.

(3) The additional settlement value caused by the superposition disturbance is fitted and integrated by the gauss formula. And then, the soil loss caused by superposition disturbance is calculated.

3.4. Back Analysis of Ground Loss Induced by Overlapping Disturbance. A total of 14 tunnel excavation cases are collected in Tables 1 and 2 to study the distribution of ground loss caused by overlapping disturbance. All cases are parallel tunnels excavated by the EPB shield machine. Table 1 summarizes the details of each tunnel project, and Table 2 summarizes the surface settlement data from the measured and calculated data. In Table 2, V'_{loss} is the ground loss caused by superposition disturbance and V_{loss1} is the ground loss caused by the preceding tunnel.

For convenience, the least-squares principle is used to carry out linear fitting of V'_{loss} in the overlapping disturbance area. All calculated V'_{loss} for cases 1–14 from the back analysis are plotted as a function of V_{loss1} in Figure 5. The approximate relationship of $V'_{\text{loss}} \sim V_{\text{loss1}}$ can be expressed as

$$V'_{\text{loss}} = 0.0249 + 0.2845 V_{\text{loss}}. \tag{13}$$

The coefficient of determination (R^2) was used to compare the goodness of fitting. 72% of the data show a good fitting result ($R^2 = 0.7146$), which indicates that V'_{loss} has a significant linear positive correlation with V_{loss1}. It can be concluded that the ground loss caused by the overlapping disturbance can be obtained through the ground loss of the following tunnel.

3.5. Calculation Process of Settlement Trough for the following Tunnel. The settlement trough calculation procedure is shown in Figure 6. Firstly, $S_1(x)$ and V_{loss1} are monitored by the measured data after the preceding tunnel excavated. Secondly, $S'(x)$ is determined by i' and V'_{loss}, which are calculated by (12) and (13). Finally, based on superposition technique, $S_2(x)$ is predicted by superimposing $S'(x)$ on $S_1(x)$.

4. Field Project Cases Validation

A total of 2 sets of data are investigated from 2 field tunnel projects to validate the calculation model for the trough width parameter and the settlement troughs above the

parallel tunnels. Parameters and known quantities are listed in Table 3.

4.1. Changsha Metro Line 2 Project. Changsha Metro Line 2 project included two tunnels constructed using an EBP shield with a diameter of 6.00 m. Field settlements were obtained from section DK16 + 265. The depth of each tunnel axis is approximately 18 m, and the spacing between the center of two adjacent tunnels is 13 m. The soil profile at the instrumented site comprises miscellaneous fill, silty clay, sand, and argillaceous siltstone. The tunnel is located in argillaceous siltstone.

4.2. Shenyang Utility Tunnel Project. Shenyang utility tunnel project, which involved two tunnels, was built in Shenhe District of Shenyang City. Two tunnels were excavated using an EBP shield with a diameter of 6.00 m. Field settlements were obtained from section K8 + 577. The depth of each tunnel axis is approximately 18 m, and the spacing between the center of two adjacent tunnels is 12 m. The soil profile at the instrumented site comprises miscellaneous fill, round gravel, medium-coarse sand, and gravelly sand. The tunnel is located in gravelly sand.

4.3. The Trough Width Parameter. The proposed formula for i (i.e., (8)) is validated in two cases. Comparison between measured data and the i calculated results is shown in Table 4. In the first case, the relative error of i calculated by the proposed formula is 9.1%, and in the second case, the relative error is 1.4%.

It can be seen that different soil properties in the layered soils affect the trough width parameters induced by the tunnel, and it must be considered in the calculation. The proposed formulas for i could accurately calculate the trough width parameters in the field project.

4.4. The Settlement Troughs above the Parallel Tunnels. In two cases, the Gaussian curve is used to describe the surface settlement troughs above the parallel tunnels. The calculation results of the modification factor method are shown in Figures 7(a) and 8(a), and the calculation results of the proposed method based on the superposition technique are also presented in Figures 7(b) and 8(b), respectively.

A comparison between the calculated settlement troughs and the data points is shown in Figures 7 and 8. In the first case, only 50% of the data using the modification factor method show a good fitting result ($R^2 = 0.645$), while 80% of the data using the calculation method based on the superposition technique show a good fitting result ($R^2 = 0.852$). But in the second case, 75% of the data using the modification factor method show a good fitting result ($R^2 = 0.928$), and 83% of the data using the calculation method based on superposition technique show a good fitting result ($R^2 = 0.952$). The comparison demonstrates that the proposed method based on the superposition technique reasonably describes the feature of surface settlement trough above the following tunnel.

TABLE 1: Engineering details.

Case NO.	Project name	Ground conditions	D (m)	Reference
1	Bangkok MRTA project	Soft clay, hard clay	6.45	Suwansawat and Einstein [12]
2	The new Milan metro line 5	Gravelly sand	6.7	Fargnoli et al. [7]
3	Wuhan Yangtze river tunnel	Miscellaneous fill, silty clay, Mucky soil, silty clay, silt, silty clay, fine sand	12.6	Ma [30]
4	Nanjing metro line 1	Silt, mucky silt clay	6.4	Li [31]

TABLE 2: Data obtained from measurement and fitting.

Case NO.	Monitoring section	h (m)	B (m)	L (m)	i' (m)	S'_{max} (mm)	V'_{loss} (m³/m)	i_1 (m)	S_{max1} (mm)	V_{loss1} (m³/m)
1	CS-8D	20.1	15	19.26	3.85	3.4	0.033	9	6.5	0.147
2	SS-5T-52E-S	22.2	20	16.45	3.29	4.3	0.035	13	15.4	0.501
3	S19	15	15	10.42	2.08	1.9	0.010	7	8.8	0.154
4	S35	15	16.5	8.72	1.74	1.8	0.007	6	8.8	0.131
5	HS-2	17.4	20	17.46	3.49	27.0	0.236	8	43.7	0.873
6	HS-3	18.4	20	20.98	4.19	19.1	0.201	7	29.9	0.523
7	HS-5	35.6	20	39.91	7.98	7.7	0.155	15	22.6	0.733
8	HS-6	37.6	20	42.15	8.43	7.0	0.148	15	12.8	0.482
9	HS-7	44	20	49.26	9.85	3.3	0.083	22	6.4	0.352
10	HS-8	46.5	20	51.9	10.38	4.1	0.116	23	6.0	0.347
11	H1	11	13	12.09	2.42	4.4	0.026	6	19.0	0.285
12	H6	16.4	13	20.08	4.02	6.6	0.067	8	15.8	0.316
13	H7	17	13	21.20	4.24	4.3	0.046	9	17.8	0.401
14	H15	14	13	16.77	3.35	5.7	0.048	7	13.9	0.243

Note: Cases 1-2 are from Project 1, Cases 3-4 are from Project 2, Cases 3–10 are from Project 3, and Cases 11–14 are from Project 4.
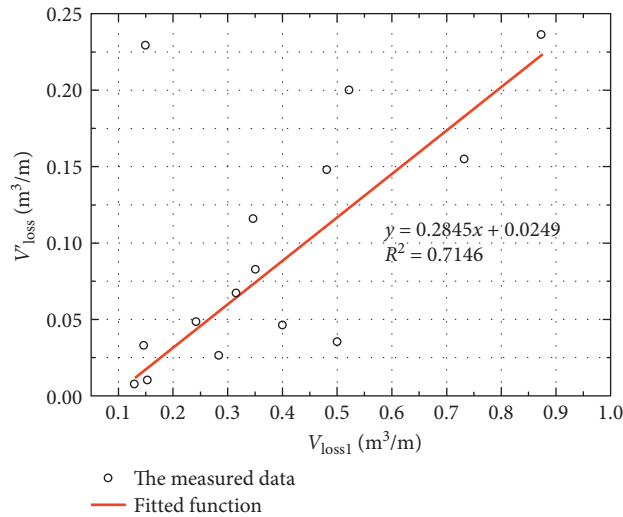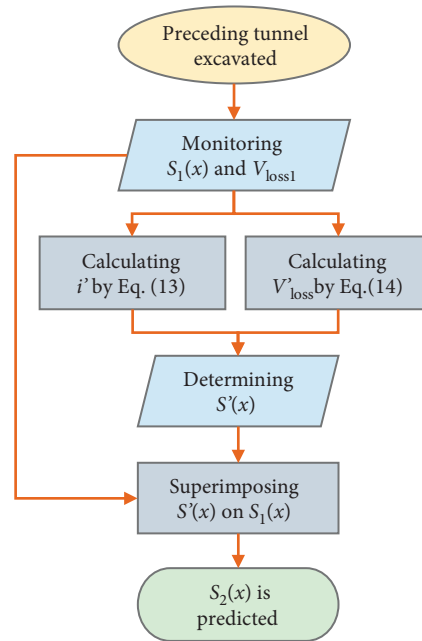

FIGURE 5: Fitting results.

FIGURE 6: Flowchart of the calculation procedure.

TABLE 3: Information of the investigated tunnel cases.

Case no.	Soil profile	h (m)	γ (kN/m^3)	c (kPa)	φ (°)	References
1	Miscellaneous fill	3.1	19.4	16.2	50	Huang [32]
	Silty clay	4.3	19.8	59	15.3	
	Sand	3.1	19			
	Argillaceous siltstone	10.5	20.5	125	32	
2	Miscellaneous fill	4	18	15	10	Li [33]
	Round gravel	6	19.8	25.9	31	
	Medium-coarse sand	4.5	20.3	27	29.5	
	Gravelly sand	9.4	20.2	29	30	

TABLE 4: Calculation results of trough width parameters.

Case NO.	Monitoring section	Field data (m)	Calculation result (m)
1	DK16 + 265	5.5	6.0
2	K8+577	6.8	6.7
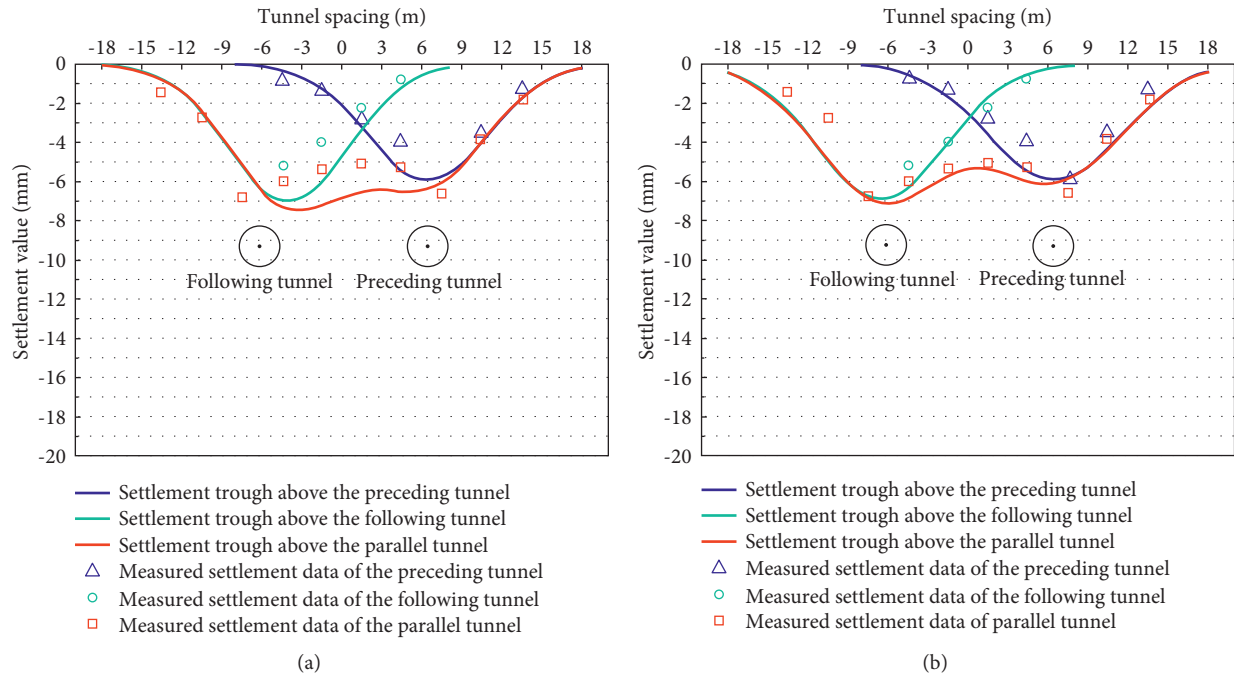
Figure 7: Comparison between the measured data and the calculated curves in case 1.
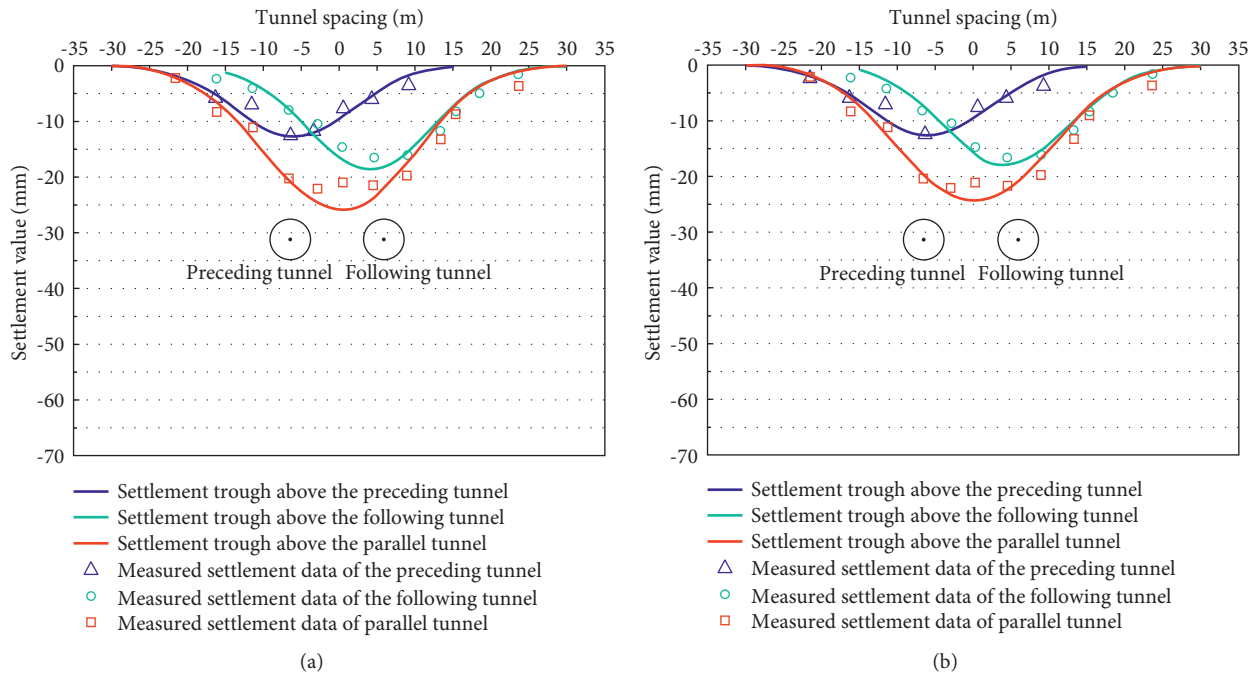
Figure 8: Comparison between the measured data and the calculated curves in case 2.

5. Conclusion

This paper establishes a new calculation method of surface settlement trough induced by the parallel tunnels in layered soils. The primary aim was to address the problem that settlement trough above the following tunnel was affected by the preceding tunnel in adjacent and parallel tunnels event.

The following conclusions can be obtained based on the results of the work:

(1) The difference of soil properties in layered soils significantly affects the width parameter of surface settlement trough. In the calculation, the plastic zone and unloading disturbance zone are firstly

determined in layered soils. And then, according to the linear relationship between the width parameter and the width of the unloading disturbance zone, the width parameter is calculated by the linear formula.

(2) Based on the superposition technique of tunnel settlement, the surface settlement above the following tunnel can be divided into the single tunneling-induced surface settlement and additional settlement induced by overlapping disturbance. The Gaussian curve can approximate the additional settlement trough according to the fitting results.

(3) Through extensive data exploration, the method for calculating the ground loss V'_{loss} induced by overlapping disturbance is proposed. With the increase of V_{loss1}, the value of V'_{loss} is gradually increased. The approximate relationship of $V'_{\text{loss}} \sim V_{\text{loss1}}$ can be expressed as

$$V'_{\text{loss}} = 0.0249 + 0.2845 V_{\text{loss}}, \tag{14}$$

(4) The calculated and measured settlement troughs above the parallel tunnels are in good agreement for the case study. Generally, the proposed model is effective and convenient for use in practice.

Data Availability

The data used to support the findings of this study are included in the article.

Conflicts of Interest

The authors declare that they have no conflicts of interest.

Acknowledgments

References

[1] E. Leca and B. New, "Settlements induced by tunneling in soft ground," *Tunnelling and Underground Space Technology*, vol. 22, no. 2, pp. 119–149, 2007.

[2] I. Elkayam and A. Klar, "Nonlinear elastoplastic formulation for tunneling effects on superstructures," *Canadian Geotechnical Journal*, vol. 56, no. 7, pp. 956–969, 2019.

[3] A. Franza and M. J. DeJong, "Elastoplastic solutions to predict tunneling-induced load redistribution and deformation of surface structures," *Journal of Geotechnical and Geoenvironmental Engineering*, vol. 145, no. 4, 2019.

[4] C. Gong, W. Ding, and D. Xie, "Twin EPB tunneling-induced deformation and assessment of a historical masonry building on shanghai soft clay," *Tunnelling and Underground Space Technology*, vol. 98, pp. 1–11, 2020.

[5] A. Klar, "Elastic continuum solution for tunneling effects on buried pipelines using fourier expansion," *Journal of Geotechnical and Geoenvironmental Engineering*, vol. 144, no. 9, pp. 1–10, 2018.

[6] P. Ni and S. Mangalathu, "Fragility analysis of gray iron pipelines subjected to tunneling induced ground settlement," *Tunnelling and Underground Space Technology*, vol. 76, pp. 133–144, 2018.

[7] V. Fargnoli, D. Boldini, and A. Amorosi, "Tbm tunnelling-induced settlements in coarse-grained soils: the case of the new milan underground line 5," *Tunnelling and Underground Space Technology*, vol. 38, pp. 336–347, 2013.

[8] R. Mair and R. Taylor, "Theme lecture: bored tunnelling in the urban environment," in *Proceedings of the Fourteenth International Conference on Soil Mechanics and foundation engineering*, pp. 2353–2385, Rotterdam, Netherlands, 1997.

[9] R. B. Peck, "Deep excavations and tunneling in soft ground," in *Proceedings of the 7th International Conference on Soil Mechanics and Foundation Engineering*, pp. 225–290, Mexico, 1969.

[10] M. L. Cooper, D. N. Chapman, C. D. F. Rogers, and W. Hansmire, "Prediction of settlement in existing tunnel caused by the second of twin tunnels," *Transportation Research Record: Journal of the Transportation Research Board*, vol. 1814, no. 1, pp. 103–111, 2002.

[11] V. Fargnoli, D. Boldini, and A. Amorosi, "Twin tunnel excavation in coarse grained soils: observations and numerical back-predictions under free field conditions and in presence of a surface structure," *Tunnelling and Underground Space Technology*, vol. 49, pp. 454–469, 2015.

[12] S. Suwansawat and H. H. Einstein, "Describing settlement troughs over twin tunnels using a superposition technique," *Journal of Geotechnical and Geoenvironmental Engineering*, vol. 133, no. 4, pp. 445–468, 2007.

[13] F. Hage Chehade and I. Shahrour, "Numerical analysis of the interaction between twin-tunnels: influence of the relative position and construction procedure," *Tunnelling and Underground Space Technology*, vol. 23, no. 2, pp. 210–214, 2008.

[14] H. N. Wang, X. Gao, L. Wu, and M. J. Jiang, "Analytical study on interaction between existing and new tunnels parallel excavated in semi-infinite viscoelastic ground," *Computers and Geotechnics*, vol. 120, pp. 1–18, 2020.

[15] C. Dong, J. Lin, C. Hua et al., "Calculation method of surface deformation of adjacent parallel tunnel considering construction sequence," *Water Resources and Hydropower Engineering*, vol. 52, no. 01, pp. 159–166, 2021.

[16] D. N. Chapman, S. K. Ahn, and D. V. Hunt, "Investigating ground movements caused by the construction of multiple tunnels in soft ground using laboratory model tests," *Canadian Geotechnical Journal*, vol. 44, no. 6, pp. 631–643, 2007.

[17] X. J. Wei and G. Wei, "Research on calculation method of ground settlement caused by horizontal parallel jacking," *Rock and Soil Mechanics*, vol. 27, no. 7, pp. 111–114, 2006.

[18] L. Ma, L. Ding, and H. Luo, "Non-linear description of ground settlement over twin tunnels in soil," *Tunnelling and Underground Space Technology*, vol. 42, pp. 144–151, 2014.

[19] G. Zheng, J. Tong, T. Zhang et al., "Experimental study on surface settlements induced by sequential excavation of two parallel tunnels in drained granular soil," *Tunnelling and Underground Space Technology*, vol. 98, pp. 1–11, 2020.

[20] P. Jia, W. Zhao, A. Khoshghalb et al., "A new model to predict ground surface settlement induced by jacked pipes with flanges," *Tunnelling and Underground Space Technology*, vol. 98, pp. 1–16, 2020.

[21] P. Attewell, I. Farmer, and N. Glossop, "Ground deformation caused by tunnelling in a silty alluvial clay," *Ground Engineering*, vol. 11, no. 8, pp. 32–41, 1978.

[22] D. Hunt, *Predicting the Ground Movements above Twin Tunnels Constructed in London Clay*, University of Birmingham, Birmingham, UK, 2005.

[23] A. A. Ata, "Ground settlements induced by slurry shield tunnelling in stratified soils," *Proc. North American Tunnelling*, vol. 96, no. 1, pp. 43–50, 1996.

[24] B. M. New, "Tunnelling induced ground movements: predicting their magnitude and effects," in *Proceedings of the 4th Int. Conf. Ground Movements and Structures*, pp. 671–697, Cardiff, UK, 1991.

[25] S. Stallebrass, R. Grant, and R. Taylor, "A finite element study of ground movements measured in centrifuge model tests of tunnels," *Geotechnical Aspects of Underground Construction in Soft Ground,* Rotterdam, Netherlands, pp. 595–600, 1996.

[26] G. W. Wei, *Study on Standard of the Ground Surface Settlement and Structures Deformation by Shield Tunnelling Construction in Beijing Subway*, Beijing Jiaotong University, China, 2008.

[27] Faisal, *Research on Surface Subsidence Caused by Shield Construction of Two Parallel Tunnels*, Dalian Maritime University, China, 2017.

[28] R. P. Chen, J. Zhu, W. Liu, and X. W. Tang, "Ground movement induced by parallel epb tunnels in silty soils," *Tunnelling and Underground Space Technology*, vol. 26, no. 1, pp. 163–171, 2011.

[29] Y. Mahmutoğlu, "Surface subsidence induced by twin subway tunnelling in soft ground conditions in istanbul," *Bulletin of Engineering Geology and the Environment*, vol. 70, no. 1, pp. 115–131, 2011.

[30] K. S. Ma, *Research on the Ground Settlement Caused by the Shield Construction and the Protection of the Adjacent Buildings*, Huazhong University of Science and Technology, China, 2008.

[31] S. G. Li, *Analysis and Numerical Simulation of Ground Settlement Caused by Epb Shield Tunnel Construction*, Central South University, China, 2006.

[32] L. Huang, *The Forecast and Analysis of Ground Subsidence Based on the Excavation of Changsha Metro*, Central South University of Forestry and Technology, China, 2016.

[33] S. l. Li, *Study on Ground Subsidence Caused by Shield Construction of Double-Line Tunnel for Underground Pipe Gallery*, Harbin Institute of Technology, China, 2018.

Research Article

Investigation on the Effect of Probability Distribution on the Dynamic Response of Liquefiable Soils

Juncheng Wang,[1] Li Zhou [ID],[2] Wenzhi Song,[3] Houle Zhang,[1] and Yongxin Wu [ID][1]

[1]*Key Laboratory of Ministry of Education for Geomechanics and Embankment Engineering,*
 College of Civil and Transportation Engineering, Hohai University, Nanjing 210098, China
[2]*China Construction Science and Industry Corporation LTD, Shenzhen 518000, China*
[3]*Shanghai MCC20 Construction Corporation Limited, 2469 Tieli Road, Shanghai 201999, China*

Correspondence should be addressed to Yongxin Wu; yxwuhhu@163.com

This study investigated the effect of different probabilistic distributions (Lognormal, Gamma, and Beta) to characterize the spatial variability of shear modulus on the soil liquefiable response. The parameter sensitivity analysis included the coefficient of variation and scale of fluctuation of soil shear modulus. The results revealed that the distribution type had no significant influence on the liquefaction zone. In particular, the estimation with Beta distribution is the worst scenario. It illuminated that the estimation with Beta distribution can provide a conservative design if site investigation is absent.

1. Introduction

It is now well recognized that natural soil properties exhibit spatial variability because of depositional and postdepositional processes. The inherent variability in soil properties has found its place in geotechnical design and has been extensively incorporated in the analysis of slope stability [1–5], foundation bearing capacity [6, 7], foundation settlement [8–10], and liquefaction [11–13]. A lognormal distribution has been generally accepted in a geotechnical reliability analysis [14–16] because of its capability to model the randomness of positive soil parameters.

Recent studies proved that different distributions impacted the stochastic properties of soil. Popescu et al. [17] and Jimenez and Sitar [18] performed a series of random finite element analyses with different probability distributions of soil parameters, which has significant effects on the foundation settlement and bearing capacity. Most recently, Wu et al. [19] applied the random finite element method to investigate the effect of different probabilistic distributions on the tunnel convergence and demonstrated the mechanisms of tunnel convergence and the probability

of exceeding liquefaction thresholds with different probabilistic distribution types. To date, publications on the application of random field theory to soil dynamic behavior are limited and the impact of probabilistic distribution on the soil liquefiable response has not been clearly defined. Wang et al. [20] investigated the liquefaction response of soil using the spatial variability of the shear modulus by considering different values of the coefficient of variation and the horizontal scale of fluctuation.

In this study, we performed the nonlinear dynamic simulation of the liquefiable response of a sand layer with the water table 1 m below the ground level under a seismic load using the finite difference program FLAC3D. The finite difference mesh configuration is shown in Figure 1. The soil domain had a length of 40 m and a height of 10 m, a liquefiable layer of 9 m, and a nonliquefiable layer of 1 m. The Mohr–Coulomb model and the Finn model were used to simulate the nonlinear soil behavior and the accumulation of the pore pressure in sand before the liquefaction triggered by a dynamic load, respectively. The Finn model can consider variations of the volumetric strain and display the increase in excess pore pressure. The relationship between variations of
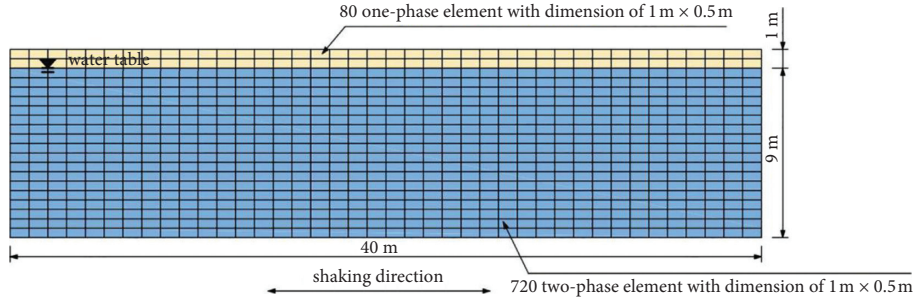
FIGURE 1: Mesh used in finite difference analysis.

volumetric strain increment ($\Delta\varepsilon_{vd}$) and cycle shearing strains (r) was defined as follows:

$$\Delta\varepsilon_{vd} = C_1\left(r - C_2\varepsilon_{vd}\right) + \frac{C_3\varepsilon_{vd}^2}{r + C_4\varepsilon_{vd}}, \tag{1}$$

where C_1, C_2, C_3, and C_4 are constant coefficients that can be obtained from cyclic triaxial tests. Following the study of Azadi and Hosseini [21], the four values were selected as 0.79, 0.52, 0.2, and 0.5, respectively. Table 1 summarizes the soil parameters in the constitutive model for the deterministic analysis. In the dynamic analysis, the boundaries were used to absorb the reflected waves and enforce the discrete half-space conditions of the numerical model. The free-field boundaries were adopted for the right and left boundaries to simulate the half-space condition. The seismic loading in the horizontal direction was applied at the bottom boundary which was assumed to be rigid.

In the stochastic analyses, the shear modulus G was assumed to be random variable and generated with the spectral representation method, which was recently developed by Shu et al. [7]. Three probabilistic distributions, including lognormal, Beta, and Gamma, were applied to model the spatial variability of G, with a mean $\mu_G = 20$ MPa and $\text{CoV}_G = 0.1, 0.3$, and 0.5. A 2D exponential correlation function [22] was adopted with the horizontal and vertical spatial correlation lengths $\delta_x = 6$ and 60 m and $\delta_y = 6$ m, respectively. 200 sets of Monte Carlo realizations were undertaken for each combination of a distribution type, a scale of fluctuation, and a CoV_G.

2. Results and Discussion

2.1. Area of Liquefied Zone A_{80}.
Figure 2 plots the mean of A_{80} ($\mu_{A_{80}}$) varying with the time history curve with different stochastic distributions. Following Popescu et al. [23], $A_{80}(t)$ from one finite difference computation is defined as

$$A_{80}(t) = \frac{\text{area}\left(u(t)/\sigma_{v0}' > 0.8\right)}{\text{area}(\text{total})}, \tag{2}$$

where σ_{v0}' and $\mu(t)$ are the initial effective stress at a specific location and the excess pore water pressure at the time instant t after the earthquake, respectively.

For the set of δ_x in this study, the difference between the distribution types merely led to a minor diversity of the peak $\mu_{A_{80}}$ by the random shear modulus $\text{CoV}_G = 0.1$. However, the

TABLE 1: Summary of soil parameters.

Parameters	Value
Shear modulus, G: MPa	20
Total unit weight, γ: kN/m^3	26.6
Poisson's ratio, ν	0.35
Permeability coefficient, k: m/s	2.64×10^{-4}
Porosity, N	0.435

peak $\mu_{A_{80}}$ by the Beta distribution was smaller than that by the Lognormal and Gamma distributions with $\text{CoV}_G = 0.3$ and $\text{CoV}_G = 0.5$ (Figures 2(b)–2(f)). In addition, the greatest peak $\mu_{A_{80}}$ was correlated with the G conformed to the Lognormal distribution in these cases.

From the perspective of the decreasing rate of A_{80}, the residual of A_{80}, and the sensitivity of A_{80} to instantaneous seismic loading, it was found that the influence of the different probability distributions on the dynamic liquefaction results was irregular, considering the results of the non-Gaussian probability distributions. However, in general, the differences among the calculated results from the three probability distributions became more obvious with the increase in CoV_G. Figure 2 presents that the irregular dynamic liquefaction results from different probability distributions, in terms of the residual A_{80} and the response of A_{80} to instantaneous seismic loading. Additionally, the increase in CoV_G can amplify the impact from the probability distribution.

2.2. Excess Pore Water Pressure Ratios Q.
The liquefication index was calculated from the mean excess pore water pressure ratio in the horizontal direction and of the form for one simulation:

$$Q(z, t) = \frac{1}{n}\sum_x r(x, z, t), \tag{3}$$

$$r(x, z, t) = \frac{u(x, z, t)}{\sigma_{v0}'}, \tag{4}$$

where x and z are the horizontal and vertical coordinates of the central point of one finite difference element, respectively; $r(x, z, t)$ is the excess pore water pressure ratio at the central point (x, z) at t-th second after the earthquake; σ_{v0}' is the initial effective stress in the vertical direction; n was set to be 40 in this study, which represents the element number of
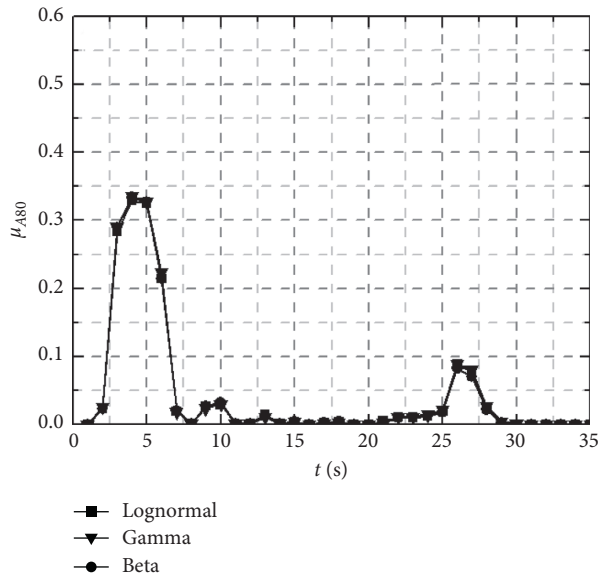
(a)
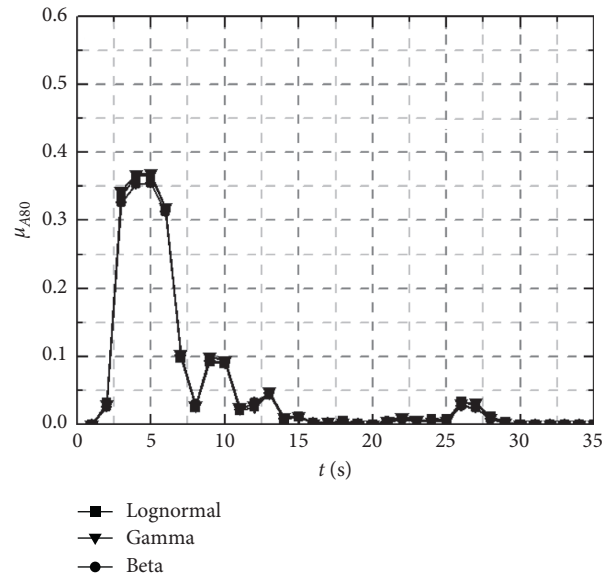
(b)
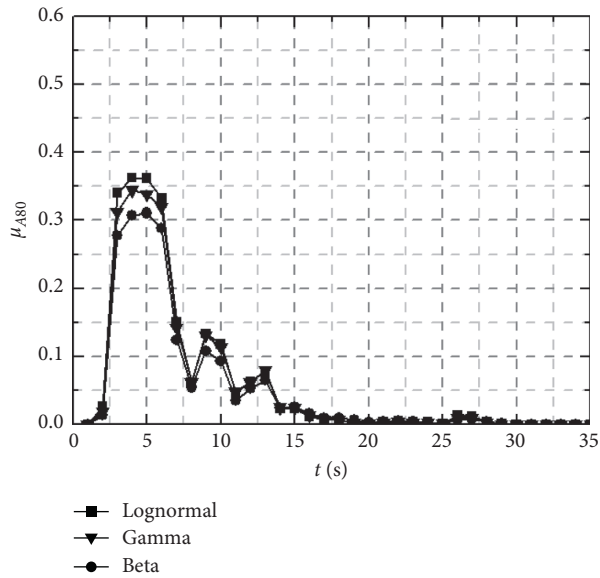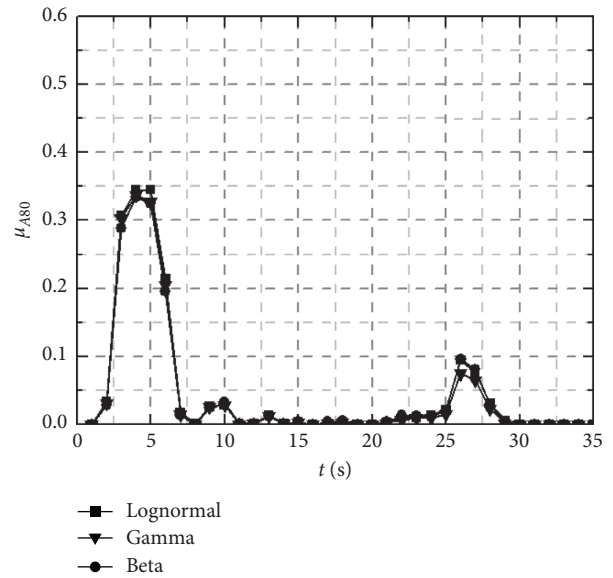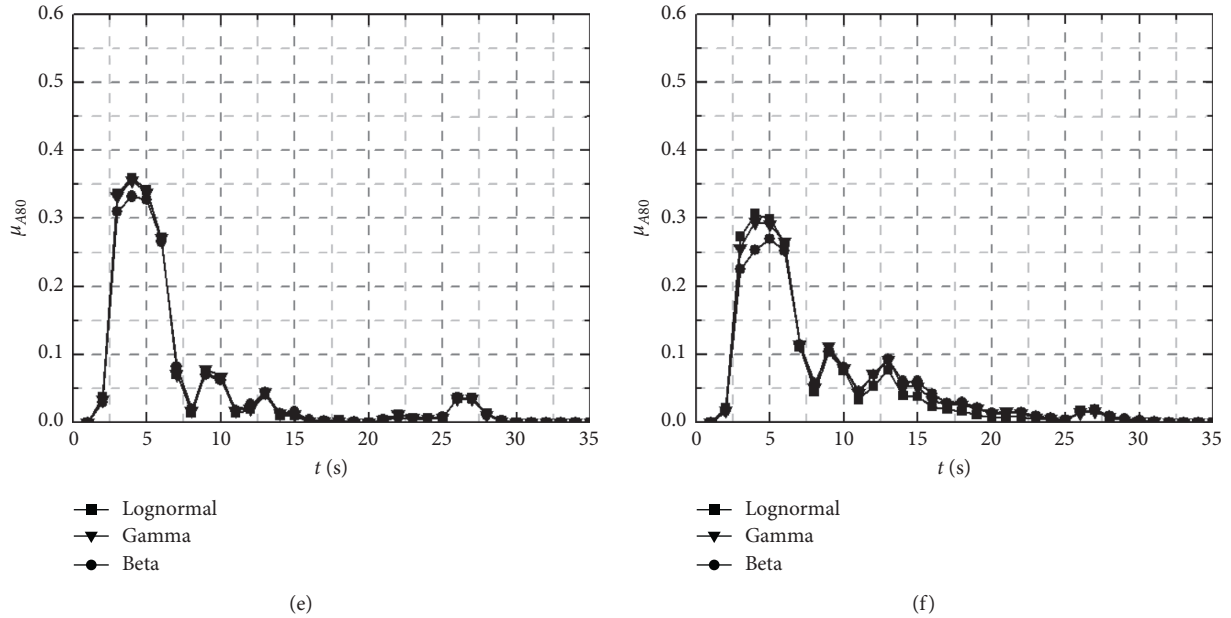
(c)

(d)

Figure 2: Continued.

(e)

(f)

FIGURE 2: Time history curve of mean liquefaction range with different distributions: (a) $\delta_x = 6$ m and $\text{CoV}_G = 0.1$; (b) $\delta_x = 6$ m and $\text{CoV}_G = 0.3$; (c) $\delta_x = 6$ m and $\text{CoV}_G = 0.5$; (d) $\delta_x = 60$ m and $\text{CoV}_G = 0.1$; (e) $\delta_x = 60$ m and $\text{CoV}_G = 0.3$; (f) $\delta_x = 60$ m and $\text{CoV}_G = 0.5$.

the finite difference model in the horizontal direction; and $Q(z, t)$ reflects the average excess pore water pressure ratio at the depth of z at t-th second after the earthquake. Due to the fact that large accumulation of pore water pressure might occur in the deep soil layer, this study paid close attention to the variation of Q at $z = 7.25$ m.

Figure 3 presents the time history curves of the mean excess pore water pressure ratio (μ_Q) at $z = 7.25$ m with different probabilistic distributions. In the case with $\text{CoV}_G = 0.1$ and $\delta_x = 6$ m or 60 m, μ_Q with varying types of distribution presents a similar trend with the seismic load imposed to the soil layer (Figures 3(a) and 3(d)). However, with the increased CoV_G, the rebound amplitude of μ_Q with different probabilistic distributions gradually declined (Figures 3(b)–3(f)). In addition, μ_Q with the Beta distribution was slightly smaller than that with the Lognormal and Gamma distributions when the CoV_G is 0.3 and 0.5, and its dissipation rate of excess pore water pressure (in terms of the slope of the descending part of μ_Q curve) was smaller than that with the Lognormal distribution and Gamma distribution.

Figure 3 also shows that μ_Q dissipated after the occurrence of the peak μ_Q appeared around $t = 4$ s. Table 2 summarizes μ_Q with shear modulus by different distributions after 7 s and 35 s occurrence of the earthquake. Table 3 tabulates the dissipation rate of pore water pressure, which was depicted from the descending section of the μ_Q time history curve. In general, the dissipation rate of μ_Q increased with the increase in CoV_G, and this increasing trend was affected by the distribution type. For instance, the amplification was 16.11% for the Beta distribution as CoV_G extended from 0.1 to 0.5, which was greater compared with that with the Gamma and Lognormal distributions.

2.3. Ground Displacement D.

In this section, the maximum surface ground horizontal movement ($D_x(t)_{\max}$) in Equation (4) and settlement ($D_z(t)_{\max}$) in Equation (5) were taken to evaluate the influence of liquefaction by earthquake, respectively:

$$D_x(t)_{\max} = \left\{ D_{x,z=0}(t) - D_{x,z=10}(t) \right\}_{\max}, \quad (5)$$

$$D_z(t)_{\max} = \left\{ D_z(t)_{\max} - D_z(t)_{\min} \right\}_{\max}, \quad (6)$$

where $D_{x,z=0}(t)$ and $D_{x,z=10}(t)$ represent the horizontal displacements at surface and bottom at the horizontal coordinate x in the soil domain and $D_z(t)_{\max}$ and $D_z(t)_{\min}$ represent the maximum and minimum settlement at t-th second after the earthquake.

Figure 4 plots the time history curve of mean ground horizontal displacement (μ_{D_x}) with different probabilistic distributions. Similar time history curves of μ_{D_x} for different distributions were obtained provided $\text{CoV}_G = 0.1$, indicating that the distribution types had little influence on the ground horizontal displacement (Figures 4(a) and 4(d)). The differences between μ_{D_x} became pronounced with the increase in CoV_G. It was worth noting that μ_{D_x} with the Beta distribution was always the largest, while μ_{D_x} with Lognormal distribution was the smallest.

As expected, the probability distributions also had certain impact on the standard deviation of the horizontal displacement (μ_{D_x}) (Figure 5). The difference of μ_{D_x} gradually increased with the increase in CoV_G, referring that the effect of different distribution on μ_{D_x} enhanced with the increase in CoV_G. If CoV_G is 0.3 or 0.5, it was obvious that μ_{D_x} with the Beta distribution was always greater than that with the Lognormal and Gamma distributions.
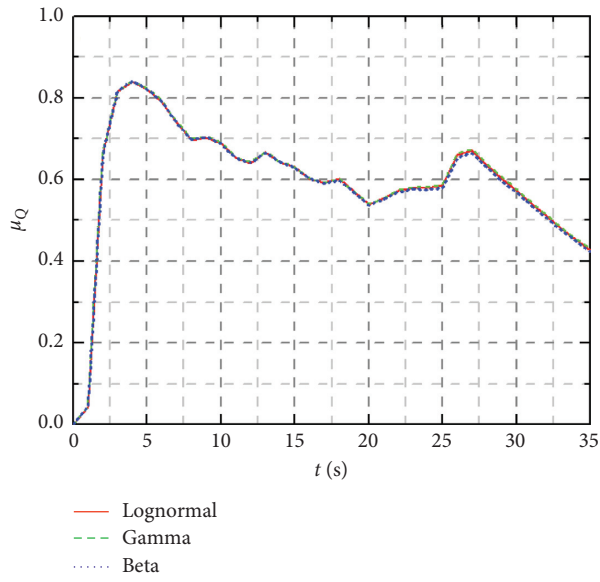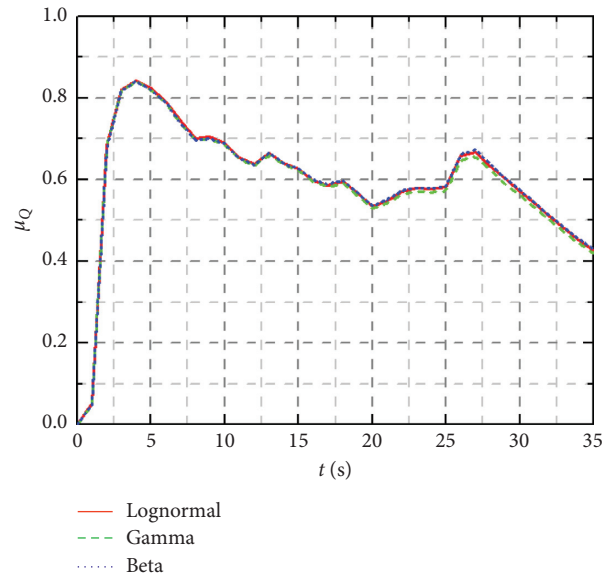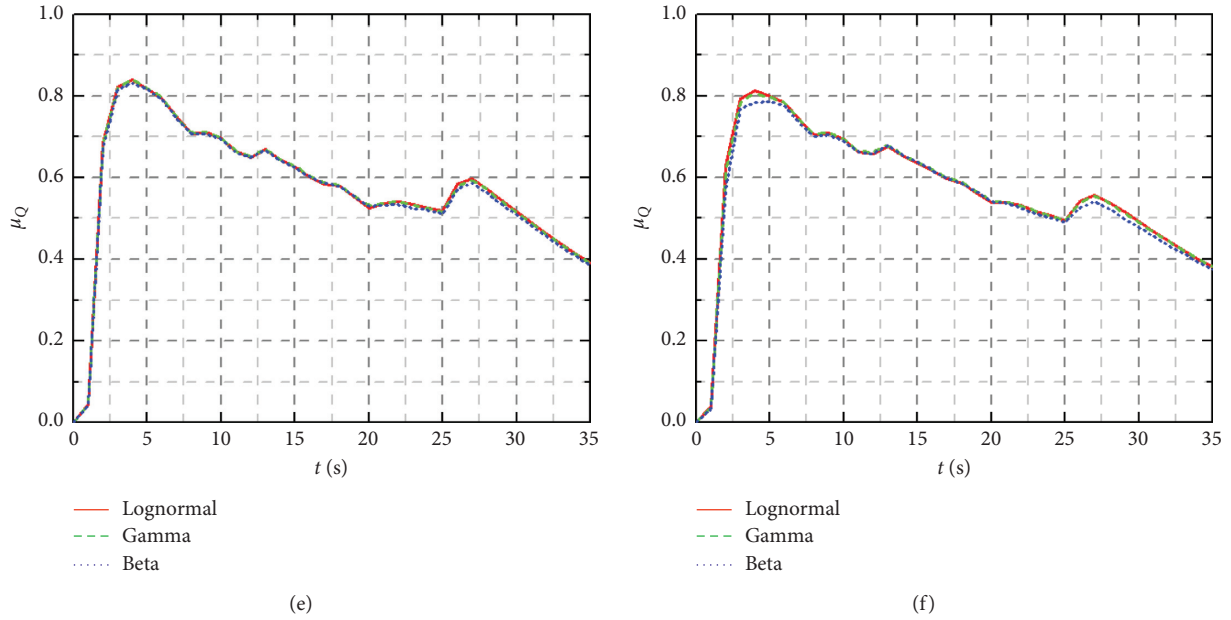
(a)
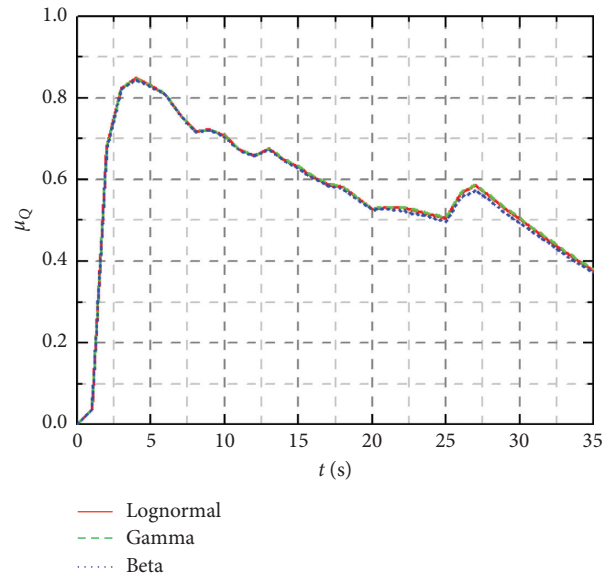
(b)
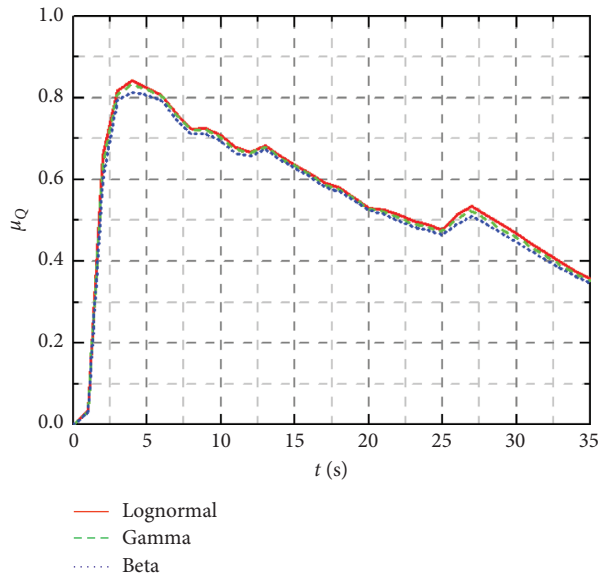
(c)

(d)

Figure 3: Continued.

(e)

(f)

Figure 3: Time history curves of μ_Q at (z) = 7.25 m with different distributions: (a) $\delta_x = 6$ m and $CoV_G = 0.1$; (b) $\delta_x = 6$ m and $CoV_G = 0.3$; (c) $\delta_x = 6$ m and $CoV_G = 0.5$; (d) $\delta_x = 60$ m and $CoV_G = 0.1$; (e) $\delta_x = 60$ m and $CoV_G = 0.3$; (f) $\delta_x = 60$ m and $CoV_G = 0.5$.

Table 2: Summary of μ_Q at $z = 7.25$ m and $t = 7$ and 35 s (10^{-2}).

δ_x (m)	Probabilistic distribution	$CoV_G = 0.1$		$CoV_G = 0.3$		$CoV_G = 0.5$	
		$t = 7$ s	$t = 35$ s	$t = 7$ s	$t = 35$ s	$t = 7$ s	$t = 35$ s
6	Lognormal	73.96	42.76	75.76	37.83	76.00	35.72
	Gamma	74.25	43.04	75.70	38.07	75.65	35.13
	Beta	74.00	42.37	75.60	37.22	74.58	34.45
60	Lognormal	74.23	42.72	74.75	39.13	74.20	38.10
	Gamma	73.88	41.96	74.75	39.02	74.12	38.23
	Beta	73.92	42.97	74.48	38.52	73.42	37.49

Table 3: Variation of dissipation rate of μ_Q ($10^{-3} \times s^{-1}$) at $z = 7.25$ m.

| δ_x (m)	Probabilistic distribution	CoV_G			Amplification (%)
		0.1	0.3	0.5	
6	Lognormal	11.14	13.55	14.39	29.17
	Gamma	11.15	13.44	14.47	29.78
	Beta	11.30	13.71	14.33	26.81
60	Lognormal	11.25	12.72	12.89	14.58
	Gamma	11.40	12.76	12.82	12.46
	Beta	11.05	12.84	12.83	16.11

Figure 6 shows the impact of CoV_G on μ_{D_x} with different distributions at $t = 35$ s. In general, an increase in CoV_G was corresponding with the increase in μ_{D_x} with different distributions. The obtained μ_{D_x} with Beta distribution was greater than that with the Gamma and Lognormal distributions. Moreover, a larger δ_x correlated with a greater $\mu_{D_{x,\max}}$ provided with the same distribution and CoV_G (Figures 6(a) and 6(b)). This finding highlighted that the worst scenario was covered by the shear modulus with Beta distribution. It illuminated that the estimation with Beta distribution is capable to provide a conservative evaluation if site investigation is absent.

The time history curves of mean and standard deviation of settlement (μ_{D_z} and σ_{D_z}) are shown in Figures 7 and 8, respectively. The influences of the distributions of G on μ_{D_z} and σ_{D_z} were similar to those on μ_{D_x} and σ_{D_x}. The differences between μ_{D_z} and σ_{D_z} with different distributions were insignificant if $CoV_G = 0.1$, which implied that the distributions had small impact on the settlement. Nonetheless, the difference was positively correlated with CoV_G. For example,
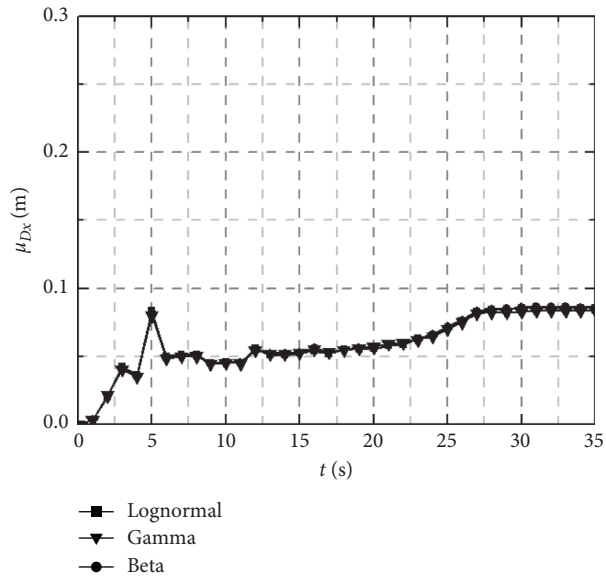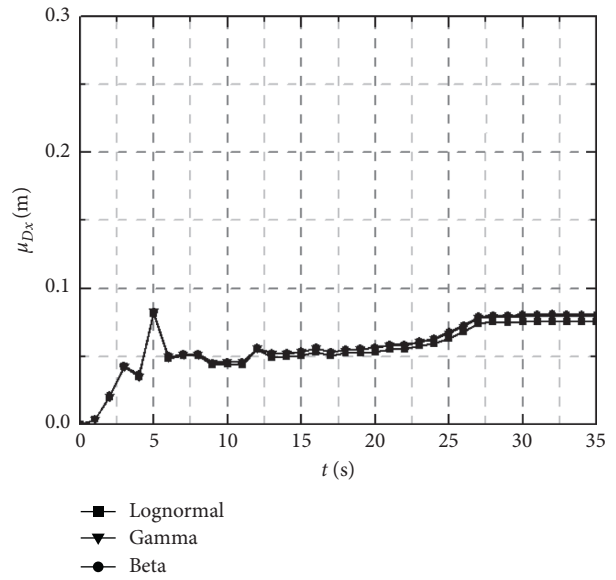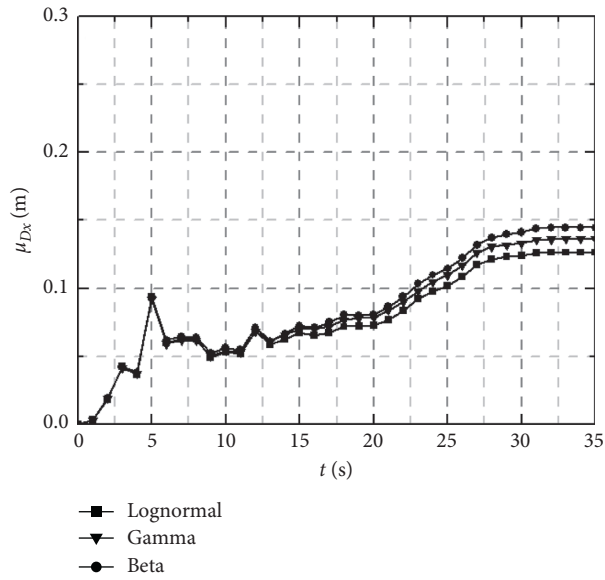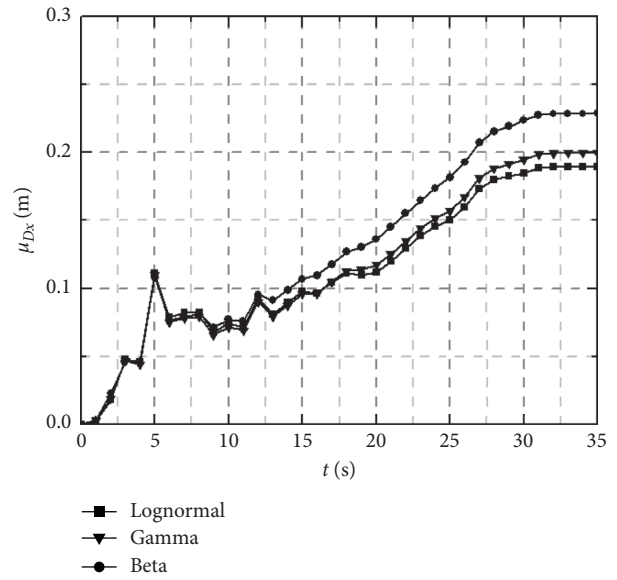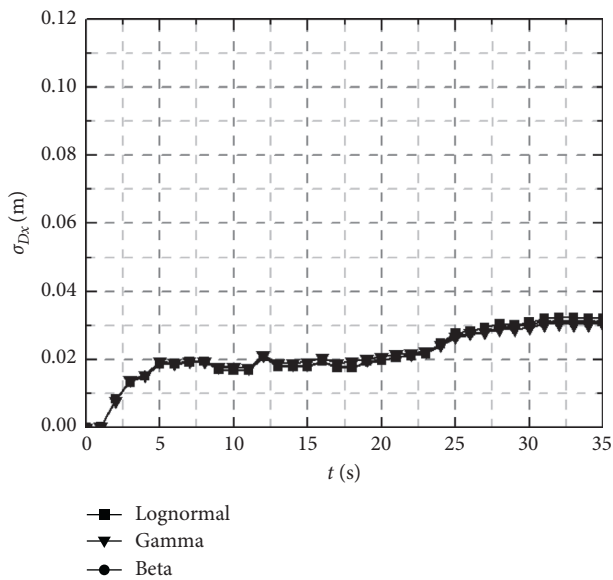
(a)
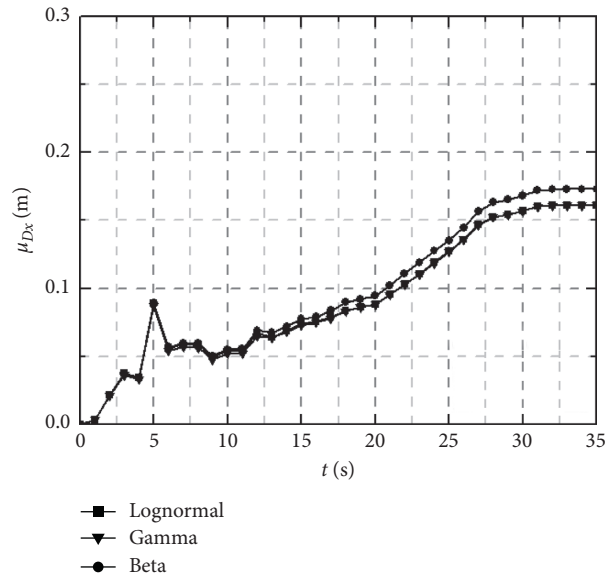
(b)
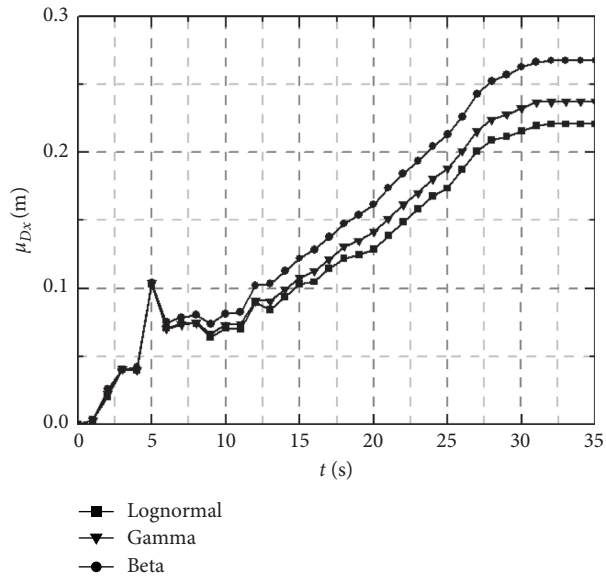
(c)

(d)

Figure 4: Continued.

(e)

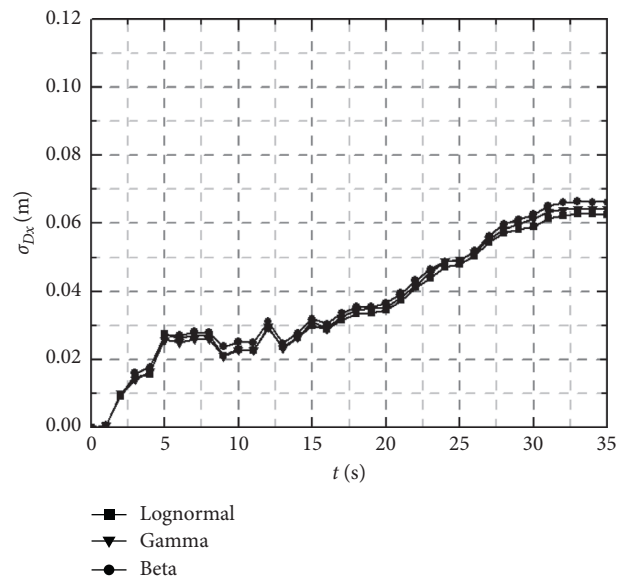

(f)

FIGURE 4: Time history curve of mean ground horizontal displacement (μ_{D_x}) with different distributions: (a) $\delta_x = 6$ m and $CoV_G = 0.1$; (b) $\delta_x = 6$ m and $CoV_G = 0.3$; (c) $\delta_x = 6$ m and $CoV_G = 0.5$; (d) $\delta_x = 60$ m and $CoV_G = 0.1$; (e) $\delta_x = 60$ m and $CoV_G = 0.3$; (f) $\delta_x = 60$ m and $CoV_G = 0.5$.
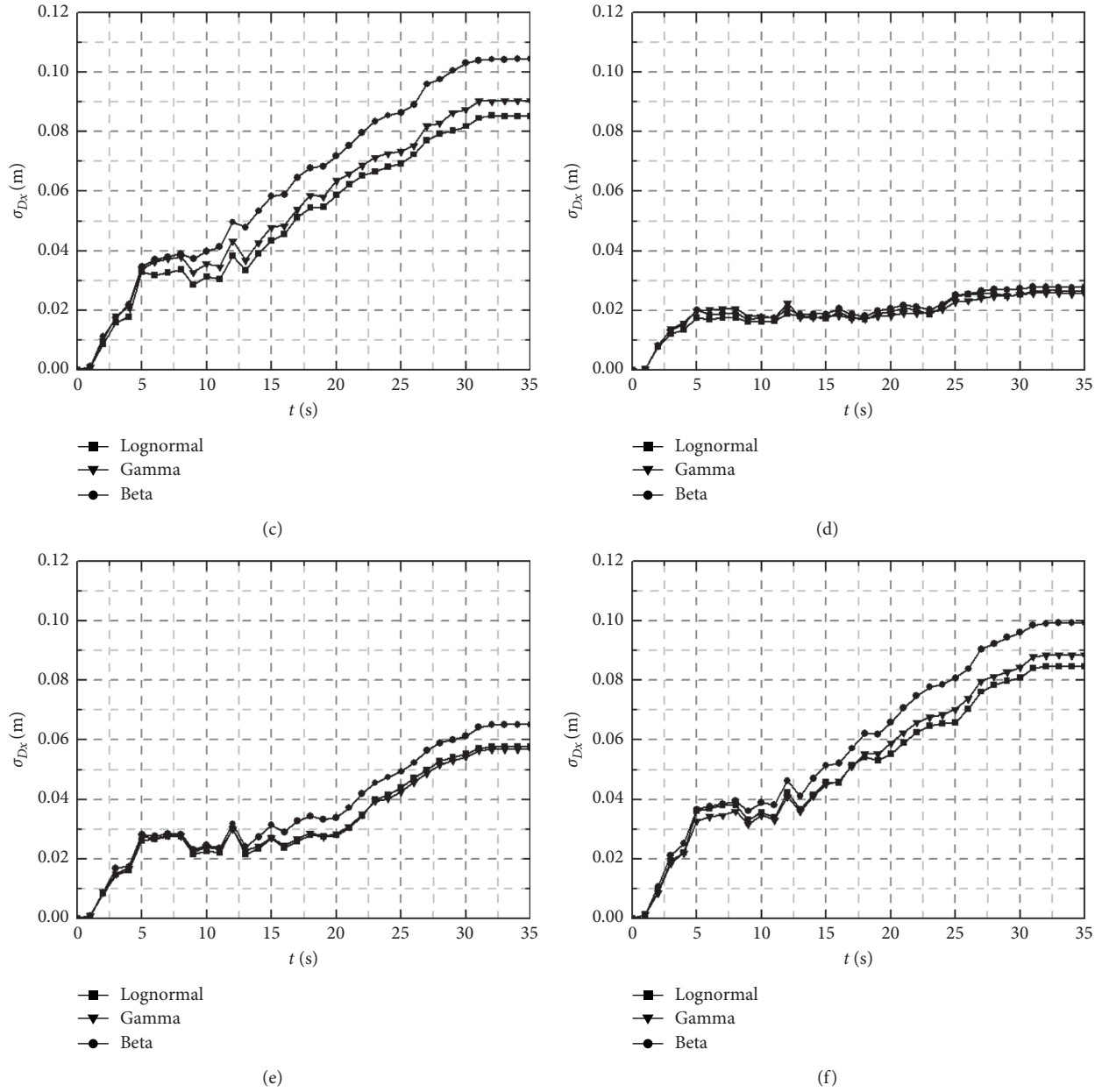

(a)

(b)

FIGURE 5: Continued.

FIGURE 5: Time history curve of standard deviation of ground horizontal displacement (μ_{D_x}) with different distributions: (a) $\delta_x = 6\,\text{m}$ and $\text{CoV}_G = 0.1$; (b) $\delta_x = 6\,\text{m}$ and $\text{CoV}_G = 0.3$; (c) $\delta_x = 6\,\text{m}$ and $\text{CoV}_G = 0.5$; (d) $\delta_x = 60\,\text{m}$ and $\text{CoV}_G = 0.1$; (e) $\delta_x = 60\,\text{m}$ and $\text{CoV}_G = 0.3$; (f) $\delta_x = 60\,\text{m}$ and $\text{CoV}_G = 0.5$.

with a given δ_x of 6 m and $\text{CoV}_G = 0.3$, μ_{D_z} with the Beta distribution was 7.81% and 7.28% larger than that with Gamma distribution and Lognormal distribution. If CoV_G was 0.5, the results enhanced 20.51% and 35.89%, respectively. It addresses the conclusion that the influence of the distributions on μ_{D_z} and σ_{D_z} increased with the increase in

CoV_G. The settlement obtained from the random fields obeying Beta distribution was greater and more dispersive than that calculated by the Lognormal distribution and Gamma distribution.

Figure 9 shows the relationship between $\mu_{D_z,\text{max}}$ and CoV_G. The distribution type had a similar impact on
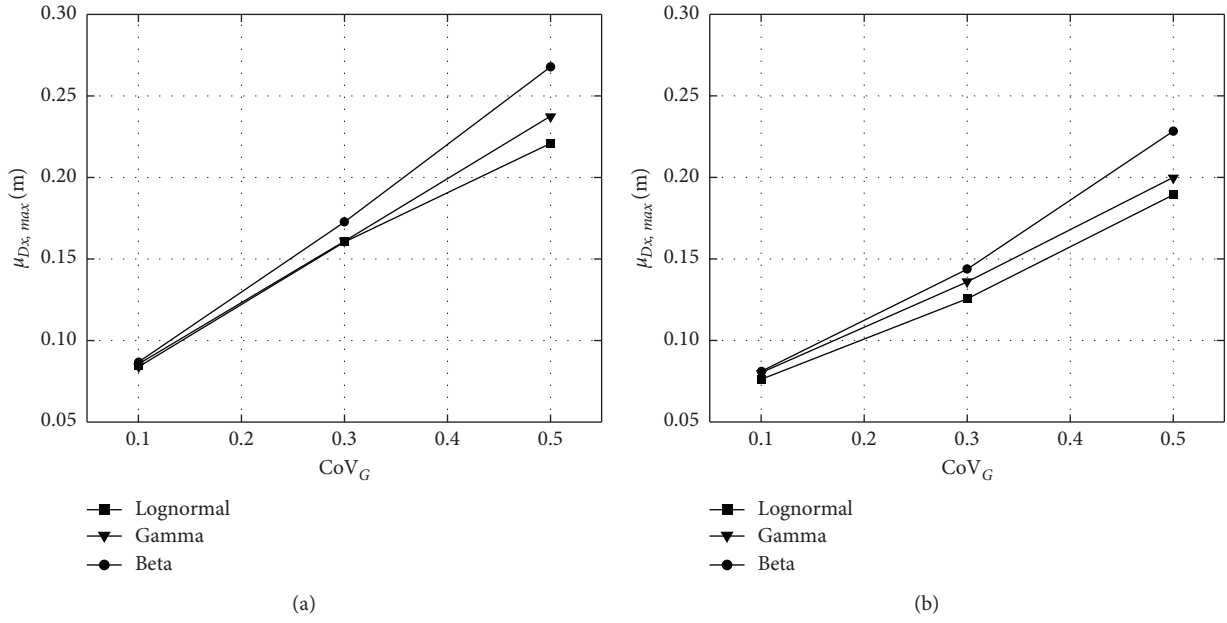
(a)

(b)

FIGURE 6: Variation of $\mu_{D_{x,\max}}$ as a function of CoV_G: (a) $\delta_x = 6\,\text{m}$ and (b) $\delta_x = 60\,\text{m}$.
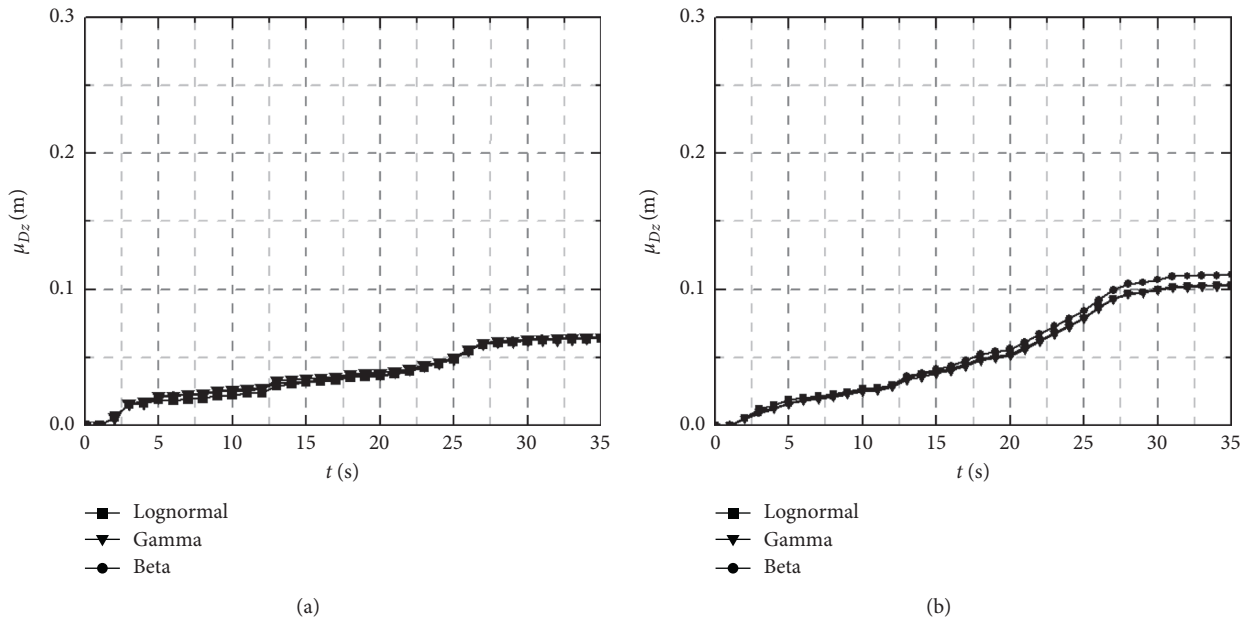

(a)

(b)

FIGURE 7: Continued.

FIGURE 7: Time history curve of μ_{D_z} with different distributions: (a) $\delta_x = 6$ m and $CoV_G = 0.1$; (b) $\delta_x = 6$ m and $CoV_G = 0.3$; (c) $\delta_x = 6$ m and $CoV_G = 0.5$; (d) $\delta_x = 60$ m and $CoV_G = 0.1$; (e) $\delta_x = 60$ m and $CoV_G = 0.3$; (f) $\delta_x = 60$ m and $CoV_G = 0.5$.

$\mu_{D_z,\max}$, which is consistent with the findings in Figure 6. A greater $\mu_{D_{X,\max}}$ was corresponding with a greater CoV_G for all three distributions. Comparing between Figures 9(a) and 9(b), it can be observed that small δ_x corresponded to large $\mu_{D_{X,\max}}$, except for the case of $CoV_G = 0.3$ under the Beta distribution.

(a)

(b)
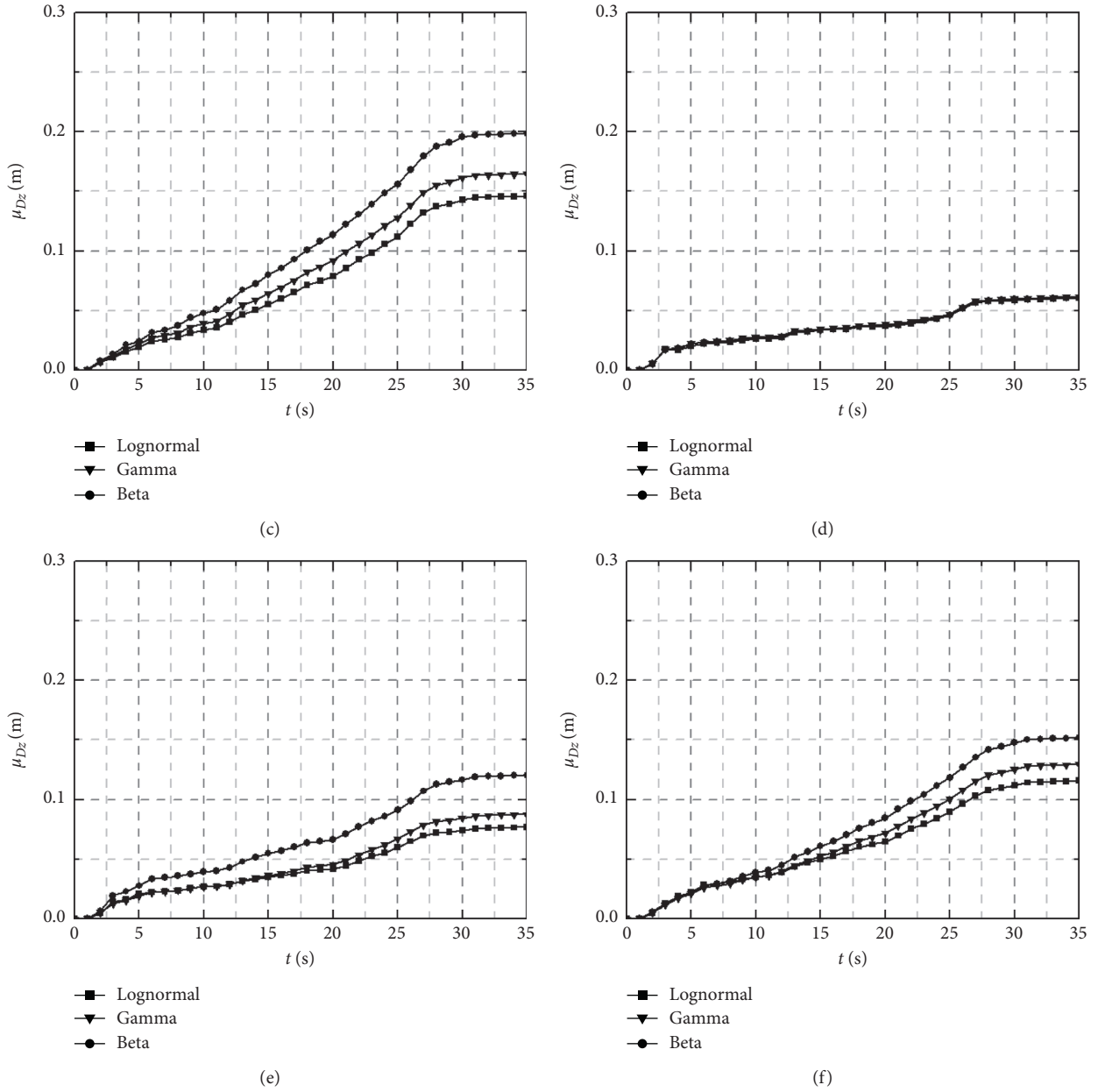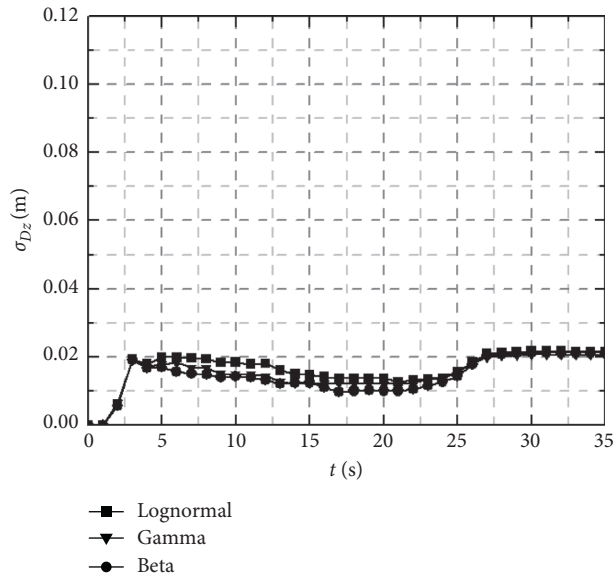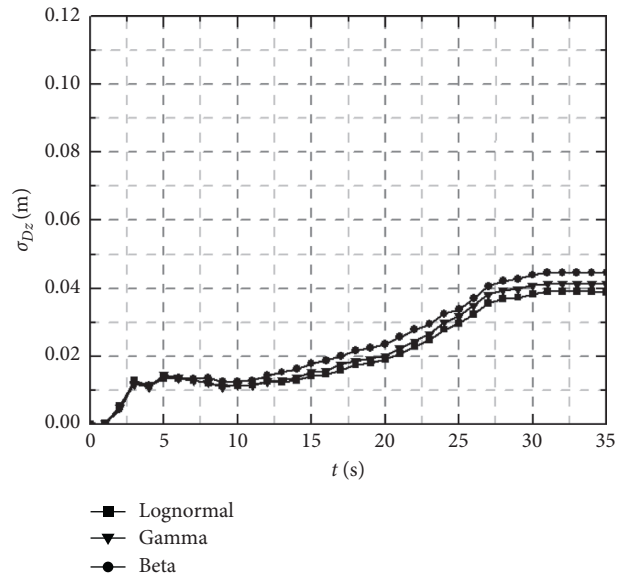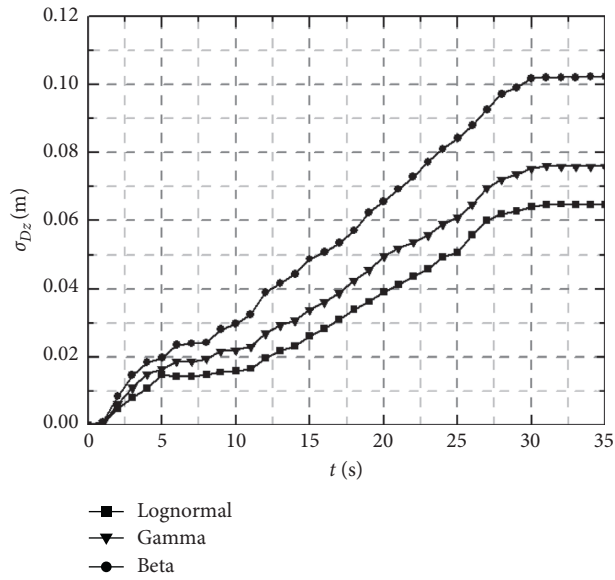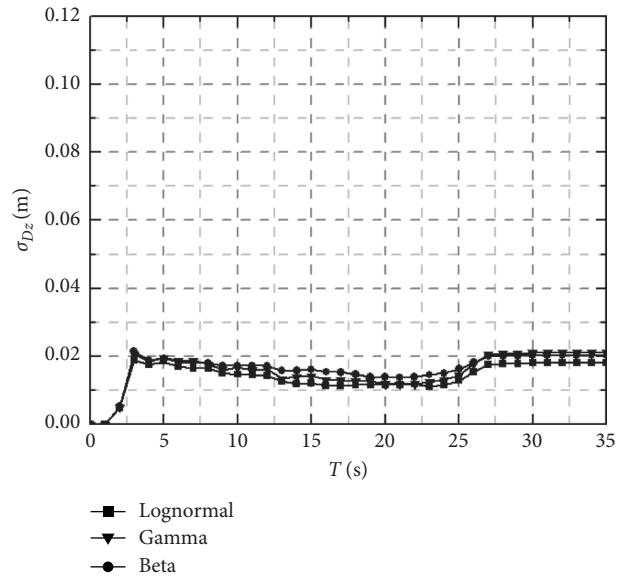

(c)

(d)

FIGURE 8: Continued.

(e)

(f)
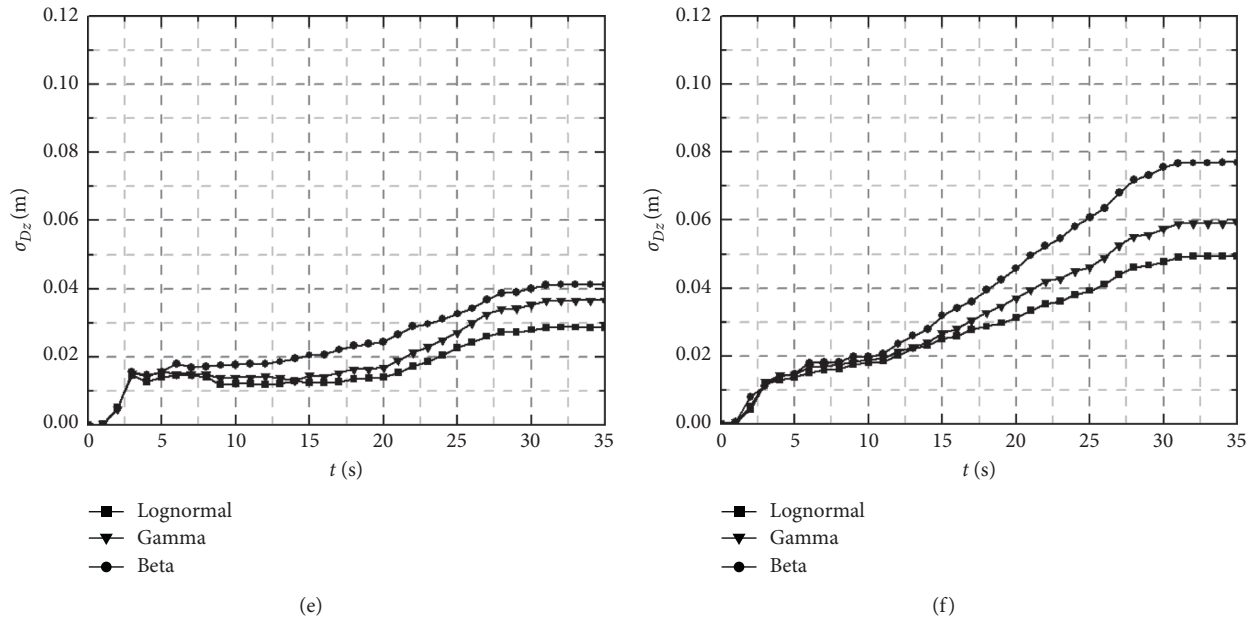
FIGURE 8: Time history curve of σ_z with different distributions: (a) $\delta_x = 6$ m and $CoV_G = 0.1$; (b) $\delta_x = 6$ m and $CoV_G = 0.3$; (c) $\delta_x = 6$ m and $CoV_G = 0.5$; (d) $\delta_x = 60$ m and $CoV_G = 0.1$; (e) $\delta_x = 60$ m and $CoV_G = 0.3$; (f) $\delta_x = 60$ m and $CoV_G = 0.5$.

(a)

(b)
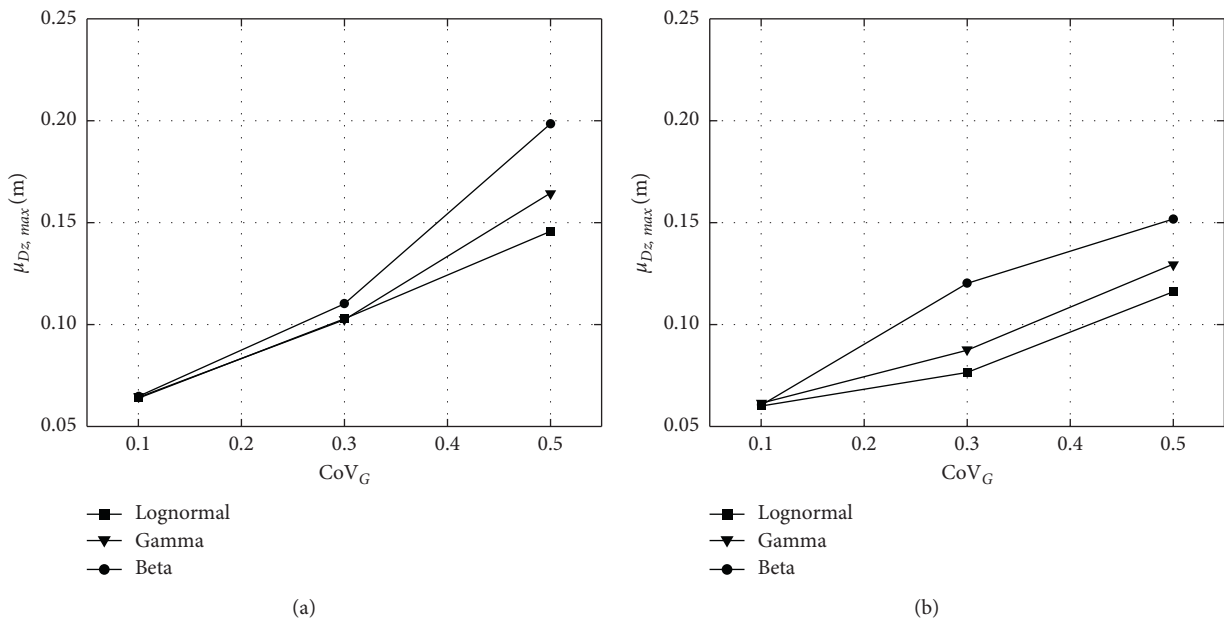
FIGURE 9: Variation of $\mu_{D_z, \max}$ as a function of CoV_G: (a) $\delta_x = 6$ m and (b) $\delta_x = 60$ m.

3. Concluding Remarks

In this study, the influence of the probability distributions of soil shear modulus on the area of liquefaction zone, the ratio of excess pore water pressure, and the ground displacement is investigated. The following conclusions can be drawn:

(1) The probability distribution type of shear modulus had no significant influence on the reduction rate of liquefaction zone and the sensitivity of the liquefaction zone to the instantaneous seismic load.

(2) Compared with the Lognormal distribution and Gamma distribution, a smaller excess pore water pressure ratio could be observed with the Beta distribution employed. The pore water pressure dissipation rate accelerated with the increase in CoV_G and was affected by the distribution type.

(3) Regarding the ground movement, the estimated horizontal displacement and settlement with Beta distribution were the worst scenario. The sensitivity of the ground horizontal displacement and

settlement to CoV_G decreased successively for Beta, Gamma, and Lognormal distribution.

Data Availability

The data used to support the findings of this study are available from the corresponding author upon request.

Conflicts of Interest

The authors declare that they have no conflicts of interest.

Acknowledgments

References

[1] S. Javankhoshdel and R. J. Bathurst, "Simplified probabilistic slope stability design charts for cohesive and cohesive-frictional (c-ϕ) soils," *Canadian Geotechnical Journal*, vol. 51, no. 9, pp. 1033–1045, 2014.

[2] S.-H. Jiang, I. Papaioannou, and D. Straub, "Bayesian updating of slope reliability in spatially variable soils with in-situ measurements," *Engineering Geology*, vol. 239, pp. 310–320, 2018.

[3] S. Jiang, J. Huang, X. Qi, and C. Zhou, "Efficient probabilistic back analysis of spatially varying soil parameters for slope reliability assessment," *Engineering Geology*, vol. 271, 2020.

[4] Y. F. Gao, F. Zhang, G. H. Lei, and D. Y. Li, "An extended limit analysis of three-dimensional slope stability," *Géotechnique*, vol. 63, no. 6, pp. 518–524, 2013.

[5] Y. Gao, F. Zhang, G. H. Lei, D. Li, Y. Wu, and N. Zhang, "Stability charts for 3D failures of homogeneous slopes," *Journal of Geotechnical and Geoenvironmental Engineering*, vol. 139, no. 9, pp. 1528–1538, 2013.

[6] J. Li, Y. Tian, and M. J. Cassidy, "Failure mechanism and bearing capacity of footings buried at various depths in spatially random soil," *Journal of Geotechnical and Geoenvironmental Engineering*, vol. 141, no. 2, 2015.

[7] S. Shu, Y. Gao, and Y. Wu, "Probabilistic bearing capacity analysis of Spudcan foundation in soil with linearly increasing mean undrained shear strength," *Ocean Engineering*, vol. 204, Article ID 106800, 2020.

[8] G. A. Fenton and D. V. Griffiths, "Three-Dimensional probabilistic foundation settlement," *Journal of Geotechnical and Geoenvironmental Engineering*, vol. 131, no. 2, pp. 232–239, 2005.

[9] A. Ahmed and A.-H. Soubra, "Probabilistic analysis of strip footings resting on a spatially random soil using subset simulation approach," *Georisk: Assessment and Management of Risk for Engineered Systems and Geohazards*, vol. 6, no. 3, pp. 188–201, 2012.

[10] M. Uzielli and P. W. Mayne, "Load-displacement uncertainty of vertically loaded shallow footings on sands and effects on probabilistic settlement estimation," *Georisk: Assessment and Management of Risk for Engineered Systems and Geohazards*, vol. 6, no. 1, pp. 50–69, 2012.

[11] C. H. Juang, C. J. Chen, D. V. Rosowsky, and W. H. Tang, "CPT-based liquefaction analysis, Part 2: reliability for design," *Géotechnique*, vol. 50, no. 5, pp. 593–599, 2000.

[12] M. K. Talukder and L. Chouinard, "Probabilistic methods for the estimation of seismic Fa and Fv maps-application to montreal," *Bulletin of Earthquake Engineering*, vol. 14, no. 2, pp. 345–372, 2016.

[13] K. O. Cetin, E. Altinci, and H. T. Bilge, "Probability-based assessment of number of equivalent uniform stress cycles," *Soil Dynamics and Earthquake Engineering*, vol. 143, no. 6, 2021.

[14] D. V. Griffiths and G. A. Fenton, "Bearing capacity of spatially random soil:The undrained clay Prandtl problem revisited," *Géotechnique*, vol. 51, no. 8, pp. 351–359, 2001.

[15] J. H. Li, M. J. Cassidy, Y. Tian, J. Huang, A. V. Lyamin, and M. Uzielli, "Buried footings in random soils: comparison of limit analysis and finite element analysis," *Georisk: Assessment and Management of Risk for Engineered Systems and Geohazards*, vol. 10, no. 1, pp. 55–65, 2015.

[16] S.-H. Jiang and J. Huang, "Modeling of non-stationary random field of undrained shear strength of soil for slope reliability analysis," *Soils and Foundations*, vol. 58, no. 1, pp. 185–198, 2018.

[17] R. Popescu, G. Deodatis, and A. Nobahar, "Effects of random heterogeneity of soil properties on bearing capacity," *Probabilistic Engineering Mechanics*, vol. 20, no. 4, pp. 324–341, 2005.

[18] R. Jimenez and N. Sitar, "The importance of distribution types on finite element analyses of foundation settlement," *Computers and Geotechnics*, vol. 36, no. 3, pp. 474–483, 2009.

[19] Y. Wu, H. Bao, J. Wang, and Y. Gao, "Probabilistic analysis of tunnel convergence on spatially variable soil: the importance of distribution type of soil properties," *Tunnelling and Underground Space Technology*, vol. 109, no. 1, 2021.

[20] Y. Wang, S. Shu, and Y. Wu, "Reliability analysis of soil liquefaction considering spatial variability of soil property," *Journal of Earthquake and Tsunami*, 2021, Article ID 2250002, DOI: 10.1142/S1793431122500026.

[21] M. Azadi and S. M. Hosseini, "Analyses of the effect of seismic behavior of shallow tunnels in liquefiable grounds," *Tunnelling and Underground Space Technology*, vol. 25, no. 5, pp. 543–552, 2010.

[22] S.-H. Jiang and J.-S. Huang, "Efficient slope reliability analysis at low-probability levels in spatially variable soils," *Computers and Geotechnics*, vol. 75, pp. 18–27, 2016.

[23] R. Popescu, J. H. Prevost, and G. Deodatis, "Effects of spatial variability on soil liquefaction: some design recommendations," *Géotechnique*, vol. 47, no. 5, pp. 1019–1036, 1997.

Research Article
Projected Moisture Index (MI) for Tropical Sri Lanka

Charuni Wickramarachchi,[1] Jayanga T. Samarasinghe [ID],[1] Yousif Alyousifi [ID],[2] and Upaka Rathnayake [ID][3]

[1]*IHE Delft Institute for Water Education, Delft, Netherlands*
[2]*Department of Mathematical Sciences, Faculty of Science and Technology, Universiti Kebangsaan Malaysia, 43600 Bangi, Selangor, Malaysia*
[3]*Department of Civil Engineering, Faculty of Engineering, Sri Lanka Institute of Information Technology, Malabe, Sri Lanka*

Correspondence should be addressed to Upaka Rathnayake; upaka.r@sliit.lk

Atmospheric moisture loading can cause a great impact on the performance and integrity of building exteriors in a tropical climate. Buildings can be highly impacted due to the changing climate conditions over the world. Therefore, it is important to incorporate the projected changes of moisture loads in structural designs under changing climates. The moisture index (MI) is widely used in many countries as a climate-based indicator to guide the building designs for their durability performance. However, this was hardly considered in structural designs in Sri Lanka, even though the country is one of the most affected countries under climate change. Therefore, this study investigates future climate change impacts on the environmental moisture in terms of MI, which can be used in climate zoning, investigating indoor air quality, understanding thermal comfort and energy consumption, etc. The moisture index was found as a function of the drying index (DI) and wetting index (WI) to the whole country for its four rainfall seasons. The temporal and spatial distributions were plotted as MI maps and showcased under two categories; including historical MI maps (1990–2004) and future projected MI maps (2021–2040, 2041–2070, and 2071–2100). Future projected MI maps were constructed using bias-corrected climatic data for two RCP climatic scenarios (RCP4.5 and RCP8.5). Results showed that the temporal and spatial variations of MIs are justifiable to the country's rainfall patterns and seasons. However, notable increases of MIs can be observed for future projected MIs in two seasons, and thus a careful investigation of their impacts should be assessed in terms of the construction of buildings and various agricultural activities. Therefore, the outcome of this research can be essentially used in policy implementation in adapting to the ongoing climate changes in Sri Lanka.

1. Introduction

Global climate change creates adverse impacts on the environment. Human living conditions are usually deteriorating due to them. Frequent natural disasters, sea-level rise, water, food scarcity, health concerns, biodiversity extinction, and so on are a few of the impacts of ongoing climate change [1, 2]. Recent studies on the global climate model (GCM) projections discuss that the global mean surface temperature would increase about 3.7°C (within a range of 2.6–4.8°C) by the end of the 21st century, in relation to time period of 1986–2005. This is under the "business as usual" high greenhouse gas emission scenario [3]. In addition, the recorded global mean temperature rise from 2006 to 2015 was much higher than that from 1850 to 1900 (which was the preindustrialized time) [4].

Increases in atmospheric temperatures can also be seen in Sri Lanka under the changing climate. The temperature increasing rate of Sri Lanka from 1961 to 1990 is 0.016°C per year, and this rate is higher than the global average rate of 0.013°C [5]. They have also reported that the 100-year warming trend of Sri Lanka from 1896–1996 is 0.003°C per year. However, the trend for 1987–1996 is 0.025°C, thus confirming the faster warming environment in more recent

years. Therefore, the annual mean temperature over Sri Lanka by the end of the 21st century would be increased by 0.8–3.2°C [6]. However, this is slightly lower compared to other South Asian counties [7]. Nevertheless, the increase is significant and can cause many adverse impacts. In addition, it is predicted that the number of days with temperatures higher than 35°C from a baseline of 20 days would increase to over 100 days by the 2090s under Representative Concentration Pathway (RCP8.5) climatic scenario [8].

Studies carried out in Sri Lanka show that there is a high tendency for the annual rainfall trends to increase in all four climate zones, which are wet, dry, intermediate, and semiarid zones. Due to the increase of rainfall in both annual and seasonal levels, there is an increased risk of floods in the southern and western provinces in the future and risk of droughts in the eastern and southeastern districts of Sri Lanka [9]. Therefore, the country is at a severe risk under the changing climates. Khaniya et al. [10, 11] and Karunanayake et al. [12] carried out extensive research work on climate change and its relationships to the water resources and other ecosystems in Sri Lanka. However, research on the construction industry under the changing climate is yet to be done in the context of Sri Lanka.

Delaying construction projects is quite frequent in Sri Lanka due to adverse climate conditions [13, 14]. In addition, the construction quality is severely affected by adverse weather conditions [15, 16]. Therefore, building design standards are updated to cope with these weather conditions in different parts of the world [3, 17]. Not only the constructions but also the maintenance and healthiness of the buildings are affected due to changing climates [18]. Walls, decks, floors, exteriors, and so on can be damaged due to the higher moisture content in the environment. This can happen in both exterior and interior of the buildings and can also cause some health risks due to fungus grown inside buildings [19, 20]. In addition, atmospheric moisture can adversely affect the performance and durability of building materials [21]. Therefore, analysis of moisture content in the atmosphere is highly important.

A moisture index (MI) was introduced by the Moisture Management of Exterior Wall Systems (MEWS), Canada, to evaluate the project areas of structural buildings in Canada on moisture-related problems [22]. The moisture index is currently used in the National Building Code of Canada (NBCC) in order to incorporate impact from moisture loading in the designs of wall assemblies to safeguard its performance and durability. The MI is the hypotenuse of normalized values of the wetting index (WI), which represents the annual rainfall recorded, and the drying index (DI), which represents the drying capacity of the air (the ability to take up water vapor) [3]. Moisture indices are known to have a significant contribution towards climate zoning for applications such as agriculture and vegetation [22, 23].

Sri Lanka, being a tropical country, experiences issues relating to warmer and humid environmental conditions. The country had many development projects in the recent past and many are in the pipeline. Colombo, the capital of Sri Lanka, is highly exposed to building construction after ending the country's war (in 2009). As stated in the

preceding paragraphs, Sri Lanka is highly vulnerable to the changing climate. Therefore, it is very important to incorporate the moisture index in structural designs to prevent cracking and moisture-related complications in construction and finishing work. However, to the authors' knowledge, this was a grey area in Sri Lanka. Therefore, this research study presents a comprehensive analysis of the moisture index over Sri Lanka and then develops the contour maps to showcase the spatial and temporal variation of MI. The research presents the MI maps for the historical climatic records (1990–2004) and for future climatic conditions (2021–2100). Future climatic conditions were assessed under two climatic scenarios (RCP4.5 and RCP8.5) for three time periods, including near-future period (2021–2040), mid-future period (2041–2070), and far-future period (2071–2100). The importance of the results was discussed along the lines of the construction industry as Sri Lanka showcases a construction boom. In addition, this is the first related study in the Sri Lankan context for future projected moisture content in the atmosphere.

2. Study Area and Data Collection

Sri Lanka is a tropical country in the Indian Ocean with a land extent of 65,610 km². Sri Lanka is rich in water resources, and thus it has around 2905 km² of inland waters [24]. The country lies in between 5.92°–9.79°N and 79.68°–81.8°E, latitudes and longitudes, respectively; therefore, it has an equatorial climate. Most of the perennial rivers originated from the central highlands of the country, and therefore the highlands are hydrologically significant. The rivers subsequently descend radially to the coast. The river system in the country is nutrified by the higher rainfalls received to the central highlands of Sri Lanka.

Sri Lanka is divided into four climatic zones based on the received annual rainfall. They are the wet zone, dry zone, intermediate zone, and semiarid zone [9]. The wet zone receives more than 2500 mm of rainfall, whereas the semiarid zone receives around 800–1200 mm rainfall per year. Rainfall is not only spatially varied but also temporally varied in seasons. Southwest monsoon (SWM) and northeast monsoon (NEM) are the two major monsoon seasons that bring the majority of rainfall to the country. SWM starts in mid-May of the year and lasts until the end of September. Western, southern, and southwestern slopes of the central hill areas receive the majority of their rainfall during SWM season [25]. Similarly, the NEM season provides rainfall to the northern, eastern, and northeastern slopes of central hills from December to February [26]. However, two intermediate seasons, the first inter-monsoon (FIM) from March to April and the second inter-monsoon (SIM) from October to November bring rainfall to the country. Thus, it is evident that the four rainfall seasons encompass rainfall regimes over the entire country resulting in a high agro-ecological diversity.

However, Sri Lanka experiences a rather homogenous temperature pattern in the lowlands with a mean annual average temperature of 27°C (altitude: 100–150 m), and it decreases to 15°C towards the highlands as the altitude increases to 1800 m [27]. Not only the spatial variation but

also the temporal variations for temperature can be seen. In the months of December to February, most of the areas have cooler temperatures, whereas warmer temperatures are experienced from April to August. In addition, the relative humidity (RH) of Sri Lanka is around 70–90% during the morning hours and 55–80% during the late afternoons. Furthermore, the country has a significant evaporation rate which varies from 3 to 8 mm per day depending on geographical region [26].

Daily rainfall data for 35 rainfall measuring stations were purchased from the Department of Meteorology, Sri Lanka. These 35 rainfall stations are well spread over Sri Lanka as shown in Figure 1. In addition, daily temperature and relative humidity data were purchased from the same department for 18 gauging stations. Sri Lanka has many gauging stations to measure daily rainfall (more than 500); however, there are only few of them for all other climatic parameters. Therefore, the available 18 stations were selected for temperature and relative humidity data collection. Depending on all data available for the total number of stations, a common time frame of 15 years from 1990–2004 was selected. The 18 meteorological stations and their spatial variation can be seen from Figure 1, and the total description including the locations and elevations can be found in Table 1.

The daily climate data were extracted for the historical years (from 1990 to 2004) and future years (from 2021 to 2100) from the climate model IS-ENES Climate4Impact. Two datasets under RCP4.5 and RCP8.5 were extracted for future climate data. All these climate data were extracted to the exact coordinates of the observed gauging station. Therefore, a clear comparison can be made between the observed and modeled climate data. RCPs showcase trajectories based on greenhouse gas concentration. RCP4.5 presents an intermediate scenario where the peak of greenhouse gas concentration is in 2040s, whereas RCP8.5 showcases an extreme case where the peak of greenhouse gas concentration goes to 2100.

Climate4Impact is a database, which has modeled regional climate model (RCM) climatic data for research purposes. The Coordinated Regional Downscaling Experiment (CORDEX) climate data can be freely extracted from this European Union-funded database. The database was widely used for many countries and areas [28–33]. The database can be found at https://climate4impact.eu/impactportal/general/index.jsp.

3. Methodology

3.1. Bias Correction.

The linear scaling method was used in order to remove the biases from the rainfall, temperature, and relative humidity data obtained from the climate model. The linear scaling bias correction method is a simple method, but it also performs other complex methods such as power transformation, quantile mapping, and delta change [12]. Measured meteorological data and historical data obtained from the climate model IS-ENES Climat4Impact for 1990–2004 were used to carry out bias corrections for the future projected meteorological data. Additive correction (refer to equation (1)) was used for temperature while
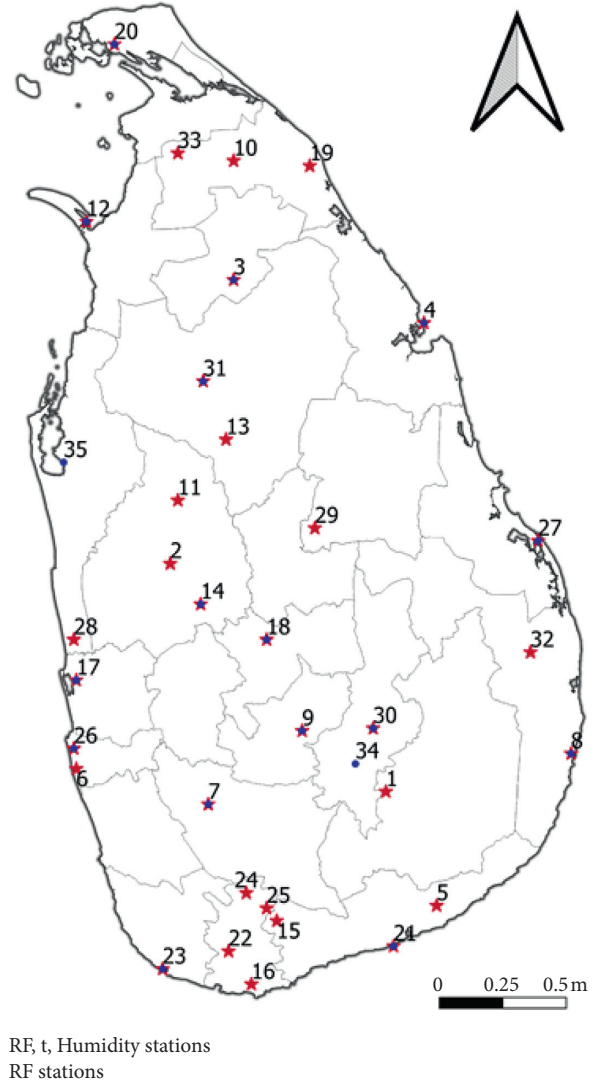

FIGURE 1: Meteorological stations used for the study.

★ RF, t, Humidity stations
● RF stations

multiplicative correction (refer to equation (2)) was used for precipitation and relative humidity data.

$$t^*_{F,d} = t_{F,d} + \left(\left(\mu_{O,t} \times t_{O,d} \right) - \left(\mu_{H,t} \times t_{H,d} \right) \right), \tag{1}$$

where $t^*_{F,d}$, $t_{F,d}$, $t_{O,d}$, and $t_{H,d}$ are the bias-corrected future temperature data, raw RCM temperature data, observed temperature data, and raw RCM temperature data for the observed duration, respectively. The subscript "d" stands for the daily basis data. $\mu_{O,t}$ and $\mu_{H,t}$ represent the long-term mean of the monthly temperature based on the observed and RCM temperature data.

$$P^*_{F,d} = P_{F,d} \times \frac{\mu_{O,P} \times P_{O,d}}{\mu_{H,P} \times P_{H,d}}, \tag{2}$$

where $P^*_{F,d}$, $P_{F,d}$, $P_{O,d}$, and $P_{H,d}$ are the bias-corrected future precipitation data, raw RCM precipitation data, observed rainfall data, and raw RCM data for the observed duration, respectively. $\mu_{O,P}$ and $\mu_{H,P}$ represent the long-term mean of the monthly precipitation based on the observed and RCM rainfalls. Some researchers have suggested using climate-

TABLE 1: List of meteorological stations and their locations.

No.	Station	Station type	Longitude	Latitude	Elevation (m)
1	Wellawaya	RF	81.1	6.73	16
2	Wariyapola	RF	80.25	7.63	16
3	Vavuniya	RF, T, RH	80.5	8.75	98
4	Trincomalee	RF, T, RH	81.25	8.58	24
5	Tissamaharama	RF	81.3	6.28	16
6	Ratmalana	RF	79.88	6.82	5
7	Ratnapura	RF, T, RH	80.4	6.68	86
8	Pottuvil	RF, T, RH	81.83	6.88	4
9	Nuwara Eliya	RF, T, RH	80.77	6.97	1894
10	Mutu Iyankaddu	RF	80.65	9.22	16
11	Mediyawa Wewa	RF	80.28	7.88	16
12	Mannar	RF, T, RH	79.92	8.98	4
13	Maha Illuppallama	RF	80.47	8.12	117
14	Kurunegala	RF, T, RH	80.37	7.47	116
15	Kirama	RF	80.67	6.22	122
16	Kekanadura	RF	80.57	5.97	49
17	Katunayake	RF, T, RH	79.88	7.17	8
18	Katugastota	RF, T, RH	80.63	7.33	417
19	Kannukkeni Tank	RF	80.8	9.2	30
20	Jaffna	RF, T, RH	80.03	9.68	3
21	Hambantota	RF, T, RH	81.13	6.12	16
22	Goluwawatta	RF	80.48	6.1	16
23	Galle	RF, T, RH	80.22	6.03	12
24	Deniyaya	RF	80.55	6.33	16
25	Dampahala	RF	80.63	6.27	176
26	Colombo	RF, T, RH	79.87	6.9	7
27	Batticoloa	RF, T, RH	81.7	7.72	8
28	Bandirippuwa	RF	79.87	7.33	16
29	Bakamuna	RF	80.82	7.77	16
30	Badulla	RF, T, RH	81.05	6.98	670
31	Anuradhapura	RF, T, RH	80.38	8.35	92
32	Amparai Tank	RF	81.67	7.28	27
33	Ambalperumalkulam	RF	80.28	9.25	16
34	Bandarawela	RF, T, RH	80.98	6.83	1220
35	Puttalam	RF, T, RH	79.83	8.03	2

modeled data directly for relative humidity due to difficulties in identifying biases [34]; however, a similar formula given in equation (2) was used to carry out the bias correction for relative humidity in this study.

3.2. The Wetting Index (WI) and Drying Index (DI).

The wetting index (WI) indicates the source or the availability of the moisture loading [3]. It can be calculated using the annual total recorded rainfall at a location normalized using 1000 mm. However, the drying index (DI) indicates the drying potential of evaporation or sink of the moisture loading [3]. The DI is calculated using the humidity ratio between saturated and ambient air conditions. The DI values are normalized using the maximum limits of DI to represent normalized DI values between zero and one. The drying index is calculated using the following equation:

$$DI = \sum_{K} \Delta w \times 1000, \tag{3}$$

$$\Delta w = w_{sat} - w_{amb}, \tag{4}$$

$$w_{sat} = 0.622 \left(\frac{V_{sat}}{P - V_{sat}} \right) \text{ and } w_{amb} = 0.622 \left(\frac{V_{amb}}{P - V_{amb}} \right), \tag{5}$$

where P, w, and K are the total pressure (assumed to be 101.1 KPa), humidity, and the number of hours in a year, respectively. The subscripts sat and amb represent the saturated and ambient levels of the atmosphere. Saturated (w_{sat}) and ambient (w_{amb}) humidity levels as shown in equation (4) are needed to calculate using the change of vapor pressures (shown in equation (5)).

The saturated vapor pressure is calculated according to equation (6) by using the monthly mean temperature values (t) [8], whereas the ambient vapor pressure is calculated according to equation (7) using the results of saturated vapor pressure obtained from the following equation:

$$V_{sat} = 6.112 \cdot \exp\left(\frac{17.62 \times t}{243.12 + t} \right), \tag{6}$$

$$V_{amb} = RH \times V_{sat} \times 100\%. \tag{7}$$

The relative humidity is the ratio of ambient vapor pressure of water (P_w) to the saturation water vapor pressure ($P_{s,w}^{pure}(t)$) and can be seen from the following equation:

$$RH = \frac{P_w}{P_{s,w}^{pure}(t)} \times 100\%. \qquad (8)$$

3.3. The Moisture Index (MI).

The moisture index (MI) formulates the potential atmospheric moisture loading as a function of wetting index (WI) and the drying index (DI) and then expresses the potential of moisture impacts when exposed to exterior climates [22]. Equation (9) shows the mathematical relationship among the indices.

$$MI = \sqrt{WI^2 + (1 - DI)^2}. \qquad (9)$$

Ideally, more parameters such as hourly wind speed and direction of wind should be considered for MI calculation; however, the comprehensive form was not used here due to data scarcity. The projected climatic data used in the model are corrected for their biases using linear bias correction technique as stated above. Therefore, the model performance in obtaining MI was kept as a higher level.

3.4. Overall Methodology.

The historical wetting index (WI) was calculated using the annual mean rainfall data of 35 rainfall stations spread all across Sri Lanka for the time period 1990–2004. The average monthly mean rainfall was calculated for observed daily rainfall data. In addition, the mean seasonal rainfalls were calculated for each monsoon (NEM, FIM, SWM, and SIM). In order to calculate the drying index, temperature data and relative humidity of 18 stations across the country for the time period of 1990–2004 were used. Finally, the MI was calculated for the time period of 1990–2004 as historical MIs and illustrated in maps. The observed climatic data were interpolated using inverse distance weighting (IDW) in generating these illustrations.

The future projections of the WI were calculated by analyzing projected daily rainfall data for three climatic cycles, including near-future period (2021–2040), mid-future period (2041–2070), and far-future period (2071–2100). Twenty years were considered for the near-future scenario, and 30 years of climate cycles were considered for the mid-future and far-future analysis based on the literature [35–37]. The climatic data were extracted under two Representative Concentration Pathways 4.5 and 8.5 (RCP4.5 and RCP8.5), and they were bias-corrected using the linear bias corrections (refer to equations (1) and (2)). These projected climate data were used to analyze the future MIs. Finally, the maps were developed for projected MIs for the three climatic cycles.

4. Results and Discussion

4.1. Historical Indices (1990–2004).

Figure 2 presents the historical indices for DI (refer to Figure 2(a)), WI (refer to Figure 2(b)), and MI (refer to Figure 2(c)) for the observed meteorological data in the 1990–2004 period. The results are given for the four seasons. As discussed in the methodology, the DI was normalized by the maximum values obtained for the DI. Therefore, the normalized drying index values ranged from zero to one. However, the WI was normalized using the minimum values obtained for the WI, and thus the normalized range was between one to values greater than one. As a result, MI ranges from 1 to values greater than one.

The literature states that drying potential can be used as the normalization factor to calculate the drying index [38]. However, the drying potential for Sri Lanka is unavailable; therefore, the corresponding minimum and maximum values of the wetting index and drying index were used in normalization. Nevertheless, the results obtained for the MI were greater than 1 [3].

The major drawbacks of using minimum and maximum values are that the normalized index does not represent the value of the index. Thus, the highest normalized WI does not represent the highest WI. The highest normalized wetting index represents the scenario with the largest range of wetting index but not the highest value.

It can be seen that the DI is higher in northwestern and western areas of the country for all four seasons (dark red patches). In addition, the northeastern and eastern regions showcase higher DI during the southwestern monsoon period. The SWM brings rain to southwestern Sri Lanka, and the wind direction is significantly towards the southwestern to northeastern direction. However, the high central hills limit the rainfall to eastern and northeastern Sri Lanka during this period. Therefore, higher DI can be expected in northeastern and eastern areas of Sri Lanka.

However, there are no significant changes in WI for the four seasons. Therefore, the moisture loading does not showcase a big difference from one season to another. Nevertheless, MI is higher in FIM and SWM for the southwestern area of the country. Therefore, the atmospheric moisture content in these two seasons is higher compared to SIM and NEM seasons. Some of the numerical values for indices are given in Table 2 for more information for the variations shown in Figure 2. The maximum MI is limited to 15.25 in SWM as shown in Table 2. In addition, the SWM season has comparably higher DI and WI values. Therefore, the numerical representation of MI can be important in identifying the maximums and minimums.

4.2. Near-Future Indices (2021–2040).

Figures 3 and 4 illustrate the DI, WI, and MI obtained for near-future climates from 2021–2040. The indices derived for RCP4.5 climate scenario are presented in Figure 3, whereas the indices for RCP8.5 are given in Figure 4. No significant differences can be identified from the corresponding indices for two RCP scenarios. Higher DI values can be seen in the northwestern region of the country for both historical and future years for all four seasons. In addition, eastern regions showcase higher DI during three seasons other than NEM. The observations are common for both RCPs.

WI and MI are found to be higher in the southwestern region for SWM season for both RCPs. Therefore, the construction industry in highly developing areas of Sri
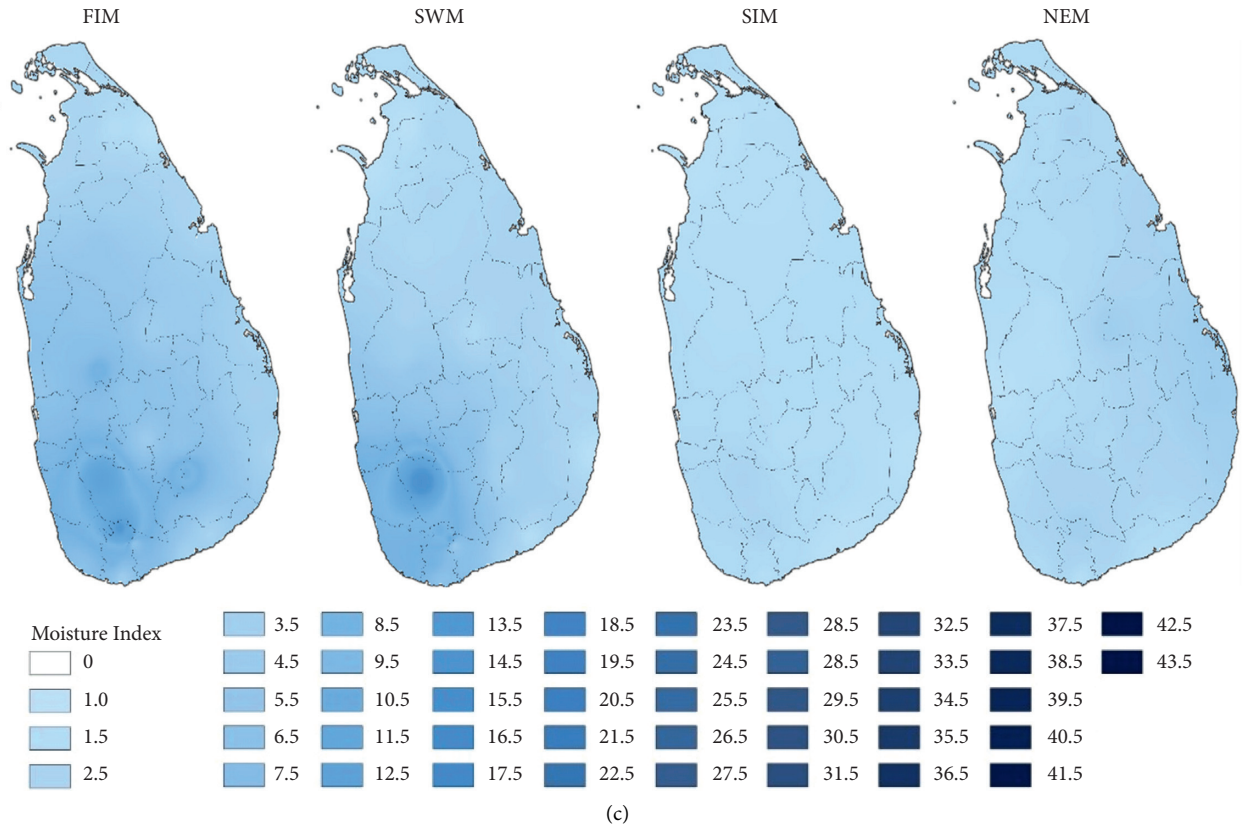
(a)

(b)
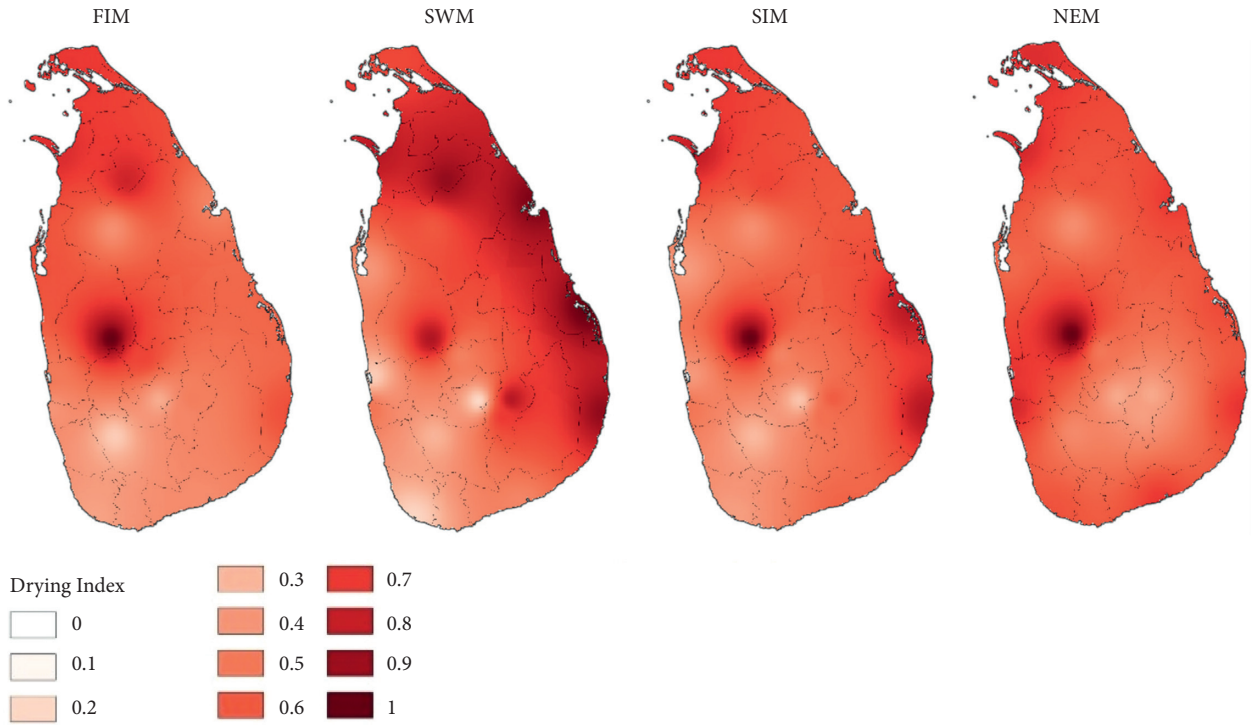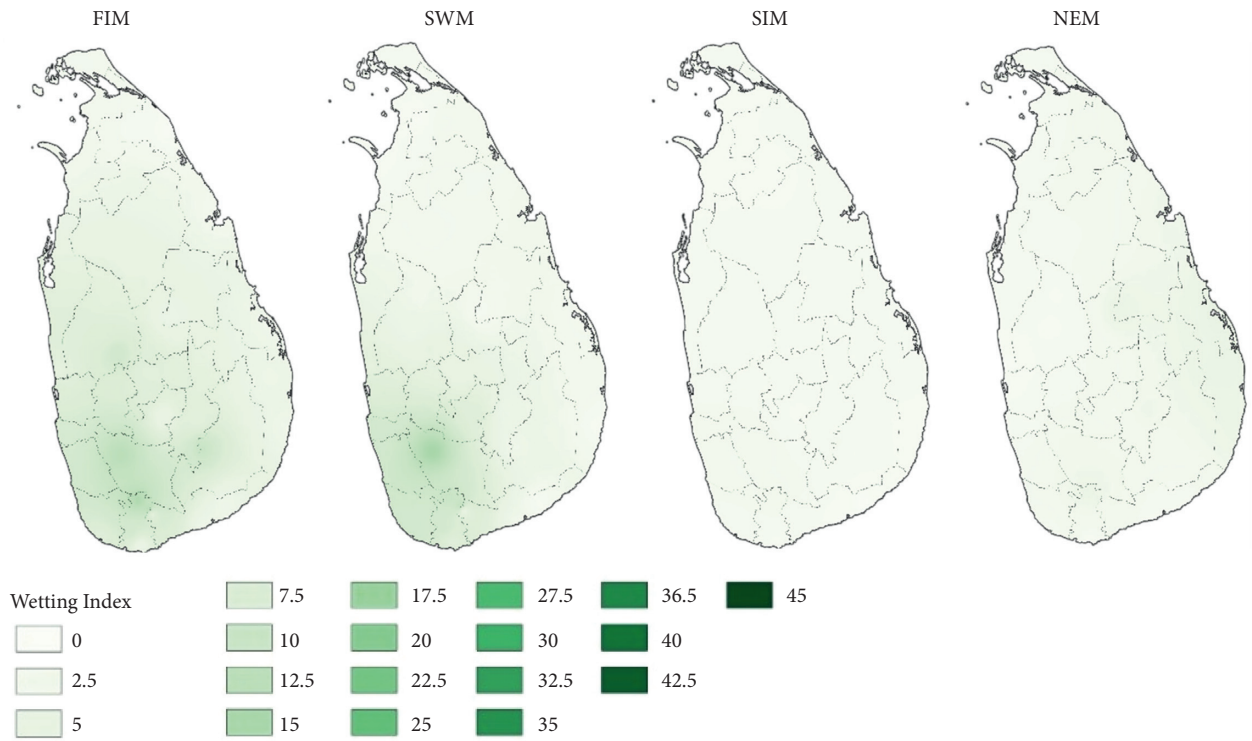
Figure 2: Continued.

FIGURE 2: Historical indices from observed climatic parameters (1990–2004). (a) For normalized DI. (b) For normalized WI. (c) Moisture index.

TABLE 2: Indices for historical meteorological observations.

Season	DI		WI		Moisture index	
	Min	Max	Min	Max	Min	Max
FIM	2.37	10.13	1.55	21.52	1.06	13.87
SWM	1.58	8.15	3.93	59.86	1.03	15.25
SIM	1.46	5.61	11.95	30.81	1.09	2.64
NEM	2.03	5.98	6.48	29.14	1.04	4.52

Lanka would be concerned. In addition, the wetting index has been increased considerably compared to historical indices, owing to the increasing trends of rainfall. Table 3 presents the minimums and maximums for DI, WI, and MI for four seasons under both RCPs. Non-normalized DI and WI do not show a significant difference from RCP4.5 to RCP8.5. This can be seen for the MI too. Therefore, the normalized DI and WI reflect the non-normalized indices. Thus, the spatial variations shown in Figures 3 and 4 are justifiable.

4.3. Mid and Far-Future Indices (2041–2070 and 2071–2100). Table 4 presents the DI, WI, and MI for mid-future and far-future periods under both RCP scenarios. DIs do not show a significant difference from mid-future to far-future periods in both minimum and maximum DIs during the RCP4.5 and RCP8.5 climatic scenarios. However, differences can be

observed in WIs from mid-future to far-future periods for RCP4.5. Nevertheless, the differences are not significant for RCP8.5. In addition, minimum MIs are always kept around 1; however, the maximum MIs have significant variations from mid-future to far-future periods in RCP4.5. Interestingly, these significant variations cannot be found for RCP8.5 climatic scenarios. The developed maps for DI, WI, and MI for mid-future and far-future periods for two RCPs are given in Figures 5–8.

The highest drying index is experienced in the southeast regions of the country for the three monsoons—FIM, SWM, and SIM, whereas for the NEM, the highest drying index is observed in the southwestern regions (refer to Figures 5–8). This phenomenon is consistent for both the time periods in both RCPs for the spatial variations of DIs. From the results given in Figures 5–8, it can be derived that the wetting index has a wide range of spatial distribution as a result of the wet regions and the dry regions of the country. Since the wetting
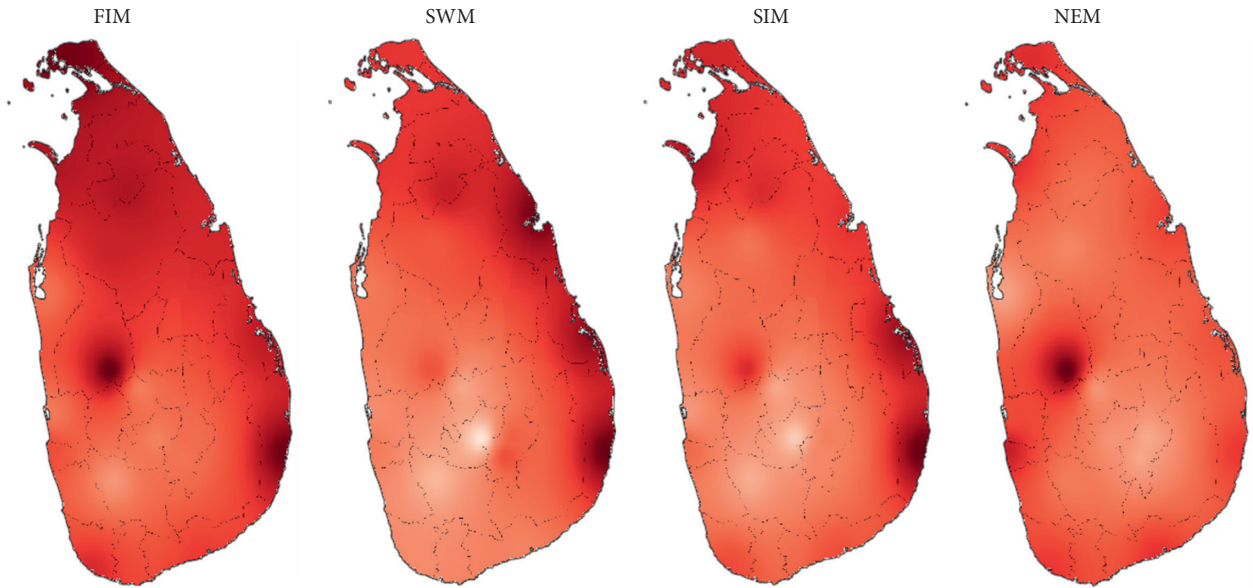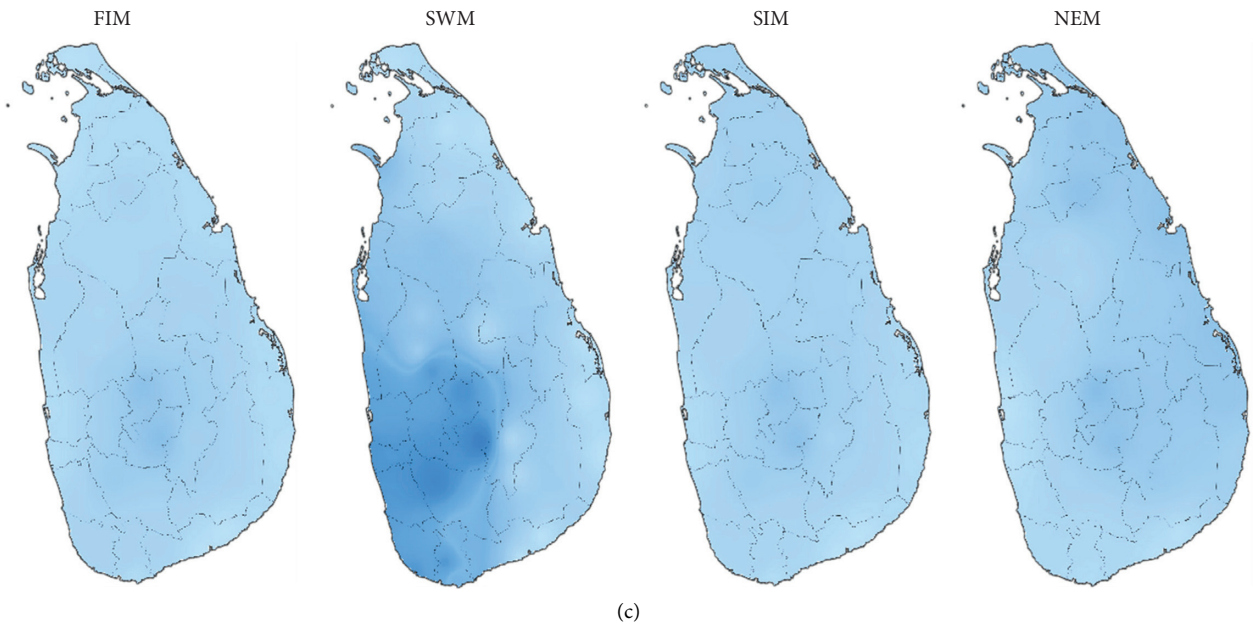
(a)
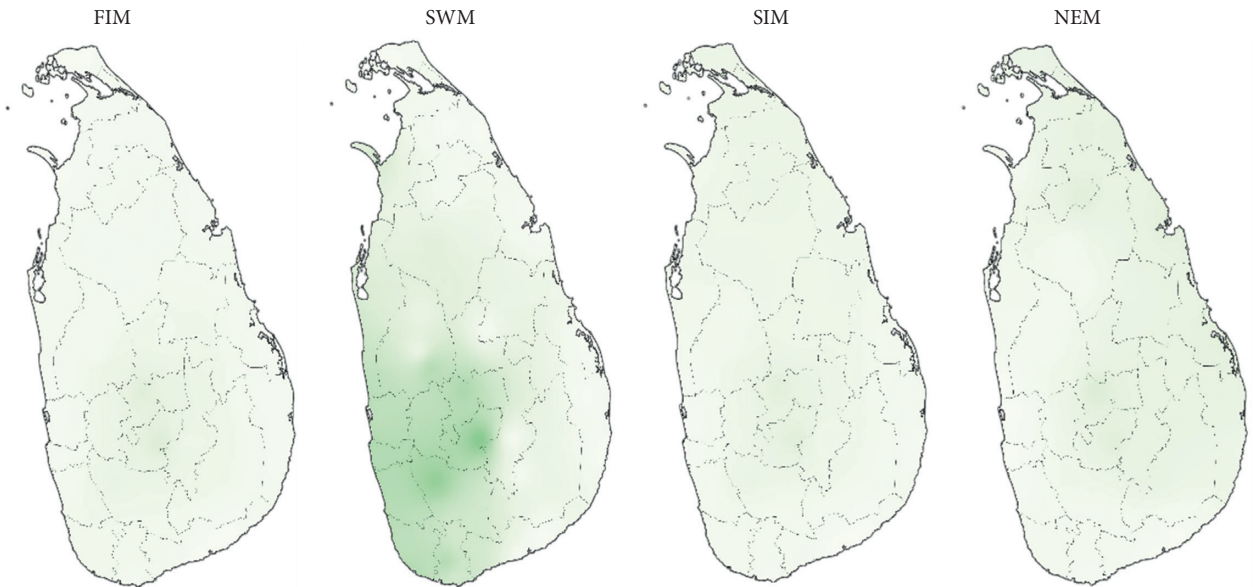
(b)

FIGURE 3: Continued.

FIM SWM SIM NEM

(c)

Figure 3: Near-future indices under RCP4.5 (2021–2040). (a) For normalized DI. (b) For normalized WI. (c) Moisture index.

FIM SWM SIM NEM

(a)

Figure 4: Continued.

FIM   SWM   SIM   NEM

(b)

FIM   SWM   SIM   NEM
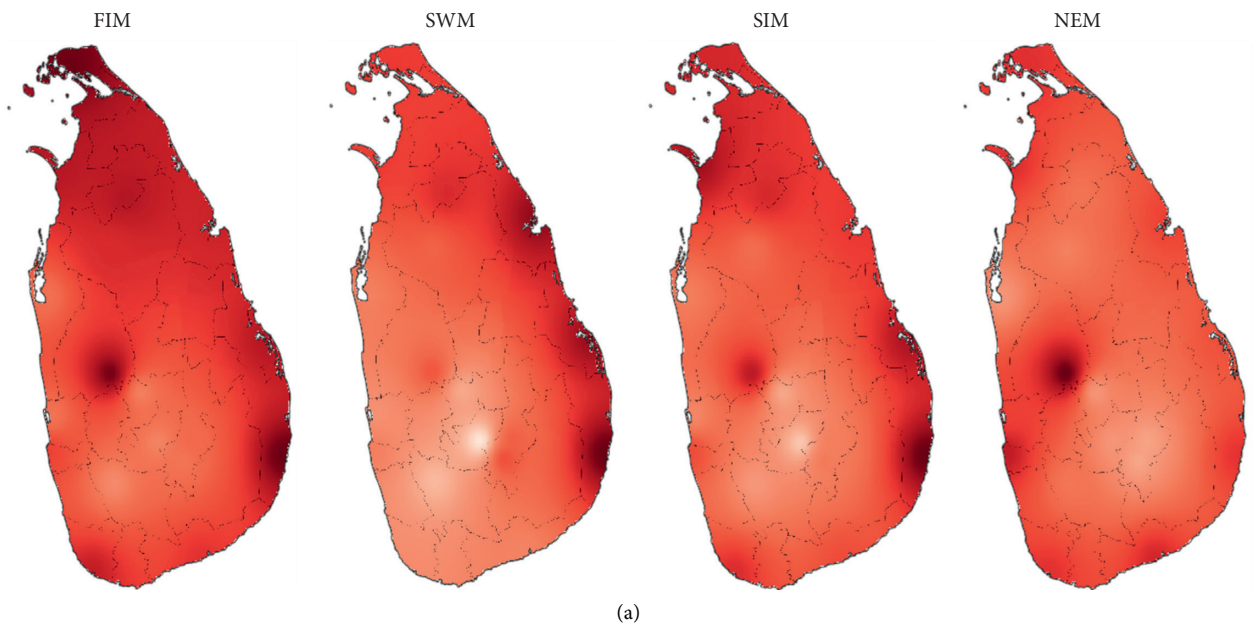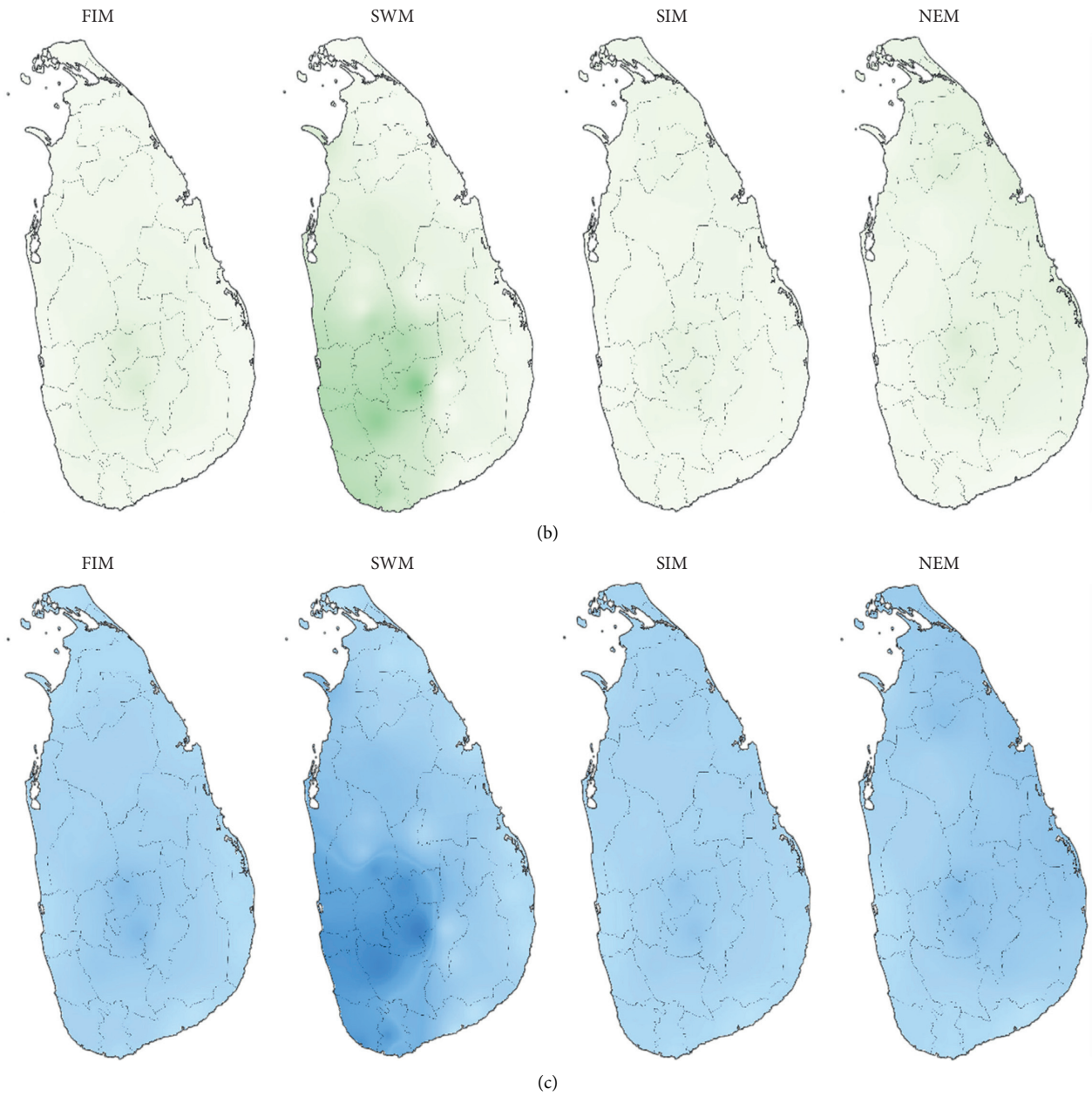

(c)

FIGURE 4: Near-future indices under RCP8.5 (2021–2040). (a) For normalized DI. (b) For normalized WI. (c) Moisture index.

TABLE 3: Minimum and maximum indices for near-future climates.

Season	DI		WI		MI	
	Min	Max	Min	Max	Min	Max
RCP4.5 (2021–2040)						
FIM	2.82	7.08	211	1428.31	1.05	6.79
SWM	1.34	8.82	12.14	2412.34	1.04	19.61
SIM	1.25	5.34	150.81	944.15	1.07	6.31
NEM	2.26	6.61	161.12	1153.98	1.06	7.19
RCP8.5 (2021–2040)						
FIM	3.36	7.63	178.82	1359.09	1.04	7.62
SWM	1.37	8.96	126.54	2479.78	1.06	19.62
SIM	1.25	4.95	201.44	1080.84	1.06	5.41
NEM	2.42	6.92	147.98	1090.29	1.03	7.40

TABLE 4: Mid and far-future indices (2041–2070 and 2071–2100).

Season	DI		WI		MI		DI		WI		MI	
	Min	Max	Min	Max	Min	Max	Min	Max	Min	Max	Min	Max
	RCP4.5 (2041–2070)						RCP4.5 (2071–2100)					
FIM	2.5	6.8	18.1	782	1.0	43.1	2.8	7.2	180.4	1382	1.0	7.7
SWM	2.4	9.9	86.9	2166	1.1	24.9	2.5	10.2	152.9	2260	1.1	14.8
SIM	1.7	5.4	340.4	1206	1.0	3.6	1.8	5.6	554.3	3424	1.1	6.2
NEM	2.4	6.2	154.7	857	1.0	5.6	2.5	6.3	201.4	1702	1.0	8.5
	RCP8.5 (2041–2070)						RCP8.5 (2071–2100)					
FIM	3.5	7.9	192	1534	1.0	8.0	4.7	9.9	200	1499	1.0	7.5
SWM	1.5	9.7	133	2253	1.1	16.9	1.7	11.1	150	2478	1.0	16.6
SIM	1.3	5.1	611	3756	1.1	6.2	1.3	5.2	872	5368	1.1	6.2
NEM	2.4	7.5	180	1789	1.1	9.9	3.2	9.0	173	1810	1.1	10.5

(a)

(b)

FIGURE 5: Continued.

FIM

SWM

SIM

NEM

(c)

Figure 5: Mid-future indices under RCP4.5 (2041–2070). (a) For normalized DI. (b) For normalized WI. (c) Moisture index.
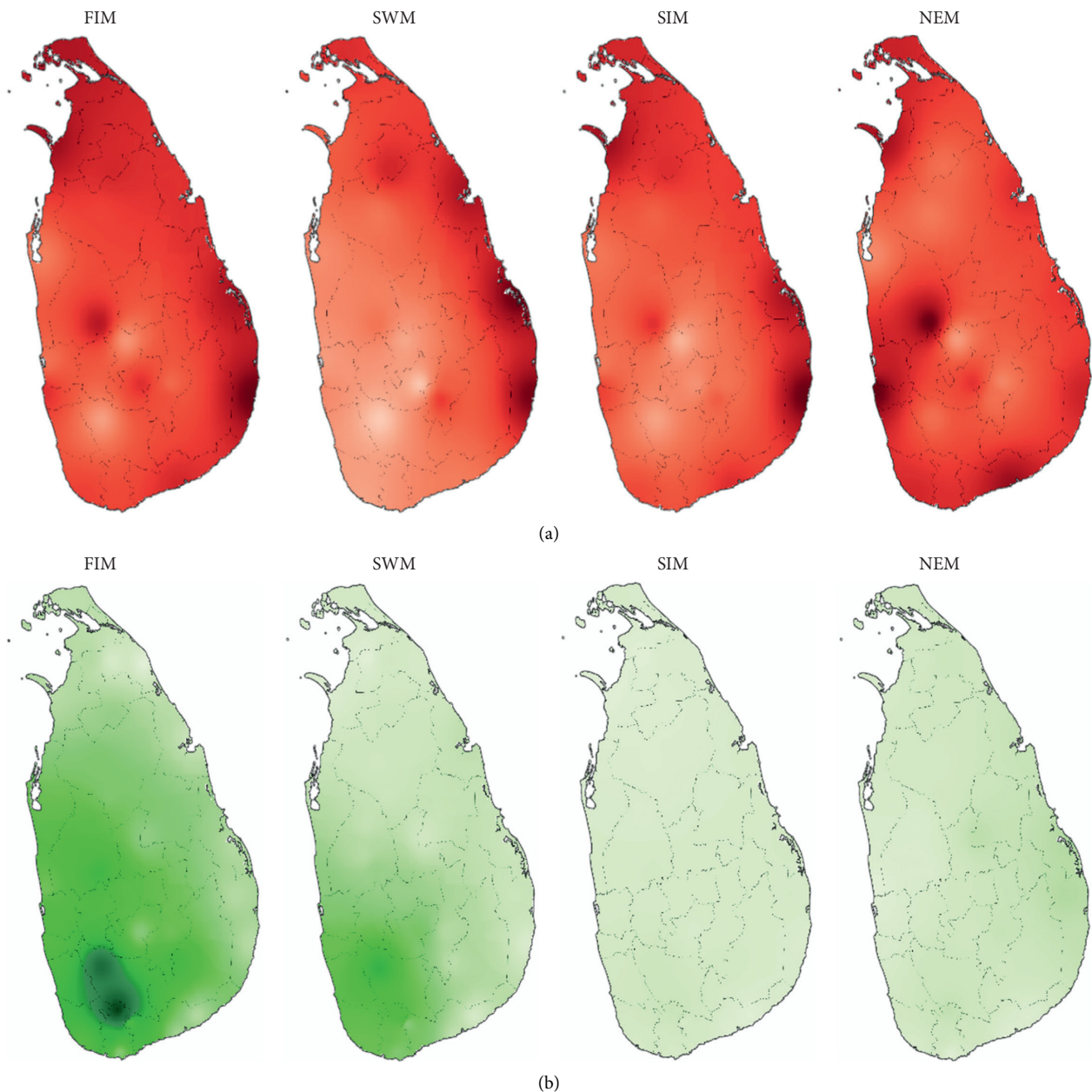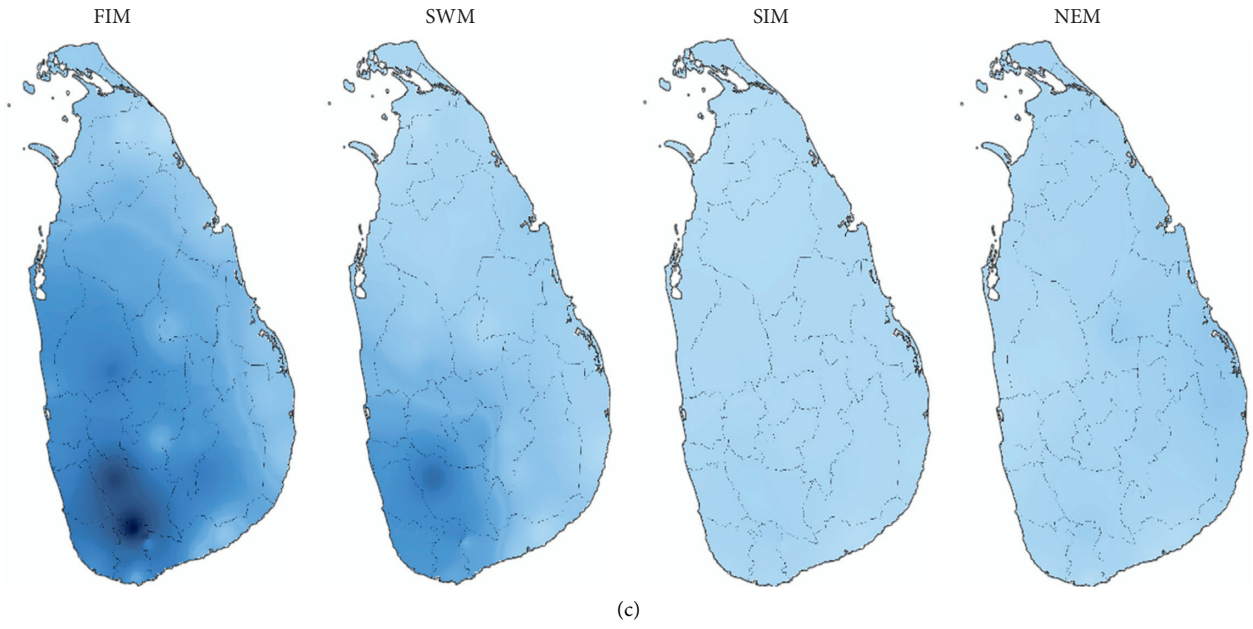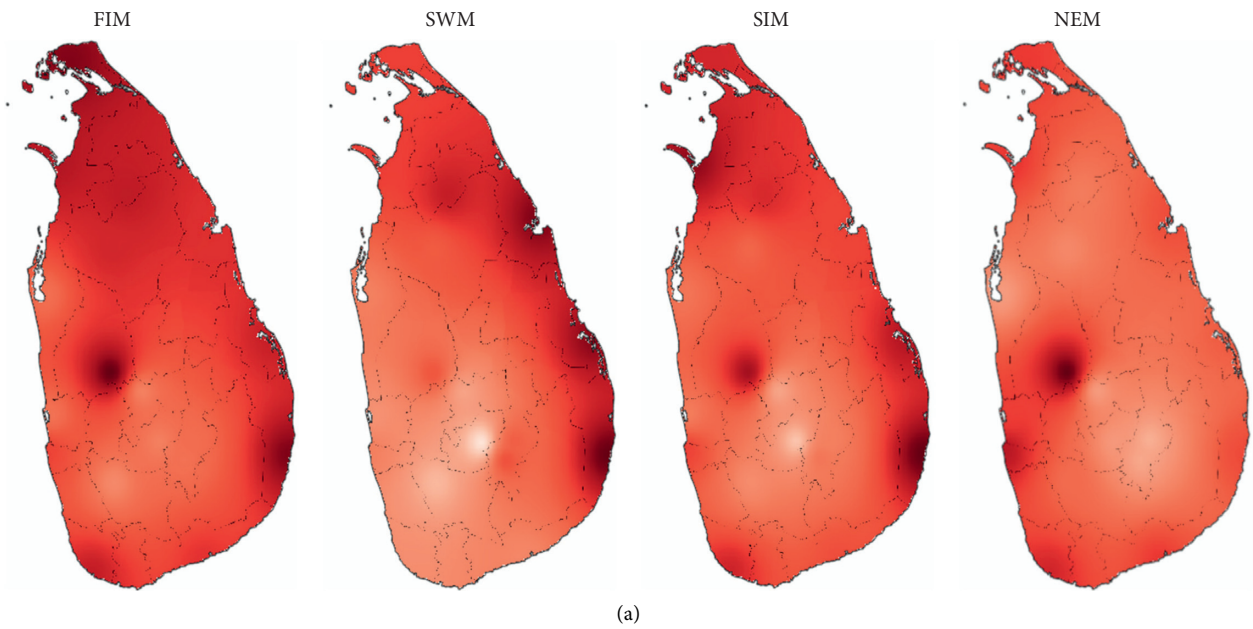
FIM

SWM
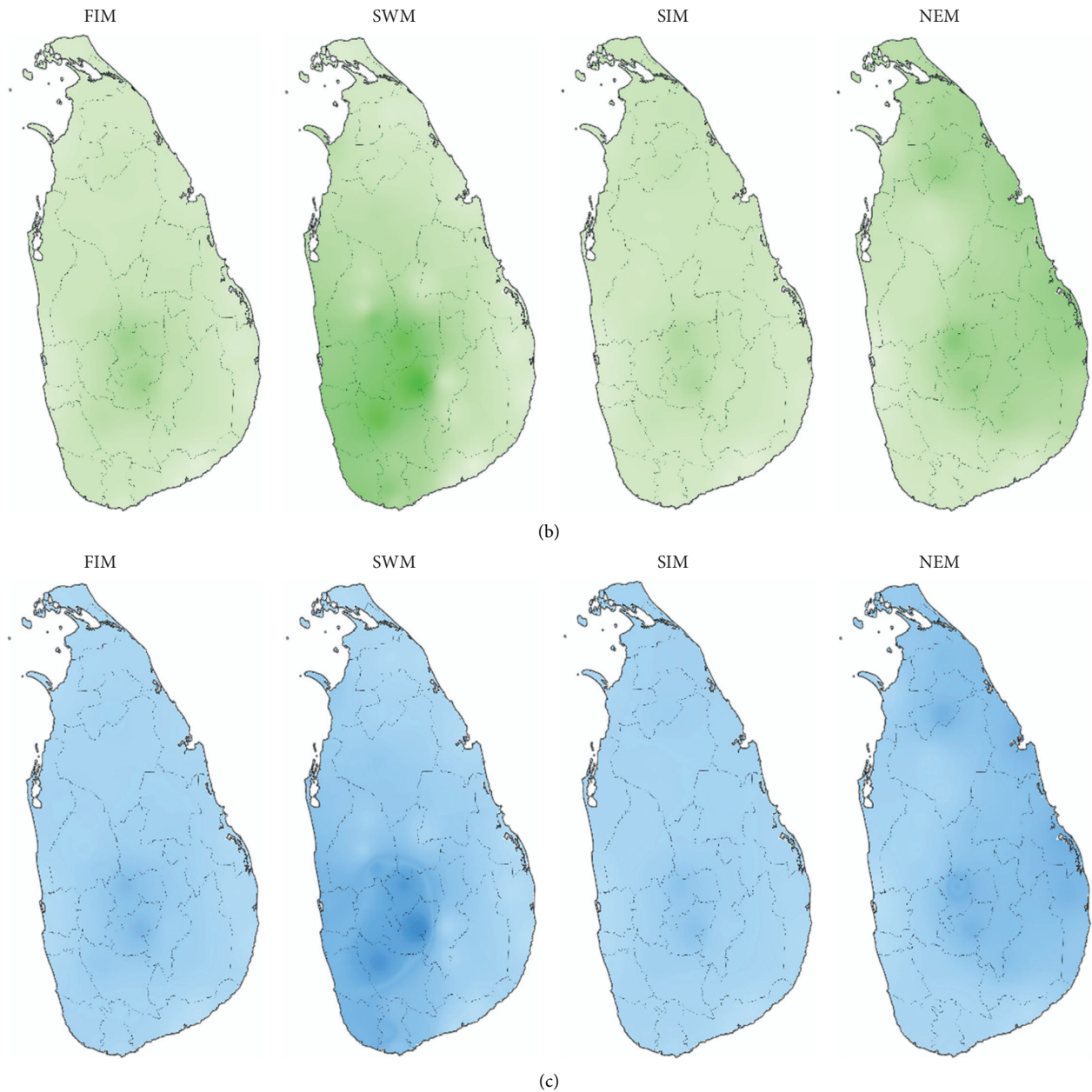
SIM

NEM

(a)

Figure 6: Continued.

(b)

(c)

FIGURE 6: Mid-future indices under RCP8.5 (2041–2070) (a) For normalized DI. (b) For normalized WI. (c) Moisture index.

index solely depends on the amount of rainfall, the pattern of the wetting index variation is evident. During the FIM and SWM, the southwestern regions experience the highest wetting index, while the northeastern regions experience the highest wetting index during the NEM. These observations clearly showcase the relationship to the rainfall seasons of the country. During the other two inter-monsoons (FIM and SIM), the central highlands of the country experience the highest wetting potential. Unlike the DI, the WI increases at a significant rate for the RCP8.5 when comparing the two-time series.

Figure 9 presents the temporal comparison of minimum and maximum moisture indices over the years for historical climatic observations and projected climatic scenarios. No significant changes can be seen for minimum MIs over the years for four seasons. However, significant variations can be seen for the maximum MIs over the years. Decreases and increases can be seen from historical MIs to near-future MIs in all four seasons. However, notable changes can be observed in FIM and SWM seasons from 2021–2040 to 2041–2070 for RCP4.5 climatic scenario. Nevertheless, SIM and NEM seasons do not show significant changes in MIs.

FIM   SWM   SIM   NEM

(a)

FIM   SWM   SIM   NEM

(b)

Figure 7: Continued.

FIM   SWM   SIM   NEM

(c)
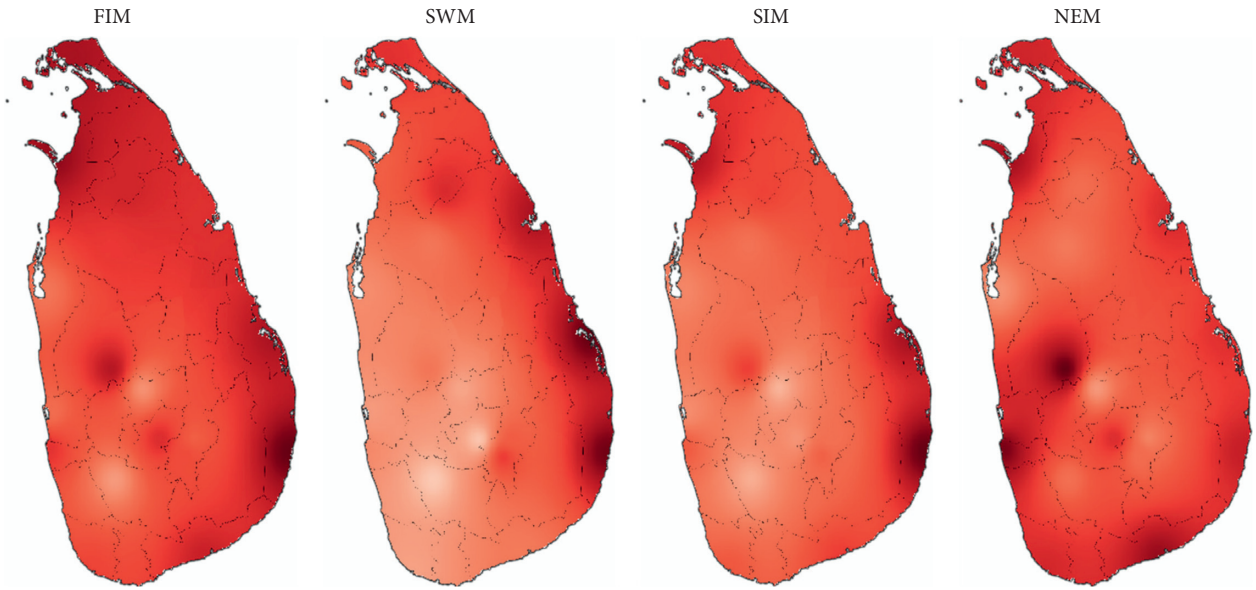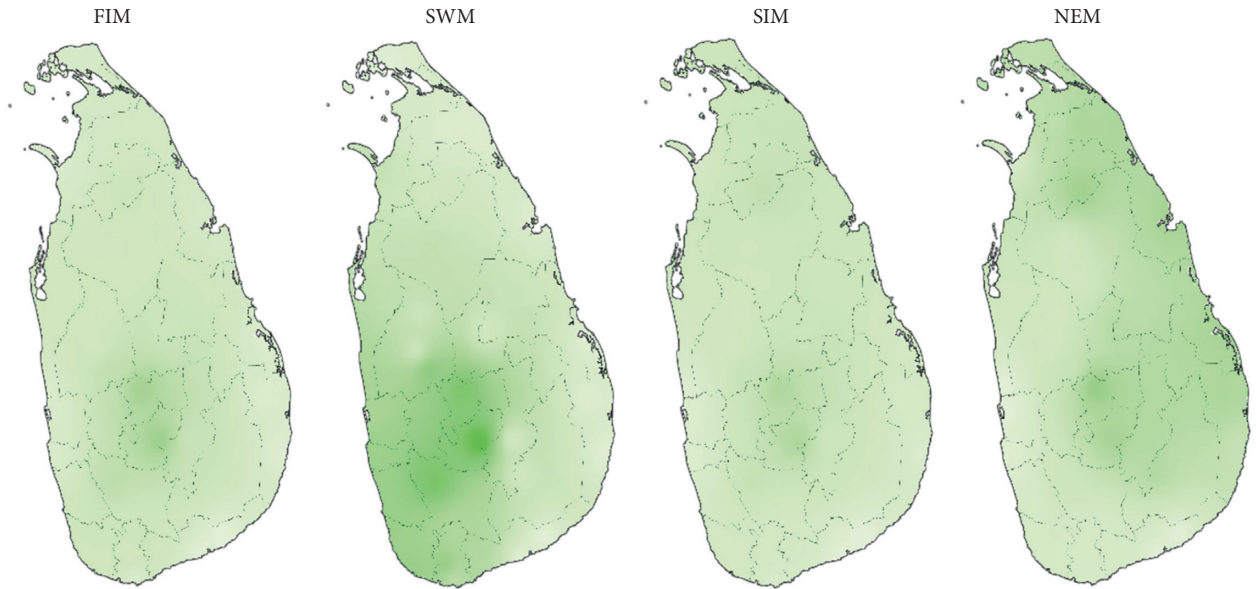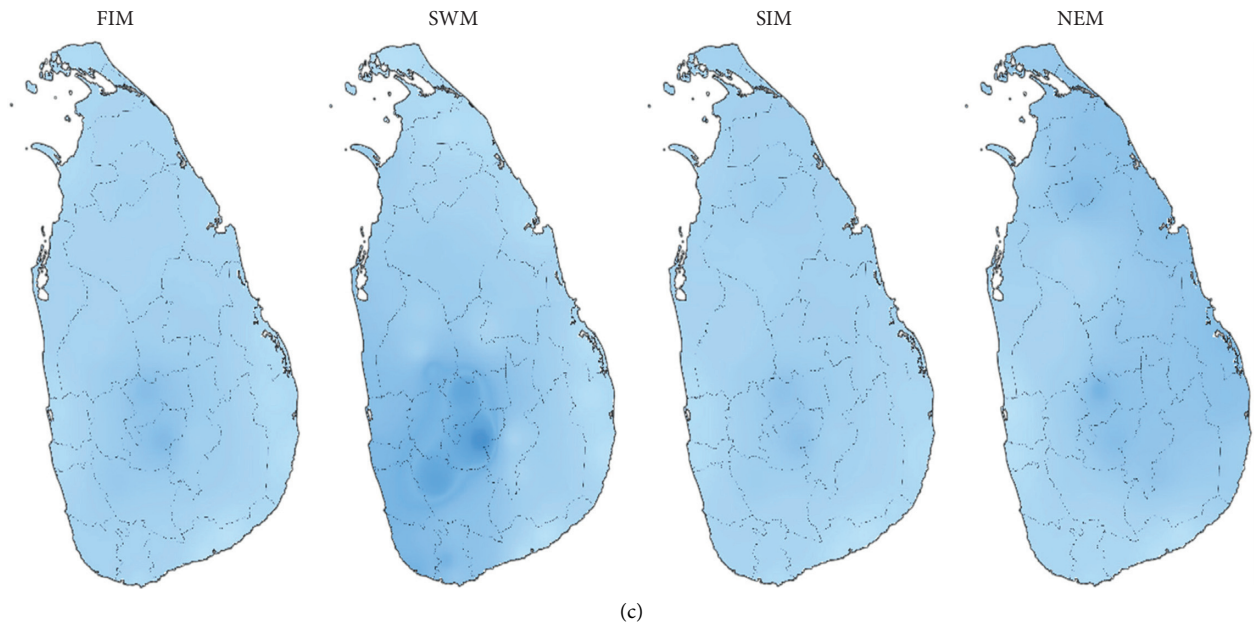
Figure 7: Far-future indices under RCP4.5 (2071–2100). (a) For normalized DI. (b) For normalized WI. (c) Moisture index.

FIM   SWM   SIM   NEM
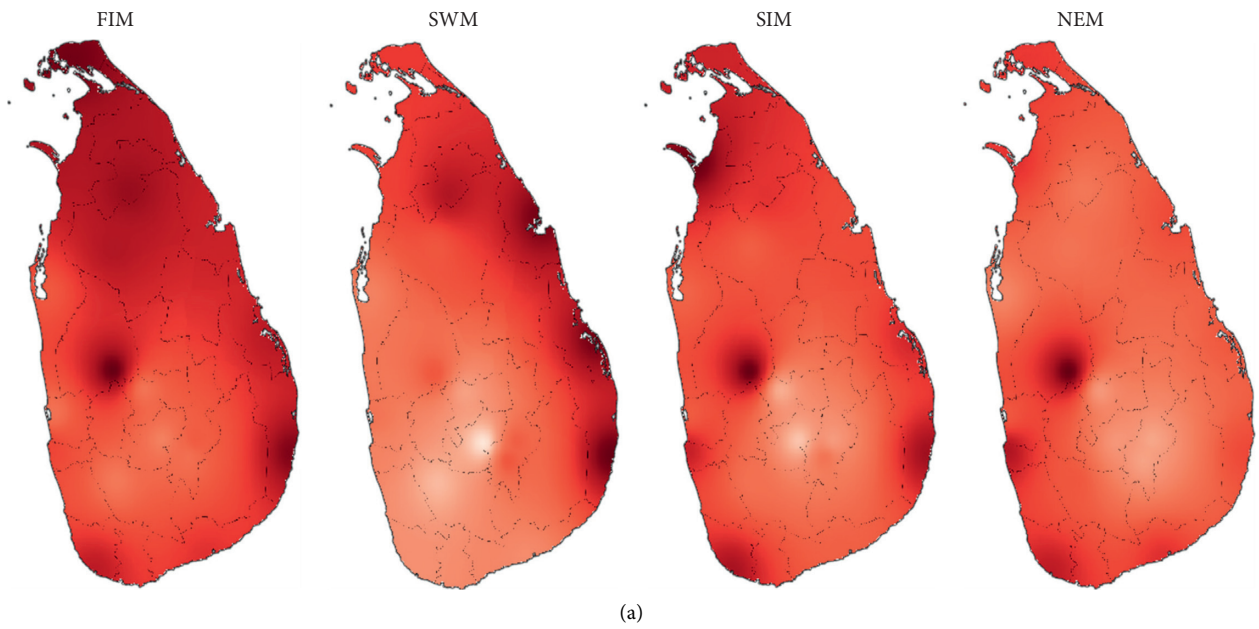
(a)
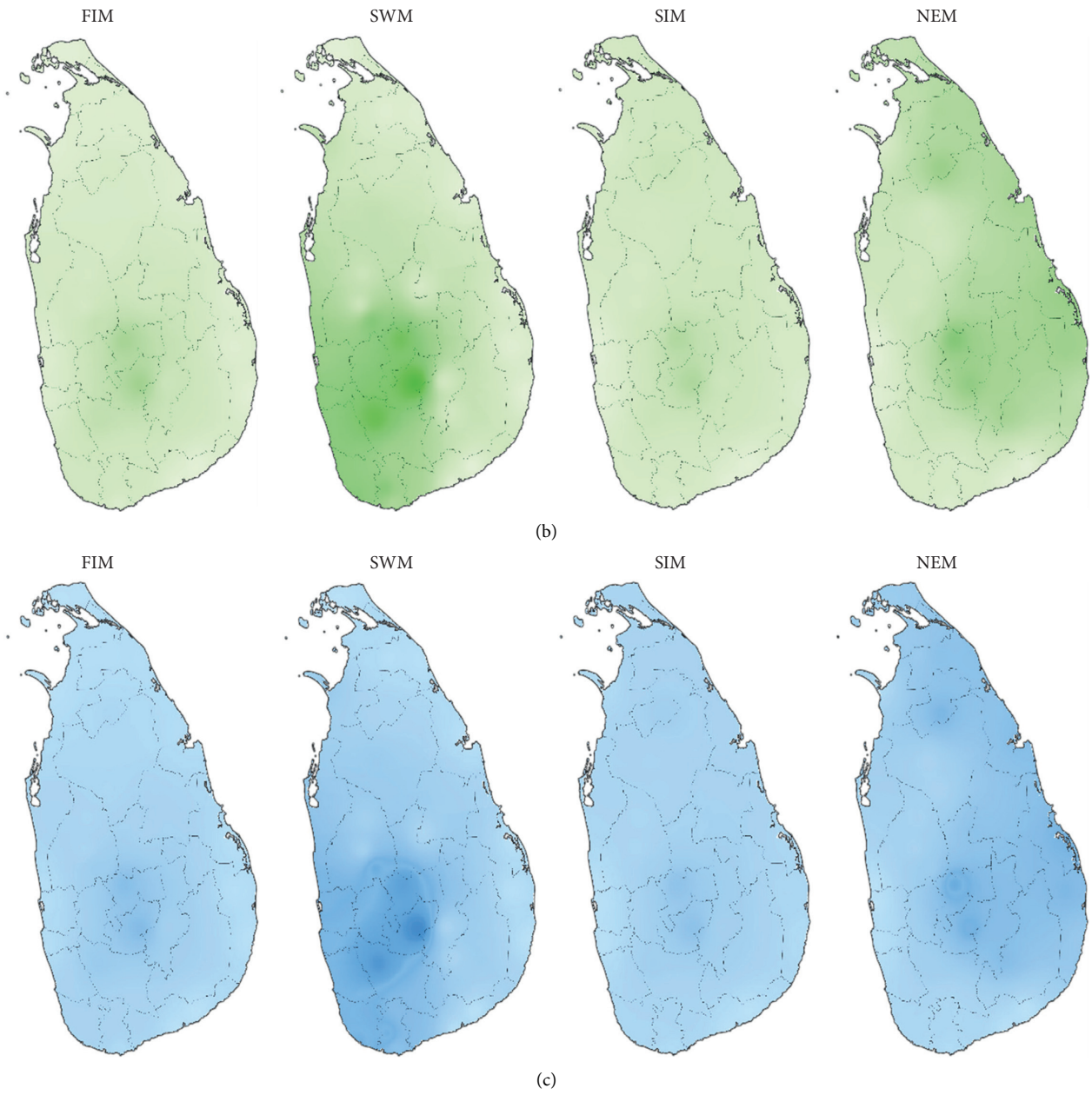
Figure 8: Continued.

(b)

(c)

FIGURE 8: Far-future indices under RCP8.5 (2071–2100). (a) For normalized DI. (b) For normalized WI. (c) Moisture index.
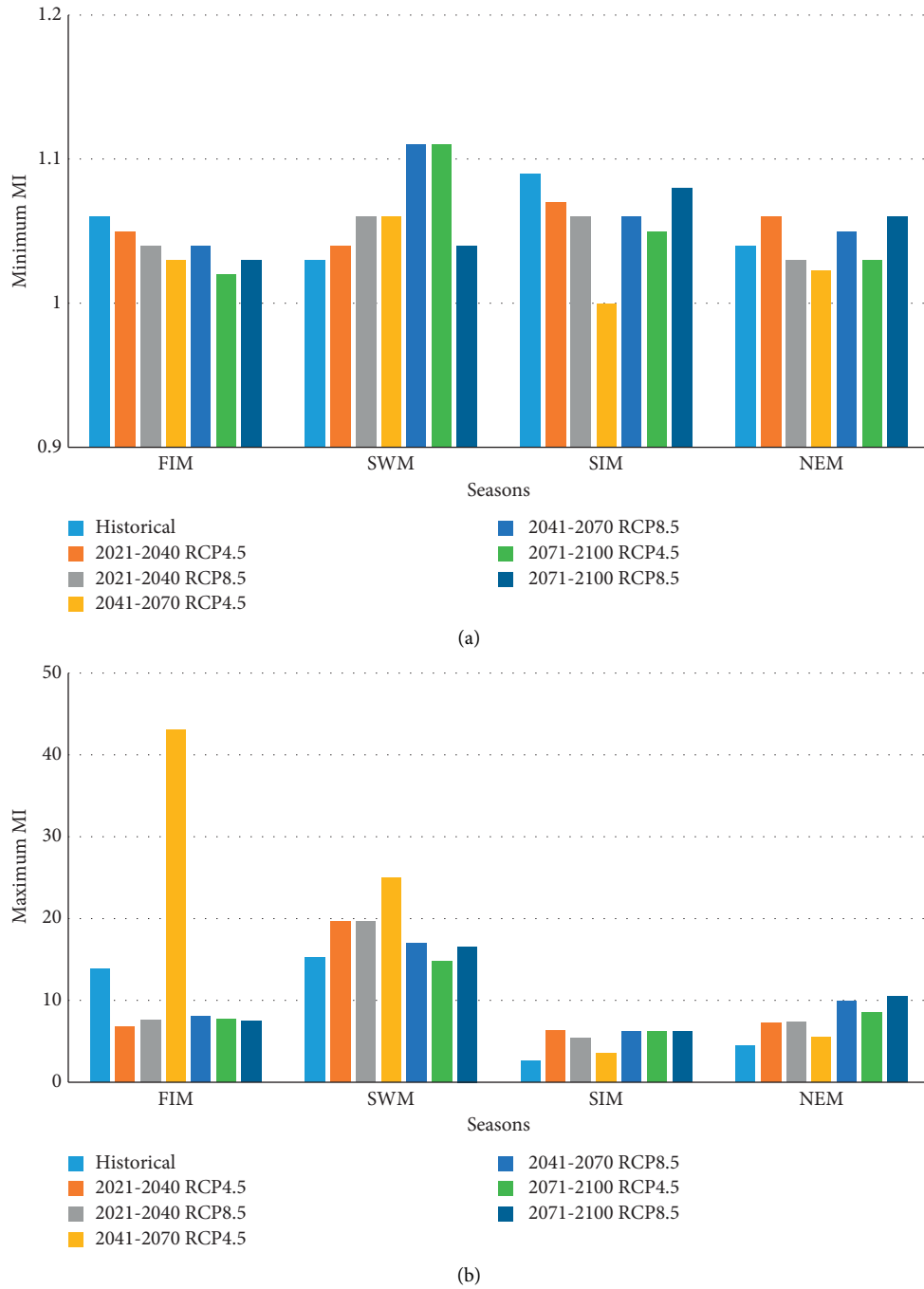
(a)

(b)

Figure 9: Comparisons of MI. (a) For minimum MI. (b) For maximum MI.

Therefore, this is very important for the construction industry in Sri Lanka in the future. The quality of the constructions can be guided along the lines of the findings of this research.

5. Summary and Conclusions

The moisture variation, in the form of the moisture index, across Sri Lanka for historical climates (1990–2004) and projected future climatic scenarios (2021–2100) was evaluated in this research work. This is the first study in Sri Lanka

to conduct such research and to come up with moisture maps for the whole country. In addition, future MI projections are significant in the changing climates. Therefore, this research clearly compiles that research gap for Sri Lanka.

The moisture load in the environment affects the durability of the building exteriors, and therefore the understanding of the moisture index over an island nation is helpful in building construction. Spatial and temporal distribution results are clearly in agreement with the country's spatial and temporal rainfall distribution. Sri Lanka's eastern and northeastern areas have and will have higher dry indices

during the SWM season. Higher WI and MI can be seen for western and southwestern areas of the country for both historical and future projected climates during the SWM and FIM seasons. However, notable changes as showcased in the results section for FIM and SWM seasons should be further investigated.

Therefore, not only the building construction but also the agricultural activities may have to be streamlined according to the results of this study. In addition, the results can effectively be used in climate zoning, investigating indoor air quality for respiratory issues, and understanding thermal comfort and energy consumption of buildings. However, a detailed investigation should be carried out related to specific disciplines including building construction and agriculture specifically to the western, southwestern, eastern, and northeastern areas of the country.

In addition, this study was carried out using the most accurate data available, yet this can be further improved by using more sophisticated and more accurate climate models and bias correction techniques. This will ensure a higher level of accuracy and less uncertainty in the results obtained. Furthermore, other climatic parameters such as wind speed, wind direction, and solar radiation which have a high impact on the moisture load in the atmosphere can be used as future improvements to this study. However, the results obtained in this study can effectively be used by decision makers in Sri Lanka and similar countries.

Data Availability

The data used in this study are available from the corresponding author upon request only for research purposes.

Conflicts of Interest

The authors declare that they have no conflicts of interest.

References

[1] M. L. Brusseau, M. Ramirez-Andreotta, I. L. Pepper, and J. Maximillian, "Environmental impacts on human health and well-being," *Environmental and Pollution Science*, pp. 477–499, 2019.

[2] M. Falkenmark and J. Lundqvist, "Towards water security: political determination and human adaptation crucial," *Natural Resources Forum*, vol. 22, no. 1, pp. 37–51, 1998.

[3] D. Jeong and A. Cannon, "Projected changes to moisture loads for design and management of building exteriors over Canada," *Building and Environment*, vol. 170, pp. 1–9, Article ID 106609, 2020.

[4] P. R. Shukla, E. Calvo Buendia, V. Masson-Delmotte, H. O. Pörtner, D. C. Roberts, and J. Malley, "IPCC, 2019: Climate Change and Land: An IPCC Special Report on Climate Change, Desertification, Land Degradation, Sustainable Land Management, Food Security, and Greenhouse Gas Fluxes in Terrestrial Ecosystems," 2019.

[5] N. Eriyagama and V. Smakhtin, "Observed and projected climatic changes, their impacts and adaptation options for Sri Lanka: a review," *The National Conference on Water, Food Security and Climate Change in Sri Lanka 2009*, pp. 99–117, BMICH, Colombo, Sri Lanka, 2010.

[6] M. Almazroui, S. Saeed, F. Saeed, M. N. Islam, and M. Ismail, "Projections of precipitation and temperature over the south asian countries in CMIP6," *Earth Systems and Environment*, vol. 4, no. 2, pp. 297–320, 2020.

[7] K. Pattnayak, S. Kar, M. Dalal, and R. Pattnayak, "Projections of annual rainfall and surface temperature from CMIP5 models over the BIMSTEC countries," *Global and Planetary Change*, vol. 152, pp. 152–166, 2017.

[8] The World Bank Group and the Asian Devolpment Bank, *Climate Risk Country Profile: Sri Lanka*, World Bank Publications, Washington, DC, USA, 2020.

[9] N. Alahacoon and M. Edirisinghe, "Spatial variability of rainfall trends in Sri Lanka from 1989 to 2019 as an indication of climate change," *ISPRS International Journal of Geo-Information*, vol. 10, no. 2-84, pp. 1–18, 2021a.

[10] B. Khaniya, C. Karunanayake, M. B. Gunathilake, and U. Rathnayake, "Projection of future hydropower generation in samanalawewa power plant, Sri Lanka," *Mathematical Problems in Engineering*, vol. 2020, pp. 1–11, Article ID 8862067, 2020.

[11] B. Khaniya, M. B. Gunathilake, and U. Rathnayake, "Ecosystem-based adaptation for the impact of climate change and variation in the water management sector of Sri Lanka," *Mathematical Problems in Engineering*, vol. 2021, pp. 1–10, Article ID 8821329, 2021.

[12] C. Karunanayake, M. B. Gunathilake, and U. Rathnayake, "Inflow forecast of iranamadu reservoir, Sri Lanka, under projected climate scenarios using artificial neural networks," *Applied Computational Intelligence and Soft Computing*, vol. 2020, pp. 1–11, Article ID 8821627, 2020.

[13] E. M. K. Ekanayake and B. A. K. S. Perera, "Appropriate delay analysis techniques to analyse delays in road construction projects in Sri Lanka," *Built Environment Project and Asset Management*, vol. 6, no. 5, pp. 521–534, 2016.

[14] T. Sivarajah, "Construction projects delays in Sri Lanka," *Journal of Research on Technology in Education*, vol. 2, no. 4, pp. 25–29, 2021.

[15] P. Ballesteros-Pérez, S. T. Smith, J. G. Lloyd-Papworth, and P. Cooke, "Incorporating the effect of weather in construction scheduling and management with sine wave curves: application in the United Kingdom," *Construction Management & Economics*, vol. 36, no. 12, pp. 666–682, 2018.

[16] S. Schuldt, M. Nicholson, Y. Adams, and J. Delorit, "Weather-related construction delays in a changing climate: a systematic state-of-the-art review," *Sustainability*, vol. 13, no. 5-2861, pp. 1–25, 2021.

[17] A. Gaur, H. Lu, M. Lacasse, H. Ge, and F. Hill, "Future projected changes in moisture index over Canada," *Building and Environment*, vol. 199, pp. 1–12, Article ID 107923, 2021.

[18] J. Hertin, F. Berkhout, D. Gann, and J. Barlow, "Climate change and the UK house building sector: perceptions, impacts and adaptive capacity," *Building Research & Information*, vol. 31, no. 3-4, pp. 278–290, 2003.

[19] S. N. Baxi, J. M. Portnoy, D. Larenas-Linnemann et al., "Exposure and health effects of fungi on humans," *The Journal of Allergy and Clinical Immunology: In Practice*, vol. 4, no. 3, pp. 396–404, 2016.

[20] J. Portnoy, K. Kwak, P. Dowling, T. VanOsdol, and C. Barnes, "Health effects of indoor fungi," *Annals of Allergy, Asthma, & Immunology*, vol. 94, no. 3, pp. 313–320, 2005.

[21] J. Berger, S. Guernouti, M. Woloszyn, and C. Buhe, "Factors governing the development of moisture disorders for integration into building performance simulation," *Journal of Building Engineering*, vol. 3, pp. 1–15, 2015.

[22] S. Cornick and A. Dalgliesh, "A moisture index approach to characterizing climates for moisture management of building envelopes," in *Proceedings of the 9th Canadian Conference on Building Science and Technology*, pp. 383–398, Vancouver, Canada, 2003.

[23] C. J. Willmott and J. J. Feddema, "A More Rational Climatic Moisture index," *The Professional Geographer*, vol. 44, pp. 84–88, 1992.

[24] B. F. A. Basnayake and C. Visvanathan, "Solid Waste Management in Sri Lanka," in *Municipal Solid Waste Management in Asia and the Pacific Islands. Environmental Science and Engineering*, A. Pariatamby and M. Tanaka, Eds., Springer, NewYork, NY, USA, 2014.

[25] B. V. Punyawardena and K. H. Premalal, "Do Trends in Extreme Positive Rainfall Anomalies in the Central highlands of Sri Lanka Exist," *Annals of the Sri Lanka Department of Agriculture*, pp. 1–12, Department of Agriculure, Ministry of Agriculture, Gannoruwa, Sri Lanka, 2013.

[26] B. Marambe, R. Punyawardena, P. Silva et al., "Climate, Climate Risk, and Food Security in Sri Lanka: The Need for Strengthening Adaptation strategies," *Handbook of Climate Change Adaptation*, pp. 1759–1789, Springer, Berlin, Heidelberg, 2014.

[27] G. Naveendrakumar, M. Vithanage, H. Kwon, M. Iqbal, S. Pathmarajah, and J. Obeysekera, "Five decadal trends in averages and extremes of rainfall and temperature in Sri Lanka," *Advances in Meteorology*, vol. 2018, Article ID 4217917, 13 pages, 2018.

[28] I. Huttunen, K. Hyytiäinen, M. Huttunen et al., "Agricultural nutrient loading under alternative climate, societal and manure recycling scenarios," *The Science of the Total Environment*, vol. 783, pp. 1–15, Article ID 146871, 2021.

[29] S. McGinnis and L. Mearns, "Building A climate service for north America based on the NA-CORDEX data archive," *Climate Services*, vol. 22, pp. 1–11, Article ID 100233, 2021.

[30] B. Mesta and E. Kentel, "Superensembles of raw and bias-adjusted regional climate models for mediterranean region, Turkey," *International Journal of Climatology*, vol. 42, pp. 1–20, 2021.

[31] S. Rennie, K. Goergen, C. Wohner, S. Apweiler, J. Peterseil, and J. Watkins, "A climate service for ecologists: sharing pre-processed EURO-CORDEX regional climate scenario data using the elter information system," *Earth System Science Data*, vol. 13, no. 2, pp. 631–644, 2021.

[32] W. Dibaba, T. Demissie, and K. Miegel, "Watershed hydrological response to combined land use/land cover and climate change in highland Ethiopia: finchaa catchment," *Water*, vol. 12, no. 6-1801, pp. 1–25, 2020.

[33] S. Suárez-Almiñana, A. Solera, J. Andreu, and L. García-Romero, "Análisis de incertidumbre de las proyecciones climáticas en relación A las aportaciones históricas en La cuenca del júcar," *Ingeniería del agua*, vol. 24, no. 2, pp. 89–99, 2020.

[34] Y. Masaki, N. Hanasaki, K. Takahashi, and Y. Hijioka, "Propagation of biases in humidity in the estimation of global irrigation water," *Earth System Dynamics*, vol. 6, no. 2, pp. 461–484, 2015.

[35] R. Seager, M. Ting, C. Li et al., "Projections of declining surface-water availability for the southwestern United States," *Nature Climate Change*, vol. 3, pp. 482–486, 2012.

[36] S. Javadi, H. Yousefi, A. Moridi, H. Khajehpour, and T. Fathi, "Determination of crisis areas of precipitation in Iran for period of 2021-2040 by climate change," *Journal of Water and Irrigation Management*, vol. 12, 2021.

[37] B. Su, J. Huang, S. Mondal et al., "Insight from CMIP6 SSP-RCP scenarios for future drought characteristics in China," *Atmospheric Research*, vol. 250, Article ID 105375, 2021.

[38] National Research Council of Canada, *National Building Code of Canada*, National Research Council Canada, Canada, 2015.

Research Article

Study on the Comfort of Pedestrians on Landscape Footpath Paved on the Suspension Monorail System

Zhou Li [ID],[1] **Yuancheng Wei,**[2] **Xiaolong Zheng,**[3] **Yongping Zeng,**[3] **Xinyu Xu** [ID]**,**[3] **Xingyu Chen,**[3] **and Qi Tao**[3]

[1]*China Construction Science and Industry Corp. Ltd., Shenzhen 518048, Guangdong, China*
[2]*Construction Affairs Bureau of Shenzhen Longhua District (Rail Transit Construction Management Center of Shenzhen Longhua District), Shenzhen 518028, Guangdong, China*
[3]*China Railway Eryuan Engineering Group Co., Ltd., Chengdu 610031, Sichuan, China*

Correspondence should be addressed to Zhou Li; 976112542@qq.com

This is the first time that the landscape footpath is realized on the suspension monorail system. To study the comfort of pedestrians on the landscape footpath when the vehicle passes, the dynamic responses of the track beam and the landscape footpath at different speeds were analyzed using the established vehicle-bridge dynamic analysis model. To evaluate the comfort of pedestrians on the landscape footpath, two indexes, Root Mean Square (RMS) value of acceleration (ISO 10137) and peak value of acceleration (EN 03), were adopted. Results show that the displacement and acceleration responses of landscape footpath and track beam are obviously different. Vertical displacement of the track beam is much larger than that of the landscape footpath due to the eccentric load of vehicles. Due to the displacement and rotation of the structural components which support the landscape footpath, the lateral response transferred to the landscape footpath would be slightly weakened. Maximum RMS values of the lateral and vertical acceleration of landscape footpath are 0.162 m/s^2 and 0.169 m/s^2, respectively, which meet the requirements of ISO 10137. Peak lateral acceleration is 0.546 m/s^2, which reaches CL3 standard, and the peak vertical acceleration is 0.548 m/s^2, which reaches CL2 standard. Lateral comfort is slightly worse than vertical comfort.

1. Introduction

Monorail transit system regards the strip beam as the pathway, where the vehicles ride on the beam or are suspended under the beam. The first suspension monorail system was built in Wuppertal in Germany along the river in 1901. Recently, the suspension monorail has been discussed as an effective transportation solution for connecting different urban areas or scenic areas. Under this circumstance, the landscape footpath has been proposed to integrate with one of the commercial-operated suspension monorails in a tourist attraction in China, to improve the tourists' experience, and to optimize the structural dynamic performance of the vehicle. It is the first case to add a landscape footpath on the track beam. Due to the large width-span ratio of the design, the proportion of the live load and dead load of the

monorail system is much larger than that of the conventional wheel-rail system. Meanwhile, for the steel structure design of the monorail, the structural damping is small. Relative standards in China, "Code for Design of Urban Rail Transit Bridge" GB/T 51234-2017 [1] and "Technical Standard for Suspension Monorail Transit" DBJ41/T217-2019 [2], have no clear requirements for the dynamic responses of the monorail bridge style. Therefore, the influence of the bridge vibration induced by the passing vehicles on the comfort of pedestrians on the footpath becomes a practical issue that needs to be explored.

With the rapid development of suspension monorail transit system in recent years, several researches on the dynamic characteristics of the system have been conducted. Bao et al. [3, 4] utilized the cosimulation method to study analysis responses of monorail vehicle and bridge, in which

the effects of tyre stiffness, crosswind, and operating condition were discussed. He et al. [5] carried out field measurement on dynamic responses of suspension monorail system for straight and curved line. Taking the curved monorail bridge as research project, Yang et al. [6] took nonlinear radial stiffness of a suspension monorail rubber tyre into consideration and analyzed several key parameters. Zou et al. [7] investigated the aerodynamic characteristics and interference effects for different spacing ratios (line distance to beam width) of track beam via wind tunnel test and CFD (Computational Fluid Dynamics) simulation.

Traditional research on the comfort of pedestrians commonly focused on pedestrian bridges. Most related works discussed the dynamic responses of bridges under the actions of pedestrians. Feng et al. [8] carried out the actual measurement and questionnaire of pedestrians on 21 footbridges, obtained a comfort design curve of pedestrian bridge based on peak acceleration, and proposed a comfort design method of pedestrian bridge. Based on the principle of probability and statistics, Chen et al. [9] combined the human body resistance and vibration effect and proposed a mathematical definition of sensitivity. Ma et al. [10] conducted an experiment to study the perception of human-induced vibrations of footbridges and proposed perception scales for lateral and vertical vibrations of footbridges. Bhowmik et al. [11] utilized an image processing technique and an automated enhanced frequency-domain decomposition technique to evaluate the damping of the suspension footbridge with 1.37 m width. Apart from the pedestrian loads, the pedestrian bridge integrated in the complex traffic system may receive other external excitations, which might have impacts on the pedestrian comfort level. Responses of the pedestrian bridge under vehicle-induced excitation were analyzed by some researchers, and the effects of the roughness of road surface, vehicle speed, and traffic flow on the responses were discussed as well [12, 13].

The article takes the aforementioned 5-span 40 m simply supported suspension monorail system with landscape footpath project as an example, and the dynamic characteristics of the monorail system with the monorail vehicle passing at operating speed are analyzed. The comfort of pedestrians on the landscape footpaths at different vehicle speeds is evaluated based on the criteria of pedestrian comfort. The results provide a helpful and reasonable reference for the future design. Section 2 presents the established vehicle-bridge coupled model for the dynamic analysis of the suspension monorail system, including the vehicle model, bridge model, and tyre model, as well as the dynamics of multibody system used in the model. Section 3 illustrates the two criteria for the comfort of pedestrians on the landscape footpath. The dynamic responses of both landscape footpath and track beam are analyzed and the comfort of pedestrians on the footpath is evaluated in Section 4. Finally, the conclusions are given in Section 5.

2. Vehicle-Bridge Coupled Model

The vehicle-bridge coupled model is a combined system composed of vehicle and bridge models on the basis of the wheel-rail motion relationship [14–17]. Unlike the traditional wheel-rail contact method, the contact method in the suspension monorail needs to take the tyre model into consideration, due to the fact that the tyre of vehicle is in contact with the beam [18–20].

In the paper, the multibody dynamic software SIMPACK and finite element software ANSYS were used to establish the monorail vehicle and bridge models, respectively. The information of bridge, including structure information (stiffness and mass information), model information, and geometry information, was obtained by substructure analysis in the finite element software. Then, the information of bridge was introduced into the multibody dynamic software via interface program, the bridge was modelled as the flexible body, and the dynamic coupled model was analyzed in multibody dynamic system.

2.1. Flexible Body in Multibody Dynamics. In the multibody system, the bridge structure is regarded as a flexible body [21, 22]. The position of point P on the flexible body can be expressed as

$$r^P(c,t) = A(t)(r + c + u(c,t)), \tag{1}$$

where A is the rotation matrix from the reference coordinate system to the inertial coordinate system of the body; r is the position in the reference coordinate system; c is the position of point P in the reference coordinate system under the nondeformation state; and $u(c,t)$ is the deformation vector of the flexible body.

The Ritz of the deformation of the flexible body can be approximated via the linear combination of the shape function $\phi_j(c)$ and the mode coordinate $q_j(t)$ as

$$u(c,t) = \sum_{j=1}^{n_q} \phi_j(c)q_j(t). \tag{2}$$

Based on the Ritz approximation and Hamilton principle, the motion equation can be expressed by the variational method as

$$M(q)\begin{Bmatrix} a \\ \dot{\omega} \\ \ddot{q} \end{Bmatrix} + k\omega(\omega, q, \dot{q}) + k(q, \dot{q}) = h, \tag{3}$$

where M is the mass matrix; k_ω is the generalized force matrix of the rotational and centrifugal items; k and h are the generalized force matrices of the internal force and external force, respectively; a, ω, and q are the absolute acceleration, angle acceleration, and modal coordinate, respectively.

2.2. Monorail Vehicle Model. The single vehicle of suspension monorail is composed of a car body and two bogies. The car body and bogie are connected by suspension devices, dampers, bolsters, and pins. The whole bogie is arranged in the C-beam body. The stiffness of the traveling tyre is defined as 13.3×10^6 N/m, which is provided by the vehicle manufacturer. The guide wheels on both sides of the bogies are

constrained by the beam webs to realize the steering function. Both the car body and frame include 5 degrees of freedom, which are lateral, vertical, yaw, pitch, and roll motions. Therefore, a single vehicle has 31 degrees of freedom in total.

In the numerical simulation, the car body and frame are regarded as rigid bodies, and the suspension and dampers are regarded as force elements. The scheme of the single vehicle model is shown in Figure 1. The monorail train applies three-vehicle marshalling, and the speeds are 20, 30, 40, 50, and 60 km/h. The load of each axle (at full capacity) is 5.5 tons.

2.3. Bridge Model. The paper employs a 5×40 m simply supported bridge. The single track beam is in the form of a thin-walled C-shaped steel box girder with an opening in the bottom. The beam height is 1.31 m at the track beam end and 2.07 m in the midspan, and it linearly increases from 1.31 m (3 m from the beam end) to 2.07 m (9 m from the beam end). The inner width of the track beam is 0.78 m, and the cross section of the beam end is shown in Figure 2. The double-track monorail track beams are all placed underneath the cover beam of the pier. The distance between the double-track lines is 5.1 m, and the width of the landscape footpath on the beam is 7.2 m. The steel pier is 16 m in height, 1.34 m in width in the longitudinal direction, and 0.9 m in the transverse direction, whose cross section is a closed rectangular cross section. The inner width of track beam is 0.78m, and the cross section of the beam end is shown in Figure 2.

The bridge model was established in the commercial finite element software ANSYS. The plate element is applied to the track beam and landscape footpath in the model, and the spatial beam element is exerted to the pier. The elastic modulus and Poisson's ratio of components are taken in accordance with the relevant design standards. The secondary dead load is evenly added to the beam elements uniformly. The finite element model has 29409 nodes and 30261 elements in total. The bridge model is shown in Figure 3. The damping ratio of the bridge is considered as 0.5%.

Natural frequency analysis of the bridge model is performed, and the typical frequencies and corresponding mode shape descriptions are shown in Table 1 and Figure 4. It can be seen from the results that the frequencies of the pier are relatively low and flexible, and the frequencies of the track beam are above 3 Hz. However, due to the small ratio of the dead load and live load on the suspension monorail beam, the dynamic responses of the bridge under the live load of the vehicle would be probably significant.

2.4. Tyre Model. Suspension monorail system adopts the rubber tyre for the link of the vehicle and track beam. The rubber traveling wheels of the vehicle directly act on the bridge, and the vertical interaction force between the vehicle and the bridge is the main force in the coupled system. The key point to establish the monorail vehicle-bridge coupled model is to precisely simulate the mechanical parameters of

the rubber tyre, which has typical nonlinear characteristics. In the dynamics of tyres in a vehicle, some simplification models, such as Fiala tyre model [23], Gim tyre model [24], and Pacejka tyre model [25], were developed and applied in the dynamic analysis.

In the paper, Pacejka tyre model is considered to simulate the dynamic characteristics of the traveling wheel. In addition, the guide wheels of the suspension monorail vehicle are in direct contact with the guide tracks on the sidewalls of the track beams. When the vehicle passes through the bridge, the guide wheels interact with the track beam to provide the lateral force to the vehicle. Therefore, it is essential to build up the mutual effect between the guide wheel and track beam as well.

2.4.1. Vertical Force of Traveling Wheel. The vertical force between the traveling wheel and the track beam is defined by the relative motion trajectory between the tyre center and the deck, as shown in Figure 5. To accurately simulate the contact between the tyre and deck, the traveling wheel can be separated from the bridge deck. When the traveling wheel jumps up, the vertical force is set to be zero, which means that the vertical force of the traveling wheel can be discontinuous. Then, it can be expressed as

$$F_Z = \begin{cases} K_z(R_0 - R_H) - F_{zN} - C_z[v_{B_k,B_l}]_z & \text{for } R_H \le R_0 \\ 0 & \text{for } R_H > R_0 \end{cases}, \tag{4}$$

where K_z and C_z are the vertical stiffness and damping coefficient of the tyre, respectively; R_0 and R_H are the height of the tyre under the nominal vertical force and the height of the tyre at the moment of movement, respectively; F_{zN} is the initial nominal force of the tyre; and $[v_{B_k,B_l}]_z$ is the vertical direction of vehicle speed of the tyre center relative to the deck.

2.4.2. Longitudinal and Side Slip Force of Traveling Wheel. The lateral and longitudinal slip force of the rubber tyre of the traveling wheel can be defined according to the creep and friction coefficient under the vertical force of the tyre as

$$F_y = -\frac{\sigma_y}{\sigma_{\text{theo}}} \frac{F_z}{F_{z_0}} \frac{\mu_y}{\mu_{y_0}} F_0\left(\sigma_{eq_y}\right),$$

$$F_x = -\frac{\sigma_x}{\sigma_{\text{theo}}} \frac{F_z}{F_{z_0}} \frac{\mu_x}{\mu_{y_0}} F_0\left(\sigma_{eq_x}\right), \tag{5}$$

where σ_x and σ_y represent longitudinal slip and lateral slip, respectively; $\sigma_{\text{theo}} = \sqrt{\sigma_x^2 + \sigma_y^2}$ is the theoretical tyre overall slip value; F_{z_0} and μ_{y_0} are the nominal tyre vertical force in the figure of lateral force against lateral slip and the friction coefficient at the moment, respectively; μ_x and μ_y are the friction coefficients of the longitudinal and lateral force in the current state of motion, respectively; σ_{eq_x} and σ_{eq_y} represent the friction performances of tyre in x-axis and y-axis directions, respectively.
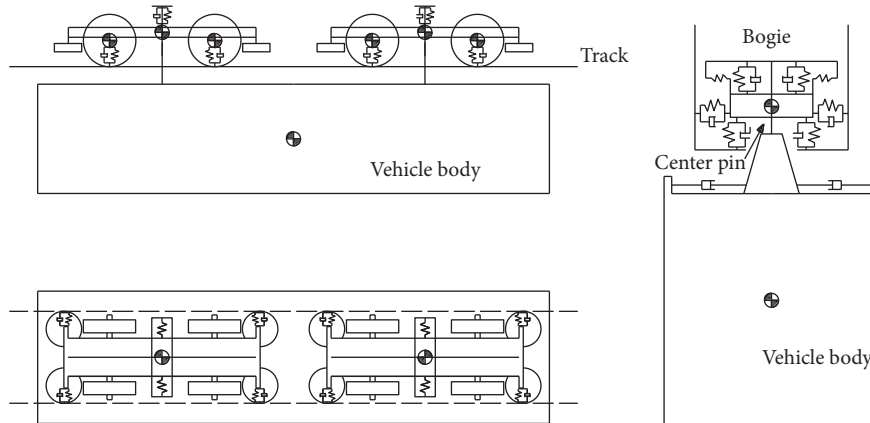
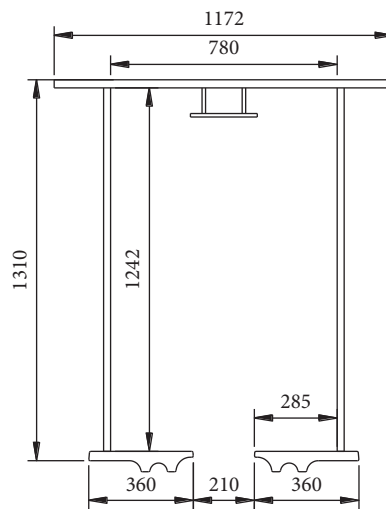Figure 1: Dynamic model of suspension monorail vehicle.

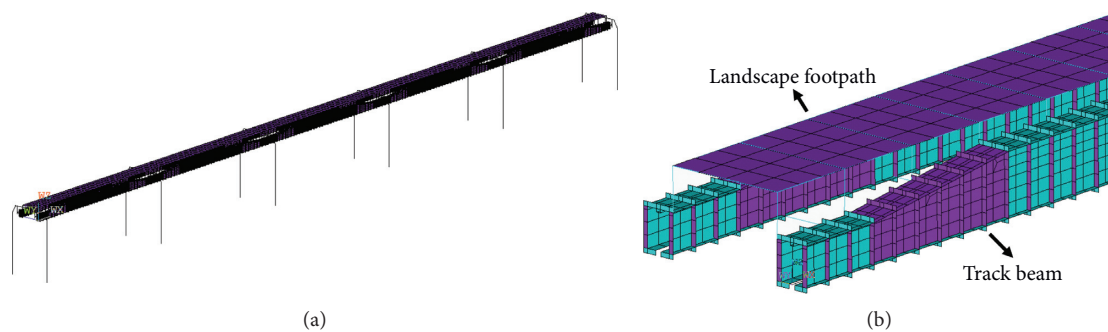Figure 2: Cross section of the track beam end (unit: mm).

(a)

(b)

Figure 3: Finite element model of the suspension monorail system. (a) Full-bridge model. (b) Schematic diagram of the partial main beam section.

2.4.3. Lateral Force of Guide Wheel.

Spring-damping force element is used to simulate the guiding force between the guide wheel and the track, which can be expressed as

$$
F_{DY} = \begin{cases} K_y (Y_r - Y_0) - C_y \left[v_{D_k, D_l} \right]_y + F_{Dy\,0} & \text{for } \Delta r > 0 \\ 0 & \text{for } \Delta r \leq 0 \end{cases},
$$

(6)

TABLE 1: Natural vibration characteristics of bridge structure.

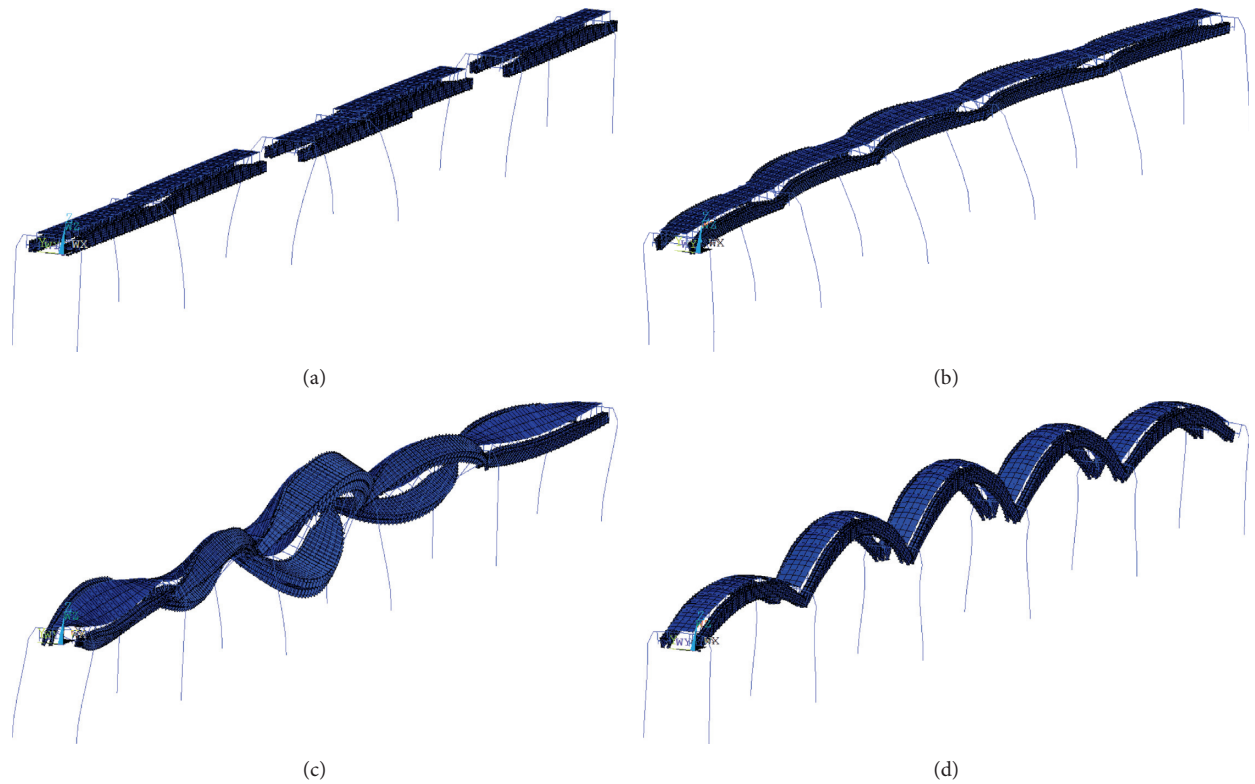| Order	Frequency (Hz)	Mode shape description
1~5	0.854~0.860	Longitudinal drift of pier
6~11	0.935~1.729	Transverse bending of pier
12	3.017	Torsion of track beam
13~16	3.066~3.453	Vertical bending of track beam and footpath
17~18	3.582~3.625	Vertical bending of track beam
19	3.715	Vertical bending of track beam and footpath
20~22	4.155~4.562	Torsion of track beam

(a)

(b)

(c)

(d)

FIGURE 4: Typical mode shapes of the structure. (a) Longitudinal drift of pier. (b) Transverse bending of pier. (c) Torsion of track beam. (d) Vertical bending of track beam and footpath.
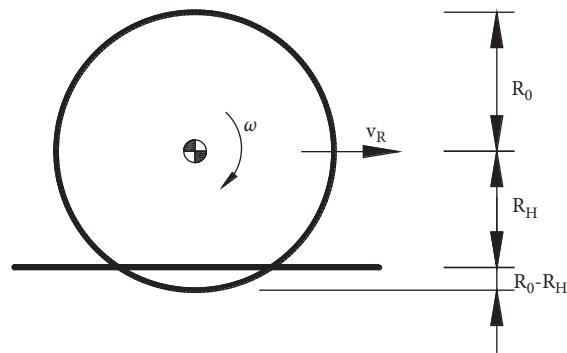

FIGURE 5: Schematic diagram of tyre loading deformation.

where Δr represents the radial compression of the guide wheel; K_y and C_y are the lateral stiffness and damping coefficient of the tyre, respectively; Y_r and Y_0 represent the radial compression of the guide wheel in operation state and preguiding state; F_{Dy0} represents preguiding force of the guide wheel; and $[v_{D_k,D_l}]_y$ represents the lateral component

of the speed of the guide wheel center relative to the guide track.

3. Criteria for Pedestrian Comfort on Landscape Footpath

Several countries and organizations have carried out a series of studies on the comfort of pedestrian bridges and formulated indicators and standards of comfort evaluation, such as BS 5400 [26], ISO 2631 [27] and ISO 10137 [28], CJJ69-95 [29], and EN 03 [30]. All of these standards provide the limit of the fundamental frequency, and some also propose that the structural dynamic response analysis is required if the fundamental frequency limit is not met. The limit of root mean square and peak value of accelerations are given as well. The standards of ISO and EN 03 propose the limits of both vertical and lateral accelerations, while other standards only confine the vertical acceleration.

In general, the pedestrian bridge is relatively flexible compared to other types of bridge. Its natural frequency is relatively low. The march of people may cause excessive amount of vibration on the bridge and discomfort themselves. The landscape footpath studied in the paper is different from ordinary pedestrian bridge, which is integrated with the monorail bridge. In this case, the walking people can be regarded to be scattered on the landscape footpath, as for the long span of the whole bridge system. Hence, the vibration of the landscape footpath caused by people themselves can be considered much smaller than that caused by the vehicle, which means the vehicle load dominates the dynamic responses of the bridge rather than the people load. Therefore, the paper concentrates on the study of pedestrian comfort influenced by the monorail vehicle-induced vibration; and ISO 2631 and ISO 10137 (root mean square of acceleration as the index) and EN 03 (peak value of acceleration as the index) are employed in the evaluation of the pedestrian's comfort.

3.1. Judgement by Root Mean Square of Acceleration. According to ISO 10137 and the reference curve of comfort specified in ISO 2631, for vertical acceleration, the limit of the root mean square is 60 times of the reference curve for walking people and 30 times of the reference curve for stationary people. For the lateral acceleration, the limit of the root mean square is 60 times of the reference curve. Then, the evaluation limit of RMS values of acceleration is shown in Figure 6.

3.2. Judgement by Peak Value of Acceleration. On the basis of EN 03, for the pedestrian bridges with the vertical fundamental frequency from 1.25 Hz to 2.3 Hz or second-order frequency from 2.5 Hz to 4.6 Hz and the lateral fundamental frequency from 0.5 Hz to 1.2 Hz, the peak value of acceleration is required to be examined; and the four-class evaluation standard is proposed, as shown in Table 2.
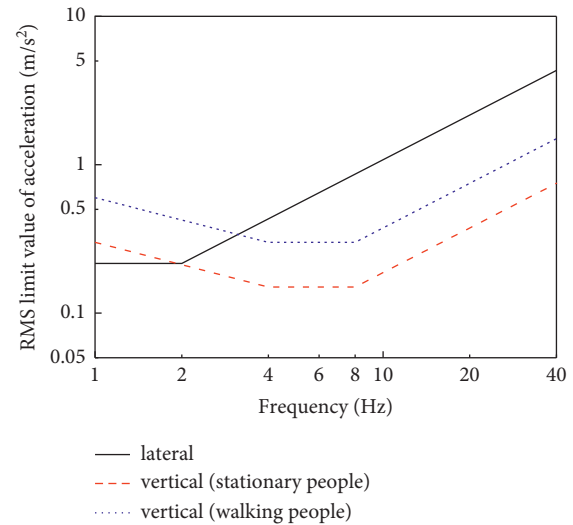

FIGURE 6: Evaluation limit of the root mean square value of acceleration.

TABLE 2: Evaluation standard of pedestrian comfort.

Comfort class	Degree of comfort	Acceleration limit (m/s^2)	
		Vertical	Lateral
CL1	Maximum	<0.5	<0.1
CL2	Medium	0.5~1.0	0.1~0.3
CL3	Minimum	1.0~2.5	0.3~0.8
CL4	Unacceptable discomfort	>2.5	>0.8

4. Vehicle-Induced Dynamic Response and Judgement of Pedestrian Comfort

The dynamic response of the third span bridge in the middle of the five-span simply-supported beam is selected for analysis in the following sections. Since the bridge structure discussed in the paper is a simply supported beam, the response of midspan is larger than those of other positions. Therefore, it is reasonable to evaluate the comfort of the midspan position as a reference of the whole bridge.

4.1. Comparison of the Dynamic Response of Landscape Footpath and Track Beam. In this section, the speed of the vehicle is selected as 60 km/h, and the lateral and vertical displacements in the midspan of the landscape footpath and track beam are shown in Figure 7.

According to Figure 7, it can be seen that the response of the landscape footpath is different from that of the track beam. The displacements of the landscape footpath and track beam basically coincide when the vehicle has not driven into or exited the span. The displacement is mainly delivered by the bridge pier, which is acted by other spans.

It can be seen from Figure 7(a) that the lateral displacement of the track beam is obviously shifted to the
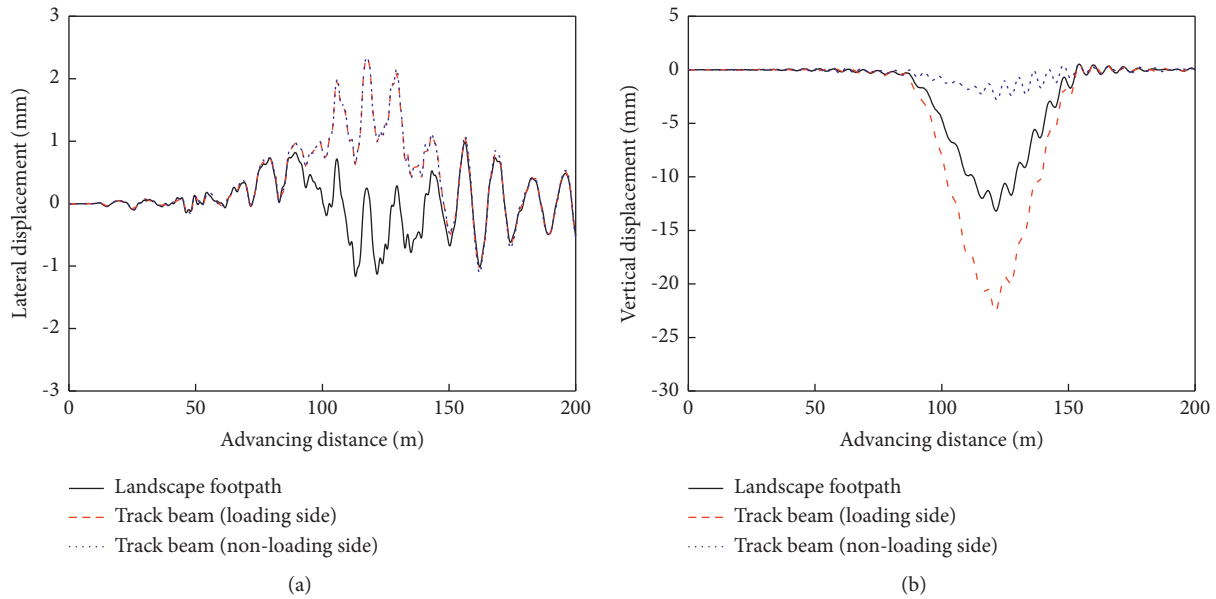
FIGURE 7: Comparison on time history of midspan displacements of landscape footpath and track beam. (a) Lateral. (b) Vertical.

loading side, and the lateral displacements of the two track beams are the same. It is simply due to the fact that the vibration on the load side is transferred to the other side via the pier. On the other hand, the landscape footpath vibrates at its equilibrium position in the lateral direction. The landscape footpath is paved on the track beam through the structure components. The responses of the landscape footpath are weakened to a certain extent when the vibration transmits from the track beam to the footpath. It is supposed that the structure components between the track beam and footpath have a certain amount of displacement and rotation. The maximum lateral displacement of the track beam is 2.34 mm, while the maximum value of the landscape footpath is only 1.16 mm.

As for the vertical displacement in Figure 7(b), when the vehicle enters the objective span section, the eccentric load of the vehicle would affect the dynamic response. The maximum vertical displacement of the track beam is 22.6 mm. The maximum value of the landscape footpath is only 13.2 mm, which is only 58.4% of the value of the track beam.

The comparison between the lateral and vertical accelerations in the midspan of the landscape footpath and track beam is shown in Figure 8.

The lateral and vertical displacements of the track beam applied to the load are greater than those of the landscape footpath, due to the fact that the track beam directly bears the vehicle load. The peak values of the lateral and vertical acceleration of the track beam (loading side) are 0.459 m/s^2 and 0.639 m/s^2, respectively. The peak values of the lateral and vertical acceleration of the landscape footpath are 0.353 m/s^2 and 0.456 m/s^2, respectively, which are 30.0% and 40.1% larger than those of the track beam, respectively.

4.2. Dynamic Response Analysis of Landscape Footpath.
The lateral and vertical displacements in the midspan of the landscape footpath at different vehicle speeds are shown in Figure 9.

It can be seen from the figure that the bridge pier will be induced to vibrate by the load applied to the adjacent beam before the vehicle enters the objective span. It results in a large lateral displacement in the midspan and a negligible vertical displacement. The peak value of the lateral displacement of the landscape footpath appears at a speed of 30 km/h; and there are two moments where relatively large displacements occur during the time in which the vehicle passes the bridge. The vertical displacement enhances with the increase of the vehicle speed. When the speed of the vehicle is 60 km/h, the vertical vibration appears during the monorail vehicle passes through the bridge.

The lateral and vertical accelerations in the midspan of the landscape footpath at different vehicle speeds are shown in Figure 10.

From Figures 10(a) and 10(b), the lateral acceleration reaches peak when the vehicle's speed is 40 km/h, while vertical acceleration reaches peak when the speed is 50 km/h. The lateral and vertical accelerations are comparatively large when the speed is over 40 km/h. The lateral acceleration is large when the vehicle passes on the bridge. The characteristics of vertical vibration are different from those of lateral vibration. When the vehicle's speed is 50 km/h, the vertical vibration of the landscape footpath markedly intensifies when the vehicle exits the span. When the vehicle's speed is 60 km/h, the landscape footpath vibrates obviously during the time in which the monorail vehicle is passing through.
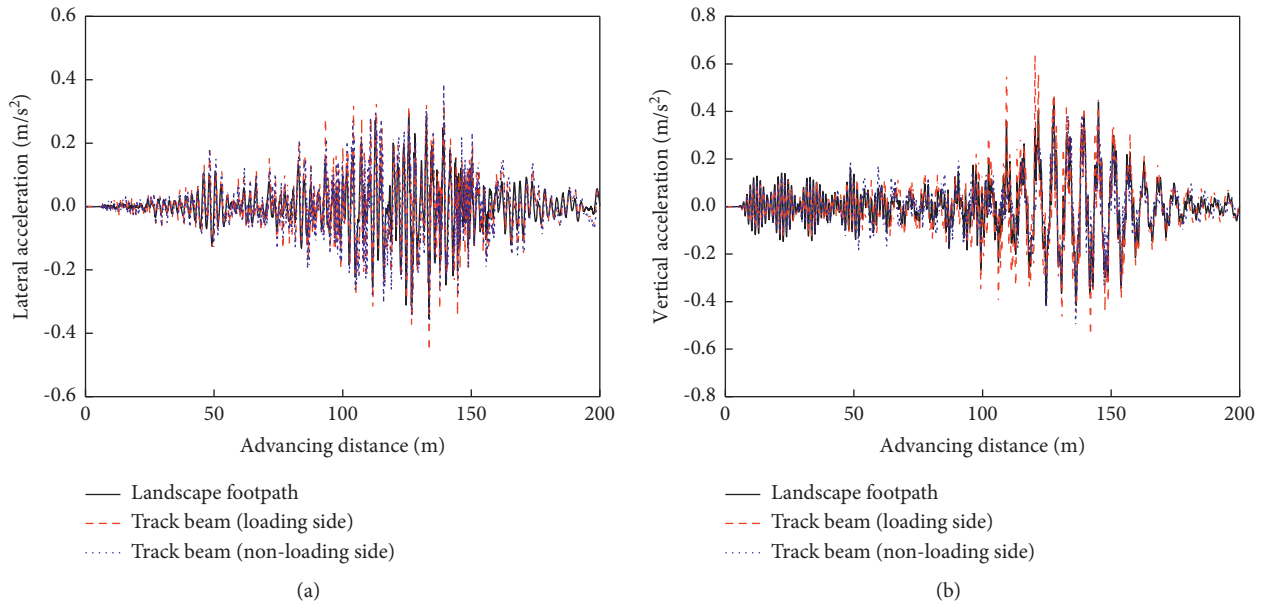
FIGURE 8: Comparison on time history of midspan accelerations of landscape footpath and track beam. (a) Lateral. (b) Vertical.
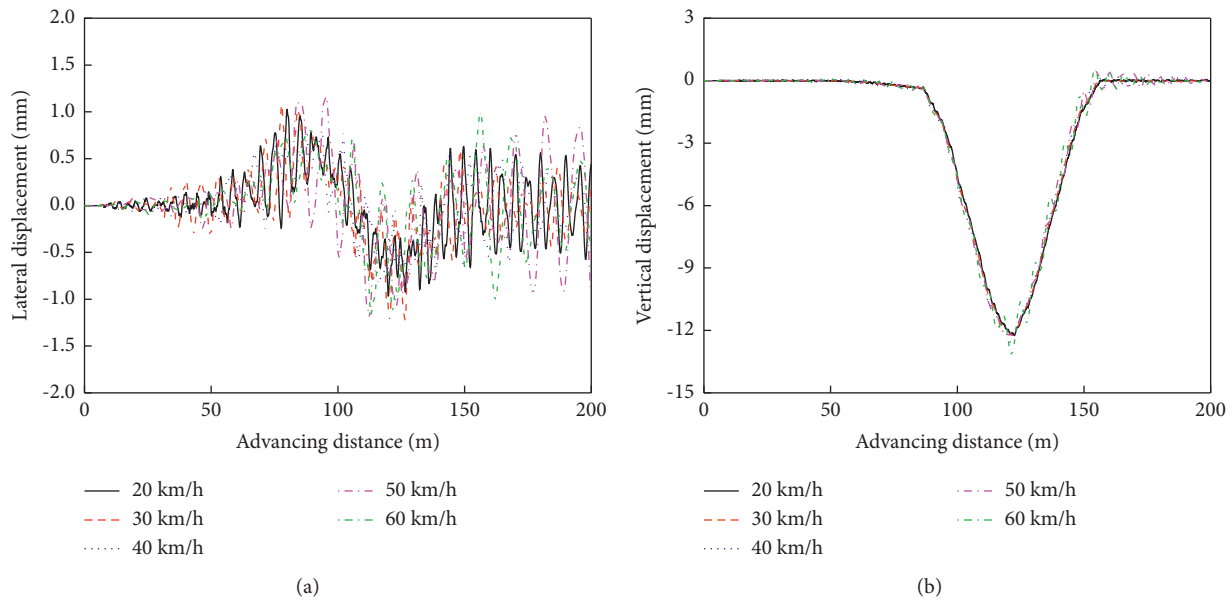

FIGURE 9: Comparison on time history of midspan displacements of landscape footpath at different vehicle speeds. (a) Lateral. (b) Vertical.

4.3. Evaluation of the Pedestrian's Comfort. By analyzing the time history of the acceleration in Figure 9, the RMS and peak values of the acceleration can be obtained; and the time histories of the acceleration during the time in which the vehicle passes the bridge can be extracted in Table 3.

Based on the RMS value evaluation of the standard ISO 10137, the maximum values of the lateral and vertical acceleration are $0.162 \, \text{m/s}^2$ and $0.169 \, \text{m/s}^2$, respectively, which meet the requirement. According to the peak value evaluation of the standard EN 03, the maximum lateral acceleration is $0.546 \, \text{m/s}^2$ which satisfies CL3 standard, while the maximum vertical acceleration is $0.548 \, \text{m/s}^2$ which meets CL2 standard.

On the whole, the pedestrian comfort of the landscape footpath paved on the suspension monorail beam meets the relevant requirements, and the lateral comfort is slightly worse than the vertical comfort.

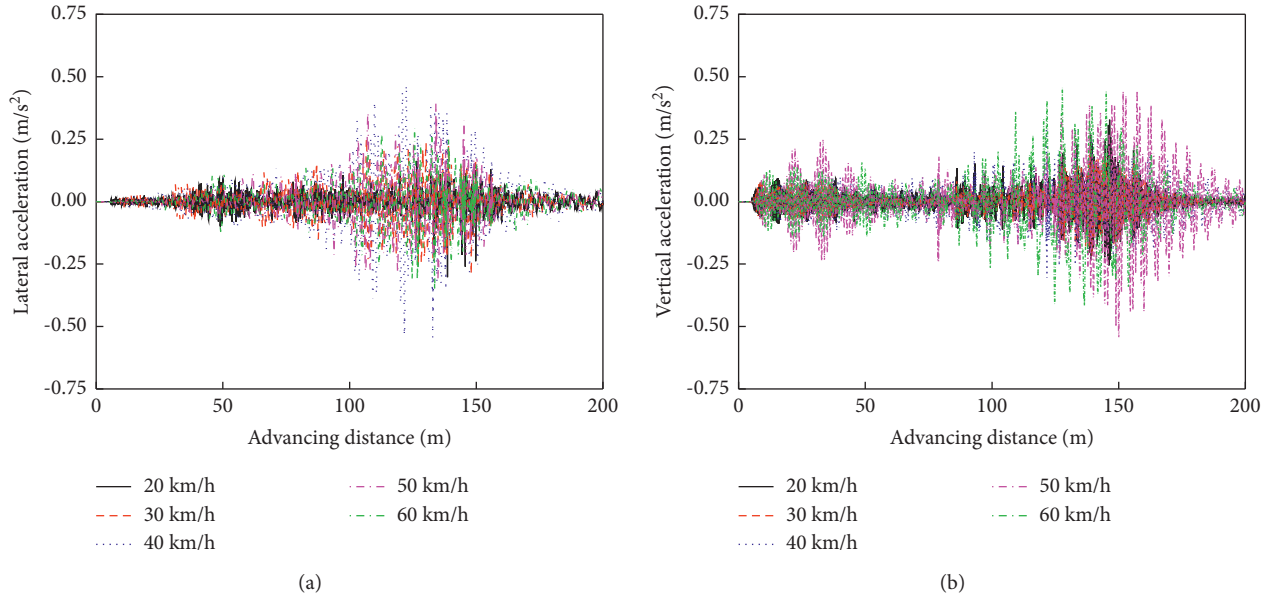(a)   (b)

FIGURE 10: Comparison on time history of midspan accelerations of landscape footpath at different vehicle speeds. (a) Lateral. (b) Vertical.

TABLE 3: Midspan acceleration values of landscape footpath at different vehicle speeds.

Acceleration		Vehicle speed				
		20 km/h	30 km/h	40 km/h	50 km/h	60 km/h
RMS value (m/s^2)	Lateral	0.041	0.093	0.162	0.121	0.105
	Vertical	0.067	0.057	0.084	0.144	0.169
Peak value (m/s^2)	Lateral	0.302	0.297	0.546	0.392	0.353
	Vertical	0.328	0.229	0.306	0.548	0.456

5. Conclusions

Under the background of the first practical application of the landscape footpath paved on the suspension monorail system, the paper analyzes the dynamic responses of track beam and landscape footpath of the suspension monorail at different vehicle speeds by establishing the monorail vehicle-bridge coupled system. The pedestrian comfort level on the landscape footpath during the time in which the vehicle is passing the bridge is evaluated. The main conclusions are as follows:

(1) The dynamic response of the landscape footpath is obviously different from that of the track beam. For the lateral displacement, due to the displacement and rotation of the structure components which support the landscape footpath, the lateral vibration transmitted to the footpath is weakened.

(2) The lateral and vertical displacements of the loaded track beam are greater than that of the landscape footpath; and the maximum acceleration of the track beam is about 1.3 to 1.4 times that of the landscape footpath.

(3) The vertical displacement generally augments with the increase of the vehicle speed. However, when the vehicle's speed is 50 km/h, the vertical acceleration of

the bridge markedly intensifies when the vehicle exits the span.

(4) The root mean square (ISO 10137) and peak value (EN 03) of acceleration are chosen to evaluate the pedestrian comfort.

Data Availability

The data generated or analyzed during this study are included within this article.

Conflicts of Interest

The authors declare that they have no conflicts of interest.

Acknowledgments

References

[1] Mohurd, *Code for Design of Urban Rail Transit Bridge. GB/T 51234-2017*, China Architecture and Building Press, Beijing, 2017.

[2] Housing and Urban-Rural Development Department of Henan Province, *Technical Standard for Suspension Monorail Transit*, Housing and Urban-Rural Development Department of Henan Province, Zhengzhou, 2019.

[3] Y. Bao, Y. Li, and J. Ding, "A case study of dynamic response analysis and safety assessment for a suspended monorail system," *International Journal of Environmental Research and Public Health*, vol. 13, no. 11, p. 1121, 2016.

[4] Y.-l. Bao, H.-y. Xiang, Y.-l. Li, C.-j. Yu, and Y.-c. Wang, "Study of wind-vehicle-bridge system of suspended monorail during the meeting of two trains," *Advances in Structural Engineering*, vol. 22, no. 8, pp. 1988–1997, 2019.

[5] Q. L. He, C. B. Cai, S. Y. Zhu, J. W. Zhang, and W. M. Zhai, "Field measurement of the dynamic responses of a suspended monorail train–bridge system," *Proceedings of the Institution of Mechanical Engineers - Part F: Journal of Rail and Rapid Transit*, vol. 234, no. 10, Article ID 095440971988073, 2019.

[6] Y. Yang, Q. He, C. Cai, S. Zhu, and W. Zhai, "Coupled vibration analysis of suspended monorail train and curved bridge considering nonlinear wheel-track contact relation," *Vehicle System Dynamics*, pp. 1–28, 2021.

[7] Y. Zou, Z. Liu, K. Shi et al., "Experimental study of aerodynamic interference effects for a suspended monorail vehicle-bridge system using a wireless acquisition system," *Sensors*, vol. 21, no. 17, p. 5841, 2021.

[8] P. Feng, Z. Wang, F. Jin, and S. Zhu, "Vibration serviceability assessment of pedestrian bridges based on comfort level," *Journal of Performance of Constructed Facilities*, vol. 33, no. 5, Article ID 04019046, 2019.

[9] D. Y. Chen, S. P. Huang, and Z. Y. Wang, "A theory of pedestrian-induced footbridge vibration comfortability based on sensitivity model," *Advances in Bridge Engineering*, vol. 24, no. 2, 2021.

[10] R. Ma, L. Ke, D. Wang, A. Chen, and Z. Pan, "Experimental study on pedestrians' perception of human-induced vibrations of footbridges," *International Journal of Structural Stability and Dynamics*, vol. 18, no. 10, Article ID 1850116, 2018.

[11] B. Bhowmik, B. Hazra, M. O'Byrne, B. Ghosh, and V. Pakrashi, "Damping estimation of a pedestrian footbridge - an enhanced frequency-domain automated approach," *Journal of Vibroengineering*, vol. 23, no. 5, pp. 14–25, 2021.

[12] B. Chen, D. Wu, X. Xie, and P. Lu, "Comfort assessment for a pedestrian passageway suspended under a girder bridge with random traffic flows," *Advances in Structural Engineering*, vol. 20, no. 2, pp. 225–234, 2017.

[13] C. J. Cui, R. J. Ma, X. H. Hu, and W. C. He, "Vibration analysis for pendent pedestrian path of a long-span extradosed bridge," *Sustainability*, vol. 11, no. 17, p. 4664, 2020.

[14] W. M. Zhai, S. L. Wang, N. Zhang, M. M. Gao, and C. F. Zhao, "High-speed train-track-bridge dynamic interactions - part II: experimental validation and engineering application," *International Journal of Reality Therapy*, vol. 1, no. 1-2, pp. 25–41, 2013.

[15] T. Arvidsson and R. Karoumi, "Train-bridge interaction - a review and discussion of key model parameters," *International Journal of Reality Therapy*, vol. 2, no. 3, pp. 147–186, 2014.

[16] Y. Li, X. Xu, Y. Zhou, C. Cai, and J. Qin, "An interactive method for the analysis of the simulation of vehicle-bridge coupling vibration using ANSYS and SIMPACK," *Proceedings of the Institution of Mechanical Engineers - Part F: Journal of Rail and Rapid Transit*, vol. 232, no. 3, pp. 663–679, 2018.

[17] H. Xiang, P. Tang, Y. Zhang, and Y. Li, "Random dynamic analysis of vertical train-bridge systems under small probability by surrogate model and subset simulation with splitting," *Railway Engineering Science*, vol. 28, no. 3, pp. 305–315, 2020.

[18] Y. Bao, W. Zhai, C. Cai, X. Yuan, and Y. Li, "Impact coefficient analysis of track beams due to moving suspended monorail vehicles," *Vehicle System Dynamics*, pp. 1–17, 2020.

[19] Q. He, C. Cai, S. Zhu, K. Wang, and W. Zhai, "An improved dynamic model of suspended monorail train-bridge system considering a tyre model with patch contact," *Mechanical Systems and Signal Processing*, vol. 144, Article ID 106865, 2020.

[20] Y. Bao, W. Zhai, C. Cai, S. Zhu, and Y. Li, "Dynamic interaction analysis of suspended monorail vehicle and bridge subject to crosswinds," *Mechanical Systems and Signal Processing*, vol. 156, no. 2, Article ID 107707, 2021.

[21] S. Dietz, G. Hippmann, and G. Schupp, "Interaction of vehicles and flexible tracks by co-simulation of multibody vehicle systems and finite element track models," *Vehicle System Dynamics*, vol. 37, no. S1, pp. 372–384, 2002.

[22] M. Rose, R. Keimer, and E. J. Breitbach, "Parallel robots with adaptronic components," *Journal of Intelligent Material Systems and Structures*, vol. 15, no. 9-10, pp. 763–769, 2004.

[23] E. Fiala, "Seitenkrafte am rollenden luftreifen," *VDI-Zeitschrift*, vol. 96, p. 973, 1954.

[24] G. Gim, Y. Choi, and S. Kim, "A semiphysical tyre model for vehicle dynamics analysis of handling and braking," *Vehicle System Dynamics*, vol. 43, no. S1, pp. 267–280, 2005.

[25] H. B. Pacejka, *Tire and Vehicle Dynamics*, Butterworth-Heinemann, UK, Third Edition, 2012.

[26] Bsi, *Steel concrete and Composite Bridges Part 2: Specification for Loads*, British Standard Institute, London, 2006.

[27] Iso, *Mechanical Vibration and Shock - Evaluation of Human Exposure to Whole-Body Vibration Part 4: Guidelines for the Evaluation of the Effects*, International Organization for Standardization, Switzerland, 2010.

[28] Iso, *Bases for Design of Structures - Serviceability of Buildings and Walkways against Vibrations*, International Organization for Standardization, Switzerland, 2007.

[29] Institute of Standard and Quota of Ministry of Construction, *Technical Specifications for Urban Pedestrian Overcrossing and Underpass*, Institute of standard and quota of Ministry of construction, Beijing, 1996.

[30] Directorate-General for Research and Innovation, *Human-induced Vibrations of Steel Structures - Design of Footbridges Guidelines. Footbridge Guidelines EN 03*, Publications Office of the European Union, Luxembourg, 2010.